The solid-state chemistry of rhodium pincer complexes

By Alexandra Longcake

A thesis submitted in partial fulfilment of the requirements for the degree of Doctor of Philosophy in Chemistry

University of Warwick, Department of Chemistry

December 2022

Contents

List of Figures

List of Tables

List of Schemes

Acknowledgements

Firstly, thanks must go to my supervisors Dr. Chaplin and Dr. Senn for providing the resources and opportunity to undertake this PhD and for feedback on this dissertation. Thank you also to Dr. Mike Probert for your support and guidance during the final months of my PhD, your help was truly invaluable.

To the wonderful experimental officers at Warwick: Dr. Ivan Prokes, thank you for running all of my low temperature NMRs and for dealing with my more troublesome complexes. Dr. Lijiang Song and Dr. Lynette Walsh, thank you for collecting high resolution mass spec data for me. Dr. Dave Walker, thank you for your guidance and patience on all things XRD.

To the past members of the Senn group: Tobie, Gabriel and Anna. I wish we could have gotten more time together, but alas, COVID prevented it. It was a pleasure to meet you all. To the current members: Jere Tidey, thank you for your support professionally and personally, especially in the last few months. By the time I've written this, you might have finally mastered 'Sweet Child O' Mine' on the ukulele. Dash, I wish you all the best in your final year. Struan, Ben & Evie, hopefully we catch-up at the BCA, but until then, may the crystal gods be ever in your favour.

To the past members of the Chaplin group, thank you making me feel so welcome when I started. To Matt Gyton, thank you for teaching me how to use a Schlenk line. Baptiste, Tom, Gemma and Matt Sinclair: thank you for the great nights out and good advice. I'm glad you all enjoyed my baking when I went through that crazy cake-lady phase!

To the amazing women who endured the highest and lowest points of my final year with me, you were the bestest-est people I could have hoped to spend my time with at Warwick, we definitely made HERstory! Jennifer, Sophie and Itxaso, thank you for the pancake evenings, the afternoon teas and all things food and musical-related over which we bonded deeply. I miss our daily coffee mornings and I hope I will remember all the useful Spanish phrases, though I doubt I will ever learn to roll my r's properly. I am amazed you managed to avoid watching the cinematic masterpiece that is 'The Mummy' with me (except Jennifer) – perhaps that can be our reunion idea over a bowl of plain rice…

Thank you, Dr. Paul Waddell, for providing extremely useful crystallographic insight into π-π interactions and thank you, Dr. Natalie Johnson, for your excellent advice, support and TV show recommendations in my final year.

I could not have finished this PhD without the support and love of my family. To my godmothers Linda and Marlene, thank you for being excellent role models and for lending an ear when I needed it. Mum, Dad and Robert, I know I was a pain throughout this whole degree, thank you for not giving up on my behalf. I continually aspire to be a person you can all be proud of. I know I don't say it enough, but I love you.

Declaration of Collaborative and Published Work

This thesis is submitted to the University of Warwick in support of my application for the degree of Doctor of Philosophy. The work presented herein has not been submitted in whole or in part for any other degree and is the original work of the author, except in the cases described below:

- Cyclic voltammetry measurements on Rh(PONOP)Cl and XRD collections of complexes **A**, **1**, **4** and **5** (chapter 2) were conducted by Dr. Adrian B. Chaplin, Reader, University of Warwick.
- SQUID measurements on complex **8** (chapter 2) were conducted by Professor Martin Lees, Professor of physics, University of Warwick.
- Assistance analysing VT-PXRD data of **A** (chapter 2) was provided by Dr. Jeremiah Tidey, PDRA, University of Warwick.
- Remote access HP-XRD studies on beamline I19 at Diamond Light Source for complexes **A** and **13** (chapters 2 & 3) were conducted with the assistance of Dr. Mark Warren, DLS beamline scientist, and Dr. Jeremiah Tidey, PDRA, University of Warwick.
- The preliminary synthesis of **12** (chapter 3) was developed by Dr. Matthew Sinclair, PhD graduate, University of Warwick.
- VT-NMR data (chapters 3 & 4) were collected by Dr. Ivan Prokes, Experimental Officer for NMR spectroscopy, University of Warwick.

Parts of this thesis have been published by the author:

- A. Longcake, M. R. Lees, M. S. Senn and A. B. Chaplin, *Organometallics*, 2022, **41**, 3557–3567.

Abbreviations

3c-2e	Three-centre two-electron
AIM	Atoms in molecules
Ar	Aryl
Ar^F	3,5-bis(trifluoromethyl)phenyl
Ar^{F20}	Pentafluorophenyl
atm	Atmosphere
ATR	Attenuated total reflectance
br	Broad
calcd	Calculated
CCDC	Cambridge Crystallographic Data Centre
CSD	Cambridge Structural Database
ClCy	Chlorocyclohexane
Cl^{i}Pr	2-chloropropane
ClPh	Chlorobenzene
COD	1,5-cyclooctadiene
COE	Cyclooctene
Cy	Cyclohexyl
d	Doublet
DAC	Diamond anvil cell
DCE	1,2-dichloroethane
DCM	Dichloromethane
DFT	Density functional theory
eq.	Equivalents
ESI	Electrospray ionisation
Et	Ethyl
fac	Facial
fwhm	Full width at half maximum
GC	Gas chromatography
gem	Geminal
h	Hours
HBcat	Catecholborane
HBpin	Pinacolborane
HOMO	Highest occupied molecular orbital
HP-XRD	High pressure X-ray diffraction

HR	High resolution
Hz	Hertz
^{i}Pr	*Iso*-propyl
IR	Infrared
LUMO	Lowest unoccupied molecular orbital
m	Multiplet
m/z	Mass-to-charge ratio
MB-DAC	Merrill-Bassett diamond anvil cell
Me	Methyl
Mes	Mesityl
mer	Meridional
mins	Minutes
MO	Molecular orbital
MS	Mass spectrometry
NBA	Norbornane
NBD	Norbornadiene
NBE	Norbornene
NBO	Natural bond orbital
^{n}Bu	*n*-butyl
NMR	Nuclear magnetic resonance
Np	Neopentyl
PASCal	Principal strain axis calculator
Ph	Phenyl
ppm	Parts per million
PTM	Pressure transmitting medium
py	Pyridine / pyridyl
r.t.	Room temperature
s	Singlet
t	Triplet
^{t}Bu	*Tert*-butyl
^{t}BuCl	2-chloro-2-methylpropane
VT	Variable temperature
XRD	X-ray diffraction

Abstract

Oxidative addition (OA) is a fundamental organometallic process which is of interest both academically and industrially, but it can be difficult to study in solution due to the highly reactive intermediates implicit in the reaction. The solid-state represents an attractive medium in which to control reactivity via external stimuli. This thesis focuses on the application of crystallographic methods to the study of OA in the solid-state. The proposed approach involved the synthesis of rhodium pincer complexes featuring Rh···X–E interactions (X–E = Cl–C, H–B) which were studied by X-ray diffraction, initially under conventional conditions, but ultimately with more elaborate variable pressure techniques, in an effort to promote pressure-induced oxidative addition. Where possible, solid-state reactivity was compared with solution phase behaviour.

The solution phase chemistry of $\{Rh(PONOP)(\kappa_{Cl}\text{-}ClR)\}^+$ (R = alkyl, aryl; PONOP = 2,6-($^tBu_2PO)_2C_5H_3N$) adducts were explored, leading to the discovery of concerted (C(sp^2)–Cl) and radical (C(sp^3)–Cl) OA mechanisms. Thermally induced oxidative addition was also achieved in solid-state samples of $[Rh(PONOP)(\kappa^1\text{-}ClCH_2Cl)][BAr^F{}_4]$. Efforts to increase the likelihood of pressure-induced reactivity in complexes of $\{Rh(pincer)\}^+$ prompted the exploration of alternative pre-activated substrates (σ-borane complexes). An isomorphous phase transition in $[Rh(PONOP)(\eta^2\text{-}HBcat)][BAr^F{}_4]$ (HBcat = $HBO_2C_6H_4$; Ar^F = 3,5-$(CF_3)_2C_6H_3$) promoted further activation of the complex from a ‘classical’ to an ‘elongated’ σ-borane complex. Furthermore, OA adducts for the structurally related complexes $[Rh(PNP)(\eta^2\text{-}HBcat)][X]$ (PNP = 2,6-($^tBu_2PCH_2)_2C_5H_3N$; X = SbF_6, $BAr^{F20}{}_4$; Ar^{F20} = C_6F_5) were obtained under ambient conditions upon crystallisation as a result of crystal packing effects. A single crystal to single crystal transformation was discovered upon exposure of $[Rh(PNP)(H)(Bcat)][BAr^{F20}{}_4]$ to carbon monoxide, which afforded $[Rh(PNP)(CO)][BAr^{F20}{}_4]$ and free HBcat. Although pressure-induced OA ultimately proved elusive, several novel SC-SC transformations induced by various control parameters such as temperature, pressure and gas were observed for a range of rhodium pincer complexes.

Chapter 1 – Introduction

Oxidative addition (OA) is a fundamental organometallic process that underpins many industrially important reactions.[1-5] OA is one of three mechanistic steps (OA, transmetalation, reductive elimination) that describe cross-coupling reactions, which are the most widely implemented synthetic methods used to generate C–C bonds.[6-8] OA is typically[i] characterised by increases in the oxidation state and coordination number of the metal complex by +2 as a result of the cleavage of the A–B bond and the formation of two new M–A and M–B bonds (Fig 1.1). Concerted mechanisms typically occur with non-polar reagents, whereas the S_N2-type mechanism is favoured by polarised substrates. These pathways are usually characterised by their second-order reaction kinetics and the respective retention (concerted) or inversion (S_N2) of substrate stereochemistry.[9]

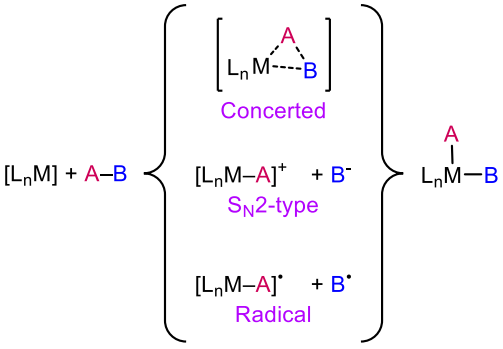

Figure 1.1 – An overview of different OA mechanistic intermediates.

Radical OA pathways, on the other hand, are characterised by their single electron transfer (SET) steps. SET from M to the A–B σ* orbital to afford M^+ and $(A–B)^{\bullet-}$ is rapidly followed by A^- transfer to M^+, liberating a $B^\bullet$ radical (Fig. 1.1). Chain radical reactions enable the transformation to proceed many times over, whilst in non-chain radical mechanisms, each radical formed causes the transformation to proceed only once. Like the S_N2 process, radical mechanisms are faster when the metal centre is more basic because electron transfer takes place more readily. Radical pathways can be challenging to definitively identify - irreproducible reaction kinetics that arise from trace impurities in the reaction mixtures can significantly influence reaction rates and,

[i] Except for cases of binuclear OA and certain radical mechanisms, which can result in increases in the oxidation state and coordination number of complexes of +1.

in extreme cases, alter the predominant mechanism by which the reaction proceeds.[9,10] Furthermore, proof of mechanism through the use of radical trapping agents has been criticised on the grounds that the radical traps might initiate a radical mechanism for reactions that would have otherwise proceeded via a non-radical pathway.[11] Even subtle changes to reagents or conditions can alter the mechanism by which OA proceeds,[9,12] therefore, it is important to fully understand mechanistic implications so that reactivity can be explained and predicted with more certainty.

1.1 – Pincer complexes

Pincer ligands are typically defined as tridentate chelating ligands that coordinate with a meridional geometry. Their nomenclature is usually derived from the principal atoms that constitute the ligand backbone. Such ligands allow complexes to maintain a well-defined coordination geometry whilst conferring thermal stability. Their reactivity can also be tuned by altering certain aspects of the ligand (Fig. 1.2).[13] Pincer ligands can be divided into several classes, depending on whether the donor atoms are neutral or anionic, and whether the pincer 'arms' are symmetrical (palindromic) or not (non-palindromic).[13] These classes can be further sub-divided, but the following literature survey is primarily focused on complexes incorporating palindromic phosphine-based pincers.

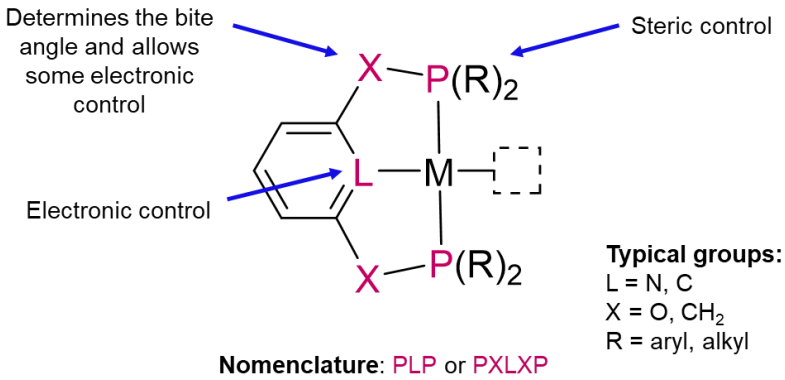

Figure 1.2 – Structure of a phosphine-based pincer ligand coordinated to a metal (M) illustrating the electronic and steric control pincer ligands facilitate.

1.1.1 – General reactivity and functionality

Late transition metal pincer complexes are a versatile class of compounds capable of activating chemically robust bonds such as C–H, C–N and C–Cl.[14-16] As a result of their propensity to facilitate OA, pincer complexes have found applications in the fields of catalysis and small molecule activation.[2,15,17-19] The seminal PCP-type scaffold alone demonstrates the versatile chemistry pincer complexes are capable of instigating, with only minor alterations made to the pincer ligand itself (Fig. 1.3).[20-24] Improved rates of alkene dehydrogenation were reported for an ^{i}Pr substituted iridium PCP complex compared to its ^{t}Bu analogue due to diminished steric congestion around the metal centre.[25] Net activation of C(sp^3)–F bonds have even been achieved via the cleavage of C–H bonds by a PCP complex.[26]

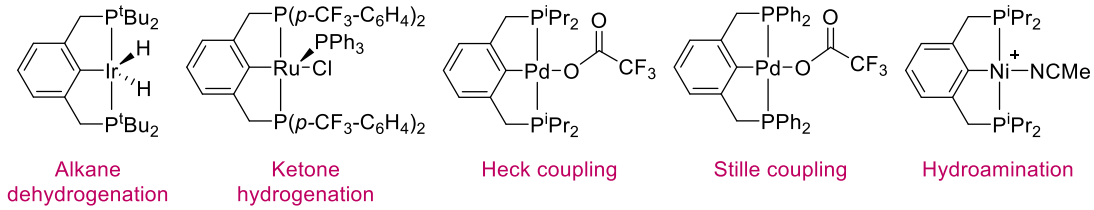

Figure 1.3 – Examples of PCP-based complexes that catalyse a range of reactions. Anions omitted for clarity.[20-24]

Modification of the pincer backbone can also promote or disfavour specific reaction pathways (Fig. 1.4).[27-36] The terminal alkyne coupling catalyst **A1** (Fig. 1.4) reported by Ozerov and co-workers resulted in higher activity and regiospecific production of *E*-enynes for the rhodium complex containing the 'tied' ligand backbones in comparison to the 'untied' analogues which lacked the connecting $(CH_2)_2$ linker. This skeletal adjustment promoted alkyne coupling more efficiently in **A1** due to the improved rigidity of the coordination environment.[33]

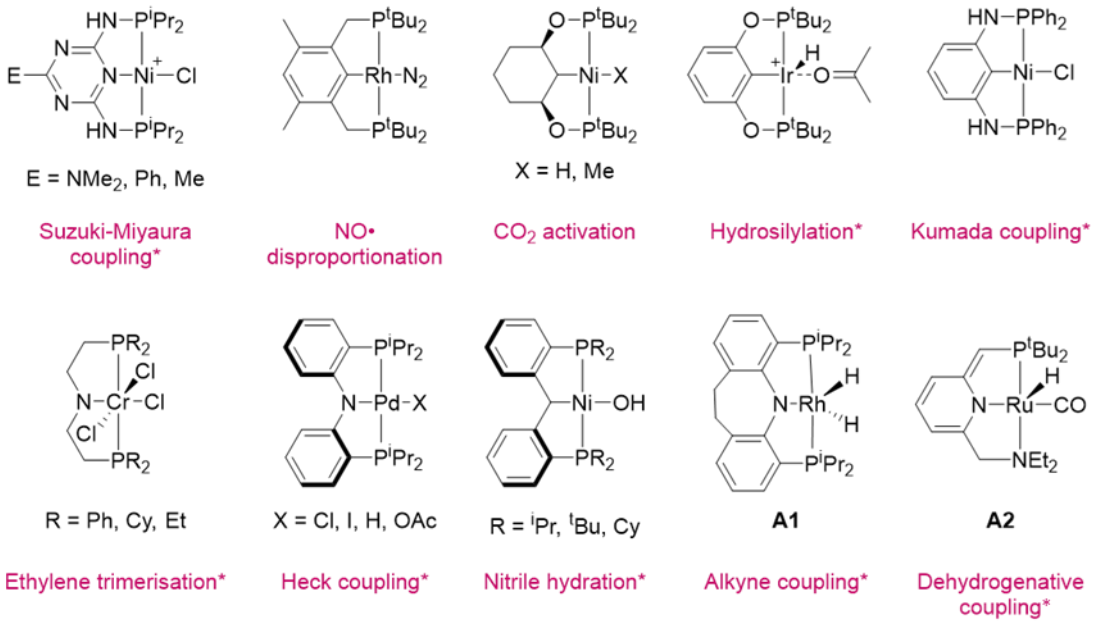

Figure 1.4 – Examples of pincer complexes featuring different pincer backbones. Anions are omitted for clarity.[27-37] * = only catalytic amounts are required.

Pincer complexes are also capable of bifunctional reactivity; for instance, (PNN)Ru(H)CO, **A2** (PNN = 6-(di-*tert*-butylphosphinomethylene)-2-(N,N-diethylaminomethyl)-1,6-dihydropyridine), is an efficient catalyst for the dehydrogenative coupling of alcohols and amines to form amides because of the unsaturated linker's ability to abstract a proton from the alcohol whilst the amine arm dissociates (Fig. 1.4). The hemilability of the pincer allowed for turnover numbers of up to 20 to be achieved in base-free conditions.[37] Complex **A2** also catalysed ester hydrogenation efficiently compared to ($^{iPr}P^{H}NP$)Ru(H)CO, **A3** ($^{iPr}P^{H}NP$ = 2-bis(di-*iso*-propylphosphinomethyl)-6-(di-*iso*-propylphosphinomethylene)pyridine), as a result of this hemilability.[38]

1.1.2 – PNP and PONOP complexes

Pincer complexes of PNP (2,6-bis(di-*tert*-butylphosphinomehyl)pyridine) and PONOP (2,6-bis(di-*tert*-butylphosphinito)pyridine) are of interest to organometallic chemists due to their propensity to facilitate bond activation as well as their aptitude to act as synthons for the generation of novel adducts.[18,19,39,40] Although complexes of PNP and PONOP are less well-known for catalytic applications in comparison to their

PCP (2,6-bis(di-*tert*-butylphosphinomehyl)benzene) and POCOP (2,6-bis(di-*tert*-butylphosphinito)benzene) counterparts, archetypes include dehydrogenations, hydrosilylations and dehydrogenative couplings.[26,41-47] Although structurally similar, complexes of PNP and PONOP have demonstrated distinct reactivity differences.[39,48] The more obtuse bite angle (∠ P-Rh-P) found in PNP complexes (relative to complexes of PONOP) results in more steric buttressing to coordinated substrates *trans* to the pincer backbone.[19,48] The PNP ligand also has more conformational flexibility as a consequence of the sp^3-hybridised CH_2 linkers. Whilst PONOP typically maintains a planar C_{2v} symmetry upon coordination to a metal, PNP can adopt either a helical C_2 or 'gullwing' C_s conformation, which can present as time averaged C_{2v} symmetry when probed by NMR spectroscopy (Fig. 1.5).[49]

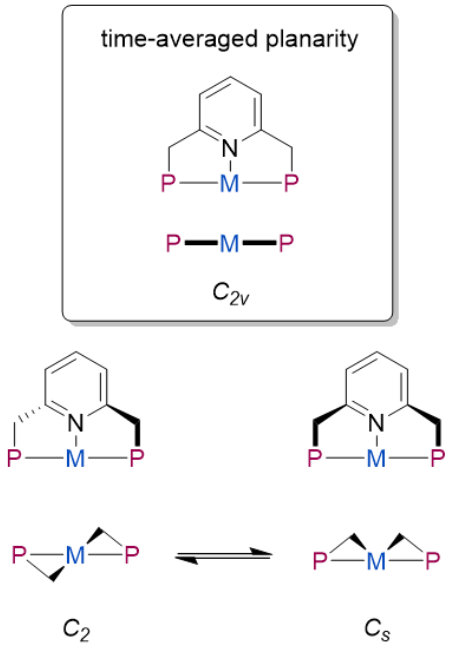

Figure 1.5 – The different conformations observed in PNP pincer ligands.

The more electron rich rhodium centre in PNP complexes has been demonstrated through observation of the decreased carbonyl infra-red (IR) frequencies of $[Rh(PNP)(CO)]^+$ *vs*. $[Rh(PONOP)(CO)]^+$ complexes as a consequence of increased π-backbonding.[39,48,50] Ligand non-innocence, where the pincer converts between monoanionic L_2X and neutral L_3 donors, is also commonly observed in PNP ligands because of the presence of acidic protons in the CH_2 linkers, which ultimately facilitate this reactivity.[38,41,44,51-53]

A more involved examination of the dissimilarities between PNP and PONOP was conducted by Daly and co-workers using solid-state X-ray absorption spectroscopy (XAS) for complexes of Rh(pincer)Cl (pincer = PONOP, **A4**; PNP, **A5**;).[48] Notable differences in the phosphorus K-edge XAS data were the more intense pre-edge feature for **A4** relative to **A5**, indicting more covalent Rh–P σ-bonding between the Rh $4d_{x2-y2}$ and P 3*p* orbitals and a higher energy P 1s → $2a_1$ transition (where the 2_{a1} transition has a lot of Rh–Cl σ* character) due to the increased stabilisation of the P 1*s* orbitals by the electronegative O linker.[48] Density functional theory (DFT) calculations confirmed that the greater electron-electron repulsions in the P–C bonds of PNP drive the calculated $4d_{yz}$ and $4d_{xy}$ orbitals of **A5** to higher energies. The higher energy Rh $4d_{yz}$ and $4d_{xy}$ orbitals in **A5** compared to **A4** provide better energy matching with ligands that contain π-acceptor orbitals, hence a greater propensity for π-backbonding was predicted for **A5** (Fig. 1.6).[48] This is reflected experimentally in rhodium(I) PNP and PONOP carbonyl complexes (ν_{CO} = 1982 cm^{-1} *vs.* 2020 cm^{-1}, respectively).[39,48]

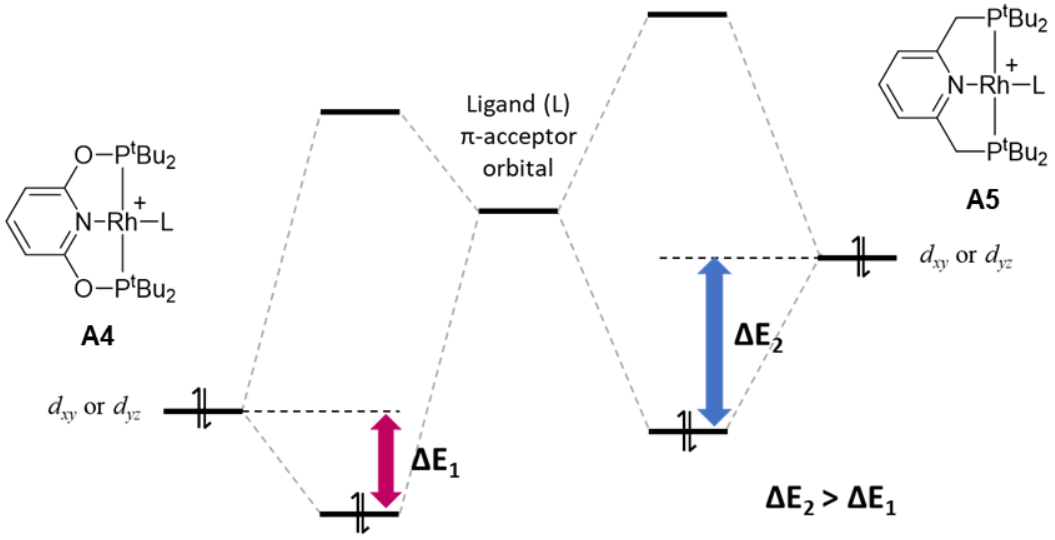

Figure 1.6 – Qualitative MO energy level diagram of **A4** vs. **A5**. ΔE = orbital interaction energy.[48]

PNP was first prepared by Milstein and co-workers and was subsequently reacted with $[M(COE)_2Cl]_2$ (M = Ir, Rh; COE = cyclooctene).[54] Under analogous conditions, the rhodium analogue generated the complex Rh(PNP)Cl, **A5**, whilst the iridium congener formed the COE-activated iridium(III) species Ir(PNP)(H)(C_8H_{13}), **A6**. This divergent

reactivity can be attributed to iridium's preference for the +3 oxidation state. Since then, Milstein and co-workers have also reported the *ortho*-selective C–H bond activation of haloarenes using [Ir(PNP)(COE)][PF_6], **A7**. [15] Whilst no C–H selectivity was observed for the activation of fluorobenzene (**A8a-c**; Scheme 1.1), prolonged heating of **A7** at 60 °C in either chlorobenzene or bromobenzene eventually resulted in the exclusive formation of the respective *ortho*-activated products (Scheme 1.1).[14,15] X-ray diffraction studies confirmed the intramolecular coordination of the halogen atoms in **A9a** and **A10a** *trans* to the hydride, accounting for the superior thermodynamic stability of the *ortho*-activated products.[15] Similar directing C–H bond activations were observed for the Np-substituted iridium analogue [Ir(^{Np}PNP)][BF_4], **A11** (^{Np}PNP = 2,6-bis(di-neopentylphosphinomethyl)-pyridine) for the *ortho*-activation of nitrobenzene and acetophenone.[55]

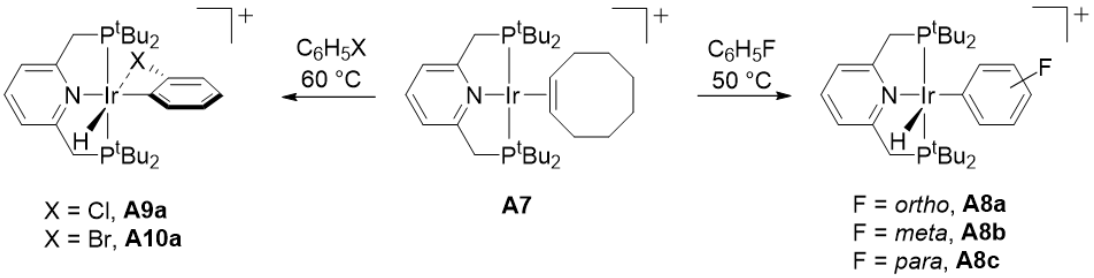

Scheme 1.1 – The reactivity of **A7** with haloarenes. Anions omitted for clarity.[14,15]

Iridium PNP complexes can also initiate intramolecular activation of the pincer ligand itself. Periana and co-workers reported the cyclometallated PNP complex **A12** which formed upon reflux of PNP with $Ir(I)_3(H_2O)_3$. Contrastingly, the analogous trichloride precursor under similar conditions did not undergo cyclometallation (Fig. 1.7).[56] A rare example of direct intramolecular C–H bond OA within a phosphine-based complex is the internal C-H activation of **A11** to form **A13** (Fig. 1.7). The original unactivated complex **A11** can be regenerated by reaction of **A13** with dihydrogen.[55]

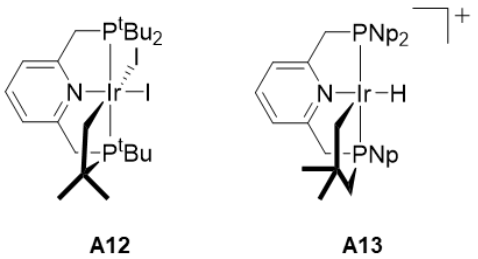

Figure 1.7 – C–H bond cyclometallation of iridium PNP complexes.[55,56]

Contrastingly, PONOP-containing complexes have demonstrated more tempered reactivity – whilst OA of C–H and H–H bonds have been facilitated by complexes of {Ir(^{R}PONOP)}$^{+}$ (R = ^{t}Bu, ^{i}Pr),[57-60] {Rh(PONOP)}$^{+}$ is better known for its ability to stabilise substrates that the analogous PNP or iridium fragments would otherwise activate. One such pivotal example was the solution phase characterisation of the first σ-methane complex [Rh(PONOP)($\eta^{2}_{C,H}$-CH_4)][BAr^{F}_4], **A14**, which was synthesised by reacting Rh(PONOP)(CH_3) with [H(Et_2O)$_2$][BAr^{F}_4] in $CDCl_2F$ at -110 °C (Scheme 1.2).[61] The poor coordination strength of the σ-methane ligand meant that **A14** was only stable at very low temperatures. The half-life for the dissociation of methane with solvent molecules was calculated to be 83 minutes at -87 °C.[61] Analogous treatment of the iridium congener with [H(Et_2O)$_2$][BAr^{F}_4] in CH_2Cl_2 resulted in protonation of the metal centre, generating [Ir(PNP)(H)(CH_3)][BAr^{F}_4], **A15** (Scheme 1.2).[57] Rapid exchange between the Ir–H and the Ir–CH_3 protons was observed by ^{1}H NMR spectroscopy, which is consistent with the formation of a transient σ-alkane complex.

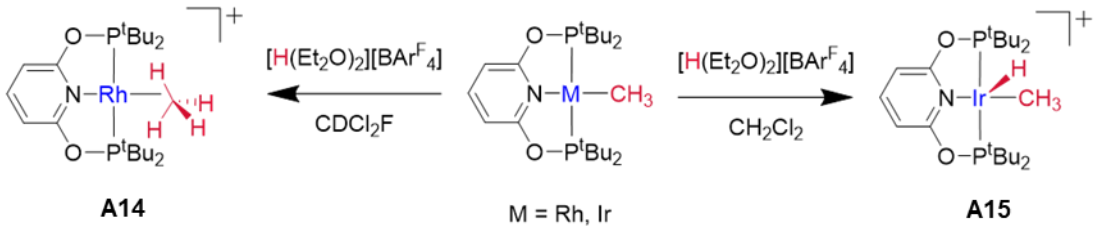

Scheme 1.2 – The synthesis of **A14** and **A15**. Counterions omitted for clarity.[57,61]

The thermodynamic preferences for the formation of **A14** and **A15** were determined to be remarkably small. The iridium(III) species was calculated to be only 5 kcal/mol more favourable than the corresponding iridium σ-methane complex. Similarly, the stability of the rhodium(I) σ-methane complex **A14** was only 8 kcal/mol more favourable than the unobserved Rh(III) activated methane complex.[57,61] Similar reactivity was reported for the equivalent ethane complexes, but the rhodium σ-ethane complex was notably less stable due to the greater steric demands of the substituent. Additionally, DFT calculations suggested that hydrogen exchange did not occur via an analogous σ-ethane intermediate for the iridium ethyl complex, but rather via a dihydride ethene species.[62]

The characterisation of **A14** in solution triggered an insurgence of interest into the use of $\{Rh(PONOP)\}^+$ and $\{Rh(PNP)\}^+$ for the stabilisation of weakly coordinating species. Weller and co-workers reported the formation of the solvent coordinated species $[Rh(PONOP)(\kappa^1\text{-}ClCH_2Cl)][BAr^F{}_4]$, **A16** (Scheme 1.3).[39] Complex **A16** was synthesised via halide abstraction from Rh(PONOP)Cl and is a convenient precursor for the generation of novel N_2, H_2 and CO derivatives via displacement of the weakly coordinated CH_2Cl_2 molecule (Scheme 1.3).[39] The PNP analogue demonstrated notably different reactivity – upon addition of $Na[BAr^F{}_4]$ to a solution of Rh(PNP)Cl in CH_2Cl_2, an approximate 1:1 mixture of $[Rh(PNP)(CH_2Cl)Cl][BAr^F{}_4]$ and $[Rh(PNP)(H)Cl][BAr^F{}_4]$ formed, alongside a number of other unidentified products. The authors did not propose a mechanism by which these species were generated due to the number of possible decomposition pathways.[39]

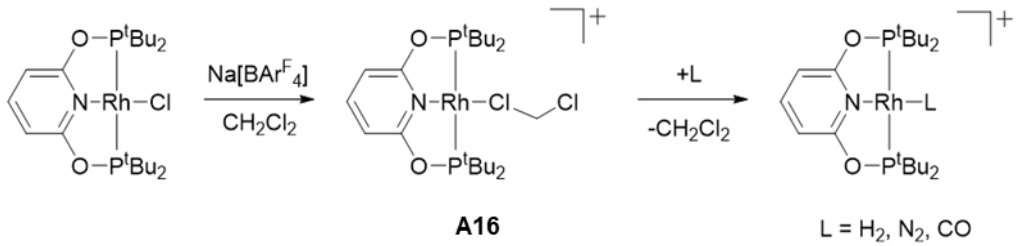

Scheme 1.3 – The preparation of **A16** and its subsequent reactivity. $[BAr^F{}_4]^-$ counterions are omitted for clarity.[39]

In a similar vein, Chaplin and co-workers reported the convenient generation of latent sources of $\{Rh(pincer)\}^+$. The reaction of $[Rh(COD)_2][BAr^F{}_4]$ (COD = 1,5-cyclooctadiene) with PONOP in 1,2-difluorobenzene formed a dynamic equilibrium mixture of the monomeric $[Rh(PONOP)(\eta^2\text{-}COD)][BAr^F{}_4]$, **A17a**, and dimeric $[\{Rh(PONOP)\}_2(\mu\text{-}\eta^2\text{:}\eta^2\text{-}COD)][BAr^F{}_4]_2$, **A17b** (Scheme 1.8).[18] Due to the steric bulk of the ^{t}Bu groups and the cationic charge of the complex, the COD ligand is weakly bound and easily displaced by solvent molecules or other weakly coordinating species. Further reactivity with CO, H_2, N_2, H_2O and N_2O demonstrated **A17a/b** to be excellent precursors for the preparation of novel adducts. Analogous behaviour was observed for the PNP complexes **A18a/b** (Scheme 1.4).[18,19]

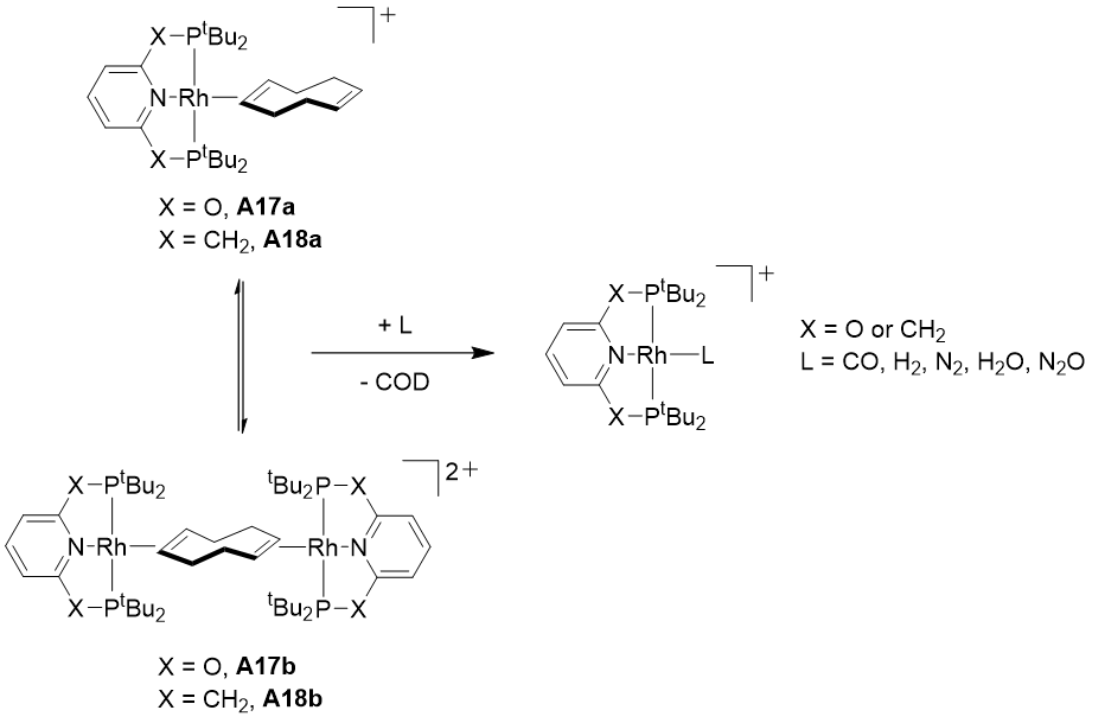

Scheme 1.4 – Reactivity of **A17a/b** and **A18a/b**. Anions omitted for clarity.[18,19]

Complexes of $\{Rh(PONOP)\}^+$ have also found applications the realms of organoborane chemistry, where amine boranes are of interest for potential utilisation as hydrogen storage materials.[63,64] Weller and co-workers reported the dehydrocoupling of amine boranes, which proceeded via the formation of the σ-amine borane complex **A19** (Fig. 1.8).[65] Several σ-amine borane complexes have been characterised over the years and can be compared to σ-silane species, such as $[Ir(POCOP)(H)(\eta^1\text{-}HSiEt_3)][BAr^{F20}{}_4]$, **A20** ($Ar^{F20}$ = pentafluorophenyl).[65-67] The silane ligand preferentially coordinates in the η^1-mode, akin to the coordination mode of **A19** (Fig. 1.8). These σ-complexes are more stable than their σ-alkane counterparts due to the more hydridic character of the E–H bonds (E = B, Si).[68]

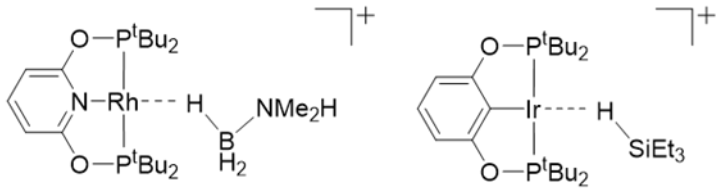

A19 **A20**

Figure 1.8 – The structures of **A19** and **A20**. Counterions omitted for clarity.[65,67]

1.2 – Single crystal to single crystal transformations

Single crystal to single crystal (SC-SC) transformations encapsulate a diverse collection of chemical and structural transformations in the solid-state. Some of the most attractive features of solid-state chemistry are the determination of absolute structure by crystallographic methods and the simplicity of the reaction medium (*i.e.*, the crystal itself as opposed to a solvent). Whilst many mechanochemical transformations are often associated with ball-milling processes,[69] SC-SC transformations can be triggered by external stimuli such as temperature, pressure and light.[70] Commonly observed transformations include phase transitions, spin-crossover (SCO) and ligand isomerism.[71-77] Because many of these transformations occur exclusively in the solid-state, traditional solution-based characterisation techniques are not always suitable. Consequently, SC-SC transformations provide a unique insight into processes that are otherwise not possible to study outside of the solid-state. A wide range of materials are known to undergo SC-SC transformations, but the review presented herein focuses only on discrete organometallic coordination complexes.

1.2.1 – Gas-induced SC-SC transformations

SC-SC transformations involving the use of gas or vapour has taken off in recent years; a range of complexes have been shown to undergo SC-SC transformations whilst retaining morphological integrity.[70] SC-SC hydrogenation reactions have by far been most extensively explored by Weller and co-workers (Scheme 1.5).[4,71,78] Hydrogenation of the norbornadiene (NBD) ligand in $Rh(Cy_2P(CH_2)_2PCy_2)(\eta^2{:}\eta^2\text{-NBD})][BAr^F{}_4]$, **A21**, resulted in the formation of the

norbornane (NBA) complex Rh($Cy_2P(CH_2)_2PCy_2$)(η^2:η^2-NBA)][BAr^F_4], **A22**, which was characterised by single crystal XRD. Dissolution of **A22** in CH_2Cl_2 led to dissociation of the NBA ligand, affording the zwitterion Rh($Cy_2P(CH_2)_2PCy_2$)(η^6-BAr^F_4), **A23**.[71] Weller and co-workers also reported the formation of several related σ-alkane adducts of {Rh($Cy_2P(CH_2)_2PCy_2$)}$^+$ via similar SC-SC transformations (Scheme 1.5).[4,78] The authors reasoned that the σ-alkane complexes were observed exclusively in the solid-state due to the presence of stabilising dispersive interactions supplied by the crystalline microenvironment of the [BAr^F_4]$^-$ anions.[4,77,79] Onward reactivity of **A22** has also been initiated by displacement of NBA with vapourised reagents, facilitating the cationic polymerisation of ethyl vinyl ether and the isomerisation of 1-butene via vapour-induced SC-SC transformations.[77,80]

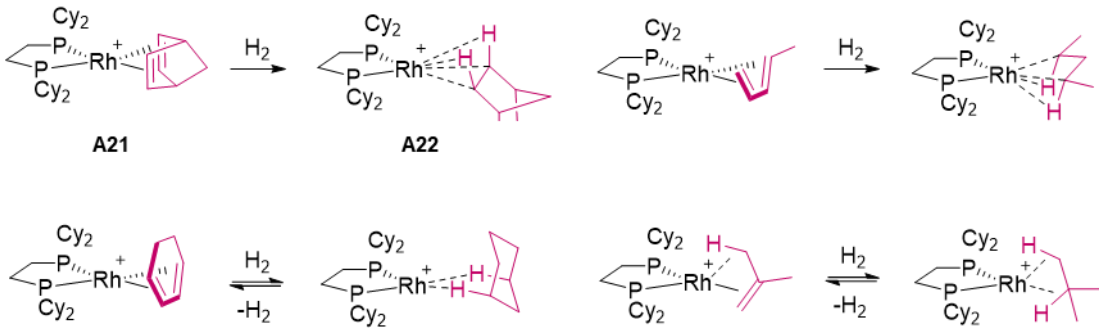

Scheme 1.5 – SC-SC transformations for adducts of {Rh($Cy_2P(CH_2)_2PCy_2$)}$^+$ with H_2. [BAr^F_4]$^-$ counterions omitted for clarity.[4,71,78]

Gas-induced SC-SC transformations in organometallic complexes are not limited to hydrogenations – ligand substitutions and addition reactions have been induced by a range of gases, ranging from small diatomic molecules up to larger ones, such as I_2.[81,82] One of the earliest examples of a gas-induced solid-state transformation was reported by van Koten and co-workers for the reversible reaction of the organoplatinum complex Pt(NCN)Cl, **A24** (NCN = 3,5-bis[(dimethylamino)methyl]phenol), with sulfur dioxide.[82] The formation of the 5-coordinate species Pt(NCN)(SO_2)Cl, **A25**, was initially suspected due to a colour change in the sample from colourless to deep orange, which was then confirmed by powder X-ray diffraction (PXRD) and infrared (IR) spectroscopy. More recently, Brookhart and co-workers reported several ligand substitutions that proceeded via SC-SC transformations for the iridium pincer complex

Ir(POCOP)(κ^1-N_2), **A26**.[83] Exposure of **A26** to atmospheres of H_2, CO, NH_3, C_2H_4 and O_2 resulted in the displacement of the N_2 ligand with the corresponding gas or vapour. Remarkably, crystals of Ir(POCOP)(η^2-C_2H_4), **A27**, demonstrated excellent catalytic activity - the hydrogenation of 120 eq. of ethene could be achieved under ambient conditions within 5 h, without any noticeable loss of crystallinity.[83]

Two sequential SC-SC transformations were reported by Crudden and co-workers for the N-heterocyclic carbene (NHC) complex Rh(SIPr)$_2$(κ^1-N_2)Cl, **A28** (SIPr = 1,3-bis(2,6-di-*iso*-propylphosphinophenyl)-4,5-dihydroimidazol-2-ylidene), each of which proceeded without noticeable degradation of the crystal (Scheme 1.6).[84] Exposure of single crystals of **A28** to air resulted in substitution of the N_2 ligand with O_2. An additional substitution was observed upon exposure of the same crystal to carbon monoxide.

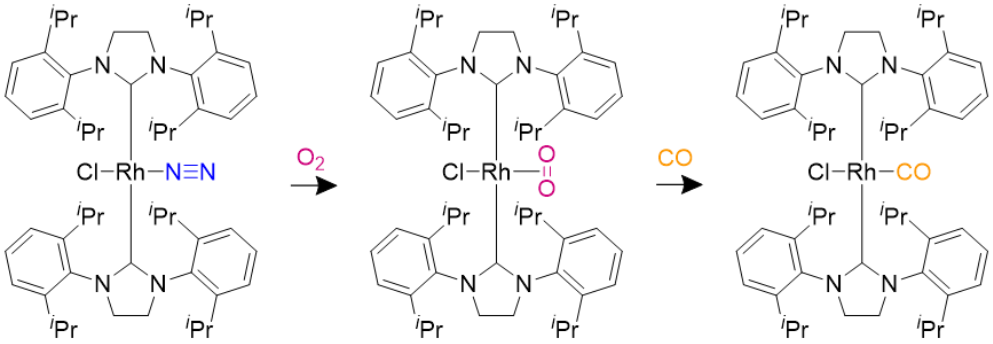

A28

Scheme 1.6 – Sequential SC-SC transformations of **A28**.[84]

1.2.2 – Photo-induced SC-SC transformations

A plethora of reports exist for photo-induced SC-SC transformations of group 10 and 11 complexes.[85] In fact, photo-induced transformations of group 11 have been so extensively explored that rare and serendipitous phenomena have been documented, such as the photosalient effect, where crystals physically 'jump' in response to light.[86] SC-SC cycloadditions are the most commonly observed transformation in dimeric species. Two simultaneous SC-SC [2+2] cycloadditions were induced by UV light between the terminal ligands of the dimeric silver complex [Ag_2(4-stilbz)$_4$][CO_2CF_3]$_2$, **A29** (4-stilbz = *trans*-1-(4-pyridyl)-2-(phenyl)ethylene), which were mediated by short argentophilic interactions.[87] Similar photo-initiated SC-SC [2+2] cycloadditions

have also been reported for polynuclear complexes of zinc, rhodium and iridium.[88,89] Photochromism has also been observed in linear gold complexes, where aurophilic contact shortening was triggered by exposure to UV light.[90,91]

A plethora of group 10 complexes have been shown to display photoactivated linkage isomerism in the solid-state by Raithby and co-workers.[92] For example, rapid photo-conversion (< 160 s) of [Pd(Bu$_4$dien)(NO$_2$)][BPh$_4$], **A30** (Bu$_4$dien = N, N, N', N'-tetrabutyl-diethylenetriamine), from the ground state nitro-(η^1-NO_2) isomer to the metastable nitrito-(η^1-ONO) isomer.[93] Soon after, it was reported that substantial proportions of the metastable excited state could be retained for crystals of **A30** at temperatures as high as 260 K.[72] Temperature and photo-dependent behaviour was also elucidated for the structurally related complex Ni(Et$_4$dien)(NO$_2$)$_2$, **A31** (Et$_4$dien = N, N, N', N'-tetraethyl-diethylenetriamine).[94] A thermally controlled equilibrium was found to exist between the linkage isomers in the absence of light – at 100 K, total occupancy of the **A31-NO$_2$** isomer was observed, establishing this isomer as the thermodynamic ground state (Table 1.1). Upon irradiation for 1 h with 400 nm light, 86 % conversion to **A31-ONO** was observed by XRD at 100 K. Reversion to **A31-NO$_2$** was only observed once the crystal was warmed to above 160 K.[94]

Table 1.1 – The crystallographically determined ratios of **A31-NO$_2$** (left) and **A31-ONO** (right) at different temperatures.[94] * = temperatures reached during heating cycle from 100 K.

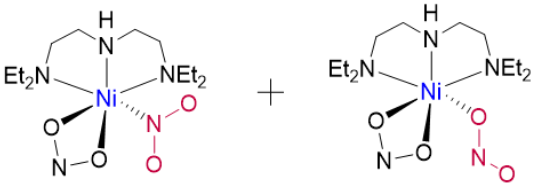

T / K	A31-NO$_2$ / %	A31-ONO / %
298	78	22
233	90	10
100	100	0
298*	78	12
350*	64	36
370*	58	42

1.2.3 – Thermally-induced SC-SC transformations

Thermally-induced SC-SC transformations are found in abundance for group 9 organometallics – perhaps, in part, as a consequence of this group's predisposition to catalytic reactivity.[70] Although many examples of thermally-induced SC-SC transformations are known,[70] most other transition metal complexes that exhibit thermally-induced SC-SC transformations have generally included reversible dehydration/rehydration cycles of non-coordinated water molecules from within the crystal. For example, heating crystals of $[(OAc)Cu(\mu\text{-hep})_2Cu(OAc)]\cdot 2H_2O$, **A32·2H₂O** ($OAc^-$ = acetate; hep^- = 2-(2-hydroxyethyl)pyridine), at 110 °C for 3 h in air produced the dehydrated analogue (**A32**) without any alterations to the structural motifs in the tetrameric core. The hydrated analogue could be recovered upon exposure of **A32** to water.[95] Similarly, reversible dehydration of $[Dy_2(phen)_2(L)_6]\cdot 2H_2O$, **A33·2H₂O** (phen = 1,10-phenanthroline; L = 4,5-bis(pinene)-2,2-bipyridine), occurred after heating crystals at 160 °C for 24 under vacuum. Dehydration of **A33·2H₂O** was accompanied by a rearrangement of the Dy centres from nine-coordinate to eight-coordinate.[96] Even phenomena such as SCO have been shown to accompany thermally-induced SC-SC transformations that involve dehydration/rehydration cycles – for example, the dehydration of the low spin complex $[Fe(tpa)\{N(CN)_2\}]_4\cdot(BF_4)_4(H_2O)_2$, **A34** (tpa = tris(2-pyridylmethyl)amine), occurred at 77 °C to the dehydrated high spin analogue, without otherwise altering the structural core.[97]

In a vein more relevant to the work presented herein, thermally-induced OA of C-N bonds were reported by Ozerov and co-workers for complexes of Rh(4-R-PNP^{Me}*)Cl, (4-R-PNP^{Me}* = bis[2-(di-*iso*-propylphosphino)-4-R-phenyl]methylamine; R = Me, **A36**; F, **A39**).[16,98] Dissolution of ligand **A35** (Scheme 1.7) in diethyl ether or C_6D_6 in the presence of 0.5 equivalents of $[(COD)RhCl]_2$ resulted in the rapid formation of complex **A36** (Scheme 1.7). When left in solution, Me^+ migration was observed by ^1H NMR spectroscopy.[16] Interestingly, Me^+ migration was also achievable in the solid-state under ambient conditions (Scheme 1.7). Two independent molecules were found in the asymmetric unit of **A36**, with the first site fully occupied by **A36** and the second site by 53(2) % **A36**; the OA product Rh(4-Me-PNP*)(Me)Cl, **A37** (4-Me-PNP* = bis[2-(di-*iso*-propylphosphino)-4-methyl-phenyl]amino), made up the remaining population at the second site. The same crystal was subjected to a second collection

after 16 days at room temperature, at which time the first site remained fully populated by **A36** but the second site was > 95 % occupied by **A37**.[16] The dependence of OA on the lattice site suggested that the two independent molecules had different activation energies.[16] Me^+ migration in **A39** to generate Rh(4-F-PNP*)(Me)Cl, **A40** (4-F-PNP* = bis[2-(di-*iso*-propylphosphino)-4-fluoro-phenyl]amino), in solution was less selective - approximately 60 % conversion was achieved alongside the generation of several other species.[98] However, heating crystals of **A39** in the solid-state improved the selectivity of the reaction - after 3 h at 70 °C, the solid was dissolved in C_6D_6 and immediately analysed by NMR spectroscopy, which revealed the exclusive formation of **A40**.[98]

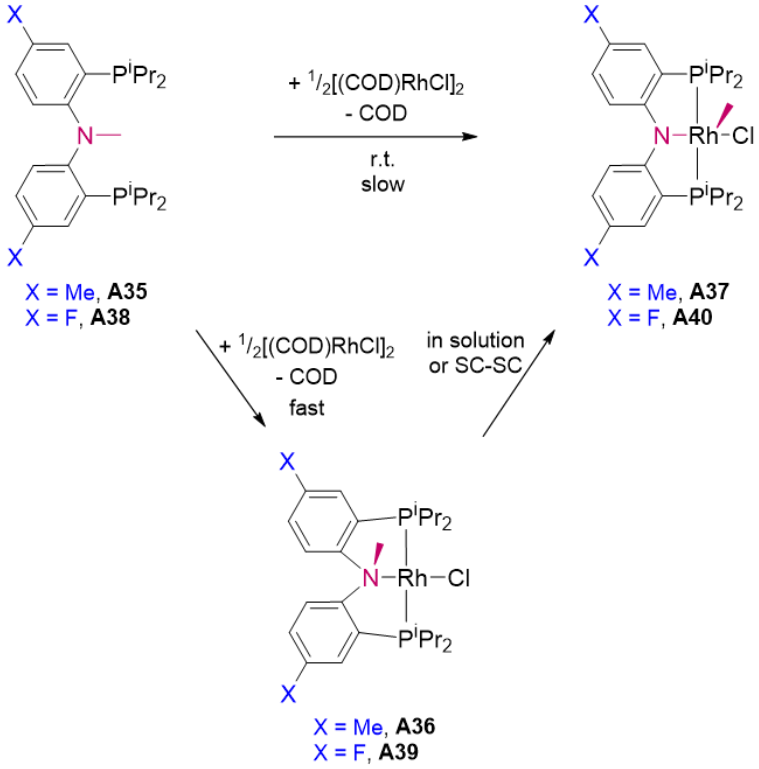

Scheme 1.7 – The synthesis and SC-SC transformations of **A36/A39**.[98]

Reaction selectivity was similarly improved for the metallocyclic complex [Ir(BINOR-S)(P^iPr_3)][$BAr^F{}_4$], **A41** (BINOR-S = 1,2,4,5,6,8-dimetheno-S-indacene), by circumventing the decomposition pathways that were more readily available in solution.[74] Heating crystals of **A41** for 20 h at 40 °C generated a mixture of the iridium(V) and iridium(III) complexes **A42a** and **A42b**, respectively (Scheme 1.8), which dynamically interconvert in the solid-state via C–C bond activation. The

crystallographic occupancy of **A42a**:**A42b** could be perturbed by temperature, with the latter isomer favoured at lower temperatures (**A42a**:**A42b** 17:83 at 100 K).

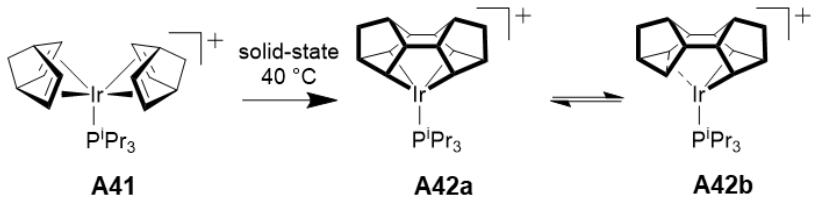

Scheme 1.8 – The SC-SC transformation of **A41** into **A42a/b**. Counterions omitted for clarity.[74]

Unprecedented temperature-induced SC-SC transformations were reported by Mobin and co-workers for the cobalt complexes $[Co(hep\text{-}H)(H_2O)_4]SO_4$, **A43**, and $[Co(hep\text{-}H)_2(H_2O)_2](NO_3)_2$, **A44** (hep-H = 2-(2-hydroxyethyl)pyridine), whereby upon heating, the non-coordinating counterions were incorporated into the coordination spheres of the complexes.[73] Dehydration of **A43** upon heating resulted in the non-coordinating sulfate ion forming bonds between two separate metal centres to generate the dimeric complex **A45** (Scheme 1.9). A similar anion migration was observed upon heating single crystals of **A44**, to generate $[Co(hep\text{-}H)_2(\kappa^2_O\text{-}NO_3)][NO_3]$, **A46** (Scheme 1.9). Interestingly, analysis of the solid-state structures of **A43** and **A44** revealed the existence of hydrogen bonds between the counterions and the water ligands that occupy the coordination sites that experience ligand exchange upon heating.[73]

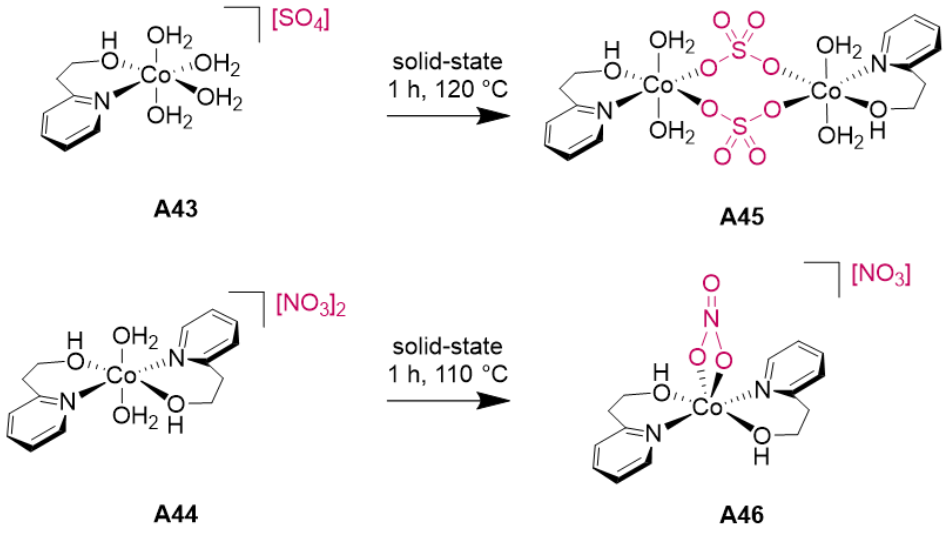

Scheme 1.9 – The SC-SC transformations of **A43** (top) and **A44** (bottom).[73]

Sundberg and co-workers reported an analogous nitrate anion migration for the polynuclear cobalt complex [{(bpbp)$Co_2(O_2)$}$_2$(NH_2bdc)](NO_3)$_4$·7H_2O, **A47** (bpbp = 2,6-bis(N,N-bis(2-pyridylmethyl)-aminomethyl)-4-*tert*-butylphenolato; NH_2bdc = 2-amino-1,4benzenedicarboxylato).[99] Upon heating crystals of **A47** to 80 °C, displacement of water and oxygen molecules from the structure promoted the coordination of a nitrate ion to one of the metal centres. This SC-SC transformation was found to be reversible upon exposure to air, facilitating the reabsorption of both water and oxygen. This particular SC-SC transformation boasts the largest reported translational movement of ions in a crystal lattice, with the nitrate anions migrating by up to 7 Å.[99] Generally speaking, SC-SC transformations consist of much smaller molecular rearrangements as opposed to changes of several angstroms, because larger rearrangements tend to result in a loss of long-range order and can cause sample damage due to large changes in the lattice volume.[77,100,101]

1.2.4 – Coordination complexes under pressure

The behaviour of coordination complexes under pressure is highly varied – this is in part due to the nature of the field, which is mostly comprised of isolated structural studies because of the specialist equipment and high level of analytical rigour required. Because a vast array of structures have been studied, a variety of intermolecular interactions,[102,103] phase transitions[104,105] and phenomena such as magnetic anisotropy,[106] negative linear compressibility[107] and piezochromism[108,109] have been elucidated. Extended structures (such as metal-organic frameworks) behave rather differently to discrete coordination complexes under pressure,[110] so are not discussed in depth herein. Instead, the following review encapsulates pressure-induced SC-SC transformations as well as the general pressure-responsive behaviour of coordination complexes, organised by group.

1.2.4.1 – Group 9 complexes

The first single crystal high pressure X-ray diffraction (HP-XRD) study conducted on a coordination complex was reported by Hazen and co-workers in 1987 for a cobalt metalloporphyrin, which underwent a reversible phase transition at 0.49 GPa that exhibited higher initial compressibility in the high pressure phase than in the ambient

pressure phase.[111] Since then, a range of cobalt complexes have been studied under pressure. Whilst some structures respond to pressure with only subtle geometrical distortions,[112] others have exhibited more pronounced changes, such as SC-SC transformations[113] and phase transitions.[104]

Sironi and co-workers reported a reversible phase transition for $[Co_2(CO)_6(PPh_3)_2]$, **A48**, upon the application of pressures > 1.3 GPa or temperatures < 120 K.[104] The phase transition resulted in a doubling of the *c* axis, reducing the space group symmetry from $R\bar{3}$ to *R*3. The loss of symmetry was attributed to the alternating compression and elongation of the P···P contacts between adjacent molecules within the 1D-molecular chains (analogous to a Peierls distortion) in conjunction with the rearrangement of the CO ligands from a staggered to eclipsed conformation (Fig. 1.9).[104]

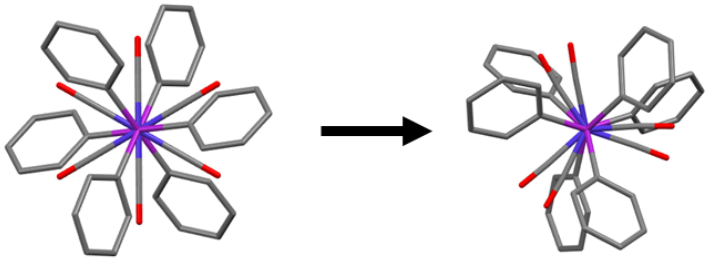

Figure 1.9 – A view of **A48** down the P–Co–Co–P axis before (left) and after (right) the phase transition.[104]

Even under extreme pressures, discrete coordination complexes can appear to be surprisingly resistant to change. Whilst void space can be removed and intermolecular interactions can become more prominent upon compression, the coordination sphere of the complex itself can often retain its integrity. For example, the octahedral complex $[Co(NH_3)_5NO_2]Cl_2$, **A49**, only displayed minor structural deformations in response to pressure. The authors attributed these deformations to a strengthening of the hydrogen-bonding network across the structure.[112] Minor structural distortions were also observed in the extended metal atom chain complex $Co_3(dpa)_4Br_2 \cdot 2CH_2Cl_2$, **A50** (dpa = 2,2'-dipyridylamide), in response to pressures up to 11.8 GPa.[114] Across the studied pressure range, a redistribution of the non-coordinating CH_2Cl_2 solvent molecule throughout the structure was observed. At higher pressures, the CH_2Cl_2 molecule shifted from predominantly its first disorder component site to its second in response

to the evolution of repulsive H···H contacts with a nearby dpa ligand. A similar redistribution of the disordered CH_2Cl_2 molecule was also reported for the isostructural complex $Co_3(dpa)_4Cl_2 \cdot 2CH_2Cl_2$, **A51**, indicating the sensitivity of solvent molecules to the compression of solvent-accessible void space.[114]

In a similar vein, extensive solvent ordering was observed within wet vitamin B_{12}, **A52**, for solvent-accessible regions of the compressed structure.[115] A 28 % reduction in the solvent-accessible void space was reported between 0 GPa and 1.0 GPa, which narrowed the channels and pockets where water molecules were found. The solvent ordering allowed for more water molecule-related electron density to be accurately modelled in **A52**, resulting in a higher quality structural model than was previously reported at ambient pressure.[115] This is an exemplary case of HP-XRD being utilised to improve the quality of a final refinement, as opposed to implementing a SQUEEZE[116] routine to 'mask' disordered solvent molecules.

There are precious few examples of pressure-induced SC-SC transformations for group 9 complexes. Reports of such transformations in cobalt complexes are uncommon when metal-organic frameworks (MOFs)[117] and SCO complexes[75,118] are discounted, but examples can be found in the literature.[119] Pressure-induced valence tautomeric interconversion (VTI) was reported for the *o*-quinone cobalt complex [Co(3,5-SQ)$_2$(phen)], **A53** (3,5-SQ^- = singly reduced 3,5-di-*tert*-butyl-*o*-quinone, phen = 1,10-phenanthroline). Between the pressures of 0.10 GPa and 2.50 GPa, **A53** was driven from the high-spin (HS) Co(II) species to the low-spin (LS) Co(III) species [Co(3,5-SQ)(3,5-CAT)(phen)], **A54** (3,5-CAT^{2-} = doubly reduced 3,5-di-*tert*-butyl-*o*-quinone).[113] The HS to LS transformation was reflected by contractions in the Co-O and Co-N bond lengths of *ca*. 10 %, despite the accompanying decrease in oxidation state. VTI occurred exclusively with pressure in the case of the non-solvated complex, whereas both pressure and temperature induced the transformation in the toluene solvate (Fig. 1.10).[113] VTI has also been induced in cobalt *o*-quinone complexes by hard X-rays.[120]

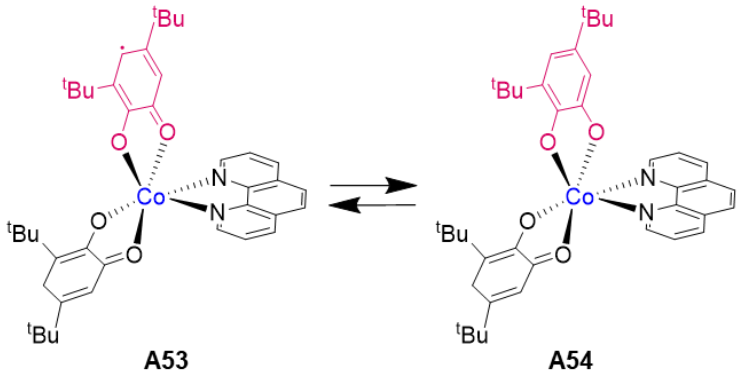

Figure 1.10 – The reversible SC-SC transformation of **A53** into **A54**.[113]

HP-XRD studies on the heavier congeners of group 9 are even more scarce - one rare example is the study of the rhodium-gold heterometallic cluster $[Rh_2(\mu\text{-}CI)_2(CNC_8H_9)_4(\mu\text{-}AuPPh_3)]_2(PF_6)_2$, **A55**, whose piezochromism was driven by a partially irreversible structural isomerisation from a *trans*, eclipsed conformation (red crystals; Rh···Rh = 3.262(2) Å) to a gauche, staggered conformation (green crystals; Rh···Rh = 3.008(4) Å).[121] Whilst there are several examples of phase transitions[122] and *in situ* high pressure syntheses for extended structures such as rhodium and iridium hydrides,[123-125] to the best of my knowledge, no examples of mononuclear rhodium or iridium complexes undergoing pressure-induced transformations have been reported, to date.

1.2.4.2 – Group 10 complexes

A comparatively large amount of HP-XRD studies have been carried out on group 10 complexes, particularly on simple planar complexes, where intermolecular M···M interactions are of particular interest.[119] Examples include $Pt(bqd)_2$, **A56**, and $Pt(dmg)_2$, **A57** (bqd = bis-1,2-benzoquinonedioximato; dmg = bis-dimethylglyoximato), which both exhibit changes in their conductive and optical properties upon the application of pressure, resulting from M···M contractions.[126-128] Pressure-induced phase transitions have also been identified in dichloride complexes of palladium and platinum.[105,129] At 0.8 GPa, *trans*-$PtCl_2(PEt_3)_2$, **A58**, underwent a reversible phase transition from $P2_1/n$ to $P2_1$, where the molecular inversion symmetry was lost across the phase transition as a result of distortions to the *trans* ligand angles

(∠P–Pt–P = 170.58°; ∠Cl–Pt–Cl = 176.82°) and the reorientation of a PEt_3 ligand.[129] These observations were supported by the splitting of spectroscopic bands observed by IR and raman spectroscopy. The authors also noted the hydrogen bonding network became more prominent in **A58** across the phase transition, as evidenced by calculated Cl···H distances of less than 2.6 Å.[129]

Intermolecular interactions becoming more pronounced in high pressure phases is extremely common, since shorter interactions naturally arise upon compression.[102] High pressure crystallography affords us the opportunity to manipulate these secondary interactions in the solid-state through mechanical means. A notable example of this was reported by Blake and co-workers for the thioether crown complex $[Pd([9]aneS_3)(PPh_3)_2](PF_6)_2$, **A59**, ([9]aneS$_3$ = 1,4,7-trithiacyclononane).[102] The effect of pressure on the π-π interactions between adjacent molecules was notable due an unprecedented deformation at the *ipso*-carbon of the PPh_3 ligands (α; Fig. 1.11). This deformation was instigated by the decrease in the horizontal ring slippage distance C from a displaced π-π interaction towards a more parallel arrangement (Fig. 1.11, Table 1.2). The significant deformation at the *ipso* carbon was rationalised by comparing the experimental structure to an idealised model containing no deformation of the phenyl ring at 6.55 GPa. The idealised model contained highly repulsive H···H contacts of only 1.742 Å between the phenyl ring in question and the symmetry related cation.[102]

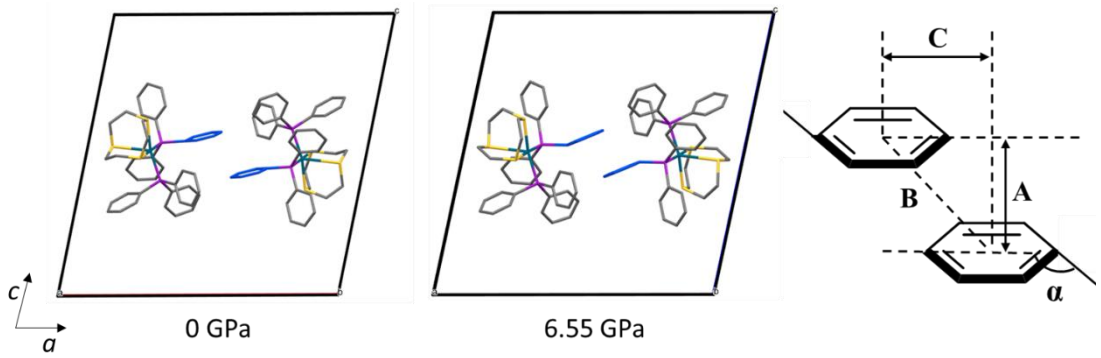

Figure 1.11 – A depiction of the π-π interactions of the phenyl embrace in **A59** as viewed along the *b* axis at 0 GPa (left) and 6.55 GPa (middle) accompanied by the definitions of the parameters supplied in Table 1.2 (right).[102]

Table 1.2 – Observed experimental parameters associated with the π-π interactions of the phenyl embrace defined in Fig. 1.11 as a function of pressure.[102]

Pressure / GPa	A / Å	B / Å	C / Å	α / °
0.00	3.058(13)	5.192(6)	4.195(10)	169.6(4)
1.05	2.96(2)	4.864(12)	3.861(18)	164.7(6)
2.88	3.01(4)	4.467(15)	3.30(3)	156.7(12)
3.67	2.819(18)	4.074(11)	2.941(18)	155.1(7)
4.02	3.016(13)	4.069(9)	2.731(13)	155.1(5)
5.57	2.996(17)	3.596(13)	1.99(2)	149.8(8)
6.55	3.016(15)	3.568(11)	1.906(18)	149.1(7)

The related complexes $[PdCl_2([9]aneS_3)]$, **A60**, and $[PdCl_2([9]aneS_2O)]$, **A61** ($[9]aneS_2O$ = 1-oxa-4,7-dithiacyclononane), were studied soon after, providing further insight into the pressure-responsive behaviour of palladium thioether crown complexes. Three different polymorphs of **A61** were studied up to pressures exceeding 9 GPa, one of which was found to undergo a reversible phase transition between 6.81-6.87 GPa that was characterised by a tripling of the unit cell volume.[105] Complex **A60** was found to undergo an isomorphous phase transition between 4.25-4.60 GPa, which was accompanied by an orange to black piezochromic response.[109] Unlike in **A59**, the M···S distances of **A60** were more sensitive to pressure, with the two Pd-S distances contracting from 3.009(5) Å and 3.204(5) Å to 2.846(7) Å and 3.117(8) Å across the

phase transition. The Pd–S contractions drove the formation of 1D-molecular chains in the high pressure phase.[109]

The effect of the coordination sphere on structure-property relationships can be profound, as was discovered for [Ni(^{Me}DABCO)$_2$Cl$_3$][ClO$_4$], **A62** (^{Me}DABCO = 1-methyl-4-aza-1-azoniabicyclo[2.2.2]octanium), where pressure-induced distortions quenched the axial magnetic anisotropy.[106] Application of pressure resulted in a loss of the ideal D_{3h} symmetry of **A62** observed at ambient pressure. The decrease in magnetic anisotropy between 0 GPa and 1.65 GPa was attributed to the angular distortions observed in the equatorial Ni–Cl plane. The loss of degeneracy between the d_{xy} and $d_{x^2-y^2}$ orbitals quenched the spin-orbit coupling (Fig. 1.12).[106]

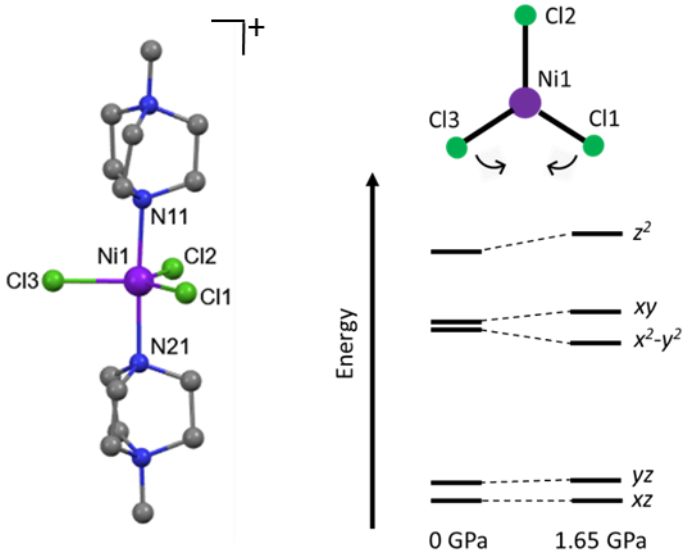

Figure 1.12 – A partially labelled cation of **A62** (left) and a diagram depicting the loss of degeneracy with increasing pressure as a result of ∠Cl–Ni–Cl distortions (right). Hydrogen atoms and anions omitted for clarity.[106]

1.2.4.3 – Group 11 complexes

Complexes of copper and gold are the most comprehensively studied complexes with respect to single crystal HP-XRD experiments. Parsons and co-workers reported pressure-induced piezochromism for the copper complex [GuH]$_4$[Cu$_2$(cit)$_2$]·2H$_2$O, **A63** (GuH = guanadiunium cation H$_4$cit = citric acid).[108] Crystals of **A63** underwent a colour change from blue to green with increasing pressure; the high pressure

absorption spectra indicated the phase transition likely occurred at 2.5 GPa. The piezochromism arose from a change in the coordination environment at the copper(II) centres in **A63**. The Cu1–O5 α-carboxylate distance decreased from 2.628(3) Å at 0 GPa to 2.407(3) Å at 2.2 GPa, which subsequently modified the geometry of **A63** from distorted pseudo-tetrahedral to distorted square-based pyramidal (Fig. 1.13).[108] The related complex $[GuH][Cu_2(OH)(cit)(Gu)_2]$, **A64** (Gu = guanidine), was shown to polymerise above 2.95 GPa due to the formation of formal intramolecular bonds from short intermolecular contacts.[130]

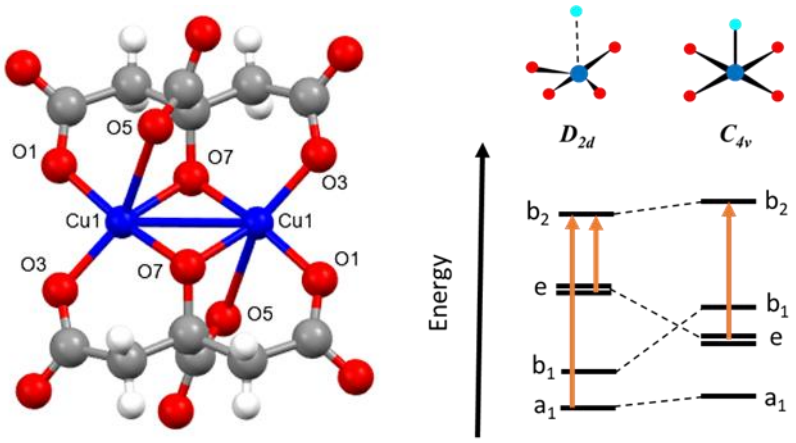

Figure 1.13 – A partially labelled structure of **A63** (left) and the energy level diagrams for C_{4v} and D_{2d} symmetry (right). Orange arrows depict allowed electronic transitions.[108]

Because of the specialist equipment, time-consuming set-up and rigorous analysis required to conduct HP-XRD experiments, systematic HP-XRD studies of coordination complexes are rare. One example of a systematic study was conducted on the dimeric complexes $[Cu_2(OH)_2(H_2O)_2(tmen)_2][ClO_4]_2$, **A65**, $[Cu_2(OH)_2(tben)_2][ClO_4]_2$, **A66**, and $[Cu_2(OH)_2(bpy)_2][BF_4]_2$, **A67** (tmen = tetramethylethylenediamine; tben = di-*tert*-butylethylenediamine; bpy = 2,2'-bipyridine), which were structurally characterised up to 2.5, 0.9 and 4.7 GPa, respectively.[131] Subtle contractions were observed in both the Cu···Cu distances and the Cu–O–Cu bridging angles for **A65-A67** with increasing pressures (Fig. 1.14). Due to the supporting $[BF_4]^-$ anions that form long contacts (~2.8 Å) at the axial positions of the copper(II) centres in **A67**, the $[Cu_2O_2]$ core was effectively 'locked' in place,

therefore, higher pressures were required to achieve the same degree of cage distortions as were observed in **A65** and **A66**.[131]

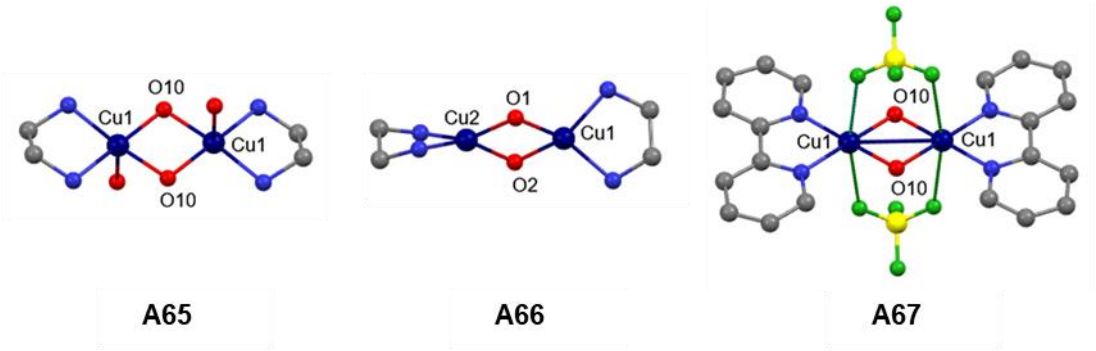

Figure 1.14 – Partially labelled structures of the molecular cores of **A65-67**.[131]

Generally speaking, the study of gold complexes under pressure has primarily been focused on their spectroscopic properties. Since there is a considerable energy gap between the ground state and lowest excited state in heavier transition metal complexes, non-radiative decay to the ground state is disfavoured. Therefore, such complexes have a propensity to be photochemically active.[132] The first systematic study into the pressure-dependence of aurophilic contacts within a coordination complex on the resulting luminescence was conducted on a series of pyrazolate-based gold(I) trimers by Raithby and co-workers. The reduction in aurophilic intertrimer distances (between 0.04-0.08 Å) with increasing pressure (up 4.3 GPa) resulted in red shifts in the luminescence spectra for all trimers that contained intermolecular Au···Au contacts.[133]

Aurophilic contact shortening with increasing pressure was also reported for [1,4-C_6H_4{PPh_2(AuCl)}$_2$], **A68**.[134] In fact, **A68** exhibited the largest Au···Au contraction for any gold(I) complex, to date, with the aurophilic distances decreasing from 3.6686(5) Å at 0 GPa to 3.0554(12) Å at 10.6 GPa (Fig. 1.15).[134] At 10.6 GPa, the π-π interactions (3.031(6) Å) became repulsive in nature and prevented further Au···Au contractions.[134]

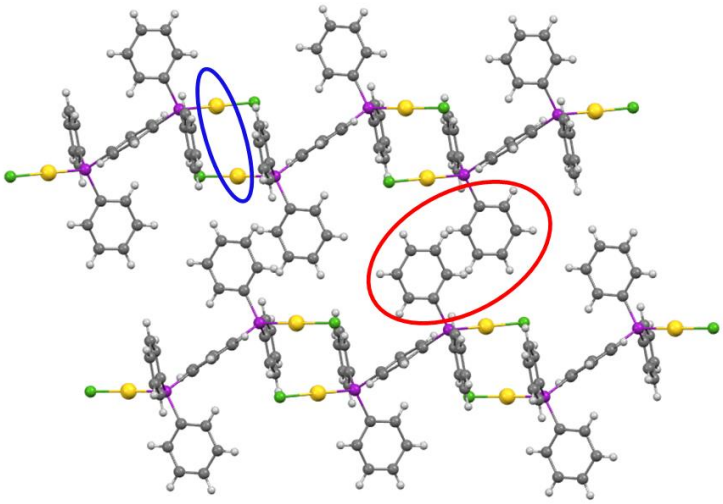

Figure 1.15 – The extended packing of **A68** at ambient pressure as viewed down the [010] direction showing the aurophilic interactions (circled in blue) and the π-π interactions (circled in red).[134]

1.2.4.4 –Main group and f-block complexes

Single crystal HP-XRD studies of coordination complexes have typically focused on transition metal complexes, however, as of 2015, Arnold, Parsons and co-workers began reporting on the pressure-responsive behaviour of lanthanoids. In the past year alone, two new reports have emerged from their collaboration, which probe fundamental properties of the f-block elements (*i.e.*, bonding and structure).[135,136] The most recent communication reported pressure-induced phase transitions between 2.8-3.3 GPa for the structurally related series $M(OAr)_4$ (OAr = 2,6-di-*tert*-butylphenoxide; M = Th, **A69**; U, **A70**; Np, **A71**), all of which were characterised by a retention of space group but a discontinuous drop in unit cell volume, caused by so-called '*c* axis collapse'. Discontinuities in the M–O bond lengths for the three complexes were found to be associated with changes to the electronic structures across the phase transitions, from primarily ionic bonding to more covalent interactions, due to greater involvement of the metals' 6*d* and 5*f* orbitals.[136]

In a similar vein, pressure-induced evolution of an agostic interaction was reported for the diuranium(III) compound $[UN''_2]_2(\mu\text{-}\eta^6\text{:}\eta^6\text{-}C_6H_6)$, **A72** (N'' = $N(SiMe_3)_2$), where the two unique contacts between the terminal carbons of the N'' ligand and the Uranium centres contracted from 3.022(3) and 3.025(3) Å at ambient pressure to

2.95(2) and 3.00(5) Å at 3.2 GPa.[103] Natural bond orbital (NBO) and quantum theory of atoms-in-molecules (QTAIM) analysis supported the evolution of a formal bond path across the CH···U interaction at 3.2 GPa – this bond path could not be located in the ambient pressure structure (Fig. 1.16). Complex **A72** was also found to undergo a phase transition at 1.8 GPa, which lowered the crystallographic symmetry from $P2_1/c$ to $P\bar{1}$. The loss of symmetry in high pressure phases has been well documented, since losing certain symmetry constraints allows more 'compressional degrees of freedom'.[104,111,137] An early observation of this phenomenon was reported in the HP-XRD study of ReO_3, where the structure's octahedra were found to have rotated slightly after the phase transition, thereby violating certain symmetry constraints.[137]

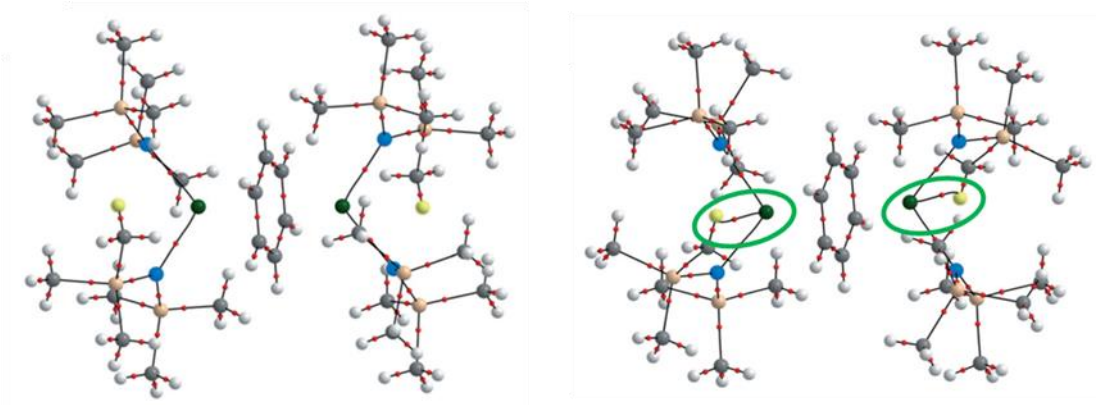

Figure 1.16 - The NBO-QTAIM molecular graphs for **A72** at ambient pressure (left) and at 3.2 GPa (right). The formal bond path calculated at 3.2 GPa is circled in green with the hydrogen atom of interest coloured yellow. Figure adapted with permission from Arnold and co-workers.[103]

Reid and co-workers systematically investigated the effects of intermolecular interactions on a homologous series of $[GeX_2\{o\text{-}C_6H_4(PMe_2)_2\}]$ complexes (X = Cl, **A73**; Br, **A74**; I, **A75**).[138] Complexes **A73** and **A74** were isomorphous ($C2/c$), whereas **A75** crystallised in the space group $P2_1/c$. Two main interfaces were present in the structures: Ge···Ge and Ar···Ar interfaces. Whilst no phase transitions were observed for **A73** or **A75** across the studied pressure range, a phase transition occurred between 2.9-4.1 GPa in **A74**, which was characterised by ring slippage at the Ar···Ar interface from an edge-to-face π-π interaction to a displaced face-to-face π-π interaction (Fig. 1.17). The packing efficiency of complex **A74** at ambient pressure was calculated to

be the lowest, which the authors noted was consistent with the findings that **A74** underwent a phase transition to a more densely packed high pressure phase. This investigation highlighted how subtle structural changes can greatly influence the structure's behaviour under pressure.[138]

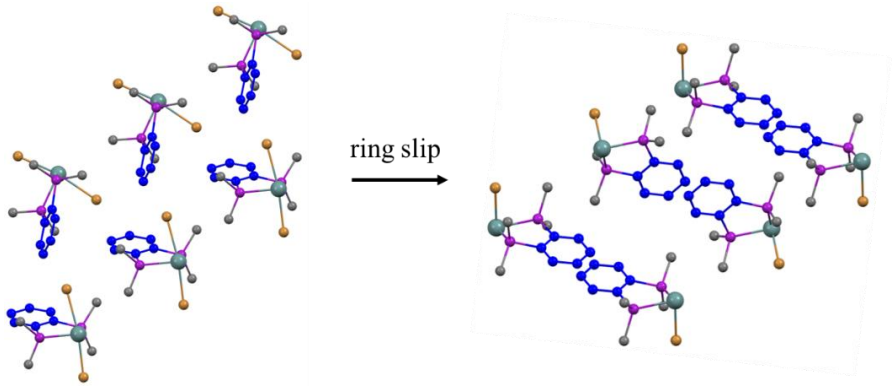

Figure 1.17 – The Ar···Ar interface in **A74**, highlighted in blue, before (left) and after (right) the phase transition.[138] Hydrogen atoms omitted for clarity. Only one disorder component is shown.

The above examples illustrate that a wealth of coordination complexes demonstrate remarkable pressure-responsive behaviour. The exploration of coordination complexes under extreme conditions remains an exciting, ever-evolving area of science.

1.3 – High pressure crystallography

Crystallographic experiments can produce some of the most comprehensive structural results for solid-state samples in the scientific field. The only stipulation is that a single crystal of appropriate size and quality must be grown in order for these experiments to be successfully executed. Advancements in technology now allow for routine crystal collections and refinements to be carried out by researchers with very limited training in the field that decades ago would have taken highly specialised crystallographers weeks, even months, to complete. Such advancements have subsequently enabled more extensive structural investigations to be developed in recent decades, such as the study of samples under extreme conditions.[139] The HP-XRD studies presented within this thesis are examples such experiments.

1.3.1 – Equipment and procedure

HP-XRD studies in the GPa regime are conventionally carried out with the use of a diamond anvil cell (DAC) – the studies presented within this thesis were conducted using a Merrill-Bassett DAC, which is comprised of two diamonds with polished flat faces mounted on backing disks housed by steel plates. The assembly is held together by Allen screws, the tightening of which controls the pressure. Diamonds are well suited towards use in pressure cells due to their hardness and transparency to not only X-rays, but UV, visible and IR radiation, allowing for both structural and spectroscopic studies to be carried out on the same sample.[139] Whilst several DAC designs exist,[140,141] the most commonly used is the Merrill-Bassett cell due to its compact size and compatibility with most modern diffractometers (Fig. 1.18).

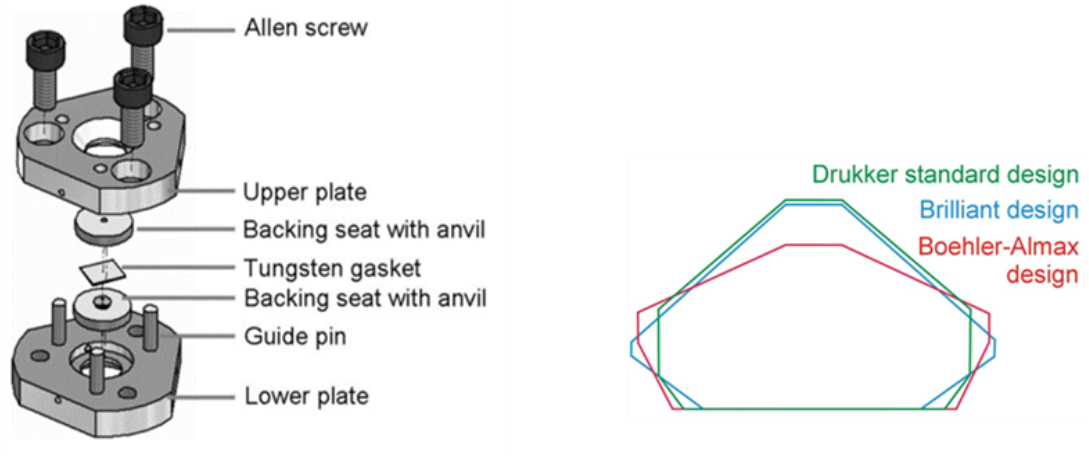

Figure 1.18 – A diagram of a Merrill-Bassett cell (left) and an illustration of different diamond cuts used in DACs (right). Figures reproduced with permissions from Parsons and co-workers[142] and Katrusiak,[139] respectively.

The diamonds are mounted on metal backing seats, with the culet faces separated by a thin piece of metal (called the gasket), in which a small hole is drilled to form the sample chamber.[139,142] Typical opening angles for Merrill-Bassett DACs are around 60-80 °, which define the accessible beam paths.[139,143] In these designs, the backing seats provide support for the anvils and transmit load from the steel plates to the diamonds - this allows considerable pressures (> 100 GPa) to be achieved within the DAC.[141] To put this in perspective, the maximum pressure exerted at the bottom of the Mariana trench, the deepest oceanic trench on earth, is ~0.11 GPa.[144]

The Merrill-Bassett cell has undergone a number of developments since its inception. Beryllium backing seats are known for their low absorption of Mo radiation (μ_{Be}(Mo Kα) = 0.048 mm^{-1}), however, they generate powder rings that are observed in the experimental frames. These powder rings contaminate the diffraction pattern, increasing the background as radiation passes through the polycrystalline material.[142,143] Due to the high number of coincident diffraction intensities with powder rings observed for molecular compounds - whose unit cell volumes can be of the order of thousands of $Å^3$ - replacing the beryllium baking seats in the DAC design has been shown to significantly increase data quality.[139,143] Tungsten carbide (WC) backing seats were thus developed that serve to mitigate the powder ring problem and can be used sparingly in the DAC design because of the hardness of the material. However, WC backing plates provided less support to Brilliant or Drukker cut anvils (which were typically used in conjunction with beryllium backing seats) and, therefore, limited access to the sample. WC is also opaque to X-rays, so larger conical holes must be used in order to maintain the opening angle of the DAC. These issues can be overcome by implementing embedded Boehler-Almax (BA) cut diamonds into the design, in conjunction with precisely matching WC backing plates, which modern DACs now favour (Fig. 1.18). [139,142,143,145] The revisions to the cell design outlined above can be made without detriment to the opening angle or size of the sample chamber.[145]

The gasket is a thin sheet of metal (typically steel or tungsten) which is required to be inserted between the diamonds to create the chamber which will house the sample. Gaskets are typically ~0.20 mm thick and are pre-indented by the diamond faces to a thickness of approximately 0.10-0.12 mm. A hole of diameter 0.2–0.4 mm (depending on the diamond culet diameter and intended pressures of operation) is then made in the centre of the pre-indented gasket.[139] Pre-indentation both increases the strength of the gasket material (a typical work-hardening property of many metals) and improves the chamber sealing in the early stages of pressure generation.[139] The degree of indentation is critical: if the gasket is too thin, the depth of the chamber can be too small to house the sample, but if the gasket is too thick then the gasket walls can deform, thereby reducing the maximum pressure achievable in the DAC. Thinner gaskets allow higher pressures to be achieved, although the size of the sample will also influence the final choice of gasket depth.[139]

A pressure transmitting medium (PTM) is also required to facilitate uniform compression of the sample; typical media include 1:1 pentane/isopentane, 4:1 methanol/ethanol and various oils.[140] The choice of PTM depends on the desired pressure range of the experiment and sample compatibility. The hydrostatic limits presented in Table 1.3 indicate the pressures at which the liquid and oil-based media become non-hydrostatic and, therefore, become unsuitable for rigorous high pressure studies. Under non-hydrostatic conditions, pressure gradients can develop, resulting in obfuscation of results, peak broadening and crystal degradation.[139,143,146]

Table 1.3 – The hydrostatic limits of popular PTM.[140,147,148]

PTM	Hydrostatic limit / GPa
4:1 methanol : ethanol	9.8
1:1 *n*-pentane : *iso*-pentane	7.0
2-propanol	4.2
Paraffin oil	3.0
Daphne-7373	2.2
Daphne-7575	4.0
Argon	1.9
Helium	11.8

Media such as Ar, N_2 or He may be used for work above 10 GPa, where the more convenient liquid media can no longer effectively operate. Although these materials crystallise at pressures of 1.9, 3 and 11.8 GPa, respectively, they behave as pseudo-hydrostatic media well beyond these limits due to their low shear strengths.[142,143,149] However, cryogenic gas loading is technically much more difficult and requires more equipment than loading with liquids or oils.[140,142,143]

The pressure generated within the DAC is most commonly measured by recording the fluorescence spectrum of a ruby chip placed in the sample chamber alongside the sample (Fig. 1.19).[139,142,143] Rubies fluoresce and display two lines at 692.7 nm (R2) and 694.2 nm (R1) at atmospheric pressure; these lines shift linearly to higher wavelengths with increasing pressure, providing an internal gauge to the pressure inside the cell.[140] By placing more than one ruby chip or sphere inside the sample

chamber, the pressure can be measured in multiple locations across the cell and an average value calculated, minimising any inaccuracies across the cell due to variations in pressure (Fig. 1.19). The comparatively small size of the rubies relative to the sample means that the rubies do not diffract strongly enough the contaminate the diffraction pattern of the sample. The fluorescence of Ruby has been calibrated up to 180 GPa,[142] however, the R1 and R2 shifts are sensitive to both non-hydrostatic conditions and temperature, which can cause systematic errors for overheated samples.[139,150] Alternative fluorescent pressure probes such as yttrium aluminium garnate have a lower temperature dependency compared to ruby, so can be useful pressure markers for low temperature HP-XRD experiments.[151]

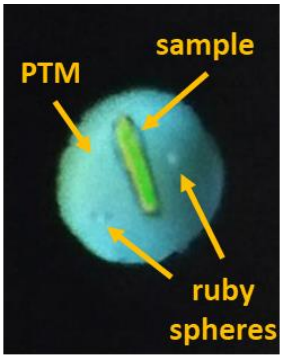

Figure 1.19 – Internal view of the sample chamber under a microscope. The gasket hole diameter is approximately 300 μm.

Pressure determination can also be achieved through use of an internal diffraction standard whose equation of state is known, such as NaCl or quartz.[139] Since the diffraction pattern of the reference is measured simultaneously with that of the sample, these materials typically possess small volume, high symmetry unit cells so as to minimise the contamination of the diffraction pattern. The measured unit cell parameters of the reference can then be converted into the corresponding pressures – this is a convenient method of pressure measurement for high pressure powder X-ray diffraction (HP-PXRD) studies.[140] Drawbacks to this method are that both the sample and the reference must be inert to the PTM and two diffraction patterns must be indexed and separated during data reduction, increasing the risk of sample reflections being contaminated.[152]

1.3.2 – Limitations of HP-XRD

The main limitation of high pressure crystallography is the restriction of accessible reciprocal space due to the body of the DAC; the completeness and redundancy of the data is greatly reduced compared to a standard collection.[139,142,143] Incomplete datasets hinder the accurate location of atomic coordinates and lower the data-to-parameter ratio, consequently increasing uncertainties associated with the final refinement. A crystallographer may attempt to improve the both data-to-parameter and signal to noise statistics by collecting to high redundancy and refining all non-hydrogen atoms isotropically.

By convention, the highest resolution achievable in a crystallographic experiment is given by the minimum value of d, which corresponds to a maximum observable angle of θ and a resolution of $\lambda/2$ of the incident radiation (as dictated by Bragg's law).[153] In other words, by using a shorter wavelength, the d-spacing values can be compressed to lower scattering angles – the implications of this for HP-XRD studies is that a larger amount of reciprocal space may be sampled by using shorter wavelength radiation sources.

The Ewald sphere is a geometric construction that describes the relationship between the wavevector of the incident and diffracted radiation and the reciprocal lattice. Since the incident wave vector, K_i, whose length is $1/\lambda$, is elastically scattered by the crystal, the diffracted wave vector, K_f, must have the same wavelength as K_i. Since $K_i = K_f$, the scattering vector, ΔK, must lie on the surface of a sphere with a radius equal to $1/\lambda$. This sphere is referred to as the Ewald sphere, and it denotes the conditions required to observe diffraction (Fig. 1.20). As a crystal is rotated in real space, the reciprocal lattice also rotates - diffraction occurs whenever the reciprocal lattice points touch the surface of the Ewald sphere. The size of the Ewald sphere can be increased by using shorter wavelength radiation, since the radius of the sphere is equal to $1/\lambda$. With a larger Ewald sphere, more lattice points will coincide with the surface of the sphere as the crystal rotates, corresponding to more diffraction events for a given scattering angle.[153]

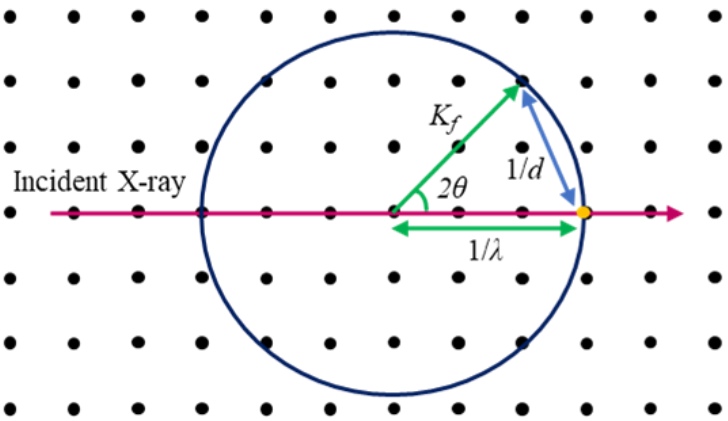

Figure 1.20 – Schematic of the Ewald sphere, denoting the incident X-ray beam in maroon, the diffracted wave vector, K_f, and its magnitude (1/λ) in green, the origin in reciprocal space in orange, the surface of the sphere in navy and the scattering vector (1/*d*) in blue.

The implication of this in real space is that shorter wavelengths have smaller scattering angles, so when considering the limited opening angle of a DAC, a larger proportion of unique reflections may be collected for a given 2θ range. However, even when short wavelength radiation is used, in extreme cases, completeness can be as low as 20% for a monoclinic cell.[142] Higher symmetry systems will of course inherently give higher data completeness due to the total number of unique reflections requiring collection being located in a smaller wedge of reciprocal space.

Another commonly encountered difficulty is solving incomplete data. Dual-space solution methods such as charge flipping algorithms typically require a certain level of completeness in order to solve structures, so alternative solution methods are sometimes required for high pressure data, such as the Patterson synthesis.[154,155] Assuming that no phase transitions or other such phenomena have occurred, isomorphous replacement can be an effective solution method for high pressure datasets, particularly for more complex structures containing large numbers of atoms.[156] Atomic coordinates are directly imported into the .ins file for the high pressure dataset, which have been harvested from an appropriate starting model (typically a previous dataset collected at ambient or lower pressures). Data quality can also suffer from gasket powder rings and diamond reflections, though their impact can

be mitigated by rejection of specific reflections during data reduction by identifying inconsistencies in intensities and/or peak profiles.[143]

1.4 – Overview and project aims

Oxidative addition is a key step in most transition metal-mediated catalytic cycles. However, intermediates of such processes are transient and, therefore, challenging to study in solution. Mechanisms are typically determined through spectroscopic analysis of product distributions as opposed to direct and continuous structural elucidation along the reaction coordinate. The solid-state has become more attractive to chemists in recent years as a reaction medium since it overcomes certain shortcomings of solution phase chemistry, such as eliminating the opportunity for competing reaction pathways involving solvent molecules to occur. Furthermore, the solid-state provides access to arguably unrivalled structural elucidation techniques, such as single crystal XRD.

The overarching aim of this project was to study oxidative addition reactions of organometallic complexes in the solid-state and monitor the transformations using crystallographic methods. More specifically, it was hypothesised that OA could be mechanically induced with pressure and monitored by HP-XRD, allowing specific structural features to be correlated to corresponding chemical behaviour (Fig. 1.21). Elucidating structure-activity relationships would improve our understanding of how to facilitate OA, subsequently improving the targeted design of future bond activation catalysts.

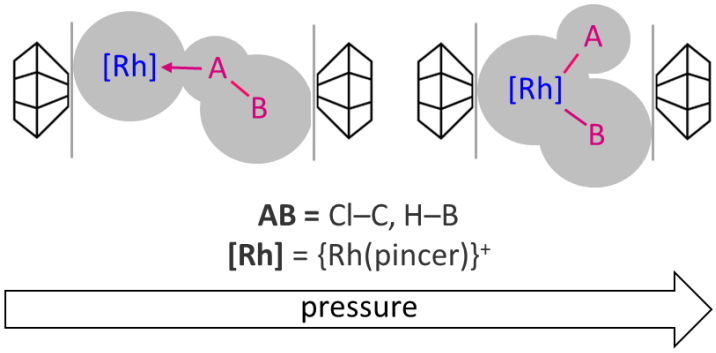

Figure 1.21 – The main project aim.

In order to study OA in the solid-state as proposed, complexes need to be prepared and isolated which are on the precipice of bond activation. Rhodium(I) pincer complexes were chosen for investigation because they are versatile complexes capable of facilitating the activation of chemically robust bonds and stabilising weakly coordinating small molecules. Both of these characteristics are important to preserve, since the substrate containing the bond of interest needs to be bound to the metal centre yet remain intact under ambient conditions.

Although pressure has not been used to induce OA in coordination complexes before, the feasibility of such studies have already been established with simple inorganics such as $Cs_2[PdX_4]\cdot I_2$ (X = Cl, **A76**; Br, **A77**; I, **A78**) and $CsAu_2Cl_6$, **A79**, which exhibit pressure-induced redox behaviour as observed by HP-PXRD and HP-XRD, respectively.[157,158] However, I aim to investigate more catalytically relevant systems involving rhodium pincer complexes. The work towards this goal is herein presented, encompassing the first systematic investigations of mononuclear rhodium pincer complexes by HP-XRD and a range of interesting pressure, temperature and gas-induced SC-SC transformations.

References

1. S. Warsink, P. D. Riekert Kotze, J. M. I. Janse van Rensburg, J. A. Venter, S. Otto, E. Botha and A. Roodt, *Eur. J. Inorg. Chem.*, 2018, 3615-3625.
2. I. Göttker-Schnetmann, P. White and M. Brookhart, *J. Am. Chem. Soc.*, 2004, **126**, 1804-1811.
3. S. D. Timpa, C. J. Pell and O. V. Ozerov, *J. Am. Chem. Soc.*, 2014, **136**, 14772-14779.
4. A. I. McKay, A. J. Bukvic, B. E. Tegner, A. L. Burnage, A. J. Marti Nez-Marti Nez, N. H. Rees, S. A. Macgregor and A. S. Weller, *J. Am. Chem. Soc.*, 2019, **141**, 11700-11712.
5. J.-P. Corbet and G. Mignani, *Chem. Rev.*, 2006, **106**, 2651−2710.
6. C. Gosmini, J. M. Begouin and A. Moncomble, *Chem. Commun.*, 2008, 3221-3233.
7. A. Suzuki, *J. Org. Chem.*, 2002, **653**, 83-90.
8. K. Juhász, Á. Magyar and Z. Hell, *Synth.*, 2020, **53**, 983-1002.
9. J. A. Labinger, *Organometallics*, 2015, **34**, 4784-4795.
10. V. W. Bowry and K. U. Ingold, *J. Am. Chem. Soc.*, 1991, **113**, 5699-5707.
11. J. Breitenfeld, J. Ruiz, M. D. Wodrich and X. Hu, *J. Am. Chem. Soc.*, 2013, **135**, 12004-12012.
12. R. H. Crabtree, *The Organometallic Chemistry of the Transition Metals: Oxidative Addition and Reductive Elimination.*, Wiley, 6th edn., 2014.
13. E. Peris and R. H. Crabtree, *Chem. Soc. Rev.*, 2018, **47**, 1959-1968.
14. E. Ben-Ari, R. Cohen, M. Gandelman, L. J. W. Shimon, J. M. L. Martin and D. Milstein, *Organometallics*, 2006, **25**, 3190-3210.
15. E. Ben-Ari, M. Gandelman, H. Rozenberg, L. J. W. Shimon and D. Milstein, *J. Am. Chem. Soc.*, 2003, **125**, 4714-4715.
16. O. V. Ozerov, C. Guo, V. A. Papkov and B. M. Foxman, *J. Am. Chem. Soc.*, 2004, **126**, 4792-4793.
17. S. Chakraborty, J. A. Krause and H. Guan, *Organometallics*, 2009, **28**, 582–586.
18. M. R. Gyton, T. M. Hood and A. B. Chaplin, *Dalton Trans.*, 2019, **48**, 2877-2880.
19. M. R. Gyton, B. Leforestier and A. B. Chaplin, *Angew. Chem. Int. Ed.*, 2019, **58**, 15295-15298.
20. M. Gupta, C. Hagen, R. J. Flesher, W. C. Kaska and C. M. Jensen, *Chem. Commun.*, 1996, 2083-2084.
21. M. Gagliardo, P. A. Chase, S. Brouwer, G. P. M. v. Klink and G. v. Koten, *Organometallics*, 2007, **26**, 2219-2227.
22. M. Ohff, A. Ohff, M. E. v. d. Boom and D. Milstein, *J. Am. Chem. Soc.*, 1997, **119**, 11687-11688.
23. D. Olsson, P. Nilsson, M. El Masnaouy and O. F. Wendt, *Dalton Trans.*, 2005, 1924-1929.
24. A. Castonguay, D. M. Spasyuk, N. Madern, A. L. Beauchamp and D. Zargarian, *Organometallics*, 2009, **28**, 2134–2141.
25. F. Liu and A. S. Goldman, *Chem. Commun.*, 1999, 655–656.
26. J. Choi, D. Y. Wang, S. Kundu, Y. Choliy, T. J. Emge, K. Krogh-Jespersen and A. S. Goldman, *Science*, 2011, **332**, 1545-1548.
27. C. Gaviglio, J. Pellegrino, D. Milstein and F. Doctorovich, *Dalton Trans.*, 2017, **46**, 16878-16884.
28. S. Park and M. Brookhart, *Organometallics*, 2010, **29**, 6057-6064.
29. K. J. Jonasson and O. F. Wendt, *Chem. Eur. J.*, 2014, **20**, 11894-11902.
30. Y. Sun, X. Li and H. Sun, *Inorg. Chim. Acta*, 2014, **415**, 95-97.
31. M. Mastalir, B. Stoger, E. Pittenauer, G. Allmaier and K. Kirchner, *Org. Lett.*, 2016, **18**, 3186-3189.
32. L. Fan, B. M. Foxman and O. V. Ozerov, *Organometallics*, 2004, **23**, 326-328.

33. W. Weng, C. Guo, R. Celenligil-Cetin, B. M. Foxman and O. V. Ozerov, *Chem. Commun.*, 2006, 197-199.
34. J. Borau-Garcia, D. V. Gutsulyak, R. J. Burford and W. E. Piers, *Dalton Trans.*, 2015, **44**, 12082-12085.
35. V. Pandarus and D. Zargarian, *Organometallics*, 2007, **26**, 4321-4334.
36. D. S. McGuinness, P. Wasserscheid, W. Keim, C. Hu, U. Englert, J. T. Dixon and C. Grove, *Chem. Commun.*, 2003, 334-335.
37. C. Gunanathan, Y. Ben-David and D. Milstein, *Science*, 2007, **317**, 790-792.
38. J. Zhang, G. Leitus, Y. Ben-David and D. Milstein, *Angew. Chem. Int. Ed.*, 2006, **45**, 1113-1115.
39. G. M. Adams, F. M. Chadwick, S. D. Pike and A. S. Weller, *Dalton Trans.*, 2015, **44**, 6340-6342.
40. M. Findlater, K. M. Schultz, W. H. Bernskoetter, A. Cartwright-Sykes, D. M. Heinekey and M. Brookhart, *Inorg. Chem.*, 2012, **51**, 4672-4678.
41. M. Vogt, A. Nerush, Y. Diskin-Posner, Y. Ben-David and D. Milstein, *Chem. Sci.*, 2014, **5**, 2043-2051.
42. M. A. Goni, E. Rosenberg, R. Gobetto and M. Chierotti, *J. Org. Chem.*, 2017, **845**, 213-228.
43. S. Kuriyama, K. Arashiba, K. Nakajima, H. Tanaka, N. Kamaru, K. Yoshizawa and Y. Nishibayashi, *J. Am. Chem. Soc.*, 2014, **136**, 9719-9731.
44. M. L. Scheuermann, S. P. Semproni, I. Pappas and P. J. Chirik, *Inorg. Chem.*, 2014, **53**, 9463-9465.
45. N. H. Anderson, J. M. Boncella and A. M. Tondreau, *Chem. Eur. J.*, 2017, **23**, 13617-13622.
46. C. Lescot, S. Savourey, P. Thuéry, G. Lefèvre, J.-C. Berthet and T. Cantat, *C. R. Chimie*, 2016, **19**, 57-70.
47. A. D. Smith, A. Saini, L. M. Singer, N. Phadke and M. Findlater, *Polyhedron*, 2016, **114**, 286-291.
48. K. Lee, H. Wei, A. V. Blake, C. M. Donahue, J. M. Keith and S. R. Daly, *Dalton Trans.*, 2016, **45**, 9774-9785.
49. T. M. Hood, B. Leforestier, M. R. Gyton and A. B. Chaplin, *Inorg. Chem.*, 2019, **58**, 7593-7601.
50. M. Feller, E. Ben-Ari, T. Gupta, L. J. W. Shimon, G. Leitus, Y. Diskin-Posner, L. Weiner and D. Milstein, *Inorg. Chem.*, 2007, **46**, 10479−10490.
51. S. Tang and D. Milstein, *Chem. Sci.*, 2019, **10**, 8990-8994.
52. J. I. van der Vlugt and J. N. Reek, *Angew. Chem. Int. Ed.*, 2009, **48**, 8832-8846.
53. Y. Wang, B. Zheng, Y. Pan, C. Pan, L. He and K. W. Huang, *Dalton Trans.*, 2015, **44**, 15111-15115.
54. D. Hermann, M. Gandelman, H. Rozenberg, L. J. W. Shimon and D. Milstein, *Organometallics*, 2002, **21**, 812-818.
55. T. Yano, Y. Moroe, M. Yamashita and K. Nozaki, *Chem. Lett.*, 2008, **37**, 1300-1301.
56. K. S. Lokare, R. J. Nielsen, M. Yousufuddin, W. A. Goddard III and R. A. Periana, *Dalton Trans.*, 2011, **40**, 9094-9097.
57. W. H. Bernskoetter, S. K. Hanson, S. K. Buzak, Z. Davis, P. S. White, R. Swartz, K. I. Goldberg and M. Brookhart, *J. Am. Chem. Soc.*, 2009, **131**, 8603–8613.
58. J. Campos, S. Kundu, D. R. Pahls, M. Brookhart, E. Carmona and T. R. Cundari, *J. Am. Chem. Soc.*, 2013, **135**, 1217-1220.
59. C. G. Royle, L. Sotorrios, M. R. Gyton, C. N. Brodie, A. L. Burnage, S. K. Furfari, A. Marini, M. R. Warren, S. A. Macgregor and A. S. Weller, *Organometallics*, 2022, **41**, 3270–3280.

60. B. S. Omar, J. Mallah, M. Ataya, B. Li, X. Zhou, S. Malakar, A. S. Goldman and F. Hasanayn, *Inorg. Chem.*, 2018, **57**, 7516-7523.
61. W. H. Bernskoetter, C. K. Schauer, K. I. Goldberg and M. Brookhart, *Science*, 2009, **326**, 553-556.
62. M. D. Walter, P. S. White, C. K. Schauer and M. Brookhart, *J. Am. Chem. Soc.*, 2013, **135**, 15933-15947.
63. I. Bustos, Z. Freixa, A. Pazos, C. Mendicute-Fierro and M. A. Garralda, *Eur. J. Inorg. Chem.*, 2021, **2021**, 3131-3138.
64. I. Bustos, J. M. Seco, A. Rodríguez-Diéguez, M. A. Garralda and C. Mendicute-Fierro, *Inorg. Chim. Acta*, 2019, **498**, 119165.
65. A. B. Chaplin and A. S. Weller, *Angew. Chem. Int. Ed.*, 2010, **49**, 581-584.
66. T. M. Douglas, A. B. Chaplin and A. S. Weller, *J. Am. Chem. Soc.*, 2008, **130**, 14432–14433.
67. J. Yang, P. S. White, C. K. Schauer and M. Brookhart, *Angew. Chem. Int. Ed.*, 2008, **47**, 4141-4143.
68. T. B. Marder and Z. Lin, *Contemporary Metal Boron Chemistry I*, Springer, 2008.
69. C. Mottillo and T. Friscic, *Molecules*, 2017, **22**, 144.
70. A. Chaudhary, A. Mohammad and S. M. Mobin, *Cryst. Growth Des.*, 2017, **17**, 2893-2910.
71. S. D. Pike, F. M. Chadwick, N. H. Rees, M. P. Scott, A. S. Weller, T. Kramer and S. A. Macgregor, *J. Am. Chem. Soc.*, 2015, **137**, 820-833.
72. L. E. Hatcher, *CrystEngComm*, 2016, **18**, 4180-4187.
73. S. M. Mobin and A. Mohammad, *Dalton Trans.*, 2014, **43**, 13032-13040.
74. A. B. Chaplin, J. C. Green and A. S. Weller, *J. Am. Chem. Soc.*, 2011, **133**, 13162-13168.
75. L. Cao, J. Tao, Q. Gao, T. Liu, Z. Xia and D. Li, *Chem. Commun.*, 2014, **50**, 1665-1667.
76. H. E. Mason, W. Li, M. A. Carpenter, M. L. Hamilton, J. A. K. Howard and H. A. Sparkes, *New J. Chem.*, 2016, **40**, 2466-2478.
77. A. J. Bukvic, D. G. Crivoi, H. G. Garwood, A. I. McKay, T. T. D. Chen, A. J. Martinez-Martinez and A. S. Weller, *Chem. Commun.*, 2020, **56**, 4328-4331.
78. F. M. Chadwick, N. H. Rees, A. S. Weller, T. Kramer, M. Iannuzzi and S. A. Macgregor, *Angew. Chem. Int. Ed.*, 2016, **55**, 3677-3681.
79. A. J. Martinez-Martinez, B. E. Tegner, A. I. McKay, A. J. Bukvic, N. H. Rees, G. J. Tizzard, S. J. Coles, M. R. Warren, S. A. Macgregor and A. S. Weller, *J. Am. Chem. Soc.*, 2018, **140**, 14958-14970.
80. A. J. Martinez-Martinez, C. G. Royle, S. K. Furfari, K. Suriye and A. S. Weller, *ACS Catal.*, 2020, **10**, 1984-1992.
81. S. I. Bezzubov, P. Kalle, A. A. Bilyalova, S. V. Tatarin and V. D. Dolzhenko, *Chem. Eur. J.*, 2018, **24**, 12779-12783.
82. M. Albrecht, M. Lutz, A. L. Spek and G. v. Koten, *Nature*, 2000, **406**, 970-974.
83. Z. Huang, P. S. White and M. Brookhart, *Nature*, 2010, **465**, 598-601.
84. O. V. Zenkina, E. C. Keske, R. Wang and C. M. Crudden, *Angew. Chem. Int. Ed.*, 2011, **50**, 8100-8104.
85. S. Dutta, D. K. Bucar, E. Elacqua and L. R. MacGillivray, *Chem. Commun.*, 2013, **49**, 1064-1066.
86. R. Medishetty, S. C. Sahoo, C. E. Mulijanto, P. Naumov and J. J. Vittal, *Chem. Mater.*, 2015, **27**, 1821-1829.
87. Q. Chu, D. C. Swenson and L. R. MacGillivray, *Angew. Chem. Int. Ed.*, 2005, **44**, 3569-3572.
88. G. S. Papaefstathiou, Z. Zhong, L. Geng and L. R. MacGillivray, *J. Am. Chem. Soc.*, 2004, **126**, 9158-9159.

89. Y. F. Han, Y. J. Lin, W. G. Jia, G. L. Wang and G. X. Jin, *Chem. Commun.*, 2008, 1807-1809.
90. T. Seki, K. Sakurada, M. Muromoto and H. Ito, *Chem. Sci.*, 2015, **6**, 1491-1497.
91. B. C. Tzeng and A. Chao, *Chem. Eur. J.*, 2015, **21**, 2083-2089.
92. M. R. Warren, S. K. Brayshaw, L. E. Hatcher, A. L. Johnson, S. Schiffers, A. J. Warren, S. J. Teat, J. E. Warren, C. H. Woodall and P. R. Raithby, *Dalton Trans.*, 2012, **41**, 13173-13179.
93. L. E. Hatcher, J. M. Skelton, M. R. Warren, C. Stubbs, E. L. da Silva and P. R. Raithby, *Phys. Chem. Chem. Phys.*, 2018, **20**, 5874-5886.
94. L. E. Hatcher, M. R. Warren, D. R. Allan, S. K. Brayshaw, A. L. Johnson, S. Fuertes, S. Schiffers, A. J. Stevenson, S. J. Teat, C. H. Woodall and P. R. Raithby, *Angew. Chem. Int. Ed.*, 2011, **50**, 8371-8374.
95. S. M. Mobin, A. K. Srivastava, P. Mathur and G. K. Lahiri, *Dalton Trans.*, 2010, **39**, 1447-1449.
96. Y. Zhu, F. Luo, M. B. Luo, X. F. Feng, S. R. Batten, G. M. Sun, S. J. Liu and W. Y. Xu, *Dalton Trans.*, 2013, **42**, 8545-8548.
97. R. J. Wei, Q. Huo, J. Tao, R. B. Huang and L. S. Zheng, *Angew. Chem. Int. Ed.*, 2011, **50**, 8940-8943.
98. W. Weng, C. Guo, C. Moura, L. Yang, B. M. Foxman and O. V. Ozerov, *Organometallics*, 2005, **24**, 3487-3499.
99. J. Sundberg, L. J. Cameron, P. D. Southon, C. J. Kepert and C. J. McKenzie, *Chem. Sci.*, 2014, **5**, 4017-4025.
100. T. M. Boyd, B. Tegner, G. Tizzard, A. Martinez-Martinez, S. Neale, M. Hayward, S. Coles, S. Macgregor and A. S. Weller, *Angew. Chem. Int. Ed.*, 2020, **59**, 6177-6181.
101. S. D. Pike and A. S. Weller, *Philos. Trans. R. Soc. A*, 2015, **373**, 20140187.
102. H. L. Wong, D. R. Allan, N. R. Champness, J. McMaster, M. Schröder and A. J. Blake, *Angew. Chem. Int. Ed.*, 2013, **52**, 5093-5095.
103. P. L. Arnold, A. Prescimone, J. H. Farnaby, S. M. Mansell, S. Parsons and N. Kaltsoyannis, *Angew. Chem. Int. Ed.*, 2015, **54**, 6735-6739.
104. N. Casati, P. Macchi and A. Sironi, *Angew. Chem. Int. Ed.*, 2005, **44**, 7736-7739.
105. J. P. Tidey, H. L. Wong, J. McMaster, M. Schröder and A. J. Blake, *Acta Cryst.*, 2016, **B72**, 357-371.
106. G. A. Craig, A. Sarkar, C. H. Woodall, M. A. Hay, K. E. R. Marriott, K. V. Kamenev, S. A. Moggach, E. K. Brechin, S. Parsons, G. Rajaraman and M. Murrie, *Chem. Sci.*, 2018, **9**, 1551-1559.
107. C. H. Woodall, C. M. Beavers, J. Christensen, L. E. Hatcher, M. Intissar, A. Parlett, S. J. Teat, C. Reber and P. R. Raithby, *Angew. Chem. Int. Ed.*, 2013, **52**, 9691-9694.
108. K. W. Galloway, S. A. Moggach, P. Parois, A. R. Lennie, J. E. Warren, E. K. Brechin, R. D. Peacock, R. Valiente, J. González, F. Rodríguez, S. Parsons and M. Murrie, *CrystEngComm*, 2010, **12**, 2516-2519.
109. D. R. Allan, A. J. Blake, D. Huang, T. J. Prior and M. Schröder, *Chem. Commun.*, 2006, 4081-4083.
110. I. E. Collings and A. L. Goodwin, *J. Appl. Phys.*, 2019, **126**, 181101.
111. R. M. Hazen, T. C. Hoering and A. M. Hofmeister, *J. Phys. Chem.*, 1987, **91**, 5042-5045.
112. E. V. Boidyreva, D. Y. Naumov and H. Ahsbahs, *J. Struc. Chem.*, 1998, **39**, 350-361.
113. C. Roux, D. M. Adams, J. P. Itié, A. Polian, D. N. Hendrickson and M. Verdaguer, *Inorg. Chem.*, 1996, **35**, 2846-2852.
114. S. R. Madsen, J. Overgaard, D. Stalke and B. B. Iversen, *Dalton Trans.*, 2015, **44**, 9038-9043.

115. F. P. A. Fabbiani, G. Buth, B. Dittrich and H. Sowa, *CrystEngComm*, 2010, **12**, 2541-2550.
116. A. L. Spek, *Acta Cryst.*, 2015, **C71**, 9-18.
117. A. A. Yakovenko, K. W. Chapman and G. J. Halder, *Acta Cryst.*, 2015, **B71**, 252-257.
118. C. Roux, J. Zarembowitch, J. P. Itié, M. Verdaguer, E. Dartyge, A. Fontaine and H. Tolentino, *Inorg. Chem.*, 1991, **30**, 3174-3179.
119. J. P. Tidey, H. L. S. Wong, M. Schröder and A. J. Blake, *Coord. Chem. Rev.*, 2014, **277-278**, 187-207.
120. T. M. Francisco, W. J. Gee, H. J. Shepherd, M. R. Warren, D. A. Shultz, P. R. Raithby and C. B. Pinheiro, *J. Phys. Chem. Lett.*, 2017, **8**, 4774-4778.
121. K. L. Bray, H. G. Drickamer, D. M. P. Mingos, M. J. Watson and J. R. Shapley, *Inorg. Chem.*, 1991, **30**, 864-866.
122. M. Sundareswari and M. Rajagopalan, *Phys. B*, 2008, **403**, 2530-2541.
123. M. Tkacz, *J. Chem. Phys.*, 1998, **108**, 2084-2087.
124. K. Niwa, D. Dzivenko, K. Suzuki, R. Riedel, I. Troyan, M. Eremets and M. Hasegawa, *Inorg. Chem.*, 2014, **53**, 697-699.
125. T. Scheler, M. Marques, Z. Konopkova, C. L. Guillaume, R. T. Howie and E. Gregoryanz, *Phys. Rev. Lett.*, 2013, **111**, 215503.
126. H. Benjamin, J. G. Richardson, S. A. Moggach, S. Afanasjevs, L. Warren, M. R. Warren, D. R. Allan, C. A. Morrison, K. V. Kamenev and N. Robertson, *Phys. Chem. Chem. Phys.*, 2020, **22**, 6677-6689.
127. K. Takeda, I. Shirotani and K. Yakushi, *Chem. Mater.*, 2000, **12**, 912-916.
128. K. Takeda, I. Shirotani, J. Hayashi, H. Fukuda and K. Ito, *Mol. Cryst. and Liq. Cryst.*, 2006, **452**, 113-122.
129. N. Bajaj, H. Bhatt, K. K. Pandey, H. K. Poswal, A. Arya, P. S. Ghosh, N. Garg and M. N. Deo, *CrystEngComm*, 2018, **20**, 3728-3740.
130. S. A. Moggach, K. W. Galloway, A. R. Lennie, P. Parois, N. Rowantree, E. K. Brechin, J. E. Warren, M. Murrie and S. Parsons, *CrystEngComm*, 2009, **11**, 2601-2604.
131. A. Prescimone, J. Sanchez-Benitez, K. K. Kamenev, S. A. Moggach, J. E. Warren, A. R. Lennie, M. Murrie, S. Parsons and E. K. Brechin, *Dalton Trans.*, 2010, 113-123.
132. C. Wegeberg and O. S. Wenger, *JACS Au*, 2021, **1**, 1860-1876.
133. C. H. Woodall, S. Fuertes, C. M. Beavers, L. E. Hatcher, A. Parlett, H. J. Shepherd, J. Christensen, S. J. Teat, M. Intissar, A. Rodrigue-Witchel, Y. Suffren, C. Reber, C. H. Hendon, D. Tiana, A. Walsh and P. R. Raithby, *Chem. Eur. J.*, 2014, **20**, 16933-16942.
134. A. E. O'Connor, N. Mirzadeh, S. K. Bhargava, T. L. Easun, M. Schröder and A. J. Blake, *Chem. Commun.*, 2016, **52**, 6769-6772.
135. A. N. Price, V. Berryman, T. Ochiai, J. J. Shephard, S. Parsons, N. Kaltsoyannis and P. L. Arnold, *Nat. Commun.*, 2022, **13**, 3931.
136. J. J. Shephard, V. E. J. Berryman, T. Ochiai, O. Walter, A. N. Price, M. R. Warren, P. L. Arnold, N. Kaltsoyannis and S. Parsons, *Nat. Commun.*, 2022, **13**, 5923.
137. J. E. Schirber, B. Morosin, R. W. Alkire, A. C. Larson and P. J. Vergamini, *Phys. Rev. B*, 1984, **29**, 4150-4152.
138. D. R. Allan, S. J. Coles, K. George, M. Jura, W. Levason, G. Reid, C. Wilson and W. Zhang, *CrystEngComm*, 2014, **16**, 8169-8176.
139. A. Katrusiak, *Acta Cryst.*, 2008, **A64**, 135-148.
140. R. Lee, J. A. Howard, M. R. Probert and J. W. Steed, *Chem. Soc. Rev.*, 2014, **43**, 4300-4311.
141. R. J. Angel, N. L. Ross, I. G. Wood and P. A. Woods, *Phase Transitions*, 2006, **39**, 13-32.
142. S. A. Moggach, S. Parsons and P. A. Wood, *Crystallogr. Rev.*, 2008, **14**, 143-184.

143. S. A. Moggach and S. Parsons, in *Spectroscopic Properties of Inorganic and Organometallic Compounds*, RSC publishing, 2009, vol. 40, ch. 11, pp. 324-354.
144. B. W. Matthews, *Proc. Natl. Acad. Sci. U. S. A.*, 2012, **109**, 6792-6793.
145. S. A. Moggach, D. R. Allan, S. Parsons and J. E. Warren, *J. Appl. Cryst.*, 2008, **41**, 249-251.
146. T. Varga, A. P. Wilkinson and R. J. Angel, *Rev. Sci. Instrum.*, 2003, **74**, 4564-4566.
147. K. Yokogawa, K. Murata, H. Yoshino and S. Aoyama, *Jpn. J. Appl. Phys.*, 2007, **46**, 3636-3639.
148. Keizo Murata and S. Aoki, *Rev. High Press. Sci. Technol.*, 2016, **26**, 3-7.
149. S. Klotz, J. C. Chervin, P. Munsch and G. Le Marchand, *J. Phys. D: Appl. Phys.*, 2009, **42**.
150. D. M. Adams, R. Appleby and S. K. Sharma, *J. Phys. E Sci. Instrum.*, 1976, **9**, 1140-1144.
151. C. Beyer, A. V. Kurnosov, T. B. Ballaran and D. J. Frost, *Phys. Chem. Miner.*, 2021, **48**, 17.
152. C. A. Cameron, Doctor of Philosophy, University of Edinburgh, 2014.
153. A. J. Blake, W. Clegg, J. M. Cole, J. S. O. Evans, P. Main, S. Parsons and D. J. Watkin, *Crystal Structure Analysis Principles and Practice*, Oxford University Press, second edn., 2009.
154. L. Palatinus, *Acta Cryst.*, 2013, **B69**, 1-16.
155. L. Palatinus, W. Steurer and G. Chapuis, *J. Appl. Cryst.*, 2007, **40**, 456-462.
156. J. P. Tidey, Doctor of Philosphy, University of Nottingham, 2016.
157. P. Heines, H.-L. Keller, M. Armbrüster, U. Schwarz and J. Tse, *Inorg. Chem.*, 2006, **45**, 9818−9825.
158. W. Denner, H. Schulz and H. D'Amour, *Acta Cryst.*, 1979, **A35**, 360-365.

Chapter 2 – C–Cl bond activation by a {Rh(PONOP)}$^+$ pincer complex

Abstract

Motivated by the prospect of inducing C–Cl bond oxidative addition in the solid-state, straightforward procedures for the synthesis of rhodium(I) κ_{Cl}-chlorocarbon complexes of the form [Rh(PONOP)(κ_{Cl}–ClR)][BAr$^F{}_4$] (PONOP = 2,6-bis(di-*tert*-butylphosphinito)pyridine; Ar^F = 3,5-bis(trifluoromethyl)phenyl; R = Ph, **1**; CH_2Cl, **A**; Cy, **5**; ^{t}Bu, **7**; CH_2CH_2Cl, **8**; ^{i}Pr, **9**) have been developed. This approach enabled the isolation and crystallographic characterisation of complexes **A**, **1**, **5**, **8** and **9**.

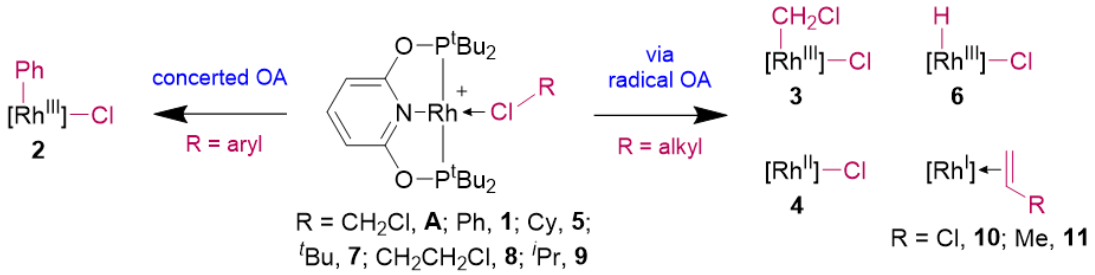

Experimental evidence indicated a concerted C(sp^2)–Cl bond oxidative addition mechanism was in operation when solutions of **1** where heated, whereas C(sp^3)–Cl bond activation of chloroalkyl adducts of {Rh(PONOP)}$^+$ were proposed to proceed via radical mechanisms that involved generation of the rhodium(II) metalloradical [Rh(PONOP)Cl][BAr$^F{}_4$], **4**. Net dehydrochlorination affording [Rh(PONOP)(H)Cl][BAr$^F{}_4$], **6**, and an alkene by-product resulted from chlorocyclohexane and 2-chloro-2-methylpropane solutions of the respective {Rh(PONOP)}$^+$ adducts by means of hydrogen atom abstraction from the corresponding alkyl radicals by **4**. Similar reactivity was observed in complexes **4** and **5**, although dehydrochlorination did not proceed cleanly.

When **A** was heated in dichloromethane in the absence of light, [Rh(PONOP)(CH_2Cl)Cl][BAr$^F{}_4$], **3**, was formed as the major product. This reactivity was masked when conducted in light by facile photo-induced reductive elimination of dichloromethane from **3**. OA was also accessible in solid-state samples of **A**. HP-XRD studies on two separate polymorphs of **A** were undertaken to assess whether OA could be induced by pressure as well as temperature, but pressure-induced bond activation proved elusive.

2.1 – Introduction

Oxidative addition (OA) is a fundamental organometallic process that underpins a wide range of industrially important reactions. For example, the formation of C–C bonds in several cross-coupling reactions requires activation of the C–X bonds of organohalides (X = Cl, Br, I).[1-4] The increased C–Cl bond strength relative to its heavier halide counterparts, however, can often result in attenuated or divergent reactivity for chlorinated substrates.[5,6] Broadening the scope of chlorocarbon functionalisation would be beneficial for both academic and industrial purposes due to their lower cost and substrate diversity.

OA of C–Cl bonds have been widely reported on and have been shown to proceed via both concerted and radical mechanisms. Studies into selective C–X activation were initially dominated by zero-valent group 10 complexes where, typically, OA was found to proceed via concerted mechanisms.[7-12] There are, however, examples of one-electron bimetallic OA of alkyl halides and C–F activation of C_6F_6 initiated by group 10 pincer complexes that proceed via radical intermediates.[13,14] Pincer-type complexes are capable of promoting a vast array of reactions, many of which involve C–H and C–X activation.[15-17] As a result, the activation of C–Cl bonds by group 9 pincer-type complexes is a growing area of interest in the field of organometallics. Several examples of selective C–Cl activation by rhodium and iridium pincer complexes are known, although iridium examples are rarer (Fig. 2.1).[18-24]

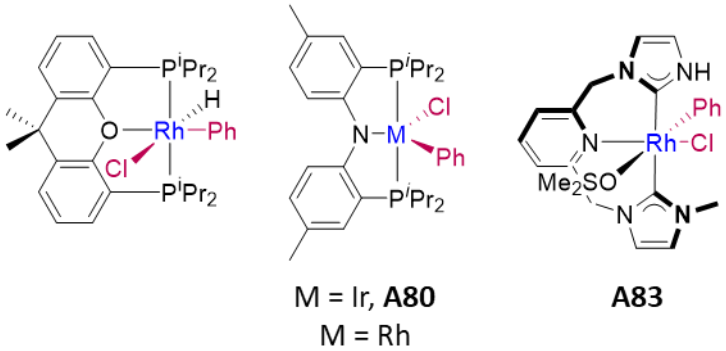

Figure 2.1 – Examples of chlorobenzene activated group 9 pincer complexes.[25-28]

Selective C–Cl activation can be challenging to achieve due to competitive alternative pathways. For example, activation of chlorobenzene by a neutral iridium complex to generate Ir(PNP*)(Ph)(Cl), **A80** (PNP* = bis[2-(di-*iso*-propylphosphino)-4-

methylphenyl]amido) was achieved in < 80 % purity via isomerisation of the *ortho*-C–H activated intermediate at elevated temperatures (60 °C; Fig. 2.1), indicating that although C–H activation was kinetically favourable, the C–Cl activated complex was the thermodynamic product.[26] Similar conclusions have been substantiated computationally for a structurally related iridium PNP-type complex by Hall and co-workers.[29]

A comparatively greater number of rhodium pincer complexes have been shown to selectively activate C(sp^2)–Cl bonds under both mild and moderate conditions via concerted mechnisms.[25,30] The structurally related rhodium complexes (PNP*)RhL_2 (L = Ph/Ph, **A81**; Ph/Me, **A82**) were later reported to demonstrate divergent reactivity, exclusively producing the C–Cl OA complex upon reductive elimination (RE) of L_2.[28] Chaplin and co-workers reported C–Cl bond activation in chlorobenzene by the N-heterocyclic carbene pincer complex [Rh(CNC-Me)($SOMe_2$)][$BAr^F{}_4$], **A83** (CNC-Me = 2,6-bis[(3-methylimidazolin-1-yl)methyl]pyridine) to generate the OA complex **A84** (Fig. 2.1), despite C–H activation being a competitive - yet ultimately endergonic - pathway by density functional theory (DFT) calculations ($\Delta\Delta G^{\ddagger}$ = +2.4 kcal mol^{-1}; Fig. 2.1).[27]

The OA of alkyl chlorides have also been investigated using group 9 pincer complexes, although a wider range of mechanisms have been proposed for the activation of such substrates. It is important to understand the mechanism by which OA occurs because competing mechanisms (*i.e.*, two-electron *vs*. radical pathways) can have unexpected effects on the outcome of a reaction and, therefore, obfuscate results. This was exemplified by the OA of dichloromethane to Rh(POP)Cl, **A85** (POP = 4,6-bis(di-*tert*-butylphosphino)dibenzo[*b*,*d*]furan), which was proposed to occur via a cascade of chloride abstraction and single-electron transfer steps in order to rationalise the formation of [Rh(POP)(=CH_2)][$BArF^{20}{}_4$], **A86** (Ar^{F20} = pentafluorophenyl), from the reaction of **A85** with K[$BArF^{20}{}_4$] in dichloromethane.[20]

Esteruelas and co-workers previously investigated the activation of chlorocarbons in Xantphos complexes (Xantphos = 9,9-dimethyl-4,5-bis(di-*iso*-propylphosphino)xanthene).[19,24] Concerted OA was achieved by RhCl(Xantphos), **A87**, which promoted C–Cl activation of chlorocyclohexane at elevated temperatures (100 °C), resulting in the formation of an unstable 6-coordinate alkyl intermediate

which subsequently underwent β-hydride elimination, affording $RhHCl_2$(Xantphos), **A88**, and cyclohexene. Catalytic dehydrochlorination of chlorocyclohexane was also demonstrated by this complex.[19] Contrastingly, competitive nucleophilic S_N2-type OA of dichloromethane to **A87** rationalised the presence of both *cis*- and *trans*-rhodium(III) dichloride products. The S_N2-type pathway has similarly been proposed for the OA of dichloromethane to Rh(PNP)Cl.[23]

Most relevant to the work herein, Weller and co-workers have previously compared the reaction outcomes between Rh(pincer)Cl (pincer = PONOP, PNP) and $Na[BAr^F{}_4]$ in dichloromethane.[31] The reaction between Rh(PONOP)Cl and $Na[BAr^F{}_4]$ generated the weakly bound and labile κ^1-$ClCH_2Cl$ adduct **A** cleanly (Scheme 2.1). However, upon crystallisation from CH_2Cl_2 solutions, samples of **A** were found to be contaminated with the dinitrogen adduct $[Rh(PONOP)(N_2)][BAr^F{}_4]$, **B**, due to the relative solubilities of CH_2Cl_2 and N_2 in the pentane antisolvent during the crystallisation process. In contrast, activation of dichloromethane was observed in the PNP analogue upon addition of $Na[BAr^F{}_4]$, affording a mixture of the OA product **C** and $[Rh(PNP)(H)Cl][BAr^F{}_4]$, **D**, amongst other undisclosed minor products (Scheme 2.1). A mechanism for the formation for $[Rh(PNP)(H)Cl][BAr^F{}_4]$ was not provided at the time by the authors, since several mechanistic pathways were deemed to be feasible, such as protonation of complexes by trace acid or decomposition of **C**.[31]

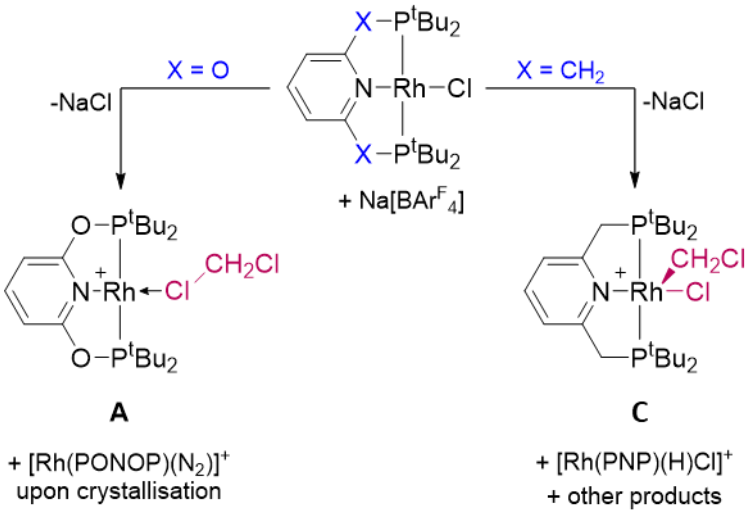

Scheme 2.1 – Reactions of $\{Rh(pincer)\}^+$ with $Na[BAr^F{}_4]$ in dichloromethane at room temperature. Anions omitted for clarity.

To date, only a handful of mononuclear rhodium complexes akin to **A** that feature a κ_{Cl}-CH_2Cl_2 ligand have been isolated as single crystals, four of which are pincer-type complexes; however, all reported examples are rhodium(III) species.[31-39] Similarly, [Rh($R_2PCH_2PR_2$)($\kappa_{Cl,Cl}$-$ClCH_2CH_2Cl$)][BAr^F_4] (R = ^{i}Pr, **A88**; ^{i}Bu, **A89**) are the only crystallographically characterised rhodium(I) examples of κ_{Cl}-dichloroethane complexes that can be found in the Cambridge Structural Database (CSD, v.5.43, update June 2022).[21,40,41]

With a view to investigating their onward reactivity, especially in connection to C–Cl bond activation in the solid-state, the isolation of new rhodium(I) κ_{Cl}-chlorocarbon complexes with general structure [Rh(PONOP)(κ_{Cl}–ClR)][BAr^F_4] (R = Ph, **1**; Cy, **6**; ^{t}Bu, **7**; CH_2CH_2Cl, **8**; ^{i}Pr, **9**; CH_2Cl, **A**) was pursued. It was hypothesised that compression of structures containing a weakly bound and partially activated Cl–C bond to a reactive rhodium(I) centre could engender OA. Reported herein are the solution-based reactivity of the chlorocarbon series **1**, **6**, **8** and **9**, along with a re-examination of the preparation and reactivity of **A**, which has been generated via an alternative synthetic route. The solid-state reactivity of **A** is also compared to its solution phase behaviour.

2.2 – Preparation and reactivity of [Rh(PONOP)(κ_{Cl}-ClPh)][BAr^F_4]

The rhodium(I) dimer [{Rh(PONOP)}$_2$(μ-η^2:η^2-COD)][BAr^F_4]$_2$, **A17b**, has previously been reported as an excellent precursor for the generation of weakly coordinated adducts of {Rh(PONOP)}$^+$ in solution by Chaplin and co-workers.[42,43] Building upon this existing methodology, the κ_{Cl}-chlorobenzene adduct **1** was synthesised by dissolution of isolated **A17b** in chlorobenzene at room temperature. Analysis of the solution by ^{1}H and ^{31}P{^{1}H} NMR spectroscopy after 6 h indicated the formation of an approximate 4:1 mixture of **1** (δ_{31P} 203.0, $^1J_{RhP}$ = 136 Hz) and [Rh(PONOP)(η^2-COD)][BAr^F_4] (δ_{31P} 202.3, $^1J_{RhP}$ = 135 Hz) alongside free cyclooctadiene (Scheme 2.2). Analytically pure material of **1** could be isolated in good yield (74 %) after two consecutive recrystallizations via liquid-liquid diffusion of hexane into the chlorobenzene solution at room temperature. Each subsequent recrystallisation encouraged preferential formation of the desired product through gradual removal of cyclooctadiene from the reaction mixture.

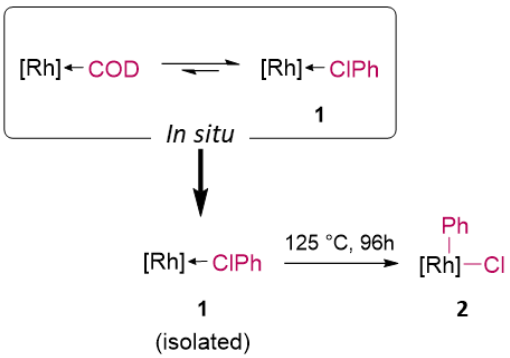

Scheme 2.2 – The synthesis and reactivity of **1**. Reactions were conducted in chlorobenzene at room temperature unless otherwise stated, [Rh] = [Rh(PONOP)][BAr^F_4].

Facile ligand exchange in **1** (*vide infra*) limited the solvent scope of **1** since it was only stable in neat chlorobenzene. As a result, characterisation by NMR spectroscopy necessitated analysis of **1** in chlorobenzene (referenced to an internal C_6D_6 capillary), however, these solutions were stable for at least 3 days at room temperature (light/dark/presence of TEMPO). Crystals suitable for XRD studies were grown using the same method described above.[ii]

Complex **1** adopts a distorted square-planar geometry in which the chlorobenzene molecule coordinates in the fourth site *trans* to the pincer ligand (Fig. 2.2). The distorted square planar geometry is evidenced by the distinctly non-linear bite angle (P1–Rh1–P2) of 161.46(3) ° and the N1–Rh1–Cl1 bond angle of 168.3(3) ° (Table 2.1). The aromatic ring of the chlorobenzene ligand is canted towards one side as a result of dative coordination through one of the lone pairs of the chlorine atom. The Rh1–Cl1 bond length of 2.340(14) Å is within 1 estimated standard deviation (esd) of that reported for **A** (2.350(2) Å),[31] but considerably shorter than observed in [Rh(Xantphos-Ar^F)H_2(κ_{Cl}-ClPh)][BAr^F_4], **A90** (Xantphos-Ar^F = 4,5-bis(di-3,5-bis(trifluoromethyl)phenylphosphino)-9,9-dimethylxanthene; 2.5207(12) Å), which is the only other crystallographically characterised κ_{Cl}-chlorobenzene adduct reported, to date, to the best of my knowledge (CSD, v.5.43, update June 2022).[37,41] This would

[ii] Crystallographic tables for all structures presented in chapter 2 can be found in the appendix and full crystallographic detail are provided in chapter 6.

suggest that the chlorine lone pair interacts more strongly with the rhodium centre in **1** than in the Xantphos-Ar^F complex.

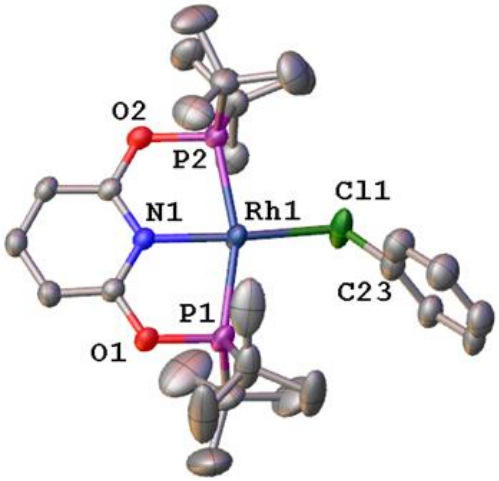

Figure 2.2 – The structure of **1**. The anion and hydrogen atoms have been omitted for clarity. Atomic displacement parameters are drawn at 50 % probability and only the major disordered component of the chlorobenzene ligand is shown for clarity.

Table 2.1 – A table of selected bond lengths and bond angles for **1**. Values with an asterisk are associated with the major disorder component.

Selected bond lengths / Å		**Selected bond angles / °**	
Rh1–P1	2.2986(9)	N1–Rh1–Cl1	168.3(3)*
Rh1–P2	2.2691(9)	P1–Rh1–P2	161.46(3)
Rh1–N1	2.006(2)	Rh1–Cl1A–C23A	116.5(2)*
Rh1–Cl1A	2.340(14)*		

Heating chlorobenzene solutions of **1** for 4 days at 125 °C did, however, quantitatively produce the rhodium(III) OA product [Rh(PONOP)(Ph)Cl][BAr$^F{}_4$], **2** (δ_{31P} 182.5, $^1J_{RhP}$ = 103 Hz; Scheme 2.2). The reaction exhibits pseudo first-order kinetics under these conditions (k = 0.480 M h^{-1}; $t_{1/2}$ = 14.4 h; Fig. 2.3) and was unaffected by addition of TEMPO as a radical scavenger. Therefore, OA of chlorobenzene in **1** was proposed to occur via a concerted OA mechanism involving selective cleavage of the C(sp^2)–Cl bond (bond dissociation energy, BDE = 400 kJ mol^{-1}).[44]

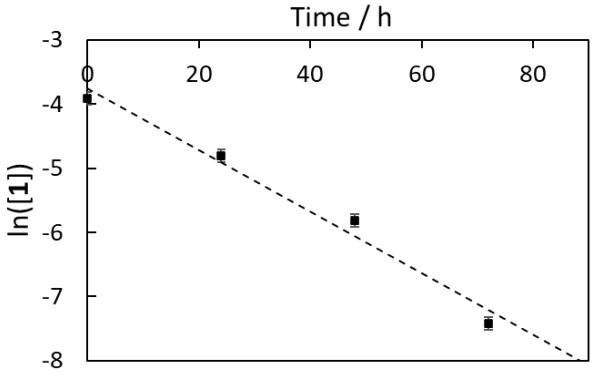

Figure 2.3 – A graph showing the first order reaction kinetics for the OA of **1** at 125 °C in chlorobenzene in the dark, as estimated by integration of the $^{31}P\{^{1}H\}$ NMR spectra.

Complex **6** was subsequently isolated in good yield (60 %) and crystals suitable for XRD studies were grown from by liquid-liquid diffusion of hexane into a chlorobenzene solution of **2** at room temperature. Complex **2** adopted a distorted square-based pyramidal geometry, with the aryl ligand coordinating in the apical position, effectively sandwiched between the flanking ^{t}Bu substituents of the pincer ligand (Rh1–C23 = 2.030(5) Å). This resulted in the molecular plane of the aryl ring adopting a perpendicular arrangement to the coordination plane of the pincer ligand (Fig. 2.4; Table 2.2). As a result of the formation of a stronger Rh–Cl bond and the higher oxidation state of +3, the Rh1–Cl1 bond length (2.3156(12) Å) is slightly contracted relative to **1** (2.340(14) Å). Complex **2** is stable in dichloromethane, with no onward reactivity detected after 24 hours at room temperature (light/dark/presence of TEMPO). The downfield ^{13}C resonance at δ 141.8 ppm (dt, $^{1}J_{RhC}$ = 34 Hz, $^{2}J_{PC}$ = 8 Hz) and the reduced $^{1}J_{RhP}$ coupling constant of 103 Hz are consistent with the results obtained by XRD.[45]

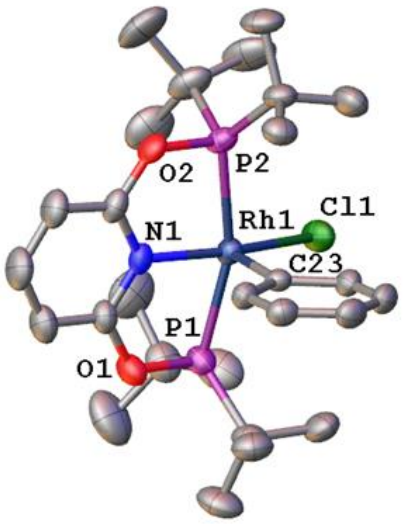

Figure 2.4 – The structure of **2**. Counterion and hydrogen atoms have been omitted for clarity. Atomic displacement parameters are drawn at 50 % probability.

Table 2.2 – A table of selected bond lengths and bond angles for **2**.

Selected bond lengths / Å		**Selected bond angles / °**	
Rh1–P1	2.3337(12)	N1–Rh1–Cl1	168.22(13)
Rh1–P2	2.3386(12)	P1–Rh1–P2	161.91(5)
Rh1–N1	2.020(4)	Cl1–Rh1–C23	101.95(15)
Rh1–C23	2.030(5)	N1–Rh1–C23	89.8(2)
Rh1–Cl1	2.3156(12)		

Although the orientation and proximity of the chlorobenzene C(sp^2)–Cl bond to the metal centre (C23A···Rh1 = 3.54(1) Å) in **1** initially suggested the complex was well set-up to probe pressure-induced OA, from a chemical standpoint, the large amount of energy required to cleave the C(sp^2)–Cl bond via thermolysis dissuaded the evaluation of **1** by HP-XRD. Furthermore, examination of the crystal packing suggested that compression of the chlorobenzene ligand into closer proximity with the rhodium(I) centre would be difficult to achieve. The extended packing in **1** shows each cation to be surrounded by an octahedral arrangement of five anions and one other cation, such that pairs of cations were encased by anions in a bicapped square prismatic arrangement. The chlorobenzene ligand is situated in a cleft created by two adjacent

Ar^F substituents, meaning that compression of the structure would be unlikely to bring about any further approach of the ligand towards the rhodium centre (Fig. 2.5). Upon compression, unfavourable sterics between the bulkier ^{t}Bu and CF_3 groups of the respective cations and anions would be more likely to dominate (Fig. 2.5; inset), thereby hindering compression around the bond of interest. Going forward, alternative substrates were targeted in an effort to optimise the chemistry of the complexes (*i.e.*, weaken the C–Cl bond to a greater extent) before HP-XRD studies were conducted.

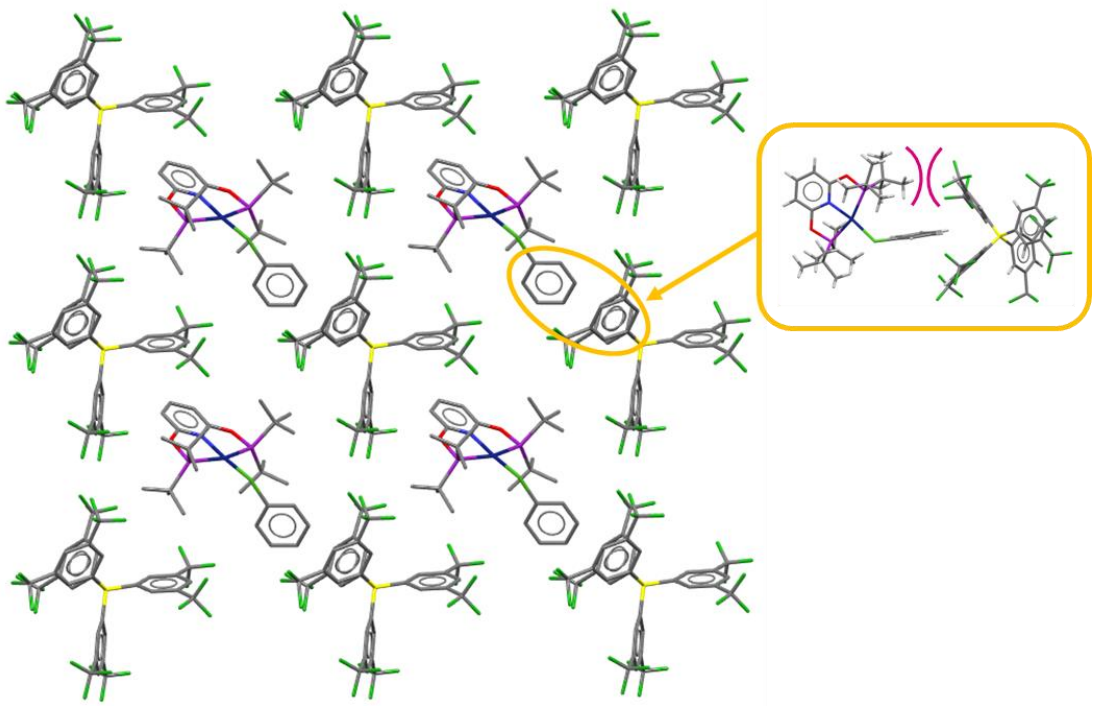

Figure 2.5 – The extended packing observed in **1**. The inset, circled in orange, shows the arrangement of the chlorobenzene ligand within the cavity of the $[BAr^F_4]^-$ anion, with the ^{t}Bu···CF_3 steric interactions depicted by burgundy lines. Hydrogen atoms omitted for clarity.

2.3 – Preparation and reactivity of [Rh(PONOP)(CH_2Cl)Cl][BAr^F_4]

Complex **1** was found to be an excellent precursor for the generation of related chloroalkyl species when dissolved in other solvents. Therefore, **1** was used as the precursor of choice for the generation of other κ_{Cl}-chlorocarbon targets through ligand substitution. Not only could the chlorobenzene by-product from these reactions be easily removed from solution during crystallisation but chlorobenzene was thought to be unlikely to participate in further metal-based reactivity. In order to prepare

complexes for HP-XRD studies that were better predisposed to C–Cl activation, the reactivity of homolytically weaker C(sp^3)–Cl bonds was targeted. Adducts of chlorocyclohexane, 2-chloro-2-methylpropane, 1,2-dichloroethane, 2-chloropropane and dichloromethane with the general structure {Rh(PONOP)(κ_{Cl}-ClR)}$^+$ were thus prepared and systematically evaluated.

Firstly, complex **A** (which has been previously reported by Weller and co-workers)[31] was prepared using an alternative synthetic route. Dissolution of **1** in dichloromethane resulted in quantitative formation of **A** at room temperature. The NMR spectra obtained in CD_2Cl_2 was in agreement with the literature (δ_{31P} 204.5, $^1J_{RhP}$ = 136 Hz).[31] Analytically pure material of **A** could be obtained in good yield (86%) by liquid-liquid diffusion of hexane into the *in situ* dichloromethane solution at room temperature. Furthermore, both CH_2Cl_2 and CD_2Cl_2 were suitable solvents for the analytically pure isolation of **A/d$_2$-A** by means of crystallisation from the *in situ* reaction mixtures, eliminating the necessity of further recrystallisation cycles.

As was previously observed by Weller and co-workers,[31] samples of **A** prepared from CH_2Cl_2 immediately generate **d$_2$-A** upon dissolution in CD_2Cl_2 due to exchange with solvent molecules. Otherwise, no onward reactivity was detected by NMR spectroscopy when solutions of **A** were left to stand at room temperature in the light for 24 h. Contrastingly, in the absence of light, partial conversion (~3 %) of **A** into a species characterised by a doublet ^{31}P resonance at δ 182.0 ppm with a smaller $^1J_{RhP}$ coupling constant of 104 Hz was observed over the course of 24 h at room temperature. Heating either CH_2Cl_2 or CD_2Cl_2 solutions of **A** at 50 °C in the dark confirmed this new species to be the OA adduct [Rh(PONOP)(CX_2Cl)Cl][BAr^F_4] (X = H, D), **d$_x$-3**, since an approximate 8:2 mixture (from 20 mM solutions) of **d$_x$-7** (δ_{31P} 182.0 (d, $^1J_{RhP}$ = 104)) and the paramagnetic rhodium(II) species [Rh(PONOP)Cl][BAr^F_4], **4** (δ_{1H} 24.46 (vbr, fwhm = 600 Hz, ^{t}Bu), was obtained after 4 days under these conditions (Scheme 2.3). This reaction exhibited pseudo first-order kinetics (k = 0.049 M h^{-1}; $t_{1/2}$ = 14.2 h; Fig. 2.6).

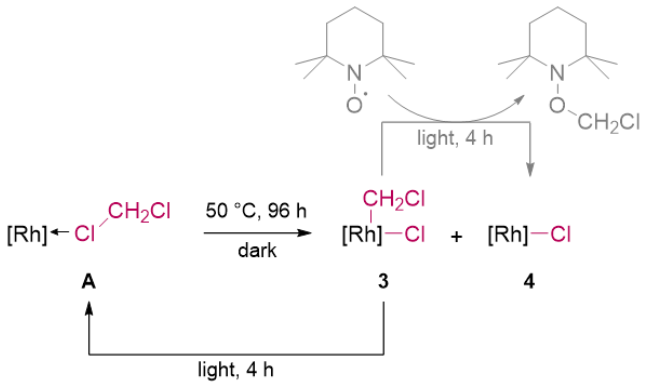

Scheme 2.3 – Reactivity of **A**. Reactions were conducted in CH_2Cl_2/CD_2Cl_2 at room temperature unless otherwise stated. [Rh] = [Rh(PONOP)][$BAr^F{}_4$].

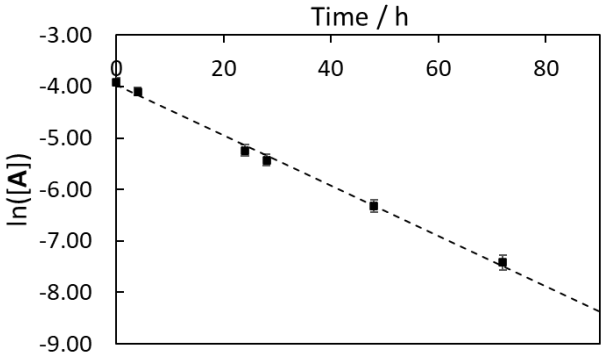

Figure 2.6 – A graph showing the first order reaction kinetics for the OA of **d_2-A** at 50 °C in CD_2Cl_2 in the dark, as estimated by integration of the ^{t}Bu ^{1}H NMR resonances relative to the [$BAr^F{}_4$]$^-$ anion.

50 mM CH_2Cl_2 solutions of **A** heated at 50 °C in the dark for 96 h produced the highest purity samples of **3** upon isolation (9:1 ratio of **3**:**4**). Since the sample was predominantly comprised of **3**, structural elucidation in CD_2Cl_2 by ^{1}H, ^{13}C and ^{31}P NMR spectroscopy (in the dark) was achievable, despite contamination by **8**. Complex **3** was spectroscopically characterised by a triplet of doublets ^{1}H resonance at δ 5.65 ppm (2H, $^3J_{PH}$ = 6.8, $^2J_{RhH}$ = 3.4 Hz) and doublet of triplets ^{13}C resonance at δ 48.0 ppm ($^1J_{RhC}$ = 30, $^2J_{PC}$ = 5 Hz), corresponding to the methylidene protons.[iii] Additionally, the ^{31}P{^{1}H} NMR (δ 182.0, $^1J_{RhP}$ = 104 Hz) was reminiscent of the spectroscopic data obtained for the rhodium(III) complex **2** (δ_{31P} 182.8, $^1J_{RhP}$ =

[iii] Spectroscopic data associated with **B** are not available, prohibiting direct comparison.

103 Hz), as was the evolution of two sets of virtual triplets between δ_{1H} 1.0-1.5 ppm, reflecting the now inequivalent ^{t}Bu environments.

Single crystals suitable for XRD studies were obtained by liquid-liquid diffusion of hexane into CH_2Cl_2 solutions of 9:1 **3**:**4** at -30 °C in the dark. Complex **3** adopts a distorted square-based pyramidal geometry, with a distinct non-linear bite angle (P1–Rh1–P2) of 160.53(3) ° (Fig. 2.7; Table 2.3). The chloride ligand, which coordinates in the fourth site *trans* to the pincer ligand, is also slightly distorted away from the equatorial coordination plane (N1–Rh1–Cl1 = 175.36(10) °). The chloroalkyl ligand coordinates in the apical position (Rh1–C23 = 2.077(4) Å) with the terminal chlorine atom projecting over the pyridine donor of the pincer ligand (Cl1–Rh1–C23–Cl2 dihedral angle = 171.52(13)°).

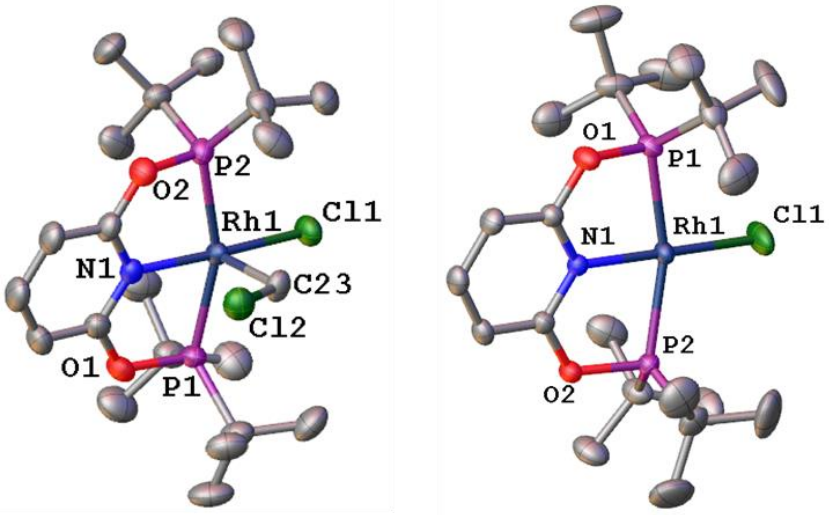

Figure 2.7 – The crystal structures of **3** (left) and **4** (right) obtained from individual crystallographic experiments, with atomic displacement parameters drawn at 50% probability. The former was established to co-crystallise as a 9:1 sample of **3** and **4**, as determined by freely refined atom site occupancies.[iv] The CH_2Cl_2 solvent molecule (**4**) and anions are omitted for clarity.

[iv] Corroborated by crystallographic refinement, combustion analysis and ^{1}H NMR spectroscopy.

Table 2.3 – Selected bond lengths and bond angles for **3** and **4**.

Complex	Selected bond lengths / Å		Selected bond angles / °	
9:1 sample of **3:4**	Rh1–P1	2.3518(9)	N1–Rh1–Cl1	175.36(10)
	Rh1–P2	2.3369(10)	P1–Rh1–P2	160.53(3)
	Rh1–N1	2.035(3)	Cl1–Rh1–C23	88.61(12)
	Rh1–C23	2.077(4)	N1–Rh1–C23	96.01(15)
	Rh1–Cl1	2.3031(8)	Rh1–C23–Cl2	115.6(2)
4	Rh1–P1	2.3048(5)	N1–Rh1–Cl1	178.09(5)
	Rh1–P2	2.3008(5)	P1–Rh1–P2	162.395(19)
	Rh1–N1	2.0231(16)		
	Rh1–Cl1	2.2955(5)		

Interestingly, the co-crystallisation observed herein of **3** with **4** reflects the co-crystallisation of the PNP homologue **C** with [Rh(PNP)(H)Cl][BAr^F_4], **D**, previously reported by Weller and co-workers.[31] As a consequence of the co-crystallisation within the respective PNP and PONOP structures, meaningful analysis of their metrics and structural comparisons are prevented.

9:1 mixtures of **3** and **4** in CD_2Cl_2 remained unchanged when left to stand for 48 h at room temperature in the dark; no H/D scrambling of the methylidene protons were observed. However, subsequent exposure of the same solution to light initiated regeneration of **A** from **3** within 4 h at room temperature (Scheme 2.3). This photo-induced reductive elimination (RE) process would suggest that **A** is best described as a photo-stationary state as opposed to the thermodynamic ground state in solution.

In an attempt to confirm the mechanism by which photo-induced RE from **3** occurred, CD_2Cl_2 solutions of **3** that contained the radical trapping reagent TEMPO were monitored over time in both the presence and absence of light. No reaction was observed between **3** and TEMPO in the dark (24 h, r.t.) but subsequent exposure of the same solution to light resulted in complete conversion of **3** into **4** within 4 h at room temperature alongside the formation of an unstable species presumed to be TEMPO–CH_2Cl (δ_{1H} 5.67 (s, OCH_2Cl); Scheme 2.3, Fig. 2.8).[46] No onward reactivity was detected from control experiments involving heated CD_2Cl_2 solutions of **4** (50 °C, 24 hours, light). Based on these experiments, a non-chain radical OA of the C(sp^3)–Cl

bond in **A** (BDE = 338 kJ mol^{-1})[44] that proceeds via homolysis of the C–Cl bond followed by incomplete radical recombination of •CH_2Cl with **4** is proposed to afford mixtures of **3** and **4**.[47,48] Since RE is known to be the microscopic reverse of OA, the photo-induced RE process is similarly proposed to proceed via the same mechanism. It is still unclear what specific organic by-product is formed alongside **4**. No evidence of 1,2-dichloroethane or any isotopologues were observed from $^{13}C\{^1H\}$ NMR experiments conducted with high scan numbers.

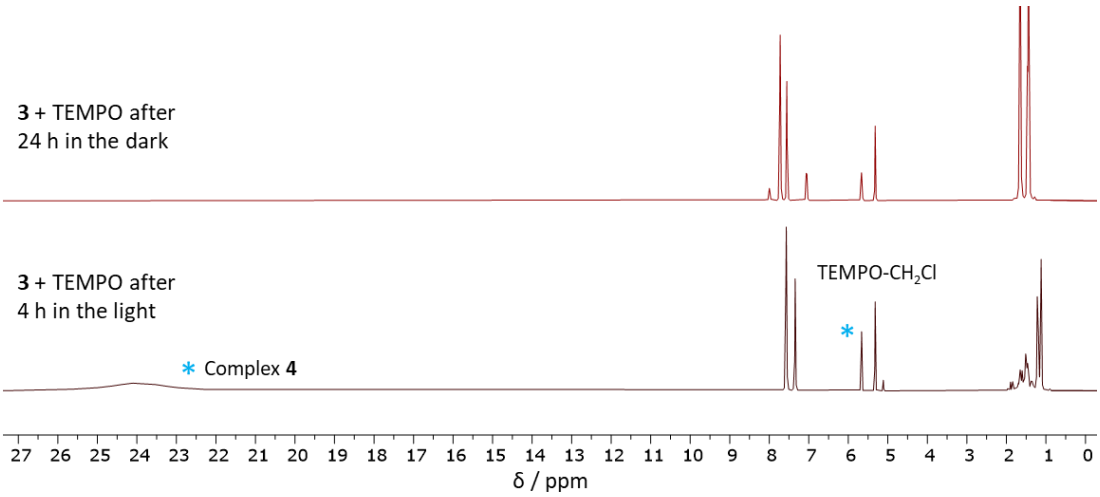

Figure 2.8 – Stacked ^1H NMR spectra of **3** in the presence of TEMPO after 24 hours at room temperature in the dark (top) and after 4 hours of exposure to light (bottom; 300 MHz, CD_2Cl_2, 298 K.)

2.4 – Characterisation of [Rh(PONOP)Cl][BAr$^F_4$]

Assignment of **4** as a paramagnetic species was apparent from the appearance of a very broad ^1H resonance at δ 25 ppm (fwhm = 650 Hz), corresponding to the ^{t}Bu groups. Observations of such metalloradicals have been reported by Hulley and co-workers,[20] and isolation of the PNP-homologue [Rh(PNP)Cl][BAr$^F_4$], **E**, was previously reported by Milstein and co-workers.[49] The formation of **4** within solutions of **3** further supports the proposed radical OA mechanism, since the paramagnetic intermediate **4** can only be produced from **A** via a single electron transfer step.

In order to fully characterise the metalloradical, **4** was prepared via an alternative synthetic method. Oxidation of [Rh(PONOP)Cl] with Fc[BAr$^F_4$] (48% yield; Fc^+ = ferrocenium) followed by crystallisation from CH_2Cl_2/hexane at room temperature

enabled the isolation of **4** as single crystals in 48 % yield. No ^{31}P resonance could be located for **4** between δ -600–600 ppm, but paramagnetically shifted ^{t}Bu (δ 24.7), 3-py (δ 1.6), and 4-py (δ -17.2) resonances were observed by ^{1}H NMR spectroscopy. XRD studies revealed that **4** adopts a distorted square planar geometry with a pincer bite angle of 162.395(19) ° and a Rh1–Cl1 bond length of 2.2955(5) Å. This bond length is notably shorter than the Rh1–Cl1 bond length reported for **A** (2.3562(7) Å; Fig. 2.7; Table 2.3)[31] and, to a certain extent, helps rationalise the shorter Rh1–Cl1 bond observed in the 9:1 sample of **3**:**4** (2.3031(8) Å) in comparison to the other structurally related rhodium(III) precedent **2** (2.3156(12) Å). A less pronounced rhodium(I/II) contraction was observed for the PNP-homologue **E** (2.381(1)/2.332(1) Å), which is attributed to enhanced chloride-to-rhodium π-donation.[49]

Interestingly, cyclic voltammetry (CV) revealed the formal potential ($E_{1/2}$) of **4** to be congruous with the ferrocene standard (-0.01 V *vs*. Fc/Fc^{+}, Fig. 2.9), rationalising the low yield (48 %) of the reaction. Since the formal potentials of the two redox species were essentially equal, the redox reaction was in equilibrium (K ~1) so approximately half of the molecules present in the solution were oxidised to rhodium(II).

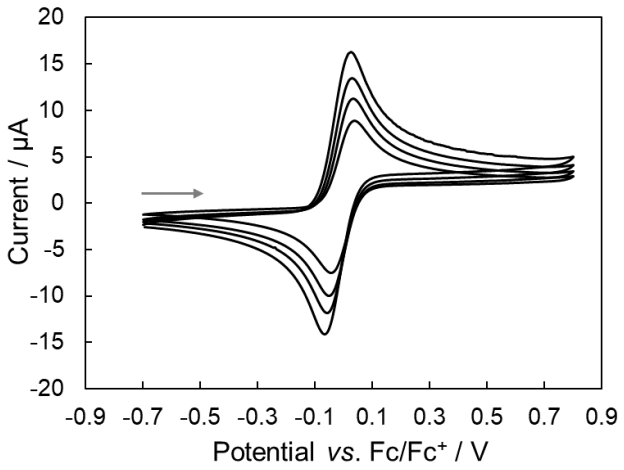

Figure 2.9 – CVs for the oxidation of Rh(PONOP)Cl in 1,2-$C_6H_4F_2$ at room temperature (2 mM complex; 0.2 M [^{n}Bu$_4$N][BAr$^{F}_4$] electrolyte; glassy carbon working electrode, coiled Pt wire counter electrode and Ag wire quasi-reference electrode; scan rates = 30, 50, 70 and 100 mV·s^{-1}). Figure and caption reproduced from Chaplin and co-workers.[50]

Magnetic susceptibility measurements were performed to confirm the spin state of the rhodium(II) centre. The temperature dependence of dc magnetic susceptibility, $\chi_{dc}(T)$, for **4** between 2 and 300 K (Fig. 2.10) and at low temperature (Fig. 2.10; inset) was probed. Complex **4** was confirmed to be paramagnetic since the sample showed no signs of magnetic order. A fit using a Curie Weiss model gave an effective moment of 2.22(2) μ_B/Rh, slightly higher than the theoretical approximation of 1.73 μ_B expected for a spin (S) = ½ ion. Similar values have been reported for other square-planar rhodium(II) complexes.[51] A Weiss temperature (Θ_W) of 0.007(5) K is also consistent with the absence of magnetic order. In magnetic fields below 10 kOe, the magnetization measurements were linear with no evidence of a hysteresis. Fig. 2.10b shows a 4 quadrant $M(H)$ curve collected at 5 K - the magnetization tends to saturate at higher fields. A saturation moment of approximately 1.10(5) μ_B/Rh at 1.8 K was obtained (Fig. 2.10b; inset), which is consistent with a rhodium(II) centre containing one unpaired electron (S = ½).

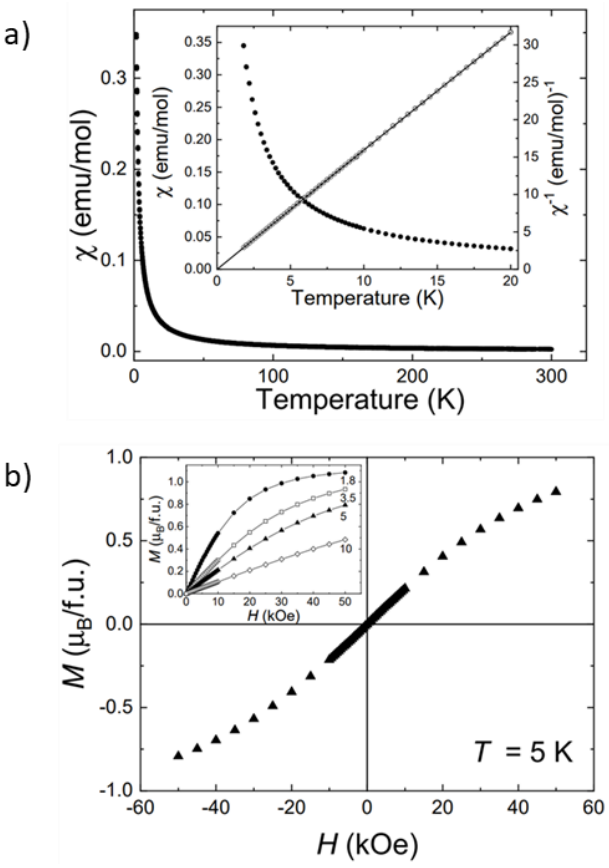

Figure 2.10 – (a) Temperature dependence of the dc magnetic susceptibility $\chi_{dc}(T)$ [●] and the inverse dc magnetic susceptibility versus temperature $\boldsymbol{\chi_{DC}^{-1}(T)}$ [○] for **4**. The data were collected while cooling in an applied field, *H*, of 1 kOe. The solid line shows a fit using a Curie–Weiss law $\left[\boldsymbol{\chi_{DC}(T) = \frac{C}{(T-\Theta_W)} + \chi_0}\right]$ between 2 and 20 K. (b) Magnetisation versus applied field for **4** at 5 K. The inset shows single quadrant *M*(*H*) curves at 1.8 [●], 3.5 [□], 5 [▲] and 10 K [◊]. Figure and caption reproduced from Chaplin and co-workers.[50]

2.5 – Preparation of other κCl-alkyl chloride

In an effort to further explore and compare the radical-based reactivity discovered in **A**, other κCl-chloroalkane adducts with lower C-centered radical enthalpies of formation were thus investigated. Dissolution of **1** in chlorocyclohexane at room temperature resulted in quantitative conversion into the rhodium(I) κ_{Cl}-chlorocyclohexane adduct **5** (δ_{31P} 204.5, $^1J_{RhP}$ = 138 Hz). Complex **5** was sufficiently stable at room temperature such that single crystals could be obtained by liquid-liquid

diffusion of hexane into the chlorocyclohexane solution at room temperature. However, the yield from the crystallisation method was low (< 35 %). In order to isolate larger quantities of analytically pure material for analysis by NMR spectroscopy and elemental microanalysis, chlorocyclohexane solutions of **1** were allowed to stand for 5 mins before all volatiles were removed *in vacuo* (yield: 79 %).

Single crystals suitable for XRD studies were grown using the crystallisation method described above. The structure of **5** revealed two crystallographically unique complexes (*Z*' = 2; Fig. 2.11). Although both unique complexes contained disordered chlorocyclohexane ligands that were modelled over two positions, both disorder components of the chlorocyclohexane ligand in the first unique complex 5A coordinated in an axial conformation, whereas one of the two chlorocyclohexane ligands in the second unique complex 5B coordinated in an equatorial conformation (Fig. 2.11). Dative coordination of chlorocyclohexane was corroborated by the Rh–Cl bond lengths, which ranged from 2.31-2.40 Å in length (Table 2.4). Notably, complex **5** represents the first crystallographic example of an organometallic κ_{Cl}-chlorocyclohexane complex (CSD, v.5.43, update June 2022).[41] Unfortunately, due to poor crystal quality, the large unit cell (Z' = 2) and the extensive disorder present in the conformationally flexible chlorocyclohexane ligands, crystals of **5** were deemed unsuitable for HP-XRD studies.

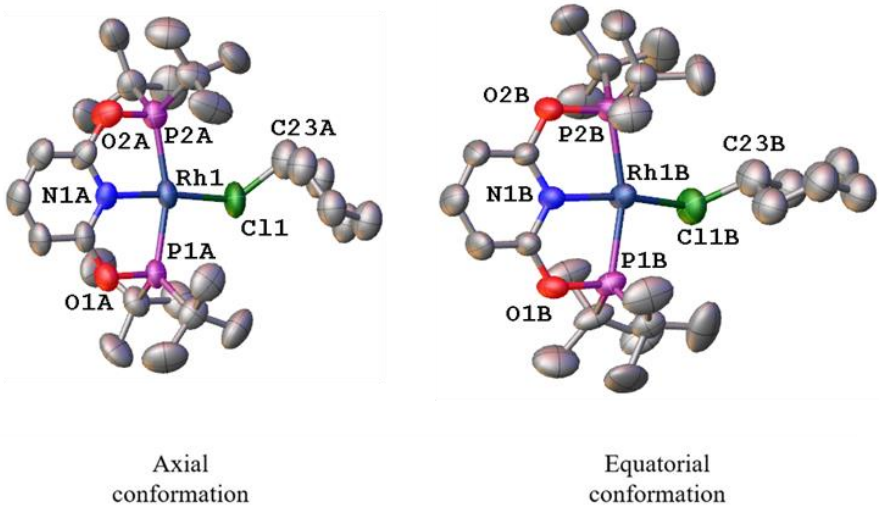

Figure 2.11 – The structures of the two crystallographically unique complexes 5A (left) and 5B (right). Atomic displacement parameters are drawn at 50 % probability. Counterions and hydrogen atoms omitted for clarity. Only one disorder component is shown.

Table 2.4 – Selected bond lengths and bond angles for **5**. Only the values associated with the major disorder components are presented. The top and bottom values correspond to the crystallographically unique complexes 2A and 2B, respectively.

Selected bond lengths / Å		**Selected bond angles / °**	
Rh1–P1	2.2814(19) 2.2737(16)	N1–Rh1–Cl1	173.3(3) 164.68(17)
Rh1–P2	2.284(2) 2.2714(16)	P1–Rh1–P2	161.90(6) 162.26(7)
Rh1–N1	2.014(5) 2.004(5)	Rh1–Cl1–C23	127.3(7) 116.2(7)
Rh1–Cl1	2.321(14) 2.378(3)		

When chlorocyclohexane solutions of **5** were allowed to stand at room temperature for 24 h, partial conversion of **5** (*ca.* 10 %) into the rhodium(III) hydride [Rh(PONOP)(H)Cl][BAr$^{F}_{4}$], **6** (δ_{31P} 197.1, $^{1}J_{RhP}$ = 102 Hz, δ_{1H} -26.16, $^{1}J_{RhH}$ = 42.3, $^{2}J_{PH}$ = 10.4 Hz) was observed alongside cyclohexene. Quantitative conversion of **5** into **6** alongside an equimolar amount of cyclohexene was observed by NMR spectroscopy upon heating solutions of **5** in chlorocyclohexane at 50 °C for 24 h (Scheme 2.4, Fig. 2.12). This dehydrochlorination process was unaffected by the presence of light and yielded identical product distributions.

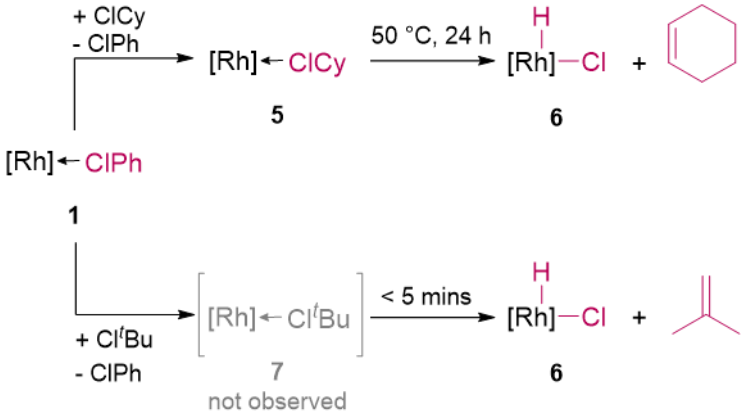

Scheme 2.4 – Synthesis and reactivity of **5** and **7**. Reactions were conducted in chlorocyclohexane (top) or 2-chloro-2-methylpropane (bottom) at room temperature unless otherwise stated. [Rh] = [Rh(PONOP)][BAr$^{F}_{4}$].

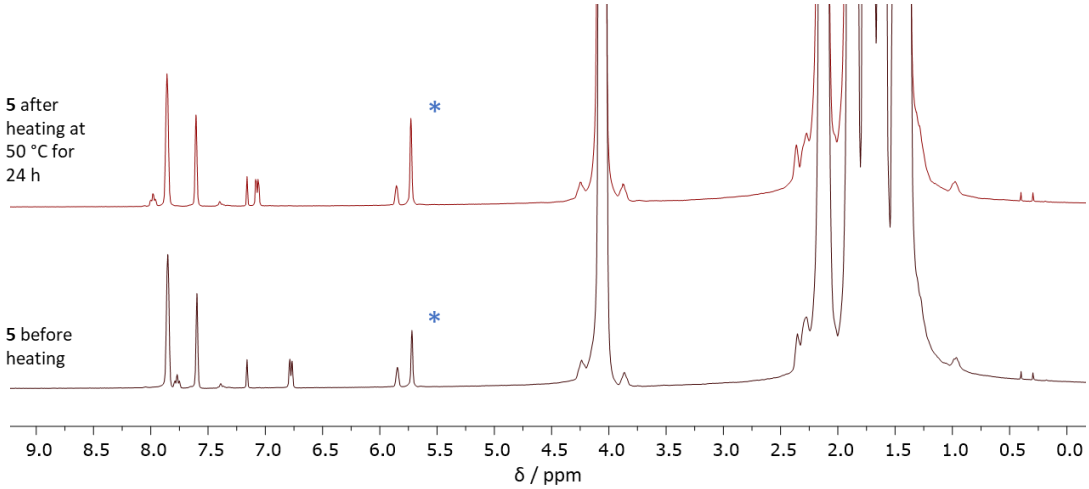

Figure 2.12 – Stacked ^{1}H NMR spectra of **5** before and after heating for 24 hours in ClCy at 50 °C in the light (400 MHz, ClCy, 298 K). Note the formation of cyclohexene (δ_{1H} 5.72 (s, CH=CH)), as denoted by an asterisk.

Considerably faster dehydrochlorination resulted upon dissolution of **1** in 2-chloro-2-methylpropane. The presumably transient κ_{Cl}-chlorocarbon complex **7** was not observed by NMR spectroscopy, instead, quantitative conversion into **6** alongside an equimolar quantity of isobutene was observed at room temperature within 5 mins, both in the presence and absence of light (Scheme 2.4). Whilst CD_2Cl_2 solutions of **6** were stable for at least 3 days in the absence of light, a small degree of decomposition into **4** (ca. 3 %) was observed when CD_2Cl_2 solutions of **6** were left to stand for 3 days in the presence of light. Therefore, analytically pure material of **6** (to the detection limit of the NMR spectrometer) was obtained in excellent yield (87 %) by liquid-liquid diffusion of hexane into 2-chloro-2-methylpropane solutions of **6** at room temperature in the absence of light. Single crystals grown using this method were also suitable for XRD studies.

Complex **6** adopted a distorted square-based pyramidal geometry, with the metal hydride coordinating in the apical position (Figure 2.13; Table 2.5). The experimental data was of sufficient quality such that the metal hydride could be located from the electron density difference map during refinement. The higher rhodium(III) oxidation state was reflected in the shorter Rh–P bond lengths (Rh1–P1 = 2.2913(8) Å; Rh1–P2 = 2.2988(8) Å) in comparison to the rhodium(I) complexes presented herein. Curiously, the Rh1–Cl1 bond length (2.3051(7)) Å) lies in between the Rh1–Cl1

distances reported for the rhodium(III) OA adduct **2** (2.3156(12) Å) and the rhodium(II) metalloradical **4** (2.2955(5) Å). The possibility that the single crystal analysed contained trace amounts of **4**, therefore, cannot be fully discounted, especially considering the propensity of these complexes to co-crystallise[31] (*vide infra*, section 2.3).[v]

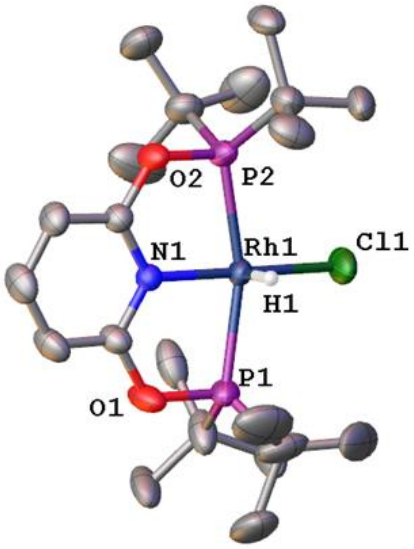

Figure 2.13 – The structure of **6**. Counterions and hydrogen atoms (except for the metal hydride) have been omitted for clarity. Atomic displacement parameters are drawn at 50 % probability.

Table 2.5 – Selected bond lengths and angles for **6**.

Selected bond lengths / Å		**Selected bond angles / °**	
Rh1–P1	2.2987(7)	N1–Rh1–Cl1	178.51(7)
Rh1–P2	2.2912(7)	P1–Rh1–P2	163.09(3)
Rh1–N1	2.0176(19)	Cl1–Rh1–H	
Rh1–Cl1	2.3051(7)	N1–Rh1–H	
Rh1–H	1.32(4)		

Extrapolating from the mechanistic work conducted on **A**, the reactivity observed for the chlorocyclohexane and 2-chloro-2-methylpropane adducts **5** and **7** is proposed to

[v] Whilst no significant decomposition of **9** was observed upon standing in CD_2Cl_2 at room temperature in the dark for 72 h, exposure of the solution to light resulted in *ca.* 3% conversation into **8** over 72 h.

proceed firstly via homolytic cleavage of the C(sp^3)–Cl bonds (BDEs = 356 and 352 kJ mol^{-1}, respectively)[44] to generate **4** and the respective C-centred alkyl radical. Compared to •CH_2Cl, •Cy and •^{t}Bu radicals are more stable and contain weaker C–H bonds (*c.f.* Table 2.6). Therefore, the subsequent formation of **6** and the corresponding alkene is proposed to occur by hydrogen atom abstraction from the alkyl radical, in preference to direct C-centered radical recombination with **4** followed by β-hydride elimination.

Table 2.6 – The calculated enthalpies of formation, C–Cl and C–H bond dissociation energies (BDEs) for various C-centered radicals. The C–Cl BDEs correspond to the chlorocarbon molecules before formation of the radicals.[44] *The C–H BDE for Ph• was derived and no tolerance values were supplied.

Radical	**$\Delta_f H^0$ / kJ mol^{-1}**	**C–H BDE / kJ mol^{-1}**	**C–Cl BDE / kJ mol^{-1}**
^{t}Bu•	48.0 ± 3.0	153 ± 3.3	352 ± 6.3
Cy•	75.3 ± 6.3	138 ± 6.3	356 ± 8.4
^{i}Pr•	88 ± 3.0	150 ± 3.3	354 ± 6.3
$ClCH_2CH_2$•	93 ± 2.4	146 ± 8.4	345 ± 5.0
$ClCH_2$•	117 ± 2.9	427 ± 10.5	338 ± 3.3
Ph•	330 ± 3.3	328*	400 ± 6.3

Supporting this hypothesis, analysis of solutions of **6** in the presence of different equivalents of TEMPO in CD_2Cl_2 indicated that TEMPO catalyses rapid transfer of the hydrogen atom between **6** and **4** (BDEs: (Rh–H) = 237–255 kJ mol^{-1}; (O–H) = 292 kJ mol^{-1}).[44] The exchange was rapid compared to the ^{1}H NMR timescale at room temperature, resulting in a broad averaged signal between the two species (400 MHz; Fig. 2.14). No hydrogen shuttling was observed when a 1:1 mixture of **4** and **6** in CD_2Cl_2 was prepared in the absence of TEMPO, confirming that the presence of TEMPO is required to mediate the hydrogen atom transfer. Additionally, partial conversion of **4** into **6** was observed upon heating solutions of **4** with dihydroanthracene in CD_2Cl_2 at 50 °C in the light, as evidenced by the evolution of sub-stoichiometric amounts of anthracene (40 % conversion) after 2 weeks in solution

(δ_{1H} 8.45 (s, 2H, CH)). Continued heating for 4 weeks at 50 °C in the light did not drive the reaction to completion.

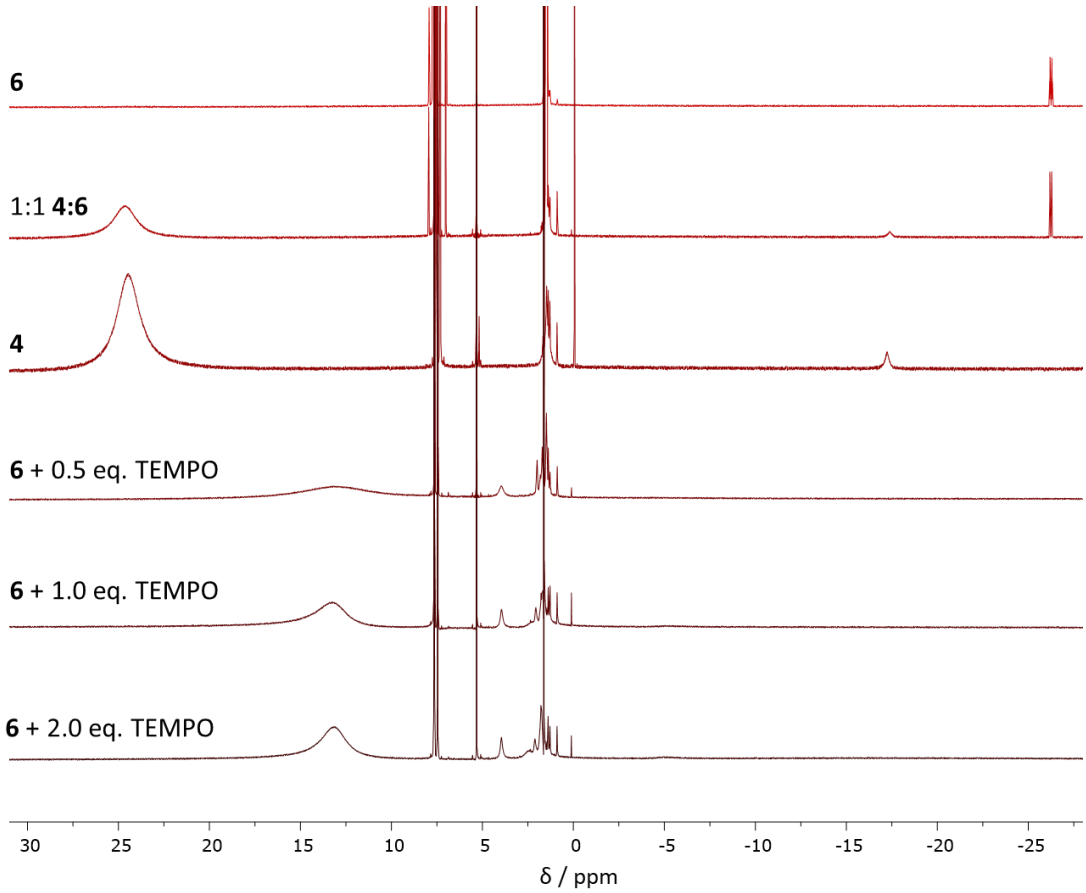

Figure 2.14 – Stacked ^{1}H NMR spectra showing the hydrogen transfer between **4** and **6** catalysed by TEMPO (400 MHz, CD_2Cl_2).

Dissolution of **1** in 1,2-dichloroethane or 2-chloropropane resulted in the respective formation of the κ_{Cl}-chlorocarbon adducts **8** and **9**. Dehydrochlorination was observed for solutions of **8** and **9** at both ambient and elevated temperatures and is proposed to proceed via a similar radical pathway to that described above for **5** and **7**. Over the course of 24 h (dark/light, room temperature), solutions of **8** (1,2-dichloroethane) and **9** (2-chloropropane) converted by *ca*. 5 % and 60 %, respectively, into mixtures of **4**, **6** and the rhodium(I) alkene complexes [Rh(PONOP)(η^2-CH_2CHR)][BAr^F_4] (R = Cl, **10**, δ_{31P} 211.6 (d, $^{1}J_{RhP}$ = 126); R = Me, **11**, δ_{31P} 212.4 (d, $^{1}J_{RhP}$ = 128); Scheme 2.5). Heating solutions of **8** and **9** for 24 h at 50 °C (dark/light) yielded similar results at an expedited rate (Table 2.7).

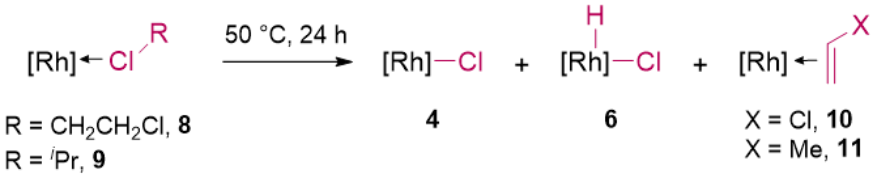

Scheme 2.5 – The reactivity observed in the dark for **8** and **9**. The reactions were conducted in 1,2-dichloroethane (**8**) or 2-chloropropane (**9**). [Rh] = [Rh(PONOP)][$BAr^F{}_4$].

Table 2.7 – Product distributions calculated by integration of the ^1H and $^{31}P\{^1H\}$ NMR spectra for the reactions of **8** and **9** depicted in Scheme 2.5.

	Product distributions / %			
Reaction	**8/9**	**4**	**6**	**10/11**
8 (dark, 50 °C, 24 h)	88	2	0	10
9 (dark, 50 °C, 24 h)	0	0	45	55

The observation of rhodium(I), (II) and (III) species in solutions of **8** and **9** are consistent with radical mechanisms, however, the product distributions of the two reactions differ (Table 2.7). The presence of **4** in heated solutions of **8** suggests the termination step (α-hydrogen abstraction) is competitive with diffusion of the $\bullet CH_2CH_2Cl$ radical away from the transient encounter complex. The observed reactivity is further complicated by the fact that the reactant is also the solvent, so termination of radical intermediates within the solvent cage (due to propagation reactions involving the solvent itself) is a distinct possibility. Additionally, the presence of trace quantities of radical stabilisers in chlorinated solvents may also facilitate alternative radical termination pathways.[52] The enhanced reactivity rate observed in solution of **9** in comparison to **8** can be rationalised by the lower $\Delta_f H^0$ of the more persistent secondary $^i Pr\bullet$ radical relative to the primary $\bullet CH_2CH_2Cl$ radical (Table 2.6).

Crystals of **8** and **9** suitable for XRD studies were grown by liquid-liquid diffusion of hexane into the respective 1,2-dichloroethane or 2-chloropropane solutions at room temperature. The crystal structures of **8** and **9** revealed that both complexes possessed similar distorted square planar geometries about the metal, with similar Rh–Cl bond lengths of *ca*. 2.35 Å, as was observed for complexes of **1**, **A** and **5** (Fig. 2.15, Table 2.8). The κ_{Cl}-ClR ligands in **8** and **9** coordinate to the rhodium centre datively via the chlorine lone pair, resulting in non-linear N1–Rh1–Cl1 bond angles (Table 2.8). Thermolysis of DCE and Cl^{i}Pr by {Rh(PONOP)}$^{+}$ proceeded readily under mild conditions, therefore, it was hypothesised that pressure-induced OA might be achievable in these systems. However, the presence of two unique complexes in the asymmetric units combined with the disorder present in each unique κ_{Cl}-coordinated ligand of interest dissuaded examination of **4** and **5** by HP-XRD, due to the complexity of the structures.

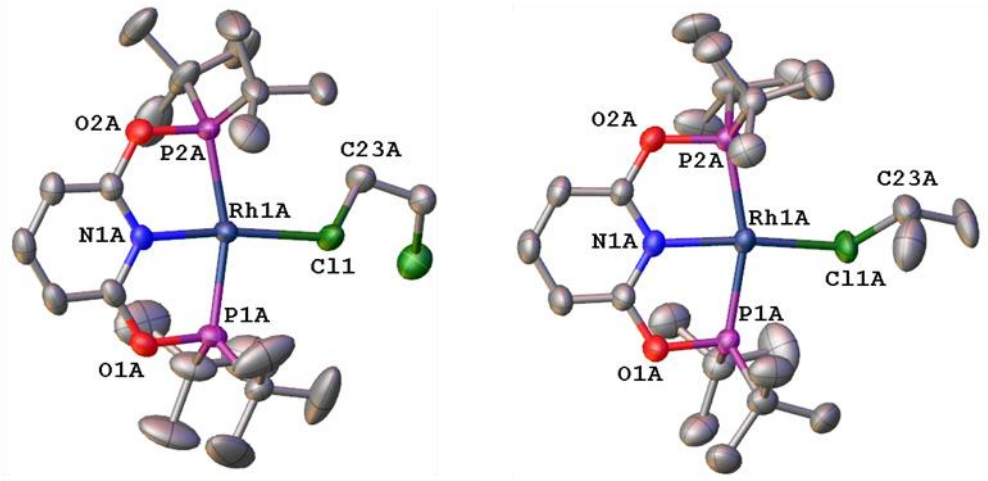

Figure 2.15 – The structures of **8** (left) and **9** (right). Counterions and hydrogen atoms have been omitted for clarity. Only the major disorder components are shown for one of the two crystallographically unique complexes in the asymmetric units. Atomic displacement parameters are drawn at 50 % probability.

Table 2.8 – A table of selected bond lengths and bond angles for **8** and **9**. The top and bottom values correspond to the major disorder components for the crystallographically unique complexes A and B, respectively, in **8** and **9**.

Bond length / Å	**8**	**9**
Rh1–P1	2.2696(6) 2.2727(6)	2.2717(9) 2.2804(10)
Rh1–P2	2.2768(6) 2.2723(6)	2.2818(9) 2.2795(10)
Rh1–N1	2.016(2) 2.0105(19)	2.027(3) 2.048(3)
Rh1–Cl1	2.3784(7) 2.3744(10)	2.3561(17) 2.3870(12)
Bond angle / °	**8**	**9**
N1–Rh1–Cl1	170.01(6) 161.85(7)	170.46(11) 170.08(9)
P1–Rh1–P2	161.96(3) 161.83(2)	161.32(3) 162.24(4)
Rh1–Cl1–C23	119.89(12) 118.2(2)	119.5(3) 120.1(2)

2.6 – Solid-state transformations of [Rh(PONOP)(κ$_{Cl}$-ClCH$_2$Cl)][BAr$^F{}_4$]

Of the κ$_{Cl}$-chloroalkyl adducts **A**, **5**, **8** and **9**, only **A** contained a ligand that was not disordered about the site of interest (*i.e.*, the C–Cl bond) and had a Z' = 1. Therefore, by process of elimination, **A** was chosen to be investigated further in the solid-state, ultimately with a view to attempting to induce C–Cl OA with pressure.

2.6.1 – VT-PXRD study of [Rh(PONOP)(κ$_{Cl}$-ClCH$_2$Cl)][BAr$^F{}_4$]

Since sample purity had been found to increase when higher concentrations of **A** were heated in solution, it was speculated that heating solid-state samples would result in quantitative formation of **3**. Unfortunately, sample purity did not improve – the solid-state thermolysis of **A** (110 °C, 18 h) yielded an approximate 5:90:5 mixture of **d$_2$-A**:**3**:**4**, as observed by ^{1}H NMR spectroscopy upon dissolution of the sample in CD_2Cl_2 after heating. Total consumption of **A** was thought to be hindered by the

rudimentary heating method employed, since crystallites of **A** adhered to areas of the NMR tube containing the sample that were not in contact with the heating mantle. Variable temperature (VT) single crystal XRD studies were initially attempted in-house up to temperatures of 380 K, but the air-sensitivity of the sample resulted in a total loss of diffraction due to degradation in air above temperatures much greater than room temperature.[vi] Attempts were made to load and seal samples of **A** into 0.5 mm and 1 mm borosilicate glass capillaries inside the glovebox, but these attempts proved fruitless.

A variable temperature powder X-ray diffraction (VT-PXRD) experiment conducted on a powdered sample of **A** on beamline I11 at Diamond Light Source sought to circumvent this issue. Samples were packed uniformly into 0.5 mm borosilicate glass capillaries to facilitate uniform heating of **A**.[vii] The sample was heated from 300 K to 380 K at a ramp rate of 360 K h^{-1}, then held at the final temperature for three further scans. Above 350 K, pronounced negative thermal expansion (NTE) was exhibited in the *b* axis, along with less extreme NTE in *c*, which produced a net NTE effect in the cell volume (Fig. 2.16). The ambient temperature structure of **A** shows the Rh1−Cl1 bonds approximately align with the *b* axis (Fig. 2.17), therefore, it would be expected that OA of **A** to afford **3** would cause a significant contraction along *b*. The less pronounced NTE in the *c* axis is likely a result of contractions in the Rh−P bonds, which are similarly aligned with the *c* axis and would be expected to contract in the event of OA (Fig. 2.16 & 2.17).

[vi] At higher temperature, the *Parabar 10312* oil that protected the sample against air exposure began to slip off the crystal.

[vii] Experimental details are described in chapter 6. Fits of the Rietveld refinements are supplied in the appendix.

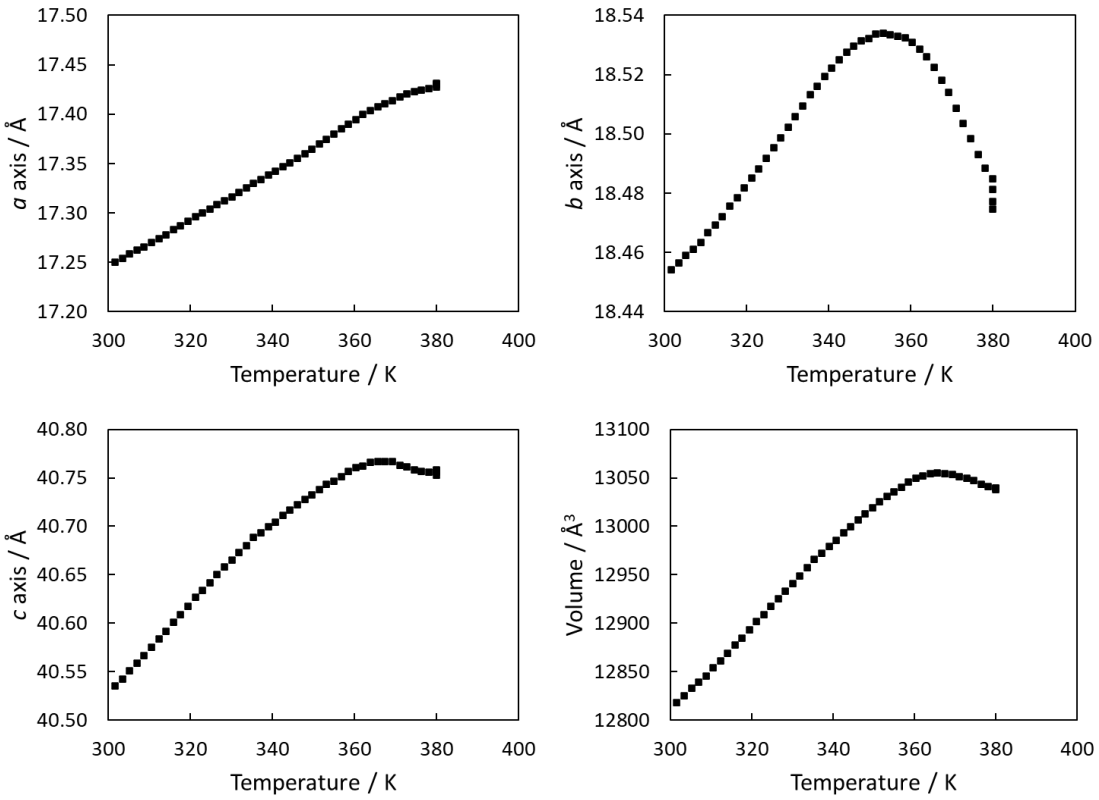

Figure 2.16 – Plots of the cell parameters of **A** as a function of temperature.

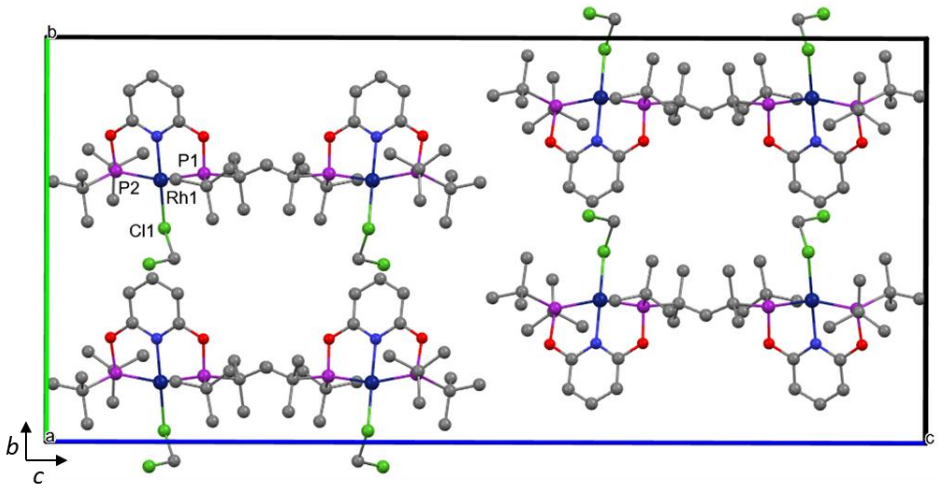

Figure 2.17 – A partially labelled depiction of the packing of cations in **A**, as viewed perpendicular to the *bc* plane. Anions and hydrogen atoms omitted for clarity.

Further studies are required to establish the kinetics of this transformation, as the preliminary VT experiment did not reach a plateau (as evidenced by the continual contraction of the *b* axis in Fig. 2.16). Furthermore, the emerging superstructure peaks

were too weak and too few to be properly indexed, so other phases could not be determined. Repeat experiments for extended periods of time would be necessary to provide more insight into the specifics of the transformation. However, problems encountered at Diamond Light Source prevented further analysis of **A** by means of VT-PXRD.[viii] It remains unclear as to why **4** was observed as one of the reaction products in the solid-state transformation of **A** into **3** by NMR spectroscopy. Whilst I am reluctant to speculate on its presence, it is possible that unforeseen decomposition pathways are available within crystals of **A** due to trace amounts of solvent operating as radical scavengers which could not be fully removed from the solid-state samples *in vacuo*. It is unlikely that solid state samples of **3** would decompose to **4** upon dissolution in CD_2Cl_2 in the dark at room temperature since the resulting 9:1 solutions of **3**:**4** were found to be stable for up to 3 days in the dark at room temperature. No indication of subsequent decomposition was observed until the solutions were exposed to light.

2.6.2 – HP-XRD studies of [Rh(PONOP)(κ$_{Cl}$-ClCH$_2$Cl)][BAr$^F{}_4$]

Since thermally induced OA was achieved in solid-state samples of **A** at modest temperatures (as observed through product distribution analysis of the heated material by ^{1}H NMR spectroscopy), it was speculated that pressure-induced OA might also be feasible in samples of **A**. As previously reported by Weller and co-workers,[31] the extended packing observed in **A** consists of two of cations encased by a bicapped square prismatic arrangement of anions, such that each cation is surrounded by an octahedral arrangement of five anions and one other cation (Fig. 2.18). Similar to what was observed in **1**, the dichloromethane ligand in **A** is situated within the cavity created by a neighbouring [BAr$^F{}_4$]$^-$ counterion, meaning that compression might not influence the bond of interest to any significant extent. However, the bond dissociation energies (BDE) of C(sp^3)–Cl bonds are *ca*. 50 kJ mol^{-1} smaller than those of C(sp^2)–Cl bonds.[44] Furthermore, the unit cell volume per complex and void volume per complex for the OA product **3** (1508.0(2) Å^3 and 335 Å^3, respectively) were found to be smaller than

[viii] No samples were studied during the final allotment of BAG time in July 2022 at I11 due to instrument misalignment. Because the outstanding experiments required a complicated execution script and manual manipulation of the hot air blower, these experiments were unable to be conducted before submission of this thesis.

those of **A** at ambient pressure (1531.0(2) Å^3 and 342 Å^3, respectively), supporting the hypothesis that compression of **A** could feasibly engender OA. These observations prompted the investigation of **A** by means of HP-XRD.

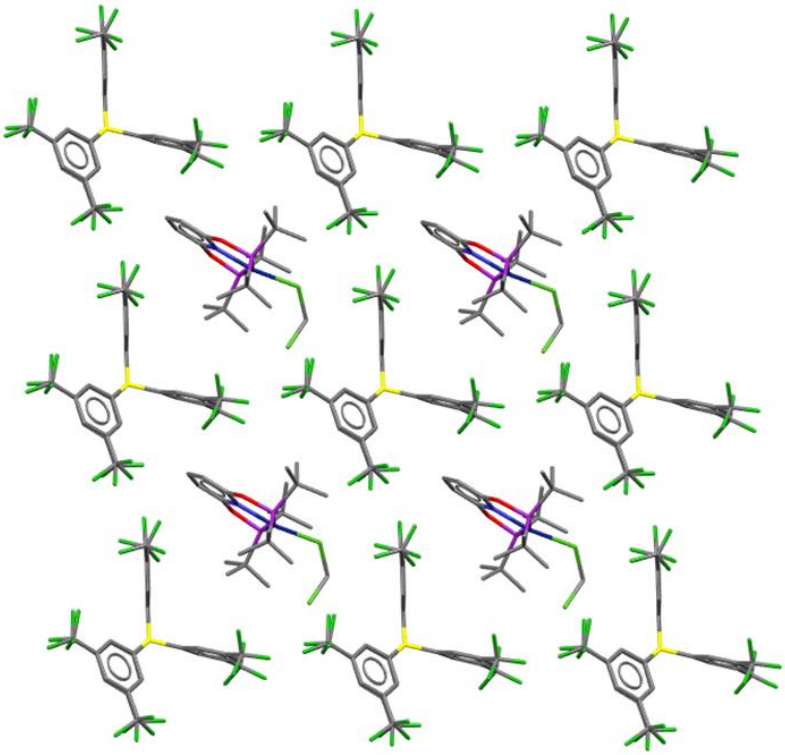

Figure 2.18 – The extended packing observed in **A**. Hydrogen atoms omitted for clarity.

Crystals of **A** were investigated under pressure at Diamond Light Source on beamline I19 at 293 K using Ag-edge radiation (λ = 0.48590 Å, 25.5 keV). Samples of **A** were individually loaded into three separate DACs - DACs 1 and 2 were loaded with the PTM Daphne-7373, whilst DAC 3 was loaded with paraffin oil as the PTM. Whilst DACs 1 and 2 contained the previously reported *C*2/*c* polymorph of **A**, **A-α**, it was discovered that DAC 3 contained a previously unknown polymorph of [Rh(PONOP)(κ$_{Cl}$-ClCH$_2$Cl)][BAr$^F{}_4$], **A-β**, which was loaded into the DAC at ambient pressure. The new polymorph crystallised in the triclinic space group $P\bar{1}$ (at 6.6 kbar: a = 12.9319(17) Å, b = 22.138(5) Å, c = 22.923(5) Å, α = 67.12(2) °, β = 86.58(2) °, γ = 87.841(16) °, V = 6035(2) Å^3, Z' = 2). It should be noted that whilst no solution was obtained for **A-β** using traditional solution methods, it became apparent that the structure was isomorphous to that of the κ$_{Cl}$-Cl^{i}Pr adduct **9**. A modified refinement of **9** in which the chloroalkane ligand was removed from the CIF was used as the starting

model to solve **A-β** via isomorphous replacement (Fig. 2.19*;* see chapter 6 and appendix). It was confirmed that **A-β** (which was initially investigated at 6.6 kbar) was not a high pressure phase of **A-α**, since no phase transitions were observed for either sample of **A-α** between ambient pressure and 15.7 kbar.

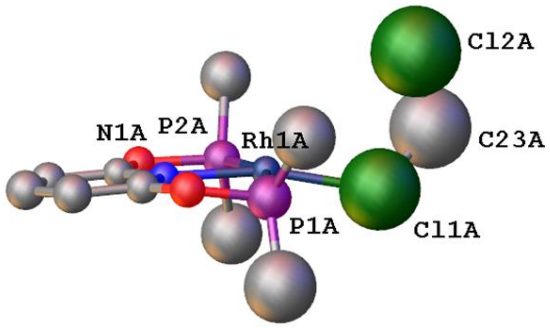

Figure 2.19 – A partially labelled structure of **A-β** at 6.6 kbar (refined isotropically). Only one unique complex is shown. Counterion, terminal ^{t}Bu groups and hydrogen atoms omitted for clarity.

Daphne-7373 and paraffin oil are reported to have hydrostatic limits of 22 kbar and 30 kbar, respectively.[53,54] Both oils were sparged with argon before use. Polymorph **A-β** (crystal C; DAC 3) was studied at pressures of 6.6, 7.0, 13.5, 18.1, 26.3 and 32.0 kbar, however, no datasets yielded a viable structural refinement.[ix] Consequently, only the pressure dependence of the unit cell parameters will be discussed herein. The same rationale applies to both crystals A and B of **A-α**, which were studied at pressures of 1.9, 7.4 and 9.5 kbar (crystal A; DAC 1) and at pressures of 6.3, 8.8, 10.6 and 15.7 kbar (crystal B; DAC 2). For both **A-α** and **A-β**, diffraction was of poor quality, resulting in low signal to noise ratios (~5) and poor resolution (*ca*. 1.6 Å). Consequently, no suitable refinements were obtained from the studies, preventing the detailed analysis of any bond lengths or bond angles. For all three crystals, sample degradation became apparent before the hydrostatic limits of the PTM were reached. Loss of diffraction was noticeable after pressures of 7.4, 10.6 and 18.1 kbar were surpassed for crystals A, B and C, respectively. Crystals failing to sufficiently diffract

[ix] Selected bond lengths, bond angles and crystallographic tables for both polymorphs are supplied in the appendix.

before the hydrostatic limit of the PTM is reached is not uncommon for high pressure studies.[55]

The unit cell parameters for **A-β** were reliably determined up to and slightly beyond the hydrostatic limit of the PTM (up to 32.0 kbar). The unit cell parameters indicated smooth compressions along all axes and the cell volume decreased at a consistent rate (Fig. 2.20). Although the 'unit cell volume per complex' value decreasing below that calculated for the ambient pressure structure of **3** ($^{V}/_{Z}$: **3** at 150 K, 0 kbar = 1508 Å^3; **A-β** at 293 K, 6.6 kbar = 1508 Å^3; 26.3 kbar = 1339 Å^3), it remains unclear whether OA was observed across the studied pressure range, due to the poor quality of the structural refinements being analysed. It cannot be definitively stated whether bond activation was achieved or not during this experiment, unfortunately.

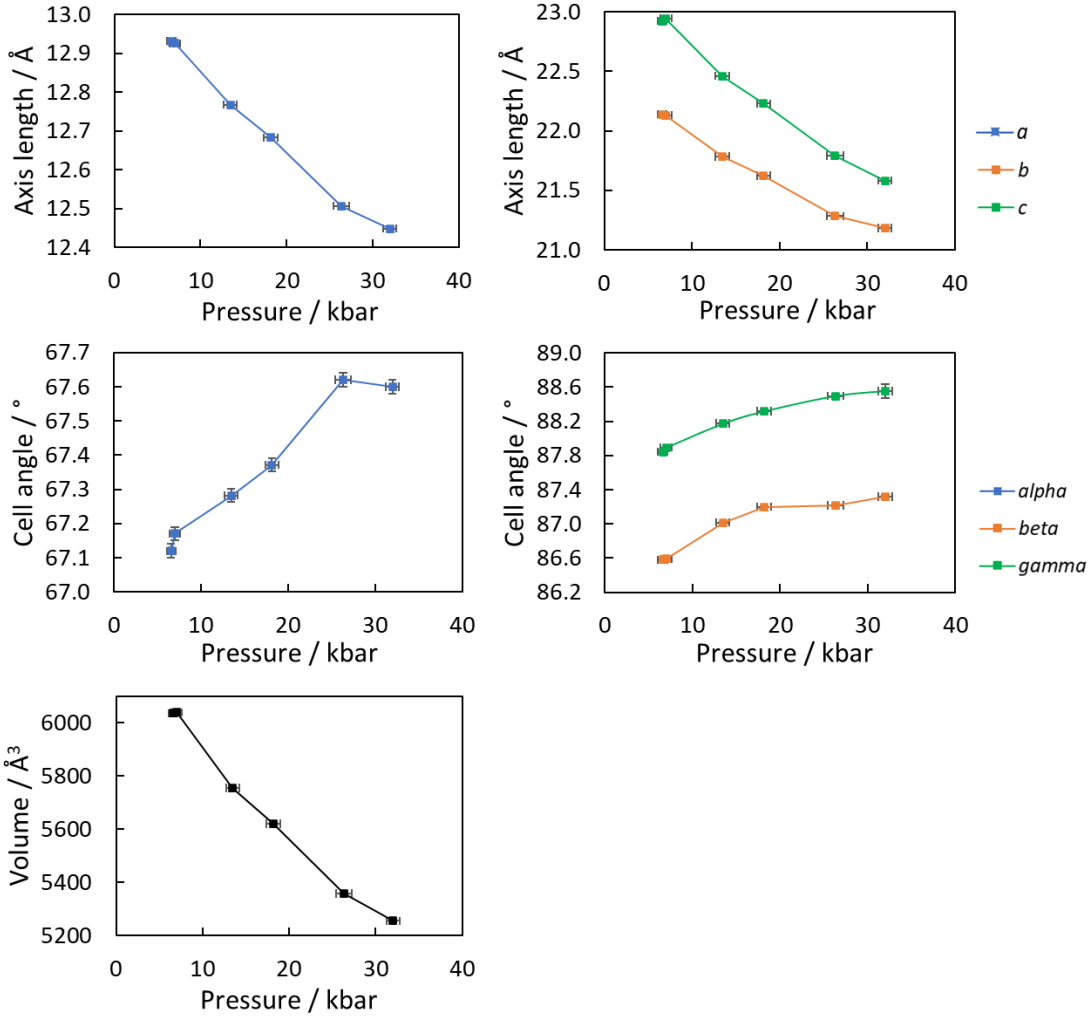

Figure 2.20 – The unit cell parameters of **A-β** as a function of pressure.

Detailed structural analysis of **A-β** proved impossible due to the low resolution and limited completeness of the datasets, which resulted in poorly determined atomic positions. Nevertheless, assessment of the unit cell parameters indicated that no bond activation or phase transitions occurred across the studied pressure range (Fig. 2.20). The poor quality of the data collected was partially attributed to the disorder of the CF_3 groups present in the counterion at room temperature and the large number of atoms in the low symmetry ($P\bar{1}$) unit cell.

The unit cell parameters for **A-α** (crystals A and B) were less reliably determined; trends between the two tested samples deviated significantly, although the cell lengths and volumes consistently decreased as pressure was applied (Fig. 2.21). The estimated standard deviations (esds) were calculated to be an order of magnitude larger than the other cell parameters for the *c* and *b* axes of crystals A and B, respectively. These larger esds are significant because they indicate that the cell parameters are less well determined. When unit cells of the crystals are closely aligned along the direction of the X-ray source, higher esds for these specific directions are obtained, since a comprehensive dataset cannot be collected due to the body of the DAC. Unfortunately, the necessity of loading the DACs within a glovebox prohibited intricate and precise reorientation of the sample relative to the diamond faces (and, therefore, the X-ray beam).

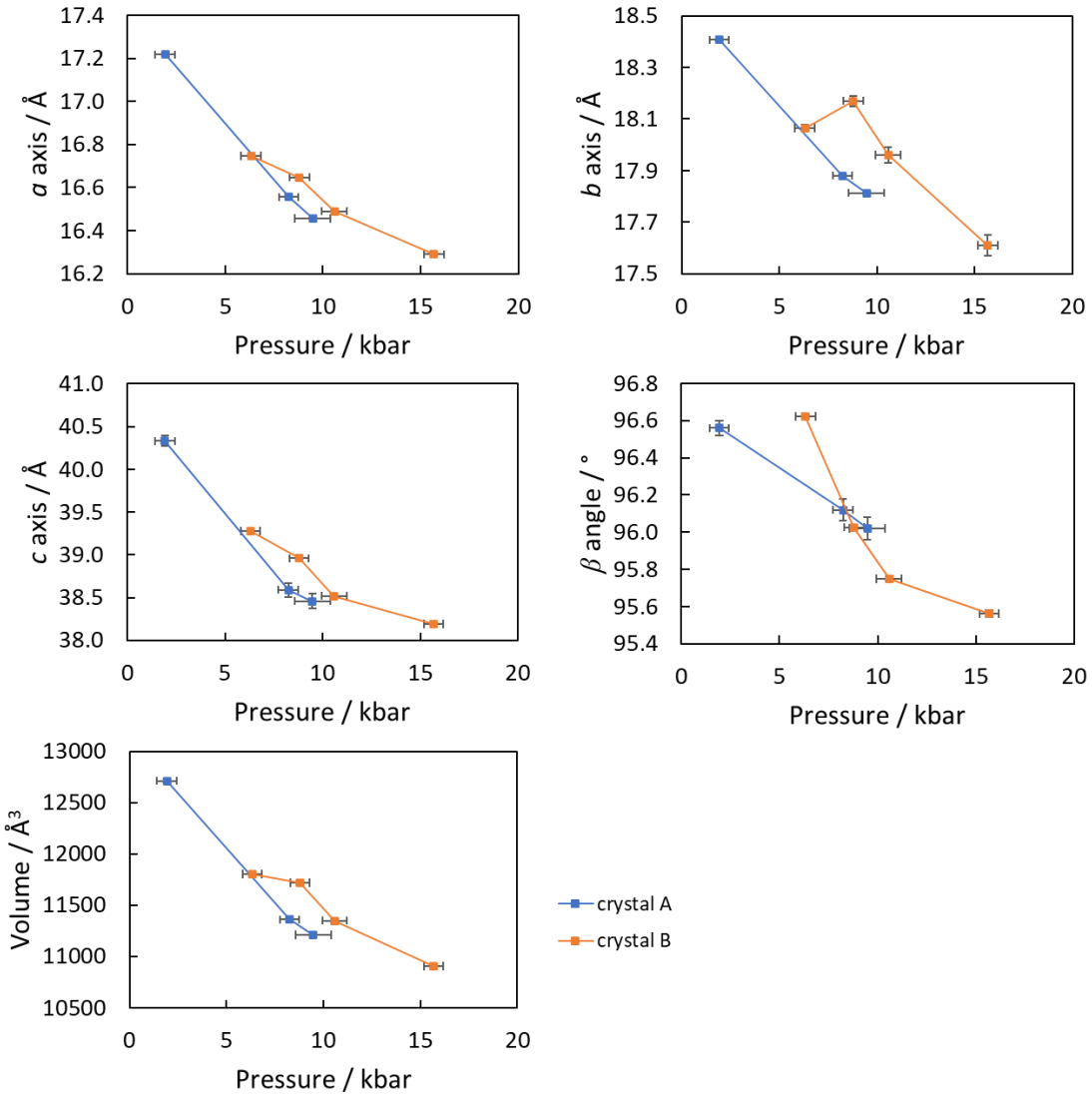

Figure 2.21 – The unit cell parameters of **A-α** as a function of pressure for crystals A (blue) and B (orange).

All datasets of **A-α** failed to yield structural refinements of good enough quality to provide meaningful analysis of the bond lengths and bond angles of **A** as a function of pressure. However, assessment of the unit cell parameters and the visual inspection of the refinements[x] for both samples of **A-α** indicated that no bond activation or phase transitions occurred across the sampled pressure range, despite the 'unit cell volume per complex' value decreasing below that calculated for the ambient pressure structure of **3** ($^{V}/_{Z}$: **3** at 150 K, 0 kbar = 1508 Å^3; **A-β** at 293 K, 1.9 kbar = 1589 Å^3; 9.5 kbar =

[x] No refinements reached convergence for either polymorph of **A**

1401 Å^3). Once again, it cannot be definitively stated whether OA occurred or not during this experiment, since the quality of the structural refinements being analysed were so poor.

2.7 – Conclusions

As a platform for investigating C–Cl bond activation, a series rhodium(I) pincer complexes with the general form [Rh(PONOP)(κ_{Cl}-ClR)][BAr$^F{}_4$] (R = CH_2Cl, **A**; Ph, **1**; Cy, **5**; CH_2CH_2Cl, **8**; ^{i}Pr, **9**) were prepared. Notably, the chlorobenzene adduct **1** served as an excellent synthon for the preparation of other κ_{Cl}-chlorocarbon complexes through ligand substitution. The first examples of rhodium(I) κ_{Cl}-complexes of chlorobenzene, 1,2-dichloroethane, 2-chloropropane and chlorocyclohexane have been synthesised and isolated using this method.

Complex **1** was stable under ambient conditions, but selective C–Cl OA could be induced under forcing conditions (125 °C, ClPh, 4 days), affording the OA adduct **2**. This reaction was unaffected by the presence of TEMPO, so was proposed to proceed via a concerted mechanism. Activation of the weaker C(sp^3)–Cl bonds of dichloromethane (96 h at 50 °C in the dark), 1,2-dichloroethane (*ca*. 20 % activation after 24 h at 50 °C), 2-chloropropane (24 h at 50 °C) chlorocyclohexane (24 h at 50 °C), and 2-chloro-2-methylpropane (< 5 min at room temperature) by the rhodium(I) pincer occurred under milder conditions. The reactivity exhibited was proposed to occur via non-chain radical mechanisms involving the generation of **4**.

Net dehydrochlorination affording [Rh(PONOP)(H)Cl][BAr$^F{}_4$] , **6**, and an alkene by-product resulted from chlorocyclohexane and 2-chloro-2-methylpropane solutions of **1**. Similarly, dehydrochlorination was observed in the 1,2-dichloroethane and 2-chloropropane adducts **8** and **9**, however, the product distributions were more complex. In addition to the formation of **8** and **9**, the respective alkene by-products were found to coordinate to the rhodium(I) pincer fragment, generating the respective rhodium(I) adducts [Rh(PONOP)(η^2-CH_2CHR)][BAr$^F{}_4$] (R = Cl, **10**; R = Me, **11**). With these substrates, hydrogen atom abstraction from the corresponding alkyl radicals is considerably faster than C-radical recombination with **4**. This proposal is supported by the hydrogen atom transfer observed between **8** and **9** on the ^{1}H NMR time scale at room temperature upon addition of TEMPO to solutions of the latter.

For dichloromethane, subsequent recombination of **4** with the •CH_2Cl radical in solution was in competition with the photo-induced reductive elimination process when the reaction was conducted in light. Contrastingly, an approximate 9:1 mixture of $\mathbf{d_x}$-**3**:**4** is observed after 4 days of heating CH_2Cl_2 or CD_2Cl_2 solutions of $\mathbf{d_x}$-**A** in the dark at 50 °C. RE of C–X bonds (X = F, Cl, Br) are usually thermodynamically uphill, so reports of this nature are scarce.[56-58] The photo-sensitive radical reactivity discovered herein could account for the product distribution Weller and co-workers previously reported for the PNP analogue [Rh(PNP)(CH_2Cl)Cl][BAr^F_4], since the authors reported the concomitant formation of the rhodium(III) species [Rh(PNP)(H)Cl][BAr^F_4], amongst other unidentified products.[31]

The transformation of **A** into **3** was also achieved in the solid-state, as observed by NMR spectroscopy upon dissolution of crystallites of **A** in CD_2Cl_2 after heating overnight at 110 °C. This transformation was further characterised by VT-PXRD, where samples of **A** displayed NTE in the *b* and *c* axes, as well decreases in the unit cell volume above 350 K. It remains unclear whether this is strictly a SC-SC transformation, since the air-sensitivity of **A** prohibited investigation of the transformation by single crystal VT-XRD. Pressure-induced OA proved elusive for single crystals of **A**, and the datasets suffered from low completeness, poor resolution and low crystal symmetry, leading to the inaccurate location of atomic coordinates. However, a new polymorph (**A-β**) was discovered that was isomorphous with the 2-chloropropane adduct **9**. This polymorph is assumed to be a minor component of the bulk sample, since experimental PXRD patterns were in good agreement with the cell parameters obtained from the originally reported polymorph **A-α**.[31]

The mechanistic differences between the OA pathways observed in **1** and **A** appear to arise from the greater amount of energy required to cleave C(sp^2)-Cl bonds compared to C(sp^3)-Cl bonds in addition to the higher enthalpy of formation of a Ph• radical (330 ± 3.3 kJ mol^{-1}) as opposed to a •CH_2Cl radical (117 ± 2.9 kJ mol^{-1}). The differences in reactivity between **1** and **A** and the relative stabilities of the respective OA products **2** and **3** highlight how even strikingly similar complexes can favour drastically different mechanistic pathways under comparable conditions. Understanding such nuances in reactivity will further improve our control over bond activation processes such as OA.

References

1. A. Zapf and M. Beller, *Chem. Eur. J.*, 2001, **7**, 2908-2915.
2. I. Kanwal, A. Mujahid, N. Rasool, K. Rizwan, A. Malik, G. Ahmad, S. A. A. Shah, U. Rashid and N. M. Nasir, *Catalysts*, 2020, **10**, 443-491.
3. L. Ackermann, R. Born, J. H. Spatz and D. Meyer, *Angew. Chem. Int. Ed.*, 2005, **44**, 7216-7219.
4. G. S. Lee, D. Kim and S. H. Hong, *Nat. Commun.*, 2021, **12**, 991.
5. C. Douvris and C. A. Reed, *Organometallics*, 2008, **27**, 807-810.
6. R. Dorta, L. J. W. Shimon, H. Rozenberg and D. Milstein, *Eur. J. Inorg. Chem.*, 2002, **2002**, 1827-1834.
7. M. Portnoy and D. Milstein, *Organometallics*, 1993, **12**, 1665-1673.
8. F. Barrios-Landeros, B. P. Carrow and J. F. Hartwig, *J. Am. Chem. Soc.*, 2009, **131**, 8141–8154.
9. F. Barrios-Landeros and J. F. Hartwig, *J. Am. Chem. Soc.*, 2005, **127**, 6944-6945.
10. J. F. Hartwig and F. Paul, *J. Am. Chem. Soc.*, 1995, **117**, 5373-5374.
11. A. K. d. K. Lewis, S. Caddick, F. G. N. Cloke, N. C. Billingham, P. B. Hitchcock and J. Leonard, *J. Am. Chem. Soc.*, 2005, **125**, 10066-10073.
12. T. T. Tsou and J. K. Kochi, *J. Am. Chem. Soc.*, 1979, **101**, 6319-6332.
13. L. Schwartsburd, R. Cohen, L. Konstantinovski and D. Milstein, *Angew. Chem.*, 2008, **47**, 3603-3606.
14. J. Breitenfeld, J. Ruiz, M. D. Wodrich and X. Hu, *J. Am. Chem. Soc.*, 2013, **135**, 12004-12012.
15. J. Choi, D. Y. Wang, S. Kundu, Y. Choliy, T. J. Emge, K. Krogh-Jespersen and A. S. Goldman, *Science*, 2011, **332**, 1545-1548.
16. M. E. v. d. Boom and D. Milstein, *Chem. Rev.*, 2003, **103**, 1759−1792.
17. M. Albrecht and M. M. Lindner, *Dalton Trans.*, 2011, **40**, 8733-8744.
18. M. Puri, S. Gatard, D. A. Smith and O. V. Ozerov, *Organometallics*, 2011, **30**, 2472-2482.
19. S. G. Curto, L. A. de las Heras, M. A. Esteruelas, M. Oliván and E. Oñate, *Organometallics*, 2019, **38**, 3074-3083.
20. T. J. Morrow, J. R. Gipper, W. E. Christman, N. Arulsamy and E. B. Hulley, *Organometallics*, 2020, **39**, 2356-2364.
21. T. M. Douglas, A. B. Chaplin and A. S. Weller, *Organometallics*, 2008, **27**, 2918-2921.
22. S. Gatard, C. Guo, B. M. Foxman and O. V. Ozerov, *Organometallics*, 2007, **26**, 6066-6075.
23. S. Gu, R. J. Nielsen, K. H. Taylor, G. C. Fortman, J. Chen, D. A. Dickie, W. A. Goddard and T. B. Gunnoe, *Organometallics*, 2020, **39**, 1917-1933.
24. L. A. de Las Heras, M. A. Esteruelas, M. Olivan and E. Onate, *Organometallics*, 2022, **41**, 716-732.
25. S. G. Curto, M. A. Esteruelas, M. Oliván, E. Oñate and A. Vélez, *Organometallics*, 2017, **36**, 114-128.
26. L. Fan, S. Parkin and O. V. Ozerov, *J. Am. Chem. Soc.*, 2005, **127**, 16772-16773.
27. A. E. Kynman, S. Lau, S. O. Dowd, T. Kramer and A. B. Chaplin, *Eur. J. Inorg. Chem.*, 2020, **2020**, 3899-3906.
28. S. Gatard, R. Celenligil-Cetin, C. Guo, B. M. Foxman and O. V. Ozerov, *J. Am. Chem. Soc.*, 2006, **128**, 2808-2809.
29. H. Wu and M. B. Hall, *Dalton Trans.*, 2009, 5933-5942.
30. S. D. Timpa, C. J. Pell and O. V. Ozerov, *J. Am. Chem. Soc.*, 2014, **136**, 14772-14779.

31. G. M. Adams, F. M. Chadwick, S. D. Pike and A. S. Weller, *Dalton Trans.*, 2015, **44**, 6340-6342.
32. F. L. Taw, H. Mellows, P. S. White, F. J. Hollander, R. G. Bergman, M. Brookhart and D. M. Heinekey, *J. Am. Chem. Soc.*, 2002, **124,**, 5100-5108.
33. J. R. Krumper, M. Gerisch, J. M. Suh, R. G. Bergman and T. D. Tilley, *J. Org. Chem.*, 2003, **68**, 9705-9710.
34. B. K. Corkey, F. L. Taw, R. G. Bergman and M. Brookhart, *Polyhedron*, 2004, **23**, 2943-2954.
35. T. Wang, J.-L. Niu, S.-L. Liu, J.-J. Huang, J.-F. Gong and M.-P. Song, *Adv. Synth. Catal.*, 2013, **355**, 927-937.
36. J. Campos and E. Carmona, *Organometallics*, 2014, **34**, 2212-2221.
37. P. Ren, S. D. Pike, I. Pernik, A. S. Weller and M. C. Willis, *Organometallics*, 2015, **34**, 711-723.
38. A. J. Martinez-Martinez, B. E. Tegner, A. I. McKay, A. J. Bukvic, N. H. Rees, G. J. Tizzard, S. J. Coles, M. R. Warren, S. A. Macgregor and A. S. Weller, *J. Am. Chem. Soc.*, 2018, **140**, 14958-14970.
39. M. R. Gyton, A. E. Kynman, B. Leforestier, A. Gallo, J. R. Lewandowski and A. B. Chaplin, *Dalton Trans.*, 2020, **49**, 5791-5793.
40. S. D. Pike, F. M. Chadwick, N. H. Rees, M. P. Scott, A. S. Weller, T. Kramer and S. A. Macgregor, *J. Am. Chem. Soc.*, 2015, **137**, 820-833.
41. I. J. Bruno, J. C. Cole, P. R. Edgington, M. Kessler, C. F. Macrae, P. McCabe, J. Pearson and R. Taylor, *Acta Cryst.*, 2002, **B58**, 389-397.
42. M. R. Gyton, T. M. Hood and A. B. Chaplin, *Dalton Trans.*, 2019, **48**, 2877-2880.
43. M. R. Gyton, B. Leforestier and A. B. Chaplin, *Angew. Chem. Int. Ed.*, 2019, **58**, 15295-15298.
44. Y.-R. Luo, *Comprehensive handbook of chemical bond energies*, CRC Press, first edn., 2007.
45. P. S. Pregosin, *NMR in Organometallic Chemistry*, Wiley, 2012.
46. K. M. van Vliet, N. S. van Leeuwen, A. M. Brouwer and B. de Bruin, *J. Org. Chem.*, 2020, **16**, 398-408.
47. L. Sheps, A. C. Crowther, C. G. Elles and F. F. Crim, *J. Phys. Chem. A*, 2005, **109**, 4296-4302.
48. P. B. Roussel, P. D. Lightfoot, F. Caralp, V. Catoire, R. Lesclaux and W. Forst, *J. Chem. Soc. Faraday Trans.*, 1991, **87**, 2367-2377.
49. M. Feller, E. Ben-Ari, T. Gupta, L. J. W. Shimon, G. Leitus, Y. Diskin-Posner, L. Weiner and D. Milstein, *Inorg. Chem.*, 2007, **46**, 10479−10490.
50. A. Longcake, M. R. Lees, M. S. Senn and A. B. Chaplin, *Organometallics*, 2022, **41**, 3557−3567.
51. M. A. Bennet and P. A. Longstaff, *J. Am. Chem. Soc.*, 1969, **91**, 6266-6280.
52. C. Heffner, I. Silwal, J. M. Peckenham and T. Solouki, *Environ. Sci. Technol.*, 2007, **41**, 5419–5425.
53. K. Yokogawa, K. Murata, H. Yoshino and S. Aoyama, *Jpn. J. Appl. Phys.*, 2007, **46**, 3636-3639.
54. R. Lee, J. A. Howard, M. R. Probert and J. W. Steed, *Chem. Soc. Rev.*, 2014, **43**, 4300-4311.
55. J. P. Tidey, H. L. S. Wong, M. Schröder and A. J. Blake, *Coord. Chem. Rev.*, 2014, **277-278**, 187-207.
56. M. Feller, Y. Diskin-Posner, G. Leitus, L. J. Shimon and D. Milstein, *J. Am. Chem. Soc.*, 2013, **135**, 11040-11047.
57. S. Gu, J. Chen, C. B. Musgrave, Z. M. Gehman, L. G. Habgood, X. Jia, D. A. Dickie, W. A. Goddard and T. B. Gunnoe, *Organometallics*, 2021, **40**, 1889−1906.
58. C. M. Frech and D. Milstein, *J. Am. Chem. Soc.*, 2006, **128**, 12434-12435.

Chapter 3 – Synthesis and characterisation of a homologous series of rhodium σ-borane complexes.

Abstract

Efforts to increase the likelihood of pressure-induced reactivity in complexes of $\{Rh(pincer)\}^+$ prompted the exploration of alternative substrates that contained the pre-activated Rh···X–E motif. A series of structurally related σ-borane complexes with the general structure $[Rh(pincer)(\eta^2\text{-}HBR_2)][BAr^F{}_4]$ (pincer = PONOP, HBR_2 = HBpin: **12**; HBcat: **13**; pincer = PNP, HBR_2 = HBpin: **14**; HBcat: **15**) were subsequently prepared and fully characterised by multinuclear NMR spectroscopy, single crystal XRD, elemental microanalysis and IR spectroscopy. The identities of both the pincer ligand and borane substrate in complexes of $\{Rh(pincer)\}^+$ were found to influence the degree of B–H activation, with the $[Rh(PNP)(\eta^2\text{-}HBcat)]^+$ complex **15** activating the borane substrate to the greatest extent.

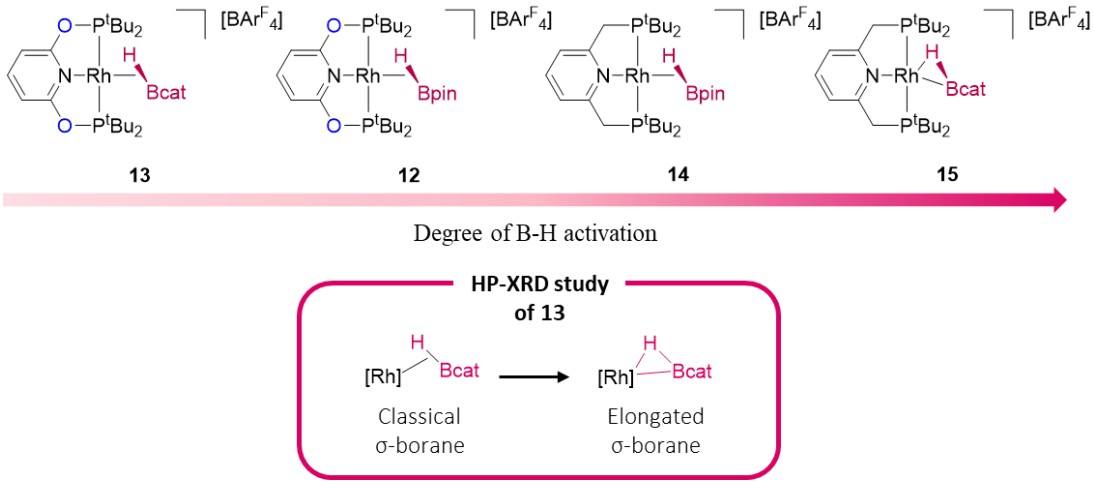

Of the four crystal structures, **13** was found to be the most suitable candidate for HP-XRD studies. Between 4.8–8.8 kbar, **13** underwent an isomorphous phase transition, whereby the σ-borane coordination mode appeared to evolve from a 'classical' σ-borane in the ambient pressure phase into an 'elongated' σ-borane in the high pressure phase. This was thought to be a consequence of enhanced orbital overlap between the HBcat ligand and the metal centre due to compression.

3.1 – Introduction

Coordination complexes containing σ-coordinated E–H groups (E = H, C, Si or B) have been extensively explored in recent years, as they play a fundamental role in both oxidative addition and reductive elimination processes, which are crucial steps in a number of catalytic cycles.[1-5] Both σ-dihydrogen and σ-silane complexes have been extensively studied for their potential uses as hydrogen storage materials and hydrosilylation chemistry.[5,6] Additionally, σ-silane complexes are more stable than their σ-alkane analogues, which tend to exist transiently in solution at very low temperature or can be generated *in situ* in the solid-state via SC-SC transformations for heavier hydrocarbon substrates under rigorously controlled conditions.[4,7-12] C–H activation and associated intermediates have also been extensively studied, but have been largely limited to intramolecular systems (*e.g.*, agostic interactions).[13-15]

3.1.1 – An introduction to σ-borane complexes

The usefulness of organoboron chemistry cannot be overstated; amine boranes have potential uses as hydrogen storage materials[2,16-18] whilst organoborane species can be used to functionalise hydrocarbon-based substrates[19-21] and facilitate the formation of carbon-carbon bonds.[22-24] One of the most frequently utilised C–C bond formation reactions in the pharmaceutical industry is the Suzuki-Miyaura cross-coupling, which typically requires a palladium catalyst, an aryl halide and boronic acid.[22-25] Complexes containing σ-borane ligands represent an emerging class of compounds which offer insight into how to control B–H bond activation. However, compared to their σ-silane and σ-dihydrogen counterparts, σ-borane complexes have been explored to a much lesser extent, with only a handful of crystal structures reported for complexes of pinacolborane (HBpin) or catecholborane (HBcat; Fig. 3.1).[16,26-34]

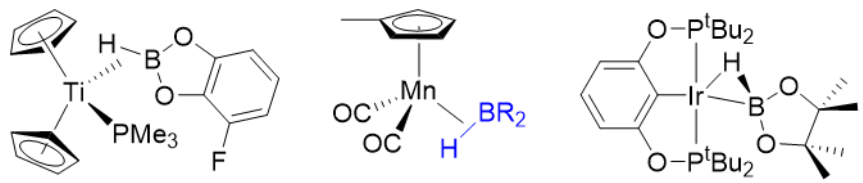

HBR$_2$ = HBcat, **A91**
HBR$_2$ = HBpin, **A92**

Figure 3.1 – Examples of isolated σ-alkoxyborane complexes.[16,33,34]

A commonality amongst many σ-H–E complexes is that the E centre satisfies the octet rule in the pre-coordination state. This is not the case for σ-boranes, which contain an electron deficient boron atom. When considering σ-borane complexes, in addition to the σ-donation (σ-H–E orbital → metal *d* orbital) and π-backbonding (metal *d* orbital → σ*-H–E orbital) components, concomitant back donation occurs from a metal *d* orbital into the 'empty' non-bonding hybrid boron orbital (Fig. 3.2).[5,35]

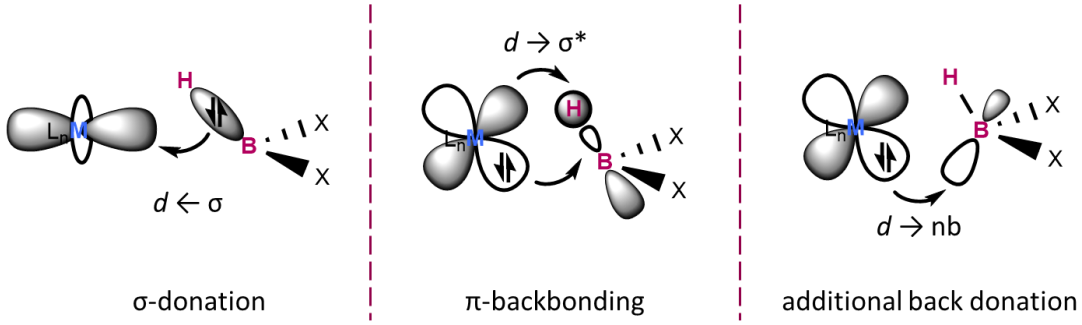

Figure 3.2 – Dewar-Chatt-Duncanson Models illustrating the bonding interactions found in σ-borane complexes.

The principal difference between σ-borane complexes and other E centres is the availability of this empty non-bonding boron orbital, which lies lower in energy than the σ* anti-bonding orbitals found in other E–H systems. Since the boron atom does not satisfy the octet rule in the precoordination state, the non-bonding orbital is available to be more involved in back donation.[5] Comparatively, for σ-alkane complexes, the backbonding interaction is less significant because the σ* orbital is so high in energy. Donation from the B–H σ-bond to the metal centre is also stronger, due to the decreased electronegativity of boron.[5] To contextualise this, the dissociation energies of the σ-borane ligands within $(MeCp)Mn(CO)_2(\eta^2\text{-HBR})$ (HBR = HBcat, **A91**; HBpin, **A92**) were calculated to be similar to the correspondent σ-triphenylsilane complex $(MeCp)Mn(CO)_2(HSiPh_3)$, **A93** (*ca.* 25 kcal mol^{-1}), but greater than the σ-alkane complex $[Co(Cy_2P(CH_2)_4PCy_2)(\eta^1{:}\eta^1\text{-NBA})][BAr^F{}_4]$, **A94** (*ca.* 19 kcal mol^{-1}),[7] and most dihydrogen complexes (13-17 kcal mol^{-1}).[34]

It is important to distinguish the characteristics of σ-borane complexes from that of the better-known tetrahydroborate complexes.[36] Particular interest has been paid to the

$[BH_4]^-$ ligand since it is isoelectronic with CH_4, making it a more accessible analogue for the study of prototype alkane activation systems.[16,37] However, tetrahydroborate is negatively charged, which allows an additional electrostatic component to contribute towards coordination of the ligand.[5]

The coordination modes of tetrahydroborates can be challenging to define due to ligand fluxionality,[38] difficulties in locating B and H atoms by XRD,[36] and difficulties interpreting complex NMR spectra involving several different spin-active nuclei.[29] One such example is the iridium pincer complex (POCOP)$IrH_2(BH_3)$, **A95**, where the highly asymmetric η^2-coordination mode of the $[BH_4]^-$ ligand presented a problem: should **A95** be considered an example of an η^2-borohydride or a σ-borane complex? The authors concluded that the highly activated B–H2 bond (1.74(5) Å) was too long to be considered a covalent interaction, therefore, assigned **A95** as a σ-borane complex with an activated B–H3 bond length of 1.45(5) Å, as opposed to a tetrahydroborate complex (Fig. 3.3).[16]

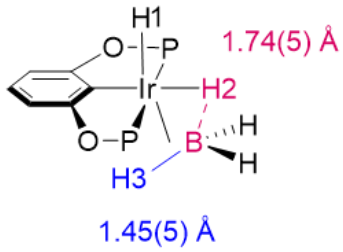

Figure 3.3 – The labelled structure of **A95** and the corresponding B–H distances as determined by neutron diffraction data.

Difficulties have also been encountered when attempting to formally assign the coordination modes of σ-borane complexes, including complexes of HBpin and HBcat. Much like their tetrahydroborate counterparts, the bonding situation can be considered to exist somewhere along the continuum between a classical σ-borane and a formal boryl hydride (Fig. 3.4). Because the B–H bonds in σ-borane complexes are partially activated, the bonding characteristics of the complexes are determined by the identity of the metal, the neighbouring ligands, and the borane itself.[20,29,31,39] The spectroscopic, crystallographic and computational data have to be carefully considered in order to correctly assign a specific coordination mode in certain cases.[26-29]

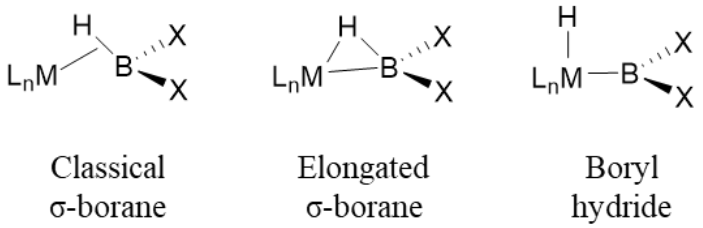

Figure 3.4 – Depictions of the different coordination modes of borane ligands.

In the case of $RuH_2(\eta^2\text{-HBcat})(\eta^2\text{-}H_2)(PCy_3)_2$, **A96** ($PCy_3$ = tricyclohexylphosphine), whilst the formation of the complex was confirmed by NMR spectroscopy in solution, single crystal XRD ultimately yielded evidence of a classical σ-borane coordination mode. All five hydrides were located using the electron density difference map when the collection was carried out at 90 K as opposed to 180 K, since the lower temperature improved data quality and prevented rotation of the H_2 ligand.[29] Although the solution phase data did not contradict the solid-state data, it gave limited insight into the exact coordination mode adopted by the borane ligand.[29]

The HBcat ligand has also demonstrated sensitivity to neighbouring ligands within a given coordination complex.[26,27] The Xantphos complexes **A97** and **A98** differ only by the identity of the ligand *trans* to the borane ligand (Fig. 3.5). The greater electronegativity and superior π-donating capabilities of the chloride ligand resulted in a greater degree of B–H activation in **A98**. The crystal structures of **A97** and **A98** confirm the elongation of the B1–H1 bond from 1.49(4) Å to 1.68(2) Å, respectively.[27] Additionally, atoms in molecules (AIM) analysis revealed that whilst both complexes contained bond critical points (BCPs) along the Os1–B1 and B1–H1 bond paths, **A98** contained an additional B1–H1 BCP as well as a ring critical point (RCP) within the centre of the Os1–B1–H1 interaction. A more significant interaction between the Os1 centre and H1 in **A98** occurred due to the more hydridic nature of H1 as a result of the greater degree of borane activation. The classical σ-borane in **A97** lacks this triangular geometry because of the less stabilising electrostatic and orbital interactions the hydride ligand provides in comparison to the chloride ligand.[27] Therefore, **A97** is best described as a classical σ-borane complex, whereas **A98** is best described as an elongated σ-borane complex.

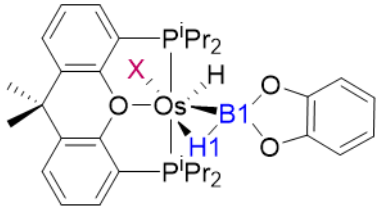

A97: X = H, H1-B1 = 1.49(4) Å
A98: X = Cl, H1-B1 = 1.68(2) Å

Figure 3.5 – The structures of **A97** and **A98**, with the B1–H1 bond length and the *trans* X atom depicted in blue and burgundy, respectively.

The definitions of 'classical' and 'elongated' coordination modes provided by Esteruelas and co-workers are that classical σ-borane complexes are normally characterised by B–H bond lengths between 1.4-1.5 Å in length, whilst elongated σ-borane complexes typically possess B–H bond lengths of between 1.6-1.7 Å.[26,27] Whilst B–H bond lengths greater than 1.5 Å are generally indicative of an elongated coordination mode for complexes of HBpin or HBcat, there are exceptions to this rule. For example, the complex OsH(η^2-HBcat)(η^3-H_2Bcat)(P^{i}Pr$_3$)$_2$, **A99**, adopts an elongated coordination mode and displays the three BCPs and RCP required to be assigned as such. However, the B–H bond length obtained by single crystal XRD for **A99** was only 1.39(3) Å.[26] What becomes increasingly apparent when surveying σ-borane complexes is that in order to formally assign a coordination mode, it is first necessary to consider the collective evidence obtained from multiple characterisation techniques. Several different methods must be utilised so as to supply definitive insight where there is otherwise ambiguity.

3.1.2 – Motivation for investigating σ-borane complexes

σ-borane complexes can be considered as structural intermediates for the concerted OA of B–H bonds, which is of particular interest to chemists due to the prevalence of organoboron chemistry in catalysis.[2,16-21] However, such intermediates are challenging to isolate and study in solution due to species reactivity and instability in solution. Studying organoborane intermediates in the solid-state is of interest because not only can solution phase decomposition pathways be circumvented, but chemical

intermediates that have only otherwise been inferred from reaction outcomes in solution can be definitively confirmed. The latter idea is exemplified by the recent work conducted by Bissember and co-workers, who unambiguously confirmed the structures of several palladium(II) boronate complexes, which are known to be transient and elusive intermediates in Suzuki-Miyaura cross coupling reactions.[40]

If an extensive series of structurally related σ-borane complexes were to be isolated, structure-activity relationships could be systematically evaluated under both ambient and extreme conditions in the solid-state. Since the B–H bonds of σ-boranes are already partially activated by the metal centre under ambient conditions, it seemed reasonable to hypothesise that pressure-induced OA might be accessible. Furthermore, to the best of my knowledge, HP-XRD has not yet been used to study B–H bond activation, so success of this study would establish a novel application of the technique.

3.2 – Preparation of the homologous σ-borane series

The σ-borane series [Rh(pincer)(η^2-HBR_2)][BAr^F_4], (pincer = PONOP, HBR_2 = HBpin: **12**; HBcat: **13**; pincer = PNP, HBR_2 = HBpin: **14**; HBcat: **15**) were synthesised by adapting a procedure previously reported by the Chaplin group for the preparation of [Rh(pincer)]$^+$ adducts (Scheme 3.1).[41] Dissolution of equimolar quantities of [$Rh(COD)_2$][BAr^F_4] and the respective pincer ligand (PONOP or PNP) in 1,2-difluorobenzene (1,2-$C_6H_4F_2$) at room temperature resulted in the formation of *in situ* mixtures of monomeric [Rh(pincer)(η^2-COD)][BAr^F_4] and dimeric [{Rh(pincer)}$_2$(μ-η^2:η^2-COD)][BAr^F_4]$_2$ (pincer = PONOP: **A17a/b**; PNP: **A18a/b**), which exist in dynamic equilibrium in solution.[41] An excess (3-4 eq.) of the appropriate borane solution (0.40 M HBcat or 0.67 M HBpin in 1,2-$C_6H_4F_2$) was subsequently added to the *in situ* reaction mixture after 5 minutes and left to stand for several hours at room temperature. The loosely coordinated COD was gradually displaced by the respective borane ligand (< 6 h), as observed by ^{1}H and ^{31}P NMR spectroscopy.

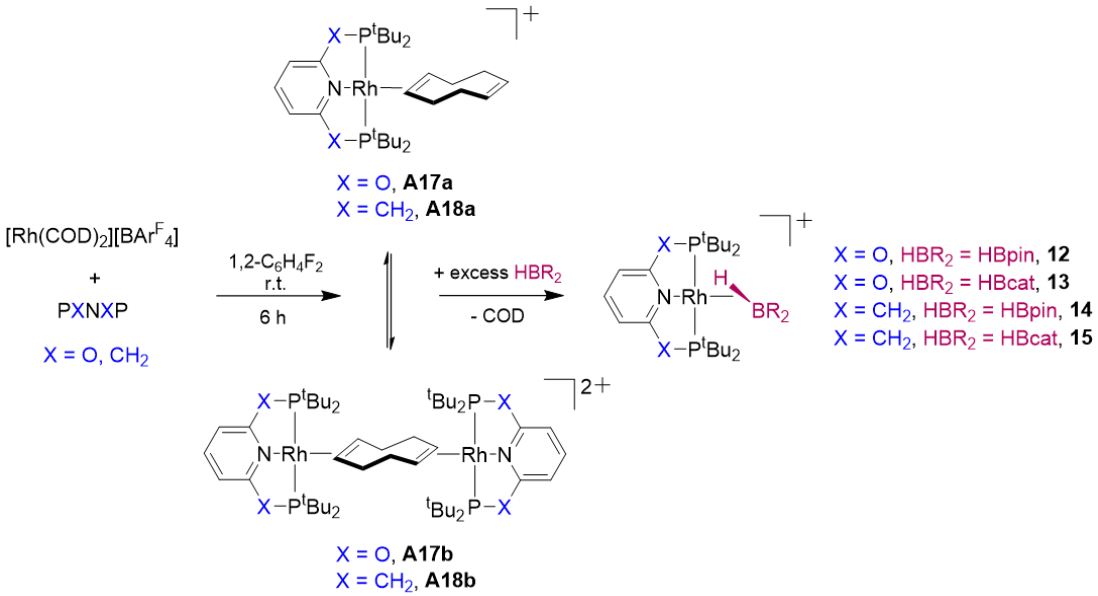

Scheme 3.1 – A scheme for the preparation of complexes **12-15**. The counterions for the labelled complexes have been omitted, for clarity.

Species **12-15** were generated *in situ* using this general methodology and could be isolated in moderate-to-good yields (60-80 %, see chapter 6) by liquid-liquid diffusion of hexane into the 1,2-$C_6H_4F_2$ reaction mixtures at room temperature. Coordination of the borane ligands were evidenced by characteristic broad resonances in the hydride region of the ^{1}H NMR spectra (δ -13.90 to -17.70 ppm) and a broad resonance between δ 35-40 ppm in the ^{11}B NMR spectra, corresponding to the coordinated proton and boron environments, respectively (Table 3.1). The boron resonances were observed in the region where 3-coordinate boranes (BR_3 or BX_3) typically occur, as expected for the alkoxyboranes HBpin and HBcat.[42] The coordinated proton environments appear in the ^{1}H NMR spectra as broad singlets (or in the case of **15**, a broad doublet; $^{1}J_{RhH}$ = 41.2), in part due to unresolved *J* couplings to different spin-active and quadrupolar nuclei present in the samples (^{103}Rh: S = $^{1}/_{2}$; ^{31}P = S = $^{1}/_{2}$; ^{11}B: S = $^{3}/_{2}$, 80.2 % abundance; ^{10}B: S = 3, 19.8 % abundance; ^{1}H: S = $^{1}/_{2}$).[43] Furthermore, examination of the ^{1}H NMR spectra showed all four complexes possess time-averaged C_{2v} symmetry (as evidenced by the equivalent ^{t}Bu environments), indicating that the borane ligands are weakly bound and highly fluxional.

Table 3.1 – A table of selected NMR data[xi] for complexes **12-15** at 298 K in 1,2-$C_6H_4F_2$ referenced to an internal C_6D_6 capillary. Only data associated with the coordinated borane environments are supplied for the ^{1}H and ^{11}B NMR spectra.

Complex	^{1}H / ppm	^{31}P{^{1}H} / ppm	^{11}B / ppm
12	-14.94 (s, br)	217.2 (d, $^1J_{RhP}$ = 129 Hz)	35.3 (s, br)
13	-13.90 (s, br)	217.8 (d, $^1J_{RhP}$ = 123 Hz)	36.6 (s, br)
14	-17.57 (s, br)	73.8 (d, $^1J_{RhP}$ = 123 Hz)	35.8 (s, br)
15	-17.70 (br d, $^1J_{RhH}$ = 41.2 Hz)	76.2 (d, $^1J_{RhP}$ = 113 Hz)	39.4 (s, br)

The chemical shifts observed in the ^{31}P{^{1}H} NMR spectra reflect the different electronic properties of the pincer ligands (Table 3.1, Fig. 3.6). Larger *J* couplings were observed within the complexes containing HBpin and/or PONOP, indicating that the interactions between the metal centre and the σ-borane ligand were influenced by the identities of both the pincer ligand and the borane substrate. These trends were expected, since HBpin is known to be a superior σ-donor to HBcat[34] and the mixing of rhodium 4d_{x2-y2} and phosphorus 3*p* orbitals has been shown to be more extensive in complexes of {Rh(PONOP)}$^+$ in comparison to {Rh(PNP)}$^+$.[44] These combined effects result in larger $^1J_{RhP}$ couplings for the HBpin and PONOP-containing complexes. The trends observed in solution by NMR spectroscopy were promising observations, since they suggested that the complexes could be systematically engineered to maximise the activation of the σ-borane ligands.

[xi] See chapter 6 for full assignments of complexes **12**-**15**.

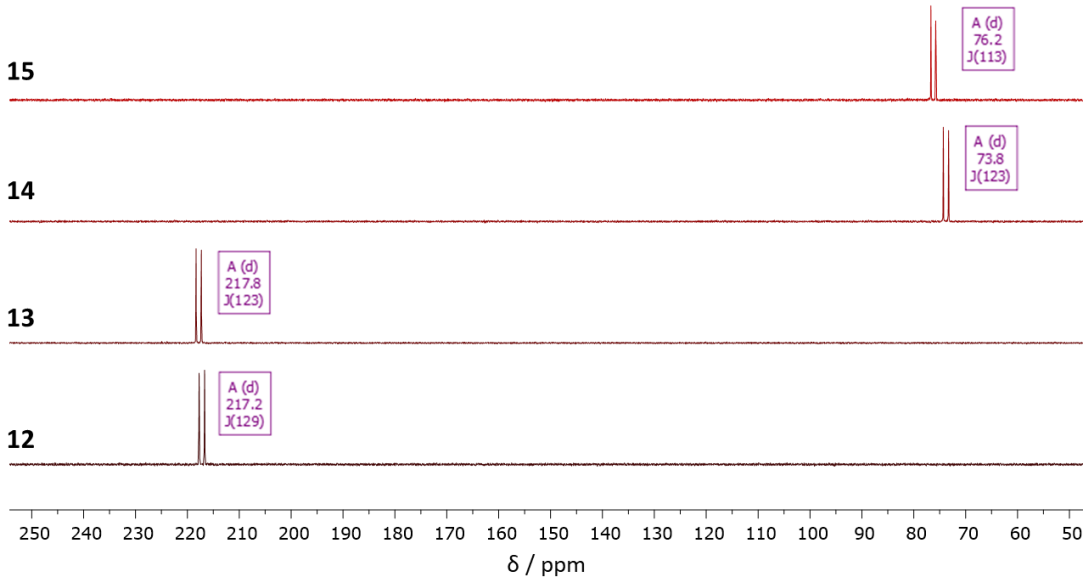

Figure 3.6 – Stacked $^{31}P\{^{1}H\}$ NMR spectra of complexes **12-15** (300 MHz, 1,2-$C_6H_4F_2$, 298 K).

The coordinated proton environments in **12-15** are particularly hydridic in nature in comparison to other reported σ-borane complexes (*c.f.* Table 3.2). The upfield chemical shifts observed for **14** and **15** in particular reflect the increased activation of the σ-borane ligands by the $\{Rh(PNP)\}^+$ fragment. The broad singlets observed in the hydride region of the ^{1}H NMR spectra for **12-14** are typical of classical σ-borane complexes,[45,46] whilst the broad doublet observed in the ^{1}H NMR spectrum of **15** suggests an enhanced association of the hydrogen atom with the rhodium centre. Such an interaction could be indicative of elongated σ-borane character, since this interaction would result in a weakening (*i.e.*, elongation) of the B–H bond (*c.f.* Table 3.2).

Table 3.2 – Table of selected NMR and IR spectroscopic data for previously reported σ-borane complexes of HBpin or HBcat.[16,26,27,33,34] Values that were not supplied by the authors are denoted with a hyphen. The asterisk denotes NMR spectra collected at -30 °C. HBcat' = 4-fluoro-catecholborane. [a]NMR spectra recorded in d^8-toluene. [b]NMR spectra recorded in C_6D_6. [c]NMR spectra recorded in d^8-THF.

Complex	^{1}H / ppm	^{11}B / ppm	B–H bond length / Å	IR ν_{BH} / cm^{-1}	σ-borane assignment
OsH(HBcat)(H_2Bcat)(P^iPr_3)$_2$[a]	-9.50 (br, 4H)	35 (br)	1.39(3)	1903	elongated
OsHCl(HBcat)(Xantphos)[b]	-15.73 (s, br)	52 (br)	1.68(2)	-	elongated
OsH_2(HBcat)(Xantphos)[b]	-1.87 (s,br)	45.5 (br)	1.49(4)	-	classical
$Cp_2Ti(PMe_3)$(HBcat')[a]	-9.4 (s, br)*	64.9 (br)*	1.35(5)	-	not specified
(MeCp)Mn(CO)$_2$(HBcat)[b]	-14.46 (s, br)	46 (br)	1.29(2)	1606	not specified
(MeCp)Mn(CO)$_2$(HBpin)[b]	-15.66 (s, br)	45 (d, $^1J_{BH}$ = 88 Hz)	1.31(2)	1603	not specified
Cp*Re(CO)$_2$(HBpin)[b]	-11.06 (s, br)	46 (br)	N/A[xii]	1603	not specified
(POCOP)Ir(HBpin)[c]	-13.15 (s, br)[xiii]	29 (br)	1.46(6)	2014	not specified

[xii] Single crystals were not obtained by the authors.
[xiii] The ^{1}H{^{11}B} NMR spectrum displayed a triplet resonance: $\delta_{^1H\{^{11}B\}}$ -13.15 (t, $^2J_{PH}$ = 5 Hz).

The argument could be made that **15** actually exists as the rhodium(III) boryl hydride complex [Rh(PNP)(H)(Bcat)][BAr^F_4] in solution, due to the small *J* coupling observed in the $^{31}P\{^1H\}$ NMR spectrum ($^2J_{RhP}$ = 113 Hz)[43] and the pronounced $^1J_{RhH}$ coupling evidenced in the ^1H NMR spectrum. In order to probe this possibility, VT-NMR experiments were conducted on samples of **12-15** in CD_2Cl_2 at 193 K and 298 K, in an attempt to freeze out the solution phase dynamics at lower temperatures (Table 3.3, Fig. 3.7). Had a temperature-dependent equilibrium between the rhodium(I) and rhodium(III) complexes existed in solution in **15**, the $^1J_{RhP}$ coupling observed in the $^{31}P\{^1H\}$ NMR spectra would have decreased substantially at lower temperatures if the rhodium(III) oxidation state was favoured.[43] However, no significant temperature dependence was observed in the $^{31}P\{^1H\}$ NMR spectra, despite rigorous preparation of the samples at -80 °C to ensure that the dynamics of the complexes were frozen out immediately upon dissolution.[xiv]

Table 3.3 – A table of selected NMR spectroscopic data (CD_2Cl_2, 500 MHz) for complexes **12-15** at 193 K (top) and 298 K (bottom).[xv] *J* couplings are supplied to two decimal places for comparative purposes. Only data associated with the coordinated proton environments are supplied for the $^1H\{^{11}B\}$ NMR spectra.

	Complex	$^1H\{^{11}B\}$ / ppm	$^{31}P\{^1H\}$ / ppm	$^{11}B\{^1H\}$ / ppm
193 K	**12**	-14.97 (br d, $^1J_{RhH}$ = 36.22 Hz)	216.54 (d, $^1J_{RhP}$ = 129.89 Hz)	not visible
	13	-14.06 (br d, $^1J_{RhH}$ = 33.35 Hz)	216.96 (d, $^1J_{RhP}$ = 123.09 Hz)	not visible
	14	-17.35 (br d, $^1J_{RhH}$ = 36.96 Hz)	72.86 (d, $^1J_{RhP}$ = 123.64 Hz)	not visible
	15	-18.20 (br d, $^1J_{RhH}$ = 41.87 Hz)	75.31 (d, $^1J_{RhP}$ = 112.36 Hz)	not visible
298 K	**12**	-14.85 (br, fwhm = 106 Hz)	217.45 (d, $^1J_{RhP}$ = 129.77 Hz)	35.1 (s, br)
	13	-13.74 (br, fwhm = 122 Hz)	218.12 (d, $^1J_{RhP}$ = 122.67 Hz)	36.5 (s, br)
	14	-17.46 (br, fwhm = 98 Hz)	73.90 (d, $^1J_{RhP}$ = 123.78 Hz)	35.4 (s, br)
	15	-17.79 (br d, J_{RhH} = 41.47 Hz)	76.14 (d, $^1J_{RhP}$ = 112.82 Hz)	39.4 (s, br)

[xiv] Low temperature NMR samples were prepared by addition of CD_2Cl_2 to the NMR tubes by vacuum transfer which were each thawed in an isopropanol / solid CO_2 ice bath before rapid transference to a pre-cooled spectrometer at 193 K. The resonances of interest in the $^{11}B\{^1H\}$ NMR spectra were unable to be visualised at this temperature due to extensive broadening.

[xv] Complexes **12**-**15** were unstable in CD_2Cl_2 and partially decomposed to the CD_2Cl_2 adduct **A** within a few hours.

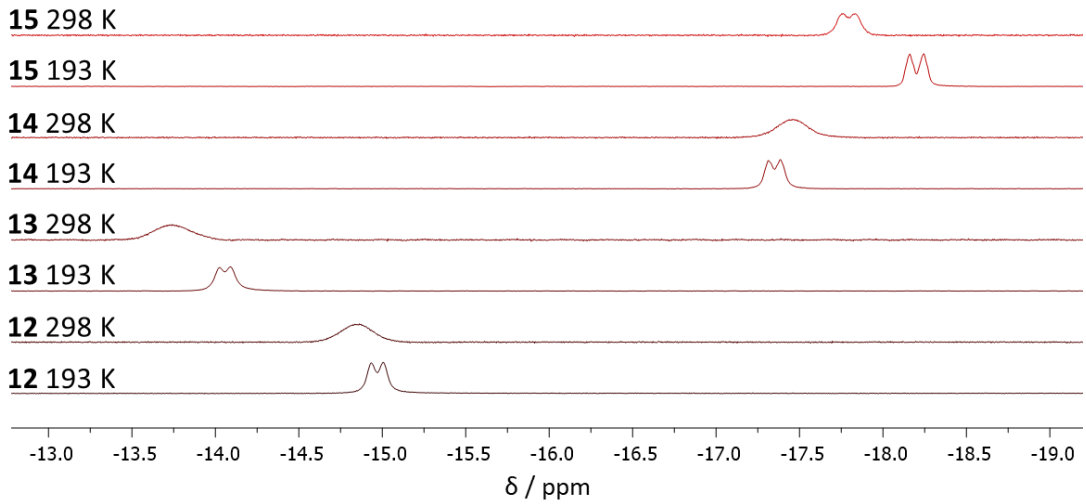

Figure 3.7 – $^{1}H\{^{11}B\}$ NMR spectra collected at 193 K and 298 K for **12-15** (CD_2Cl_2, 500 MHz).

Furthermore, had the rhodium(III) boryl hydride adduct existed at lower temperatures in solution, it was anticipated to be characterised by a doublet of triplets in the $^{1}H\{^{11}B\}$ NMR spectrum, due to coupling to the Rh and P atoms (*c.f.* Table 3.4, Fig. 3.7). Since only a broad doublet was observed across the studied temperature range with no resolved $^{2}J_{PH}$ coupling, it can only be concluded that **15** exists as a highly fluxional species in solution. The ground state of the species could feasibly be either the rhodium(I) or the rhodium(III) OA adduct, however, the temperature dependence of the $^{1}J_{RhH}$ coupling in the $^{1}H\{^{11}B\}$ NMR spectra of **15** indicates that this complex is perhaps best described as existing in dynamic equilibrium between the rhodium(I) and rhodium(III) adducts in solution. The isolated crystal structures presented in section 3.3 (*vide infra*) suggest the complexes favour the rhodium(I) oxidation state because they crystallise as rhodium(I) σ-borane complexes.

Table 3.4 – Table of selected NMR and IR spectroscopic data for previously reported metal boryl complexes of Bpin or Bcat.[21,47,48] Values that were not supplied by the authors are denoted with a hyphen. The asterisk denotes spectra collected at 258 K. [a]NMR spectra recorded in d^8-toluene. [b]NMR spectra recorded in C_6D_6. [c]NMR spectra recorded in $CDCl_3$.

Complex	M–H ^{1}H / ppm	^{11}B / ppm	^{31}P{^{1}H} / ppm
cis-Rh(Bpin)(CO)(PEt_3)$_2$[a]	N/A	42 (br)	17.0 (d, $^1J_{RhP}$ = 110 Hz)
RhH_2(Bpin)(Xantphos)[a]	-5.94 (dt, $^1J_{RhH}$ = 23.4, $^2J_{PH}$ = 15.9 Hz)*	33.3 (br)*	68.3 (d, $^1J_{RhP}$ = 131 Hz)*
RhH_2(Bcat)(Xantphos)[a]	-6.04 (dt, $^1J_{RhH}$ = 23.9 Hz, $^2J_{PH}$ = 13.5 Hz)*	34.7 (br)*	63.8 (d, $^1J_{RhP}$ = 132 Hz)*
Rh(Bpin)(Xantphos)[b]	N/A	41.9 (br)	51.9 (d, $^1J_{RhP}$ = 176 Hz)
Rh(Bcat)(Xantphos)[b]	N/A	48.7 (br)	55.1 (d, $^1J_{RhP}$ = 165 Hz)
Ir(Cp*)$(H)_2$(Bpin)$_2$[b]	-15.28 (s)	33.45	N/A
Ir(Cp*)$(H)_3$(Bcat)[b]	-14.66 (s)	35.98	N/A
Os(Bcat)(H)$(CO)_2(PPh_3)_2$[c]	-7.18 (t, $^2J_{PH}$ = 21.5 Hz)	45.2	-
Ru(Bcat)$_2(CO)_2(PPh_3)_2$[c]	N/A	48.2	-

A more noticeable temperature dependence was established by VT-NMR for complexes **12-14** (Fig. 3.7). At 193 K the coordinated proton environments appeared as broad doublets in both the ^{1}H and ^{1}H{^{11}B} NMR spectra, but upon collection of the same sample at 298 K, the resonances in question were observed as broad singlets (due to the fluxionality of the weakly bound borane ligand). The $^1J_{RhH}$ values at 193 K for **12-14** were marginally smaller (by *ca*. 5-8 Hz) than was reported for **15** (Table 3.3; 298 K). The NMR spectroscopic data indicate that **12-14** are best described as classical σ-borane complexes, since the $^1J_{RhH}$ couplings observed at lower temperatures are smaller than the $^1J_{RhH}$ coupling observed in **15**. The ^{11}B and ^{11}B{^{1}H} NMR spectra were not used to determine the coordination modes of the complexes, since the spectra were found to be poor handles for the determination of boron coordination environments (Fig. 3.8). At 193 K the resonances associated with the alkoxyboranes in **12-15** were so broad that they could not be located (Table 3.3). Additionally, examination of NMR data reported for other boryl hydride complexes verified that ^{11}B chemical shifts are unreliable indicators of both coordination environment and metal oxidation state (*c.f.* Table 3.4).

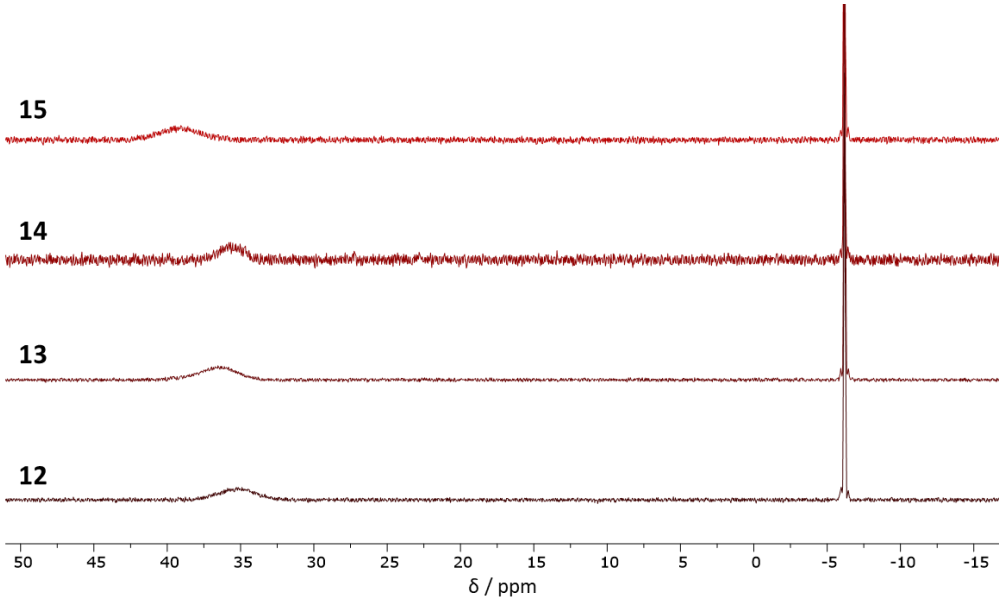

Figure 3.8 – Stacked ^{11}B NMR spectra for complexes **12-15** (96 MHz, 1,2-$C_6H_4F_2$, 298 K, *c.f.* Table 3.1).

Although the $^{1}J_{RhP}$ coupling decreases across the series in the order **12** > **13** ≈ **14** > **15**, the $^{1}J_{RhH}$ coupling does not mirror this trend, instead increasing in the order **13** < **12** ≈ **14** < **15** (Table 3.3). The chemical shifts of the ^{1}H NMR environments also move more upfield in this order (Fig. 3.7). The greater σ-donating ability of HBpin in comparison to HBcat results in a greater weakening of the B–H bond, leading to a greater interaction between the hydrogen atom and the metal centre (*i.e.*, larger $^{1}J_{RhH}$ couplings) when considering the PONOP-containing complexes **12** and **13**.[34] However, the greater π-accepting capabilities of HBcat allows the rhodium(I) centre to donate electron density more readily into the non-bonding and antibonding borane orbitals, resulting in a smaller $^{1}J_{RhP}$ coupling value in **13** compared to **12**. The pincer ligands serve to magnify these electronic differences – the higher energy frontier MO's of {Rh(PNP}$^{+}$ facilitate better donation of electron density into the π-accepting orbitals of HBcat in **15**, whereas the lower energy orbitals of {Rh(PONOP)}$^{+}$ encourage stronger σ-donation from the HBpin ligand in **12**.[44] As a result, the activation of the borane ligands appear to increase across the series in the order **13** < **12** < **14** < **15** (Table 3.3; Fig. 3.7).

The *in situ* reaction mixtures of **12-15** were stable for up to 48 h at room temperature in the presence of excess free borane (3-4 eq.). Similar timeframes with respect to the stability of σ-borane complexes of manganese and rhenium were reported by Hartwig

and co-workers.[34] Whilst it is not uncommon for σ-borane complexes to persist for extended periods of time in solution at room temperature, species such as the titanocene complex $Cp_2Ti(PMe_3)(HBcat')$, **A100**, are known to decompose rapidly above -30 °C.[33] From this work, Hartwig and co-workers concluded that the more stable complexes typically contained strong σ-donating and weak π-accepting ligands (such as phosphines) which did not compete with the π-accepting borane ligands for electron density.

Isolated solutions of **12-15** partially decomposed over the course of 24 h by approximately 10-15 % into the previously reported complexes $[Rh(PONOP)(\eta^2\text{-}H_2)][BAr^F{}_4]$ or $[Rh(PNP)(\eta^2\text{-}H_2)][BAr^F{}_4]$.[3,49] It was speculated that **12-15** could facilitate either dehydrogenative coupling between the solvent and a borane molecule or dehydrogenative coupling between two borane substrates to generate either B_2pin_2 or B_2cat_2 with H_2 as the by-product, the latter of which subsequently coordinates to the rhodium(I) centre. However, there is no experimental evidence for the presence of diboron products or any organoborane molecules that could feasibly result from coupling with 1,2-$C_6H_4F_2$ in solutions of $[Rh(pincer)(\eta^2\text{-}H_2)][BAr^F{}_4]$ analysed by mass spectrometry or by ^{11}B, ^{1}H or ^{19}F NMR spectroscopy, so this suggestion is only tentative and highly speculative. The identities of the decomposition products and the pathways to them remain unclear.

This decomposition process was expedited by heat and was ultimately determined to be an unavoidable decomposition pathway that could only be delayed by 24-48 h, even in the presence of excess borane. It was unclear whether the dehydrocoupling of the alkoxyboranes or even the hydroboration of COD were competing pathways in the *in situ* reaction mixtures, since the observed ^{11}B NMR resonances overlapped significantly with one another and the protonated solvent signals prohibited any detailed analysis of the borylation products by ^{1}H NMR spectroscopy. The organoborane adducts produced from the reactions of the alkoxyboranes with COD, solvent or another borane molecule were not observed by ESI-MS when aliquots of the decomposed reaction mixtures were analysed.

However, once **12-15** were isolated through means of crystallisation, the complexes were stable in the solid-state for several weeks. Presumably, decomposition was circumvented by removal of the solvent and additional stabilisation was supplied by the solid-state microenvironment, as was reported by Weller and co-workers for their

similarly unstable σ-alkane complexes.[7,9,50] Single crystals suitable for XRD studies were grown by liquid-liquid diffusion of hexane into the *in situ* 1,2-$C_6H_4F_2$ solutions at room temperature. Since all four samples were found to be stable enough in the solid-state for crystallographic analysis, the structures were subsequently compared and evaluated with a view to assessing their suitability for HP-XRD studies.

3.3 – Solid-state characterisation of the σ-borane series

The structures obtained from XRD studies for **12-15** are first individually presented herein, then followed by a comparison of the series (section 3.4). Full crystallographic details and considerations (including data reduction, solution, refinement and treatment of disorder) can be found in chapter 6. Where Hirschfeld surfaces are mentioned, the surface is defined as the point at which more than 50 % of the electron density belongs to the promolecule (*i.e.* the cations in these cases). Blue, white and red colouring on the surfaces indicate distances greater than, equal to, or less than the sum of the Van der Waals radii, respectively.[51]

Furthermore, it should be noted that where Rh–H or B–H bond lengths are considered, the values reported should be regarded loosely. The location of hydrogen atoms by X-ray diffraction is inherently unreliable, especially when in close proximity to a heavy atom, such as rhodium. Therefore, any comparisons being drawn from the experimental data with respect to the coordinating hydrogen atoms of the σ-borane ligands must be considered with these facts in mind.

3.3.1 – Crystal structure of [Rh(PONOP)(η^2-HBpin)][BAr$^F{}_4$], 12

Complex **12** crystallises in the monoclinic space group $P2_1/n$ (a = 13.28940(9) Å, b = 14.23474(10) Å, c = 35.08633(17) Å, β = 92.9395(5) °, V = 6628.59(7) Å^3) and can be best described as a distorted square planar complex in which the HBpin ligand coordinates in the fourth coordination site *trans* to the pincer ligand (Fig. 3.9; Table 3.5). The coordination of the pincer ligand is primarily responsible for the distortion of the complex away from idealised square planar geometry (P1–Rh1–P2 ∠ = 161.68(2) °; Table 3.5). The mean molecular plane of the HBpin ligand lies diagonal to the meridional plane of the pincer ligand - the twist angle between the planes of the HBpin ligand (as defined by the O1–B1–O2 atoms) and the PONOP ligand (as defined

by the O1, P1, Rh1, P2, O2 and N1 atoms) was calculated to be *ca*. 26.4 ° using *Mercury*.[52] The PONOP ligand distorts away from the ideal meridional coordination plane, as evidenced by the P1–O1···O2–P2 torsion angle of 13.09(8) °. This deformation can be partially attributed to the unfavourable steric encounters between the bulky substituents of the pincer and the borane ligands - yawing of the phosphine donors has been observed in other $[Rh(PONOP)]^+$ complexes.[53]

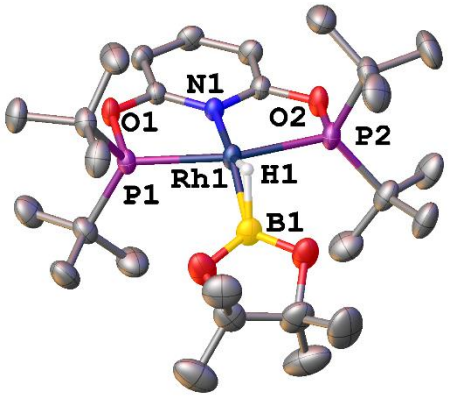

Figure 3.9 – A partially labelled structure of **12**. Atomic displacement parameters are drawn at 50 % probability. The anions and all hydrogen atoms, except for H1, omitted for clarity.

Table 3.5 – Table of selected bond lengths and bond angles for **12**.

Atoms	Bond length / Å	Atoms	Bond angle / °
Rh1–N1	2.0541(16)	P1–Rh1–P2	161.68(2)
Rh1–P1	2.2957(5)	N1–Rh1–B1	160.07(9)
Rh1–P2	2.2978(5)	Rh1–B1–H1	48.2(12)
Rh1–B1	2.111(3)	B1–H1–Rh1	91.7(16)
B1–H1	1.36(3)	H1–Rh1–B1	40.0(10)
Rh1–H1	1.58(3)		

The bonds lengths and bond angles presented in Table 3.5 are consistent with the values reported for other rhodium(I) PONOP complexes.[41,54,55] Complex **12** appears to adopt a classical σ-borane coordination mode, as evidenced by the B–H bond length of 1.36(3) Å. The hydrogen atom H1 was located using the electron density difference map and refined freely, but its location is somewhat unreliable due to the general noise

of the models' background (largest peak = 0.42 e/Å^3; largest hole = –0.39 e/Å^3). A search of the CSD (v.5.43, update June 2022)[56] confirmed the B–H bond length lies within the range of other previously reported B–H bond lengths for σ-HBpin complexes, which range from 1.30(2)-1.46(6) Å.[16,28,29,32,34]

The extended packing in **12** consists of alternating chains of cationic and anionic pairs (horizontal rows; Fig 3.10), such that each cation is surrounded by an octahedral arrangement of five counterions and one other cation. The HBpin ligand is situated within a cavity created by two adjacent Ar^F groups of a neighbouring anion (Fig. 3.10). Examination of the cation's Hirshfeld surface showed that no notable short contacts exist around the borane ligand at ambient pressure, however, compression would be expected to force the HBpin ligand into closer proximity with the metal centre as the cell volume decreased.

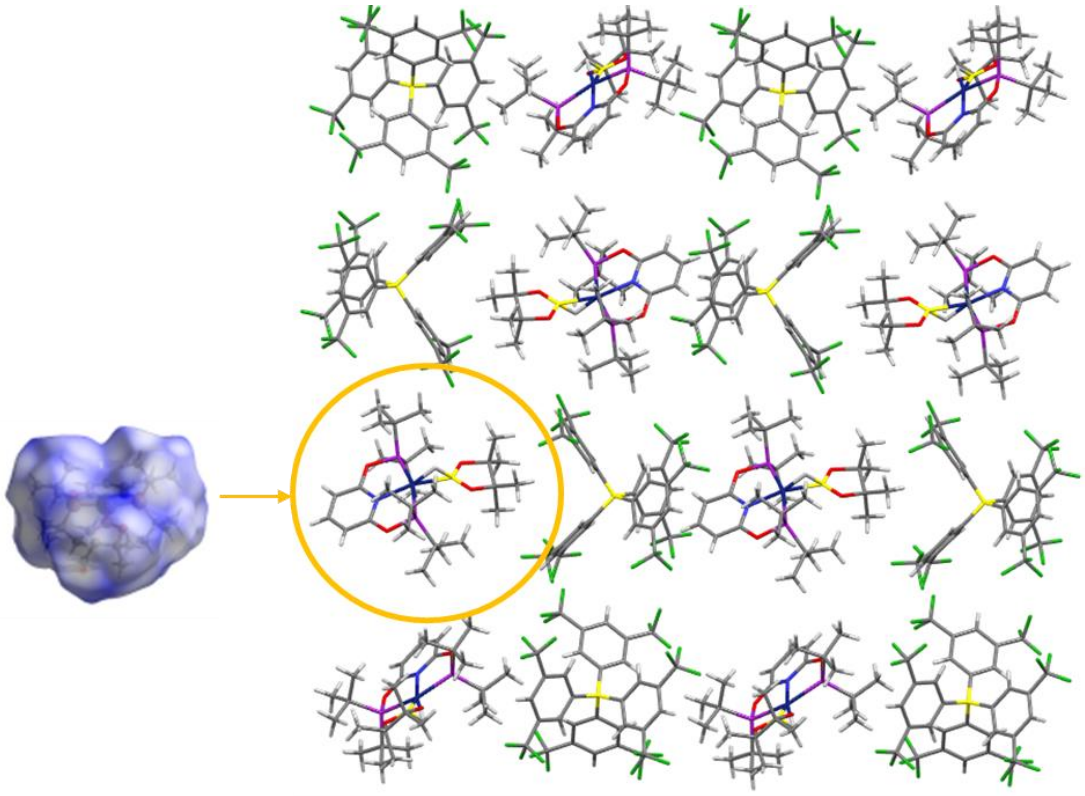

Figure 3.10 – The extended packing in **12**, as viewed along the [111] direction. The cation's Hirshfeld surface is shown for reference.

3.3.2 – Crystal structure of [Rh(PONOP)(η^2-HBcat)][BAr$^F{}_4$], 13

Complex **13** is chemically analogous to **12** with the exception of the identity of the σ-borane ligand. Complex **13** crystallises in the monoclinic space group $P2_1/c$ (a = 18.1285(2) Å, b = 17.9092(2) Å, c = 20.1931(2) Å, β = 92.314(1) °, V = 6550.69(12) Å^3), and is best described as a distorted square planar complex in which the HBcat ligand coordinates in the fourth coordination site *trans* to the pincer ligand (Fig. 3.11). The coordination of the pincer ligand is primarily responsible for the distortion of the complex away from idealised square planar geometry (P1–Rh1–P2 ∠ = 162.03(2) °; Table 3.6). The molecular plane of the HBcat ligand lies diagonal to the coordination plane of the pincer ligand; the twist angle between the planes of the borane ligand (as defined by all non-hydrogen atoms of the HBcat ligand) and the PONOP ligand (as defined by the O1, P1, Rh1, P2, O2 and N1 atoms) was calculated to be *ca*. 37.5 ° using *Mercury*.[52] Unfavourable steric interactions between the planar, more compact HBcat ligand and the phosphine donors of the PONOP ligand appear to be diminished in comparison to those observed in **12** - the P1–O1···P2–O2 torsion angle was calculated to be 7.21(9) ° for **13** (**12**: P1–O1···P2–O2 = 13.07(8)°). It is apparent from these observations that σ-borane ligand sterics contribute in some capacity to the minor structural deformations observed in the pincer ligand.

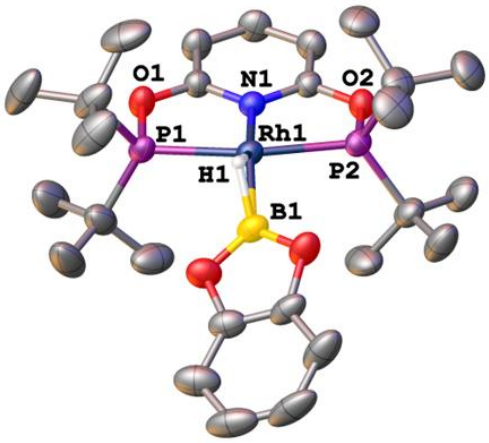

Figure 3.11 – A partially labelled structure of **13**. ADPs are drawn at 50 % probability. The anion and all hydrogen atoms, except for H1, omitted for clarity.

Table 3.6 – Table of selected bond lengths and bond angles for **13**.

Atoms	Bond length / Å	Atoms	Bond angle / °
Rh1–N1	2.0528(16)	P1–Rh1–P2	162.03(2)
Rh1–P1	2.2933(6)	N1–Rh1–B1	160.14(9)
Rh1–P2	2.2939(6)	Rh1–B1–H1	45.7(10)
Rh1–B1	2.079(2)	B1–H1–Rh1	91.5(14)
B1–H1	1.41(3)	H1–Rh1–B1	42.8(10)
Rh1–H1	1.49(3)		

The bond lengths and bond angles of **13** are consistent with those reported for **12** and similar coordination complexes of {Rh(PONOP)}$^+$ (Table 3.6).[41,54,55] Complex **13** appears to adopt a classical σ-borane coordination mode, as evidenced by the B–H bond length of 1.41(3) Å, which lies within the range of other σ-HBcat complexes found within the CSD (v.5.43, update June 2022),[56] whose B–H bond lengths range from 1.250(5)-1.45(13) Å.[26,27,29-31,34] The hydrogen atom H1 was located using the electron density difference map and refined freely, but its location is unreliable due to the general noise of the models' background (largest peak = 0.40 e/Å^3; largest hole = –0.78 e/Å^3). The coordination mode of the HBcat ligand is unsurprisingly similar to that observed for the HBpin ligand in **13**, however, the marginally contracted Rh1–B1 bond exhibited by **13** in comparison to **12** reflects the subtle differences in the interactions between the borane ligands and the rhodium(I) centre (Fig. 3.12; Table 3.6). These differences arise due to both the different electronic properties and steric profiles of the two boranes (see section 3.4).

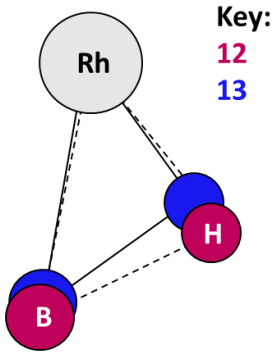

Figure 3.12 – A qualitative diagram of the marginally different borane coordination geometries observed in **12** and **13**. Diagram not to scale.

The extended packing consists of alternating chains of cations and anions (diagonal rows; Fig. 3.13), such that each cation is encased by an octahedral arrangement of anions. The HBcat ligands are situated within cavities created by two adjacent Ar^F groups of a neighbouring counterion. Examination of the Hirshfeld surface of the cation showed a close contact (depicted in red on the surface) exists between the face of the HBcat ligand and a nearby CF_3 substituent (circled in orange; Fig. 3.13). The % void volume for the unit cells of **12** and **13** were calculated to be 23.3 % and 25.6 %, respectively, using *Mercury*.[52] Despite the overall less efficient packing of **13**, the planar HBcat ligand allows for more efficient packing of the borane into cavities created by adjacent anions, resulting in the evolution of close contacts between the borane and counterion in the ambient pressure structure, which might feasibly evolve upon compression of the structure.

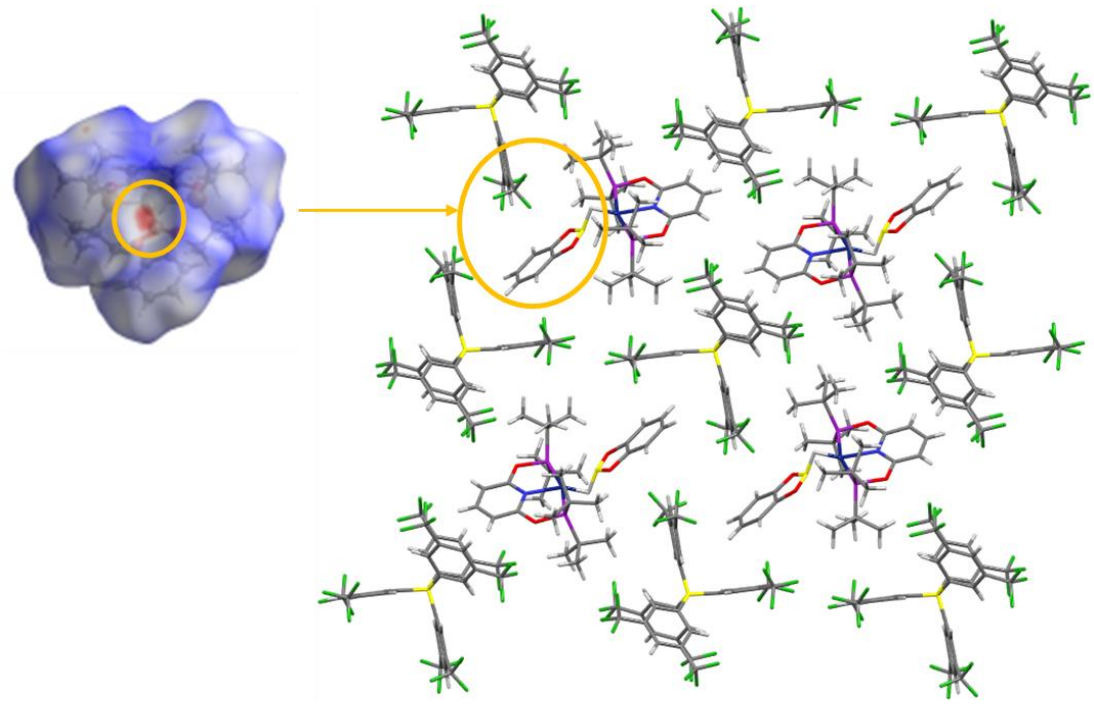

Figure 3.13 – The octahedral arrangement of the anions around each cation in **13**, as viewed along the [010] direction. Only four of the six anions of the surrounding octahedron are shown for clarity. The cation's Hirschfeld surface is shown for reference.

3.3.3 – Crystal structure of [Rh(PNP)(η^2-HBpin)][BAr$^F_4$], 14

Complex **14** is isomorphous to its PONOP analogue **12** and crystallised in the monoclinic space group $P2_1/n$ (a = 13.0589(1) Å, b = 14.2536(1) Å, c = 35.8756(4) Å, β = 93.247(1) °, V = 6667.03(10) Å^3). Complex **14** is best described as a distorted square planar complex in which the HBpin ligand coordinates in the fourth coordination site *trans* to the pincer ligand (Fig. 3.14). The coordination of the pincer ligand is primarily responsible for the distortion of the complex away from idealised square planar geometry (P1–Rh1–P2 ∠ = 165.17(2) °; Table 3.7). Disorder of the HBpin ligand was treated by modelling the C and O atoms of the borane as a two-components which were related to one another via rotation about the mean plane of the ligand. Full details are supplied in chapter 6. The HBpin ligand coordinates diagonally to the coordination plane of the pincer ligand for both disorder components. The twist angle between the planes of the major disordered components for the HBpin ligand (as defined by the O1–B1–O2 atoms) and the pincer ligand (as defined by the P1, Rh1, P2 and N1 atoms) was calculated to be *ca*. 40.2 ° using *Mercury*.[52] The PNP ligand adopts a C_2 conformation, in which the CH_2 linkers point towards opposing faces of the py ring, as viewed along the pincer backbone, resulting in a helical appearance (Fig. 3.14). The P1–C7···C8–P2 torsion angle was calculated to be 35.03(16) ° using *Mercury*.[52]

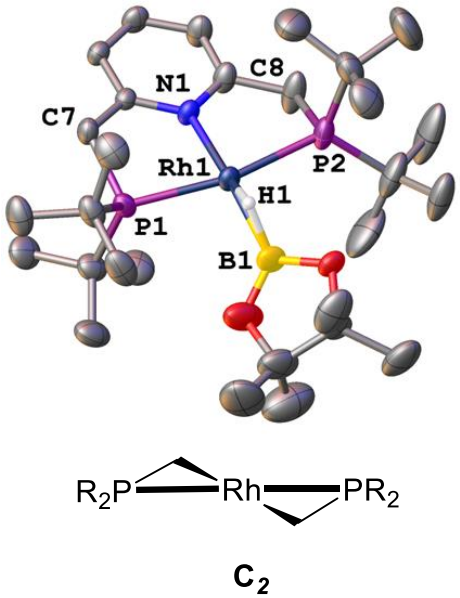

Figure 3.14 – A partially labelled structure of **14** (top) and a depiction of the C_2 conformation adopted by the PNP ligand (bottom). Atomic displacement parameters are drawn at 50 % probability. The anion and all hydrogen atoms, except for H1, are omitted for clarity. Only one disorder component is shown.

Table 3.7 – Table of selected bond lengths and bond angles for **14**.

Atoms	Bond length / Å	Atoms	Bond angle / °
Rh1–N1	2.127(2)	P1–Rh1–P2	165.17(2)
Rh1–P1	2.3138(7)	N1–Rh1–B1	168.18(13)
Rh1–P2	2.3376(7)	Rh1–B1–H1	45.7(14)
Rh1–B1	2.083(3)	B1–H1–Rh1	92(2)
B1–H1	1.40(3)	H1–Rh1–B1	42.0(13)
Rh1–H1	1.49(3)		

The bond lengths and bond angles associated with **14** are consistent with the values reported for other rhodium(I) PNP complexes (Table 3.7).[3,41] Complex **14** appears to adopt a classical σ-borane coordination mode, as evidenced by the B–H bond length of 1.36(3) Å. The hydrogen atom H1 was located using the electron density difference map and refined freely, but its location is unreliable due to the general noise of the models' background (largest peak = 1.47 e/Å^3; largest hole = –0.58 e/Å^3). A search of the CSD (v.5.43, update June 2022)[56] does, however, confirm that the B–H bond length lies within the range reported for other σ-coordinated HBpin complexes (see section 3.3.1).[16,28,29,32,34]

The extended packing comprises of alternating chains of cations and anions (horizontal rows; Fig. 3.15), such that each cation is surrounded by five anions and one other cation in an octahedral arrangement. The structure and packing is isomorphous to that observed in **12** (*c.f.* Fig. 3.12), differing only by the identity of the pincer ligand and small differences in the relative orientations of the borane ligands when the unit cells of **12** and **14** are superimposed over one another. The subtly different crystal packing facilitates the evolution of a close contact between the HBpin ligand and an adjacent CF_3 group belonging to a neighbouring counterion, as depicted on the Hirshfeld surface of a cation in Fig. 3.15 (circled in orange). This suggests that **14** may be a better candidate for HP-XRD studies than **12**, due to the greater abundance of short contacts observed in the ambient pressure structure of **14** and PNP's proclivity to activate bonds more readily than PONOP.[44,54]

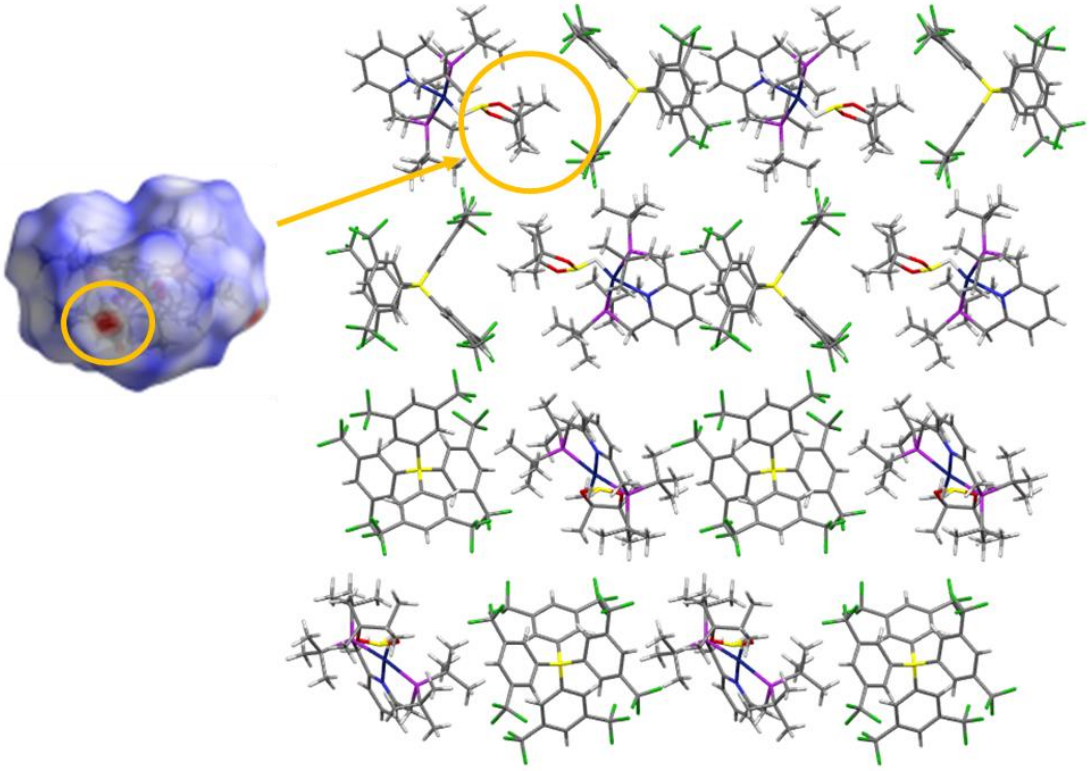

Figure 3.15 – The extended packing in **14**, as viewed along the [111] direction. The cation's Hirshfeld surface is shown for reference. Only one disorder component is shown.

3.3.4 – Crystal structure of [Rh(PNP)(η^2-HBcat)][BAr$^F{}_4$], 15

Complex **15** is the PNP analogue of **13**, differing by the identity of the pincer ligand. Complex **15** crystallises in the monoclinic space group $P2_1/c$ (a = 19.2532(4) Å, b = 17.6224(3) Å, c = 19.3155(3) Å, β = 98.960(2) °, V = 6473.5(2) Å^3). Whole molecule disorder is exhibited by the cation of **15**, where the minor disorder component (32 % occupancy) is related to the major disorder component (68 % occupancy) via a pseudo-inversion centre that is independent of the space group symmetry (Fig. 3.16). Merohedral twinning was also considered as a possible explanation for the disorder, but upon further inspection of the data, it was believed that the correct space group ($P2_1/c$) had been assigned. Distorted square planar geometries are adopted by both disorder components (P1–Rh1–P2 ∠ = 164.63(5) °, major disorder component; Table 3.8). The HBcat ligand was found to coordinate similarly in both disorder components with respect to the pincer ligand coordination plane. The twist angle between the planes of the HBcat ligand (as defined by the non-hydrogen atoms of the borane) and

the PNP ligand (as defined by the P1, Rh1, P2 and N1 atoms) were calculated to be *ca*. 50.3 ° and 50.1 ° (*i.e*. within error of one another) for the major and minor disorder components, respectively, using *Mercury*.[52] The PNP ligand adopts a helical C_2 conformation, as was observed in **14**. The P1–C7···C8–P2 torsion angle was calculated to be 40.8(9) ° for **15**.

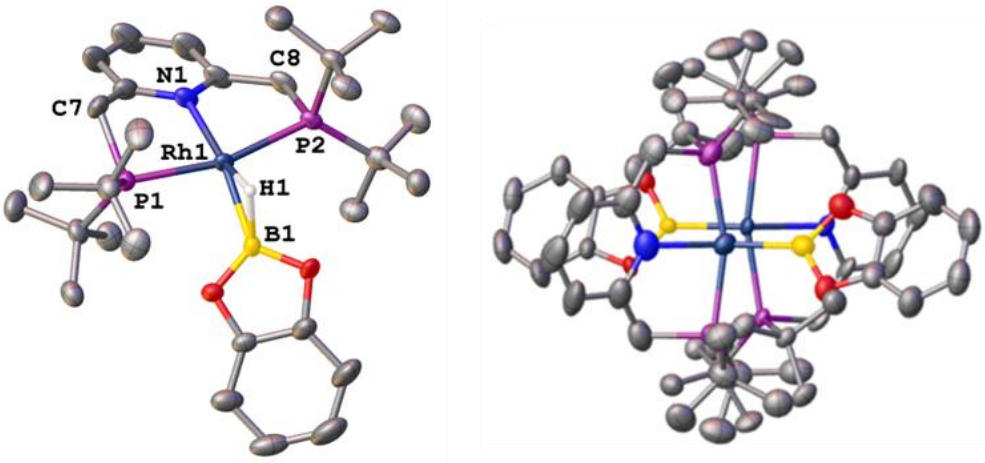

Figure 3.16 – A partially labelled structure of the major disorder component of **15** (left) and a depiction of the two disorder components related to one another by pseudo-inversion (right). Atomic displacement parameters are drawn at 50 % probability. The anion and all hydrogen atoms, except for H1 (leftmost figure), are omitted for clarity.

Table 3.8 – Table of selected bond lengths and bond angles for the major disorder component of **15**.

Atoms	Bond length / Å	Atoms	Bond angle / °
Rh1–N1	2.1050(4)	P1–Rh1–P2	164.63(5)
Rh1–P1	2.3308(14)	N1–Rh1–B1	149.92(18)
Rh1–P2	2.3354(14)	Rh1–B1–H1	47(2)
Rh1–B1	2.024(6)	B1–H1–Rh1	83(3)
B1–H1	1.56(5)	H1–Rh1–B1	50(2)
Rh1–H1	1.50(6)		

The Rh1–N1 bond length is slightly shorter than reported for the HBpin analogue **14** (**14**: 2.127(2) Å; **15**: 2.1050(4) Å), which is indicative of the subtly different donor / acceptor properties of the HBpin and HBcat ligands (Table 3.8). HBpin is a slightly stronger σ-donor whilst HBcat is a better π-acceptor, due to the delocalisation of

electron density from the oxygen atoms into the aromatic substituent on HBcat.[34] The increased σ-donation capability of HBpin results in a greater *trans* influence on the Rh1–N1 bond.

The substitution of HBpin for HBcat in the $\{Rh(PNP)\}^+$ system (**14** *vs*. **15**) appears to enhance the overlap between the rhodium 4*d* orbital and the 'empty' non-bonding boron orbital, as evidenced by the significantly smaller N1–Rh1–B1 angle (149.92(18) °)[30] and elongated B–H bond (1.56(5) Å) relative to the other σ-borane complexes presented herein (Table 3.8; Fig. 3.17). The B–H bond is similar in length to other reported elongated σ-HBcat complexes (1.58(3)-1.68(2) Å).[26,27] These two structural indicators suggest that **15** is best described as an elongated σ-borane complex, due to enhanced interactions between the rhodium centre and the boron and hydrogen atoms. The hydrogen atom H1 was located using the electron density difference map and refined freely, but it should be noted that its location is unreliable due to the general noise of the models' background (largest peak = 1.32 e/Å^3; largest hole = –1.02 e/Å^3). The background noise of this refinement is higher than most other structures presented within, so the location of the hydrogen atoms in this case are particularly unreliable.

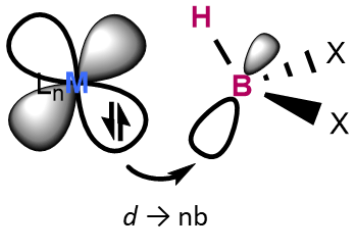

Figure 3.17 – A Dewar–Chatt–Duncanson model of *d* → nb back donation within a σ-borane complex.

The extended packing consists of alternating chains of cations and anions which stack together in layers (Fig. 3.18). The packing arrangement indicates the existence of weak aromatic interactions between the Ar^F substituents of the anions and the Ph and py rings of the cations, which are disrupted by the bulky CF_3 and phosphine substituents (Fig. 3.18, circled in red). The centroid-to-centroid distances between the adjacent rings were calculated to be greater than 4.0 Å (ranging from 4.27-4.70 Å), indicating that these were not formal π-π interactions and are, therefore, better described as dipole-induced dipole interactions.[57,58]

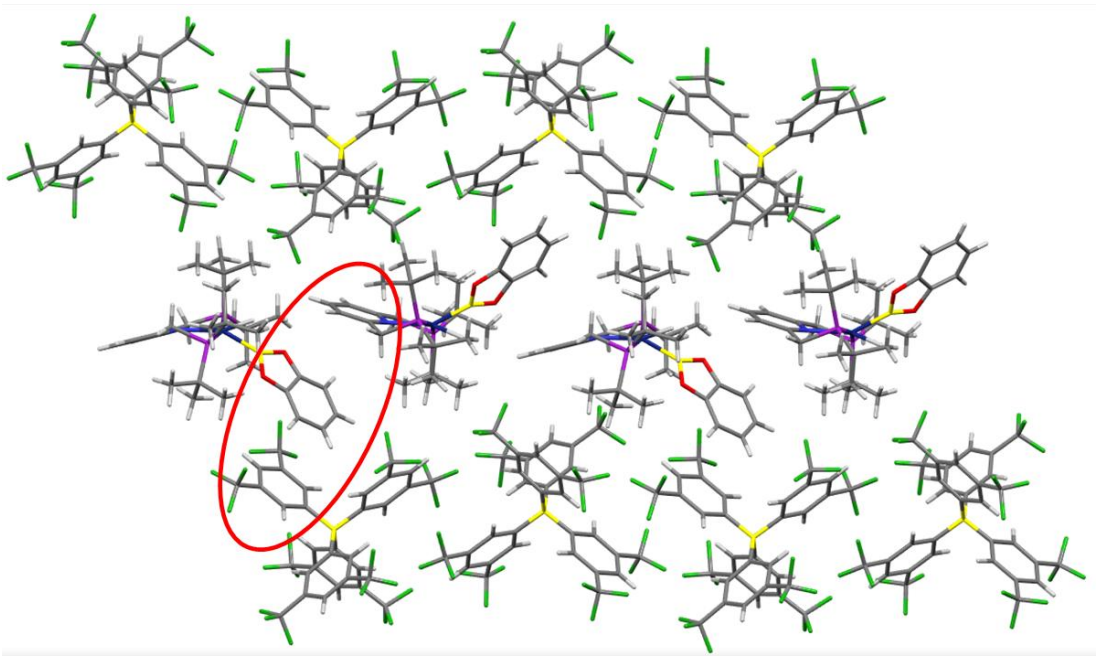

Figure 3.18 – The packing of **15**, as viewed along the [100] direction. Only the major disorder component is shown.

Nevertheless, these interactions could potentially contribute towards the distinctive coordination geometry of the HBcat ligand to the $\{Rh(PNP)\}^+$ fragment in **15**, which differed from the coordination geometries observed in the other σ-borane complexes (**12**-**14**) presented herein. Unfortunately, the full cation disorder in **15** would likely prohibit any viable structural solution being obtained from HP-XRD studies (Fig. 3.16).

3.4 – Comparison of the σ-borane complexes

Whilst the HBpin-containing structures **12** and **14** are isomorphous, the HBcat-containing structures **13** and **15** are not, since they exhibit different packing arrangements (Table 3.9). Smaller 'unit cell volume per complex' values ($^{V}/_{Z}$; Table 3.9) calculated for **13** and **15** were expected, since they contain the more rigid and compact HBcat substrate. Unfortunately, the 'void volume per complex' values supplied in Table 3.9 should be regarded loosely, since *Mercury* does not account for disorder components when calculating voids. Problems were also encountered when calculating voids with *CrystalExplorer*,[51] because although all disorder components

were taken into account, individual parts could not be separated. Therefore, a direct comparison of the packing efficiencies across the series was not possible.

Table 3.9 – A table of crystallographic information for **12-15**. The unit cell void volumes were calculated using *Mercury*[52] with a probe radius of 0.4 Å and a grid spacing of 0.2 Å.

	PONOP		**PNP**	
	HBpin	**HBcat**	**HBpin**	**HBcat**
Complex	**12**	**13**	**14**	**15**
Space group	$P2_1/n$	$P2_1/c$	$P2_1/n$	$P2_1/c$
Crystal system	monoclinic	monoclinic	monoclinic	monoclinic
T **/ K**	150	150	150	150
a **/ Å**	13.28940(9)	18.1285(2)	13.0589(1)	19.2532(4)
b **/ Å**	14.23474(10)	17.9092(2)	14.2536(1)	17.6224(3)
c **/ Å**	35.08633(17)	20.1931(2)	35.8756(4)	19.3155(3)
α **/ °**	90	90	90	90
β **/ °**	92.9395(5)	92.314(1)	93.247(1)	98.960(2)
γ **/ °**	90	90	90	90
V **/ Å^3**	6628.59(7)	6550.69(12)	6667.03(10)	6473.5(2)
Z'	1	1	1	1
R_1 **($I \geq 2\sigma$)**	0.0341	0.0328	0.0410	0.0693
wR_2 **(all data)**	0.0828	0.0871	0.1067	0.2096
GooF	1.1290	1.0290	1.0170	1.0380
R_{int}	0.0274	0.0431	0.0287	0.0458
Largest peak	0.4300	0.3900	1.4700	1.3300
Largest hole	-0.4000	-0.7800	-0.5800	-1.0200
μ **/ mm^{-1}**	3.55	3.59	3.50	3.61
V/Z **/ Å^3**	1657	1638	1667	1618
$\textit{unit cell void volume}/Z$ **/ Å^3**	387	418	366	432

Comparison of cations in **12-15** show subtle variations across the series as a result of changing the identity of the borane ligand and/or the pincer ligand (Tables 3.10 & 3.11). The angle between the borane and pincer ligand coordination planes increased from 26.36 ° in **12** to 40.23 ° in **14** and from 37.46 ° in **13** to 50.26 ° in **15** (although some distortion can perhaps be attributed to the intermolecular aromatic interactions

described for **15** in section 3.3.4). These geometric changes are likely due to the change in hybridisation state from an sp^2-hybridised O linker to an sp^3-hybridised CH_2 linker within the pincer ligand. The different linkers also influence the bite angles, which are *ca*. 3-4 ° smaller for **12** and **13** relative to **14** and **15**, respectively (Table 3.10). The bite angles themselves are within the typical ranges expected for monomeric rhodium PONOP and PNP complexes.[17,41,54]

Table 3.10 – Selected bond angles reported for **12-15**.

Bond angle / °	12	13	14	15
P1–**Rh1**–**P2**	161.68(2)	162.03(2)	165.71(2)	164.63(5)
N1–**Rh1**–**B1**	160.07(9)	160.14(9)	163.18(13)	149.92(18)
Rh1–**B1**–**H1**	48.2(12)	45.7(10)	45.7(14)	47(2)
H1–**Rh1**–**B1**	40.0(10)	42.8(10)	42.0(13)	50(2)
B1–**H1**–**Rh1**	91.7(16)	91.5(14)	92(2)	83(3)

Table 3.11 – Selected bond lengths reported for **12-15**.

Bond length / Å	12	13	14	15
Rh1–**P1**	2.2957(5)	2.2933(6)	2.3138(7)	2.3308(14)
Rh1–**P2**	2.2978(5)	2.2939(6)	2.3376(7)	2.3354(14)
Rh1–**N1**	2.0541(16)	2.0528(16)	2.127(2)	2.1050(4)
Rh1–**B1**	2.111(3)	2.079(2)	2.083(3)	2.024(6)
Rh1–**H1**	1.58(3)	1.49(3)	1.49(3)	1.50(6)
B1–**H1**	1.36(3)	1.41(3)	1.40(3)	1.56(5)
Rh1···B–**H centroid**	1.57(5)	1.49(3)	1.49(4)	1.49(5)

The Rh1–B1 bond lengths are generally similar across the series, but the HBpin analogues **12** and **14** exhibit slightly longer Rh1–B1 bonds than their HBcat counterparts **13** and **15** (Table 3.11). The weaker π-accepting ability of HBpin results in longer Rh1–B1 bonds in **12** and **14**, relative to their HBcat counterparts (Table 3.11).[46] The shortest Rh1–B1 bond length was observed in **15** (2.024(6) Å), which is indicative of a more prevalent interaction between the boron and rhodium atoms. The Rh1–N1 bonds in the PNP complexes are also slightly elongated relative to their PONOP analogues (**12** = 2.0541(16) Å; **13** = 2.0528(16) Å; **14** = 2.127(2) Å; **15** =

2.1050(4) Å; Table 3.11). The differences observed in the Rh1–N1 bond lengths principally originate from the different electronic properties of the pincer ligands, as Daly and co-workers have previously established.[44] The identity of the borane ligand likely has a similar, albeit less pronounced effect on the Rh1–N1 bond lengths, due to the more subtle electronic differences between the two boranes outlined above.[34]

The B1–H1 bond lengths range from 1.36(3)-1.56(5) Å across the series, which are significantly elongated relative to the B–H bond lengths calculated for uncoordinated monomeric alkoxyboranes (*ca.* 1.17 Å),[34] due to partial activation by the {Rh(PXNXP)}$^+$ fragment. The B1–H1 bond lengths increase across the series in the order **12** < **14** ≈ **13** < **15**, indicating that both the pincer ligand and the borane ligand identities influence the degree of B–H activation. HBcat and PNP containing complexes possess longer B–H bonds than their HBpin or PONOP containing variants (Fig. 3.19). The PNP ligand makes the rhodium centre more basic in nature,[44] allowing electron density to be more readily donated into the 'empty' non-bonding orbital of the HBcat ligand, the better π-acceptor of the two alkoxyboranes,[34] which leads to enhanced B–H activation.

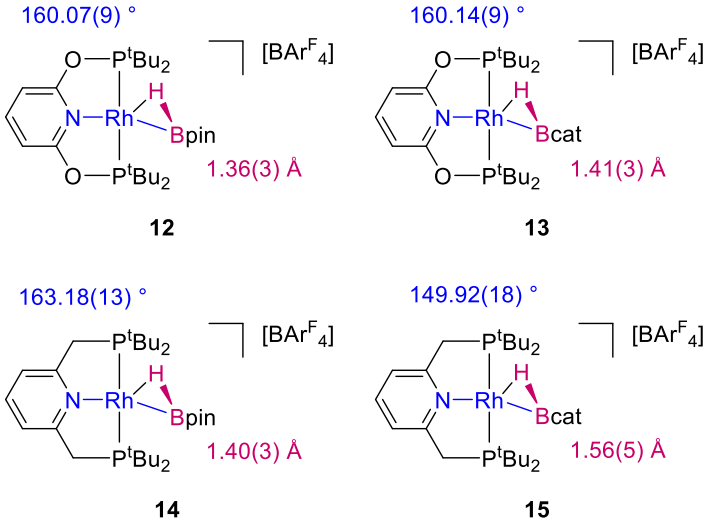

Figure 3.19 – Annotated chemical structures of **12-15**. The burgundy and blue values correspond to the B1–H1 bond lengths and N1–Rh1–B1 bond angles, respectively.

Using equation 3.1, where σx_n is the standard deviation of the n^{th} measurement and Δx is the difference between the two measurements, the confidence interval of two measurements can be calculated. A 3σ confidence interval means that there is a 99.7 % probability that the true value lies within three standard deviations (σ) of the mean.[59]

Equation 3.1 $$\frac{\Delta x}{\sqrt{\sigma x_1{}^2 + \sigma x_2{}^2}} > 3$$

The differences in the B–H bond lengths of **12-14** are less than two standard deviations, so are not statistically significant. Although the difference between the B–H bond lengths calculated for **13** and **15** (*ca*. 0.15 Å) is statistically significant (3.4σ), given the inherent difficulties associated with locating hydrogen atoms by XRD, the trends observed in solution by NMR spectroscopy may better represent the degree of borane activation across the series (section 3.2). Keeping in mind the inherent uncertainty in the B–H bond lengths obtained from XRD, assignments made based on the crystallographic data are supported by the spectroscopic data – both the solid-state and solution phase data are in good agreement and indicate that the coordination mode of the HBcat substrate in **15** is enhanced relative to the rest of the series.

The structures obtained by XRD for **12-14** are in line with structures expected for classical σ-borane complexes, because the B–H bond lengths in **12-14** are shorter than 1.5 Å (*c.f.* Table 3.2.; Fig. 3.19).[26,27] On the other hand, a B–H bond length of greater than 1.5 Å (as is observed for **15**) is more characteristic of an elongated σ-borane complex – Esteruelas and co-workers defined elongated σ-borane complexes as having B–H bond lengths of between 1.6-1.7 Å typically. The assignment of **15** as an elongated σ-borane complex is supported not only by the elongated B1–H1 bond (1.56(5) Å), but the different coordination geometry of the borane substrate (*c.f.* H1–Rh1–B1 & B1–H1–Rh1 values; Table 3.10) and the much smaller N1–Rh1–B1 bond angle (149.92(18) °), which reflects the enhanced interaction between the metal *d* orbital and the 'empty' boron orbital.[30] Better orbital overlap accommodates stronger back donation and, therefore, weakens (*i.e.*, elongates) the B–H bond. The 'elongated' coordination mode assigned to **15** is supported by the ^{1}H NMR spectrum – a broad doublet is observed for the coordinated proton environment in **15** ($^1J_{RhH}$ = 41 Hz), indicating that an enhanced and more persistent interaction exists between the metal and the borane in solution, unlike the analogous proton environments in **12-14** that appear as broad singlets at room temperature (Table 3.3).

The infrared (IR) spectra collected for **12-15** exhibit bands between 1605-1613 cm^{-1}, with the PONOP analogues possessing higher energy B–H stretches than their PNP counterparts ($\nu_{B\text{-}H}$: **12** = 1613 cm^{-1}; **13** = 1612 cm^{-1}; **14** = 1609 cm^{-1}; **15** = 1605 cm^{-1}), but the differences are marginal (Fig. 3.20). Complex **15** possesses the lowest energy B–H stretch and an additional Rh–H stretch was assigned at 1471 cm^{-1}, suggesting this complex contains the most activated borane of the series (Fig.3.20). These assignments should be treated with caution because the bands of interest are weak and obscured by overlapping stretches – Braunschweig and co-workers encountered similar problems when assigning their σ-borane complexes.[60] Consequently, the IR data should not be held in as high regard as the XRD and NMR data, although the assigned B–H stretches are in line with the literature (*c.f.* Table 3.2, section 3.2). The B–H stretches for all complexes indicate a significant decrease in bond order from the uncoordinated borane species (HBpin $\nu_{B\text{-}H}$ = 2580 cm^{-1}; HBcat $\nu_{B\text{-}H}$ = 2660 cm^{-1}).[61] Although only 8 cm^{-1} separates the B–H stretches for **12-15**, the B–H stretch of free HBcat is *ca*. 80 cm^{-1} higher in wavenumber than free HBpin. Therefore, the degree of B–H activation in the HBcat analogues **13** and **15** is thought to be greater than in the HBpin analogues **12** and **14** due to the higher Lewis acidity of the HBcat ligand.[34,61]

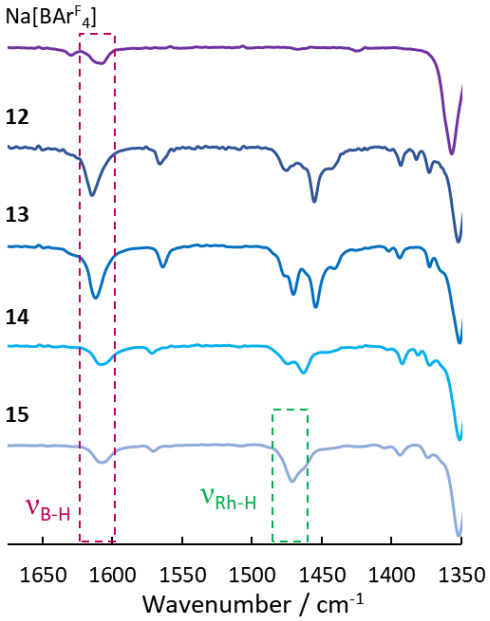

Figure 3.20 – Partially labelled IR spectra of **12-15** in the region of interest. IR spectrum of Na[BAr^F_4] supplied for reference.

Examination of the collective data suggests that B–H activation is achieved to the greatest extent by incorporating PNP and HBcat ligands into the complex. The PNP

ligand makes the rhodium centre more basic in nature,[44] allowing electron density to be more readily donated into the 'empty' non-bonding orbital of the HBcat ligand, the better π-acceptor of the two alkoxyboranes investigated herein,[34] leading to enhanced B–H activation. Generally speaking, the more upfield the chemical shift of the proton environment in the ^{1}H NMR spectrum, the lower the wavenumber of the $\nu_{B\text{-}H}$ stretch and the longer the B–H bond length (Table 3.12).

Table 3.12 – Selected spectroscopic data for complexes **12-15**. The $^{1}H\{^{11}B\}$ NMR data corresponds to the coordinated proton environment (CD_2Cl_2, 500 MHz).

Complex	$\nu_{B\text{-}H}$ / cm^{-1}	$^{1}H\{^{11}B\}$ NMR / ppm		B–H bond length / Å
		298 K	193 K	
12	1613	-14.85 (br, fwhm = 106 Hz)	-14.97 (br d, $^{1}J_{RhH}$ = 36.2 Hz)	1.36(3)
13	1612	-13.74 (br, fwhm = 122 Hz)	-14.06 (br d, $^{1}J_{RhH}$ = 33.4 Hz)	1.41(3)
14	1609	-17.46 (br, fwhm = 98 Hz)	-17.35 (br d, $^{1}J_{RhH}$ = 37.0 Hz)	1.40(3)
15	1605	-17.79 (br d, $^{1}J_{RhH}$ = 41.5 Hz)	-18.20 (br d, $^{1}J_{RhH}$ = 41.9 Hz)	1.56(5)

3.5 – High pressure studies of [Rh(PONOP)(η^2-HBcat)][BAr$^F{}_4$]

Due to the good sample quality and minimal disorder present in the structure at ambient pressure, crystals of **13** were determined to be the most suitable starting point for investigation by HP-XRD by process of elimination. The extensive disorder present in **14** and **15** made these samples unsuitable for HP-XRD studies, since additional challenges may be expected when attempting to solve potential high pressure phases with limited resolution and completeness. Additionally, the HBcat ligand in **13** was evaluated to be more straightforward to interrogate under pressure than the HBpin analogue **12** because the molecular plane of HBcat is more rigid and well-defined. The structural flexibility of HBpin could potentially be more challenging to correctly model in datasets suffering from limited completeness.

3.5.1 – Pressure limits of the study

Two separate crystals of **13** were studied under pressure on the I19 beamline at Diamond light source using Ag-edge synchrotron radiation (λ = 0.4859 Å) at 293 K. Daphne-7373 and paraffin oil were used as the pressure transmitting media (PTM),

which are reported as having a hydrostatic limits of 22 kbar[62] and 30 kbar,[63] respectively. Both oils were sparged with argon before use. A PTM is required in high pressure studies in order to facilitate isotropic compression of the sample, which is applied up to the hydrostatic limit of the PTM. Once the non-hydrostatic regime is entered, pressure gradients can develop in the sample, which can lead to degradation of the crystal, false promotion or suppression of certain phenomena (such as phase transitions) and the impingement of data trends.[64,65]

Crystal A was studied in Daphne-7373 at pressures of 2.5, 4.8, 14.0, 22.4, 25.8, 32.8 and 45.1 kbar, with viable refinements obtained for data sets up to 25.8 kbar. Crystal B was studied in paraffin oil at pressures of 8.8, 13.9, 15.4, 20.6, 25.2 and 26.5 kbar, with viable structural refinements obtained up to 15.4 kbar (Tables 3.13 & 3.14). Pressures were determined using the ruby fluorescence method.[66] Full data reduction, solution and refinement details are supplied in chapter 6.

Table 3.13 – Table of crystallographic data collected for crystal B of **13** at 293 K.[xvi]

Pressure / kbar	**8.8**	**13.9**	**15.4**
Space group	$P2_1/c$	$P2_1/c$	$P2_1/c$
Crystal system	monoclinic	monoclinic	monoclinic
$\boldsymbol{T}$ **/ K**	293	293	293
$\boldsymbol{\lambda}$ **/ Å**	0.4859	0.4859	0.4859
$\boldsymbol{a}$ **/ Å**	18.577(4)	18.251(4)	18.216(5)
$\boldsymbol{b}$ **/ Å**	16.577(2)	16.349(2)	16.327(2)
$\boldsymbol{c}$ **/ Å**	19.44(2)	19.06(2)	18.95(3)
$\boldsymbol{\beta}$ **/ °**	93.27(5)	92.93(6)	92.93(7)
$\boldsymbol{V}$ **/ Å^3**	5978(6)	5680(6)	5629(8)
$\boldsymbol{R_1}$ **($\boldsymbol{I \geq 2\sigma}$)**	0.1247	0.1229	0.1334
$\boldsymbol{wR_2}$ **(all data)**	0.3672	0.3556	0.3869
GooF	1.041	1.154	1.154
$\boldsymbol{R_{int}}$	0.4748	0.3619	0.3706
Data/rest/param	2477/2692/400	2392/2686/400	2369/2695/400

[xvi] Full crystallographic tables can be found in the appendix.

Table 3.14 – Table of crystallographic data collected for crystal A of **13** at 293 K. The asterisk denotes the ambient pressure collection conducted at 150 K on a separate crystal, for reference.

Pressure / kbar	**0.0***	**2.5**	**4.8**	**14.0**	**22.4**	**25.8**
Space group	$P2_1/c$	$P2_1/c$	$P2_1/c$	$P2_1/c$	$P2_1/c$	$P2_1/c$
Crystal system	monoclinic	monoclinic	monoclinic	monoclinic	monoclinic	monoclinic
***T* / K**	150	293	293	293	293	293
λ / Å	1.54184	0.4859	0.4859	0.4859	0.4859	0.4859
***a* / Å**	18.1285(2)	18.186(2)	18.020(3)	18.2732(19)	18.011(2)	17.923(2)
***b* / Å**	17.9092(2)	17.958(2)	17.501(3)	16.3352(18)	16.0971(19)	16.012(2)
***c* / Å**	20.1931(2)	20.14(2)	19.94(3)	19.06(2)	18.79(2)	18.75(2)
β / °	92.314(1)	92.58(2)	91.84(3)	93.43(3)	93.33(3)	92.91(3)
***V* / Å^3**	6550.69(12)	6572(7)	6285(9)	5678(6)	5440(6)	5373(7)
R_1 ($I \geq 2\sigma$)	0.0329	0.0837	0.0936	0.0704	0.0774	0.0781
wR_2 (all data)	0.0874	0.2425	0.2817	0.1812	0.2070	0.2056
GooF	1.027	1.052	1.068	1.046	1.051	1.056
R_{int}	0.0431	0.1811	0.1698	0.1209	0.1284	0.1456
Data/rest/param	13059/3405/1022	2672/2788/486	2587/2776/460	2278/2790/460	2165/2784/460	2127/3183/473

The study did not include a 0 kbar collection for a combination of reasons. First and foremost, the air sensitivity of the sample made it necessary to ensure that the sample was sealed in an airtight environment. To do this in the absence of a PTM would almost certainly result in the significant compression of the gasket hole and likely the sample would be crushed, or otherwise exposed to air. Thus, the samples were loaded immediately with PTM. In this context, there were difficulties in deciphering when the screws were suitably tightened through the thick gloves fitted to the glovebox and, to further ensure a closed system, modest amounts of pressure were invariably applied. This decision was further motivated by the fact that the study was conducted shortly after Diamond Light Source had reopened following the COVID-19 pandemic and samples were to be sent ahead of time to the facility to be run remotely. Thus, it was ensured that each cell was slightly pressurised so as to avoid any possibility of sample deterioration through leaching of air into the cell over time.

In the case of crystal B, sample degradation was noticeable before the hydrostatic limit of the PTM was reached (the last viable dataset used for structure refinement and unit cell determination was collected at 15.4 kbar), leading to lower resolution data in comparison to the data collected for crystal A. Crystals failing to sufficiently diffract before the hydrostatic limit of the PTM is reached is not uncommon for high pressure studies.[64] The unit cell parameters for crystal A were reliably determined up to and slightly beyond the hydrostatic limit of the PTM (the last viable dataset used was collected at 25.8 kbar). In fact, at higher pressures the R_{int} improved for crystal A (Table 3.15), another phenomenon that has been observed in other HP-XRD studies.[67]

Crystal A remained well-diffracting until the hydrostatic limit of the PTM was surpassed (beyond 30 kbar), however, datasets collected above 25.8 kbar will not be discussed as it became apparent from the structural refinements that the bond lengths and bond angles deviated significantly from the trends observed under hydrostatic conditions. The dataset at 25.8 kbar is included in the discussion despite being collected in the non-hydrostatic regime because that particular refinement did not appear suffer excessively from non-hydrostatic conditions.

3.5.2 – Pressure dependence of cell parameters

Between 4.8 and 8.8 kbar, an isomorphous phase transition occurred in **13**, as indicated by a noticeable increase in the *a* axis (Fig. 3.21). The b and *c* axes were less noticeably affected by the phase transition, although the high pressure phase appeared to have a distinct compression regime from the ambient pressure phase along the *b* axis. The phase transition may account for why the R_{int} improved for crystal A between 4.8 kbar and 14.0 kbar, as the removal of excess void space may have helped reduce the amount of dynamic motion the structure experienced at 293 K (particularly the disordered $[BAr^{F}{}_{4}]^{-}$ anion).

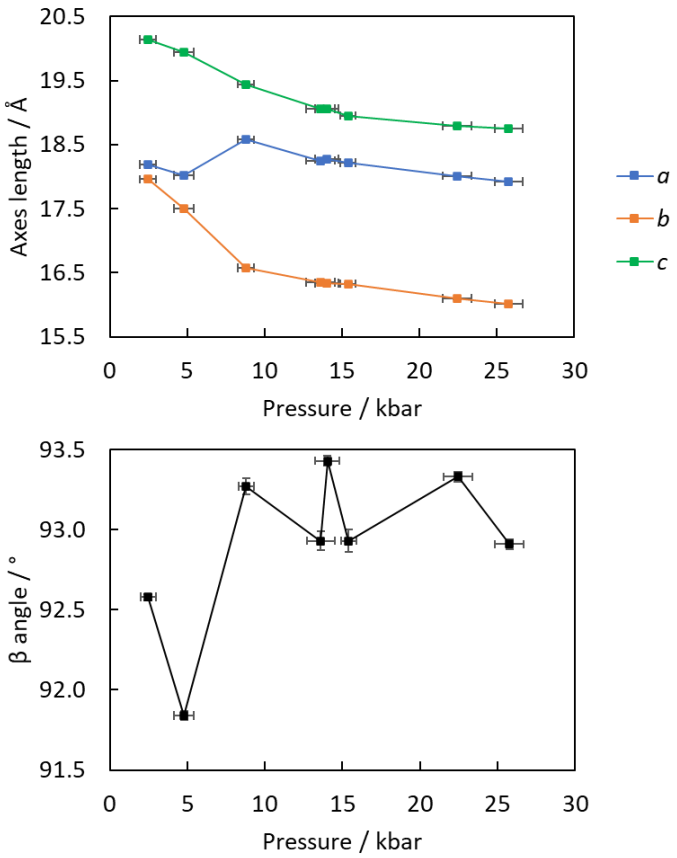

Figure 3.21 – Graph of the unit cell axes of **13** as a function of pressure (top) and of the *β* angle as a function of pressure (bottom)

Examination of the *β* angle as a function of pressure showed a small increase across the phase transition from 91.84(3) ° to 93.27(5) ° (Fig. 3.21). Between pressures of 8.8-25.8 kbar, *β* was less consistently determined but appeared to be larger in the high

pressure phase, **13-β** (average β angle in **13-β** = 93.13(5) °).[xvii] Discrepancies in the β angle could result from differences in crystal quality between samples and crystal orientation in relation to the incident beam during the separate experiments.

Smooth compression was observed for the cell volume as a function of pressure up to 25.8 kbar (Fig 3.22). The phase transition is imperceptible in Fig. 3.22, although it is apparent at higher pressures that the structure became less compressible. The bulk moduli and principal axis analysis of the two phases are discussed in section 3.5.4.

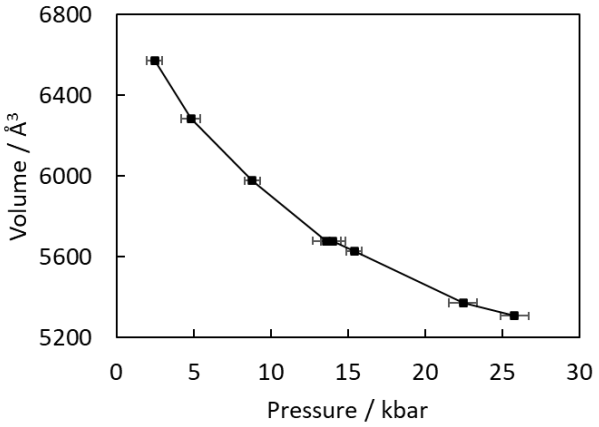

Figure 3.22 – Graph of the unit cell volume of **13** as a function of pressure.

3.5.3 – Phase transition in [Rh(PONOP)(η^2-HBcat)][BAr$^F{}_4$]

Between 4.8 and 8.8 kbar an isomorphous phase transition occurred, generating the high pressure phase **13-β**, which retained both the space group ($P2_1/c$) and commensurate cell parameters of the original phase, **13-α**. There was an appreciable structural reorientation of the anion and cation across the phase transition in addition to more subtle rearrangements to the coordination geometry within the cation (Fig. 3.23). Examination of the two phases showed that although the cations rotated by roughly 45 ° across the phase transition, the octahedral arrangement of anions around each cation was effectively preserved. The HBcat ligand remained 'sandwiched' between two adjacent Ar^F rings of a neighbouring anion across the phase transition

[xvii] The average standard deviation (Δz) was calculated using the equation $\Delta z = (\sqrt{\Sigma(\Delta x_n)^2})/n$, where n is the number of datapoints and Δx is the esd of β for each dataset.

because the rotation of the cation was accompanied by a complementary rotation of the surrounding anions (Fig. 3.23).

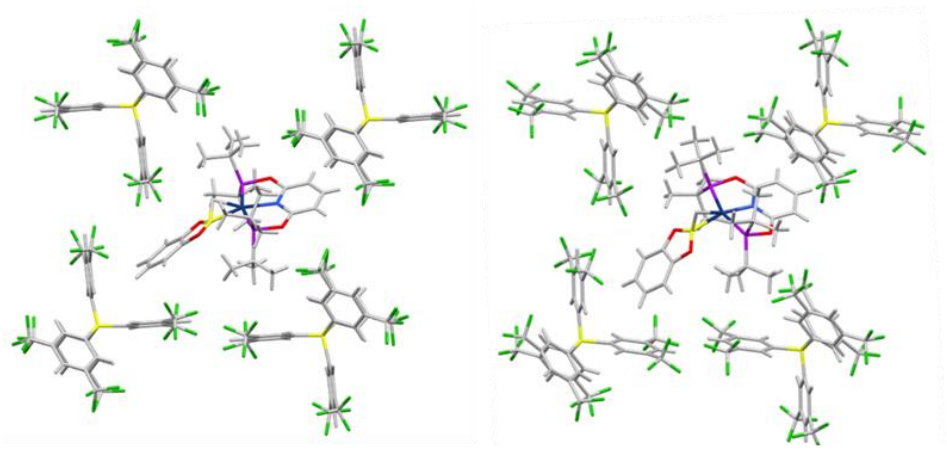

Figure 3.23 – A stick frame depiction of the packing observed in the ambient pressure (**13-α**, left) and high pressure (**13-β**, right) phases, as viewed approximately down the [100] direction.

The cation rotates in such a way that the width of the pincer ligand becomes better aligned with respect to the *a* axis in **13-β** – this accounts for the slight increase in the *a* axis across the phase transition (Fig. 3.21; Fig 3.22). Using *Mercury*,[52] the angle between the planes of the pincer ligands before and after the phase transition (as defined by the py rings of the pincer ligand) was calculated to be 44.92 °; the structures were overlaid such that the cell axes were best aligned. Interestingly, Weller and co-workers recently reported a similar transformation in the solid-state upon addition of H_2 to single crystals of [Ir($^{i\mathrm{Pr}}$PONOP)(η^2-propene)][BAr$^{\mathrm{F}}{}_4$], **A101** ($^{i\mathrm{Pr}}$PONOP = 2,6-bis(di-*iso*-propylphosphinito)pyridine), in which the pincer ligand was found to rotate by approximately 90 ° about the P–Ir–P vector in preference to rotation of the propene substrate.[68]

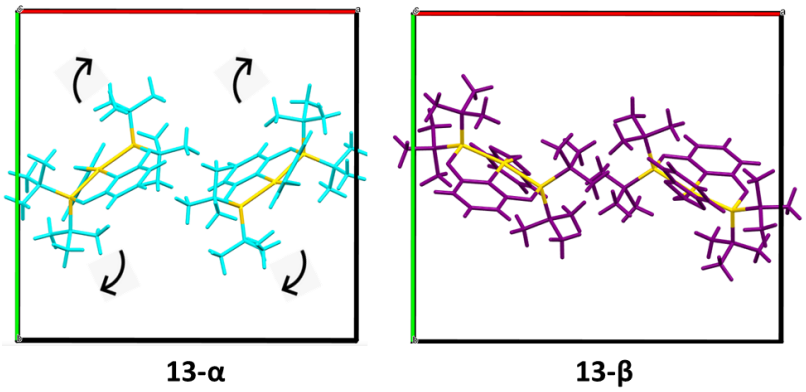

Figure 3.24 – The rotation of two cations in **13** across the phase transition, as viewed down the *c* axis. The coordination plane of the pincer ligand is highlighted in yellow. Red and green lines depict the *a* and *b* axes, respectively.

Interestingly, upon closer inspection of the phase transition overlay, whilst the planes defining pincer ligand were displaced by approximately 45 °, the planes of the HBcat ligands appeared almost orthogonal to one another (Fig. 3.25). In fact, the calculated angle between the HBcat planes across the phase transition calculated in *Mercury* was 99.04 °.[52] The HBcat planes were defined in both cases by all non-hydrogen atoms of the borane. The rotation of the HBcat ligand with respect to the coordination plane of the pincer ligand was synchronous with the rotation of the cation as a whole across the phase transition. Furthermore, the rotation of the HBcat ligand with respect to the pincer coordination plane occurred in the same direction as the rotation of the coordination complex as a whole across the phase transition (Fig. 3.25) The angle between the planes of the HBcat ligand and the pincer complex in **13-α** was reported by *Mercury* as 34.84 °, with the HBcat plane tilting off to the right-hand side, whereas the angle between the HBcat and pincer ligand planes in **13-β** was calculated to be 47.55 °, with the HBcat ligand tilting towards the left-hand side (Fig. 3.25).[52]

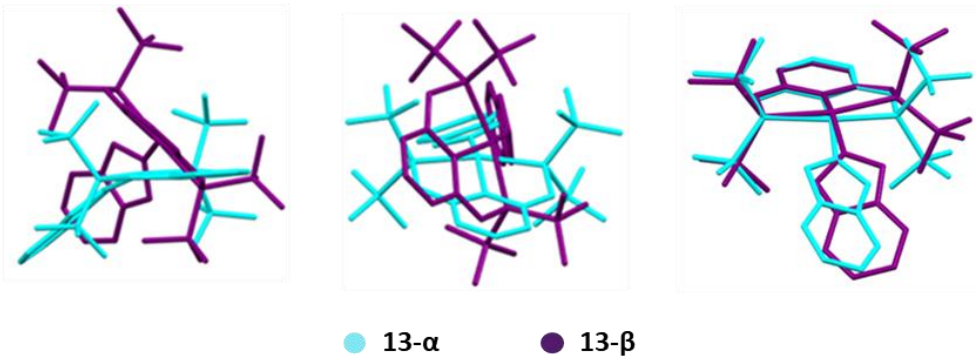

Figure 3.25 – Overlaid structures visualised in *Mercury*[52] of the orientation of the cations with respect to one another before (cyan, 4.8 kbar) and after (purple, 8.8 kbar) the phase transition, as viewed along (left) and from above (middle) the coordination plane of the pincer ligand, as well as the cations of **13-α** and **13-β** superimposed on one another (right).[xviii]

The coordination geometry of the pincer ligand itself was also altered across the phase transition – the plane defined by the P1–O1 and P2–O2 bonds of the pincer noticeably twisted away from coplanarity with respect to the aromatic backbone of the pincer ligand in **13-β** (Fig. 3.25). The offset of the phosphorus atoms, albeit small, consequently result in larger offsets for the ^{t}Bu substituents. The distortion observed in **13-β** better emulates the C_2 symmetry observed in PNP pincer ligands, as opposed to the C_{2v} symmetry typically exhibited by PONOP.[44] The origin of the pincer ligand deformation is explored in greater detail in section 3.5.4.

Analysis of the associated bond lengths and bond angles of the structural refinements between 2.5 kbar and 25.8 kbar revealed several trends across the data sets. Before the phase transition, in refinements up to 4.8 kbar, the N1–Rh1–B1 angle was determined to be approximately 160 °, but in **13-β**, decreased to approximately 152 ° as a consequence of the reorientation of the HBcat ligand (Fig. 3.26; Table 3.15). The decrease in the N1–Rh1–B1 angle across the phase transition suggests an improved overlap between the rhodium *d* orbital and the empty boron *p* orbital (Fig 3.26). Stronger back donation would result in enhanced activation of the B–H bond, which

[xviii] The overlays of the leftmost and central figures were made with the unit cell axes best aligned across the two phases. The rightmost figure was created by overlaying the cations of interest, not the unit cells.

could be considered a prerequisite to OA. Furthermore, the smaller N1–Rh1–B1 bond angle observed in the high pressure phase emulates the geometry of the elongated σ-borane complex **16**. The application of pressure appears to facilitate the evolution of the classical σ-borane (**13-α**) into an elongated σ-borane (**13-β**) through enhancement of the metal-borane orbital overlap.

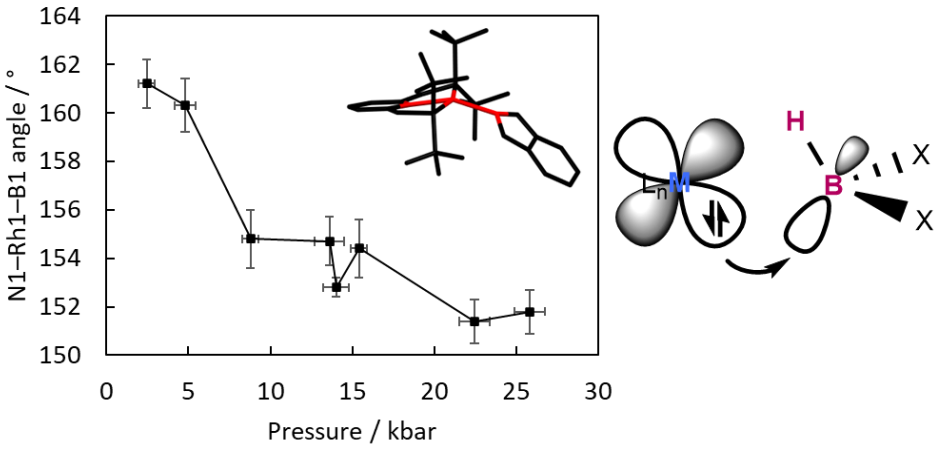

Figure 3.26 – A graph of the N1–Rh1–B1 angle of **13** as a function of pressure with an inset depicting the angle of interest in red (left) and a Dewar–Chatt–Duncanson model of the *d* → nb back donation found within a σ-borane complex (right).

Table 3.15 – Table of selected bond angles as a function of pressure. The asterisk denotes the ambient pressure collection previously conducted at 150 K, for reference.

Pressure / kbar	**N1–Rh1–B1 / °**	**P1–Rh1–P2 / °**
0.0*	160.14(9)	162.03(2)
2.5	161.2(10)	162.1(5)
4.8	160.3(11)	163.0(5)
8.8	154.8(12)	161.8(7)
13.9	154.7(10)	161.2(6)
14.0	152.8(8)	161.2(4)
15.4	154.4(12)	161.0(7)
22.4	151.4(9)	160.6(4)
25.8	151.8(9)	160.9(5)

The confidence interval between the N1–Rh1–B1 angles reported at 4.8 kbar (160.3(11) °) and 8.8 kbar (154.8(12) °) was calculated to be 3.4 σ, indicating that this change is statistically significant. Contrastingly, the confidence interval for the decrease in the P1–Rh1–P2 angle between 2.5 kbar and 25.8 kbar was calculated to be 1.7σ, meaning that the bite angle deformation was statistically insignificant (Table 3.15). A search of the CSD (v.5.43, update June 2022) [56] confirmed that the bite angle values reported in Table 3.15 were within the expected range for monomeric PONOP pincer complexes (160.6-163.3 °).

Crystal B's data are excluded from Figure 3.27 due to the considerably high R_{int} values (~40 %), which hindered the accurate assessment of bond lengths. For the sake of clarity, only the higher quality data (R_{int} < 16 %) collected for crystal A are discussed. The Rh–P bond lengths remained approximately the same across the studied pressure range, although gradual contractions (confidence interval < 3σ) were observed (Fig. 3.27, Table 3.16). These contractions, whilst statistically insignificant, are nevertheless complementary to the evolution of the elongated σ-borane interaction and, therefore, the activation of the rhodium(I) complex. The observation of such consistent structural metrics within this HP-XRD study was promising, since pincer complexes were purposefully selected for investigation due to their ability to maintain a well-defined and rigid coordination environment.[69] A well-defined coordination environment was hypothesised to make the location of atoms easier in datasets of limited quality, should new pressure-induced phases be discovered.

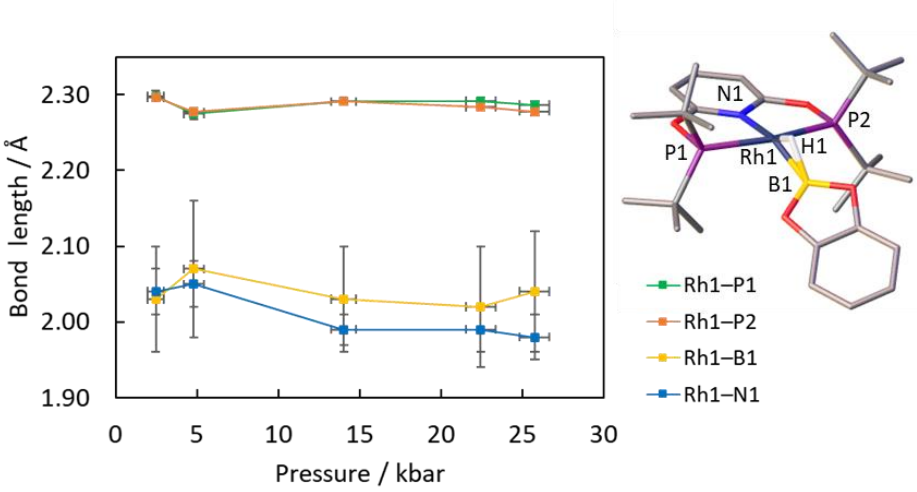

Figure 3.27 – A graph of the selected bond lengths against pressure for crystal A (bottom) and a partially labelled structure of the cation (top).

Table 3.16 – Table of selected bond lengths against pressure. The ambient pressure collection previously conducted at 150 K, denoted with an asterisk, is supplied for reference.

Pressure / kbar	Rh1–P1 / Å	Rh1–P2 / Å	Rh1–B1 / Å	Rh1–N1 / Å	B1–H1 / Å
0.0*	2.2933(6)	2.2939(6)	2.079(2)	2.0528(17)	1.41(3)
2.5	2.295(5)	2.298(7)	2.03(7)	2.05(3)	1.49(19)
4.8	2.275(7)	2.277(5)	2.07(9)	2.05(3)	1.4(2)
8.8	2.280(14)	2.292(11)	2.15(8)	2.06(2)	1.41(11)
13.9	2.290(13)	2.290(13)	2.13(5)	2.04(2)	1.39(11)
14.0	2.291(4)	2.291(4)	2.03(7)	1.99(2)	1.51(17)
15.4	2.264(16)	2.292(12)	2.11(6)	2.03(2)	1.43(11)
22.4	2.292(5)	2.284(5)	2.02(8)	1.99(3)	1.42(16)
25.8	2.287(5)	2.278(5)	2.04(8)	1.98(3)	1.47(15)

Interestingly, the Rh1–B1 bond length remained approximately the same across the phase transition, although the associated esds were significantly larger than for the other bond lengths presented (Table 3.16). The larger esds can be attributed, in part, to the low number of electrons found in boron, which prohibit the accurate location of the atom by HP-XRD. The Rh1-N1 bond length appears to contract across the phase transition, but only slightly. The confidence interval between the N1–Rh1 bond lengths reported at 4.8 kbar (2.05(3) Å) and 14.0 kbar (1.99(2) Å) was calculated to be 1.7 σ, indicating that the contraction is not statistically significant. The Rh1–N1 contraction can be attributed to the increased activation of the σ-borane – as the lone pair of the nitrogen atom donates electron density into the rhodium centre, the metal becomes more basic and can more readily donate electron density into the 'empty' boron orbital. This explanation is supported by the complimentary decrease observed in the N1–Rh1–B1 bond angle (Fig. 3.26).

As anticipated, accurate location of the coordinated hydrogen atom within each of the refinements proved impossible. Whilst many of the refinements allowed for the location of the hydrogen atom by way of the electron density difference map, the bond angles and bond lengths associated with the hydrogen atom between datasets varied significantly. In cases where the atom could not be located from the electron density difference map, the hydrogen atom was generated and constrained to a sensible

distance from the boron and rhodium atoms using fixed bond lengths which were informed by the 150 K ambient pressure collection.

3.5.4 – Compressibility and void space analysis

Both phases before and after the phase transition smoothly compress with increasing pressure. As anticipated, **13-β** was less compressible, with higher pressures being required to induce the same percentage of volume contraction. The second-order Birch-Murnaghan equation of states (BM EoS) for both phases were calculated using *PASCal*.[70] For the low-pressure phase, B_0 = 3.4(7) GPa , B'_0 = 4, V_0 = 7004(118) Å^3 and for the high pressure phase, B_0 = 10.5(15) GPa , B'_0 = 4, V_0 = 6356(94) Å^3. Analysis of the principal strain axes (also calculated using *PASCal*) indicated that before the phase transition, the principal axis X_1 had the highest compressibility coefficient (K) whereas X_3 had the lowest (Table 3.17). Phase **13-β** compressed more uniformly with respect to each principal component axes, with less variety observed between the calculated compressibility coefficients.

Table 3.17 – Table of the principal compressibilities, corresponding principal axes components and the approximate directions of compression determined for both phases, calculated using *PASCal*.[70]

Structure	Principle axis, i	K_i / TPa^{-1}	**Component of X_i along the crystallographic axes**			Approximate axis
			a	*b*	*c*	
13-α	1	109(8)	0	-1	0	[010]
	2	67(4)	-0.61	0	0.79	[$\bar{2}$03]
	3	12.3(6)	-0.83	0	-0.55	[201]
13-β	1	14(4)	0	-1	0	[010]
	2	13.9(16)	0.92	0	0.39	[301]
	3	11(5)	-0.37	0	0.93	[$\bar{1}$03]

In **13-α**, the principal strain axis with the highest calculated compressibility coefficient K_i was calculated to act approximately along the [010] Miller plane, followed by the second most compressible axis along [$\bar{2}$03] (Table 3.17). These directions of compression correspond to alignment of the lengths and widths, respectively, of the

largest volumes of void space calculated using *Mercury* within **13-α** (Fig. 3.28). The larger volumes of calculated void space tend to be located either within or adjacent to the cavities established by the counterion.

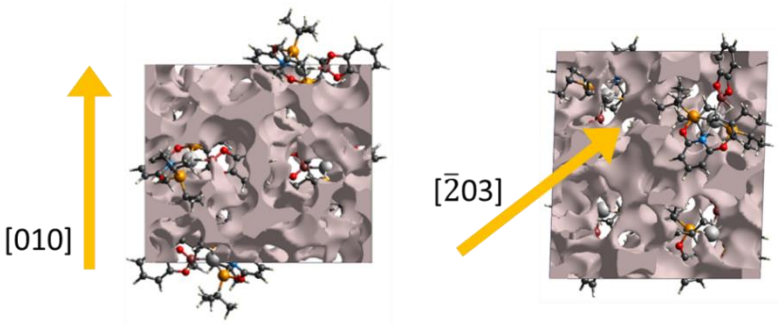

Figure 3.28 – The unit cell void volumes of **13-α** at 4.8 kbar visualised in *CrystalExplorer* with an isovalue of 0.002 e Å^{-3}, as viewed along the *a* axis (left) and the *b* axis (right). The [010] and [$\bar{2}$03] directions are depicted by orange arrows. For clarity, only the cations and voids are shown.

Across the phase transition, there was a decided decrease in the calculated void space within **13** (Fig. 3.29). The void volume, which was calculated using *CrystalExplorer*,[51] decreased smoothly across the studied pressure range and was accompanied by an increase in the calculated bulk modulus across the phase transition. A total of 352 Å^3 of void space was removed from the unit cell between 8.8 kbar and 25.8 kbar from **13-β** (Fig. 3.29).

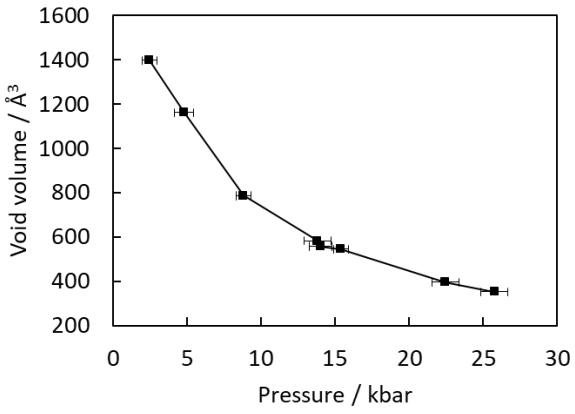

Figure 3.29 – A graph of the calculated void space across the pressure range studied for **13**, calculated by *CrystalExplorer* with an isovalue of 0.002 e Å^{-3}.[51,71]

This particular HP study was limited by the hydrostatic limit of the PTM, due to the obvious effect of non-hydrostatic conditions on the quality of the data and the deviation of trends observed in datasets collected above 25.8 kbar. However, it is apparent from the void volume calculations that at 25.8 kbar that a significant amount of void space is still present in **13-β**. The void space located near the HBcat ligand in **13-β** at 25.8 kbar, circled in yellow in Fig. 3.30, indicates that the application of more pressure would be required before any bond activation is likely to occur. Higher pressures could potentially remove more void space and subsequently force the bonds of interest into closer proximity with the metal centre and, therefore, engender OA.

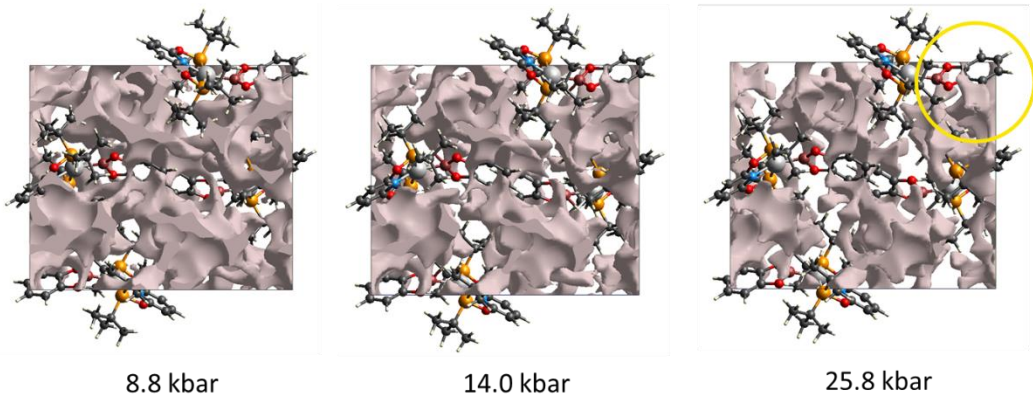

Figure 3.30 – The void volumes for **13-β** visualised in *CrystalExplorer* with an isovalue of 0.002 e Å-3 at 8.8, 14.0 and 25.8 kbar (left to right), as viewed along the *b* axis. Note the void space located next to the top face of the HBcat ligand in the structure at 25.8 kbar, circled in yellow. For clarity, only the cations are shown.

Inspection of the calculated Hirschfeld surfaces associated with the cation across the sampled pressure range suggests that further compression could promote the closer approach of the borane ligand to the metal centre. Figure 3.31 shows the evolution of the close contacts between the top HBcat face and the counterion (circled in yellow) at higher pressures. The phase transition appears to relieve the close contacts on the face of the HBcat ligand, which then continue to evolve as pressure increases. However, other unfavourable close contacts develop between the CF_3 groups of an anion and the ^{t}Bu groups of the pincer ligand (circled in red) at higher pressures in **13-β** (Fig. 3.31 & 3.32). The Hirschfeld surfaces indicate these ^{t}Bu···F_3C contacts are more severe than those experienced by the HBcat ligand, as they are displayed in a

more saturated red hue in Fig. 3.31. This observation is supported by the short contact values supplied in Fig. 3.32.

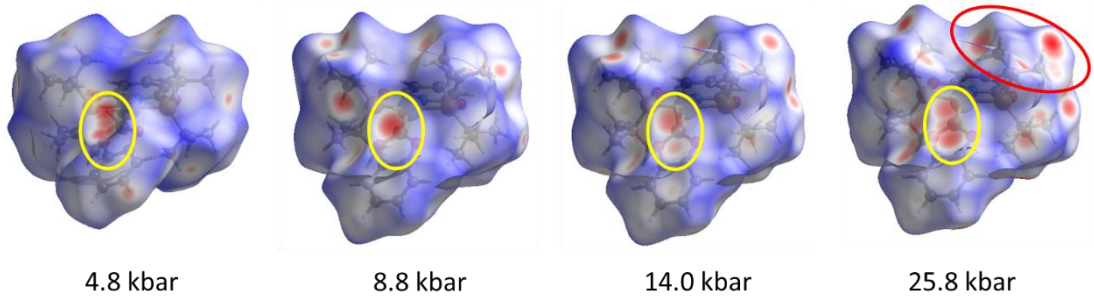

Figure 3.31 – The calculated Hirschfeld surfaces associated with the cation for structures of **13**. The close contacts near the HBcat ligand and ^{t}Bu group are circled in yellow and red, respectively.

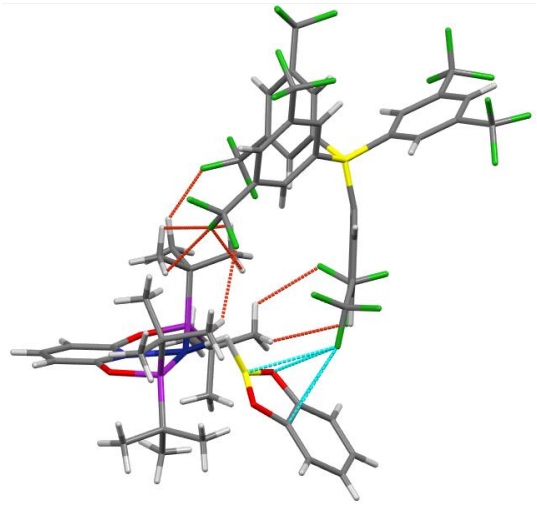

Contact type	Colour	Contact length / Å	Length - VdW radii / Å
$CF_3\cdots$HBcat		2.75(2) – 3.20(5)	−0.42(2) – −0.28(5)
$CF_3\cdots{}^{t}$Bu		2.07 – 2.67	−0.60 – −0.01

Figure 3.32 – The short contacts observed in **13-β** at 25.8 kbar. The accompanying table denotes the contact type and distance range calculated by *Mercury*.[52]

Higher pressures would presumably eliminate void space and continue to push the counterion into closer proximity of the borane of interest. In turn, this would bring the B–H bond into closer proximity with the metal centre and, therefore, encourage OA. However, the concern with this particular structure is that the close contacts that

develop between the cation and the counterion could hinder the effective compression of the HBcat ligand towards the metal centre, due to the steric bulk of the cation's ^{t}Bu groups and the anion's CF_3 groups.

3.6 – Conclusions

The preparation and characterisation of the first homologous series of rhodium σ-borane complexes was achieved by adapting a methodology previously reported in the Chaplin group for the convenient preparation of weakly coordinated novel adducts of {Rh(pincer)}$^{+}$.[41] Complexes **12-15** could be isolated in good yield and were fully characterised by multinuclear VT-NMR spectroscopy, single crystal XRD, elemental microanalysis and IR spectroscopy. The degree of borane activation under ambient conditions was found to depend on the identity of both the pincer and borane ligands, with PNP and HBcat-containing complex **15** activating the B–H bond to the greatest extent, as evidenced by VT-NMR spectroscopy and XRD. Because of the highly fluxional borane substrates, the ground state of the structures are ambiguous in solution (time averaged C_{2v} symmetry), although the temperature dependence of the $^{1}J_{RhH}$ coupling in **15** suggests that the complex is best described as existing in dynamic equilibrium between the rhodium(I) and rhodium(III) adducts.

HP-XRD studies conducted on **13** indicated that an isomorphous phase transition occurred between 4.8-8.8 kbar, which incited several notable geometric changes to the coordination geometry of the σ-borane ligand. Most notably, the N1–Rh1–B1 bond angle decreased from *ca*. 160 ° to *ca*. 152 ° across the phase transition, indicating the evolution of the classical σ-borane complex in the ambient pressure phase into an elongated σ-borane complex in the high pressure phase as a result of enhanced orbital overlap between the boron *p* and rhodium *d* orbitals due to compression. Ultimately, the study of **13** was restricted by the $[BAr^{F}_{4}]^{-}$ counterion, which hindered the approach of the HBcat ligand into closer proximity with the metal centre at higher pressures due to competing close contacts between the anion and ^{t}Bu substituents of the pincer ligand.

Keeping in mind that the overall aim of the project was to develop systems which undergo OA upon the application of pressure, the σ-borane complexes prepared herein – whilst thought to be chemically sensible targets – required further refinement in

order to engender pressure-induced OA. One logical avenue to pursue would be to study **13** at higher pressures using a different PTM. However, loading the DAC in a glove box with liquid media such as 1 : 1 pentane : *iso*-pentane or argon presents a significant challenge. Alternatively, complexes analogous to **12-15** which incorporated smaller, more rigid counterions could be prepared. This would improve dataset resolution through removal of the dynamic disorder experienced by the CF_3 groups. Additionally, changes to the crystal packing upon substitution of the bulky $[BAr^F{}_4]^-$ counterion could improve the compressibility of the structures. Given the already inherent difficulty of the air-sensitive HP-XRD experiments without the added challenge of handling volatile liquid media or cryogenic gas loading equipment, the latter avenue was thus pursued. All four systems were subsequently reengineered using alternative counterions in an attempt to encourage pressure-induced OA upon compression.

References

1. A. B. Chaplin and A. S. Weller, *Angew. Chem. Int. Ed.*, 2010, **49**, 581-584.
2. T. M. Douglas, A. B. Chaplin and A. S. Weller, *J. Am. Chem. Soc.*, 2008, **130**, 14432–14433.
3. M. Findlater, K. M. Schultz, W. H. Bernskoetter, A. Cartwright-Sykes, D. M. Heinekey and M. Brookhart, *Inorg. Chem.*, 2012, **51**, 4672-4678.
4. W. H. Bernskoetter, C. K. Schauer, K. I. Goldberg and M. Brookhart, *Science*, 2009, **326**, 553-556.
5. T. B. Marder and Z. Lin, *Contemporary Metal Boron Chemistry I*, Springer, 2008.
6. G. Alcaraz, A. B. Chaplin, C. J. Stevens, E. Clot, L. Vendier, A. S. Weller and S. Sabo-Etienne, *Organometallics*, 2010, **29**, 5591-5595.
7. T. M. Boyd, B. Tegner, G. Tizzard, A. Martinez-Martinez, S. Neale, M. Hayward, S. Coles, S. Macgregor and A. S. Weller, *Angew. Chem. Int. Ed.*, 2020, **59**, 6177-6181.
8. S. D. Pike, F. M. Chadwick, N. H. Rees, M. P. Scott, A. S. Weller, T. Kramer and S. A. Macgregor, *J. Am. Chem. Soc.*, 2015, **137**, 820-833.
9. F. M. Chadwick, N. H. Rees, A. S. Weller, T. Kramer, M. Iannuzzi and S. A. Macgregor, *Angew. Chem. Int. Ed.*, 2016, **55**, 3677-3681.
10. A. I. McKay, A. J. Bukvic, B. E. Tegner, A. L. Burnage, A. J. Marti Nez-Marti Nez, N. H. Rees, S. A. Macgregor and A. S. Weller, *J. Am. Chem. Soc.*, 2019, **141**, 11700-11712.
11. A. J. Martinez-Martinez, B. E. Tegner, A. I. McKay, A. J. Bukvic, N. H. Rees, G. J. Tizzard, S. J. Coles, M. R. Warren, S. A. Macgregor and A. S. Weller, *J. Am. Chem. Soc.*, 2018, **140**, 14958-14970.
12. R. N. Perutz, S. Sabo-Etienne and A. S. Weller, *Angew. Chem. Int. Ed.*, 2022, **61**, e202111462.
13. J. J. Race, A. L. Burnage, T. M. Boyd, A. Heyam, A. J. Martinez-Martinez, S. A. Macgregor and A. S. Weller, *Chem. Sci.*, 2021, **12**, 8832-8843.
14. M. R. Gyton, B. Leforestier and A. B. Chaplin, *Organometallics*, 2018, **37**, 3963-3971.
15. M. Brookhart, M. L. H. Green and G. Parkin, *PNAS*, 2007, **104**, 6908–6914.
16. T. J. Hebden, M. C. Denney, V. Pons, P. M. B. Piccoli, T. F. Koetzle, A. J. Schultz, W. Kaminsky, K. I. Goldberg and D. M. Heinekey, *J. Am. Chem. Soc.*, 2008, **130**, 10812–10820.
17. E. A. K. Spearing-Ewyn, N. A. Beattie, A. L. Colebatch, A. J. Martinez-Martinez, A. Docker, T. M. Boyd, G. Baillie, R. Reed, S. A. Macgregor and A. S. Weller, *Dalton Trans.*, 2019, **48**, 14724-14736.
18. M. C. Denney, V. Pons, T. J. Hebden, D. M. Heinekey and K. I. Goldberg, *J. Am. Chem. Soc.*, 2006, **128**, 12048-12049.
19. J. F. Hartwig, K. S. Cook, M. Hapke, C. D. Incarvito, Y. Fan, C. E. Webster and M. B. Hall, *J. Am. Chem. Soc.*, 2005, **127**, 2538–2552.
20. J. F. Hartwig, S. Bhandari and P. R. Rablen, *J. Am. Chem. Soc.*, 1994, **116**, 1839-1844.
21. M. A. Esteruelas, M. Oliván and A. Vélez, *Organometallics*, 2015, **34**, 1911-1924.
22. J. F. Hartwig, *Acc. Chem. Res.*, 2012, **45**, 864–873.
23. A. Suzuki, *Proc. Jpn. Acad., Ser. B*, 2004, **80**, 359-371.
24. B. J. Foley, N. Bhuvanesh, J. Zhou and O. V. Ozerov, *ACS Catal.*, 2020, **10**, 9824-9836.
25. D. Blakemore, *Synthetic methods in drug discovery: volume 1*, The Royal Society of Chemistry, first edn., 2016.
26. J. C. Babon, M. A. Esteruelas, I. Fernandez, A. M. Lopez and E. Oñate, *Inorg. Chem.*, 2018, **57**, 4482-4491.

27. M. A. Esteruelas, I. Fernández, C. García-Yebra, J. Martín and E. Oñate, *Organometallics*, 2017, **36**, 2298-2307.
28. V. Montiel-Palma, M. Lumbierres, B. Donnadieu, S. Sabo-Etienne and B. Chaudret, *J. Am. Chem. Soc.*, 2002, **124**, 5624–5625.
29. S. Lachaize, K. Essalah, V. Montiel-Palma, L. Vendier, B. Chaudret, J.-C. Barthelat and S. Sabo-Etienne, *Organometallics*, 2005, **24**, 2935-2943.
30. J. F. Hartwig, C. N. Muhoro and X. He, *J. Am. Chem. Soc.*, 1996, **118**, 10936-10937.
31. D. R. Lantero, D. H. Motry, D. L. Ward and M. R. Smith, *J. Am. Chem. Soc.*, 1994, **116**, 10811-10812.
32. L. P. Press, A. J. Kosanovich, B. J. McCulloch and O. V. Ozerov, *J. Am. Chem. Soc.*, 2016, **138**, 9487-9497.
33. C. N. Muhoro, X. He and J. F. Hartwig, *J. Am. Chem. Soc.*, 1999, **121**, 5033-5046.
34. S. Schlecht and J. F. Hartwig, *J. Am. Chem. Soc.*, 2000, **122**, 9435-9443.
35. G. Alcaraz, M. Grellier and S. Sabo-Etienne, *Acc. Chem. Res.*, 2009, **42**, 1640-1649.
36. S. V. Safronov, E. I. Gutsul, I. E. Golub, F. M. Dolgushin, Y. V. Nelubina, O. A. Filippov, L. M. Epstein, A. S. Peregudov, N. V. Belkova and E. S. Shubina, *Dalton Trans.*, 2019, **48**, 12720-12729.
37. T. J. Marks and J. R. Kolb, *Chem. Rev.*, 1977, **77**, 263-293.
38. J. Zhang, E. Balaraman, G. Leitus and D. Milstein, *Organometallics*, 2011, **30**, 5716-5724.
39. J. F. Hartwig and S. R. D. Gala, *J. Am. Chem. Soc.*, 1994, **116**, 3661-3662.
40. A. Olding, C. Ho, A. Canty, N. Lucas, J. Horne and A. C. Bissember, *Angew. Chem. Int. Ed.*, 2021, **60**, 14897-14901.
41. M. R. Gyton, T. M. Hood and A. B. Chaplin, *Dalton Trans.*, 2019, **48**, 2877-2880.
42. G. R. Eaton, *J. Chem. Educ.*, 1969, **46**, 547-556.
43. P. S. Pregosin, *NMR in Organometallic Chemistry*, Wiley, 2012.
44. K. Lee, H. Wei, A. V. Blake, C. M. Donahue, J. M. Keith and S. R. Daly, *Dalton Trans.*, 2016, **45**, 9774-9785.
45. J. F. Hartwig, K. S. Cook, M. Hapke, C. D. Incarvito, Y. Fan, C. E. Webster and M. B. Hall, *J. Am. Chem. Soc.*, 2005, **127**, 2538-2552.
46. K. K. Pandey, *Coord. Chem. Rev.*, 2009, **253**, 37-55.
47. S. I. Kallane, T. Braun, M. Teltewskoi, B. Braun, R. Herrmann and R. Laubenstein, *Chem. Commun.*, 2015, **51**, 14613-14616.
48. C. E. F. Rickard, W. R. Roper, A. Williamson and L. J. Wright, *Organometallics*, 2000, **19**, 4344-4355.
49. A. B. Chaplin and A. S. Weller, *Organometallics*, 2011, **30**, 4466-4469.
50. S. K. Furfari, B. E. Tegner, A. L. Burnage, L. R. Doyle, A. J. Bukvic, S. A. Macgregor and A. S. Weller, *Chem. Eur. J.*, 2021, **27**, 3177-3183.
51. P. R. Spackman, M. J. Turner, J. J. McKinnon, S. K. Wolff, D. J. Grimwood, D. Jayatilaka and M. A. Spackman, *J. Appl. Cryst.*, 2021, **54**, 1006-1011.
52. C. F. Macrae, I. Sovago, S. J. Cottrell, P. T. A. Galek, P. McCabe, E. Pidcock, M. Platings, G. P. Shields, J. S. Stevens, M. Towler and P. A. Wood, *J. Appl. Crystallogr.*, 2020, **53**, 226-235.
53. T. M. Hood, B. Leforestier, M. R. Gyton and A. B. Chaplin, *Inorg. Chem.*, 2019, **58**, 7593-7601.
54. G. M. Adams, F. M. Chadwick, S. D. Pike and A. S. Weller, *Dalton Trans.*, 2015, **44**, 6340-6342.
55. M. R. Gyton, B. Leforestier and A. B. Chaplin, *Angew. Chem. Int. Ed.*, 2019, **58**, 15295-15298.
56. I. J. Bruno, J. C. Cole, P. R. Edgington, M. Kessler, C. F. Macrae, P. McCabe, J. Pearson and R. Taylor, *Acta Cryst.*, 2002, **B58**, 389-397.

57. C. Janiak, *J. Chem. Soc., Dalton Trans.*, 2000, 3885-3896.
58. K. Avasthi, L. Shukla, R. Kant and K. Ravikumar, *Acta. Cryst.*, 2014, **C70**, 555-561.
59. A. J. Blake, W. Clegg, J. M. Cole, J. S. O. Evans, P. Main, S. Parsons and D. J. Watkin, *Crystal Structure Analysis Principles and Practice*, Oxford University Press, second edn., 2009.
60. C. Lenczyk, D. K. Roy, B. Ghosh, J. Schwarzmann, A. K. Phukan and H. Braunschweig, *Chem. Eur. J.*, 2019, **25**, 8585-8589.
61. Y. B. Hleba, Doctor of Philosophy, Queen's University, 2007.
62. K. Yokogawa, K. Murata, H. Yoshino and S. Aoyama, *Jpn. J. Appl. Phys.*, 2007, **46**, 3636-3639.
63. R. Lee, J. A. Howard, M. R. Probert and J. W. Steed, *Chem. Soc. Rev.*, 2014, **43**, 4300-4311.
64. J. P. Tidey, H. L. S. Wong, M. Schröder and A. J. Blake, *Coord. Chem. Rev.*, 2014, **277-278**, 187-207.
65. T. Boffa Ballaran, A. Kurnosov and D. Trots, *High Pressure Res.*, 2013, **33**, 453-465.
66. J. D. Barnett, S. Block and G. J. Piermarini, *Rev. Sci. Instrum.*, 1973, **44**, 1-9.
67. F. P. A. Fabbiani, G. Buth, B. Dittrich and H. Sowa, *CrystEngComm*, 2010, **12**, 2541-2550.
68. C. G. Royle, L. Sotorrios, M. R. Gyton, C. N. Brodie, A. L. Burnage, S. K. Furfari, A. Marini, M. R. Warren, S. A. Macgregor and A. S. Weller, *Organometallics*, 2022, **41**, 3270−3280.
69. E. Peris and R. H. Crabtree, *Chem. Soc. Rev.*, 2018, **47**, 1959-1968.
70. M. J. Cliffe and A. L. Goodwin, *J. Appl. Cryst.*, 2012, **45**, 1321-1329.
71. M. J. Turner, J. J. McKinnon, D. Jayatilaka and M. A. Spackman, *CrystEngComm*, 2011, **13**, 1804-1813.

Chapter 4 – Anion effects in a series of {Rh(pincer)}$^{+}$ σ-borane complexes

Abstract

Based on the HP-XRD study of **13**, it was thought that substitution of the $[BAr^{F}{}_{4}]^{-}$ counterion in complexes **12-15** would improve structure compressibilities by inciting changes in the crystal packing, thereby encouraging pressure-induced OA to occur. Through anion substitution, the largest structurally related collection of rhodium σ-borane complexes have been isolated and compared. Notably, OA products were obtained upon crystallisation under ambient conditions for samples of [Rh(PNP)(HBcat)][X] (X = SbF_6: **19**; $BAr^{F20}{}_{4}$: **23**; Ar^{F20} = pentafluorophenyl), whereas the $[BAr^{F}{}_{4}]^{-}$ analogue **15** crystallised as the rhodium(I) σ-borane adduct. The solid-state isolation of complexes with different oxidation states were thought to be the result of crystal packing effects.

HP-XRD studies were carried out on co-crystal **19** in an effort to induce OA in the remaining rhodium(I) complex; unfortunately, analysis was limited by the complexity of the structure and the poor data-to-parameter ratio. Pressure-indued OA also remained elusive in [Rh(PNP)(η^2-HBpin)][$BAr^{F20}{}_{4}$], **22**, but the evolution of formal π-π interactions between adjacent Ar^{F20} rings was observed at pressures beyond 11.2 kbar. X-ray diffraction techniques were instrumental in elucidating the solid-state behaviour of these species.

Chapter 4 Key

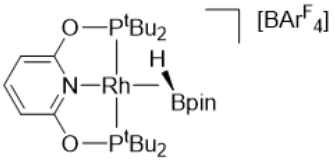

12

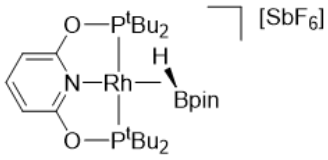

16

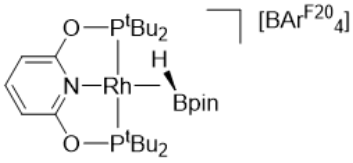

20

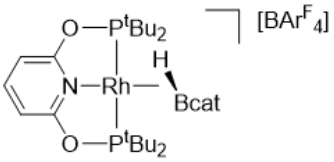

13

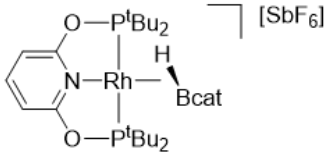

17
not isolated

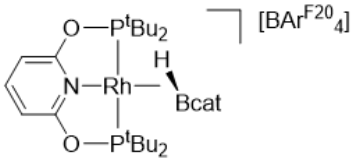

21
not isolated

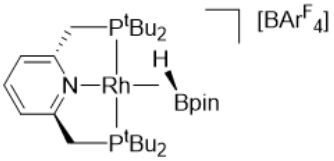

14

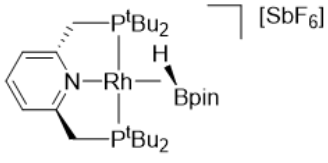

18

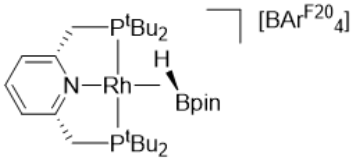

22

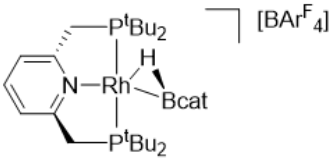

15

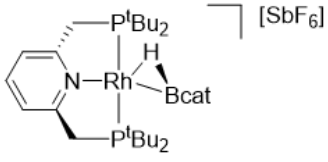

19a

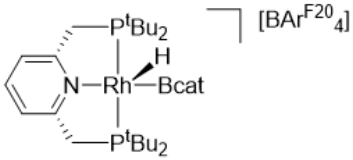

23

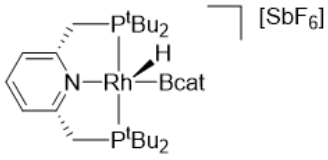

19b

4.1 – Introduction

Crystal engineering is of continuing interest to scientists striving to understand structure-property relationships. Coordination polymers and polyoxometalates, for example, have been probed extensively by solid-state chemists because their high-dimensional arrays and flexible architectures permit the modulation of properties such as conduction, luminescence and gas adsorption.[1-4] Whilst many factors contribute to the structure and subsequent properties of a complex,[5] one of the most straightforward modifications to make to a charged species is substitution of the counterion.

Factors to consider include the size and electronic properties of the different anions – for example, substitution of the weakly coordinating anions in linear chain networks of $[Ag(4\text{-pytz})_2][X]$ (X = BF_4, **A102**; PF_6, **A103**; 4-pytz = 1,4-bis-(4-pyridyl)-2,3,4,5-tetrazine) for the more coordinating $[NO_3]^-$ anion lead to the formation of an extended helical staircase structure.[6] Substitution of the difluorophosphate anion in $\{[Ag(pybut)][PO_2F_2]\}_\infty$, **A104** (pybut = 1,4-bis(4-pyridyl)butadiyne) for $[NO_3]^-$ also resulted in disruptions to the laddered π-π and Ag···Ag aurophilic interactions by disturbing the linear chain networks.[7] Similar disruptions in extended networks have been observed with cationic counterions too – the cation in $[NHEt_3][Rh(C_6Cl_2O_4)(CO)_2]$, **A105**, had an adverse influence on the formation of metallic stacks as a result of hydrogen bonding interactions with the carbonyl ligands of the anionic complex. Whilst some rhodium atoms were separated by 3.2130(6) Å, the hydrogen bonding network interrupted the continuous stacking arrangement (Fig. 4.1).

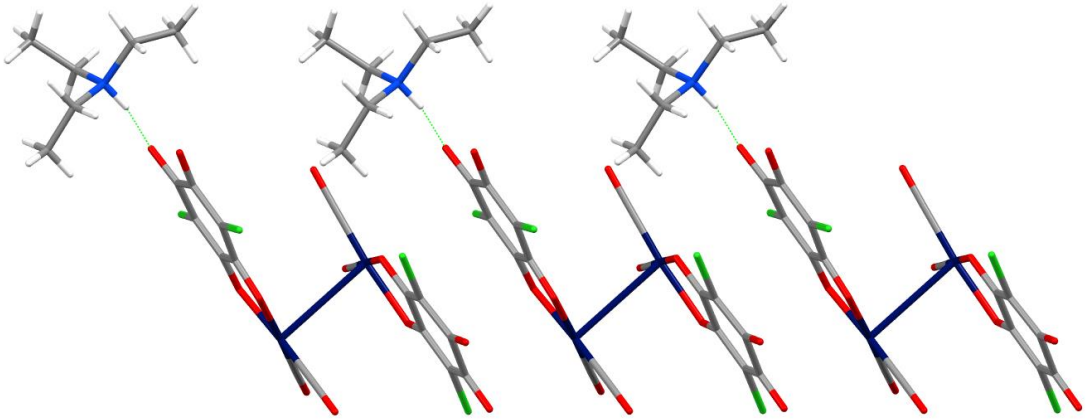

Figure 4.1 – The interrupted packing of Rh···Rh stacks observed in **A105**, as viewed approximately down the [111] direction. Hydrogen-bonds depicted by green dotted lines. Key: white = H, grey = C, red = O, green = Cl, blue = N, navy = Rh.

The formation of continuous 1D metal-metal interactions is one methodology for the production of nanowires, so the interruption of such stacking arrangements is unfavourable. Single crystals of the related complex $[NMe_4][Rh(C_6Cl_2O_4)(CO)_2]$, **A106**, were not successfully produced by Oro and co-workers at the time, however, spectroscopic data indicated the formation of intermetallic interactions, presumably due to the removal of the disruptive hydrogen bonding interactions.[8]

Perturbations created by adjusting the steric and electronic properties of a non-coordinating counterion can also have a significant influence on the activity of the complex. The catalytic efficiency of hydrogen isotope exchange in solution increased with anion size in [Ir(COD)(IMes)(PPh_3)][X] (IMes = 1,3-Bis(2,4,6-trimethylphenyl)-1,3-dihydro-2*H*-imidazol-2-ylidene; X = BF_4, **A107**; OTf, **A108**; BAr^F_4, **A109**).[9] The larger anions additionally allowed wider solvent scopes to be employed. Through crystal engineering, Duan and co-workers were able to increase the effective quantum efficiencies (EQEs) of thin films of $[Ir(ppy)_2(bpy)][X]$ (ppy = 2-phenylpyridine; bpy = 2,2′-bipyridine; X = BF_4, **A110**; PF_6, **A111**; BPh_4, **A112**; BAr^F_4, **A113**) from 1.2 % up to 14.8 %.[10] By substituting the counterions and ancillary ligands, larger sterically hindered 'spacers' were incorporated into the functional materials, resulting in higher EQEs. Counterion substitution in cobalt(II), iron(II) and iron(III) SCO complexes have been shown to provoke drastic changes behaviour, ranging from influencing the cooperativity of the system to fully supressing the phenomenon altogether.[11]

However, counterion substitutions do not always change the properties of the resulting material significantly. For example, Rodriguez and co-workers reported that whilst the aurophilic contacts and, therefore, the luminescence spectra of $[\{^{Ph}PNP(AuCl)_2\}_2][X]$ (^{Ph}PNP = 2,6-bis(diphenylphosphinomethyl)pyridine; X = BF_4, **A114**; SbF_6, **A115**) were similar, the gold(I) atoms in the **A115** adopted a near-linear arrangement in the solid-state, as opposed to a zig-zag arrangement, as was observed in **A114**.[12]

Perhaps most relevant to this work are the anion effects Weller and co-workers have described for their solid-state molecular organometallic (SMOM) chemistry. The synthesis of many of their σ-alkane complexes via SC-SC transformations relies on the ability of the $[BAr^F_4]^-$ anion to provide a stabilising microenvironment.[13-20] Recently the group investigated the effect of the anion on the solid-state chemistry of $[Rh(Cy_2PCH_2CH_2PCy_2)(\eta^2{:}\eta^2\text{-NBD})]^+$ – of the four different $[BAr^X_4]^-$ anions studied

($[BAr^{F}{}_4]^-$ = $[B(3,5\text{-}\{CF_3\}_2C_6H_3)_4]^-$, **A116**; $[BAr^{F*}{}_4]^-$ = $[B(3,5\text{-}F_2C_6H_3)_4]^-$, **A117**; $[BAr^{Cl}{}_4]^-$ = $[B(3,5\text{-}Cl_2C_6H_3)_4]^-$, **A118**; $[BAr^{H}{}_4]^-$ = $[B(C_6H_5)_4]^-$, **A119**), only the $[BAr^{F}{}_4]^-$ analogue **A116** afforded an indefinitely stable σ-alkane complex upon hydrogenation in the solid-state. For the other $[BAr^{X}{}_4]^-$ analogues, hydrogenation proceeded at a protracted rate (in the case of **A118**), only partially (in the case of **A117**) or so slowly that the resulting unstable σ-alkane species was unobserved (in the case of **A119**).[21] The stability of the resulting σ-alkane analogues confirmed that the $-CF_3$ groups of the $[BAr^{F}{}_4]^-$ anion clearly play a significant role in facilitating the movement of H_2 through the crystal whilst stabilising the structure to prevent collapse.

The non-coordinating anion also affected the coordination mode adopted by the σ-alkane product – whilst the NBA ligand in **A118** adopted an *exodentate* conformation, the NBA ligand in **A116** adopted an *endodentate* conformation.[21] Similar distinctions had previously been observed by Weller and co-workers for the substitution of the R groups in $[Rh(R_2PCH_2CH_2PR_2)(\eta^2{:}\eta^2\text{-NBD})][BAr^{F}{}_4]$ from R = Cy (**A116**, *endodentate*) to R = ^{t}Bu (**A120**, *exodentate*).[22] In both cases, the conformational preferences were attributed to crystal packing effects and the localised crystalline microenvironment. The catalytic activity of the four $[BAr^{X}{}_4]^-$ analogues **A116**-**A119** were also controlled using this anion templating approach. It was found that although the selectivity of butene isomerisation could not be improved, **A116** was the most efficient catalyst in the early stages of the reaction compared to **A117** and **A118**. Complex **A119** was inactive since the σ-alkane species could not be efficiently generated from this initial NBE complex.[21]

4.2 – Crystal engineering as a control parameter

Non-coordinating counterions can have profound effects on the overall behaviour of a structure, even under ambient conditions. This prompted the exploration of alternative counterions to incorporate into complexes **12**-**15**, with the expectation that substitution of the counterion could alter the structure and packing in a beneficial manner so as to enable pressure-induced OA. Replacement of the $[BAr^{F}{}_4]^-$ counterion was speculated to improve the pressure-responsive behaviour of the systems in two ways: Firstly, replacing $[BAr^{F}{}_4]^-$ with a smaller or more rigid anion may improve crystal quality by removal of the disordered CF_3 groups, thereby, potentially enhancing the resolution of

the HP-XRD data. Secondly, by perturbing the solid-state microenvironment around the borane ligands, perhaps packing efficiencies and structure compressibilities could be improved so as to encourage pressure-induced OA. Two different anions were selected to interrogate the counterion's effect on the solid-state chemistry of the σ-borane complexes: hexafluoroantimonate, $[SbF_6]^-$, and tetrakis(pentafluorophenyl)borate, $[BAr^{F20}{}_4]^-$.

The $[SbF_6]^-$ analogues [Rh(pincer)(η^2-HBR_2)][SbF_6] (pincer = PONOP, HBR_2 = HBpin, **16**; HBcat, **17**; pincer = PNP, HBR_2 = HBpin, **18**; HBcat, **19**) were proposed since the structures were anticipated to be less disordered in comparison to **12**-**15**. Less disorder would, in theory, improve data resolution and lead to higher quality refinements. The $[BAr^{F20}{}_4]^-$ analogues [Rh(pincer)(η^2-HBR_2)][$BAr^{F20}{}_4$] (pincer = PONOP, HBR_2 = HBpin, **20**; HBcat, **21**; pincer = PNP, HBR_2 = HBpin, **22**; HBcat, **23**) were proposed as suitable alternatives to $[BAr^F{}_4]^-$ because whilst the size and general shape of the $[BAr^F{}_4]^-$ anion is preserved, the CF_3 groups (which had previously hindered the dataset resolution in the HP-XRD studies of **A** and **13**) were removed. In fact, it was thought that the $[BAr^{F20}{}_4]^-$ anion may even enhance the stabilising secondary interactions in the solid-state, due to the abundance of electronegative fluorine atoms present in $[BAr^{F20}{}_4]^-$ capable of forming favourable dipole-dipole interactions.[23]

It was decided that the cations themselves would remain unchanged, since the existing NMR, IR and XRD data indicated that the σ-borane ligands were activated to a reasonable extent under ambient conditions. The existing reactivity of the cations are controlled by the slightly Lewis acidic alkoxyboranes in combination with the stabilising electronic properties of the pincer ligands. By methodically altering the identity of the pincer ligand, the borane ligand and the non-coordinating anion, a series of twelve different σ-borane complexes were produced that were compared and systematically interrogated both in solution and the solid-state.

4.3 – Preparation and characterisation of the $[SbF_6]^-$ and $[BArF^{20}{}_4]^-$ analogues

The σ-borane complexes [Rh(pincer)(η^2-HBR_2)][X] (pincer = PONOP or PNP; HBR_2 = HBpin or HBcat; X = SbF_6 or $BAr^{F20}{}_4$; Table 4.1) were synthesised following the

general procedure previously outlined in chapter 3 for the preparation of complexes **12-15**. Equimolar quantities of $[Rh(COD)_2][X]$ (X = SbF_6, $BAr^{F20}{}_4$) and the respective pincer ligand (PONOP or PNP) were dissolved in 1,2-$C_6H_4F_2$ at room temperature, after which addition of the respective borane solution (3-4 eq.; 0.40 M HBcat or 0.67 M HBpin in 1,2-$C_6H_4F_2$) afforded *in situ* solutions of complexes **16-23** (Table 4.1) and free COD. The reactions were monitored over the course of several hours (< 6 h) by ^1H and ^{31}P NMR spectroscopy until quantitative formation of the respective σ-borane complex was observed. The NMR spectra collected for complexes **16-23** were equivalent to their respective $[BAr^F{}_4]^-$ counterparts **12-15** (see chapter 6).

Table 4.1 – The numbering scheme and isolated yields of **12-23**.

Complex	Numbering scheme	Isolated yield / %
$[Rh(PONOP)(\eta^2\text{-HBpin})][BAr^F{}_4]$	**12**	83
$[Rh(PONOP)(\eta^2\text{-HBcat})][BAr^F{}_4]$	**13**	80
$[Rh(PNP)(\eta^2\text{-HBpin})][BAr^F{}_4]$	**14**	72
$[Rh(PNP)(\eta^2\text{-HBcat})][BAr^F{}_4]$	**15**	60
$[Rh(PONOP)(\eta^2\text{-HBpin})][SbF_6]$	**16**	19
$[Rh(PONOP)(\eta^2\text{-HBcat})][SbF_6]$	**17**	Not isolated
$[Rh(PNP)(\eta^2\text{-HBpin})][SbF_6]$	**18**	39
$[Rh(PNP)(\eta^2\text{-HBcat})][SbF_6]$	**19**	35
$[Rh(PONOP)(\eta^2\text{-HBpin})][BAr^{F20}{}_4]$	**20**	79
$[Rh(PONOP)(\eta^2\text{-HBcat})][BAr^{F20}{}_4]$	**21**	Not isolated
$[Rh(PNP)(\eta^2\text{-HBpin})][BAr^{F20}{}_4]$	**22**	79
$[Rh(PNP)(\eta^2\text{-HBcat})][BAr^{F20}{}_4]$	**23**	75

Complexes **16**, **18**, **19**, **20**, **22** and **23** could be isolated by liquid-liquid diffusion of hexane into the 1,2-$C_6H_4F_2$ solutions at room temperature in varying yields (Table 4.1). Complexes **17** and **21** could be generated *in situ* but were unable to be isolated because crystallisation attempts resulted in precipitation of an oil. Spectroscopic analysis of the oil indicated that the substance was comprised of several unidentified decomposition products. All of the isolated complexes partially decomposed by *ca*. 10 % into their respective dihydrogen adducts $[Rh(pincer)(\eta^2\text{-}H_2)][X]$ (pincer =

PONOP, PNP; X = SbF_6, $BAr^{F20}{}_4$) in solutions of 1,2-$C_6H_4F_2$ at room temperature over the course of 24 h, as was observed for the original series **12-15**. The spectroscopic data obtained for the dihydrogen adducts were consistent with the literature.[24,25]

Given the large number of structurally similar complexes prepared, for clarity, the crystal structures of the $[SbF_6]^-$ and $[BAr^{F20}{}_4]^-$ analogues are first individually presented and analysed in the following section, then the overall series is widely compared (section 4.4). Crystallographic details that are not described herein are provided in the experimental section (chapter 6) or the appendix. Furthermore, it should be noted that where Rh–H or B–H bond lengths are considered, the values reported should be regarded loosely. The location of hydrogen atoms by X-ray diffraction is inherently unreliable, especially when in close proximity to a heavy atom, such as rhodium. Therefore, any comparisons being drawn from the experimental data with respect to the coordinating hydrogen atoms of the σ-borane ligands must be considered with these facts in mind.

4.3.1 – Crystal structure of [Rh(PONOP)(η^2-HBpin)][SbF_6], 16

Complex **16** crystallised as a 1,2-$C_6H_4F_2$ solvate in the triclinic space group $P\bar{1}$ (a = 14.5639(2) Å, b = 15.7044(2) Å, c = 16.7452(3) Å, α = 95.625(1) °, β = 94.853(1) °, γ = 95.136(1) °, V = 3779.29(10) Å^3, Z' = 2) with two crystallographically unique complexes (A and B) in the asymmetric unit. Both of the crystallographically unique cations adopt distorted square planar geometries and are structurally similar to the $[BAr^F{}_4]^-$ analogue **12** (Fig. 4.2; Table 4.2). The twist angles between the mean molecular planes of the HBpin ligands (as defined by the O1–B1–O2 atoms) and the pincer ligands (as defined by the O1, P1, Rh1, P2, O1 and N1 atoms) were calculated to be *ca*. 24.2 ° and 33.5 ° for complexes A and B, respectively, using *Mercury*.[26] Both complexes A and B are best described as classical σ-borane complexes, as evidenced by their B–H bond lengths of 1.37(4) Å and 1.41(4) Å, respectively (Table 4.2), which are similar to the B–H bond length reported for **12** (1.36(3) Å). The hydrogen atoms H1A and H1B were located using the electron density difference map and refined freely, but their locations are unreliable due to the general noise of the models' background (largest peak = 0.91 e/Å^3; largest hole = –1.31 e/Å^3).

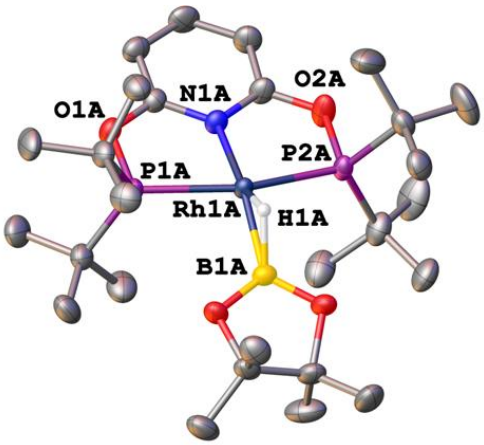

Figure 4.2 – A partially labelled structure of complex A in **16**. Atomic displacement parameters are drawn at 50 % probability. Counterions, solvent molecules and all hydrogen atoms, except for the HBcat hydrogen, are omitted for clarity. Complex A is representative of the coordination sphere of complex B.

Table 4.2 – Table of selected bond lengths and bond angles for the two unique complexes A (top values) and B (bottom values) in **16**.

Atoms	Bond length / Å	Atoms	Bond angle / °
Rh1–N1	2.057(2) 2.056(2)	P1–Rh1–P2	161.93(3) 161.69(3)
Rh1–P1	2.2928(7) 2.2978(7)	N1–Rh1–B1	163.68(11) 155.27(10)
Rh1–P2	2.2882(7) 2.3017(7)	Rh1–B1–H1	44.0(16) 44.8(18)
Rh1–B1	2.120(3) 2.103(3)	B1–H1–Rh1	96(2) 93(2)
B1–H1	1.37(4) 1.41(4)	H1–Rh1–B1	40.0(14) 42.1(17)
Rh1–H1	1.48(4) 1.48(4)		

The extended packing of **16** consists of chains of cations assembled in rows, with anions interspersed between the cations such that each anion is surrounded by an octahedral arrangement of cations. The torsion angle between the P1–O1···O2–P2 bonds of PONOP in complexes A and B were calculated to be 1.88(12) ° and

17.50(11) °, respectively. The enhanced deformation of the pincer ligand in complex B in combination with the smaller N1–Rh1–B1 angle (155.27(10) °) emulates the geometry observed in the high pressure phase of [Rh(PONOP)(η^2-HBcat)][$BAr^F{}_4$]. This distortion can be attributed, in part, to close contacts observed between the HBpin ligand of complex B and a 1,2-$C_6H_4F_2$ solvent molecule (Fig. 4.3; circled in red). Complex A does not experience the same interaction with the solvent molecule.

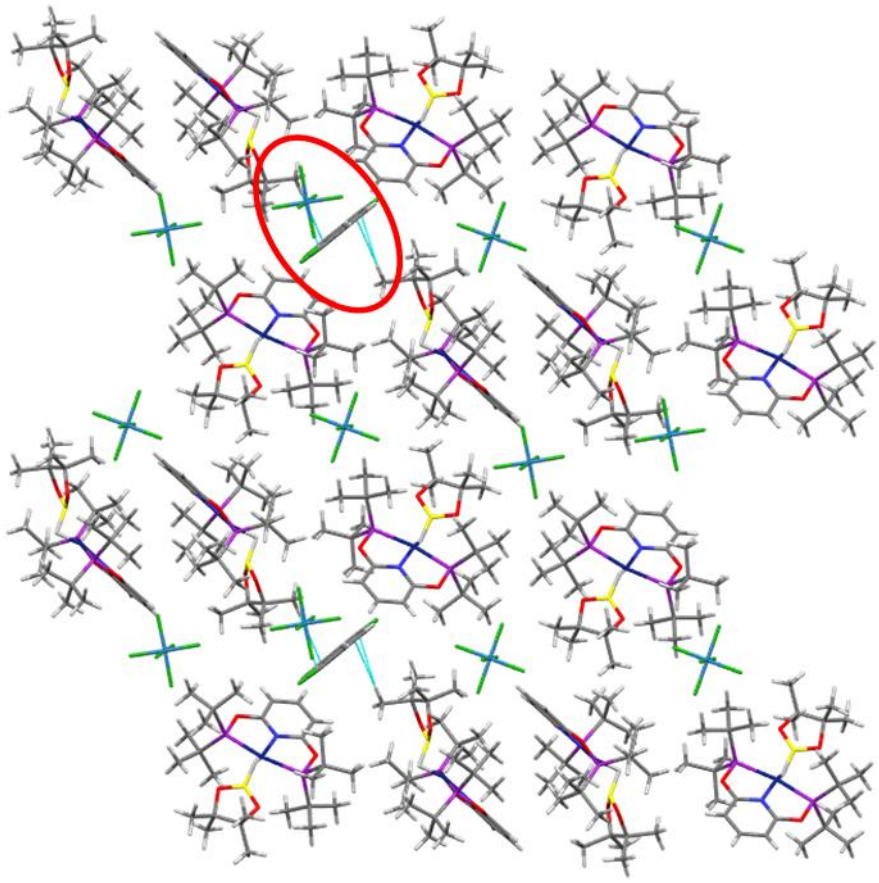

Figure 4.3 – The extended packing observed in **16**. The close contacts calculated by *Mercury*[26] between complex B and the 1,2-$C_6H_4F_2$ solvent molecule are depicted by cyan lines (circled in red).

The lack of notable close contacts surrounding the two unique cations suggests that the structure is held together predominantly by dipole-induced dipole interactions, courtesy of the fluorine-rich anions (Fig. 4.3). The low symmetry of the crystal system and the large number of atoms in the asymmetric unit (Z' = 2) makes **16** an unsuitable candidate for HP-XRD studies.

4.3.2 – Crystal structure of [Rh(PNP)(η^2-HBpin)][SbF$_6$], 18

Complex **18** crystallised in the monoclinic space group $P2_1/c$ (a = 12.7624(2) Å, b = 16.8181(3) Å, c = 17.3698(2) Å, β = 91.416(1) °, V = 3727.33(10) Å^3). A distorted square planar geometry (P1–Rh1–P2 ∠ = 164.55(3) °; N1-Rh1-B1 = 160.77(1) °) is adopted by **18**; the cation is structurally similar to the $[BAr^F{}_4]^-$ analogue **14** (Fig. 4.4, Table 4.3). The twist angle between the mean molecular planes of the HBpin (as defined by the O1–B1–O2 atoms) and the pincer ligand (as defined by the P1, Rh1, P2 and N1 atoms) was calculated to be *ca*. 40.3 ° in *Mercury*.[26]

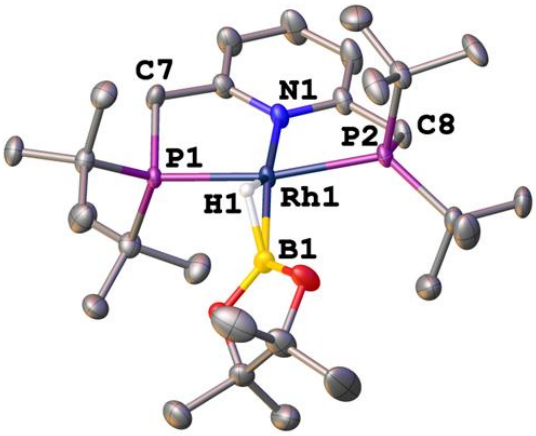

Figure 4.4 – A partially labelled structure of **18**. Atomic displacement parameters are drawn at 50 % probability and all hydrogen atoms, except for the HBcat hydrogen, are omitted for clarity.

Table 4.3 – Table of selected bond lengths and bond angles for **18**.

Atoms	Bond length / Å	Atoms	Bond angle / °
Rh1–N1	2.129(2)	P1–Rh1–P2	164.55(3)
Rh1–P1	2.3038(7)	N1–Rh1–B1	160.77(12)
Rh1–P2	2.3368(7)	Rh1–B1–H1	45(2)
Rh1–B1	2.088(3)	B1–H1–Rh1	91(3)
B1–H1	1.45(5)	H1–Rh1–B1	44(2)
Rh1–H1	1.47(5)		

The N1–Rh1–B1 bond angle of 160.77(12) ° and the B–H bond length of 1.45(5) Å support the assignment of **18** as a classical σ-borane complex, since these values are

in line with those reported for **14** (chapter 3). The hydrogen atom H1 was located using the electron density difference map and refined freely, but its location is unreliable due to the general noise of the models' background (largest peak = 0.81 e/Å^3; largest hole = –1.36 e/Å^3). The PNP ligand adopts a C_2 conformation, resulting in the twisting of the –$CH_2P^tBu_2$ moieties away from one another (P1–C7···C8–P2 torsion angle = 42.84(16) °). This helical conformation is commonly observed in PNP complexes.[27,28]

The extended packing in **18** consists of an alternating staggered arrangement of cations and anions (Fig. 4.5). Examination of the Hirschfeld surface[29] of a cation indicated that no close contacts were present in the structure at ambient pressure (Fig. 4.5). Whilst the smaller $[Sb^F{}_6]^-$ anion was less disordered than $[BAr^F{}_4]^-$, fewer close contacts near the borane ligand were observed in comparison to the $[BAr^F{}_4]^-$ analogue **14**, suggesting that greater pressures might be required in order to facilitate pressure-induced B–H bond activation. Furthermore, **18** crystallised unreliably, meaning that if **18** was studied further using HP-XRD, there would be limited sample available.

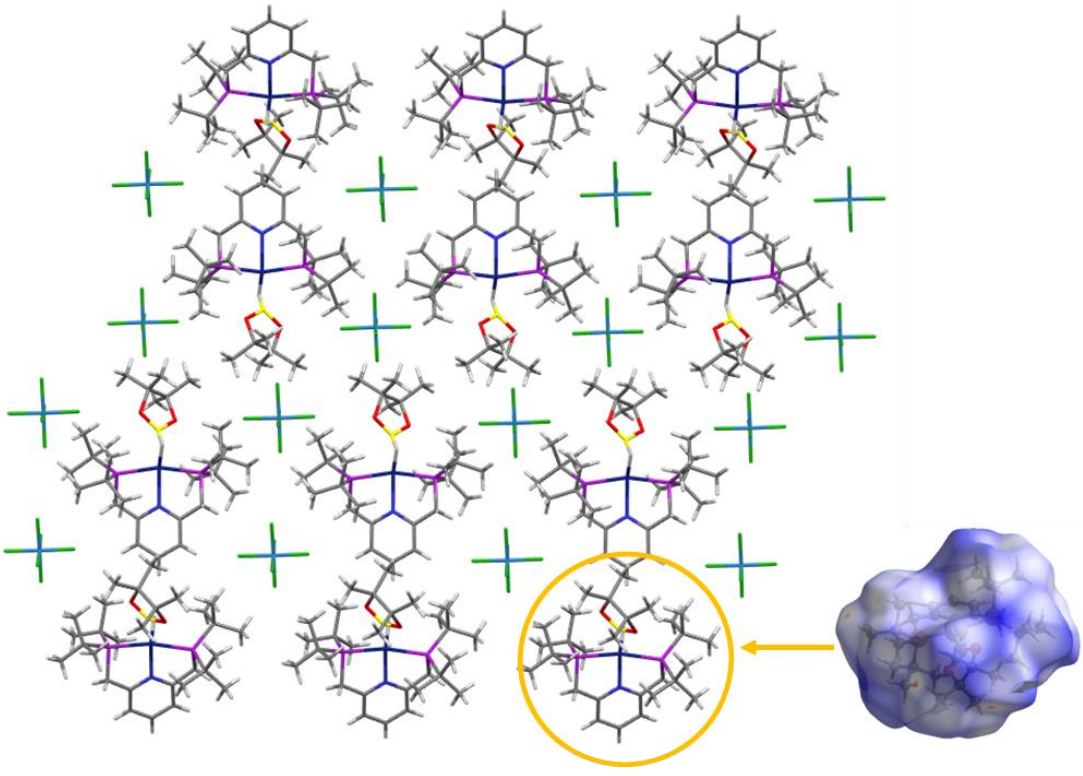

Figure 4.5 –The extended packing of **18**, accompanied by the calculated Hirshfeld surface of the cation.

4.3.3 – Crystal structure of [Rh(PNP)(HBcat)][SbF_6], 19

Remarkably, complex **19** crystallises as a co-crystal comprised of two distinct complexes with different oxidation states. The first unique complex within the crystal structure is the rhodium(I) σ-borane complex [Rh(PNP)(η^2-HBcat)][SbF_6], **19a**,[xix] and the second is the rhodium(III) OA adduct [Rh(PNP)(H)(Bcat)][SbF_6], **19b**. Co-crystal **19** crystallises in the orthorhombic space group $P2_12_12_1$ (a = 12.9296(1) Å, b = 17.8215(2) Å, c = 31.0623(3) Å, V = 7157.53(12) Å^3). The rhodium(I) complex **19a** adopts a distorted square planar geometry as a consequence of the pincer ligand coordination geometry (P1–Rh1–P2 ∠ = 165.54(6) °). The cation of **19a** is structurally similar to the [BAr^F_4]$^-$ analogue **15** (Fig. 4.6, Table 4.4). The twist angle between the molecular planes of the HBcat (as defined by the non-hydrogen atoms) and pincer ligand (as defined by the P1, Rh1, P2 and N1 atoms) was calculated to be *ca*. 39.8 ° by *Mercury*.[26]

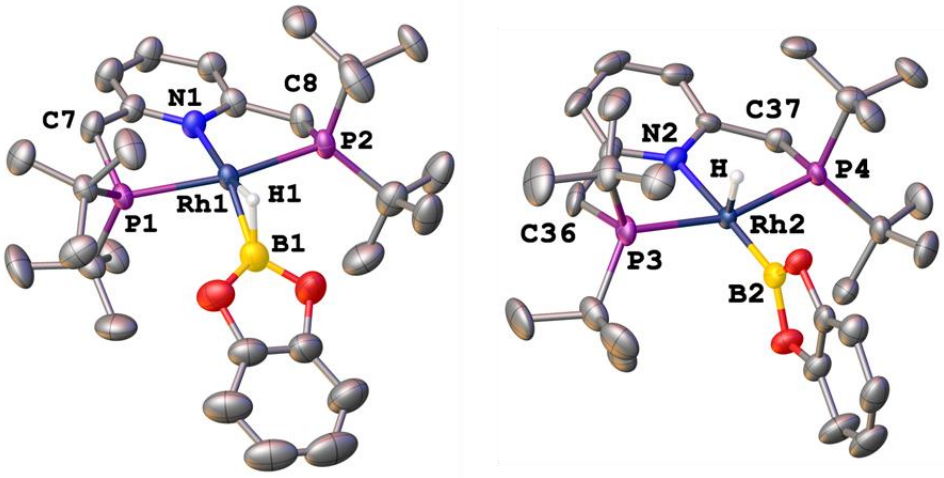

Figure 4.6 – Partially labelled structures of **19a** (left) and **19b** (right). Atomic displacement parameters are drawn at 50 % probability and all hydrogen atoms, except for the HBcat hydrogens of interest, are omitted for clarity.

[xix] '**19a**' and '**19b**' refer to the two crystallographically unique complexes in the crystal structure.

Table 4.4 – Table of selected bond lengths and bond angles for **19a** (top values) and **19b** (bottom values)**.** Hyphens correspond to values that are not applicable.

Atoms	Bond length / Å	Atoms	Bond angle / °
Rh1–N1 Rh2–N2	2.112(6) 2.167(5)	P1–Rh1–P2 P3–Rh2–P4	165.54(6) 162.76(7)
Rh1–P1 Rh2–P3	2.3270(16) 2.3072(15)	N1–Rh1–B1 N2–Rh2–B2	156.8(3) 177.6(3)
Rh1–P2 Rh2–P4	2.3338(16) 2.3085(15)	Rh1–B1–H1	58(3) -
Rh1–B1 Rh2–B2	2.053(9) 2.012(8)	B1–H1–Rh1	82(3) -
B1–H1	1.33(6) -	H1–Rh1–B1	40(2) -
Rh1–H1 Rh2–H	1.76(6) 1.42(7)		

Complex **19a** is best described as an elongated σ-borane complex, as evidenced by the N1–Rh1–B1 bond angle of 156.8(3) °, which is reminiscent of the related analogue **15**. Despite the short B–H bond length of only 1.33(6) Å, **19a** is assigned as an elongated σ-borane complex due to the reactivity presented herein. Whilst B–H bond lengths of greater than 1.5 Å are certainly characteristic of many elongated σ-borane complexes, it is not an absolute requirement to be assigned as such, merely a structural indicator (*c.f.* Table 3.2, chapter 3). Other examples of elongated σ-borane complexes containing shorter B–H bond lengths include OsH(η^2-HBcat)(η^3-H_2Bcat)(P^iPr_3)$_2$, **A99** (1.39(3) Å),[30] and Ir(POCOP)(η^2-HBpin), **A121** (1.47(6) Å).[31,xx] Both hydrogen atoms H and H1 were located using the electron density difference map and refined freely, but their locations are unreliable due to the general noise of the models' background (largest peak = 1.15 e/Å^3; largest hole = –1.25 e/Å^3). The background noise of this refinement is higher than most other structures presented within, so the location of the hydrogen atoms in this case are particularly unreliable.

The rhodium(III) complex **19b** adopts a distorted square-based pyramidal geometry (P1–Rh1–P2 ∠ = 162.76(7) °), with the hydride ligand coordinating in the axial

[xx] Bond lengths determined by single crystal XRD.

position and the Bcat ligand in the equatorial site *trans* to the pincer ligand (Fig. 4.6, Table 4.4). The distortion of **19b** can be mainly attributed to the pincer bite angle since coordination of the Bcat ligand is characterised by the near-linear N2–Rh2–B2 angle of 177.6(3) ° (Table 4.4). The molecular plane of the Bcat ligand is almost perfectly orthogonal to the pincer ligand, as defined by the py ring plane (*ca*. 88.9 ° calculated by *Mercury*).[26]

The different oxidation states of **19a** and **19b** are reflected in their metal-ligand bond lengths (Table 4.4). Despite being the higher oxidation state of the metal, **19b** exhibits a longer Rh–N bond than **19a** (2.167(6) Å and 2.113(6) Å, respectively) due to the greater *trans* influence of the monoanionic Bcat ligand. This is further supported by the contracted Rh–B bond length of **19b** (2.012(8) Å; **19a**: 2.053(9) Å). Shorter Rh–P bond lengths in **19b** (*ca.* 0.02 Å shorter than **19a**) also reflect the higher oxidation state (Table 4.4).

Notably, the conformations of the PNP ligand differ between the two complexes (Fig. 4.7). A C_2 conformation is adopted by **19a** (P1–C8···C7–P2 torsion angle = 38.7(4) °), whereas a symmetrical C_s conformation is adopted by **19b** (P1–C8···C7–P2 torsion angle = 0.7(3) °). The different conformations are reflected in the bite angles presented in Table 4.4 (**19a**: 165.54(6) °; **19b**: 162.76(7) °). Sterics could also contribute towards the different pincer conformations adopted by the complexes - since the Bcat ligand is firmly 'sandwiched' between the flanking ^{t}Bu substituents in **19b**, a greater steric influence is likely exerted on the ^{t}Bu groups, resulting in a yawing of the phosphine substituents and a contraction in the bite angle.

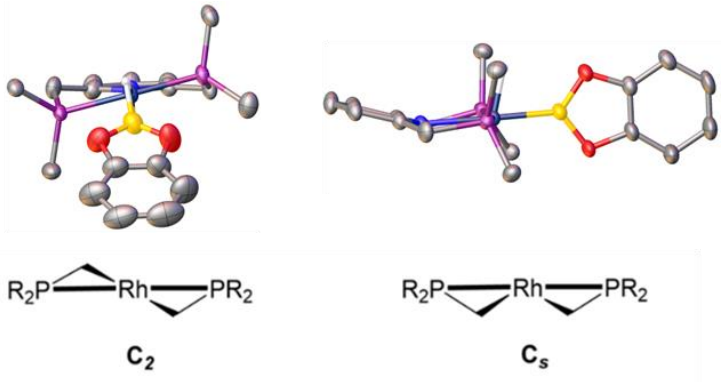

Figure 4.7 – A comparison of the pincer conformations adopted by **19a** (left) and **19b** (right). Atomic displacement parameters are drawn at 50 % probability. Hydrogen atoms (except for H and H1) and the ^{t}Bu groups are omitted for clarity.

The extended packing in **19** was comprised of alternating pairs of rhodium(I) and rhodium(III) cations which assemble into chains (Fig. 4.8; horizontal rows). Between these cationic chains, rows of anions are also interspersed. Identical cationic chains pack together in matching pairs, such that the vertical columns alternate between the complexes **19a** and **19b** every two sites (Fig. 4.8; Key). The origin of the formation of the rhodium(III) complex **19b** in the solid-state can be, to some extent, explained by the presence of prevalent short contacts between the F1···Rh2 (2.905(5) Å) and F1···N2 (2.905(5) Å) atoms, which are 0.57 Å and 0.17 Å shorter than the Van der Waals radii of the atoms involved, respectively, as calculated by *Mercury*[26] (Fig. 4.9).

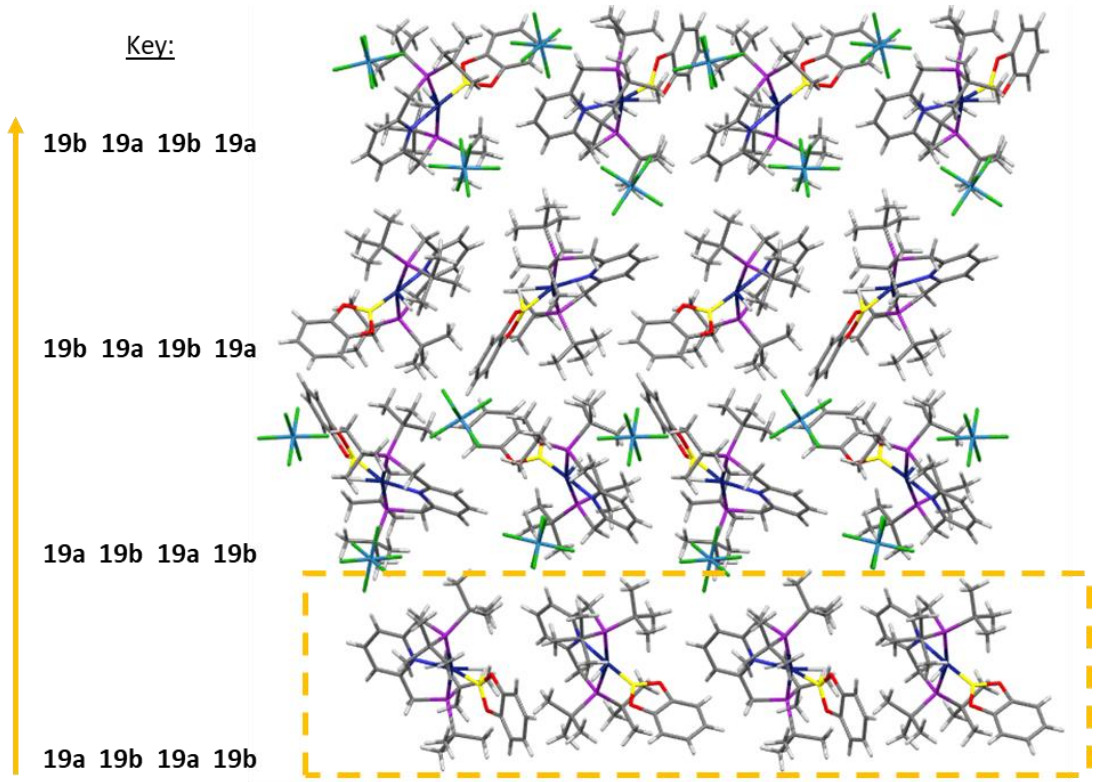

Figure 4.8 – The extended packing observed in **19**, accompanied by a key.

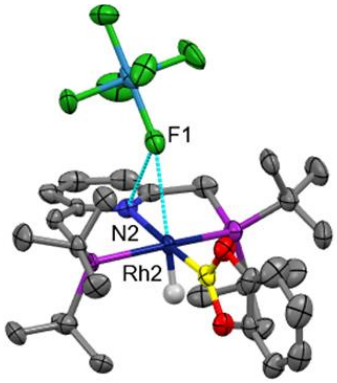

Figure 4.9 – The short contacts (cyan lines) observed between the cation of **19b** and the anion. All hydrogen atoms, except for the metal hydride, are omitted for clarity.

The presence of the OA adduct at only one of the two crystallographically independent sites suggests that the activation energies of the two independent complexes in the structure might be different; similar observations were previously made by Ozerov and co-workers during their investigation of C–N bond OA to a rhodium pincer complex.[32] However, VT-NMR experiments (discussed in section 4.4.3) suggest that this proposal does not correctly describe the behaviour exhibited by these systems. Despite the large number of atoms present in co-crystal **19**, the accessibility of the rhodium(III) oxidation state (**19b**) under ambient conditions suggests that OA may also be achievable under non-ambient conditions (*i.e.*, with pressure) at the other unique site (**19a**) if the energetic barrier is small enough.

4.3.4 – Crystal structure of [Rh(PONOP)(η^2-HBpin)][BAr$^{F20}{}_4$], 20

Complex **20** crystallises in the orthorhombic space group $Pca2_1$ (a = 20.5241(1) Å, b = 14.2767(1) Å, c = 37.7165(2) Å, V = 11051.55(11) Å^3, Z' = 2). The cations of the two crystallographically unique complexes (A and B, respectively) are structurally similar not only to each other, but to the [Rh(PONOP)(η^2-HBpin)]$^+$ analogues **12** and **16** (Fig. 4.10, Table 4.5). The twist angles between the mean molecular planes of the HBpin ligands (as defined by the O3–B1–O4 atoms) and the pincer ligands (as defined by the P1, O1, Rh1, N1, O2 and P2 atoms) were calculated to be *ca*. 31.3 ° and 30.5 ° using *Mercury*[26] for complexes A and B, respectively. The P1–O1···O2–P2 torsion angles for complexes A and B were also similar (0.2(5) ° and 2.8(5) °, respectively).

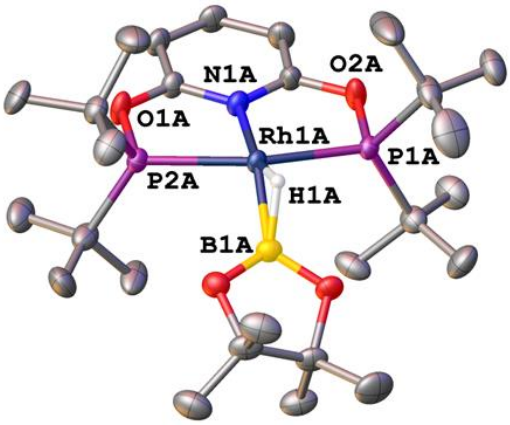

Figure 4.10 – A partially labelled structure of complex A in **20**. Atomic displacement parameters are drawn at 50 % probability. The counterion and all hydrogen atoms, except for the HBpin hydrogen, are omitted for clarity.

Table 4.5 – Selected bond lengths and bond angles for complexes A (top values) and B (bottom values) in **20**.

Atoms	Bond length / Å	Atoms	Bond angle / °
Rh1–N1	2.060(8) 2.053(8)	P1–Rh1–P2	161.67(10) 161.09(9)
Rh1–P1	2.288(4) 2.302(2)	N1–Rh1–B1	158.8(4) 158.3(4)
Rh1–P2	2.301(3) 2.314(4)	Rh1–B1–H1	43(5) 43(5)
Rh1–B1	2.112(12) 2.131(12)	B1–H1–Rh1	98(7) 95(7)
B1–H1	1.34(10) 1.43(12)	H1–Rh1–B1	39(4) 42(5)
Rh1–H1	1.45(11) 1.46(12)		

Both of the crystallographically distinct complexes are best described as classical σ-borane complexes because their B–H bond lengths (1.34(10) Å and 1.43(12) Å, respectively) lie with the range of the other classical σ-borane complexes reported herein (see chapters 3 & 4). The hydrogen atoms H1A and H1B were located using the electron density difference map and refined freely, but their locations are unreliable

due to the general noise of the models' background (largest peak = 0.48 e/Å^3; largest hole = -1.11 e/Å^3). The difference in their B–H bond lengths cannot, therefore, be reliably determined.

The extended packing in **20** consists of alternating layers of cations and anions, such that a 3-dimensional 'checkerboard' arrangement is adopted (Fig. 4.11). The result of this is that each cation is surrounded by an octahedral arrangement of anions and vice versa. The cations can be seen to pack together in a pseudo-herringbone arrangement (Fig. 4.11). The Hirschfeld surface of Complex A (Fig. 4.11) indicates that the close contacts between the $[BAr^{F20}{}_4]^-$ anion and the bulky ^{t}Bu groups of the pincer ligand (circled in orange) are more prevalent that those between the HBpin ligand and the cleft created by the Ar^{F20} substituents of the anion (circled in burgundy). This is likely a consequence of the steric demands of the bulky ^{t}Bu groups. Although compression of **20** might facilitate the evolution of closer contacts between the anion and the borane so as to enable OA, the large number of atoms present in **20** (Z' = 2) would negatively impact the data-to-parameter ratio. Therefore, **20** is an unsuitable candidate for investigation by HP-XRD.

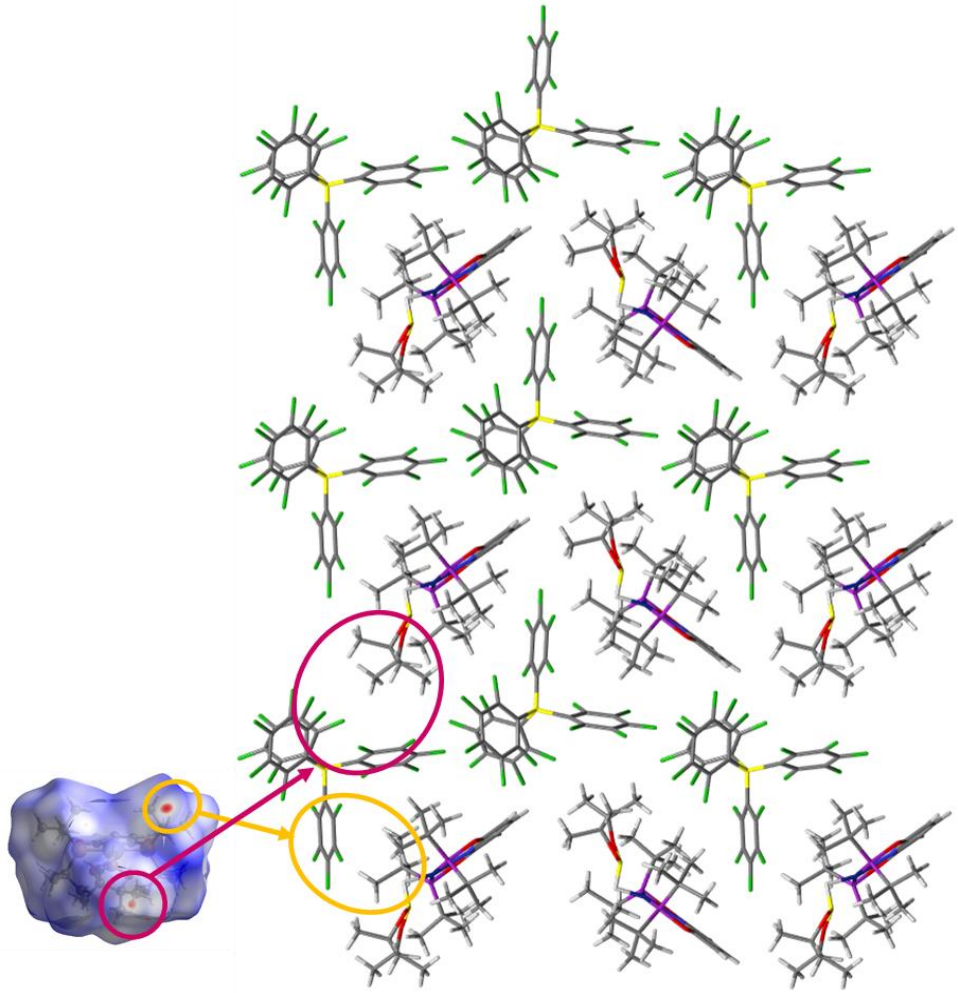

Figure 4.11 – The crystal packing observed in **20**, as viewed down the *c* axis, with the Hirshfeld surface of cation A.

4.3.5 – Crystal structure of [Rh(PNP)(η^2-HBpin)][BAr$^{F20}{}_4$], 22

Complex **22** crystallises in the monoclinic space group $P\bar{1}$ (a = 11.7094(2) Å, b = 14.2312(2) Å, c = 17.4132(2) Å, α = 104.046(1) °, β = 99.239(1) °, γ = 91.173(1) °, V = 2773.08(7) Å^3) and is as a distorted square planar species (P1–Rh1–P2 ∠ = 166.558(16) °) that is structurally similar to the analogues **14** and **18** (Fig. 4.12, Table 4.6). The HBpin ligand is disordered over two sites which are related to one another by rotation about the mean molecular plane of the borane (*c.f.* chapter 6). The twist angle between the mean molecular plane of the major disordered component of the HBpin ligand (defined by the O1–B1–O2 atoms) and the pincer ligand plane (defined by the P1, Rh1, P2 and N1 atoms) was calculated to be *ca*. 43.5 ° using *Mercury*.[26] Complex **22** is assigned as a classical σ-borane complex, since the B–H bond length

of 1.44(2) Å is similar to the B–H bond lengths reported for the related [Rh(PNP)(η^2-HBpin)]$^+$ analogues **14** (1.40(3) Å) and **18** (1.45(5) Å). The hydrogen atom H1 was located using the electron density difference map and refined freely, but its location is somewhat unreliable due to the general noise of the models' background (largest peak = 0.32 e/Å^3; largest hole = –0.36 e/Å^3).

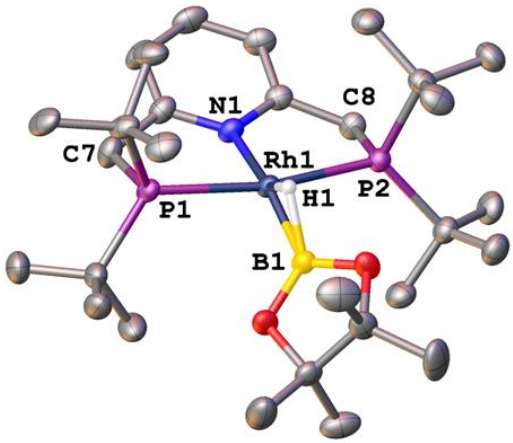

Figure 4.12 – A partially labelled structure of **22**. Atomic displacement parameters are drawn at 50 % probability. The counterion and all hydrogen atoms, except for the HBpin hydrogen, are omitted for clarity. Only one disorder component is shown.

Table 4.6 – A table of selected bond lengths and bond angles associated with **22**.

Atoms	Bond length / Å	Atoms	Bond angle / °
Rh1–N1	2.1371(11)	P1–Rh1–P2	166.558(16)
Rh1–P1	2.3283(4)	N1–Rh1–B1	165.58(5)
Rh1–P2	2.3328(4)	Rh1–B1–H1	44.5(8)
Rh1–B1	2.0836(15)	B1–H1–Rh1	91.6(11)
B1–H1	1.44(2)	H1–Rh1–B1	43.9(8)
Rh1–H1	1.46(2)		

Notably, the PNP ligand adopts a C_s conformation (P1–C7···C8–P2 torsion angle = 3.67(7) °), resulting in a symmetrical gull-wing appearance (Fig. 4.13). Whilst PNP can readily adopt both C_2 and C_s conformations due to the flexibility of the

sp^3-hybridised CH_2 linkers, the C_s conformation is less common.[25,28] All other $\{Rh^I(PNP)\}^+$ complexes presented herein adopted C_2 conformations, except for **22**. The C_s conformation was only otherwise observed in the rhodium(III) boryl hydride complexes **19b** and **23** (*vide infra*).

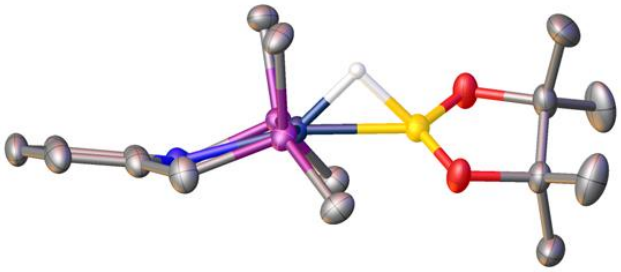

Figure 4.13 – Structure of the cation of **22** viewed along the plane of the pincer ligand. The terminal ^{t}Bu groups and all hydrogen atoms except for H1 are omitted for clarity.

The extended packing in **22** consists of alternating chains of cations and anions (Fig. 4.14; horizontal rows) which packing together vertically in pairs. The $[BAr^{F20}{}_4]^-$ anions appear to assemble into layers due to favourable dipole-induced aromatic interactions between neighbouring Ar^{F20} groups, which are assisted by the abundance of electronegative fluorine atoms in the anion.[23] The anions interact with each other through a 'phenyl embrace' (Fig. 4.14; cyan lines) which is comprised of a displaced face-to-face interaction (3.070(1) Å) and two symmetry related edge-to-face interactions (3.134(2) Å). The centroid-to-centroid distance between the face-on rings is 4.348(2) Å. Because the centroid-to centroid distance between the Ar^{F20} rings in **22** is greater than 4.0 Å (the typical threshold distance that defines a π-π interaction),[xxi] this interaction is not a formal π-π interaction.[33,34] It has also been noted in the literature that edge-to-face interactions commonly form between fluorine-rich aromatics due to the electrostatic attractions between electron-rich fluorine substituents and comparatively electron-poor ring centroids.[23] Merz Jr. and co-workers previously reported that, for simple aromatics, the more fluorine

[xxi] The definition and thresholds of a π-π interaction is discussed in greater detail in section 4.7.4

substituents an aromatic ring possessed, the shorter the edge-to-face interactions were.[35]

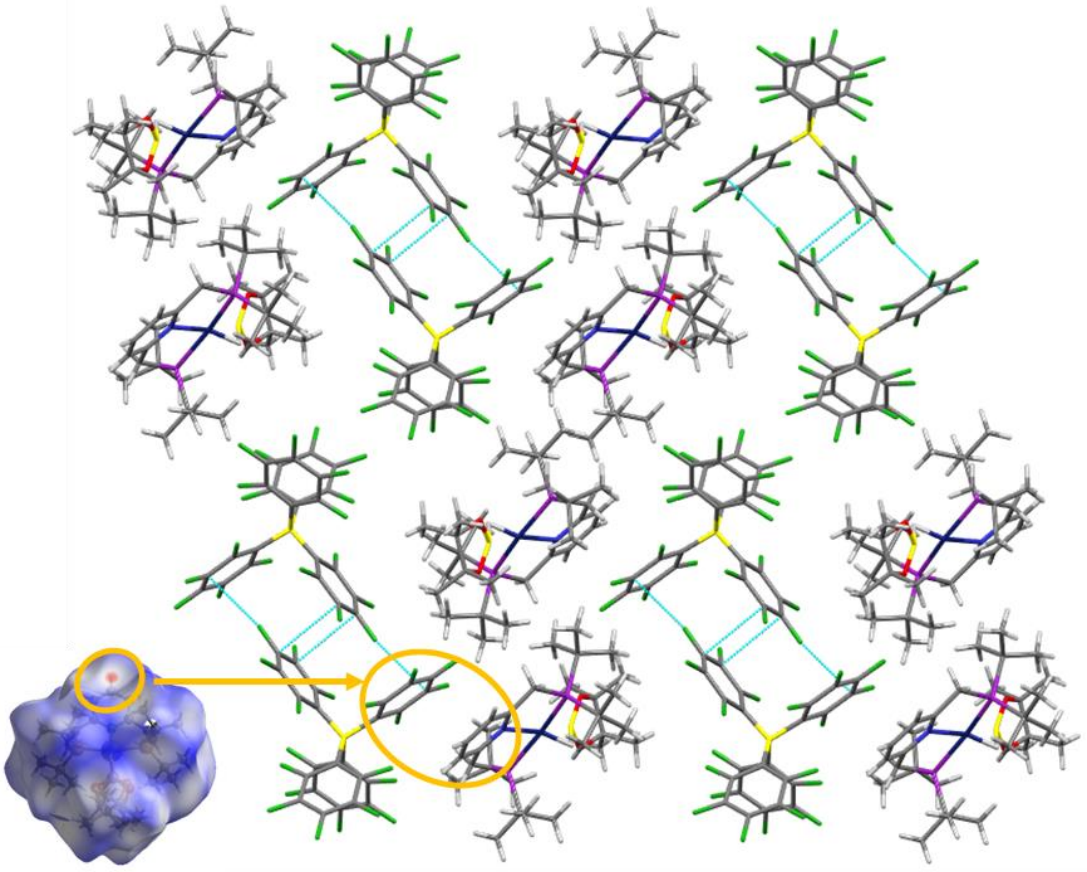

Figure 4.14 – The extended packing observed in **22** and the calculated Hirshfeld surface of the cation. The phenyl embrace is depicted by cyan lines.

Whilst no notable close contacts are present on the Hirschfeld surface of the cation around the borane ligand at ambient pressure, a π-π interaction (centroid-to-centroid distance = 3.815(2) Å, interplanar distance = 3.347(2) Å) exists between the py ring of the pincer ligand and a neighbouring anion (Fig. 4.14, circled in orange). The C_s conformation adopted by the PNP ligand might be stabilised in the solid-state by this secondary interaction. The C_s conformation could potentially be a structural indicator that the complex is on the precipice of OA, since this conformation is only otherwise observed in the rhodium(III) boryl hydride complexes **19b** and **23** (*vide infra*). Therefore, **22** was determined to be a potential candidate for further study by HP-XRD.

4.3.6 – Crystal structure of [Rh(PNP)(H)(Bcat)][BAr$^{F20}_4$], 23

Complex **23** crystallised in the monoclinic space group $P\bar{1}$ (a = 11.6375(2) Å, b = 14.3262(2) Å, c = 17.0942(2) Å, α = 78.270(1) °, β = 81.446(1) °, γ = 88.973(1) °, V = 2759.18(7) Å^3) and was found to crystallise as the rhodium(III) boryl hydride adduct [Rh(PNP)(H)(Bcat)][BAr$^{F20}_4$]. The cation adopts a distorted square-based pyramidal geometry, with the Bcat ligand coordinating in the fourth equatorial coordination site and the metal hydride coordinating in the axial site (Fig. 4.15). The molecular plane of the Bcat ligand is orthogonal to the coordination plane of the pincer ligand and is reinforced by the steric demands of the flanking ^{t}Bu substituents of the PNP ligand (Fig. 4.15). The hydrogen atom H1 was located using the electron density difference map and refined freely, but its location is unreliable due to the general noise of the models' background (largest peak = 0.60 e/Å^3; largest hole = –1.18 e/Å^3).

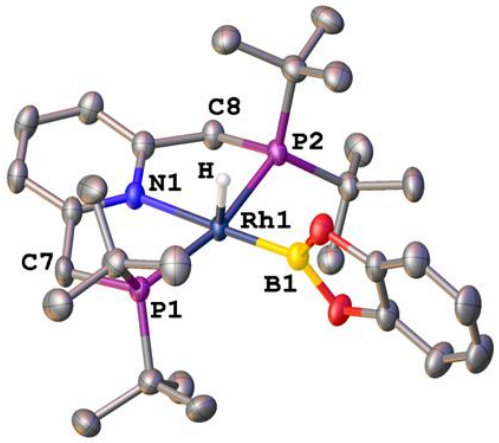

Figure 4.15 – A partially labelled structure of **23**. Atomic displacement parameters are drawn at 50 % probability. The counterion and all hydrogen atoms, except for the metal hydride, are omitted for clarity.

Table 4.7 – A table of selected bond lengths and bond angles associated with **23**.

Atoms	Bond length / Å	Atoms	Bond angle / °
Rh1–N1	2.1715(15)	P1–Rh1–P2	166.317(16)
Rh1–P1	2.3131(5)	N1–Rh1–B1	178.93(7)
Rh1–P2	2.3103(5)		
Rh1–B1	2.000(2)		
Rh1–H1	1.51(3)		

The rhodium(III) oxidation state is confirmed by the almost linear N1–Rh1–B1 bond angle (178.93(7) °) and the contracted Rh–P bond lengths (2.3103(5)-2.3131(5) Å; Table 4.7) relative to the [Rh(PNP)(η^2-HBcat)]$^+$ analogues **14** (2.328(5)-2.334(4) Å) and **19a** (2.3270(16)-2.3338(16) Å). The Rh1–N1 bond length (2.1705(15) Å) is also marginally longer than the rhodium(I) analogues (**14**: 2.127(2) Å; **19a**: 2.112(6) Å) as a result of the greater *trans* influence of the monoanionic Bcat ligand (Table 4.7). The PNP ligand adopts a slightly distorted C_s conformation (P1–C7···C8–P2 torsion angle = 5.84(9) °), as was similarly observed in **19b** and **22** (Fig. 4.16).

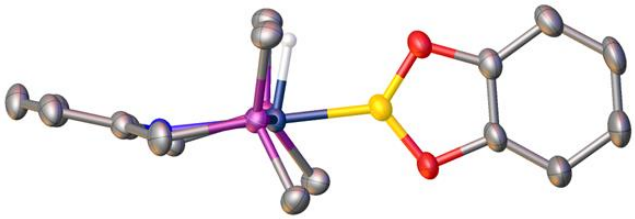

Figure 4.16 – Structure of the cation of **23** as viewed along the plane of the pincer ligand. The terminal ^{t}Bu groups and all hydrogen atoms except for the metal hydride are omitted for clarity.

The extended packing in **23** is comprised of alternating chains of cations and anions (Fig. 4.17; vertical columns). The [BAr$^{F20}{}_4$]$^-$ anions appear to assemble into layers through favourable dipole interactions. Sites 1 and 2 in Fig. 4.17 depict two different aromatic interactions. The former is between the Bcat ligand and an Ar^{F20} group (centroid-to-centroid distance = 4.382(3) Å) and the latter is between the py ring of the pincer ligand and an Ar^{F20} group (centroid-to-centroid distance = 3.926(3) Å). Furthermore, a prominent close contact is visible upon examination of the Hirshfeld surface of the cation between the edge of the Bcat ligand and the fluorine substituent of a neighbouring anion. This suggests that the favourable secondary interactions observed in **23** contribute to stabilising the rhodium(III) OA adduct in the solid-state (see section 4.4.3).

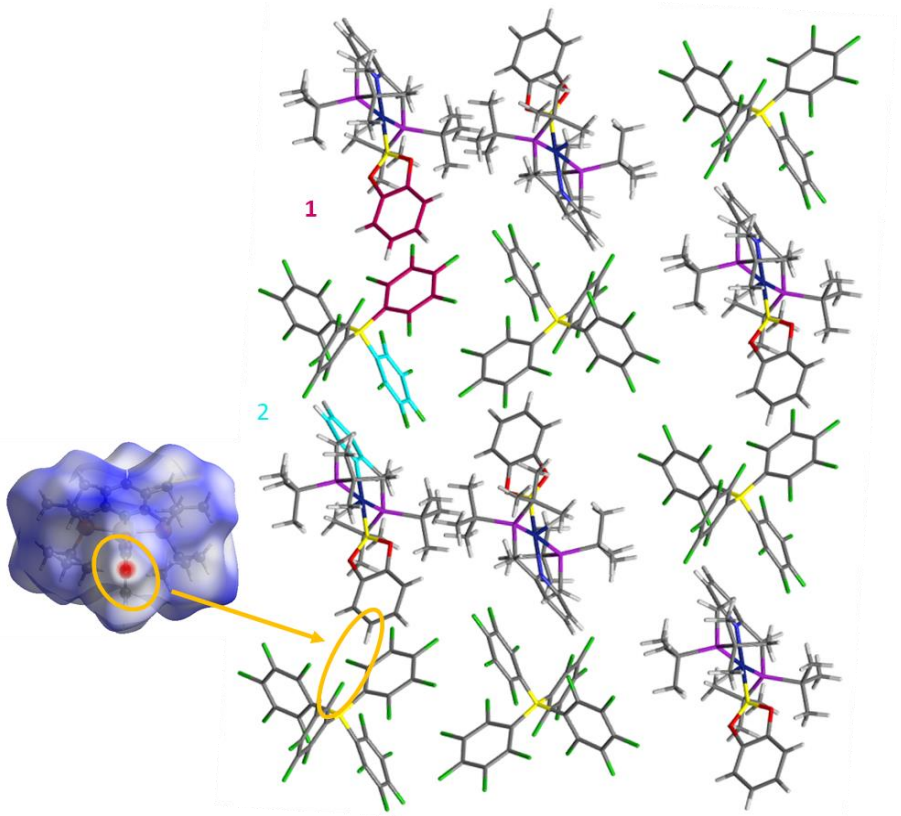

Figure 4.17 – The extended packing observed in **23**. Sites 1 and 2 depict different aromatic interactions in burgundy and cyan, respectively. The Hirshfeld surface of the cation is supplied for reference.

4.4 – Comparison of the σ-borane complexes

A total of ten out of the twelve σ-borane complexes were isolated – unfortunately, the $[BAr^{F20}{}_4]^-$ and $[SbF_6]^-$ analogues of $[Rh(PONOP)(\eta^2\text{-HBcat})]^+$ precipitated out as oils, so could not be studied further. The average exposure times for each standard collection with Cu Kα radiation at 150 K were shortened from *ca*. 10 s (low angle) for the $[BAr^F{}_4]^-$ analogues down to *ca*. 1-4 s (low angle) for the $[BAr^{F20}{}_4]^-$ and $[SbF_6]^-$ analogues. This was thought to be advantageous for subsequent HP-XRD studies, since exposure times for high pressure collections tend to be significantly longer than for standard collections.

Table 4.8 – A table of crystallographic information and refinement statistics for **12-16**, **18-20**, **22** and **23**.

	$[BAr^F_4]^-$				$[SbF_6]^-$			$[BAr^{F20}_4]^-$		
	PONOP		**PNP**		**PONOP**	**PNP**		**PONOP**	**PNP**	
	HBpin	**HBcat**	**HBpin**	**HBcat**	**HBpin**		**HBcat**	**HBpin**		**HBcat**
Complex	**12**	**13**	**14**	**15**	**16**	**18**	**19**	**20**	**22**	**23**
Space Group	$P2_1/n$	$P2_1/c$	$P2_1/n$	$P2_1/c$	$P\bar{1}$	$P2_1/c$	$P2_12_12_1$	$Pca2_1$	$P\bar{1}$	$P\bar{1}$
Crystal System	monoclinic	monoclinic	monoclinic	monoclinic	triclinic	monoclinic	orthorhombic	orthorhombic	triclinic	triclinic
***T* / K**	150	150	150	150	150	150	150	150	150	150
***a* / Å**	13.28940(9)	18.1285(2)	13.0589(1)	19.2532(4)	14.5639(2)	12.7624(2)	12.9296(1)	20.5241(1)	11.7094(2)	11.6375(2)
***b* / Å**	14.23474(10)	17.9092(2)	14.2536(1)	17.6224(3)	15.7044(2)	16.8191(3)	17.8215(2)	14.2767(1)	14.2312(2)	14.3262(2)
***c* / Å**	35.08633(17)	20.1931(2)	35.8756(4)	19.3155(3)	16.7452(3)	17.3698(2)	31.0623(3)	37.7165(2)	17.4132(2)	17.0942(2)
***α* / °**	90	90	90	90	95.625(1)	90	90	90	104.046(1)	78.270(1)
***β* / °**	92.9395(5)	92.314(1)	93.247(1)	98.960(2)	94.853(1)	91.416(1)	90	90	99.239(1)	81.446(1)
***γ* / °**	90	90	90	90	95.136(1)	90	90	90	91.173(1)	88.973(1)
***V* / Å^3**	6628.59(7)	6550.69(12)	6667.03(10)	6473.5(2)	3779.29(10)	3727.33(10)	7157.53(12)	11051.55(11)	2773.08(7)	2759.18(7)
Z'	1	1	1	1	2	1	1	2	1	1
***μ* / mm^{-1}**	3.55	3.59	3.50	3.61	10.57	10.63	11.07	4.06	4.02	4.04
Radiation	Cu Kα	Cu Kα	Cu Kα	Cu Kα	Cu Kα	Cu Kα	Cu Kα	Cu Kα	Cu Kα	Cu Kα
R_1 **($I \geq 2\sigma$)**	0.0341	0.0328	0.0410	0.0693	0.0287	0.0320	0.0380	0.0663	0.0207	0.0295
wR_2 **(all data)**	0.0828	0.0871	0.1067	0.2096	0.0716	0.0790	0.0993	0.1758	0.0530	0.0751
GooF	1.129	1.029	1.017	1.0380	1.031	1.033	1.050	1.038	1.022	1.025
R_{int}	0.0274	0.0431	0.0287	0.0458	0.0423	0.0341	0.0411	0.0549	0.0184	0.0285
Largest peak	0.43	0.39	1.47	1.33	0.90	0.81	1.16	0.48	0.32	0.60
Largest hole	-0.40	-0.78	-0.58	-1.02	-1.34	-1.36	-1.26	-1.11	-0.36	-1.18

Ambient pressure void space analysis of all ten crystal structures indicated that incorporation of $[BAr^{F20}{}_4]^-$ or $[SbF_6]^-$ anions into the structures resulted in more efficient packing in comparison to the $[BAr^F{}_4]^-$ analogues (Table 4.9). When the 'void volume per complex' is considered, it is clear that the $[SbF_6]^-$ complexes (**16**, **18** and **19**) contain the least void space (Table 4.9). However, with the exception of **19**, the crystal growth of the $[SbF_6]^-$ analogues are very unreliable, so are not the most suitable samples for HP-XRD studies. The $[BAr^{F20}{}_4]^-$ analogues (**20**, **22** and **23**) also contain less 'void volume per complex' than the $[BAr^F{}_4]^-$ analogues, indicating that the removal of the CF_3 groups from the counterion allowed for more efficient packing. However, as previously mentioned in chapter 3, *Mercury* does not account for disorder components when calculating void space, therefore, the 'void volume per complex' values supplied in Table 4.9 should be regarded loosely. A direct comparison of the packing efficiencies across the series is impossible for this reason.

Table 4.9 – Table of volume and void space values calculated using *Mercury*[26] for **18-24**, implementing a probe radius of 0.4 Å and a grid spacing of 0.2 Å.

Complex	V/Z / Å^3	Void volume per unit cell / Å^3	Void volume per complex / Å^3
12	1657	1547	387
13	1638	1674	418
14	1667	1464	366
15	1618	1728	432
16	945	947	237
18	933	929	232
19	895	1816	227
20	1381	2598	325
22	1387	617	309
23	1380	703	352

Nonetheless, the decrease in void volume upon substitution of $[BAr^F{}_4]^-$ with the two new counterions was a promising observation, as the easily accessible voids are more likely to be compressed out in the early stages of pressure generation. In the case of the $[SbF_6]^-$ systems, the voids are no longer 'trapped' inside the Ar^F cavities found the

$[BAr^{F}{}_4]^-$ analogues, making them potentially easier to remove upon compression. The perfluorinated rings in $[BAr^{F20}{}_4]^-$ improve the rigidity of the anion and the size of the cavities between adjacent substituents are smaller due to the abundance of the larger fluorine substituents.

4.4.1 – Assessment of the σ-borane coordination geometries

Substutution of $[BAr^{F}{}_4]^-$ with $[SbF_6]^-$ or $[BAr^{F20}{}_4]^-$ influenced the relative coordination geometry of the borane ligands to a minor extent (Fig. 4.18). The angles between the coordination planes of the borane and pincer ligands were similar across the series, varying by < 5 ° amongst analogues with a shared cation. The largest discrepancy in this twist angle was observed between **15** (*ca*. 50.26 °) and **19a** (*ca*. 39.77 °). The significant difference in coordination geometry is attributed to crystal packing effects, which are discussed in greater detail in section 4.4.3. M*ost* of the cations do not change significantly upon substitution of the non-coordinating anion. Small inconsistencies across the series can be, in part, attributed to crystal packing effects – secondary interactions likely influence the coordination geometries of the weakly bound and fluxional σ-borane substrates. Notably, the PNP backbone of **22** adopts a C_s confirmation, unlike all other structures depicted in Fig. 4.18, which adopt C_2 conformations. This conformational change has a negligible effect on the Rh–P bond lengths and the pincer bite angle, however, the slightly larger N1–Rh1–B1 angle (165.85(8) °) suggests that the coordination geometry of the borane ligand is sensitive to the pincer ligand.

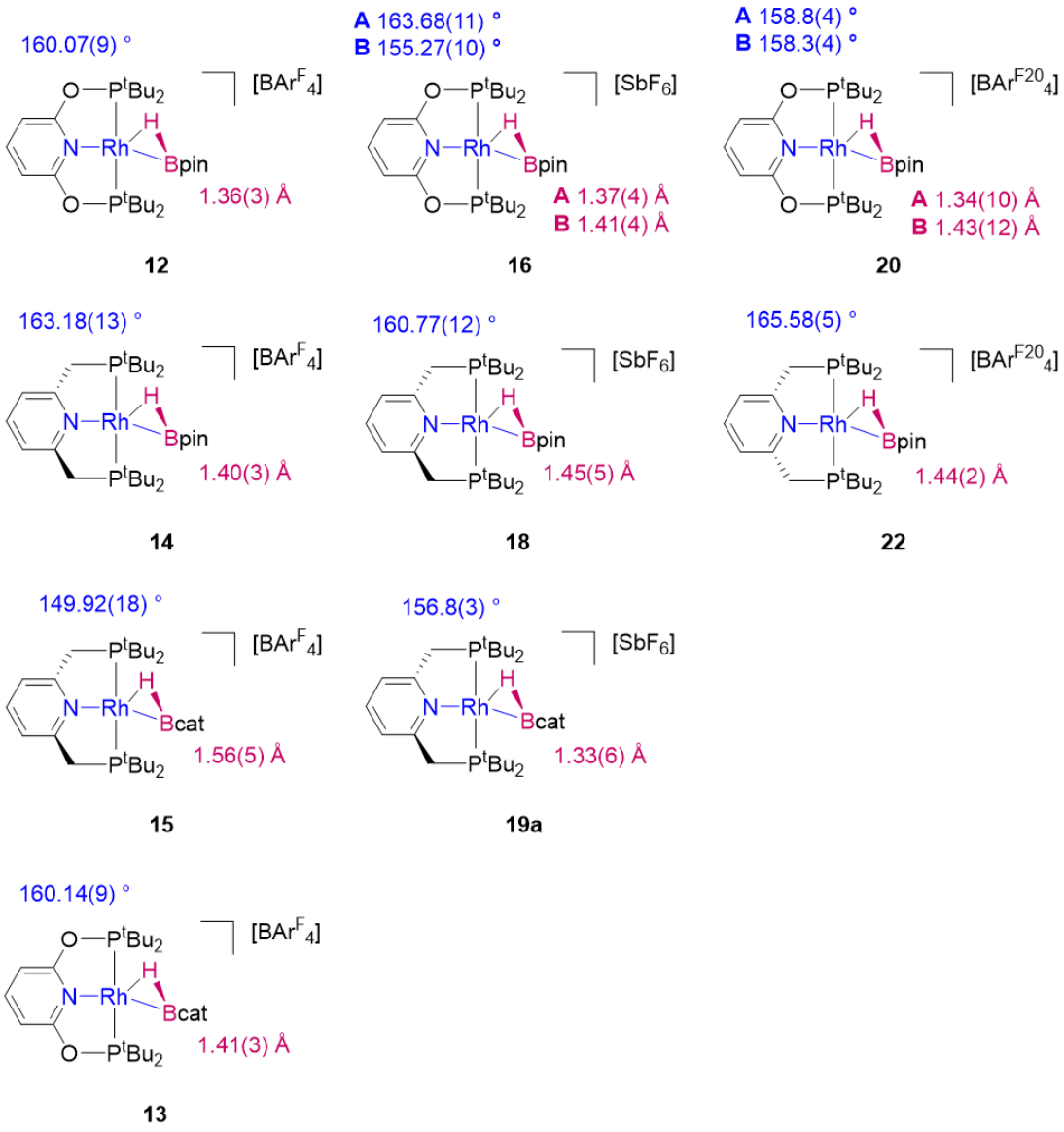

Figure 4.18 – Structures of the rhodium(I) adducts. The blue and burgundy values correspond to the N1–Rh1–B1 bond angles and B1–H1 bond lengths, respectively.

4.4.2 – General trends

The rhodium(I) PNP complexes are characterised by slightly elongated Rh1–N1 bond lengths in comparison to their PONOP counterparts (*ca.* 2.12 Å vs. *ca.* 2.05 Å, respectively) due to the different electronic properties of the linkers.[36] The crystal structures of **12-14**, **16**, **18**, **20** and **22** support the assignment of classical σ-borane coordination modes (B1–H1 = < 1.5 Å; N1–Rh1–B1 ∠ = *ca.* 160 °; Tables 4.10 & 4.11).[30,37]

Table 4.10 – Selected bond lengths reported for **12-16, 18-20**, **22** and **23**. Where two values are given, these correspond to the two crystallographically unique molecules A and B, respectively. The rhodium(III) complexes are denoted with asterisks.

Complex	Rh1–N1 / Å	Rh1–B1 / Å	Rh1–H1 / Å	B1–H1 / Å	Rh1–P1 / Å	Rh1–P2 / Å
12	2.0541(16)	2.111(3)	1.58(3)	1.36(3)	2.2957(5)	2.2978(5)
13	2.0528(16)	2.079(2)	1.49(3)	1.41(3)	2.2933(6)	2.2939(6)
14	2.127(2)	2.083(3)	1.49(3)	1.40(3)	2.3138(7)	2.3376(7)
15	2.114(10)	2.088(14)	1.56(10)	1.47(6)	2.328(5)	2.334(4)
16	2.057(2) 2.056(2)	2.120(3) 2.103(3)	1.48(4) 1.48(4)	1.37(4) 1.41(4)	2.2928(7) 2.2978(7)	2.2882(7) 2.3017(7)
18	2.129(2)	2.088(3)	1.47(5)	1.45(5)	2.3038(7)	2.3368(7)
19a **19b***	2.112(6) 2.167(5)*	2.053(9) 2.012(8)*	1.76(6) 1.42(7)*	1.33(6) -	2.3270(16) 2.3072(15)*	2.3338(16) 2.3085(15)*
20	2.060(8) 2.053(8)	2.112(12) 2.131(12)	1.45(11) 1.46(12)	1.34(10) 1.43(12)	2.288(4) 2.302(2)	2.301(3) 2.314(4)
22	2.1371(11)	2.0836(15)	1.46(2)	1.44(2)	2.3283(4)	2.3328(4)
23*	2.1715(15)*	2.000(2)*	1.51(3)*	-	2.3131(5)*	2.3103(5)*

Table 4.11 – Selected bond angles reported for **12**-**16, 18**-**20**, **22** and **23**. Where two values are given, these correspond to the two unique complexes – A and B, respectively – in the asymmetric unit. Asterisks denote the rhodium(III) complexes.

Complex	P1–Rh1–P2 / °	N1–Rh1–B1 / °
12	161.68(2)	160.07(9)
13	162.03(2)	160.14(9)
14	165.71(2)	163.18(13)
15	166.11(13)	156.0(6)
16	161.93(3) 161.69(3)	163.68(11) 155.27(10)
18	164.55(3)	160.77(12)
19a **19b***	165.54(6) 162.76(7)*	156.8(3) 177.6(3)*
20	161.67(10) 161.09(9)	158.8(4) 158.3(4)
22	166.558(16)	165.58(5)
23*	166.317(16)*	178.93(7)*

On the other hand, **15** and **19a** are assigned as elongated σ-borane complexes due to their smaller N1–Rh1–B1 bond angles (< 155 °), which are suggestive of enhanced metal-borane interactions (Tables 4.10 & 4.11; see chapter 3).[37] The marginally shorter Rh1–B1 bond length in **19a** (2.053(9) Å) compared to **15** (2.088(14) Å) is suggestive of a more prevalent metal $d \rightarrow$ 'empty' non-bonding boron orbital interaction, although the difference is statistically insignificant (confidence interval = 2.1σ). The difference in the B1–H1 bond lengths of **19a** (1.33(6) Å) and **15** (1.56(6) Å) cannot be entirely accounted for, although it should be noted that the location of the hydrogen atoms by XRD studies are inherently inaccurate.

4.5 – Anion effects on [Rh(PNP)(HBcat)]$^+$

Interestingly, the oxidation state of solid-state samples of [Rh(PNP)(HBcat)]$^+$ could be controlled through substitution of the non-coordinating anion. In solution, the NMR spectra of **15**, **19** and **23** were almost identical with respect to the cations (see appendix

for ^{1}H NMR spectra). A pronounced interaction between the coordinating hydrogen of the HBcat ligand and the rhodium centre was indicated by broad doublets ($^{1}J_{RhH}$ = *ca*. 41 Hz) in the ^{1}H NMR spectra at 298 K (500 MHz, 1,2-$C_6H_4F_2$, see chapter 6). However, upon isolation, the $[BAr^{F}{}_4]^-$ analogue **15** was found to crystallise as the rhodium(I) complex [Rh(PNP)(η^2-HBcat)][$BAr^{F}{}_4$], whereas the $[BAr^{F20}{}_4]^-$ analogue **23** crystallised as the rhodium(III) OA complex [Rh(PNP)(H)(Bcat)][$BAr^{F20}{}_4$]. More surprisingly, the $[Sb^{F}{}_6]^-$ analogue **19** crystallised with two unique molecules in the asymmetric unit, one of which adopted the rhodium(I) oxidation state, **19a**, and the other the rhodium(III) oxidation state, **19b** (Scheme 4.1).

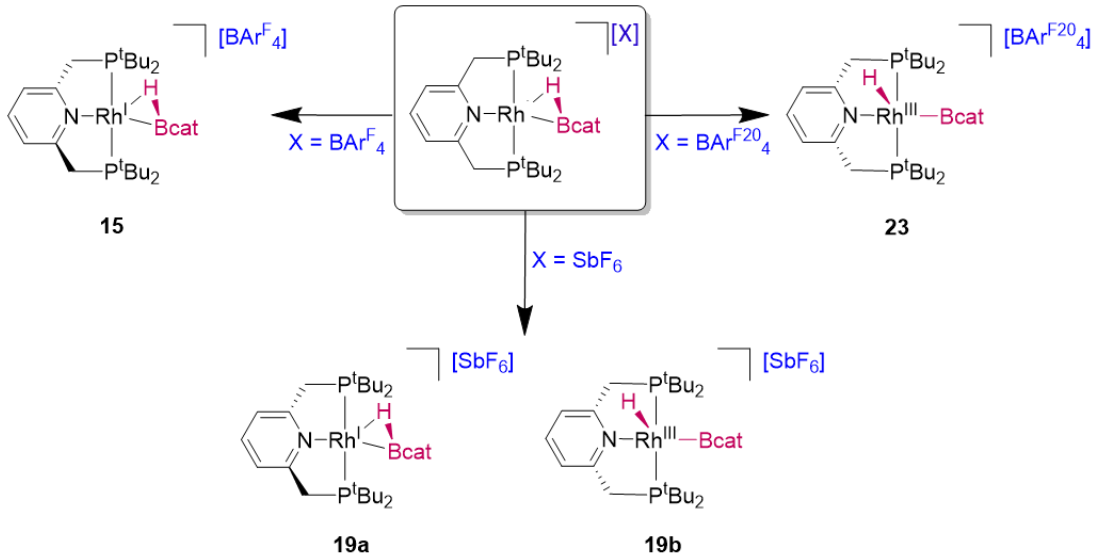

Scheme 4.1 – The different oxidation states observed in single crystals of [Rh(PNP)(HBcat)][X] (X = $BAr^{F}{}_4$, $BAr^{F20}{}_4$, SbF_6).

The OA adducts **19b** and **23** are characterised by near-linear N–Rh–B bond angles (177.6(3) ° and 178.93(7) °, respectively), which are indicative of formal Rh–B bonds (*ca*. 2.0 Å; Table 4.11). The elongated Rh1–N1 bond lengths (2.167(5) Å and 2.1715(15) Å) and conversely contracted Rh1–B1 bond lengths (2.012(8) Å and 2.000(2) Å) in comparison to the rhodium(I) complexes presented in Table 4.10 reflect the enhanced *trans* influence of the anionic Bcat ligands in **19b** and **23**, respectively. The higher oxidation state is also responsible for contractions in the Rh–P bond lengths (*ca*. 0.3 Å in **19b** and **23**) relative to the rhodium(I) precedents **15** and **19a** (Table 4.10).

PXRD diffractograms collected at Diamond Light Source on beamline I11 for the $[Rh(PNP)(HBcat)]^+$ series (λ = 0.82606 Å, 15 keV, 300 K) confirmed that the structures obtained by single crystal XRD for **15**, **19** and **23** were representative of the bulk material (Fig. 4.19). Whilst the PXRD patterns of **15** and **19** were in good agreement with the original structures obtained by single crystal XRD, the simulated PXRD pattern of **23** (derived from the single crystal CIF) did not originally match the experimental powder pattern. In order to reach an agreement with the powder pattern, a $[\bar{1}00/010/00\bar{1}]$ transformation matrix was applied to the lattice vectors of the original cell obtained by single crystal XRD (a = 11.6375(2) Å, b = 14.3262(2) Å, c = 17.0942(2) Å, α = 78.270(1) °, β = 81.446(1) °, γ = 88.973(1) °), thereby generating a non-reduced cell that was in better agreement with the experimental PXRD pattern obtained for **23** (a = 12.15454(4) Å, b = 14.21393(5) Å, c = 17.11746(8) Å, α = 104.0313(9) °, β = 81.6925(6) °, γ = 94.7915(8) °; Fig. 4.19).

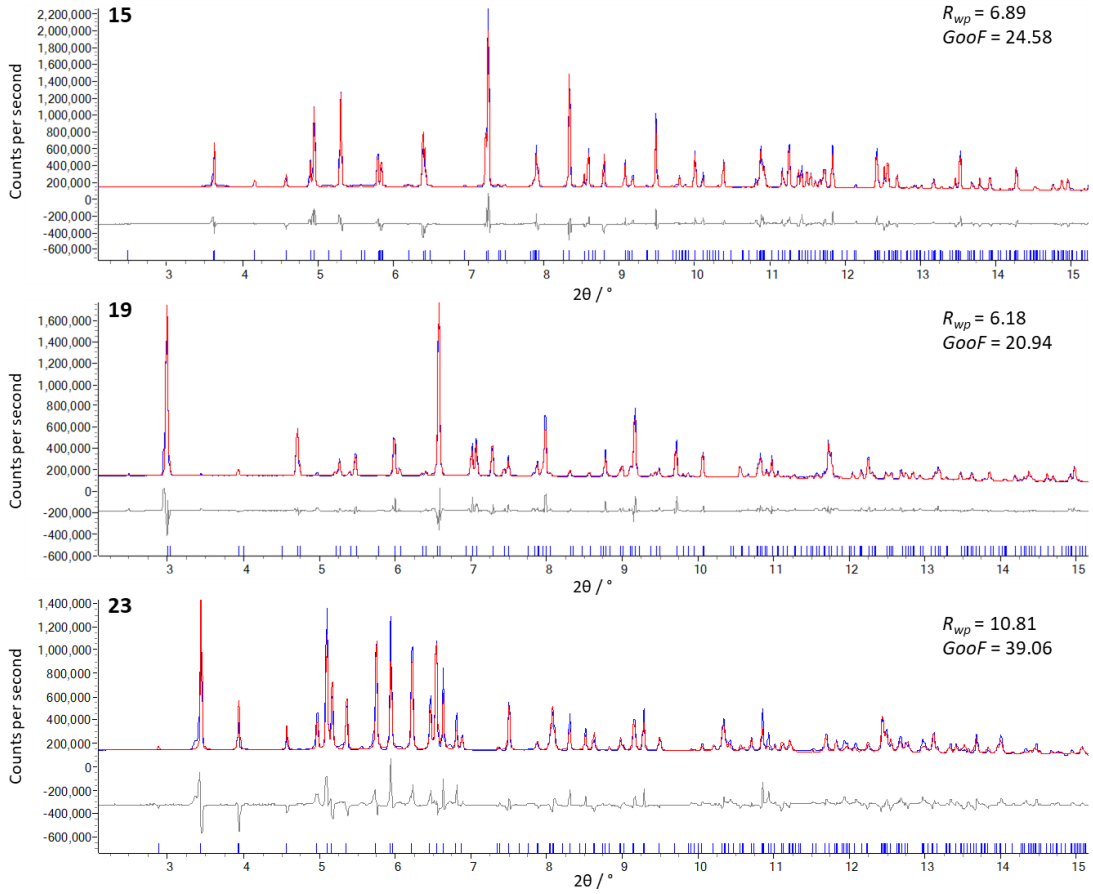

Figure 4.19 – Experimental (blue) and simulated (red) PXRD data for **15**, **19** and **23** (top to bottom). The difference between the simulated and experimental results as a function of 2θ are depicted in grey. Indexed peaks are indicated by blue tick marks.

The R_{wp} factors are slightly high, which can be partially attributed to the complexity of the structures being analysed, strain that may have developed in the crystals upon grinding of the samples and discrepancies between the experimental PXRD pattern and the SC-XRD CIFs used to simulate the idealised PXRD patterns (e.g., due to disorder). More dynamic disorder would be expected within the PXRD structures because of the higher temperatures (300 K) used during the experiments compared to the SC-XRD collections (150 K). Additionally, the single crystal and powder XRD experiments were conducted at different temperatures, so there will be differences between the unit cells due to temperature. Therefore, some discrepancies between the intensities and peak profiles is expected.

The quality of the single crystals used to make the powder sample of **23** were particularly poor, which may account for the elevated R_{wp} factor of 10.81 % in Fig. 4.19 in comparison to the refinement statistics reported for **15** and **19**. The highly air-sensitive nature of the samples could have also resulted in partial sample decomposition or loss of crystallinity to a minor extent. The samples were loaded into borosilicate glass capillaries in an argon-filled glove box and sealed with superglue in order to protect the samples from exposure to air. However, since the samples were prepared almost 1 week ahead of time in order to be transported to Diamond Light Source, small volumes of air could have feasibly leached into the samples (thus contaminating them) in this time period.

Solid-state IR spectra of **15**, **19** and **23** were also collected, but were difficult to assign due to weak and overlapping absorption bands (Fig. 4.20). In **15**, the ν_{BH} stretch was assigned at 1605 cm^{-1}, whilst in **23**, the $\nu_{Rh^{III}H}$ stretch was assigned at 1600 cm^{-1}. The $\nu_{Rh^{III}B}$ stretch was not identified because of the large number of the overlapping bands in the region of interest (Fig. 4.20). Both rhodium(I) and rhodium(III) components were thought to be present in **19** ($\nu_{Rh^{III}H}$ & ν_{BH} = 1595-1610 cm^{-1}), but again, the two stretches of interest were overlapped and weak, which effectively precluded a definitive and comprehensive assignment of the IR spectra (Fig. 4.20).

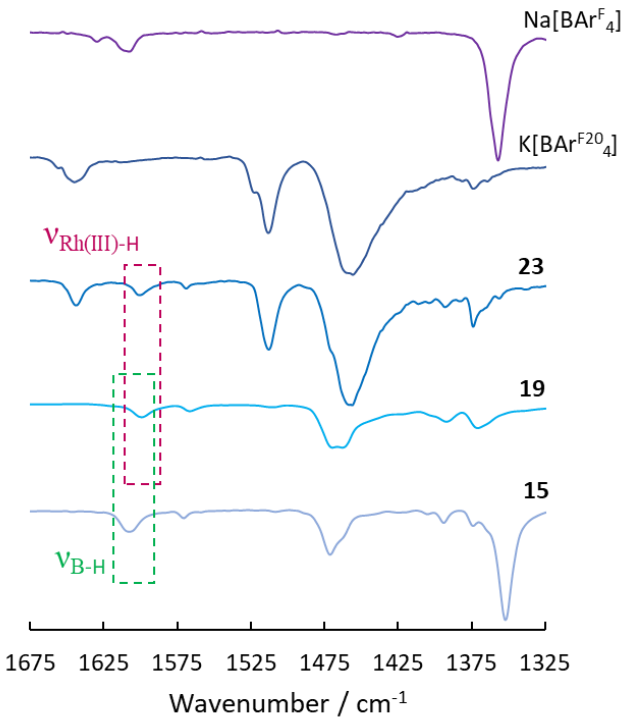

Figure 4.20 – Partially annotated IR spectra of **15**, **19** and **23** with reference spectra of Na[BAr$^{F}_4$] and K[BAr$^{F20}_4$].

To establish whether the rhodium(III) boryl hydride adducts were in any way persistent in solution, VT-NMR experiments were conducted on samples of **23** and **15** (as a control experiment). To ensure that dynamic processes were minimised in solution, samples were prepared and maintained at low temperatures (see chapter 6). Each NMR tube was charged with the appropriate amount of complex (10 μmol) then submerged in liquid nitrogen before addition of CD_2Cl_2 via vacuum transfer. The sample was then thawed in a 2-propanol / solid CO_2 ice bath (~193 K) and maintained at this temperature before being transferred into a pre-cooled NMR spectrometer.

The $^{1}H\{^{11}B\}$ NMR spectra collected for **15** and **23** at 193 K indicated that the complex was highly fluxional in solution, even at low temperatures. The coordinated proton resonance, whilst slightly more upfield and hydridic in nature for **23**, appeared as a broad doublet in both samples (**15** and **23**) across the studied temperature range. The only couplings observed in both samples in the $^{1}H\{^{11}B\}$ NMR spectra were to the respective rhodium atoms (**15**, 298K: -17.80 ($^{1}J_{RhH}$ = 35.6); 193 K: -18.20 ($^{1}J_{RhH}$ =

41.6); **23**, 298K: -17.83 ($^1J_{RhH}$ = 36.8); 193 K: -18.28 ($^1J_{RhH}$ = 42.2)),[xxii] as would be expected for elongated σ-borane complexes.

Although the lack of $^2J_{PH}$ coupling in the $^1H\{^{11}B\}$ NMR spectra indicates the absence of a formal metal hydride (which would be characterised by a doublet of triplets), the $^1J_{RhH}$ couplings observed in the $^1H\{^{11}B\}$ NMR spectra increased as the temperature decreased. Changes to *J* couplings are indicative of different metal oxidation states,[38] therefore, solutions of **15**, **19** and **23** are perhaps best described as existing in dynamic equilibrium between the rhodium(I) σ-borane and the rhodium(III) boryl hydride adducts,[xxiii] as opposed to simply highly activated σ-borane complexes which are on the precipice of OA. The coupling observed in the $^{31}P\{^1H\}$ NMR spectra, however, appeared to be temperature independent, which arguably supports the latter description. With that being said, the proton environment is a more direct spectroscopic handle for the determination of the borane coordination mode than the inferred electronics provided by the phosphorus environments of the pincer ligand.

Taking into account the collective data, the oxidation states adopted by the $[Rh(PNP)(\eta^2\text{-HBcat})]^+$ analogues in the solid-state appear to be dependent on crystal packing effects. Although in solution a dynamic equilibrium exists between the rhodium(I) and rhodium(III) analogues, upon crystallisation, perturbations to the solid-state thermodynamics (as a result of crystal packing effects) cause either the rhodium(I) or rhodium(III) adduct to crystallise more favourably.

The solid-state microenvironments of the $[Rh(PNP)(HBcat)]^+$ complexes were examined in greater detail using *Mercury*[26] in an attempt to rationalise the experimental observations. As previously described, short contacts were identified between the $[SbF_6]^-$ anion and the Rh and N atoms of **19b**, as evidenced by the elongated ADP of the involved F atom (Fig. 4.21). This suggests the anion provides a significant stabilising effect to the rhodium(III) complex within co-crystal **19**. Short contacts have previously been documented for 5-coordinate group 9 complexes of $[M(CNC\text{-}12)(biph)][BAr^F{}_4]$ (M = Rh, Ir), but the contacts in these cases were indicative of agostic interactions (Fig. 4.21).[39]

[xxii] The small differences in chemical shifts were attributed to solution-based counterion effects (*i.e.* different halogen bonding interactions).

[xxiii] The slight differences between the low temperature NMR spectra obtained for **15** and **23** could be due to perturbations to the equilibrium in solution due to the different anions.

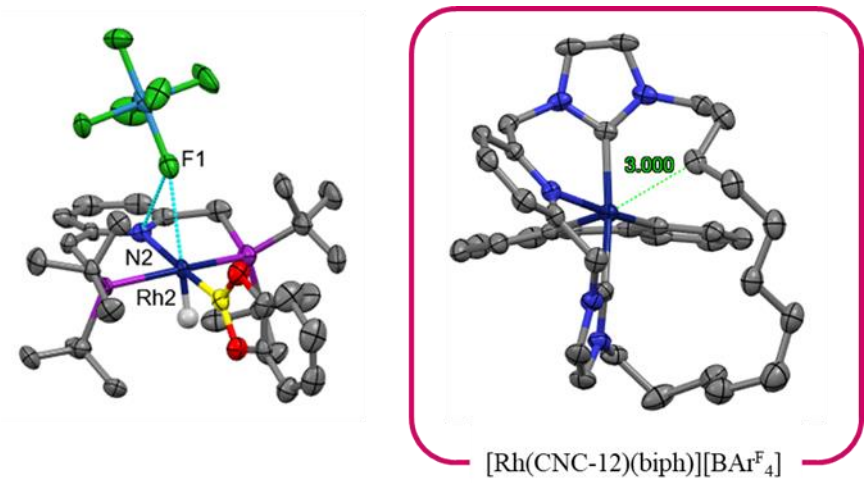

Figure 4.21 – The short contacts (cyan lines) observed between the cation of **19b** and the anion (left) and the structure of [Rh(CNC-12)(biph)][BAr$^F_4$][39] with the agostic interaction distance depicted in green (right). All hydrogen atoms except for the metal hydride of **19b** are omitted for clarity.

The different oxidation states adopted in **15** and **23**, on the other hand, appeared to be stabilised by specific aromatic interactions. In **23**, the rhodium(III) oxidation state appeared to be stabilised through reinforcement of the Bcat ligand coordination geometry by dipole-induced dipole interactions between the Bcat ligand and adjacent ArF[20] groups (Fig. 4.22). Examination of the extended packing in **15** showed the existence of similar dipole-induced interactions. However, in the case of **15**, these interactions preferentially reinforce the rhodium(I) oxidation state by maintaining the 'diagonal' coordination mode of the HBcat ligand, as opposed to the 'orthogonal' conformation adopted by the Bcat ligand in **23** (Fig. 4.22 & 4.23). The interactions are best described as dipole-induced dipole interactions as opposed to formal π-π interactions because the centroid-to-centroid distances between the rings depicted in Figures 4.22 & 4.23 are greater than 4.0 Å. Rings with centroid-to-centroid distances of greater than 4.0 Å and interplanar separations of greater than 3.4 Å (*i.e.*, the Van der Waals radii of two carbon atoms) are not generally regarded as genuine π-π interactions.[33,34]

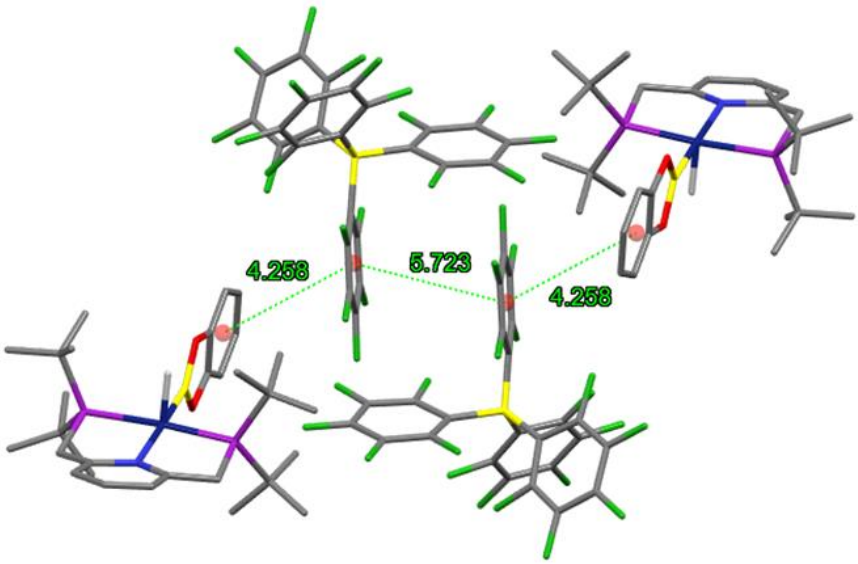

Figure 4.22 – The aromatic interactions observed in **23**. The centroid-to-centroid distances reported by *Mercury*[26] (red spheres, green values) are given in angstroms. All hydrogen atoms except for the metal hydrides are omitted for clarity.

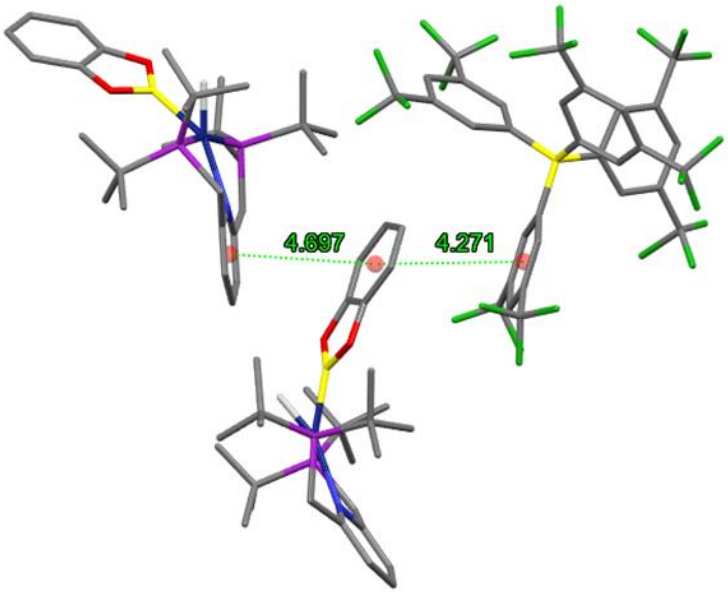

Figure 4.23 – The aromatic interactions observed in **15**. The centroid-to-centroid distances reported by *Mercury*[26] (red spheres, green values) are given in angstroms. All hydrogen atoms except for the B–H hydrogens are omitted for clarity.

4.5.1 – The gas-induced SC-SC transformation of [Rh(PNP)(H)(Bcat)][BAr$^{F20}_4$]

Attempts to stabilise the rhodium(III) boryl hydride adduct **23** for solution phase analysis led to the discovery of a SC-SC transformation. Initially, a powdered sample of **23** was exposed to an atmosphere of carbon monoxide for 24 h, in an attempt to 'trap' the complex with carbon monoxide in the solid-state as a 6-coordinate species. Within 10 minutes, the powder had turned from pale yellow to bright yellow in colour. The carbon monoxide atmosphere was purged by exposing the tube to a continuous flow of argon, followed by dissolution of the sample in CD_2Cl_2. Immediate analysis by ^{1}H, ^{31}P and ^{11}B NMR spectroscopy confirmed the formation of the rhodium(I) carbonyl adduct [Rh(PNP)(CO)][BAr$^{F20}_4$], **24**, (δ_{31P}: 78.3 (d, $^1J_{RhP}$ = 121 Hz)[25] alongside free HBcat (δ_{11B}: 28.9 (d, $^1J_{BH}$ = 191 Hz)),[40-42] the latter of which decomposed slowly over time into molecular hydrogen (δ_{1H}: 4.60 (s))[43] and B_2cat_2 (δ_{11B}: 22.59 (br)).[44] This decomposition process is presumably assisted by complex **24**, since dehydrogenative borylations catalysed by late transition metal pincer complexes are well-documented.[45-49] A control experiment where **23** was dissolved in CD_2Cl_2 without exposure to carbon monoxide showed only partial decomposition (*ca*. 10 %) of **23** into the dihydrogen adduct [Rh(PNP)(H_2)][BAr$^{F20}_4$] (δ_{31P} 81.7 ($^1J_{RhP}$ = 121 Hz))[24] over the course of 24 h. Exposure of CD_2Cl_2 solutions of **23** to carbon monoxide similarly afforded **24** alongside free HBcat within 5 minutes at room temperature, as observed by ^{1}H and ^{31}P NMR spectroscopy.

It was initially assumed that upon exposure of **23** to carbon monoxide the 6-coordinate complex [Rh(PNP)(H)(Bcat)(CO)][BAr$^{F20}_4$] was generated in the solid-state and that **24** was subsequently afforded via reductive elimination of HBcat upon dissolution of the sample. However, analysis by single crystal XRD definitively confirmed that **24** was directly generated in the solid-state alongside free HBcat via a SC-SC transformation (Scheme 4.2). The bond lengths and bond angles[xxiv] associated with the cation of **24** are commensurate with the previously reported analogues [Rh(PNP)(CO)][X] (X = BAr$^F_4$, **F**; BF_4, **G**).[25,27] Furthermore, the carbonyl ($\nu_{C=O}$ = 1981 cm^{-1})[25] and free HBcat (ν_{B-H} = 2655 cm^{-1})[50] stretches obtained by IR spectroscopy for a solid-state sample of **23** after exposure to carbon monoxide (1bar,

[xxiv] Crystallographic tables and selected bond lengths and bond angles for **24** are supplied in the appendix.

24 h) are consistent with the literature and corroborate the SC-SC transformation. Straightforward coordination of carbon monoxide to generate the 6-coordinate complex [Rh(PNP)(H)(Bcat)(CO)][$BAr^{F20}{}_4$] was initially anticipated because such behaviour would mirror the solution-based reactivity reported by Milstein and co-workers for carbon monoxide addition to rhodium PCP and PNP-type complexes.[51,52] With that being said, several SC-SC transformations involving ligand substitution with carbon monoxide have been reported, notably for iridium PONOP and rhodium NHC complexes.[53,54]

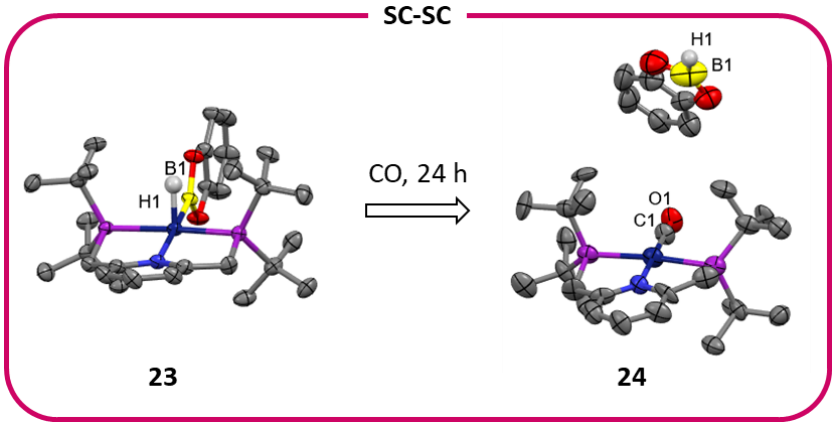

Scheme 4.2 – Partially labelled structures showing the SC-SC transformation of **23** into **24**. All anions and hydrogen atoms, except for H1, are omitted for clarity.

The SC-SC transformation of **23** (a = 11.6375(2) Å, b = 14.3262(2) Å, c = 17.0942(2) Å, α = 78.270(1) °, β = 81.446(1) °, γ = 88.973(1) °, V = 2759.18(7) $Å^3$) into **24** (a = 12.1335(13) Å, b = 13.4392(14) Å, c = 17.6394(16) Å, α = 86.300(8) °, β = 80.679(8) °, γ = 83.559(9) °, V = 2817.3(5) $Å^3$) compromised the morphological integrity of the single crystals, so much so that dataset resolution of the latter was limited to *ca*. 1.5 Å. The net unit cell volume change for this transformation was calculated to be 2.1 % - this is typical for SC-SC transformations, which tend to change cell volume by < 4 %.[56] These observations are unsurprising considering that not only does the PNP ligand experience a conformational change from C_s to C_2 during the transformation, but the boron atom of the free HBcat migrates over 6.3 Å away from its previous coordinated position, as calculated from structural overlays of **23** and **24** in *Mercury* (Scheme 4.2).[26] Furthermore, large gradients between the surface and bulk material in single crystals during SC-SC transformations caused by exposure to stimuli

such as irradiation or gaseous reagents are known to produce phase separations, leading to more polycrystalline products.[55]

Migrations of this magnitude are rarely reported due to the impact of large structural rearrangements on sample crystallinity during SC-SC transformations,[56,57] with only the nitrate anion migrations reported for the polynuclear cobalt complex **A47**[xxv] (~7 Å) being comparable.[58] Furthermore, SC-SC transformations involving reductive elimination are rare because this process requires a significant structural rearrangement[56] - more common SC-SC transformations include facile ligand substitutions or, in the case of photo-induced transformations, templated cycloadditions.[57] However, photo-induced N_2 extrusion via an SC-SC transformation has been previously reported by Powers and co-workers for two different azide-containing polynuclear rhodium complexes at 100 K, although the N_2 migrations observed during the transformations were small (< 1.4 Å).[59,60] Nevertheless, the SC-SC transformation of **23** into **24** is particularly notable because it is characterised by the large migration (up to 6.3 Å) of a relatively large HBcat molecule (Van der Waals volume = *ca*. 143 Å^3).[61,62]

Given the reactivity observed in **23**, for comparative purposes, the reactivity of **15** with carbon monoxide was also probed. Exposure of CD_2Cl_2 solutions of **15** to carbon monoxide resulted in the formation of the previously reported carbonyl complex [Rh(PNP)(CO)][BAr$^F_4$], **F** (δ_{31P} 78.3, J_{RhP} = 121 Hz),[25,27] alongside free HBcat (δ_{11B}: 28.9 (d, $^1J_{BH}$ = 194)).[40-42] Similarly, exposure of crystallites of **15** to carbon monoxide (24 h, 1 atm) afforded the same products, as observed spectroscopically upon dissolution of the sample in CD_2Cl_2. Furthermore, analysis of a solid-state sample of **15** after exposure to carbon monoxide by IR spectroscopy indicated quantitative formation of **F**·HBcat (ν_{CO} = 1981 cm^{-1}; ν_{BH} = 2655 cm^{-1}).[25,50] The solid-state transformation of **15** into **F** is not a SC-SC transformation because single crystals of **15** did not diffract after exposure to carbon monoxide. This transformation is an example of straightforward ligand exchange, as opposed to ligand exchange that proceeds via RE (as observed during the transformation of **23** into **24**).

[xxv] **A47** = [{(bpbp)$Co_2(O_2)$}$_2$(NH_2bdc)](NO_3)$_4$·7H_2O, (bpbp = 2,6-bis(N,N-bis(2-pyridylmethyl)-aminomethyl)-4-tert-butylphenolato; NH_2bdc = 2-amino-1,4benzenedicarboxylato)

Not only has it been verified that OA can be achieved in complexes of $[Rh(PNP)(\eta^2\text{-HBcat})]^+$ under ambient conditions, but the oxidation state of the cationic fragment can be controlled in the solid-state through substitution of the non-coordinating counterion. It is apparent that complexes of $[Rh(PNP)(HBcat)]^+$ are capable of undergoing OA without the need for added stimulus (such as pressure) when the surrounding solid-state microenvironment does not otherwise prohibit it (Fig. 4.24). Additionally, the OA observed upon crystallisation is reversible, since dissociation of the borane ligand is facilitated rapidly upon dissolution of the crystalline samples or, in the case of **23**, upon exposure to carbon monoxide.

4.6 – Selection of candidates for reconceived HP-XRD studies

HP-XRD studies on selected PNP-containing complexes were of particular interest so that the pressure-responsive behaviour of the more activated σ-borane analogues could be explored. Because the PNP complexes more readily pre-activate the σ-borane ligands, it was hypothesised that there was a greater likelihood of inducing OA upon the application of pressure. The OA observed in **19** and **23** (section 4.4.3) was also particularly encouraging, since it confirmed that these complexes were capable of undergoing B–H activation when the crystal packing was perturbed.

The most suitable candidates for further investigation by means of HP-XRD were chosen based on the following criteria:

1. Single crystals could be reliably grown and were of suitable quality, size and morphology
2. The complex contained the PNP pincer ligand, in order to enhance the activation of the borane ligand
3. The complex had not already fully undergone OA at ambient pressure upon crystallisation

With this criteria in mind, the best candidates for subsequent studies under pressure were decided upon by a process of elimination. The PONOP-based systems (**12**, **16** and **20**) were discounted from subsequent study, since the PNP-based complexes showed greater activation of the B–H bond under ambient conditions. Furthermore, the $[SbF_6]^-$ systems **16** and **18** were discounted from further study because crystal

growth was unreliable. High pressure studies generally require a reliable and steady supply of suitable crystals because of the difficulties associated with the DAC loading procedure. The loading procedure, in this case, was further complicated by the air-sensitivity of the samples.

Based on the conclusions drawn from the initial HP-XRD study of **13**, structures either containing HBpin or precluding $[BAr^{F}{}_{4}]^{-}$ were considered to be the most suitable samples to interrogate via HP-XRD. It was thought that the *gem*-methyl groups of the HBpin ligands might help prevent the borane ligand becoming too well encased in cavities created by adjacent Ar^{F20} groups in $[BAr^{F20}{}_{4}]^{-}$, whilst removal of the $[BAr^{F}{}_{4}]^{-}$ anion could improve the resolution of the HP datasets.

With this collective information in mind, **19** and **22** were chosen to be studied using HP-XRD. Co-crystal **19** was thought to be a promising system to investigate since OA had already been achieved in half of the independent molecules in the asymmetric unit under ambient conditions. However, the presence of two unique complexes in the asymmetric unit was a less desirable attribute, due to the large number of parameters requiring refinement. Since the OA adduct was crystallised for the $[BAr^{F20}{}_{4}]^{-}$ analogue **23**, the next logical candidate for investigation by HP-XRD (after, of course, co-crystal **19**) was the closely related complex [Rh(PNP)(η^2-HBpin)][$BAr^{F20}{}_{4}$] (**22**). Although **22** crystallises in a triclinic crystal system, the C_s conformation adopted by the PNP ligand suggests that onward reactivity to the OA product is feasible, since the only other complexes that adopt this configuration are the rhodium(III) boryl hydride complexes.

4.7 – HP-XRD study of co-crystal 19

Since one of the two unique complexes present in the asymmetric unit of **19** was the rhodium(III) OA adduct, an HP-XRD study on co-crystal **19** was conducted in an attempt to induce OA with pressure in the remaining rhodium(I) σ-borane complex.

4.7.1 – Pressure limits of the study

Crystals of **23** were studied at 300 K within an Easy-Almax Mini-Bragg DAC on a Rigaku XtaLAB Synergy-S diffractometer equipped with a Hypix pixel array detector.

Daphne-7575 was used as the PTM, whose hydrostatic limit is reported to be *ca*. 40 kbar.[63,64] Three separate crystals of **19** were studied under pressure: Crystal A (0.09 mm x 0.11 mm x 0.20 mm) was studied at 0.9 kbar. Crystal B (0.04 mm x 0.06 mm x 0.12 mm) was studied at pressures of 3.5, 9.5 and 12.1 kbar, with viable structural refinements obtained up to 9.5 kbar (Table 4.12). Crystal C (0.08 mm x 0.13 mm x 0.18 mm) was studied at pressures of 15.5, 20.7, 29.5 and 34.6 kbar, with viable structural refinements obtained up to 34.6 kbar (Table 4.13). Pressures were determined using the ruby fluorescence method.[65] Due to the necessity to handle samples within a glovebox, ambient pressure datasets were not collected for **19** at 300 K. The lowest pressure reported is 0.9 kbar, whose structure was found to be comparable to the ambient pressure collection conducted at 150 K (Table 4.12).

Table 4.12 – Table of crystallographic data collected for crystals A and B at 300 K. The asterisk denotes the 150 K ambient pressure collection conducted on a separate sample, for reference.

Pressure / kbar	**0.0***	**0.9**	**3.5**	**9.5**
Space group	$P2_12_12_1$	$P2_12_12_1$	$P2_12_12_1$	$P2_12_12_1$
Crystal system	orthorhombic	orthorhombic	orthorhombic	orthorhombic
***T* / K**	150	300	300	300
***a* / Å**	12.9296(1)	12.9338(4)	12.8683(3)	12.7419(3)
***b* / Å**	17.8215(2)	17.86815(18)	17.7842(15)	17.5948(14)
***c* / Å**	31.0623(3)	30.7579(6)	30.4739(14)	29.5095(12)
***V* / Å³**	7157.53(12)	7108.2(3)	6974.0(7)	6615.8(6)
R_1 **(*I* ≥ 2σ)**	0.0369	0.1296	0.1054	0.1125
wR_2 **(all data)**	0.0965	0.3206	0.3156	0.2935
GooF	1.053	1.076	1.087	1.080
R_{int}	0.0411	0.0690	0.0705	0.0786
Data/rest/param	13887/0/808	6865/1497/395	3709/1050/370	3100/1050/370
Flack parameter	0.003(3)	0.185(18)	0.13(2)	0.15(2)

Table 4.13 – Table of crystallographic data collected for crystal C at 300 K.

Pressure / kbar	**15.5**	**20.7**	**29.5**	**34.6**
Space group	$P2_12_12_1$	$P2_12_12_1$	$P2_12_12_1$	$P2_12_12_1$
Crystal system	orthorhombic	orthorhombic	orthorhombic	orthorhombic
***T* / K**	300	300	300	300
***a* / Å**	12.63380(19)	12.57770(19)	12.5073(2)	12.4616(3)
***b* / Å**	17.5246(2)	17.4485(2)	17.3543(3)	17.4875(4)
***c* / Å**	28.649(5)	28.304(5)	27.969(5)	26.620(7)
***V* / Å^3**	6343.1(11)	6211.7(10)	6070.9(11)	5801.1(16)
R_1 **($I \geq 2\sigma$)**	0.1194	0.1111	0.0968	0.1124
wR_2 **(all data)**	0.2680	0.2438	0.2103	0.3187
GooF	1.219	1.164	1.225	1.757
R_{int}	0.0404	0.0397	0.0426	0.0535
Data/rest/param	2353/1074/365	2054/1070/365	1797/1076/370	1482/1073/360
Flack parameter	0.212(16)	0.185(17)	0.172(17)	0.10(2)

Although it would have been preferable to interrogate the same crystal across a range of pressures, in the end, three separate crystals were studied. Several other samples were loaded into DACs, but major physical defects (cracking, fragmentation) were observed upon initial application of pressure. Additionally, rapid decomposition of the samples were observed upon contact with the laser used to excite the ruby spheres inside the DAC, so great care was taken with pressure measurements conducted before and after each collection. It also would have been preferable to collect datasets at interspersed pressure points for the three samples presented herein so that the structures could be better compared to one another, but sample decomposition and the limited time frame allotted to this preliminary study made this unfeasible.

For crystals A and B, sample degradation was noticeable before the hydrostatic limit of the PTM was reached (0.9 kbar and 9.5 kbar, respectively). In the case of crystal A, upon increasing the pressure after the first collection, the crystal fractured in several areas due to the sudden force exerted on the sample. In the case of crystal B, sample degradation was noticeable above pressures of 9.5 kbar, beyond which diffraction became very poor. Crystals failing to sufficiently diffract before the hydrostatic limit of the PTM is reached is not uncommon for HP-XRD studies.[66]

4.7.2 – Pressure dependence of cell parameters

The unit cell parameters collected for all three crystals were robust and reliably determined up to just below 30 kbar (the last viable dataset was collected at 29.5 kbar). Examination of the unit cell parameters indicted that no bond activation events or phase transitions were observed in the studied pressure range (Fig. 4.24). The most pronounced compression by far was observed along the *c* axis, which decreased by *ca*. 2.8 Å in length between the pressures of 0.9 kbar and 29.5 kbar (*ca*. 9 % contraction). The *b* and *a* axes compress by approximately 0.43 Å and 0.51 Å, respectively, (*ca*. 3 % contraction) across the same pressure range (Fig. 4.24). The final collection for crystal C at 34.6 kbar presented large deviations in cell parameters which could not be accounted for by phase transitions or other structural rearrangements, but a noticeable loss of high angle diffraction was evident at this pressure. Non-hydrostatic conditions were initially suspected, but the hydrostatic limit of Daphne-7575 is reported as being closer to 40 kbar.[63,64] Therefore, the poor determination of cell parameters was attributed to loss of diffraction in the already compromised crystal at 34.6 kbar.

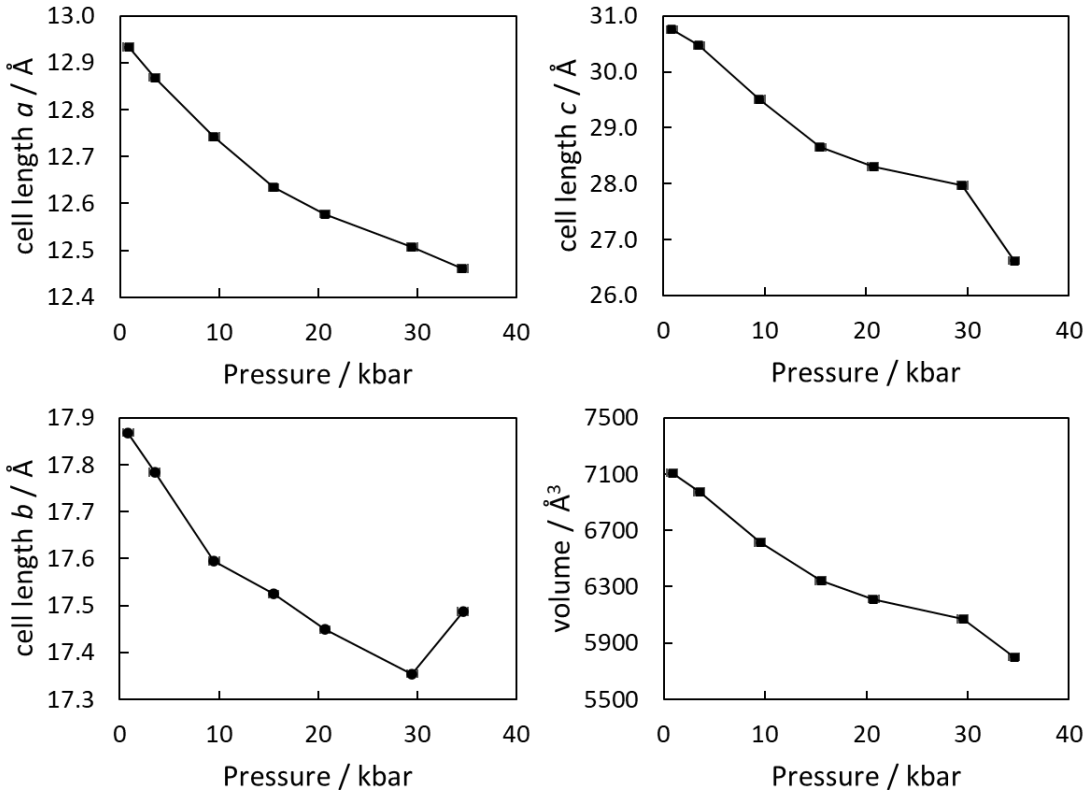

Figure 4.24 – Various cell parameters for **19** against pressure**.**

The subsequent increase in pressure from 0.9-34.6 kbar in **23** resulted in a decrease in the calculated void volume present in the structure (Fig. 4.24 & 4.25). The reported void volume decreased from 1599 $Å^3$ at 0.9 kbar to 772 $Å^3$ at 29.5 kbar. It is apparent from examination of Fig. 4.25 that the structure became less compressible as pressure was increased. The third-order Birch-Murnaghan equation of states (BM EoS) for **19** was calculated using *PASCal* (B_0 = 116(38) GPa , B'_0 = 3.8(24), V_0 = 7145(115) $Å^3$).[67] The error associated with these calculations is high due to the lack of data points across the studied pressure range, as well as the inaccuracies associated with pressure measurement across the experiment.

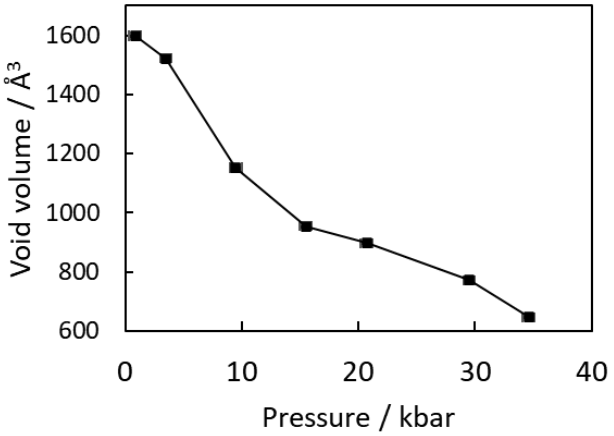

Figure 4.25 – Graph of total unit cell void volume as a function of pressure calculated in *Mercury* using a probe radius of 0.4 Å and a grid spacing of 0.2 Å.[26]

4.7.3 – Other limitations

The samples studied were of generally good quality (R_{int} < 8 %), however, none of the refinements reached convergence. The main cause of this was the constant motion/rotation of the ^{t}Bu groups associated with the PNP ligand. Additionally, the low completeness (*ca*. 40 %), poor data/restraints/parameter ratio (*ca*. 3000/1000/400) and limited resolution (~1.2 Å at higher pressures) resulted in consistently unstable refinements. Consequently, the calculated bond lengths and bond angles across all refinements have extremely high esds associated with the values and little else can be remarked on due to this. Some bond lengths were calculated to vary by over 10 % across the study, which was due to the poor data-to-parameter ratio and low I/σ. The B–H and Rh–H bond lengths for all HP refinements presented herein were constrained

to suitable values in order to maintain sensible bonding positions. As a result, the evaluation of **19**'s behaviour under pressure in the following section is more qualitative in nature and any structural metrics that are mentioned should be regarded loosely. Specific bond lengths and bond angles are not discussed in detail herein but are supplied in the appendix.

4.7.4 – Notable structural features

Despite the overall poor quality of the data collected in-house, limited insights can be made. Firstly, the coordination geometry of the HBcat ligand in **19a** remained similar across the study, indicating that bond activation was not achieved within the sampled pressure range. Initially, the insensitivity of the HBcat ligand to pressure was surprising, since the plane of the HBcat ligand lies roughly orthogonal to the *c* axis, the most compressible axis in the structure. The large decrease of 9 % in the *c* axis between the pressures of 0.9 kbar and 29.5 kbar did not translate to a large geometric rearrangement of the HBcat ligand. However, inspection of the Hirshfeld surfaces of **19a** across the studied pressure range rationalised why OA was not observed. At 0.9 kbar, only the right-hand side of the HBcat ligand experiences close contacts with a ^{t}Bu substituent of a neighbouring cation (Fig. 4.26, left). At 29.5 kbar, however, the force exerted on the HBcat ligand is less selective and close contacts are observed more uniformly across the top and bottom faces of the HBcat ligand (Fig. 4.26, right).

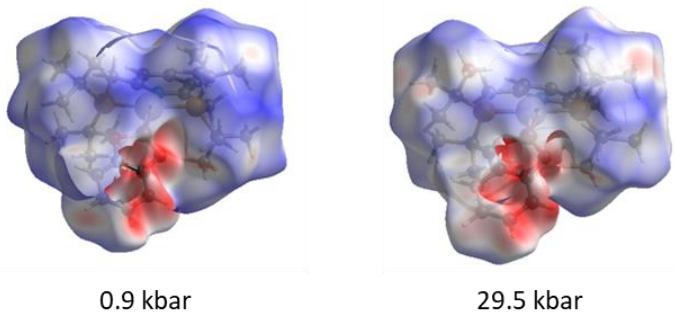

Figure 4.26 – The calculated Hirshfeld surfaces for the cation of **19a** at 0.9 kbar (left) and 29.5 kbar (right).

Assuming that upon OA the borane would adopt the coordination geometry observed in **19b**, a rotation of the HBcat ligand would be required (Fig. 4.27). To achieve this

rotation, pressure would most likely have to be exerted on the edge of the HBcat ligand (as was initially observed at 0.9 kbar), as opposed to pressure being exerted indiscriminately over the entire face, as appears to occur at higher pressures in this experiment (Fig. 4.26). The HBcat ligand of **19a** remains surrounded by ^{t}Bu substituents from neighbouring cations throughout the HP-XRD study. Unfortunately, these bulky ^{t}Bu groups appear to prohibit the more precise directional compression that would be required to encourage OA in **19a**.

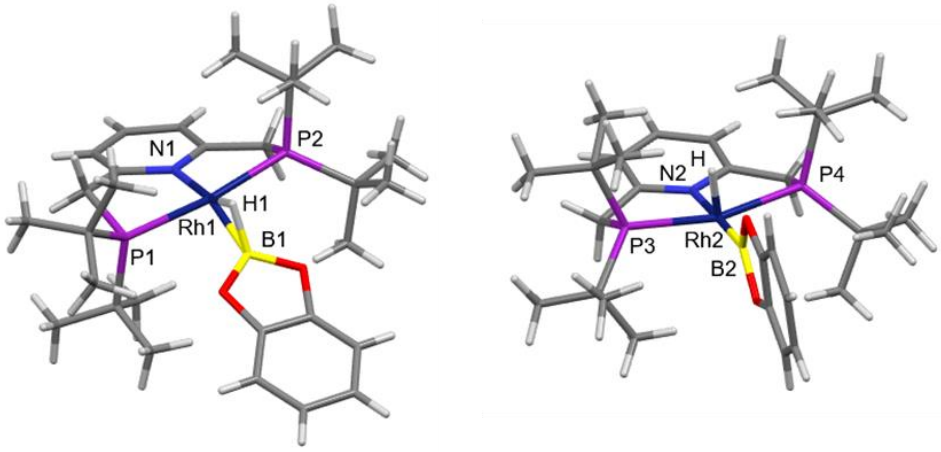

Figure 4.27 – Partially labelled structures of **19a** (left) and **19b** (right) from the 150 K ambient pressure collection.

Unexpectedly, whilst the coordination geometry of the HBcat ligand in **19a** was largely unaffected by pressure, the Bcat ligand of **19b** experienced noticeable pressure-induced distortions. At 0.9 Kbar, very few short contacts exist between **19b** and neighbouring molecules, as evidenced by the large amount of saturated blue depicted on the Hirshfeld surface in Fig. 4.28. However, between 0.9 kbar and 29.5 kbar, short contacts developed between the ^{t}Bu substituents of a neighbouring cation of **19a** and one of the faces of the Bcat ligand in **19b** (Fig. 4.28, right). The inset in Fig. 4.28 clearly indicates the displacement of the Bcat ligand away from collinearity with the *trans* Rh–N bond as a result of unfavourable close contacts with a neighbouring cation. The N2–Rh2–B2 bond angle was, for the most part, unaffected by the increase in pressure, changing only from 172.2(10) ° at 0.9 kbar to 175(2) ° at 29.5 kbar. This bond angle was most likely preserved due to the steric buttressing of the ^{t}Bu groups which flank the Bcat ligand in **19b**. The direction of compression – shown by orange arrows in the inset of Fig. 4.28 – is approximately parallel to the least

compressible axes in the structure (the *a* axis), as calculated by *PASCal*.[67] This suggests that the ^{t}Bu groups help support the Bcat ligand and hinder further pressure-induced distortion.

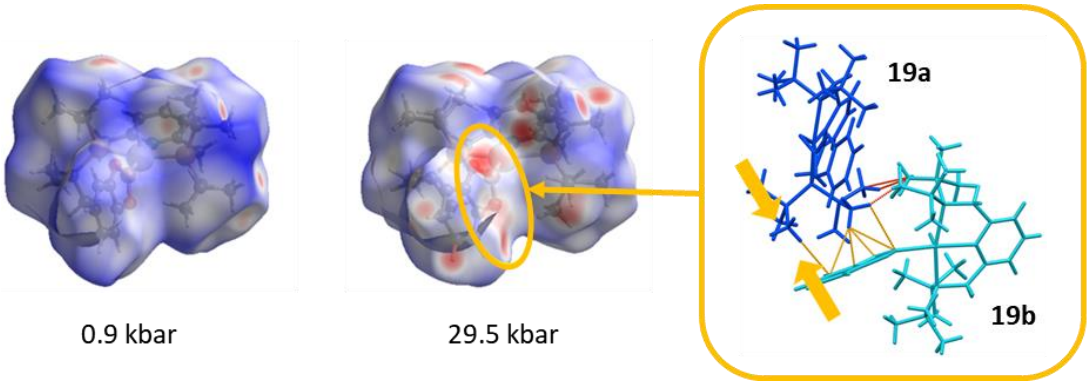

Figure 4.28 – The calculated Hirshfeld surfaces for the cation of **19b** at 0.9 kbar (left) and 29.5 kbar (right). The inset depicts the deformation of the Bcat ligand in **19b** (light blue) due to the close approach of **19a** (dark blue) at 29.5 kbar. The close contacts between ^{t}Bu···^{t}Bu and ^{t}Bu···Bcat are depicted by red and orange lines, respectively, and the orange arrows depict the approximate direction of compression.

4.8 – HP-XRD study of [Rh(PNP)(η^2-HBpin)][BAr$^{F20}{}_4$], 22

The combination of HBpin and PNP ligands within **22** were thought to be an effective pairing for achieving the desired pressure-responsive reactivity from a chemical standpoint, since OA was observed under ambient conditions for the HBcat analogue **23**. Furthermore, examination of **22** by HP-XRD would allow us to ascertain whether OA could be encouraged in a rhodium(I) complex where a C_s PNP conformation was adopted in preference to the C_2 conformation, which was observed in all other σ-borane complexes (see section 4.4.1). It should be noted, however, that ligand geometry has previously been calculated to have negligible effect on MO energies of PNP complexes, rather, the electrostatic component of the CH_2 linkers principally contribute to the higher energy frontier orbitals.[36,68] Fortunately, good quality crystals of **22** are reproducible and of suitable size and morphology for HP-XRD studies.

4.8.1 – Pressure limits of the study

Crystals of **22** were studied at 293 K within an Easy-Almax Mini-Bragg DAC using Mo Kα radiation (λ = 0.71073 Å) on a Rigaku XtaLAB Synergy-S diffractometer equipped with a Hypix pixel array detector. Daphne-7575 was used as the PTM, which is reported as having a hydrostatic limit of *ca*. 40 kbar.[63,64] Two separate crystals of **22** were studied under pressure: Crystal A (0.08 mm x 0.15 mm x 0.21 mm) was studied at 4.7, 14.7, 20.3, 25.1 and 32.9 kbar, with viable structural refinements obtained up to 25.1 kbar (Table 4.14). Crystal B (0.06 mm x 0.09 mm x 0.16 mm) was studied at pressures of 6.9, 11.2, 18.1, 30.8 and 39.9 kbar, with viable structural refinements obtained up to 30.8 kbar (Table 4.15). Pressures were determined using the ruby fluorescence method.[65] An ambient pressure dataset was not collected because of difficulties encountered with the DAC loading procedure within the glovebox. Therefore, the 4.7 kbar collection is the first recorded pressure point for this HP-XRD study. A comparison of the ambient pressure 150 K collection and the 4.7 kbar 293 K collection did not indicate any significant structural deviations when the structures were overlayed in *Mercury*,[26] however, the 150 K dataset is included in Table 4.14 and the discussion in section 4.7.3, for reference.

Table 4.14 – Table of crystallographic data collected for crystal A of **22** at 293 K. The asterisk denotes the ambient pressure collection conducted at 150 K on a separate sample, for reference.

Pressure / kbar	**0.0***	**4.7**	**14.7**	**20.3**	**25.1**
Space group	$P\bar{1}$	$P\bar{1}$	$P\bar{1}$	$P\bar{1}$	$P\bar{1}$
Crystal system	triclinic	triclinic	triclinic	triclinic	triclinic
***T* / K**	150	293	293	293	293
***λ* / Å**	1.54184	0.71073	0.71073	0.71073	0.71073
***a* / Å**	11.7094(2)	11.6616(4)	11.5115(3)	11.4585(3)	11.4279(3)
***b* / Å**	14.2312(2)	14.0971(6)	13.8210(5)	13.7141(4)	13.6530(3)
***c* / Å**	17.4132(2)	17.1094(10)	16.4891(8)	16.2902(8)	16.1691(9)
***α* / °**	104.046(1)	104.172(5)	104.806(4)	104.938(4)	105.035(3)
***β* / °**	99.239(1)	99.146(4)	98.854(4)	98.781(4)	98.703(3)
***γ* / °**	91.173(1)	90.958(3)	90.180(3)	89.969(2)	89.8231(18)
***V* / Å^3**	2773.08(7)	2687.9(2)	2503.60(17)	2442.37(16)	2406.66(16)
R_1 ($I \geq 2\sigma$)	0.0207	0.0650	0.0583	0.0609	0.0601
wR_2 (all data)	0.0530	0.1648	0.1365	0.1393	0.1428
GooF	1.022	1.084	1.080	1.093	1.085
R_{int}	0.0184	0.0514	0.0456	0.0271	0.0260
Data/rest/param	11031/1021/827	2970/462/387	2788/462/387	2623/462/387	2605/460/387

Table 4.15 – Table of crystallographic data collected for crystal B of **22** at 293 K.

Pressure / kbar	**6.9**	**11.2**	**18.1**	**30.8**
Space group	$P\bar{1}$	$P\bar{1}$	$P\bar{1}$	$P\bar{1}$
Crystal system	triclinic	triclinic	triclinic	triclinic
***T* / K**	293	293	293	293
***λ* / Å**	0.71073	0.71073	0.71073	0.71073
***a* / Å**	11.6412(5)	11.5545(3)	11.4630(4)	11.3799(2)
***b* / Å**	14.0705(5)	13.9378(4)	13.7354(4)	13.5844(4)
***c* / Å**	17.0322(11)	16.7316(12)	16.3314(11)	15.8652(11)
***α* / °**	104.268(4)	104.640(5)	105.029(4)	104.956(5)
***β* / °**	99.146(4)	98.973(5)	98.804(4)	98.645(4)
***γ* / °**	90.883(3)	90.460(2)	89.942(3)	89.5465(19)
***V* / Å^3**	2665.1(2)	2572.0(2)	2452.1(2)	2341.4(2)
***R*$_1$ (*I* ≥ 2σ)**	0.0893	0.0889	0.0771	0.0871
***wR*$_2$ (all data)**	0.2707	0.2461	0.1972	0.2243
GooF	1.115	1.085	1.111	1.068
***R*$_{int}$**	0.0459	0.0470	0.0376	0.0545
Data/rest/param	2887/408/350	2809/408/350	2653/406/350	2553/396/350

Rapid sample degradation was noticeable before the hydrostatic limit of the PTM was reached (< 32.9 kbar). Whilst both crystals remained physically and optically in-tact, amorphisation at higher pressures was apparent beyond ~30 kbar. The final collections for crystals A and B at 32.9 kbar and 39.9 kbar, respectively, failed to index a sensible unit cell (Fig. 4.29). The intensity profiles were very broad and resolution did not extend far beyond 2.5 Å.

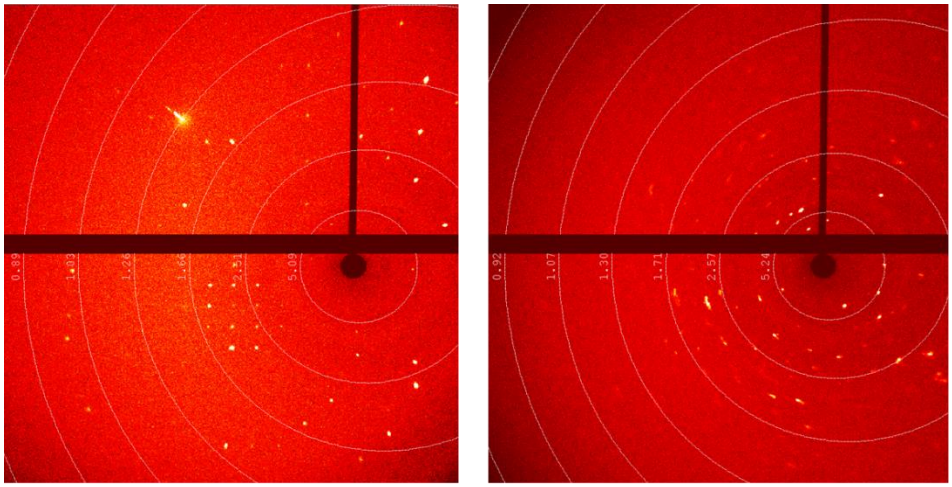

Figure 4.29 – Frames from the 25.1 kbar (left) and 32.9 kbar (right) collections for crystal A showing the loss of high-angle diffraction above pressures of *ca*. 31 kbar.

4.8.2 – Pressure dependence of cell parameters

Smooth compressions were observed along all axes in **22** across the studied pressure range. Between 4.7 kbar and 30.8 kbar, the *a*, *b* and *c* axes decreased by approximately 2 %, 4 % and 7 %, respectively (Fig. 4.30). Across the same pressure range the α angle increased slightly (~ 1 %,), whilst β and γ angles decreased by *ca*. 0.5 % and 1.5 %, respectively (Fig. 4.30). The unit cell volume also contracted at a steady rate across the study by 12.9 %, reducing smoothly from 2687.2(9) at 4.7 kbar to 2341.4(2) at 30.8 kbar (Fig. 4.30).

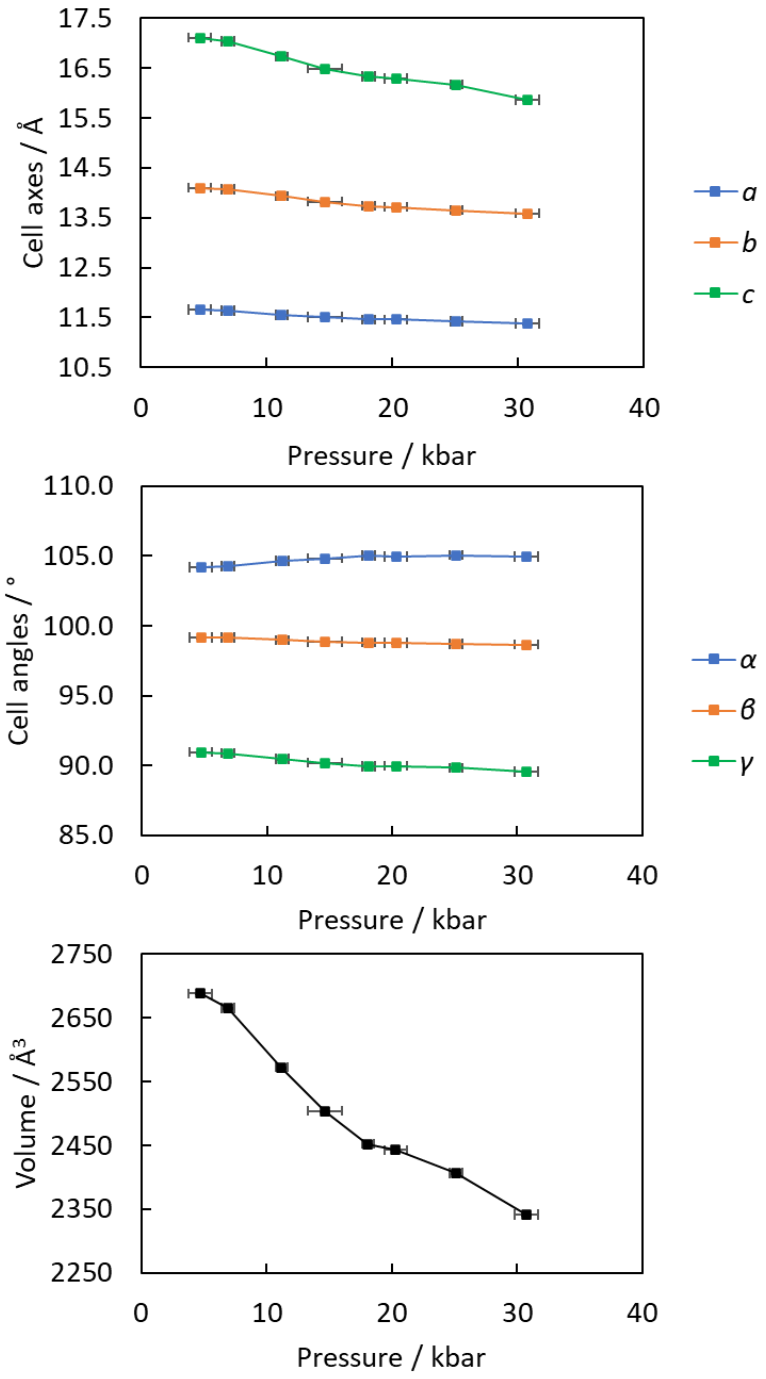

Figure 4.30 – Graphs of the unit cell axes, cell angles and cell volume against pressure for **22** (top to bottom).

4.8.3 – Notable structural features

The coordination environment surrounding the metal centre remained largely unaffected by pressure. Minor contractions were observed cross the study of *ca*. 0.03-0.05 Å in the Rh–P bond lengths (Fig. 4.31; Table 4.16), reflecting the enhanced conformational flexibility of PNP in comparison to PONOP. The Rh1–N1 bond length remained a similar length throughout the study (~2.13 Å) whereas the Rh1–B1 distance varied from 2.057(13)-2.129(12) Å (Fig. 4.31; Table 4.16). The general trend, however, showed the Rh1–B1 distance was generally shorter than the Rh1–N1 bond length, which is consistent with the ambient pressure structure (Tables 4.16 & 4.17). Excluding the 14.7 kbar and 30.8 kbar collections, the Rh1–B1 distance generally decreased with increasing pressure (Fig. 4.31), however, this contraction was statistically insignificant (confidence interval < 3σ). The invariance of the Rh1–B1 bond length and the N1–Rh1–B1 bond angle across the study suggests that the σ-borane coordination mode is not significantly affected by pressure and **22** remains a classical σ-borane complex.

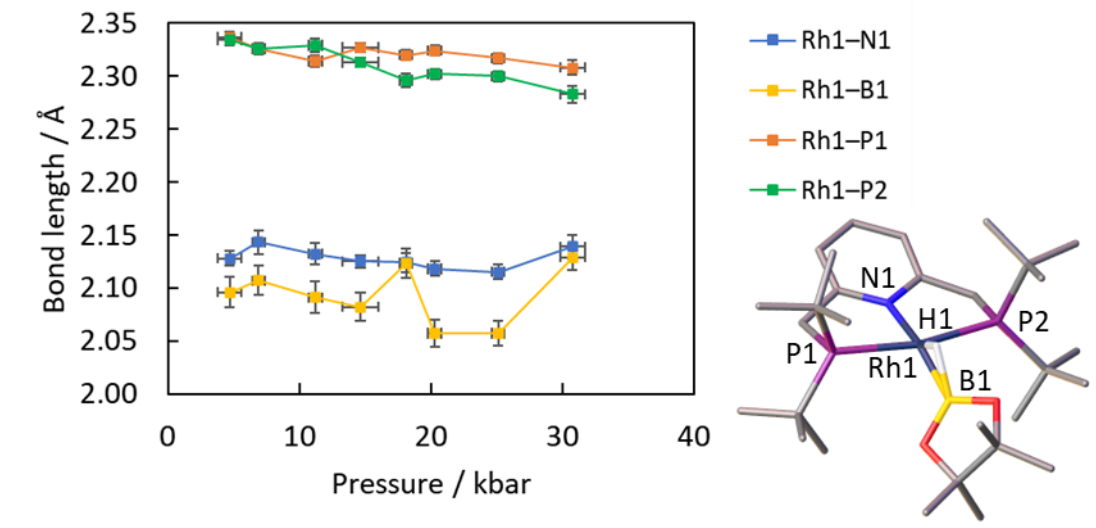

Figure 4.31 –Plot of selected bond lengths against pressure (left) accompanied by a partially labelled cation of **22** (bottom right).

Table 4.16 – Table of selected bond lengths of **22** at different pressures. The asterisk denotes the ambient pressure collection conducted at 150 K.

Pressure / kbar	Rh1–P1 / Å	Rh1–P2 / Å	Rh1–B1 / Å	Rh1–N1 / Å	B1–H1 / Å
0.0*	2.3328(4)	2.3283(4)	2.0836(15)	2.1371(11)	1.44(2)
4.7	2.337(5)	2.334(5)	2.096(14)	2.128(7)	1.36(12)
6.9	2.326(5)	2.326(5)	2.107(14)	2.143(11)	1.44(9)
11.2	2.314(5)	2.329(6)	2.091(15)	2.132(10)	1.34(10)
14.7	2.327(4)	2.313(4)	2.082(13)	2.125(6)	1.36(10)
18.1	2.320(5)	2.296(6)	2.123(14)	2.124(9)	1.31(9)
20.3	2.324(5)	2.302(5)	2.057(13)	2.118(7)	1.42(10)
25.1	2.317(5)	2.300(5)	2.057(12)	2.115(7)	1.39(16)
30.8	2.308(7)	2.283(8)	2.129(12)	2.139(11)	1.29(10)

Table 4.17 – Table of selected bond angles in **22** at different pressures. The asterisk denotes the ambient pressure collection conducted at 150 K.

Pressure / kbar	P1–Rh1–P2 / °	N1–Rh1–B1 / °
0.0*	168.558(14)	165.58(5)
4.7	167.13(14)	165.2(7)
6.9	166.89(17)	165.5(12)
11.2	166.77(19)	168.0(11)
14.7	168.12(11)	165.9(7)
18.1	168.18(12)	166.2(10)
20.3	168.54(10)	167.5(7)
25.1	168.73(9)	166.8(7)
30.8	169.26(13)	164.8(11)

Examination of the cation Hirschfeld surfaces of **22** rationalises why the HBpin ligand was not significantly influenced by pressure. At 4.7 kbar, an Ar^{F20} substituent of an anion adopts a face-one arrangement opposite the HBpin ligand and a flanking ^{t}Bu group on the PNP ligand (Fig. 4.32, site 1). At 30.8 kbar, whilst close contacts evolve between this Ar^{F20} group and the right-hand side of the borane ligand, as viewed in at site 1 in Fig. 4.32, the close approach of the anion to the borane ligand is hindered by the much bulkier nearby ^{t}Bu substituent. This arrangement prevented any substantial

compression of the borane ligand because repulsive electron-electron interactions between the Ar^{F20} ring and the adjacent ^{t}Bu substituent dominated.

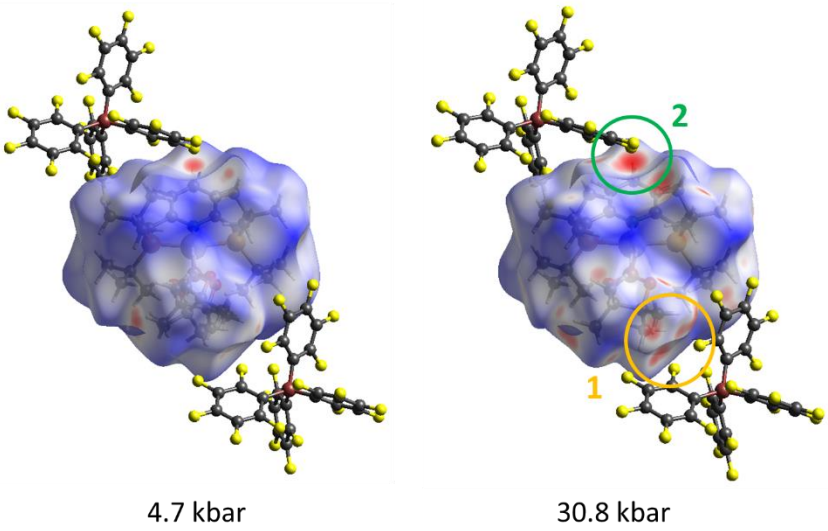

Figure 4.32 – Calculated Hirschfeld surfaces for a cation of **22** at 4.7 kbar (left) and 30.8 kbar (right). Sites 1 and 2, depicted in orange and green, respectively, show the short contacts between anions with 1) the HBpin and PNP ligands 2) the py ring.

Closer inspection of the face-on interaction at site 1 in Fig 4.32 revealed another limitation to borane compression - the Ar^{F20} ring, **Ar^{F20}-2**, experiences a significant structural deformation at the *ipso*-position at higher pressure (Fig. 4.33). This deformation is not observed at the Ar^{F20} substituent which is in close contact with the py ring of the PNP ligand (Fig. 4.32, site 2). Between 4.7 kbar and 30.8 kbar, the δ angle (as defined by the boron, *ipso*-carbon and *para*-carbon atoms) of **Ar^{F20}-2**, depicted in Fig. 4.33, decreased from 172.8(5) ° at 4.7 kbar to 165.4(9) ° at 30.8 kbar (confidence interval of 8.2σ). The origin of this phenomenon is most likely electrostatic in nature; since the Ar^{F20} ring contains enhanced regions of negative charge localised on the F atoms, repulsive electron-electron interactions between **Ar^{F20}-2** and the bulky alkyl groups of the cation will become significant upon compression (Fig. 4.34, site 1). The Ar^{F20} substituents of the counterion are also more prone to distortion than the ^{t}Bu groups, which are fixed firmly in place by the chelating pincer ligand. The surrounding steric demands of neighbouring ^{t}Bu and *gem*-methyl groups further hinder deformation of the ^{t}Bu group in question. Indeed, as the bite angle of **22** increased with higher pressures (Table 4.17), the ^{t}Bu groups were pushed

forward so as to better 'enfold' the HBpin ligand.[69] This subsequently forced the bending of **Ar^{F20}-2** at the *ipso*-carbon, giving rise to the contractions observed in the δ angle (Fig. 4.33 & 4.34).

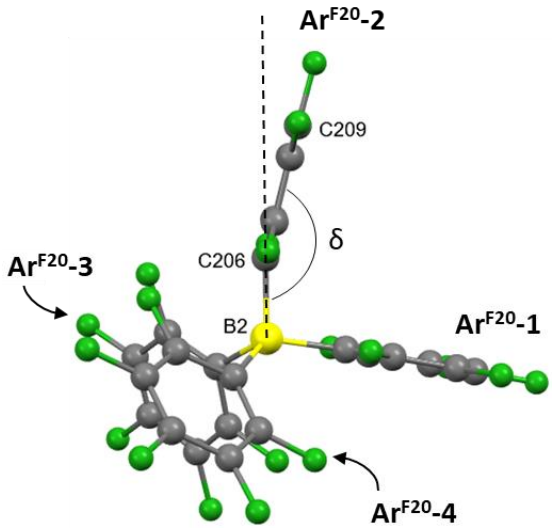

Pressure / kbar	δ / °
0.0*	172.82(9)
4.7	172.8(5)
6.9	172.1(7)
11.2	170.9(7)
14.7	169.8(5)
18.1	168.8(7)
20.3	168.9(6)
25.1	168.0(6)
30.8	165.4(9)

Figure 4.33 – A partially labelled anion depicting **Ar^{F20}-2** in the apical position, accompanied by tabulated values of the B2–C206···C209 angle against pressure. The asterisk denotes the ambient pressure collection conducted at 150 K.

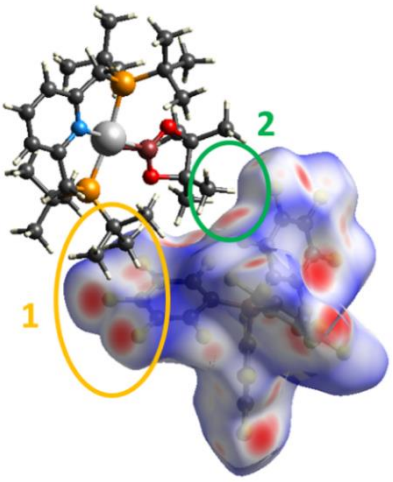

Figure 4.34 – The calculated Hirschfeld surface for the anion of **22** at 30.8 kbar. The close contacts between **Ar^{F20}-2** and the cation (site 1, orange) and **Ar^{F20}-4** and the cation (site 2, green) are highlighted.

Whilst the δ angle in **Ar^{F20}-2** decreased across the study, the other three Ar^{F20} rings, **Ar^{F20}-1**, **Ar^{F20}-3** and **Ar^{F20}-4**, did not experience the same magnitude of deformation to their respective ipso-positions (Fig. 4.35). This suggests that the distortion experienced by **Ar^{F20}-2** is unique to that particular Ar^{F20} environment. The beginnings of a similar trend developed at pressures above 20.3 kbar for the analogous δ angle in **Ar^{F20}-4** (Fig. 4.35), which upon closer examination of the Hirschfeld surface (Fig. 4.34, site 2) can be reconciled by the indication of similar repulsive interactions between the **Ar^{F20}-4** and the *gem*-methyl groups of the HBpin ligand.

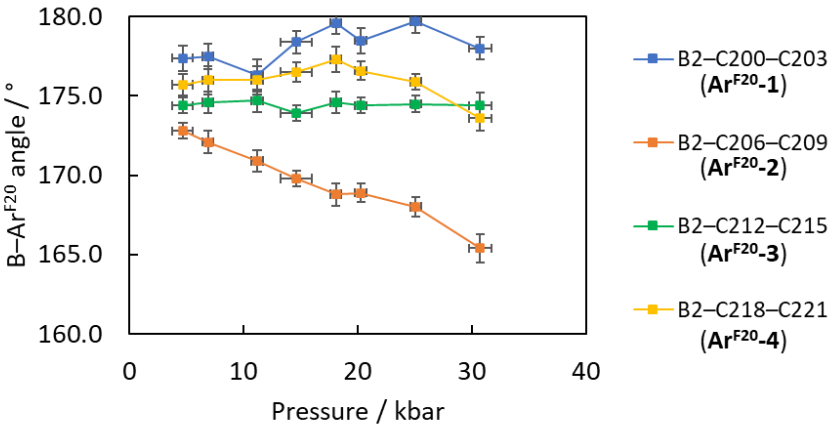

Figure 4.35 – A graph of the four B – *ipso*-C – *para*-C angles of the [BAr$^{F20}{}_4$]$^-$ anion against pressure.[xxvi]

4.8.4 – Pressure-induced evolution of π-π interactions

It was discovered that aromatic interactions between adjacent counterions in **22** could be modulated by the application of pressure. In the ambient pressure structure, anions assemble into 1-dimentional chains which contain favourable dipole-dipole interactions between adjacent Ar^{F20} rings. The resulting 'phenyl embrace' consists of one displaced face-to-face interaction and two edge-to-face interactions. With increasing pressure, the displaced face-to-face rings gradually slide horizontally closer to one another (Fig. 4.36).

[xxvi] Tabulated values are supplied in the appendix.

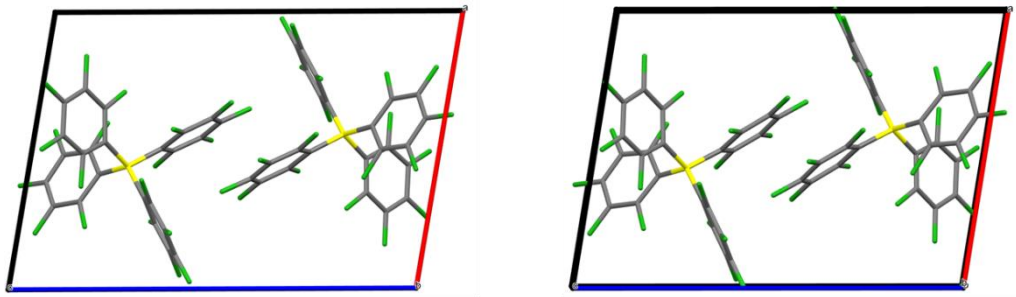

Figure 4.36 – The phenyl embrace between two anions in **22** at 4.7 kbar (left) and 30.8 kbar (right), as viewed along the *b* axis. The *a* and *c* axes are depicted in red and blue, respectively, and the cations are omitted, for clarity.

The most significant contraction across the study was observed in the centroid-to-centroid distance B, as defined in Fig. 4.37. Between the pressures of 4.7 kbar and 30.8 kbar, distance B decreased from 4.348(2) Å to 3.56(2) Å , respectively (Table 4.18). Formal π-π interactions are typically defined by centroid-to-centroid distances of 3.8-4.0 Å and interplanar separation distances of less than 3.4 Å, because this distance corresponds to the Van der Waals radii of two carbon atoms.[33,34] By these definitions, the phenyl embrace observed in **22** gradually evolves into an interaction that can be formally described as a displaced π-π interaction at pressures > 11.2 kbar (Table 4.18).

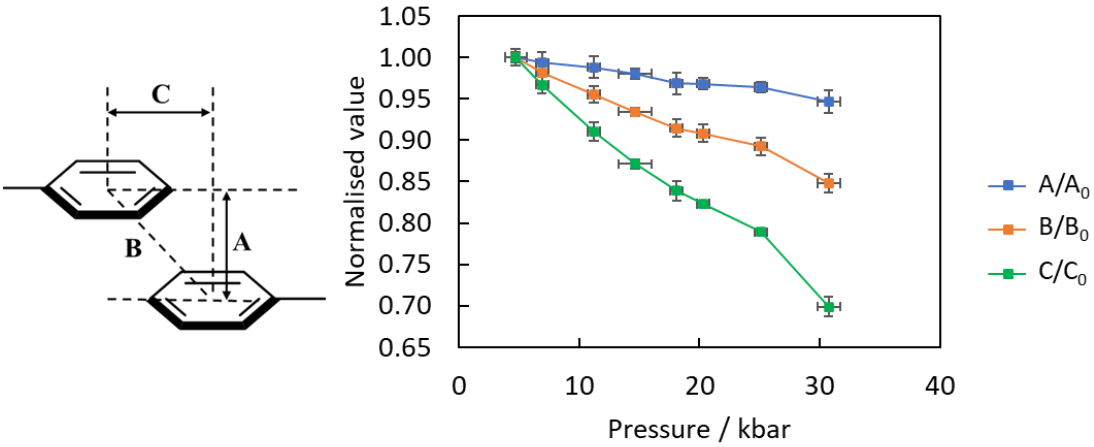

Figure 4.37 – A labelled diagram depicting parameters A-C for the phenyl embrace (left) and a graph of the normalised parameters against pressure (right). The parameters obtained from the 4.7 kbar collection were used to normalise the data, since an ambient pressure structure was not collected at 293 K.

Table 4.18 – Table of the parameters depicted in Fig. 4.37. The asterisk denotes the ambient pressure collection conducted at 150 K, for reference.

Pressure / kbar	A / Å	B / Å	C / Å
0.0*	3.178(2)	4.348(2)	2.967(18)
4.7	3.163(10)	4.21(2)	2.771(5)
6.9	3.14(2)	4.13(3)	2.67(14)
11.2	3.13(2)	4.02(2)	2.52(15)
14.7	3.100(10)	3.929(10)	2.413(7)
18.1	3.06(2)	3.84(2)	2.324(13)
20.3	3.062(10)	3.82(2)	2.281(4)
25.1	3.049(10)	3.75(2)	2.186(4)
30.8	2.99(2)	3.56(2)	1.937(11)

There is much contention surrounding how to properly describe true π-π interactions, so much so that articles are regularly published about how to correctly quantify them.[70-74] Given the nebulousness of the definition, it could be argued that a highly displaced π-π interaction is present in **22** at ambient pressure, since the interplanar ring separations are < 3.2 Å and the large centroid-to-centroid and horizontal displacement distances are likely a consequence of the fluorine substituted rings.[75] The normalised parameters A-C as functions of pressure clearly show that whilst the interplanar spacing (A) is consistently close to the optimal distance for π-π interactions (3.0-3.3 Å),[33] the horizontal displacement (C) and centroid-to-centroid (B) distances can be regulated. Irrespective of which values are used to define the threshold of π-π interactions, it is clear that the application of pressure to **22** either a) modulates the interaction, if the ambient pressure motif is considered a displaced π-π interaction from the start, or b) prompts the dipole-induced interaction to evolve into a formal π-π interaction.

Curiously, despite expectations that contractions in distance C would be limited by the edge-to-face interactions, C appeared to reduce at a steady rate up to the point of crystal degradation (30.8 kbar), indicating that a plateau had yet to be reached (Fig. 4.37). Distance D (*c.f.* Fig. 4.38) decreased as pressure increased – complementary

increases were also observed in ε (Fig. 4.38).[xxvii] The contraction of distance D was likely assisted initially by the electrostatically attractive edge-to-face interactions at lower pressure, until the energetic minima of the interaction was reached.[23,35] Whilst the edge-to-face interactions may have restricted the rate of contraction in C at higher pressures, it did not fully impede the motion. Feasibly, had higher pressures been possible to reach, further decreases in C would have been observed. It should be noted, however, that one of the rings involved in the phenyl embrace was **Ar^{F20}-4**, a ring that exhibited the signs of *ipso*-carbon deformation beyond 20.3 kbar (Fig. 4.35). Consequently, the modulation of the phenyl embrace with pressure should be considered dependent on several interconnected interactions.

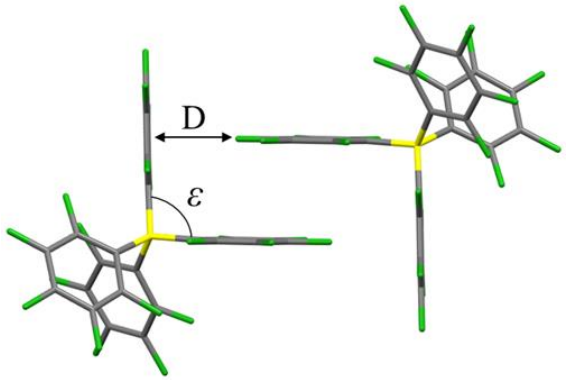

Pressure / kbar	ε / °	D / Å
0.0*	89.45(9)	3.016(2)
4.7	92.7(7)	2.91(10)
6.9	92.4(10)	2.81(4)
11.2	94.9(10)	2.80(6)
14.7	96.6(7)	2.77(10)
18.1	97.3(10)	2.75(10)
20.3	97.7(7)	2.71(10)
25.1	98.8(7)	2.72(7)
30.8	102.1(10)	2.63(2)

Figure 4.38 – A depiction of the phenyl embrace with the edge-to-face distance (D) and adjacent Ar^{F20} substituent angle (ε) labelled, accompanied by tabulated values as a function of pressure. The asterisk denotes the ambient pressure 150 K collection.

Similar π-π interactions modulated by pressure were reported by Blake and co-workers for the palladium thioether complex [Pd([9]aneS$_3$)(PPh$_3$)$_2$](PF$_6$)$_2$,[xxviii] **A59**, although the π-π interactions found in **A59** were affected by pressure to a much greater extent.[76] Between 0 kbar and 65.5 kbar, the equivalent distances B and C reported for the phenyl embrace of **A59** contracted significantly (B: 5.192(6) Å to 3.568(11) Å; C:

[xxvii] ε is defined by the angle between the *ipso*-C, B and *ipso*-C atoms of the two adjacent Ar^{F20} groups.
[xxviii] [9]aneS$_3$ = 1,4,7-trithiacyclononane.

4.195(10) Å to 1.906(18) Å), transforming the highly displaced phenyl embrace into a formal π-π stacking interaction. However, these results pertain to a phenyl embrace between unsubstituted aromatic substituents as opposed to the perfluorinated rings found in **22**, thereby, precluding a direct comparison of these phenyl embraces.

A search of the CSD (v5.43, update June 2022)[77] for phenyl embrace motifs between $-C_6F_5$ substituents returned a range of centroid-to-centroid distances with a mean value of 4.39 Å (Fig. 4.39). Distance B was calculated to be shorter than this mean value for both the 4.7 kbar (B = 4.21(2) Å) and ambient pressure (B = 4.348(2) Å) collections. At 30.8 kbar, distance B decreased to 3.56(2) Å, one of the shortest separations reported for Ar^{F20} phenyl embraces (Fig. 4.39). Due to the extreme conditions of the collection, this result is not unexpected. The centroid-to-centroid distance B decreased by 0.83 Å from 4.21(2) Å at 4.7 kbar to 3.56(2) Å 30.8 kbar in **22**, indicating that pressure brought about the evolution of a formal displaced π-π interaction[33,34] between the $-C_6F_5$ rings involved in the phenyl embrace. The mean interplanar separation of Ar^{F20} phenyl embrace motifs found within the CSD (v5.43, update June 2022)[77] was 3.33 Å – even at ambient pressure distance A in **22** is shorter than this average (3.178(2) Å; Table 4.18), indicating that the Ar^{F20} interactions are reasonably well developed in **22** at ambient pressure.

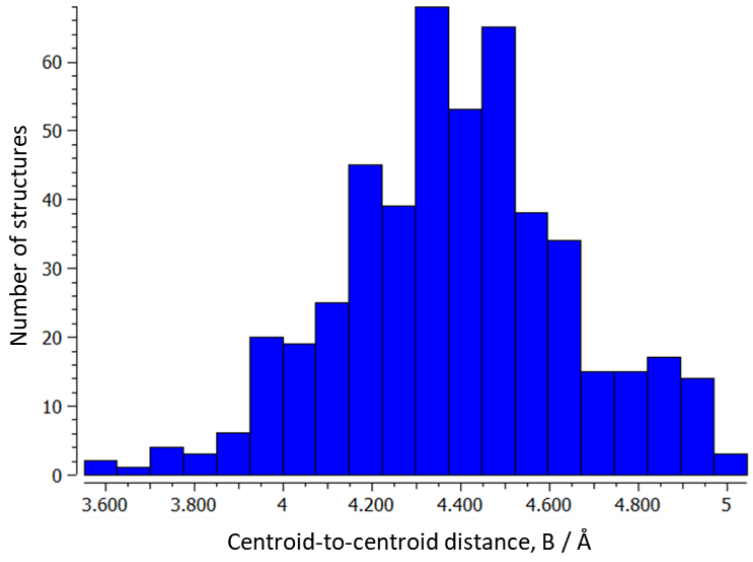

Figure 4.39 – A histogram of centroid-to-centroid distances calculated for phenyl embraces between B–C_6F_5 rings found within the CSD (v5.43, update June 2022).[77]

4.8.5 – Compressibility and void space analysis

The second-order Birch-Murnaghan equation of state (BM EoS) for **22** was calculated using *PASCal* (B_0 = 122(10) GPa , B'_0 = 4, V_0 = 2781(22) Å^3).[67] The larger B_0 indicates that **22** is much less compressible than the related $[BAr^{F}{}_4]^-$ complex **13**, whose BM EoS values were almost one order of magnitude lower. This confirms that substitution of the $[BAr^{F}{}_4]^-$ anion for $[BAr^{F20}{}_4]^-$ improves overall structural rigidity and packing efficiency. Across the studied pressure range the calculated void volume calculated by *CrystalExplorer*[29] decreased by over 220 Å^3 at a steady rate to 139 Å^3 at 30.8 kbar (Fig. 4.40). The void volume occupancy as a percentage of the total cell volume decreased from 13.4 % to 5.9 % between 4.7 kbar and 30.8 kbar.

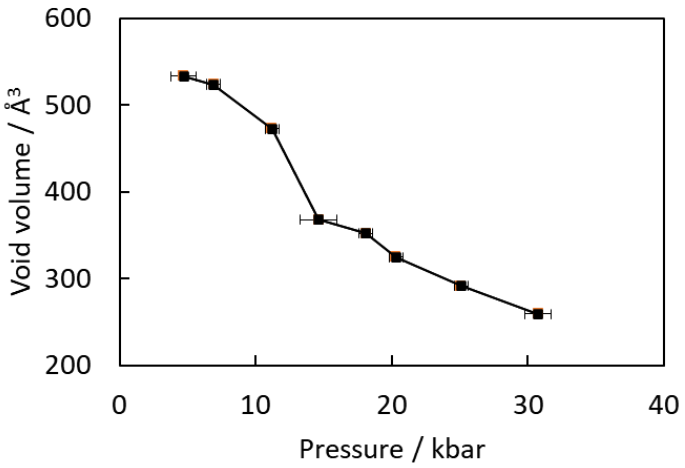

Figure 4.40 – A graph of void volume as a function of pressure calculated in *CrystalExplorer* using an isovalue of 0.002 e Å^{-3}.

The principal strain axes for **22** were also calculated using *PASCal*.[67] The principal axis with the highest compressibility coefficient, K_i, was calculated to act approximately along the $[\bar{1}47]$ lattice direction (Table 4.19). The magnitude of X_1 was roughly four times larger than X_3, the least compressible axis, and was found to align approximately with the vector defined by the horizontal displacement distance (C) of the phenyl embrace, as well as the mains channels of void space present in the structure at lower pressures (Fig. 4.41). In contrast, X_3 approximately aligns with the vector defined by the vertical displacement distance A, the parameter that was found to be most resistant to compression. The *PASCal* compressibility calculations support the experimental results and indicate that horizontal ring slippage in phenyl embraces

appears more significantly affected by pressure than vertical displacement distances. This observation is in agreement with the results obtained by Blake and co-workers for the HP-XRD study of **A59**.[76]

Table 4.19 – Table of the principal axes and compressibilities determined by *PASCal*.[67]

Structure	Principle axis, *i*	K_i / TPa^{-1}	Component of X_i along the crystallographic axes			Approximate axis
			a	*b*	*c*	
22	1	2.89(35)	-0.14	0.48	0.86	$[\bar{1}47]$
	2	1.43(14)	-0.57	0.78	-0.27	$[\bar{2}3\bar{1}]$
	3	0.50(5)	0.90	0.43	0.10	[210]

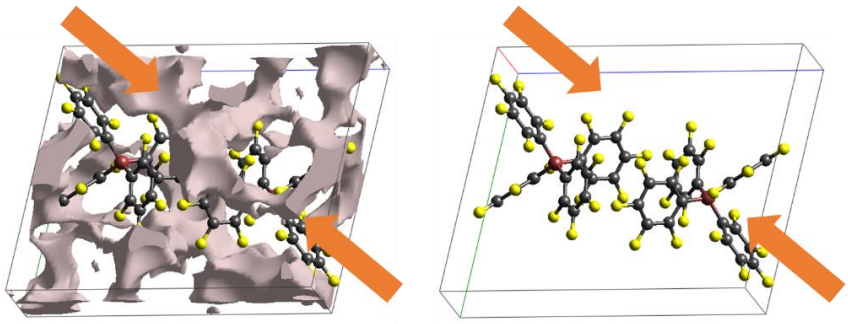

Figure 4.41 – The unit cell of **22** at 4.7 kbar with (left) and without (right) void space depicted, as viewed along the $\bar{1}47$ miller plane. The orange arrows indicate the approximate direction of X_1 (*c.f.* Table 4.19). The *a*, *b* and *c* axes are depicted by red, green and blue lines, respectively.

4.9 – Conclusions

A total of twelve σ-borane complexes with the general structure [Rh(pincer)(η^2-HBR_2)][X] have been disclosed over the previous two chapters which were prepared *in situ* using a methodology previously developed in the Chaplin group.[27] Ten of these complexes were isolated as single crystals, facilitating the direct comparison of their structures, with a view to investigating the most crystallographically suitable structures by HP-XRD. For the most part, only subtle

variations were observed across the series with respect to the coordination geometries of the σ-borane ligands in the solid-state, as observed by single crystal XRD. The most suitable candidates for HP-XRD studies were selected using the following criteria:

1. Single crystals could be reliably grown and were of suitable size, shape and quality
2. The structure contained a rigid and well-defined anion
3. The complex had not already undergone OA in the solid-state under ambient conditions

Interestingly, although the $[Rh(PNP)(HBcat)]^+$ complexes (**15**, **19** and **23**) were seemingly similar in solution, upon crystallisation, the $[BAr^F{}_4]^-$ analogue **15** crystallised as the rhodium(I) σ-borane complex, the $[BAr^{F20}{}_4]^-$ analogue **23** crystallised as the rhodium(III) boryl hydride complex and, even more surprisingly, the $[SbF_6]^-$ analogue **19** crystallised as a rhodium(I)-rhodium(III) co-crystal. Furthermore, the structures obtained by single crystal XRD were conformed to be representative of the bulk material by PXRD. Solutions of **15**, **19** and **23** were thought to be in dynamic equilibrium between the rhodium(I)/(III) adducts, as evidenced by VT-NMR experiments conducted on **15** and **23**. It is proposed that the solid-state thermodynamics of the complexes are perturbed by crystal packing effects, such that either the rhodium(I) or the rhodium(III) adduct crystallises out more favourably in certain circumstances.

Attempts to generate a 6-coordinate carbon monoxide adduct from **23** resulted in the discovery of a gas-induced SC-SC transformation which was also corroborated by NMR and IR spectroscopy. Exposure of **23** to carbon monoxide (1 atm, 24 h) afforded $[Rh(PNP)CO][BAr^{F20}{}_4]$, **24**, and free HBcat, whose boron atom was found to migrate by over 6.3 Å away from its original location upon reductive elimination. Although this SC-SC transformation somewhat compromised the crystallinity of the sample, single crystals were still of suitable enough quality for analysis by single crystal XRD.

By virtue of their reliable crystal growth and optimised chemical make-up, **19** and **22** were selected for investigation by HP-XRD in an effort to engender pressure-induced OA. Unfortunately, the large number of parameters in co-crystal **19** that required refinement impacted the quality of the high pressure datasets, limiting the level of insight that could be gained from the study. Despite the lack of reliable structural

metrics, examination of the Hirshfeld surfaces of the rhodium(III) complex at higher pressures indicated that the Bcat ligand in **19b** was more sensitive to compression than the σ-borane ligand in **19a**. The more noticeable pressure-induced deformations in **19b** can be attributed to the constraints of the stronger Rh–B bond as opposed to the more ambiguous 3c-2e σ-borane interaction found in **19a**.

Likewise, OA was not observed in **22** upon compression, however, the application of pressure prompted the evolution of a formal π-π interaction between Ar^{F20} substituents of adjacent $[BAr^{F20}{}_4]^-$ counterions, which were previously better described as dipole-induced interactions in the ambient pressure structure. Contractions in the vectors defined by the horizontal slippage distance C and the centroid-to-centroid distance B between the Ar^{F20} rings of **22** were found to approximately align with the most compressible principal axis calculated with *PASCal*,[67] providing the rational as to why the most pronounced compression was observed in that direction. Had higher pressures been achievable with this system, it is possible a larger contraction would have been observed in C, since no obvious plateau had been reached in its contraction rate before crystal degradation became a problem. The evolution of the π-π interactions with pressure was accompanied by bending of select Ar^{F20} substituents (**Ar^{F20}-2** and **Ar^{F20}-4**) away from idealised geometry due to unfavourable repulsive interactions with a neighbouring cation.

References

1. E. Bosch, J. Matheny, A. E. Brown and B. Eichler, *CrystEngComm*, 2011, **13**, 5755-5762.
2. M. Cano, J. V. Heras, M. L. Gallego, J. Perles, C. Ruiz-Valero, E. Pinilla and M. R. Torres, *Helv. Chim. Acta*, 2003, **86**, 3194-3203.
3. X. Kang, X. Wei, S. Jin, S. Wang and M. Zhu, *Inorg. Chem.*, 2021, **60**, 4198-4206.
4. C. B. Aakeröy, N. R. Champness and C. Janiak, *CrystEngComm*, 2010, **12**, 22-43.
5. H.-Y. Deng, J.-R. He, M. Pan, L. Li and C.-Y. Su, *CrystEngComm*, 2009, **11**.
6. A. J. Blake, N. R. Champness, P. Hubberstey, W.-S. Li, M. A. Withersby and M. Schröder, *Coord. Chem. Rev.*, 1999, **183**, 117–138.
7. A. J. Blake, G. Baum, N. R. Champness, S. S. M. Chung, P. A. Cooke, D. Fenske, A. N. Khlobystov, D. A. Lemenovskii, W.-S. Li and M. Schröder, *J. Chem. Soc., Dalton Trans.*, 2000, 4285-4291.
8. A. Elduque, Y. Garcés, F. J. Lahoz, J. A. López, L. A. Oro, T. Pinillos and C.Tejel, *Inorg. Chem. Commun.*, 1999, **2**, 414–418.
9. A. R. Kennedy, W. J. Kerr, R. Moir and M. Reid, *Org. Biomol. Chem.*, 2014, **12**, 7927-7931.
10. D. Ma, R. Liu, C. Zhang, Y. Qiu and L. Duan, *ACS Photonics*, 2018, **5**, 3428-3437.
11. A. Galet, A. B. Gaspar, M. C. Muñoz and J. A. Real, *Inorg. Chem.*, 2006, **45**, 4413−4422.
12. M. Casciotti, G. Romo-Islas, M. Álvarez, F. Molina, J. M. Muñoz-Molina, T. R. R. Belderrain and L. Rodríguez, *Dalton Trans.*, 2022, **51**, 17162-17169.
13. T. M. Boyd, B. Tegner, G. Tizzard, A. Martinez-Martinez, S. Neale, M. Hayward, S. Coles, S. Macgregor and A. S. Weller, *Angew. Chem. Int. Ed.*, 2020, **59**, 6177-6181.
14. A. J. Bukvic, D. G. Crivoi, H. G. Garwood, A. I. McKay, T. T. D. Chen, A. J. Martinez-Martinez and A. S. Weller, *Chem. Commun.*, 2020, **56**, 4328-4331.
15. F. M. Chadwick, N. H. Rees, A. S. Weller, T. Kramer, M. Iannuzzi and S. A. Macgregor, *Angew. Chem. Int. Ed.*, 2016, **55**, 3677-3681.
16. A. J. Martinez-Martinez, C. G. Royle, S. K. Furfari, K. Suriye and A. S. Weller, *ACS Catal.*, 2020, **10**, 1984-1992.
17. A. J. Martinez-Martinez, B. E. Tegner, A. I. McKay, A. J. Bukvic, N. H. Rees, G. J. Tizzard, S. J. Coles, M. R. Warren, S. A. Macgregor and A. S. Weller, *J. Am. Chem. Soc.*, 2018, **140**, 14958-14970.
18. A. I. McKay, A. J. Bukvic, B. E. Tegner, A. L. Burnage, A. J. Marti Nez-Marti Nez, N. H. Rees, S. A. Macgregor and A. S. Weller, *J. Am. Chem. Soc.*, 2019, **141**, 11700-11712.
19. S. D. Pike, F. M. Chadwick, N. H. Rees, M. P. Scott, A. S. Weller, T. Kramer and S. A. Macgregor, *J. Am. Chem. Soc.*, 2015, **137**, 820-833.
20. C. G. Royle, L. Sotorrios, M. R. Gyton, C. N. Brodie, A. L. Burnage, S. K. Furfari, A. Marini, M. R. Warren, S. A. Macgregor and A. S. Weller, *Organometallics*, 2022, **41**, 3270−3280.
21. A. I. McKay, A. J. Martínez-Martínez, H. J. Griffiths, N. H. Rees, J. B. Waters, A. S. Weller, T. Krämer and S. A. Macgregor, *Organometallics*, 2018, **37**, 3524-3532.
22. S. K. Furfari, B. E. Tegner, A. L. Burnage, L. R. Doyle, A. J. Bukvic, S. A. Macgregor and A. S. Weller, *Chem. Eur. J.*, 2021, **27**, 3177-3183.
23. C. R. Martinez and B. L. Iverson, *Chem. Sci.*, 2012, **3**.
24. A. B. Chaplin and A. S. Weller, *Organometallics*, 2011, **30**, 4466-4469.
25. M. Feller, E. Ben-Ari, T. Gupta, L. J. W. Shimon, G. Leitus, Y. Diskin-Posner, L. Weiner and D. Milstein, *Inorg. Chem.*, 2007, **46**, 10479−10490.
26. C. F. Macrae, I. Sovago, S. J. Cottrell, P. T. A. Galek, P. McCabe, E. Pidcock, M. Platings, G. P. Shields, J. S. Stevens, M. Towler and P. A. Wood, *J. Appl. Crystallogr.*, 2020, **53**, 226-235.

27. M. R. Gyton, T. M. Hood and A. B. Chaplin, *Dalton Trans.*, 2019, **48**, 2877-2880.
28. T. M. Hood, B. Leforestier, M. R. Gyton and A. B. Chaplin, *Inorg. Chem.*, 2019, **58**, 7593-7601.
29. P. R. Spackman, M. J. Turner, J. J. McKinnon, S. K. Wolff, D. J. Grimwood, D. Jayatilaka and M. A. Spackman, *J. Appl. Cryst.*, 2021, **54**, 1006-1011.
30. J. C. Babon, M. A. Esteruelas, I. Fernandez, A. M. Lopez and E. Oñate, *Inorg. Chem.*, 2018, **57**, 4482-4491.
31. T. J. Hebden, M. C. Denney, V. Pons, P. M. B. Piccoli, T. F. Koetzle, A. J. Schultz, W. Kaminsky, K. I. Goldberg and D. M. Heinekey, *J. Am. Chem. Soc.*, 2008, **130**, 10812–10820.
32. O. V. Ozerov, C. Guo, V. A. Papkov and B. M. Foxman, *J. Am. Chem. Soc.*, 2004, **126**, 4792-4793.
33. C. Janiak, *J. Chem. Soc., Dalton Trans.*, 2000, 3885-3896.
34. K. Avasthi, L. Shukla, R. Kant and K. Ravikumar, *Acta. Cryst.*, 2014, **C70**, 555-561.
35. K. E. Riley and J. Kenneth M. Merz, *J. Phys. Chem. B*, 2005, **109**, 17752-17756.
36. K. Lee, H. Wei, A. V. Blake, C. M. Donahue, J. M. Keith and S. R. Daly, *Dalton Trans.*, 2016, **45**, 9774-9785.
37. M. A. Esteruelas, I. Fernández, C. García-Yebra, J. Martín and E. Oñate, *Organometallics*, 2017, **36**, 2298-2307.
38. P. S. Pregosin, *NMR in Organometallic Chemistry*, Wiley, 2012.
39. M. R. Gyton, B. Leforestier and A. B. Chaplin, *Organometallics*, 2018, **37**, 3963-3971.
40. G. Alcaraz and S. Sabo-Etienne, *Coord. Chem. Rev.*, 2008, **252**, 2395-2409.
41. H. Nöth and M. Warchhold, *Eur. J. Inorg. Chem.*, 2004, **2004**, 1115-1124.
42. H. R. Morales, H. Tlahuext, F. Santiesteban and R. Contrera, *Spectrochim. Acta*, 1984, **40A**, 855-862.
43. G. R. Fulmer, A. J. M. Miller, N. H. Sherden, H. E. Gottlieb, A. Nudelman, B. M. Stoltz, J. E. Bercaw and K. I. Goldberg, *Organometallics*, 2010, **29**, 2176-2179.
44. W. Clegg, A. J. Scott, C. Dai, G. Lesley, T. B. Marder, N. C. Norman and L. J. Farrugia, *Acta Cryst.*, 1996, **C52**, 2545-2547.
45. J. Takaya, N. Kirai and N. Iwasawa, *J. Am. Chem. Soc.*, 2011, **133**, 12980-12983.
46. C. I. Lee, J. Zhou and O. V. Ozerov, *J. Am. Chem. Soc.*, 2013, **135**, 3560-3566.
47. C. J. Pell and O. V. Ozerov, *Inorg. Chem. Front.*, 2015, **2**, 720-724.
48. S. Jiang, S. Quintero-Duque, T. Roisnel, V. Dorcet, M. Grellier, S. Sabo-Etienne, C. Darcel and J. B. Sortais, *Dalton Trans.*, 2016, **45**, 11101-11108.
49. S. G. Curto, M. A. Esteruelas, M. Oliván and E. Oñate, *Organometallics*, 2019, **38**, 2062-2074.
50. Y. B. Hleba, Doctor of Philosophy, Queen's University, 2007.
51. M. Feller, Y. Diskin-Posner, G. Leitus, L. J. Shimon and D. Milstein, *J. Am. Chem. Soc.*, 2013, **135**, 11040-11047.
52. C. M. Frech and D. Milstein, *J. Am. Chem. Soc.*, 2006, **128**, 12434-12435.
53. O. V. Zenkina, E. C. Keske, R. Wang and C. M. Crudden, *Angew. Chem. Int. Ed.*, 2011, **50**, 8100-8104.
54. Z. Huang, P. S. White and M. Brookhart, *Nature*, 2010, **465**, 598-601.
55. I. Halasz, *Cryst. Growth Des.*, 2010, **10**, 2817-2823.
56. S. D. Pike and A. S. Weller, *Philos. Trans. R. Soc. A*, 2015, **373**, 20140187.
57. A. Chaudhary, A. Mohammad and S. M. Mobin, *Cryst. Growth Des.*, 2017, **17**, 2893-2910.
58. J. Sundberg, L. J. Cameron, P. D. Southon, C. J. Kepert and C. J. McKenzie, *Chem. Sci.*, 2014, **5**, 4017-4025.

59. A. Das, Y. S. Chen, J. H. Reibenspies and D. C. Powers, *J. Am. Chem. Soc.*, 2019, **141**, 16232-16236.
60. A. Das, C. H. Wang, G. P. Van Trieste, 3rd, C. J. Sun, Y. S. Chen, J. H. Reibenspies and D. C. Powers, *J. Am. Chem. Soc.*, 2020, **142**, 19862-19867.
61. A. Bondi, *J. Phys. Chem.*, 1964, **68**, 441-451.
62. Y. H. Zhao, M. H. Abraham and A. M. Zissimos, *J. Org. Chem.*, 2003, **68**, 7368-7373.
63. Keizo Murata and S. Aoki, *Rev. High Press. Sci. Technol.*, 2016, **26**, 3-7.
64. D. Staško, J. Prchal, M. Klicpera, S. Aoki and K. Murata, *High Press. Res.*, 2020, **40**, 525-536.
65. J. D. Barnett, S. Block and G. J. Piermarini, *Rev. Sci. Instrum.*, 1973, **44**, 1-9.
66. J. P. Tidey, H. L. S. Wong, M. Schröder and A. J. Blake, *Coord. Chem. Rev.*, 2014, **277-278**, 187-207.
67. M. J. Cliffe and A. L. Goodwin, *J. Appl. Cryst.*, 2012, **45**, 1321-1329.
68. F. Fang, J. X. Kang, C. Q. Xu, J. Chang, J. Zhang, S. Li and X. Chen, *Inorg. Chem.*, 2021, **60**, 18924-18937.
69. D. M. Roddick, *Topics in Organometallic Chemistry: Organometallic Pincer Chemistry*, Springer, 2012.
70. A. Banerjee, A. Saha and B. K. Saha, *Cryst. Growth Des.*, 2019, **19**, 2245-2252.
71. R. Thakuria, N. K. Nath and B. K. Saha, *Cryst. Growth Des.*, 2019, **19**, 523-528.
72. S. Grimme, *Angew. Chem. Int. Ed.*, 2008, **47**, 3430-3434.
73. T. Chen, M. Li and J. Liu, *Cryst. Growth Des.*, 2018, **18**, 2765-2783.
74. K. Molčanov and B. Kojić-Prodić, *IUCrJ*, 2019, **6**, 156-166.
75. K. Carter-Fenk and J. M. Herbert, *Chem. Sci.*, 2020, **11**, 6758-6765.
76. H. L. Wong, D. R. Allan, N. R. Champness, J. McMaster, M. Schröder and A. J. Blake, *Angew. Chem. Int. Ed.*, 2013, **52**, 5093-5095.
77. I. J. Bruno, J. C. Cole, P. R. Edgington, M. Kessler, C. F. Macrae, P. McCabe, J. Pearson and R. Taylor, *Acta Cryst.*, 2002, **B58**, 389-397.

Chapter 5 – Conclusions & outlook

The initial aim of this project was to attempt to induce oxidative addition in organometallic species in the solid-state through the application of pressure. Although pressure-induced OA remained elusive, the project evolved to include the investigation of novel rhodium pincer complexes in the solid-state by means of several alternative control parameters, such as temperature, gas and *ex situ* crystal engineering. Crystallographic methods have been implemented throughout this research in order to provide direct insight into a range of solid-state transformations.

5.1 – Activation of C–Cl bonds by a {Rh(PONOP)}$^+$ complex

As a platform for investigating the activation of C–Cl bonds in the solid-state and comparing reactivity to the solution phase chemistry, a series of κ_{Cl}-coordinated adducts of {Rh(PONOP)}$^+$ were prepared by developing a methodology previously reported in the Chaplin group.[1] The chlorobenzene adduct **1** proved an effective synthon for the generation of other κ_{Cl}-ClR adducts in solution and afforded the first examples of κ_{Cl}- adducts of chlorocyclohexane, 1,2-dichloroethane and 2-chloropropane (Scheme 5.1).

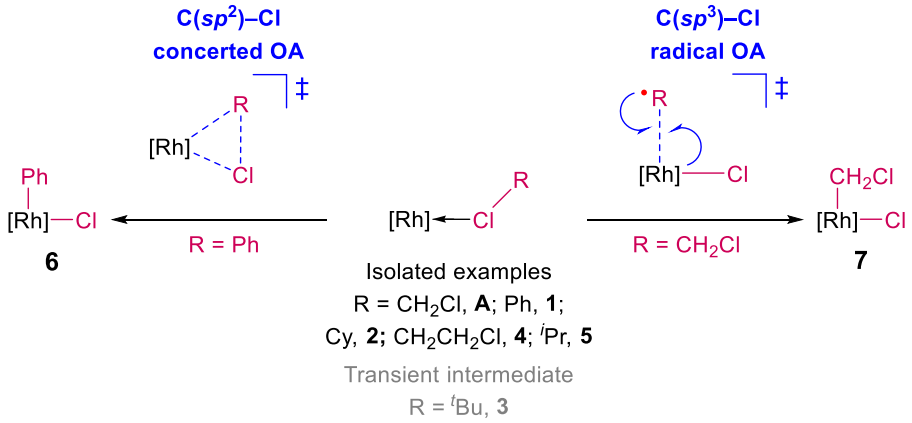

Scheme 5.1 – C–Cl OA in complexes of [Rh(PONOP)][BAr$^F{}_4$] ([Rh]).

The previously reported dichloromethane complex **A** was prepared by dissolution of **1** in CH_2Cl_2, which circumvented the formation of the contaminant [Rh(PONOP)(N_2)][BAr$^F{}_4$] species that Weller and co-workers encountered when isolating **A** after their halide abstraction method.[2] In solution, the {Rh(PONOP)}$^+$

fragment facilitated C–Cl bond activation of the respective substrate. C–Cl activation was proposed to occur via both concerted (C(sp^2)–Cl) and radical (C(sp^3)–Cl) mechanisms under mild to moderate conditions (Scheme 5.1).

Oxidative addition of the C–Cl bond in **A** was accessible both in the solid-state and in solution at elevated temperatures in the absence of light. Interestingly, the photo-stability of the OA product **7** was found to be phase dependent – whilst solid-state samples were stable for extended periods of time (several weeks) in light, exposure of solutions of **7** to light triggered facile reductive elimination. Initial VT-PXRD studies showed that NTE occurred in **A** above 350 K – this could be caused by the early stages of OA, since such reactivity was observed spectroscopically upon dissolution of solid-state samples of **A** after heating (110 °C, 18 h). However, since the cell parameters of the new phase could not be obtained, in order to comprehensively quantify the order of the phase transition and the kinetics of the transformation, further VT-PXRD studies for prolonged periods of time would be required.

Attempts to induce OA in **A** using pressure as an alternative control parameter were unsuccessful, although a new polymorph of **A** (**A-β**, 6.6 kbar: a = 12.9319(17) Å, b = 22.138(5) Å, c = 22.923(5) Å, α = 67.12(2) °, β = 86.58(2) °, γ = 87.841(16) °, V = 6035(2) Å^3, Z' = 2) was discovered to have been inadvertently loaded into one of the DACs. Despite the generally poor quality of the data obtained from Diamond Light Source for both polymorphs of **A**, assessment of the cell parameters and visual inspection of the unstable refinements indicated that no phase transitions or other bond activation events were induced upon compression.

5.2 – The impact of the pincer ligand, borane substrate and anion on a homologous series of rhodium σ-borane complexes

Owing to the robust nature of the C–Cl bonds explored in chapter 2, alternative substrates containing Rh···X–E bonding motifs were pursued in an effort to engender pressure-induced OA more readily going forward. As a result, a total of twelve structurally related σ-borane complexes of {Rh(pincer)}$^+$ were synthesised, ten of which were isolated as single crystals. These complexes represent the largest structurally related collection of rhodium σ-borane complexes reported, to date.

Examination of the $[BAr^{F}_4]^-$ series **12-15** indicated that the identity of both the pincer ligand and the borane influenced the degree of B–H activation in the complexes under ambient conditions. The higher energy frontier MOs of the $\{Rh(PNP)\}^+$ fragment are best matched in energy with the HBcat ligand, the better π-acceptor, whereas better energy matching was experienced for the lower energy MOs of $\{Rh(PONOP)\}^+$ with HBpin, the stronger σ-donor.[3,4] Consequently, the HBpin ligand (**12**) was more activated than HBcat (**13**) in $\{Rh(PONOP)\}^+$ complexes, whereas the inverse was true for the $\{Rh(PNP)\}^+$ complexes **14** and **15**. Although the experimental data supports the assignment of **12-14** as classical σ-borane complexes and **15** as an elongated σ-borane complex, ideally, supporting DFT calculations such as AIM analysis or energy decomposition analysis should be carried out so as to quantitively distinguish the different bonding situations across the series, especially because the solution phase data are ambiguous due to the highly fluxional borane ligands.

For complexes of $[Rh(PNP)(\eta^2\text{-HBcat})]^+$, whilst their solution phase data was near identical, the non-coordinating anions appeared to perturb the thermodynamics of the crystalline microenvironments such that, under ambient conditions, different oxidation states were favoured in the solid-state. The $[BAr^{F}_4]^-$ analogue crystallised as the rhodium(I) adduct (**15**), the $[BAr^{F20}_4]^-$ analogue crystallised as the rhodium(III) boryl hydride adduct (**23**) and the $[SbF_6]^-$ analogue crystallised as a mixed valence co-crystal (**19**). Going forward, DFT calculations including periodic boundary conditions may help elucidate the thermodynamic origin for the preferential formation of the different adducts. These supporting calculations could provide crucial quantitative insight into the energetics of the systems that the experimental data presented herein cannot.

5.3 - Pressure-responsive behaviour of rhodium σ-borane complexes

The fact that B–H activation was observed under ambient conditions in complexes of $[Rh(PNP)(\eta^2\text{-HBcat})]^+$ indicated that the borane ligands were highly activated by the $\{Rh(PNP)\}^+$ fragment and only small amounts of energy might be required to activate the structurally related analogues. This encouraged subsequent HP-XRD studies on crystallographically suitable and/or chemically intriguing samples, in an effort to engender pressure-induced OA.

Owing to the large volume of void space present in the ambient pressure structure, [Rh(PONOP)(η^2-HBcat)][BAr^F_4], **13-α**, underwent an isomorphous phase transition between 4.8-8.8 kbar, generating the more densely packed and less compressible high pressure phase, **13-β**. The coordination mode of the HBcat ligand in **13-β** is indicative of an elongated σ-borane complex, as evidenced by the decrease in the N1–Rh1–B1 bond angle across the phase transition from *ca*. 160 ° to *ca*. 152 ° (Fig. 5.1). In order to determine whether the elongated σ-borane interaction or the high pressure phase is persistent when pressure is removed, decompression studies could be pursued in the future. Ultimately this study was hindered by the bulky and disordered $[BAr^F_4]^-$ anion, which restricted compression about the site of interest at higher pressures and limited the resolution of the datasets at room temperature. Therefore, with a view to improving the σ-borane systems for subsequent interrogation by HP-XRD, complexes incorporating smaller, more rigid and less disordered anions were synthesised and isolated.

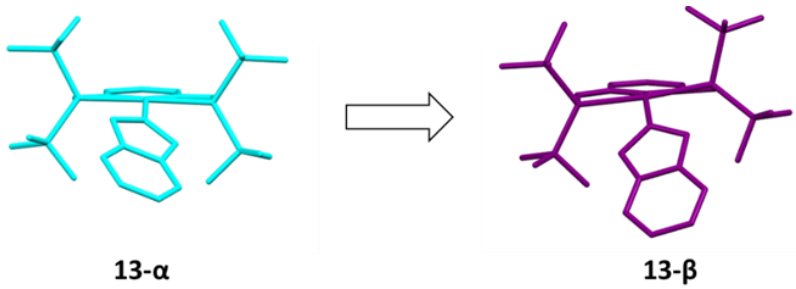

Figure 5.1 – Structure of the cation of **13** before (cyan, 4.8 kbar) and after (purple, 14.0 kbar) the phase transition.

Unfortunately, the HP-XRD study of the [Rh(PNP)(η^2-HBcat)][SbF_6] / [Rh(PNP)(H)(Bcat)][SbF_6] co-crystal was challenging to analyse in any great detail due to the extremely low data-to-parameter ratio of the high pressure datasets. However, visual inspection of the refinements indicated that the rhodium(III) boryl hydride complex experience more pronounced pressure-induced deformations than the rhodium(I) σ-borane complex on account of the more restrictive coordination environment surrounding the Bcat ligand.

Similarly, the cation of [Rh(PNP)(η^2-HBpin)][BAr^{F20}_4] only experienced minor structural distortions in response to pressure. However, the development of a formal

displaced π-π interaction[5] between two $[BAr^{F20}{}_4]^-$ anions was observed upon compression (centroid-to-centroid distance at 4.7 kbar = 4.21(2) Å; 30.8 kbar = 3.56(2) Å). The vector describing the centroid-to-centroid separation coincided with the largest principal strain axes calculated by *PASCal*.[6] Distortion of the Ar^{F20} substituents away from ideal geometry at the *ipso*-carbon position was also observed at higher pressures due to the evolution of unfavourable repulsive interactions with the neighbouring cation.

5.4 – Final remarks & perspectives

Through systematic substitution of the pincer ligand, weakly coordinated substrate and anion, structure-activity relationships in reactive species of $\{Rh(pincer)\}^+$ have been determined. The elongated σ-borane complexes were very well set-up from a chemical standpoint to undergo pressure-induced OA. The combination of the σ-donating PNP pincer ligand in conjunction with the π-accepting HBcat substrate resulted in complexes that crystallised as either the rhodium(I) σ-borane adduct or the rhodium(III) OA product, depending on the crystal packing effects invoked by the non-coordinating counterion. Unfortunately, the poor crystal quality and whole molecule disorder present in **15** prohibited examination of the sample by HP-XRD. The $[Rh(PNP)(HBcat)]^+$ complexes in particular highlight that chemical suitability is only one of several factors that must be considered when attempting to control organometallic chemistry in the solid-state. Other challenges include polymorphism,[7] crystal packing effects[8] and the crystallographic unsuitability of certain samples.[9] An ongoing challenge for solid-state chemists is designing systems which target specific interactions, since solid-state microenvironments can have such profound effects on complexes that are otherwise seemingly similar in solution.

It is clear that as more systematic studies on structurally related systems are carried out, the unexpected contributions of serendipity to solid-state transformations will wane as it is 'designed out' of the systems.[10] Raithby and co-workers exemplify this concept with their 'reaction cavity' theory, which predicts that photo-isomerisation reactions in the solid-state proceed more readily in larger reaction cavities.[11,12] Although other factors were acknowledged by the authors to play a part in photoconversion efficiency, their approach and methodology was heavily reliant on

extensive investigations of similar structures which informed the subsequent prediction of SC-SC transformations in likewise closely related systems through the post-rationalisation of experimental results.[11-20] Crystal engineering still has a way to go before structures can be reliably predicted and designed with any degree of certainty for specific functionality.

References

1. M. R. Gyton, T. M. Hood and A. B. Chaplin, *Dalton Trans.*, 2019, **48**, 2877-2880.
2. G. M. Adams, F. M. Chadwick, S. D. Pike and A. S. Weller, *Dalton Trans.*, 2015, **44**, 6340-6342.
3. K. Lee, H. Wei, A. V. Blake, C. M. Donahue, J. M. Keith and S. R. Daly, *Dalton Trans.*, 2016, **45**, 9774-9785.
4. S. Schlecht and J. F. Hartwig, *J. Am. Chem. Soc.*, 2000, **122**, 9435-9443.
5. C. Janiak, *J. Chem. Soc., Dalton Trans.*, 2000, 3885-3896.
6. M. J. Cliffe and A. L. Goodwin, *J. Appl. Cryst.*, 2012, **45**, 1321-1329.
7. J. P. Tidey, H. L. Wong, J. McMaster, M. Schröder and A. J. Blake, *Acta Cryst.*, 2016, **B72**, 357-371.
8. A. I. McKay, A. J. Martínez-Martínez, H. J. Griffiths, N. H. Rees, J. B. Waters, A. S. Weller, T. Krämer and S. A. Macgregor, *Organometallics*, 2018, **37**, 3524-3532.
9. J. P. Tidey, H. L. S. Wong, M. Schröder and A. J. Blake, *Coord. Chem. Rev.*, 2014, **277-278**, 187-207.
10. I. Halasz, *Cryst. Growth Des.*, 2010, **10**, 2817-2823.
11. M. R. Warren, S. K. Brayshaw, L. E. Hatcher, A. L. Johnson, S. Schiffers, A. J. Warren, S. J. Teat, J. E. Warren, C. H. Woodall and P. R. Raithby, *Dalton Trans.*, 2012, **41**, 13173-13179.
12. L. E. Hatcher and P. R. Raithby, *Acta Cryst.*, 2013, **C69**, 1448-1456.
13. L. E. Hatcher, E. J. Bigos, M. J. Bryant, E. M. MacCready, T. P. Robinson, L. K. Saunders, L. H. Thomas, C. M. Beavers, S. J. Teat, J. Christensen and P. R. Raithby, *CrystEngComm*, 2014, **16**, 8263-8271.
14. L. E. Hatcher and P. R. Raithby, *Coord. Chem. Rev.*, 2014, **277-278**, 69-79.
15. L. E. Hatcher and P. R. Raithby, *CrystEngComm*, 2017, **19**, 6297-6304.
16. L. E. Hatcher, J. M. Skelton, M. R. Warren and P. R. Raithby, *Acc. Chem. Res.*, 2019, **52**, 1079-1088.
17. L. E. Hatcher, J. M. Skelton, M. R. Warren, C. Stubbs, E. L. da Silva and P. R. Raithby, *Phys. Chem. Chem. Phys.*, 2018, **20**, 5874-5886.
18. L. E. Hatcher, M. R. Warren, D. R. Allan, S. K. Brayshaw, A. L. Johnson, S. Fuertes, S. Schiffers, A. J. Stevenson, S. J. Teat, C. H. Woodall and P. R. Raithby, *Angew. Chem. Int. Ed.*, 2011, **50**, 8371-8374.
19. M. R. Warren, S. K. Brayshaw, A. L. Johnson, S. Schiffers, P. R. Raithby, T. L. Easun, M. W. George, J. E. Warren and S. J. Teat, *Angew. Chem. Int. Ed.*, 2009, **48**, 5711-5714.
20. M. R. Warren, T. L. Easun, S. K. Brayshaw, R. J. Deeth, M. W. George, A. L. Johnson, S. Schiffers, S. J. Teat, A. J. Warren, J. E. Warren, C. C. Wilson, C. H. Woodall and P. R. Raithby, *Chem. Eur. J.*, 2014, **20**, 5468-5477.

Chapter 6 - Experimental

6.1. – General Considerations

All manipulations were performed under an atmosphere of argon using Schlenk and glove box techniques. Glassware was dried at 150 °C in an oven overnight and flame-dried under vacuum prior to use. Molecular sieves were activated by heating at 300 °C *in vacuo* overnight. Gases (argon and carbon monoxide) were purchased from BOC and used as supplied.

6.1.1 – Solvents

1,2-difluorobenzene (1,2-$C_6H_4F_2$) was purchased from Fluorochem Ltd. and was pre-dried over Al_2O_3, distilled from calcium hydride, then dried twice over 3 Å molecular sieves. Anhydrous hexane was purchased form Sigma Aldrich, sparged for two hours with argon and then stored over 3 Å molecular sieves. TMS was purchased from Sigma Aldrich, distilled from liquid Na/K_2 alloy and stored over a potassium mirror. All other anhydrous solvents were purchased from Sigma Aldrich or Acros organics, freeze-pump-thaw degassed and then stored over 3 Å molecular sieves. CD_2Cl_2 was purchased from Goss scientific in sealed ampoules, freeze-pump-thaw degassed and dried over 3 Å molecular sieves.

6.1.2 – Reagents

The compounds $Na[BAr^F_4]$,[1] PONOP,[2] PNP,[3] $Fc[BAr^F_4]$,[4] $[Rh(COD)Cl]_2$,[5] Rh(PONOP)Cl,[6] $[Rh(COD)_2][SbF_6]$,[7] $[Rh(COD)_2][BAr^F_4]$[8] and $[\{Rh(PONOP)\}_2(\mu\text{-}\eta^2\text{:}\eta^2\text{-COD})][BAr^F_4]_2$[9] were synthesised according to published procedures. HBpin and HBcat were purchased from VWR. Solutions of HBpin and HBcat were made by dissolving a known mass of the respective borane in a known volume of 1,2-$C_6H_4F_2$. The solutions were then titrated against a known concentration of COD to confirm the concentration of the borane solution. The pressure transmitting media for the HP-XRD studies (Daphne-7575, Daphne-7373 and paraffin oil) were sparged with argon and stored in an argon-filled glovebox before use. All other reagents were purchased from Sigma Aldrich or VWR and used as received.

6.1.3 – Other analyses

NMR spectra were recorded on Bruker 300 MHz, 400 MHz, 500 MHz or 600 MHz spectrometers under argon at 298 K unless otherwise stated. Chemical shifts are quoted in ppm and coupling constants in Hz. Virtual coupling constants are reported as the separation between the first and third lines.[10] All NMR spectra collected with protonated solvents were recorded and referenced to an internal capillary of C_6D_6. NMR spectra of ^{31}P and ^{11}B were referenced to external standards. ATR FTIR spectra were recorded on a Bruker Alpha spectrometer at 298 K. ESI-MS were recorded on Bruker Maxis Plus (High Res) or Agilent 6130B single Quad (Low Res) instruments. GC-MS were recorded on an Agilent 5977B (Low Res) instrument. Elemental microanalyses were performed by Elemental Microanalysis Ltd.

Cyclic voltammograms of Rh(PONOP)Cl were conducted at scan rates of 30, 50, 70 and 100 $mV \cdot s^{-1}$ in an inert atmosphere glovebox under argon using a PalmSens EmStat3+ Blue potentiostat and a 3-electrode set-up comprising a glassy carbon working electrode (CH Instruments, 3.0 mm-diameter), a coiled platinum wire counter electrode and a silver wire quasi-reference electrode. [^{n}Bu$_4$N][BAr$^F{}_4$] (^{n}Bu$_4$N$^+$ = tetrabutylammonium) was used as the electrolyte in 2 mM concentrations throughout. The potential was calibrated to the ferrocene/ferrocenium (Fc/Fc^+) redox couple. The half-wave potentials, $E_{1/2}$, were determined from: $E_{1/2} = (E_P^{red} + E_P^{ox})/2$, where E_P^{red} and E_P^{ox} are the reduction and oxidation peak potential values, respectively.

Measurements of dc magnetization of [Rh(PONOP)Cl][BAr$^F{}_4$] were made using a Quantum Design MPMS-5S SQUID (superconducting quantum interference device) magnetometer. The powder sample was immobilised in a small quantity of n-eicosane and sealed in a quartz tube. Measurements of dc magnetic susceptibility, χ_{dc}, versus temperature, *T*, were made between 2 - 300 K in zero-field-cooled warming (ZFCW) and field-cooled cooling (FCC) modes in applied fields, *H*, between 50 Oe and 5 kOe. Magnetization versus field measurements were made at fixed temperatures in magnetic fields between -50 and 50 kOe.

6.1.4 – Crystallography

Ambient pressure single crystal X-ray diffraction data for all complexes were collected on a Rigaku-Agilent SuperNova diffractometer using mirror-monochromated Cu Kα radiation (λ = 1.54180 Å) generated using a microfocus sealed X-ray tube source and detected at an Atlas S2 CCD area detector. Samples were flash-cooled to 150 K under N_2 using an Oxford Cryosystems N-Helix cryostat. Crystals were mounted onto borosilicate glass fibres using the perfluoroether *Fomblin-Y*. Unit cell measurement, data collection and data reduction were performed using the software *CrysAlisPRO*.[11] Numerical absorption correction was applied therein using Gaussian integration over multi-faceted crystal models. All structures were solved using *SHELXT*[12] and refined with *SHELXL*[13] in *Olex2*.[14]

Atomic displacements for all non-hydrogen atoms were refined as anisotropic. The σ-hydrogens of the borane ligands in structures **12-16**, **18-20**, **22** and **23** were located using the electron density difference map and refined freely. The σ-hydrogen of the free HBcat molecule in **24** was constrained to a sensible distance from the boron atom (1.17 Å).[15] All other hydrogen atoms for all structures were constrained to an idealised geometry and displacement parameters were constrained using a riding model. In structures **12-15**, CF_3 rotational disorder in $[BAr^F{}_4]^-$ was sufficiently treated by modelling the fluorine atoms of the CF_3 groups over two sites and restraining the 1,2- C–F and 1,3- C–F and F–F positions to be alike. A rigid body was applied to the whole anion and atomic displacement parameter (ADP) restraints were applied, where appropriate, to select CF_3 groups to better model the disorder.

Disorder of the first chlorocyclohexane ligand in **5** was treated by modelling the ligand over two sites then restraining the 1,2- C–Cl and C–C distances to be alike. Disorder of the second chlorocyclohexane ligand was treated by splitting the second ligand over two sites so that each component was fixed to 0.5 occupancy, then restraining the 1,2- C–Cl and C–C distances to be alike. Disorder of all DCE and Cl^{i}Pr ligands in **8** and **9**, respectively, were treated by modelling the respective ligands over two sites then restraining all 1,2- Rh–Cl, C–Cl and C–C distances to be alike. Where appropriate, ADP restraints were then applied to the disorder components. Disorder of the chlorobenzene ligand in **1** was treated by modelling the arene ring over two sites, restraining the 1,2- C–Cl distances to be alike and constraining each arene ring to an

idealised geometry. ADP restraints were applied to each disorder component of the chlorobenzene ligand. Disorder of the cation in **15** was treated by modelling all non-hydrogen atoms over two sites and restraining all 1,2- Rh–P, Rh–B, Rh–N, P–C, B–O, C–C and C–O distances to similarity in each disorder component. The entire structure was modelled as a rigid body. The HBcat ligands were additionally restrained to planarity. ADP restraints were then applied to each disorder component, as well as strong ADP restraints to all coordinated B and H atoms. Disorder of the HBpin ligands in structures **14** and **22** were each treated by modelling all non-hydrogen atoms of the borane ligand except for the B atom over two sites and restraining the 1,2- B–O, C–O and C–C distances to be alike. ADP restraints were applied therein to each disorder component.

6.2 – Data related to Chapter 2

NMR scale reaction of [{Rh(PONOP)}$_2$(COD)][BAr$^F{}_4$]$_2$ with ClPh

ClPh (0.5 mL) was added to a J. Young's valve NMR tube charged with [{Rh(PONOP)}$_2$(COD)][BAr$^F{}_4$]$_2$ (14.1 mg, 5.0 μmol) at room temperature. The resulting orange homogenous solution was analysed *in situ* using ^{1}H and ^{31}P NMR spectroscopy, with constant mixing at room temperature when not in the spectrometer. Liberation of COD and formation of [Rh(PONOP)(κ$_{Cl}$-ClPh)][BAr$^F{}_4$] (**1**; δ_{31P} 203.0 (d, $^1J_{RhP}$ = 136)) was observed, with a 5:1 equilibrium mixture of **1** and [Rh(PONOP)(η^2-COD)][BAr$^F{}_4$] (δ_{31P} 202.3 (d, $^1J_{RhP}$ = 135))[9] obtained after 6 hours.

Preparation of [Rh(PONOP)(κ$_{Cl}$-ClPh)][BAr$^F{}_4$], 1

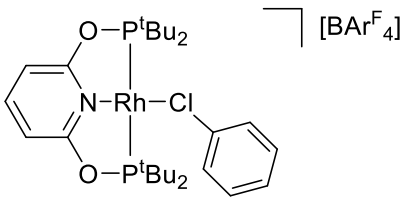

ClPh (10 mL) was added to a flask charged with [{Rh(PONOP)}$_2$(COD)][BAr$^F{}_4$]$_2$ (100.7 mg, 35.5 μmol) at room temperature with vigorous stirring. The resulting orange solution was left to stand for 18 h at room temperature and the analytically pure

material obtained as orange crystals after two consecutive crystallisations from ClPh and hexane by liquid-liquid diffusion at room temperature. Yield: 77.4 mg (52.4 µmol, 74%). Crystals grown in this way were suitable for analysis by X-ray diffraction.

^{1}H NMR (400 MHz, ClPh; selected data): δ 8.04 – 8.10 (m, 8H, Ar^{F}), 7.43 (br, 4H, Ar^{F}), 6.12 (d, $^{3}J_{HH}$ = 8.1, 2H, 3-py), 0.91 (vt, J_{PH} = 14.7, 36H, ^{t}Bu). No paramagnetic signals observed in the range -50 – +50 ppm.

^{31}P{^{1}H} NMR (162 MHz, ClPh): δ 203.0 (d, $^{1}J_{RhP}$ = 138).

LR ESI-MS: only $[Rh(PONOP)(N_2)]^+$ was observed (m/z = 530.3, calc. = 530.2).

Anal. Calcd for $C_{59}H_{56}BClF_{24}NO_2P_2Rh$ (1478.18 gmol^{-1}): C, 47.94; H, 3.82; N, 0.95. Found: C, 48.16; H, 3.84; N, 1.00.

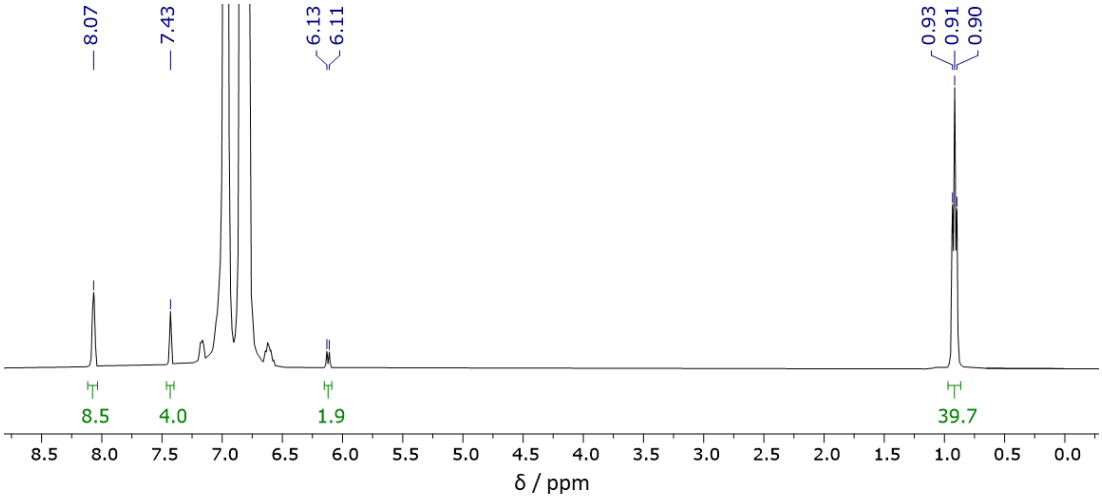

Figure 6.1 – ^{1}H NMR spectrum of **1** (400 MHz, ClPh, 298 K, light).

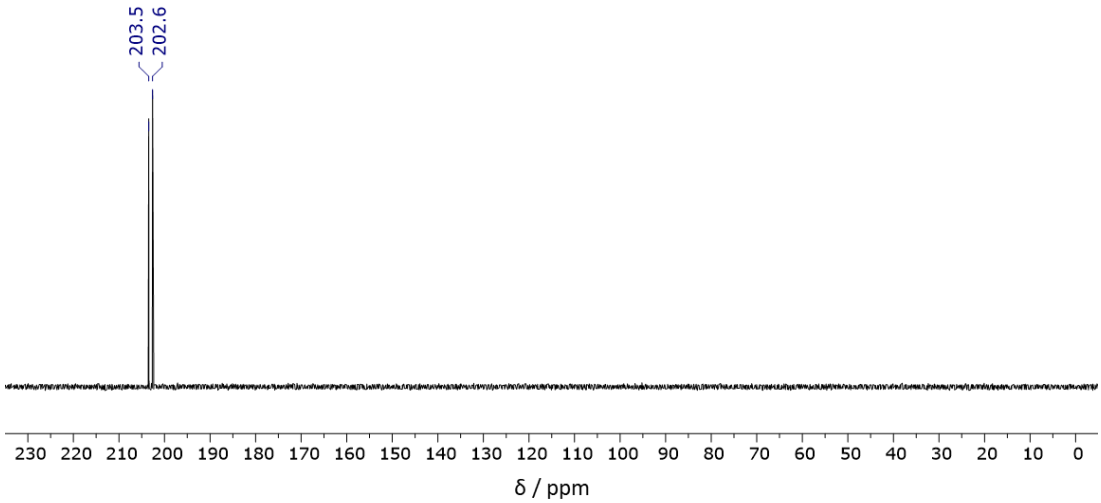

Figure 6.2 – ^{31}P{^{1}H} NMR spectrum of **1** (162 MHz, ClPh, 298 K, light).

Preparation of [Rh(PONOP)(Ph)Cl][BAr$^{F}_{4}$], 2

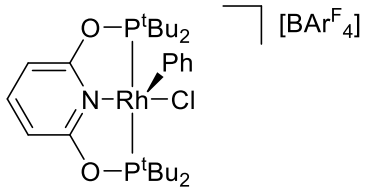

A 20 mM solution of **1** in ClPh (0.5 mL) was prepared *in situ* as described above. Volatiles were removed *in vacuo* and the analytically pure product obtained as dark orange crystals following recrystallisation from CH_2Cl_2 and pentane by liquid-liquid diffusion at 5 °C. Yield: 8.9 mg (6.0 µmol, 60%). Crystals suitable for analysis by X-ray diffraction were grown from ClPh and hexane by liquid-liquid diffusion at room temperature.

^{1}H NMR (500 MHz, CD_2Cl_2): δ 8.10 (t, $^3J_{HH}$ = 8.2, 1H, 4-py), 8.04 (br d, $^3J_{HH}$ = 7.0, 1H, *o*-Ph), 7.70 – 7.76 (m, 8H, Ar^F), 7.56 (br, 4H, Ar^F), 7.17 (d, $^3J_{HH}$ = 8.2, 2H, 3-py), 6.91–6.98 (m, 2H, *m*-Ph+*p*-Ph), 6.53 (ddt, $^3J_{HH}$ = 9.1, 6.5, $^4J_{HH}$ = 3.3, 1H, *m*-Ph), 5.01 (dt, $^3J_{HH}$ = 8.6, $^4J_{HH}$ = 2.5, 1H, *o*-Ph), 1.46 (vt, J_{PH} = 15.5, 18H, ^{t}Bu), 1.07 (vt, J_{PH} = 16.5, 18H, ^{t}Bu). No paramagnetic signals observed in the range -50 – +50 ppm.

^{13}C{^{1}H} NMR (126 MHz, CD_2Cl_2): δ 164.5 (s, 2-py), 162.2 (q, $^1J_{BC}$ = 50, Ar^F), 147.6 (s, 4-py), 141.8 (dt, $^1J_{RhC}$ = 34, $^2J_{PC}$ = 4, *i*-Ph), 139.9 (br, *o*-Ph), 135.2 (s, Ar^F), 132.0 (br, *o*-Ph), 130.8 (s, *m*-Ph), 129.5 (s, *m*-Ph), 129.3 (qq, $^2J_{FC}$ = 32, $^3J_{CB}$ = 3, Ar^F), 127.7 (s, *p*-Ph), 125.0 (q, $^1J_{FC}$ = 272, Ar^F), 117.9 (sept, $^3J_{FC}$ = 4, Ar^F), 106.7 (vt, J_{PC} = 4, 3-py), 44.2 (vt, J_{PC} = 10, *t*Bu{C}), 43.3 (vtd, $^1J_{PC}$ = 10, $^2J_{RhC}$ = 2, ^{t}Bu{C}), 28.3 (vt, J_{PC} = 5, ^{t}Bu{CH_3}), 27.7 (vt, J_{PC} = 5, ^{t}Bu{CH_3}).

^{31}P{^{1}H} NMR (162 MHz, CD_2Cl_2): δ 182.8 (d, $^1J_{RhP}$ = 103).

HR ESI-MS (positive ion 4 kV): 614.1580 ([*M*]$^+$, calcd 614.1585) *m/z*.

Anal. Calcd for $C_{59}H_{56}BClF_{24}NO_2P_2Rh$ (1478.18 gmol^{-1}): C, 47.94; H, 3.82; N, 0.95. Found: C, 48.25; H, 3.83; N, 1.00.

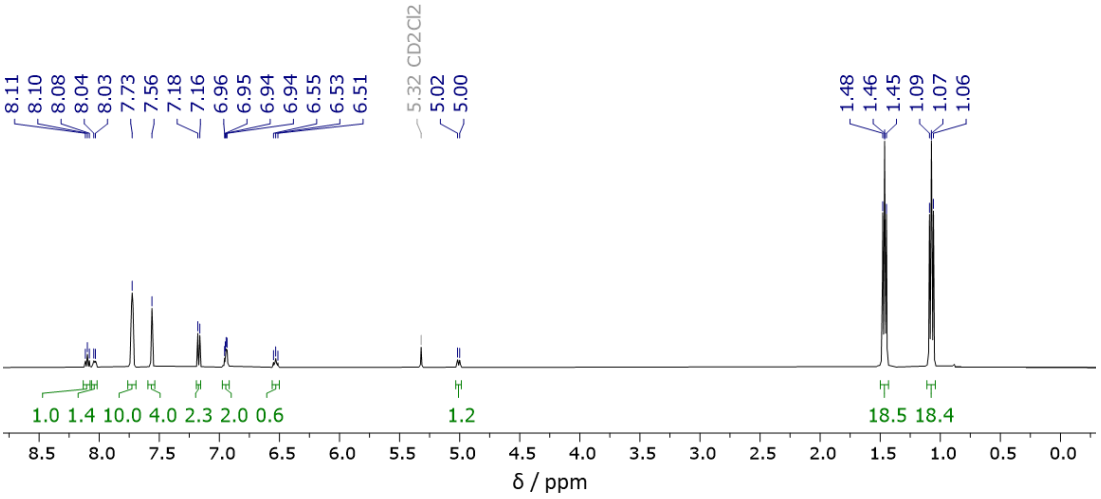

Figure 6.3 – ^{1}H NMR spectrum of **2** (500 MHz, CD_2Cl_2, 298 K, light).

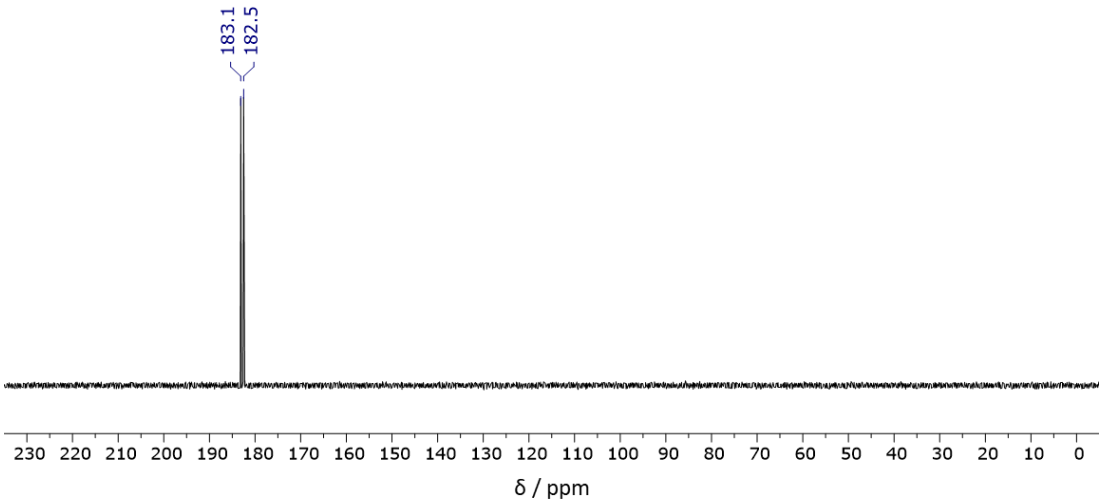

Figure 6.4 – $^{31}P\{^{1}H\}$ NMR spectrum of **2** (162 MHz, CD_2Cl_2, 298 K, light).

Preparation of [Rh(PONOP)(κ$_{Cl}$-ClCH$_2$Cl)][BAr$^F_4$], A

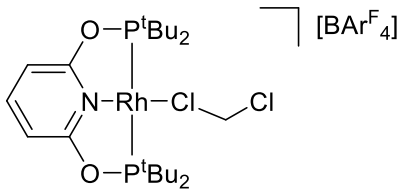

CH_2Cl_2 (1.0 mL) was added to a flask charged with **1** (34.8 mg, 23.6 µmol) in the light at room temperature. The resulting orange solution was left to stand for 5 min at room temperature. Analytically pure material was obtained as orange crystals upon

crystallisation from CH_2Cl_2 and hexane by liquid-liquid diffusion at room temperature. Yield: 29.2 mg (20.1 µmol, 86 %). Spectroscopic data are in agreement with data reported in the literature for this compound.[16] Use of paramagnetic ^{1}H NMR spectroscopy in the dark confirmed that < 1% [Rh(PONOP)Cl][BAr^F_4], **4**, was present. Instantaneous exchange of coordinated dichloromethane, resulting in the liberation of CH_2Cl_2 and formation of **d$_2$-A**, was apparent upon dissolution of **A** in CD_2Cl_2 by ^{1}H NMR spectroscopy.

^{1}H NMR (500 MHz, CD_2Cl_2): δ 7.73 (obscured t, $^3J_{HH}$ = 8.1, 1H, 4-py), 7.70 – 7.74 (m, 8H, Ar^F), 7.56 (br, 4H, Ar^F), 6.73 (d, $^3J_{HH}$ = 8.1, 2H, 3-py), 1.43 (vt, J_{PH} = 15.2, 36H, ^{t}Bu). Coordinated CH_2Cl_2 was not observed, due to rapid ligand exchange.

^{31}P{^{1}H} NMR (161 MHz, CD_2Cl_2): δ 204.5 (d, J_{RhP} = 136).

Characterisation of [Rh(PONOP)(CH_2Cl)Cl][BAr^F_4], 3

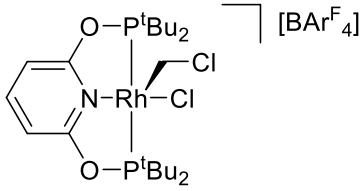

A 50 mM solution of **A** was prepared within a J. Young's valve NMR tube in the dark by dissolution of **1** (36.4 mg, 24.6 µmol) in CH_2Cl_2 (0.5 mL). The resulting orange solution was heated at 50 °C in the dark and periodically monitored *in situ* using ^{1}H and ^{31}P NMR spectroscopy. The spectra were collected at room temperature and the samples were kept in the dark during transport to and from the spectrometer. After heating for 96 h, **3** and [Rh(PONOP)Cl][BAr^F_4], **4**, were observed in an approximate 9:1 ratio by NMR spectroscopy. Recrystallisation from CH_2Cl_2 and hexane by liquid-liquid diffusion in the dark afforded 29.5 mg of dark orange crystals. Analysis of the sample in CD_2Cl_2 in the dark by ^{1}H, ^{13}C and ^{31}P NMR spectroscopy indicated co-crystallisation of **3** and **4** in a 9:1 ratio. Single crystals of **3** suitable for analysis by X-ray diffraction were able to be isolated from the mixture by crystallisation via liquid-liquid diffusion of CH_2Cl_2 into hexane in the dark at -30 °C.

Selected data for **3**:

^{1}H NMR (500 MHz, CD_2Cl_2, selected data): δ 7.99 (t, $^{3}J_{HH}$ = 8.2, 1H, py), 7.69 – 7.74 (m, 8H, Ar^F), 7.55 (br, 4H, Ar^F), 7.05 (d, $^{3}J_{HH}$ = 8.2, 2H, py), 5.65 (dt, $^{3}J_{PH}$ = 6.8, $^{2}J_{RhH}$ = 3.4, 2H, CH_2Cl), 1.64 (vt, J_{PH} = 16.1, 18H, ^{t}Bu), 1.43 (vt, J_{PH} = 15.6, 18H, ^{t}Bu).

^{13}C{^{1}H} NMR (126 MHz, CD_2Cl_2, selected data): δ 164.2 (s, 2-py), 162.2 (q, $^{1}J_{BC}$ = 50, Ar^F), 147.5 (s, 4-py), 135.2 (s, Ar^F), 129.3 (qq, $^{2}J_{FC}$ = 32, $^{3}J_{CB}$ = 3 Ar^F), 125.0 (q, $^{1}J_{FC}$ = 272, Ar^F), 117.9 (sept, $^{3}J_{FC}$ = 4, Ar^F), 106.4 (vt, J_{PC} = 5, 3-py), 48.0 (dt, $^{1}J_{RhC}$ = 30, $^{2}J_{PC}$ = 5, CH_2Cl), 43.9 (vt, $^{1}J_{PC}$ = 10, ^{t}Bu{C}), 42.7 (vtd, J_{PC} = 10, $^{2}J_{RhC}$ = 2, ^{t}Bu{C}), 28.3 (vt, J_{PC} = 6, ^{t}Bu{CH_3}), 28.2 (vt, J_{PC} = 6, ^{t}Bu{CH_3}).

^{31}P{^{1}H} NMR (162 MHz, CD_2Cl_2, selected data): δ 182.0 (d, J_{RhP} = 104).

HR ESI-MS (positive ion 4 kV): 586.1034 ($[M]^+$, calcd 586.1039) *m/z*.

Data for the 9:1 **3**:**2** mixture:

Anal. Calcd for $(C_{54}H_{53}BCl_2F_{24}NO_2P_2Rh)_{0.9}(C_{53}H_{51}BClF_{24}NO_2P_2Rh)_{0.1}$ (1445.60 $gmol^{-1}$): C, 44.78; H, 3.68; N, 0.97. Found: C, 45.06; H, 3.61; N, 1.05.

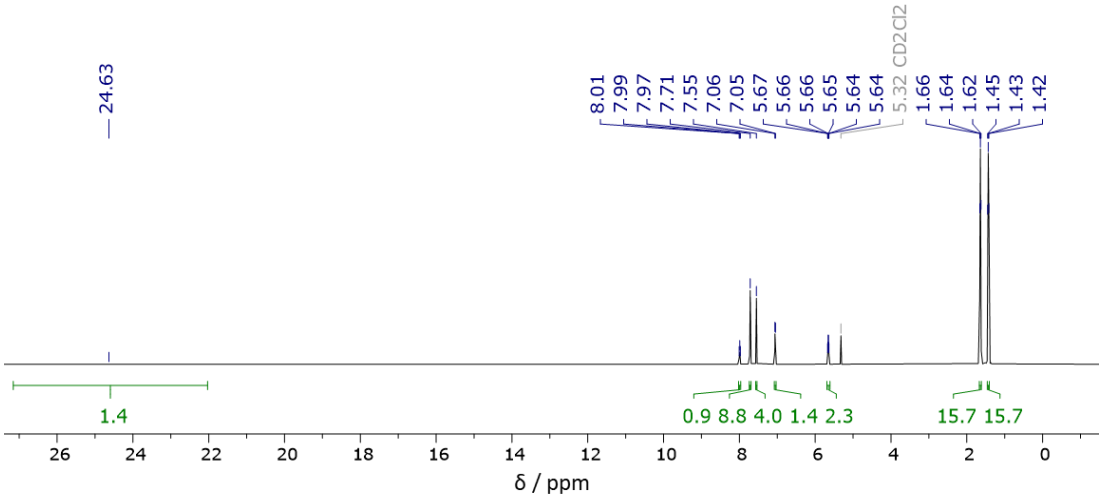

Figure 6.5 – ^{1}H NMR spectrum of the 9:1 ratio of **3:4** (500 MHz, CD_2Cl_2, 298 K, dark).

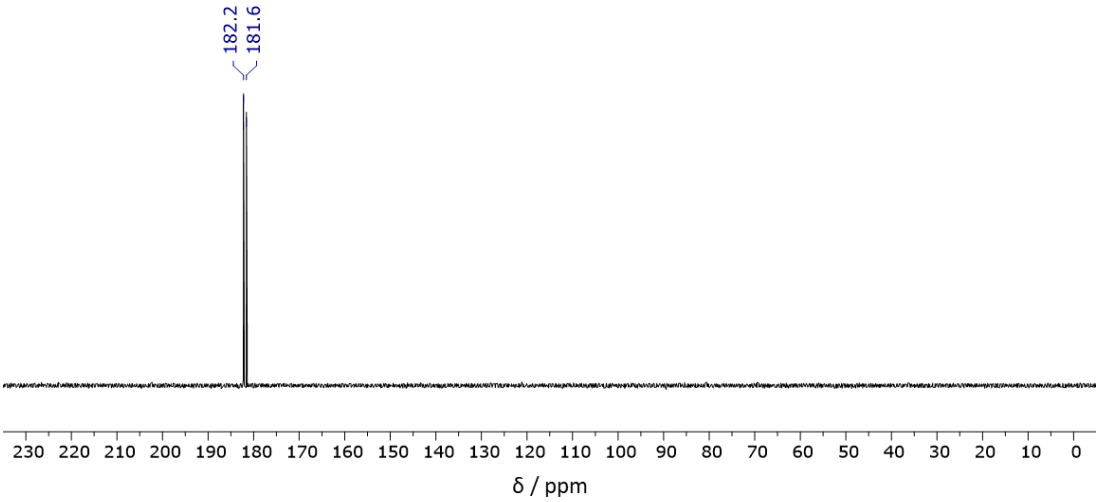

Figure 6.6 – $^{31}P\{^{1}H\}$ NMR spectrum of the 9:1 ratio of **3:4** (162 MHz, CD_2Cl_2, 298 K, dark).

Preparation of [Rh(PONOP)Cl][BAr$^F_4$], 4

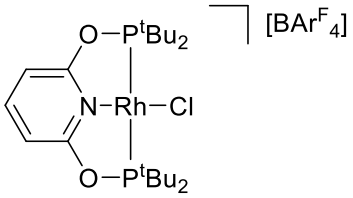

To a flask charged with [Rh(PONOP)Cl] (30.0 mg, 55.7 μmol) and Fc[BAr$^F_4$] (55.6 mg, 52.9 μmol) was added 1,2-$C_6H_4F_2$ (2 mL). The resulting dark green solution was stirred at room temperature for 1 h before volatiles were removed *in vacuo*. The residue was washed with hexane (2 × 5 mL) and then dried *in vacuo*. Recrystallisation from CH_2Cl_2 and hexane by liquid-liquid diffusion at room temperature afforded the analytically pure product as purple crystals. Yield: 35.4 mg (25.3 μmol, 48%). Crystals grown in this way were suitable for analysis by X-ray diffraction.

^{1}H NMR (400 MHz, CD_2Cl_2): δ 24.71 (vbr, fwhm = 600 Hz, 36H, *t*Bu), 7.64 – 7.75 (m, 8H, Ar^F), 7.46 (br, 4H, Ar^F), 1.59 (vbr, fwhm = 60 Hz, 2H, 3-py), -17.17 (vbr, fwhm = 110 Hz, 1H, 4-py).

^{31}P{^{1}H} NMR (162 MHz, CD_2Cl_2): no resonances observed between δ -600 and +600.

HR ESI-MS (positive ion 4 kV): not sufficiently stable under the analysis conditions employed.

Magnetic moment (Evan's method; 20.83 mM, 298 K, 400 MHz): $\Delta f = 60.1$ Hz, $\mu_{eff} = 2.33\ \mu_B$ (spin only approximation for n = 1: 1.73 μ_B).

Anal. Calcd for $C_{53}H_{51}BClF_{24}NO_2P_2Rh$ (1401.07 $gmol^{-1}$): C, 45.44; H, 3.67; N, 1.00. Found: C, 45.59; H, 3.67; N, 1.03.

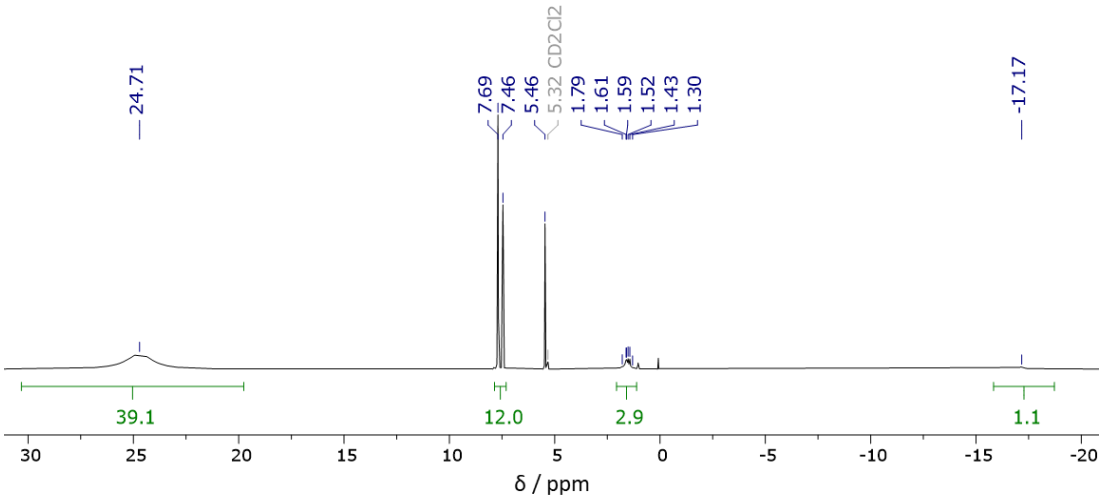

Figure 6.7 – ^{1}H NMR spectrum of **4** (400 MHz, CD_2Cl_2, 298 K, light).

Preparation of [Rh(PONOP)(κ$_{Cl}$-ClCy)][BAr$^F{}_4$], 5

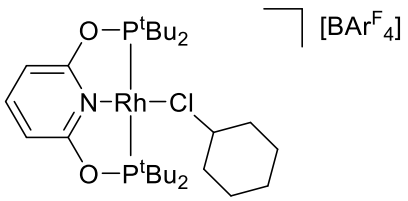

ClCy (0.5 mL) was added to a flask charged with **1** (18.4 mg, 12.5 µmol) at room temperature and left to stand at room temperature for 5 minutes before all volatiles were removed *in vacuo* to afford the analytically pure product as a yellow powder. Yield: 14.6 mg (9.8 µmol, 79%). The presence or absence of light did not affect the reaction. Crystals suitable for analysis by X-ray diffraction were grown from ClCy and hexane by liquid-liquid diffusion at room temperature.

^{1}H NMR (400 MHz, ClCy, selected peaks): δ 7.82 – 7.88 (m, 8H, Ar^F), 7.77 (t, $^3J_{HH}$ = 8.2, 1H, 4-py), 7.60 (br, 4H, Ar^F), 6.78 (d, $^3J_{HH}$ = 8.2, 2H, 3-py). No paramagnetic signals observed in the range -50 – +50 ppm.

^{31}P{^{1}H} NMR (162 MHz, ClCy): δ 204.5 (d, J_{RhP} = 138).

LR ESI-MS: only $[Rh(PONOP)(N_2)]^+$ was observed (m/z = 530.2, calc. = 530.2).

Anal. Calcd for $C_{59}H_{62}BClF_{24}NO_2P_2Rh \cdot C_6H_{11}Cl$ (1602.83 $gmol^{-1}$): C, 48.71; H, 4.59; N, 0.87. Found: C, 49.09; H, 4.53; N, 0.96.

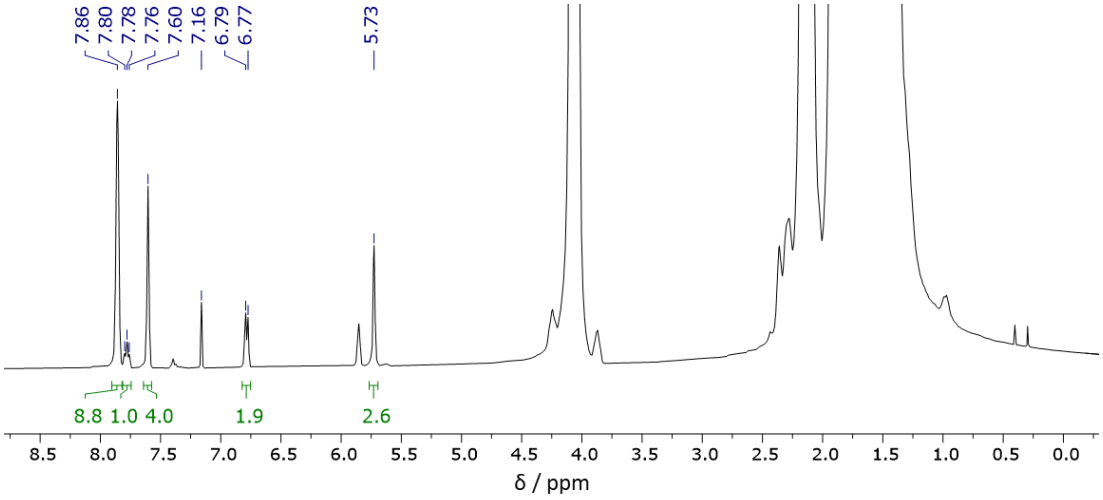

Figure 6.8 – ^1H NMR spectrum of **5** (400 MHz, ClCy, 298 K, light).

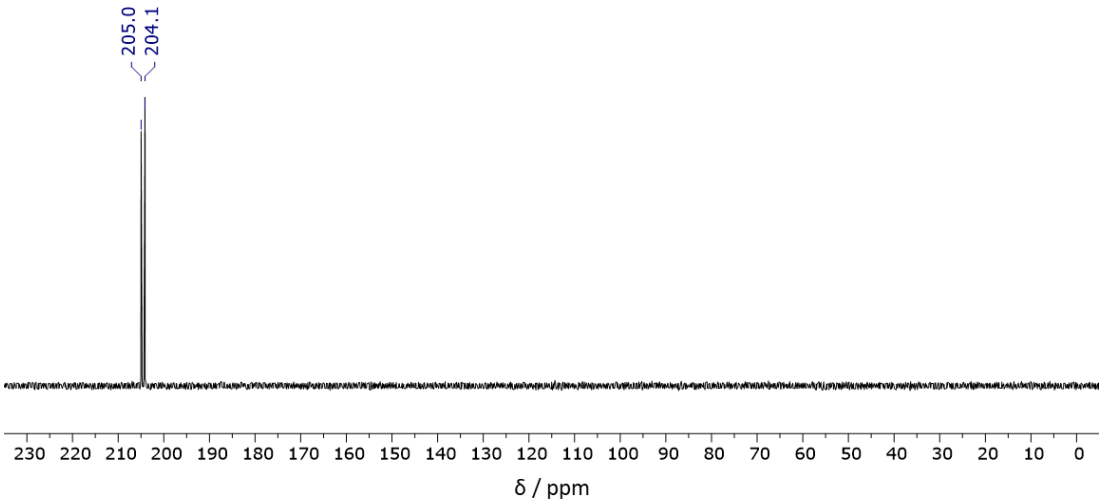

Figure 6.9 – $^{31}P\{^1H\}$ NMR spectrum of **5** (162 MHz, ClCy, 298 K, light).

Preparation of [Rh(PONOP)(H)Cl][BAr$^F_4$], 6

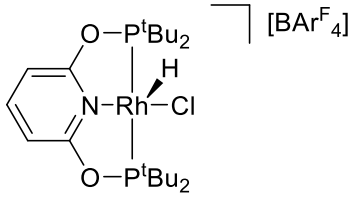

^{t}BuCl (1 mL) was added in the dark at room temperature to a flask charged with **1** (29.6 mg, 20.0 µmol). The complex [Rh(PONOP(κ$_{Cl}$-Cl^{t}Bu)][BAr$^F_4$], **7**, was not observed spectroscopically or otherwise. The solution was left to stand for 5 min before all volatiles were removed under vacuum. Recrystallisation from CH_2Cl_2 and hexane by liquid-liquid diffusion at room temperature in the dark afforded the analytically pure product as yellow crystals. Yield: 24.3 mg (17.3 µmol, 87%). Crystals grown in this way were suitable for analysis by X-ray diffraction.

^{1}H NMR (500 MHz, CD_2Cl_2): δ 7.96 (t, $^3J_{HH}$ = 8.2, 1H, 4-py), 7.68 – 7.74 (m, 8H, Ar^F), 7.55 (br, 4H, Ar^F), 7.01 (d, $^3J_{HH}$ = 8.3, 2H, 3-py), 1.50 (vt, J_{PH} = 16.3, 18H, ^{t}Bu), 1.46 (vt, J_{PH} = 16.8, 18H, ^{t}Bu), -26.25 (dt, $^1J_{RhH}$ = 41.9, $^2J_{PH}$ = 10.1, 1H, RhH).

^{13}C{^{1}H} NMR (126 MHz, CD_2Cl_2): δ 164.8 (vt, J_{PC} = 8, 2-py), 162.2 (q, $^1J_{BC}$ = 50, Ar^F), 147.1 (s, 4-py), 135.2 (s, Ar^F), 129.3 (qq, $^2J_{FC}$ = 32, $^3J_{CB}$ = 3, Ar^F), 125.0 (q, $^1J_{FC}$ = 272, Ar^F), 117.9 (sept, $^3J_{FC}$ = 4, Ar^F), 105.6 (vt, J_{PC} = 5, py), 43.0 (vt, J_{PC} = 12, ^{t}Bu{C}), 40.8 (vtd, $^1J_{PC}$ = 14, $^2J_{RhC}$ = 2, *t*Bu{C}), 27.17 (vt, J_{PC} = 6, ^{t}Bu{CH_3}), 27.15 (vt, J_{PC} = 6, ^{t}Bu{CH_3}).

^{31}P{^{1}H} NMR (162 MHz, CD_2Cl_2): δ 197.7 (d, $^1J_{RhP}$ = 100).

HR ESI-MS (positive ion 4 kV): not sufficiently stable under the analysis conditions employed.

Anal. Calcd for $C_{53}H_{52}BClF_{24}NO_2P_2Rh$ (1402.08 $gmol^{-1}$): C, 45.40; H, 3.74; N, 1.00. Found: C, 45.54; H, 3.80; N, 1.04.

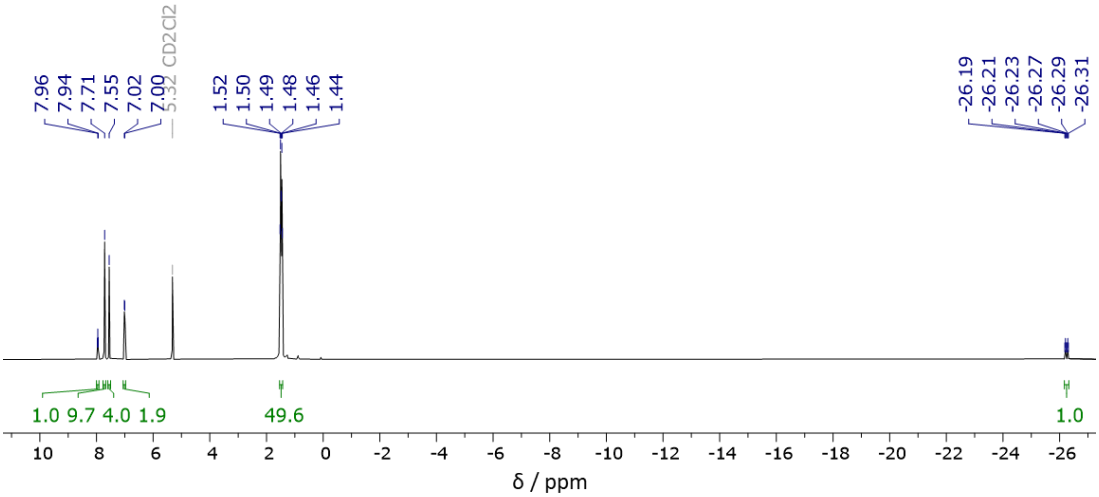

Figure 6.10 – ^{1}H NMR spectrum of **6** (500 MHz, CD_2Cl_2, 298 K, dark).

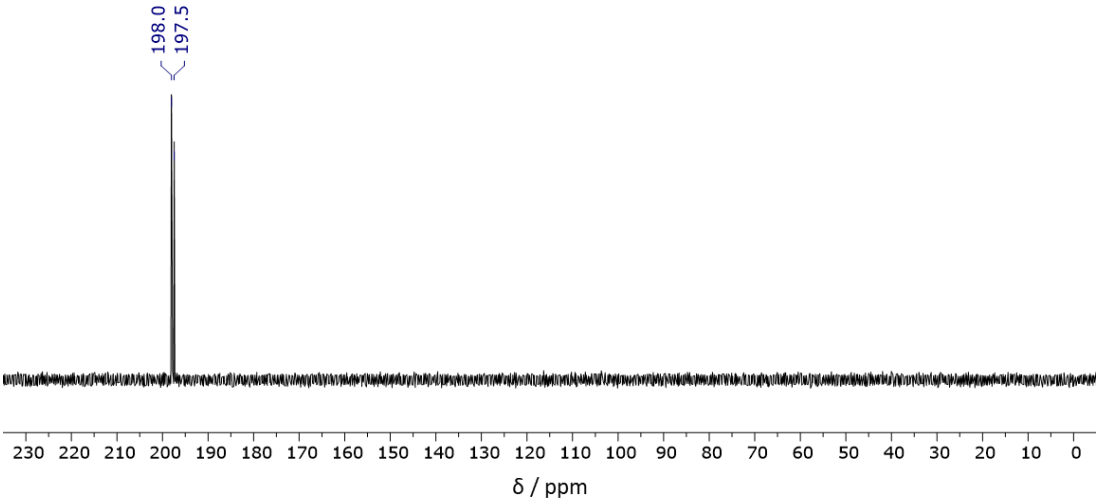

Figure 6.11 – $^{31}P\{^{1}H\}$ NMR spectrum of **6** (162 MHz, CD_2Cl_2, 298 K, dark).

Preparation of [Rh(PONOP)(κCl-ClCH$_2$CH$_2$Cl)][BAr$^F_4$], 8

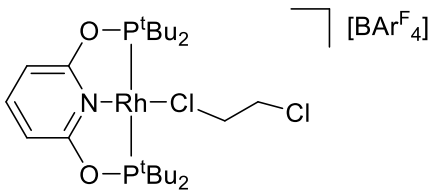

DCE (0.5 mL) was added to a flask charged with **1** (17.4 mg, 11.8 µmol) at room temperature. The resulting orange solution was left to stand at room temperature for 5 minutes before the volatiles were removed *in vacuo* to afford the analytically pure product as a yellow powder. Yield: 14.6 mg (10.0 µmol, 85%). The presence or absence of light did not affect the reaction. Crystals suitable for analysis by X-ray diffraction were grown from DCE and hexane by liquid-liquid diffusion at room temperature.

^{1}H NMR (400 MHz, DCE, selected peaks): δ 7.64 – 7.66 (m, 8H, Ar^F), 7.59-7.62 (obscured t, 1H, 4-py), 7.44 (br, 4H, Ar^F), 6.59 (d, $^3J_{HH}$ = 8.1, 2H, 3-py), 1.29 (vt, J_{PH} = 15.1, 36H, ^{t}Bu). No paramagnetic signals observed in the range -50 – +50 ppm.

^{31}P{^{1}H} NMR (162 MHz, DCE): δ 203.7 (d, J_{RhP} = 136).

LR ESI-MS: only [Rh(PONOP)(N$_2$)]$^+$ was observed (m/z = 530.4, calc. = 530.2).

m.p.: 171-174 °C

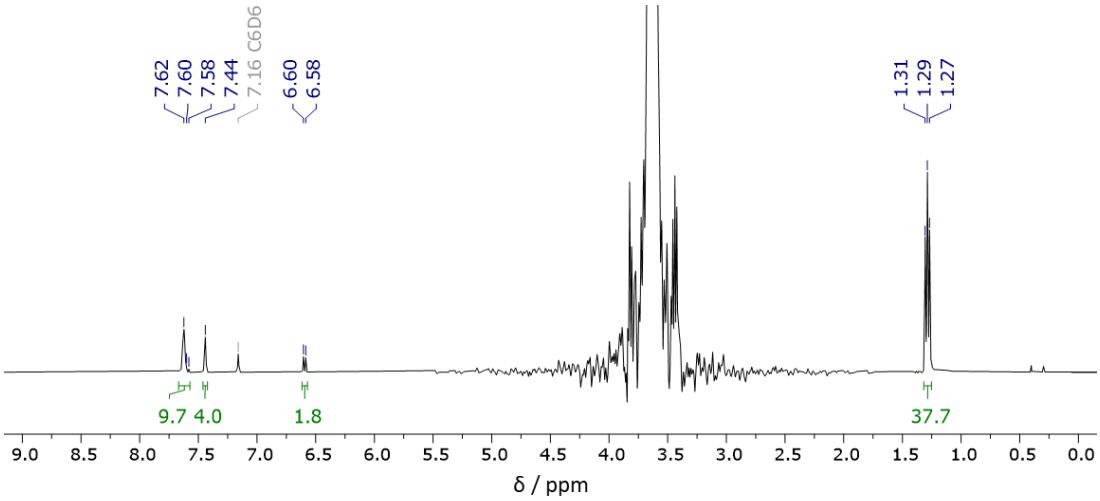

Figure 6.12 – ^{1}H NMR spectrum of **8** (400 MHz, DCE, 298 K, light).

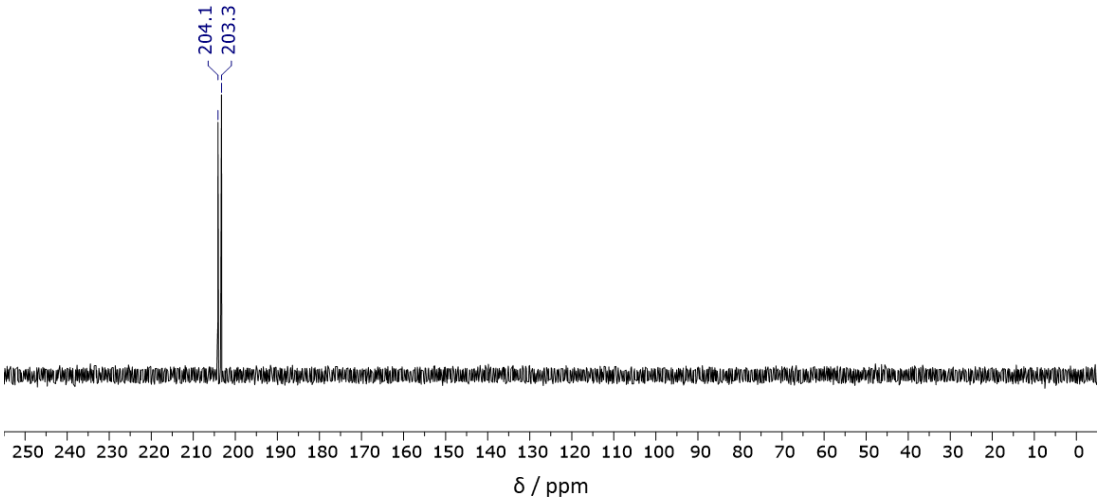

Figure 6.13 – $^{31}P\{^{1}H\}$ NMR spectrum of **8** (162 MHz, DCE, 298 K, light).

Preparation of [Rh(PONOP)(κ$_{Cl}$-Cl^{i}Pr)][BAr$^{F}_{4}$], 9

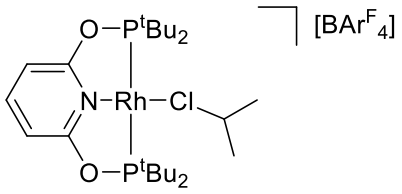

Cl^{i}Pr (0.5 mL) was added to a flask charged with **1** (17.2 mg, 11.6 µmol) at room temperature. The resulting orange solution was left to stand at room temperature for 5 minutes before the volatiles were removed *in vacuo* to afford the analytically pure product as a yellow powder. Yield: 13.2 mg (9.2 µmol, 79 %). The presence or absence of light did not affect the reaction. Crystals suitable for analysis by X-ray diffraction were grown via liquid-liquid diffusion of Cl^{i}Pr into hexane at room temperature.

^{1}H NMR (400 MHz, Cl^{i}Pr, selected peaks): δ 8.17-8.20 (obscured t, 1H, 4-py), 8.14-8.19 (m, 8H, Ar^{F}), 7.94 (br, 4H, Ar^{F}), 7.14 (d, $^{3}J_{HH}$ = 8.2, 2H, 3-py). No paramagnetic signals observed in the range -50 – +50 ppm.

^{31}P{^{1}H} NMR (162 MHz, Cl^{i}Pr): δ 204.7 (d, J_{RhP} = 139).

LR ESI-MS: only [Rh(PONOP)(N$_2$)]$^{+}$ was observed (m/z = 530.5, calc. = 530.2).

m.p.: 178-181 °C

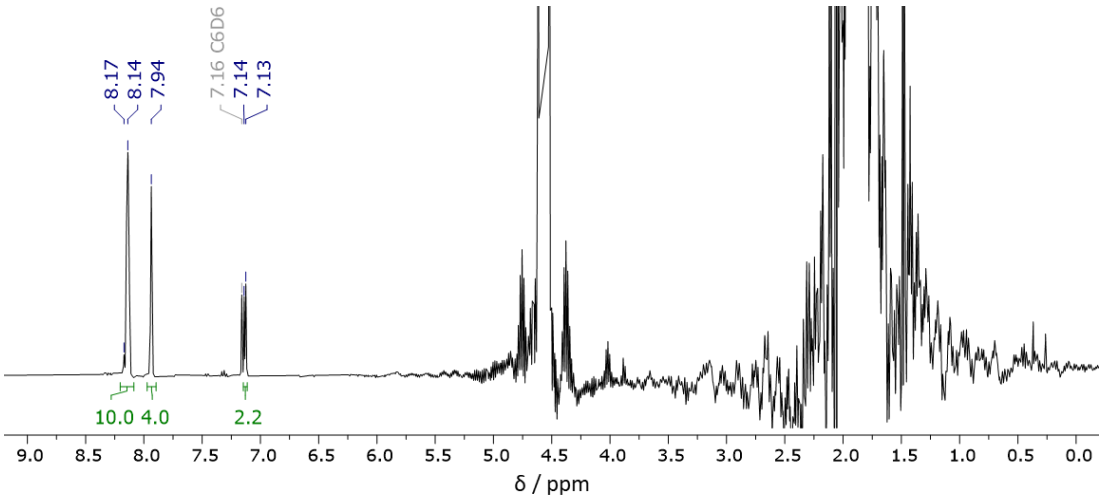

Figure 6.14 – ^{1}H NMR spectrum of **9** (400 MHz, Cl^{i}Pr, 298 K, light).

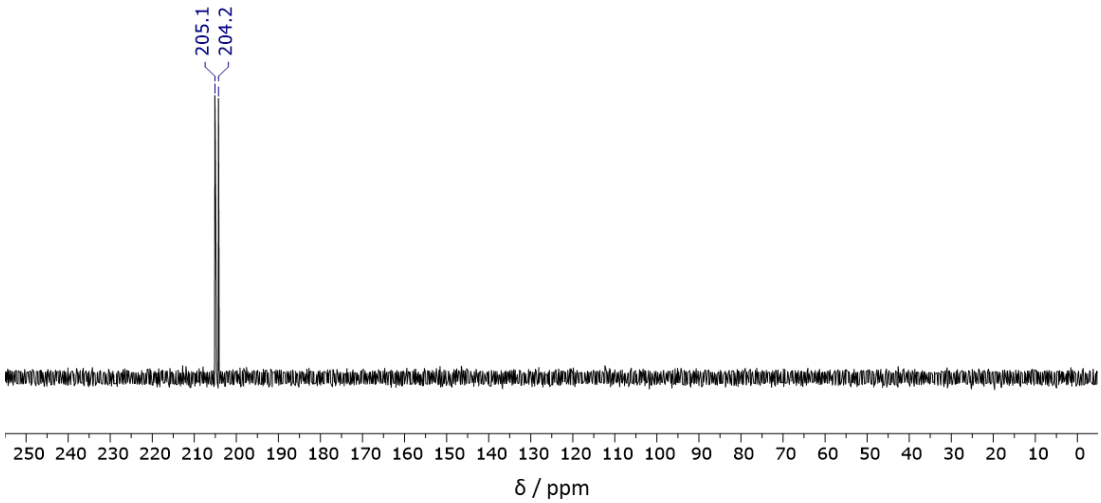

Figure 6.15 – ^{31}P{^{1}H} NMR spectrum of **9** (162 MHz, Cl^{i}Pr, 298 K, light).

NMR scale reactions of 1

Reactions were performed within J. Young's valve NMR tubes using 20 mM solutions of **1** (14.8 mg, 10.0 µmol) in the respective solvent (0.5 mL) and monitored *in situ* using ^{1}H and ^{31}P NMR spectroscopy. Solutions of **1** were stable in ClPh at room temperature for 72 h both in the presence and the absence of light (orange solutions).

Stability of 1 at 125 °C in ClPh

Heating **1** in ClPh at 125 °C for 96 h in either the light or the dark resulted in quantitative formation of [Rh(PONOP)(Ph)Cl][BAr^F_4] (**2**; δ_{31P} 182.5 (d, $^1J_{RhP}$ = 103); dark orange solution). Upon removal of the solvent and dissolution in CD_2Cl_2, no biphenyl was observed by ^{1}H NMR spectroscopy.

Stability of 1 at 125 °C in ClPh in the presence of TEMPO.

Heating a solution of **1** (14.8 mg, 10 µmol) and TEMPO (1.6 mg, 10 µmol) in ClPh at 125 °C for 24 h in the dark resulted in the formation of [Rh(PONOP)(Ph)Cl][BAr^F_4] (**2**; δ_{31P} 182.5 (d, $^1J_{RhP}$ = 103); dark orange solution) in approximately 40 % yield. No paramagnetic signals were observed by ^{1}H NMR spectroscopy.

NMR scale reactions of 2

Stability of 2 in the presence of TEMPO in CD_2Cl_2

CD_2Cl_2 (0.5 mL) was added to a J. Young's valve NMR tube charged with **2** (14.8 mg, 10.0 µmol) and TEMPO (1.6 mg, 10.2 µmol) at room temperature in the dark. The solution remained orange in colour and no onward reactivity with TEMPO was apparent from analysis *in situ* using ^{1}H and ^{31}P NMR spectroscopy after 24 h in the dark at room temperature. The same outcome was observed when the same solution was subsequently exposed to light for 24 h at room temperature.

NMR scale reactions of A / d_2-A

Stability of d_2-A at room temperature in CD_2Cl_2

20 mM solutions of **d_2-A** (14.5 mg, 10.0 µmol) in CD_2Cl_2 (0.5 mL) were prepared within J. Young's valve NMR tubes in the presence and absence of light, and thereafter monitored *in situ* using ^{1}H and ^{31}P NMR spectroscopy. In the dark, standing at room temperature for 24 h resulted in partial conversion (3%) of **d_2-3** into [Rh(PONOP)(CD_2Cl)Cl][BAr^F_4] (**d_2-3**; δ_{31P} 182.0 (d, $^1J_{RhP}$ = 104)); orange solution).

No onward reaction of **d$_2$-3** was apparent upon standing at room temperature for 24 h in the light (orange solution). Similar reactivity was observed for solutions of **A**.

Stability of d$_2$-A at 50 °C in CD_2Cl_2

A 20 mM solution of **d$_2$-A** (14.5 mg, 10.0 μmol) in CD_2Cl_2 (0.5 mL) was prepared within a J. Young's valve NMR tube in dark, heated at 50 °C in the dark, and periodically monitored *in situ* using ^{1}H and ^{31}P NMR spectroscopy at room temperature in the dark. After heating for 96 h, **d$_2$-A** was completely consumed and [Rh(PONOP)(CD_2Cl)Cl][BAr^F_4] (**d$_2$-3**; δ_{31P} 182.0 (d, $^1J_{RhP}$ = 104)) and [Rh(PONOP)Cl][BAr^F_4] (**4**; δ_{1H} 24.56 (vbr, fwhm = 600 Hz, ^{t}Bu)) were observed in an approximate 8:2 ratio by ^{1}H NMR spectroscopy (orange solution). The formation of methyl chloride (~δ_{13C} 25.1) or 1,2-dichloroethane (~δ_{13C} 44.4) was not observed by ^{13}C NMR spectroscopy. Similar reactivity and product distributions were observed for solutions of **A**.

Solid-state stability of A

Crystallites of **A** (14.5 mg, 10.0 μmol) were heated in the solid-state at 110 °C for 18 h, during which time they changed colour from pale to dark orange. The sample was dissolved in CD_2Cl_2 (0.5 mL) and analysed by ^{1}H and ^{31}P NMR spectroscopy in the dark, revealing generation of a 5:90:5 mixture of d$_2$-**A**, [Rh(PONOP)(CH_2Cl)Cl][BAr^F_4] (**3**; δ_{31P} 182.0 (d, $^1J_{RhP}$ = 104)) and [Rh(PONOP)Cl][BAr^F_4] (**4**; δ_{1H} 24.46 (vbr, fwhm = 610 Hz, ^{t}Bu).

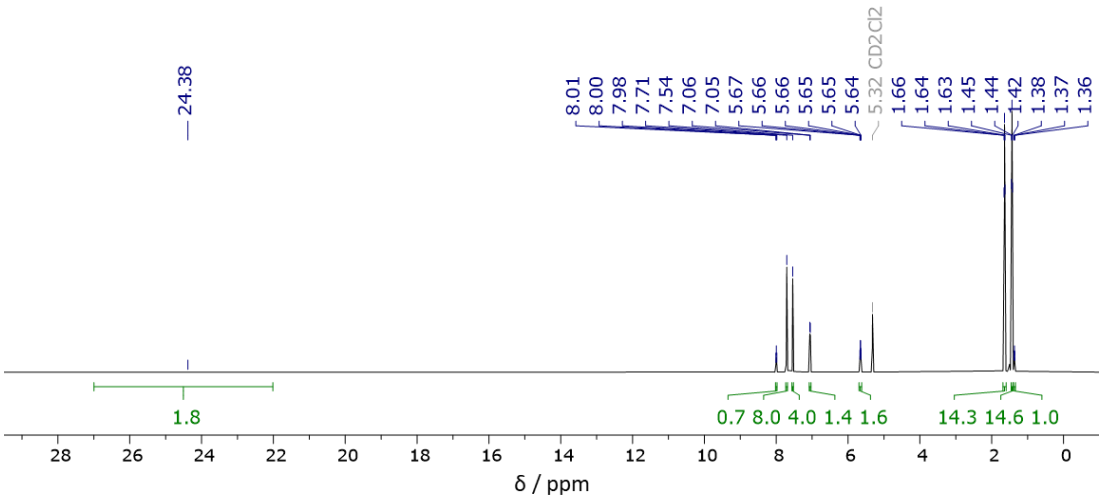

Figure 6.16 – ^{1}H NMR spectrum of **A** after 18 h at 110 °C in the solid-state (600 MHz, CD_2Cl_2, 298 K, dark).

NMR scale reactions of [Rh(PONOP)(CH_2Cl)(Cl)][BAr^F_4], 3

Stability of 3 at room temperature in CD_2Cl_2

A solution of a 9:1 mixture of **3** and **4** (14.5 mg) in CD_2Cl_2 (0.5 mL) was prepared within a J. Young's valve NMR tube in dark and monitored *in situ* using ^{1}H and ^{31}P NMR spectroscopy. No onward reaction was apparent after standing at room temperature for 48 h in the dark. The solution was exposed to light and quantitative conversion of **3** into **A** (δ_{31P} 204.5 (d, $^{1}J_{RhP}$ = 136)) was observed within 4 h at room temperature (orange solution). The concentration of **4** remained constant.

Stability of 3 in the presence of TEMPO in CD_2Cl_2

CD_2Cl_2 (0.5 mL) was added To a J. Young's valve NMR tube charged with a 9:1 mixture of **3** and **4** (14.5 mg) and TEMPO (1.6 mg, 10.2 µmol) at room temperature in the dark. The resulting solution was left to stand at room temperature for 24 h in the dark. No onward reaction was apparent from analysis *in situ* using ^{1}H and ^{31}P NMR spectroscopy. The solution was exposed to light resulting in a gradual change in colour from orange to deep red. Generation of a species tentatively assigned as TEMPO-CH_2Cl (δ_{1H} 5.67 (s, OCH_2Cl))[17] and quantitative conversion of **3** into **4** (δ_{1H} 23.94 (vbr, fwhm = 600 Hz, ^{t}Bu) was observed within 4 h.

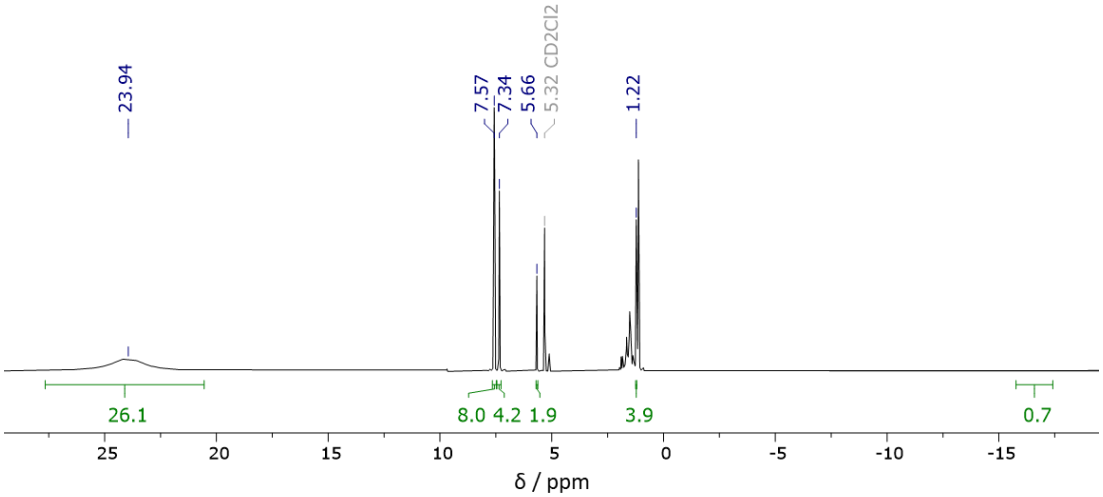

Figure 6.17 – ^{1}H NMR spectrum of **3** after 4 hours in light in the presence of TEMPO (400 MHz, CD_2Cl_2, 298 K, light).

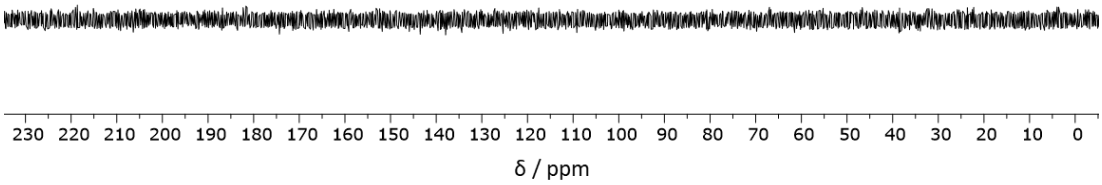

Figure 6.18 – ^{31}P{^{1}H} NMR spectrum of **3** after 4 hours in light in the presence of TEMPO (162 MHz, CD_2Cl_2, 298 K, light).

NMR scale reactions of [Rh(PONOP)Cl][BAr$^{F}_{4}$], 4

Stability of 4 at 50 °C in CD_2Cl_2

A 21 mM solution of **4** (14.5 mg, 10.3 µmol) in CD_2Cl_2 (0.5 mL) was prepared within J. Young's valve NMR tube in the dark, heated at 50 °C in the dark, and periodically monitored *in situ* using ^{1}H and ^{31}P NMR spectroscopy at room temperature in the dark. No onward reaction was apparent after heating for 24 h (purple solution). The same outcome was observed when repeated in the presence of light.

Reaction of 4 with dihydroanthracene

CD_2Cl_2 (0.5 mL) was added to a J. Young's valve NMR tube charged with **4** (14.5 mg, 10.3 µmol) and 9,10-dihydroanthracene (1.2 mg, 6.7 µmol) at room temperature in the dark. The resulting purple solution was heated at 50 °C in the dark for 1 week. No onward reaction was apparent from analysis *in situ* by ^{1}H and ^{31}P NMR spectroscopy. A separate solution [**4** (14.0 mg, 10.0 µmol) and 9,10-dihydroanthracene (1.4 mg, 7.8 µmol) dissolved in CD_2Cl_2 (0.5 mL)] was exposed to light and heated for 1 week at 50 °C, after which time partial conversion (~10 %) of **4** into **5** (δ_{1H} -25.89 (br d, $^{1}J_{RhH}$ = 42.3, 1H, RhH), δ_{31P} 197.3 (d, $^{1}J_{RhP}$ = 102)) with concomitant generation of anthracene (δ_{1H} 8.45 (s, 2H, CH)) was observed. This was accompanied by a colour change of the solution from purple to maroon. Full conversion to **5** was not observed after 4 weeks under these conditions.

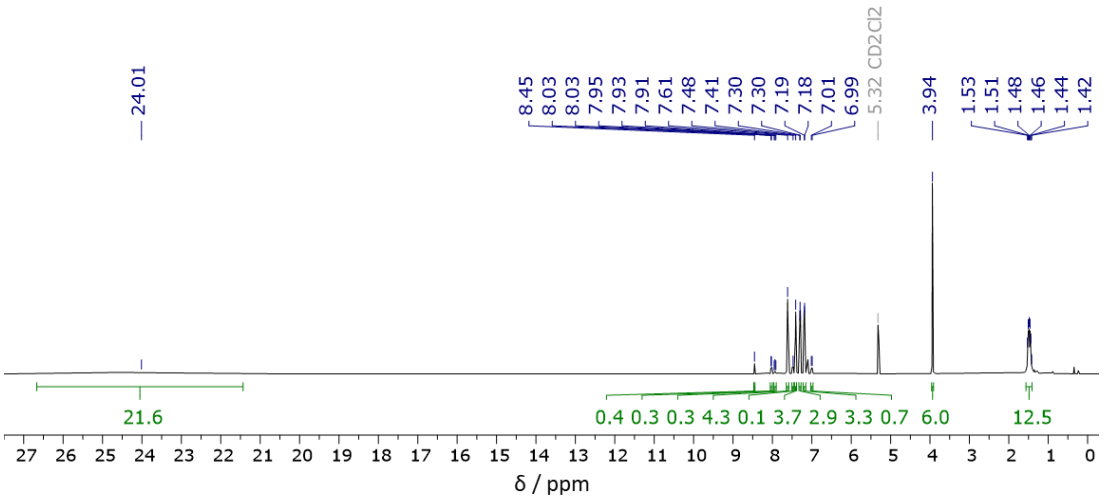

Figure 6.19 – ^{1}H NMR spectra of the reaction of **4** with 9,10-dihydroanthracene after 1 week in the presence of light at 50 °C (300 MHz, CD_2Cl_2, 298 K, light).

NMR scale reactions of 5

Reactions were performed within J. Young's valve NMR tubes using 20 mM solutions of **5** (14.8 mg, 10.0 µmol) in ClCy (0.5 mL) and monitored *in situ* using ^{1}H and ^{31}P NMR spectroscopy.

Stability of 5 at room temperature in ClCy

Standing at room temperature for 24 h in the dark resulted in partial conversion (*ca*. 10%) of **5** into [Rh(PONOP)(H)Cl][BAr^{F}_{4}], **6** (δ_{1H} -26.15 (dt, $^{1}J_{RhH}$ = 42.3, $^{2}J_{PH}$ = 10.5, RhH), δ_{31P} 197.1 (d, $^{1}J_{RhP}$ = 102)) with concomitant generation of cyclohexene (δ_{1H} 5.72 (s, CH=CH); yellow solution). The same outcome was observed when repeated in the presence of light.

Stability of 5 at 50 °C in ClCy

Heating **5** in ClCy at 50 °C for 24 h in the dark generated equimolar quantities of cyclohexene (δ_{1H} 5.72 (s, CH=CH)) and **6** (δ_{1H} -26.16 (dt, $^{1}J_{RhH}$ = 42.3, $^{2}J_{PH}$ = 10.4, 1H, RhH), δ_{31P} 197.1 (d, $^{1}J_{RhP}$ = 102); yellow solution). The same outcome was observed when repeated in the presence of light.

LR GC-MS: cyclohexene was observed (m/z = 82.1, calc. = 82.1).

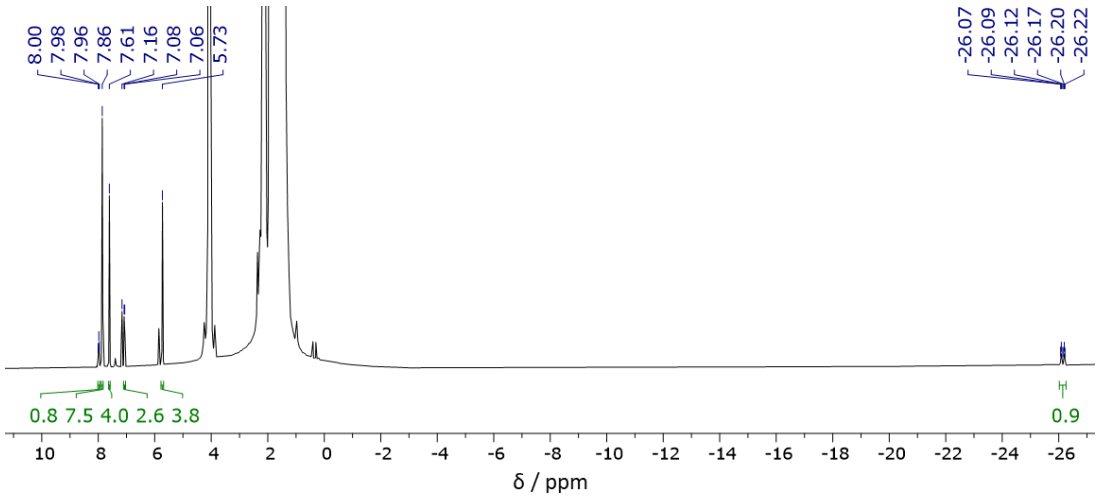

Figure 6.20 – ^{1}H NMR spectrum of **5** after heating for 24 hours at 50 °C in the presence of light (400 MHz, ClCy, 298 K, light).

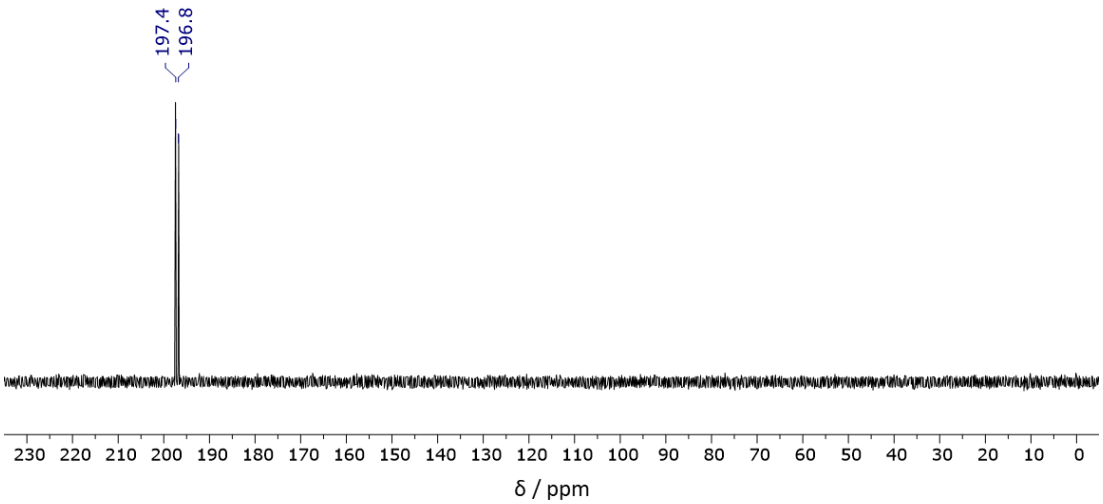

Figure 6.21 – $^{31}P\{^{1}H\}$ NMR spectrum of **5** after heating for 24 hours at 50 °C in the presence of light (162 MHz, ClCy, 298 K, light).

NMR scale reactions of 6

Stability of 6 at room temperature in CD_2Cl_2

20 mM solutions of **5** (14.0 mg, 10.0 µmol) in CD_2Cl_2 (0.5 mL) were prepared within J. Young's valve NMR tubes in the presence and absence of light and were monitored *in situ* using ^{1}H and ^{31}P NMR spectroscopy. No significant onward reaction of **6** was apparent upon standing at room temperature for 72 h in the dark, but partial decomposition (~3%) into **4** (δ_{1H} 24.2 (vbr, fwhm = 650 Hz, ^{t}Bu)) was observed in the presence of light under the same conditions (yellow solution).

Stability of 6 in the presence of TEMPO in CD_2Cl_2

CD_2Cl_2 (0.5 mL) was added to a J. Young's valve NMR tube charged with **6** (14.0 mg, 10.0 µmol) and TEMPO (1.6 mg, 10.2 µmol) at room temperature in the dark. The solution immediately turned red in colour. Quantitative consumption of **6** was apparent from analysis *in situ* using ^{1}H and ^{31}P NMR spectroscopy within 5 min. The species produced were assigned as a dynamic mixture of TEMPO-H and **4** – the ^{1}H signals shifted due to dynamics in solution that were unable to be resolved on the NMR timescale.

NMR scale reactions of 8

Reactions were performed within J. Young's valve NMR tubes using 20 mM solutions of **8** (14.6 mg, 10.0 µmol) in DCE (0.5 mL) and monitored *in situ* using ^{1}H and ^{31}P NMR spectroscopy.

Stability of 8 at room temperature in DCE

Standing at room temperature for 24 h in the dark resulted in partial conversion (5 %) of DCE solutions of **8** into [Rh(PONOP)(η^2-CH_2CHCl)][BAr^F_4] (**10**; δ_{31P} 211.6 (d, $^{1}J_{RhP}$ = 126)) and trace quantities of **4** (< 1 %). The same outcome was observed when repeated in the presence of light.

Stability of 8 at 50 °C in DCE

Heating **8** in DCE at 50 °C for 24 h in the dark resulted in partial conversion (~10 %) of DCE solutions of **2** into [Rh(PONOP)(η^2-CH_2CHCl)][BAr^F_4] (**10**; δ_{31P} 211.6 (d, $^{1}J_{RhP}$ = 126)) and trace quantities of **4** (~2 %). The same outcome was observed when repeated in the presence of light.

Selected data for **10**:

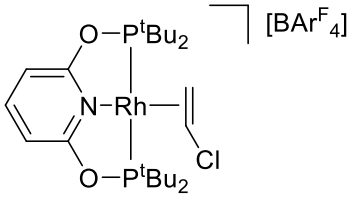

^{1}H NMR (400 MHz, DCE, selected peaks): δ 7.86-7.79 (obscured t, 1H, 4-py), 7.60 (m, 8H, Ar^F), 7.37 (br, 4H, Ar^F), 7.04 (d, $^{3}J_{HH}$ = 8.2, 2H, 3-py), 1.27 (vt, J_{PH} = 14.8, 36H, ^{t}Bu).

^{31}P{^{1}H} NMR (162 MHz, DCE, selected peaks): δ 211.6 (d, $^{1}J_{RhP}$ = 126).

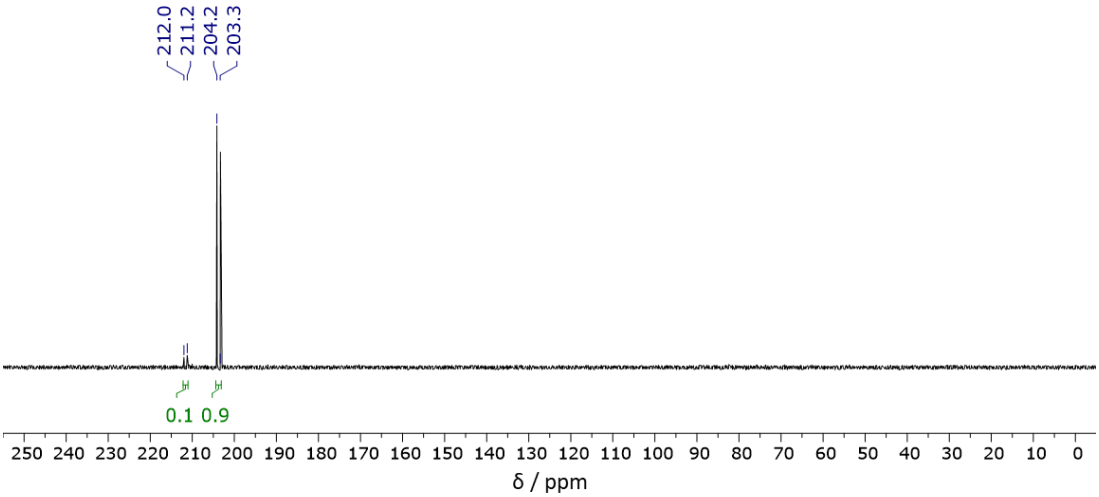

Figure 6.22 – $^{31}P\{^{1}H\}$ NMR spectrum of **8** after 24 hours heating at 50 °C in DCE in the presence of light (162 MHz, DCE, 298 K, light).

NMR scale reactions of 9

Reactions were performed within J. Young's valve NMR tubes using 20 mM solutions of **9** (14.5 mg, 10.0 µmol) in Cl^{i}Pr (0.5 mL) and monitored *in situ* using ^{1}H and ^{31}P NMR spectroscopy.

Stability of 9 at room temperature in Cl^{i}Pr

Standing at room temperature for 24 h in the dark resulted in partial conversion (*ca*. 60 %) of Cl^{i}Pr solutions of **9** into approximately equal quantities of **5** and [Rh(PONOP)(η^{2}-CH_2CHCH_3)][BAr^{F}_4] (**11**; δ_{31P} 212.4 (d, $^{1}J_{RhP}$ = 128)) with trace quantities of [Rh(PONOP)(N_2)][BAr^{F}_4] also being generated. The same outcome was observed when repeated in the presence of light.

Stability of 9 at 50 °C in Cl^{i}Pr

Heating **9** in Cl^{i}Pr at 50 °C for 24 h in the dark generated an approximate 1:1 mixture of **5** and [Rh(PONOP)(η^{2}-CH_2CHCH_3)][BAr^{F}_4] (**11**; δ_{31P} 212.4 (d, $^{1}J_{RhP}$ = 128)). The same outcome was observed when repeated in the presence of light.

Selected data for **11**:

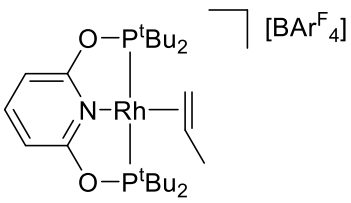

^{1}H NMR (400 MHz, Cl^{i}Pr, selected peaks): δ 8.35 (t, $^3J_{HH}$ = 8.2, 1H, 4-py), 8.16-8.20 (m, 8H, Ar^F), 7.98 (br, 4H, Ar^F), 7.36 (d, $^3J_{HH}$ = 8.2, 2H, 3-py).

^{31}P{^{1}H} NMR (162 MHz, Cl^{i}Pr, selected peaks): δ 212.4 (d, $^1J_{RhP}$ = 128).

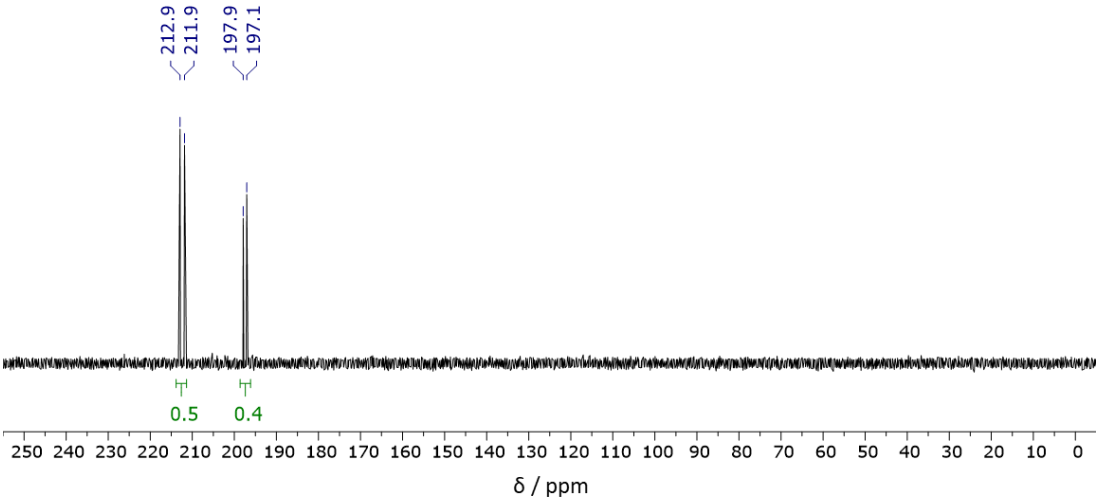

Figure 6.23 – ^{31}P{^{1}H} NMR spectrum of **9** after 24 hours heating at 50 °C in Cl^{i}Pr in the presence of light (162 MHz, Cl^{i}Pr, 298 K, light).

6.2.1 – Variable temperature powder X-ray diffraction

Powder X-ray diffraction data of **A** was collected on the I11 beamline at Diamond Light Source, England, using synchrotron radiation (λ = 0.82662 Å). The sample was heated from 300 K to 380 K at a rate of 360 K hr^{-1}, allowing 30 s for sample equilibration before collections were carried out approximately every 2 °C. Once the final temperature was reached the sample was held at 380 K while a further three patterns were collected with continued equilibration times. The sample was packed in a 0.5 mm diameter borosilicate glass capillary within an Argon atmosphere and sealed with superglue to avoid air exposure. Rietveld refinements were carried out using

TOPAS *Academic*[18] and fitted to powder simulations derived from the single crystal CIFs (see appendix).

6.2.2 – High-pressure crystallography

High-pressure data of **A** were collected on the I19 beamline at Diamond Light Source using Ag-edge synchrotron radiation (λ = 0.48590 Å, 25.5 keV) with a Pilatus 300 K detector at 293(2) K. High-pressure data for crystal A (**A-α**; dimensions 0.02 x 0.06 x 0.08 mm) was studied in Daphne-7373 at pressures of 1.9, 7.4 and 9.5 kbar. High-pressure data for crystal B (**A-α**; dimensions 0.02 x 0.06 x 0.08 mm) was studied in paraffin oil at pressures of 6.3, 8.8, 10.6 and 15.7 kbar. High-pressure data for crystal C (**A-β**; dimensions 0.03 x 0.05 x 0.07 mm) was studied in Daphne-7373 at pressures of 6.6, 7.0, 13.5, 18.1, 26.3 and 32.0 kbar.

The sample chambers of the Merrill-Bassett diamond anvil cells (DAC) were formed by the 500 μm (crystal B) or 600 μm (crystals A & C) culet faces of the Boehler-Almax diamonds and a laser-cut tungsten sheet (Goodfellow Metals, thickness 200 μm) indented to a thickness of *ca*. 120 μm with a gasket hole of diameter 240 μm, drilled using a BETSA electric discharge machine. In each case, the sample crystal was fixed to one culet face by means of high vacuum hydrocarbon grease alongside two ruby chips which allowed for pressure measurement using the ruby fluorescence method.[19] After each pressure ramp, the pressure inside the DAC was allowed to equilibrate for a minimum of 1 hour before data collection was initiated. Pressure measurements were taken immediately before and after each collection and the pressure reported as the average. The average uncertainty in pressure across the studies of **A-α** and **A-β** were 0.9 kbar and 0.8 kbar, respectively, with specific error bars drawn on Figures as 0.5 times the magnitude of the individual drift plus 0.5 kbar attributed to the inherent uncertainty in the pressure determination of the ruby fluorescence method.[20] Error bars associated with bond lengths and angles for specific refinements are drawn on Figures as the esd, as calculated by *SHELXL*.[13]

Cell refinement and data reduction was carried out using the software *CrysAlis*^{PRO}.[11] Special settings (smart background setting, profile agreement rejection parameters, angle-dependent profile changes) were implemented in the data reduction step. Contaminating diamond reflections and powder rings were removed during data

reduction in this manner. Multi-scan absorption corrections were applied with an empirical absorption correction using spherical harmonics, implemented in the *SCALE3 ABSPACK* scaling algorithm[21] through *CrysAlis*^{PRO}.[11] All datasets of **A-α** and **A-β** were solved by isomorphous replacement using an appropriate starting model taken from a previous ambient pressure collection. Structure solution and refinement were carried out with *SHELXL*[13] using the *Olex2* interface.[14]

Atomic displacements for all non-hydrogen atoms were refined isotopically except for the rhodium atom in certain refinements, which was refined anisotropically, where appropriate. All aromatic rings were constrained to an idealised 6-membered ring geometry. Appropriate distance restraints were applied to all B–Ar^F, C–O, O–P and C–Cl bond distances across all refinements, as were all 1,2- and 1,3- distances associated with the CF_3 groups of the counterion and the ^{t}Bu groups of the cation. Where appropriate, C–Cl distance constraints were implemented. Where appropriate, the CF_3 group disorder was modelled over two positions. ADP restraints were placed on the counterion to suppress chemically unsensible ADPs in select CF_3 groups, where the combination of geometric restraints and disorder models proved insufficient. All other hydrogen atoms were automatically generated and refined using a riding model. No refinements reached convergence, given the limited data available and the complexity of the structures, therefore, the bond lengths and bond angles supplied in the appendix should be regarded very loosely. Only the cell parameters should be regarded with any degree of certainty.

6.3 – Data related to Chapter 3

General procedure – NMR scale reactions

A stoichiometric mixture of $[Rh(COD)_2][BAr^F{}_4]$ and pincer ligand (PONOP or PNP) were dissolved in 1,2-$C_6H_4F_2$ ([Rh] = 50 mmol L^{-1}) and allowed to equilibrate for 5 minutes at room temperature before an excess of borane (*ca*. 3 eq.) in 1,2-$C_6H_4F_2$ (HBpin, 0.67 M; HBcat, 0.40 M) was added to the orange solution at room temperature by syringe. The reaction mixture was allowed to stand at room temperature for several hours, during which time the solution turned yellow. In all cases, complete conversion to the rhodium(I) σ-borane complex within 6 hours was confirmed upon *in situ* analysis by ^{1}H, ^{31}P and ^{11}B NMR spectroscopy. Layering the

1,2-$C_6H_4F_2$ solution with hexane afford the product as yellow crystals suitable for analysis by single crystal X-ray diffraction upon diffusion at room temperature.

General stability in solution

In the presence of excess borane, 1,2-$C_6H_4F_2$ solutions of the rhodium σ-borane complexes were persistent at room temperature for up to 48 h. Dissolution of isolated material led to partial decomposition (*ca.* 10–15%) into [Rh(pincer)(H_2)][BAr^F_4] (pincer = PONOP, δ_{31P} 224.4 (J_{RhP} = 126 Hz); PNP, δ_{31P} 81.7 (J_{RhP} = 121 Hz)) within 24 hours at room temperature. The spectroscopic data for these complexes match the literature.[22,23]

Selected data for [Rh(PONOP)(H_2)][BAr^F_4]:

^{1}H NMR (300 MHz, 1,2-$C_6H_4F_2$, selected peaks): δ 6.28 (d, $^3J_{HH}$ = 8.0, 2H, 3-py), 1.17 (vt, J_{PH} = 15.8, 18H, ^{t}Bu), -8.40 (br d, $^1J_{RhH}$ = 27.4, 2H, σ-H_2).

^{31}P{^{1}H} NMR (121 MHz, 1,2-$C_6H_4F_2$, selected peaks): δ 224.4 (d, J_{RhP} = 126).

Selected data for [Rh(PNP)(H_2)][BAr^F_4]:

^{1}H NMR (300 MHz, 1,2-$C_6H_4F_2$, selected peaks): δ 3.40-3.43 (obscured m, 4H, CH_2P), 1.07-1.12 (obscured vt, 18H, ^{t}Bu), -11.02 (br d, J_{RhH} = 25.8, 2H, σ-H_2).

^{31}P{^{1}H} NMR (121 MHz, 1,2-$C_6H_4F_2$, selected peaks): δ 81.7 (d, J_{RhP} = 121).

Preparation of [Rh(PONOP)(η²-HBpin)][BAr$^F_4$], 12

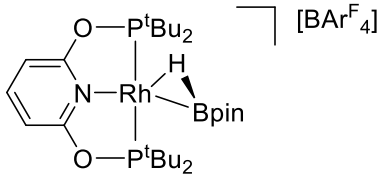

The general procedure detailed above was followed, using PONOP (10.0 mg, 25.0 µmol), [Rh(COD)$_2$][BAr$^F_4$] (30.0 mg, 25.3 µmol) and a 0.67 M solution of HBpin in 1,2-$C_6H_4F_2$ (120 µL, 80.4 µmol). The product was purified by crystallisation; yellow crystals suitable for X-ray diffraction studies were produced by liquid-liquid diffusion of hexane into the *in situ* 1,2-$C_6H_4F_2$ solution at room temperature. Yield: 30.8 mg (20.6 µmol, 83 %).

^{1}H NMR (600 MHz, 1,2-$C_6H_4F_2$, 298 K, selected peaks): δ 8.12-8.15 (br s, 8H, Ar^F), 7.61 (t, $^3J_{HH}$ = 8.2, 1H, 4-py), 7.49 (br s, 4H, Ar^F), 6.63 (d, $^3J_{HH}$ = 8.1, 2H, 3-py), 1.26 (vt, J_{PH} = 15.6, 36H, ^{t}Bu), 1.15 (s, 12H, HBpin), -14.94 (br s, 1H, HBpin).

^{13}C{^{1}H} NMR (126 MHz, 1,2-$C_6H_4F_2$, 298 K, selected peaks): δ 164.2 (vt, J_{PC} = 6, 2-py), 162.5 (q, $^1J_{BC}$ = 50, Ar^F), 147.1 (s, 4-py), 135.1 (s, Ar^F), 129.7 (qq, $^2J_{FC}$ = 32, $^3J_{BC}$ = 3, Ar^F), 124.9 (q, $^1J_{FC}$ = 272, Ar^F), 117.6 (sept, $^3J_{FC}$ = 4, Ar^F), 102.6 (vt, J_{PC} = 5, 3-py), 86.1 (s, HBpin{C}), 40.4 (vtd, $^1J_{PC}$ = 6, $^2J_{RhC}$ = 2, ^{t}Bu{C}), 26.8 (vt, J_{PC} = 8, ^{t}Bu{CH_3}), 24.1 (s, HBpin{CH_3}).

^{31}P{^{1}H} NMR (121 MHz, 1,2-$C_6H_4F_2$, 298 K): δ 217.2 (d, J_{RhP} = 129).

^{11}B NMR (96 MHz, 1,2-$C_6H_4F_2$, 298 K): 35.25 (br s, HBpin), -6.18 (s, BAr$^F_4$).

^{1}H{^{11}B} NMR (500 MHz, CD_2Cl_2, 298 K): δ 7.92 (t, $^3J_{HH}$ = 8.1, 1H, 4-py), 7.70-7.74 (br s, 8H, Ar^F), 7.55-7.57 (br s, 4H, Ar^F), 6.87 (d, $^3J_{HH}$ = 8.1, 2H, 3-py), 1.41 (vt, J_{PH} = 15.5, 36H, ^{t}Bu), 1.30 (s, 12H, HBpin), -14.85 (br, 1H, HBpin).

^{31}P{^{1}H} NMR (202 MHz, CD_2Cl_2, 298 K): δ 217.5 (d, J_{RhP} = 130).

^{11}B{^{1}H} NMR (160 MHz, CD_2Cl_2, 298 K): 35.07 (br s, HBpin), -6.59 (s, BAr$^F_4$).

^{1}H{^{11}B} NMR (500 MHz, CD_2Cl_2, 193 K): δ 7.83 (t, $^3J_{HH}$ = 8.1, 1H, 4-py), 7.69-7.75 (br s, 8H, Ar^F), 7.50-7.54 (br s, 4H, Ar^F), 6.81 (d, $^3J_{HH}$ = 8.2, 2H, 3-py), 1.23-1.33 (br s, 36H, ^{t}Bu), 1.17 (s, 12H, HBpin), -14.97 (br d, $^1J_{RhH}$ = 36.2, 1H, HBpin).

^{31}P{^{1}H} NMR (202 MHz, CD_2Cl_2, 193 K): δ 216.5 (d, J_{RhP} = 130).

$^{11}B\{^1H\}$ NMR (160 MHz, CD_2Cl_2, 193 K): -6.79 (s, BAr^F_4).

IR (KBr, cm^{-1}) 1613 (ν_{BH}), 1563 (ν_{RhH}).

LR ESI-MS: only $[Rh(PONOP)(N_2)]^+$ was observed (m/z = 530.2, calc. = 530.2).

Anal. Calcd for $C_{59}H_{64}B_2F_{24}NO_4P_2Rh$ (1493.58 $gmol^{-1}$): C, 47.45; H, 4.32; N, 0.94. Found: C, 47.36; H, 4.26; N, 0.88.

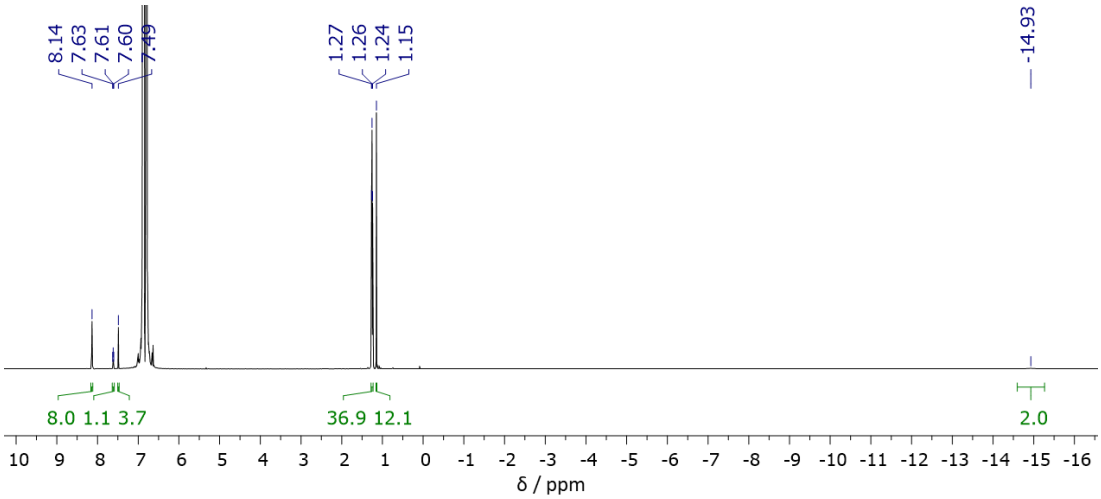

Figure 6.24 – ^1H NMR spectrum of **12** (600 MHz, 1,2-$C_6H_4F_2$, 298 K).

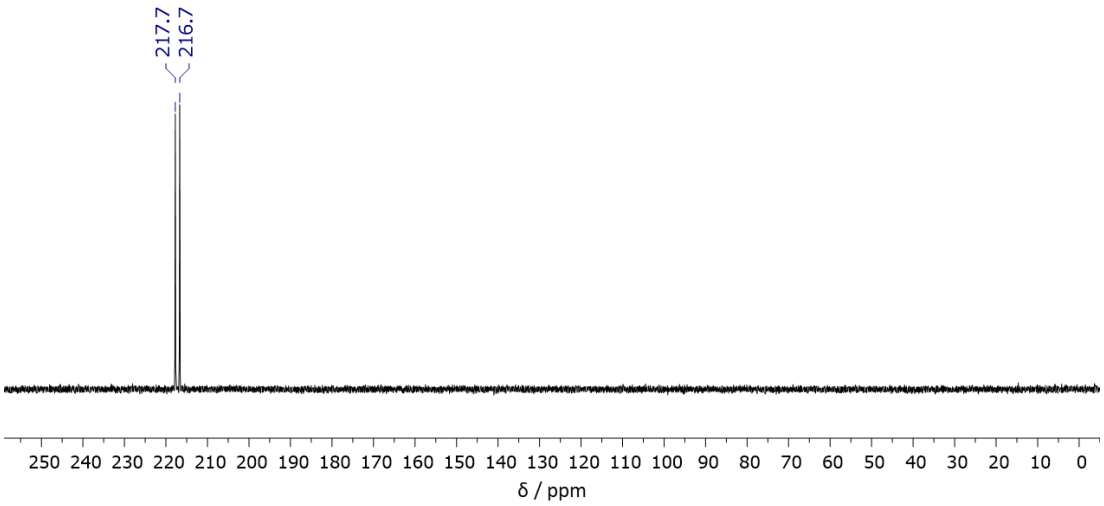

Figure 6.25 – $^{31}P\{^1H\}$ NMR spectrum of **12** (121 MHz, 1,2-$C_6H_4F_2$, 298 K).

Preparation of [Rh(PONOP)(η²-HBcat)][BAr$^F_4$], 13

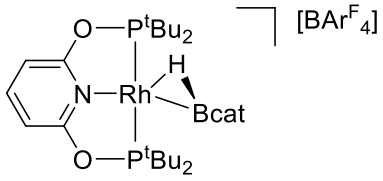

The general procedure detailed above was followed, using PONOP (9.9 mg, 24.8 µmol), [Rh(COD)$_2$][BAr$^F_4$] (29.9 mg, 25.1 µmol) and a 0.40 M solution of HBcat in 1,2-$C_6H_4F_2$ (225 µL, 90.0 µmol). The product was purified by crystallisation; yellow crystals suitable for X-ray diffraction studies were produced by liquid-liquid diffusion hexane into the *in situ* 1,2-$C_6H_4F_2$ solution at room temperature. Yield: 29.4 mg (19.8 µmol, 80 %).

^{1}H NMR (500 MHz, 1,2-$C_6H_4F_2$, 298 K, selected peaks): δ 8.11-8.15 (br s, 8H, Ar^F), 7.70 (t, $^3J_{HH}$ = 8.1, 1H, 4-py), 7.49 (br s, 4H, Ar^F), 6.71-6.74 (obscured d, 2H, 3-py), 1.30 (vt, J_{PH} = 15.6, 36H, ^{t}Bu), -13.90 (br s, 1H, HBcat).

^{13}C{^{1}H} NMR (126 MHz, 1,2-$C_6H_4F_2$, 298 K, selected peaks): δ 164.1 (vt, J_{PC} = 6, 2-py), 162.6 (q, $^1J_{BC}$ = 50, Ar^F), 149.6 (s, HBcat{C}), 147.9 (s, 4-py), 135.1 (s, Ar^F), 129.7 (qq, $^2J_{FC}$ = 32, $^3J_{BC}$ = 3, Ar^F), 124.9 (q, $^1J_{FC}$ = 272, Ar^F), 123.2 (s, HBcat{CH}), 117.6 (sept, $^3J_{FC}$ = 4, Ar^F), 111.7 (s, HBcat{CH}), 103.1 (vt, J_{PC} = 4, 3-py), 40.8 (vtd, $^1J_{PC}$ = 6, $^2J_{RhC}$ = 2, ^{t}Bu{C}), 26.5 (vt, J_{PC} = 7, ^{t}Bu{CH$_3$}).

^{31}P{^{1}H} NMR (121 MHz, 1,2-$C_6H_4F_2$, 298 K): δ 217.8 (d, J_{RhP} = 123).

^{11}B NMR (96 MHz, 1,2-$C_6H_4F_2$, 298 K): 36.60 (br s, HBcat), -6.20 (s, BAr$^F_4$).

^{1}H{^{11}B} NMR (500 MHz, CD_2Cl_2, 298 K): δ 7.99 (t, $^3J_{HH}$ = 8.1, 1H, 4-py), 7.70-7.75 (br s, 8H, Ar^F), 7.54-7.58 (br s, 4H, Ar^F), 7.23 (dd, $^3J_{HH}$ = 5.8, $^4J_{HH}$ = 3.4, 2H, HBcat 3-py), 7.14 (d, $^3J_{HH}$ = 5.8, $^4J_{HH}$ = 3.4, 2H, HBcat 2-py), 6.96 (d, $^3J_{HH}$ = 8.1, 2H, 3-py), 1.46 (vt, J_{PH} = 15.8, 36H, ^{t}Bu), -13.74 (br, 1H, HBcat).

^{31}P{^{1}H} NMR (202 MHz, CD_2Cl_2, 298 K): δ 218.1 (d, J_{RhP} = 123).

^{11}B{^{1}H} NMR (160 MHz, CD_2Cl_2, 298 K): 36.54 (br s, HBcat), -6.59 (s, BAr$^F_4$).

^{1}H{^{11}B} NMR (500 MHz, CD_2Cl_2, 193 K): δ 7.90 (t, $^3J_{HH}$ = 8.2, 1H, 4-py), 7.68-7.76 (br s, 8H, Ar^F), 7.50-7.55 (br s, 4H, Ar^F), 7.20 (dd, $^3J_{HH}$ = 5.8, $^4J_{HH}$ = 3.4, 2H, HBcat

3-py), 7.07 (d, $^{3}J_{HH}$ = 5.8, $^{4}J_{HH}$ = 3.4, 2H, HBcat 2-py), 6.91 (d, $^{3}J_{HH}$ = 8.1, 2H, 3-py), 1.27-1.43 (br s, 36H, ^{t}Bu), -14.06 (br d, $^{1}J_{RhH}$ = 33.3, 1H, HBcat).

^{31}P{^{1}H} NMR (202 MHz, CD_2Cl_2, 193 K): δ 217.0 (d, J_{RhP} = 123).

^{11}B{^{1}H} NMR (160 MHz, CD_2Cl_2, 193 K): -6.79 (s, BAr^{F}_{4}).

IR (KBr, cm^{-1}) 1612 (ν_{BH}), 1566 (ν_{RhH}).

LR ESI-MS: only $[Rh(PONOP)(N_2)]^+$ was observed (m/z = 530.3, calc. = 530.2).

Anal. Calcd for $C_{59}H_{56}B_2F_{24}NO_4P_2Rh$ (1485.53 $gmol^{-1}$): C, 47.70; H, 3.80; N, 0.94. Found: C, 47.62; H, 3.74; N, 0.88.

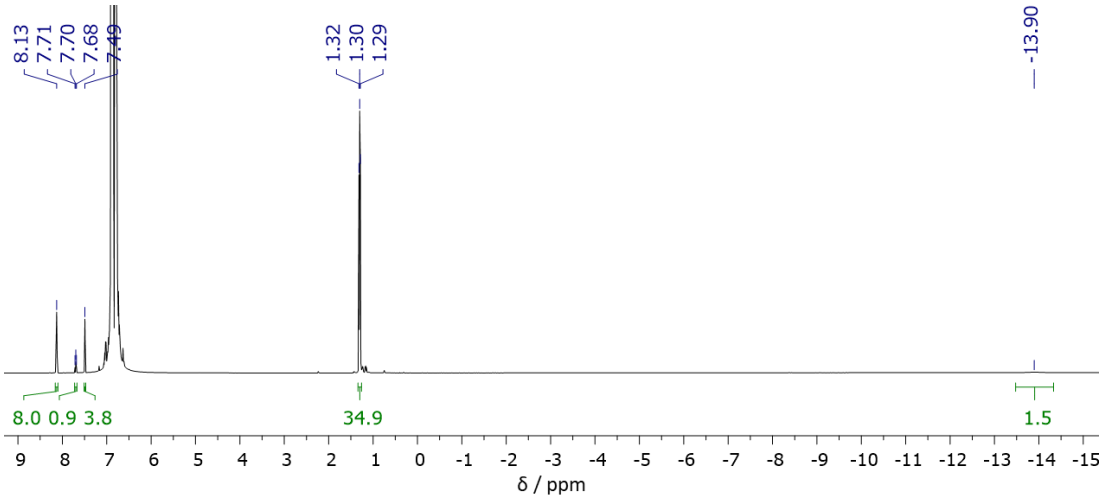

Figure 6.26 – ^{1}H NMR spectrum of **13** (500 MHz, 1,2-$C_6H_4F_2$, 298 K).

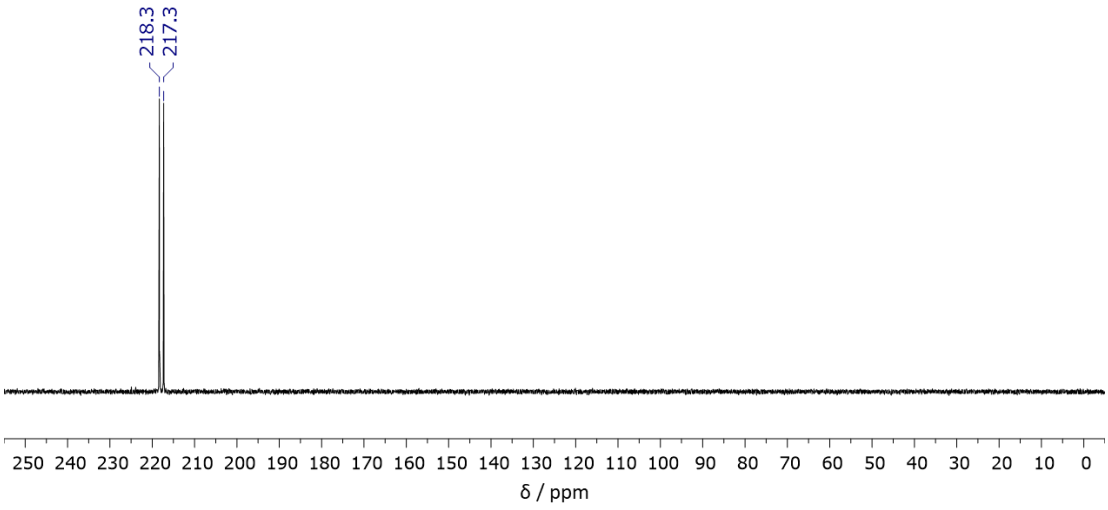

Figure 6.27 – ^{31}P{^{1}H} NMR spectrum of **13** (121 MHz, 1,2-$C_6H_4F_2$, 298 K).

Preparation of [Rh(PNP)(η²-HBpin)][BAr$^F_4$], 14

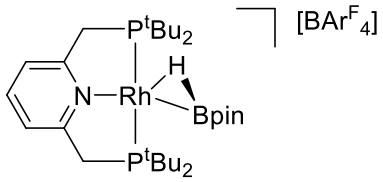

The general procedure detailed above was followed, using PNP (9.9 mg, 25.0 µmol), [Rh(COD)$_2$][BAr$^F_4$] (30.0 mg, 25.3 µmol) and a 0.67 M solution of HBpin in 1,2-$C_6H_4F_2$ (120 µL, 80.4 µmol). The product was purified by liquid-liquid diffusion of hexane into the *in situ* 1,2-$C_6H_4F_2$ solution at room temperature. Yield: 18.2 mg (18.1 µmol, 72 %). Yellow crystals suitable for X-ray diffraction studies were produced by liquid-liquid diffusion of tetramethyl silane (TMS) into the *in situ* 1,2-$C_6H_4F_2$ solution at -30 °C or by room temperature diffusion of hexane into the 1,2-$C_6H_4F_2$ solution.

^{1}H NMR (500 MHz, 1,2-$C_6H_4F_2$, 298 K, selected peaks): δ 8.11-8.15 (br s, 8H, Ar^F), 7.55 (t, $^3J_{HH}$ = 7.8, 1H, 4-py), 7.49 (br s, 4H, Ar^F), 7.23 (d, $^3J_{HH}$ = 7.7, 2H, 3-py), 3.45-3.47 (m, 4H, PCH_2), 1.18 (vt, J_{PH} = 14.2, 36H, ^{t}Bu), 1.13 (s, 12H, HBpin), -17.57 (br s, 1H, HBpin).

^{13}C{^{1}H} NMR (126 MHz, 1,2-$C_6H_4F_2$, 298 K, selected peaks): δ 164.4 (vt, J_{PC} = 8, 2-py), 162.5 (q, $^1J_{BC}$ = 50, Ar^F), 140.8 (s, 4-py), 135.0 (s, Ar^F), 129.6 (qq, $^2J_{FC}$ = 32, $^3J_{BC}$ = 3, Ar^F), 124.8 (q, $^1J_{FC}$ = 272, Ar^F), 120.7 (vt, J_{PC} = 8, 3-py), 117.5 (sept, $^3J_{FC}$ = 4, Ar^F), 84.5 (s, HBpin{C}), 36.3 (vt, J_{PC} = 7, PCH_2), 35.2 (vtd, $^1J_{PC}$ = 8, $^2J_{RhC}$ = 2, ^{t}Bu{C}), 28.9 (vt, J_{PC} = 6, ^{t}Bu{CH_3}), 24.2 (s, HBpin{CH_3}).

^{31}P{^{1}H} NMR (121 MHz, 1,2-$C_6H_4F_2$, 298 K): δ 73.8 (d, J_{RhP} = 123).

^{11}B NMR (96 MHz, 1,2-$C_6H_4F_2$, 298 K): 35.75 (br s, HBpin), -6.17 (s, BAr$^F_4$).

^{1}H{^{11}B} NMR (500 MHz, CD_2Cl_2, 298 K, selected peaks): δ 7.82 (t, $^3J_{HH}$ = 7.7, 1H, 4-py), 7.70-7.74 (br s, 8H, Ar^F), 7.54-7.57 (br s, 4H, Ar^F), 7.46 (d, $^3J_{HH}$ = 7.7, 2H, 3-py), 3.63-3.66 (m, 4H, PCH_2), 1.35 (vt, J_{PH} = 14.1, 36H, ^{t}Bu), 1.28 (s, 12H, HBpin), -17.46 (br, 1H, HBpin).

^{31}P{^{1}H} NMR (202 MHz, CD_2Cl_2, 298 K): δ 73.9 (d, J_{RhP} = 124).

^{11}B NMR (160 MHz, CD_2Cl_2, 298 K): 35.43 (br s, HBpin), -6.59 (s, BAr$^F_4$).

$^{1}H\{^{11}B\}$ NMR (500 MHz, CD_2Cl_2, 193 K): δ 7.73 (obscured t, 1H, 4-py), 7.68-7.75 (br s, 8H, Ar^F), 7.50-7.55 (obscured br s, 4H, Ar^F), 7.38 (d, $^{3}J_{HH}$ = 7.8, 2H, 3-py), 3.52-3.57 (br s, 4H, PCH_2), 1.18-1.26 (br s, 36H, ^{t}Bu), 1.15 (s, 12H, HBpin), -17.35 (br d, $^{1}J_{RhH}$ = 36.9, 1H, HBpin).

$^{31}P\{^{1}H\}$ NMR (202 MHz, CD_2Cl_2, 193 K): δ 72.9 (d, J_{RhP} = 124).

^{11}B NMR (160 MHz, CD_2Cl_2, 193 K): -6.79 (s, BAr^F_4).

IR (KBr, cm^{-1}) 1609 (ν_{BH}), 1572 (ν_{RhH}).

LR ESI-MS: only $[Rh(PONOP)(N_2)]^+$ was observed (m/z = 530.2, calc. = 530.2).

Anal. Calcd for $C_{61}H_{68}B_2F_{24}NO_4P_2Rh$ (1489.63 $gmol^{-1}$): C, 49.18; H, 4.60; N, 0.94. Found: C, 48.70; H, 4.51; N, 0.97.

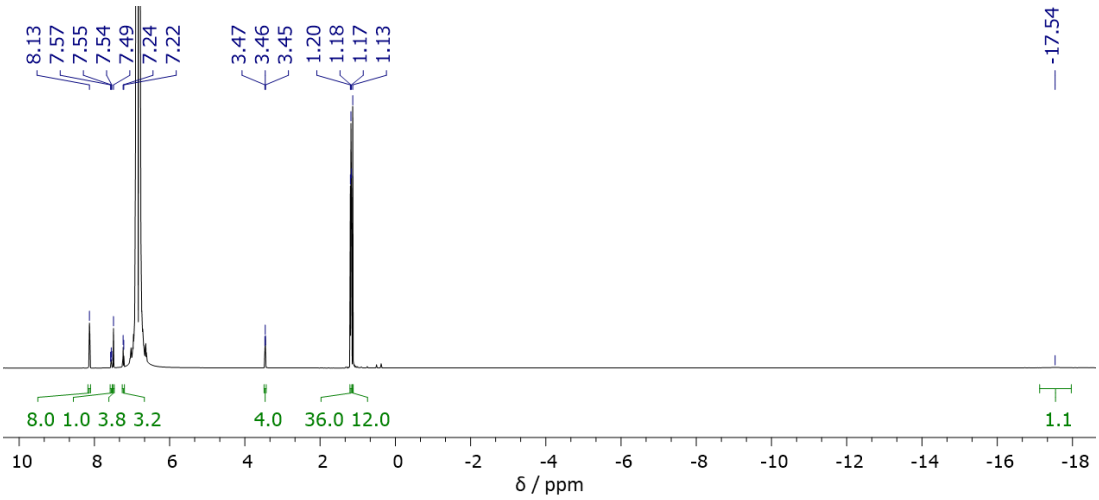

Figure 6.28 – ^{1}H NMR spectrum of **14** (500 MHz, 1,2-$C_6H_4F_2$, 298 K).

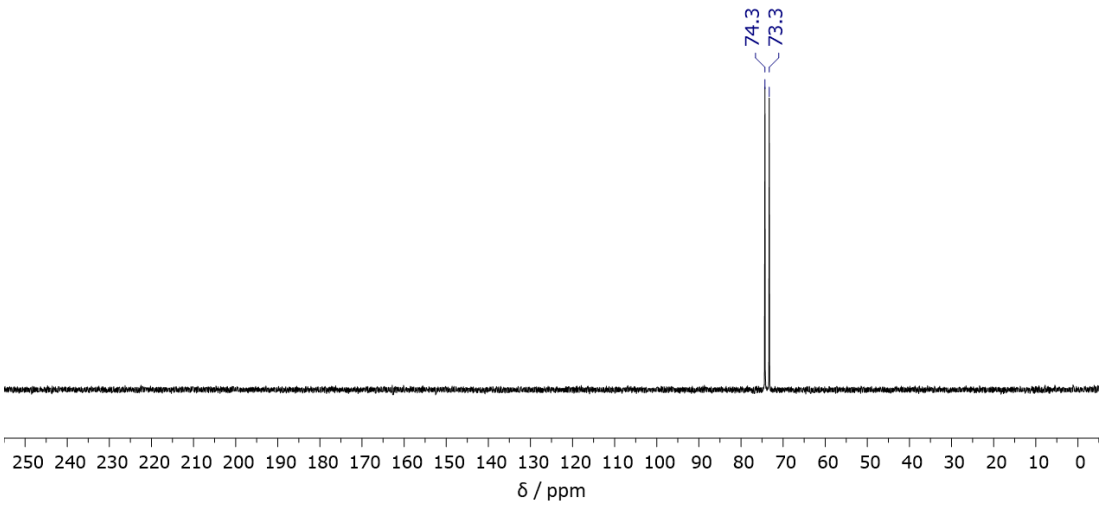

Figure 6.29 – $^{31}P\{^{1}H\}$ NMR spectrum of **14** (121 MHz, 1,2-$C_6H_4F_2$, 298 K).

Preparation of [Rh(PNP)(η^2-HBcat)][BAr$^F_4$], 15

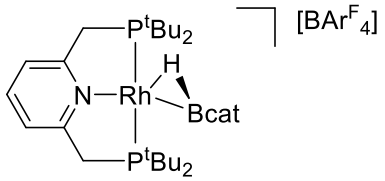

The general procedure detailed above was followed, using PNP (10.0 mg, 25.3 μmol), [Rh(COD)$_2$][BAr$^F_4$] (30.0 mg, 25.3 μmol) and a 0.40 M solution of HBcat in 1,2-$C_6H_4F_2$ (225 μL, 90.0 μmol). The product was purified by crystallisation; yellow crystals suitable for X-ray diffraction studies were produced by liquid-liquid diffusion of hexane into the *in situ* 1,2-$C_6H_4F_2$ solution at room temperature. Yield: 15.1 mg (15.3 μmol, 60 %).

^{1}H NMR (500 MHz, 1,2-$C_6H_4F_2$, 298 K, selected peaks): δ 8.12-8.16 (br s, 8H, Ar^F), 7.63 (t, $^3J_{HH}$ = 7.8, 1H, 4-py), 7.49 (br s, 4H, Ar^F), 7.34 (d, $^3J_{HH}$ = 7.8, 2H, 3-py), 3.63-3.65 (m, 4H, PCH$_2$), 1.14 (vt, J_{PH} = 14.2, 36H, ^{t}Bu), -17.70 (br d, J_{RhH} = 41.2, 1H, HBcat).

^{13}C{^{1}H} NMR (126 MHz, 1,2-$C_6H_4F_2$, 298 K, selected peaks): δ 163.7 (vt, J_{PC} = 8, 2-py), 162.8 (q, $^1J_{BC}$ = 50, Ar^F), 149.2 (s, HBcat{C}), 141.1 (s, 4-py), 135.1 (s, Ar^F), 129.7 (qq, $^2J_{FC}$ = 32, $^3J_{BC}$ = 3, Ar^F), 124.9 (q, $^1J_{FC}$ = 272, Ar^F), 122.5 (s, HBcat{CH}), 121.3 (vt, J_{PC} = 9, 3-py), 117.6 (sept, $^3J_{FC}$ = 4, Ar^F), 111.4 (s, HBcat{CH}), 36.7 (vt, $^1J_{PC}$ = 8, PCH$_2$), 35.7 (vtd, J_{PC} = 9, $^2J_{RhC}$ = 2, ^{t}Bu{C}), 28.5 (vt, J_{PC} = 5, ^{t}Bu{CH$_3$}).

^{31}P{^{1}H} NMR (121 MHz, 1,2-$C_6H_4F_2$, 298 K): δ 76.2 (d, J_{RhP} = 113).

^{11}B NMR (96 MHz, 1,2-$C_6H_4F_2$, 298 K): 39.38 (br s, HBcat), -6.18 (s, BAr$^F_4$).

^{1}H{^{11}B} NMR (500 MHz, CD_2Cl_2, 298 K, selected peaks): δ 7.88 (t, $^3J_{HH}$ = 7.8, 1H, 4-py), 7.70-7.74 (br s, 8H, Ar^F), 7.54-7.57 (obscured br s, 4H, Ar^F), 7.53-7.56 (obscured d, 2H, 3-py), 7.18 (d, $^3J_{HH}$ = 5.8, $^4J_{HH}$ = 3.4, 2H, HBcat 3-py), 7.06 (d, $^3J_{HH}$ = 5.8, $^4J_{HH}$ = 3.4, 2H, HBcat 2-py), 3.79-3.82 (m, 4H, PCH$_2$), 1.30 (vt, J_{PH} = 14.7, 36H, ^{t}Bu), -17.79 (br d, $^1J_{RhH}$ = 41.5, 1H, HBcat).

^{31}P{^{1}H} NMR (202 MHz, CD_2Cl_2, 298 K, selected peaks): δ 76.1 (d, J_{RhP} = 113).

^{11}B NMR (160 MHz, CD_2Cl_2, 298 K): 39.43(br s, HBcat), -6.59 (s, BAr$^F_4$).

^{1}H{^{11}B} NMR (500 MHz, CD_2Cl_2, 193 K): δ 7.75-7.80 (obscured t, $^{3}J_{HH}$ = 7.9, 1H, 4-py), 7.71-7.76 (br s, 8H, Ar^F), 7.51-7.54 (br s, 4H, Ar^F), 7.47 (d, $^{3}J_{HH}$ = 7.9, 2H, 3-py), 7.14 (dd, $^{3}J_{HH}$ = 5.8, $^{4}J_{HH}$ = 3.5, 2H, HBcat 3-py), 7.00 (dd, $^{3}J_{HH}$ = 5.8, $^{4}J_{HH}$ = 3.4, 2H, HBcat 2-py), 3.68-3.75 (m, 4H, PCH_2), 1.17 (vt, J_{PH} = 13.9, 36H, ^{t}Bu), -18.20 (br d, J_{RhH} = 41.9, 1H, HBcat).

^{31}P{^{1}H} NMR (202 MHz, CD_2Cl_2, 193 K, selected peaks): δ 75.3 (d, J_{RhP} = 112).

^{11}B NMR (160 MHz, CD_2Cl_2, 193 K): -6.79 (s, BAr^F_4).

IR (KBr, cm^{-1}) 1605 (ν_{BH}), 1571 (ν_{RhH}).

LR ESI-MS: only $[Rh(PONOP)(N_2)]^+$ was observed (m/z = 530.2, calc. = 530.2).

Anal. Calcd for $C_{61}H_{60}B_2F_{24}NO_4P_2Rh$ (1481.59 $gmol^{-1}$): C, 49.45; H, 4.08; N, 0.95. Found: C, 49.42; H, 4.02; N, 0.89.

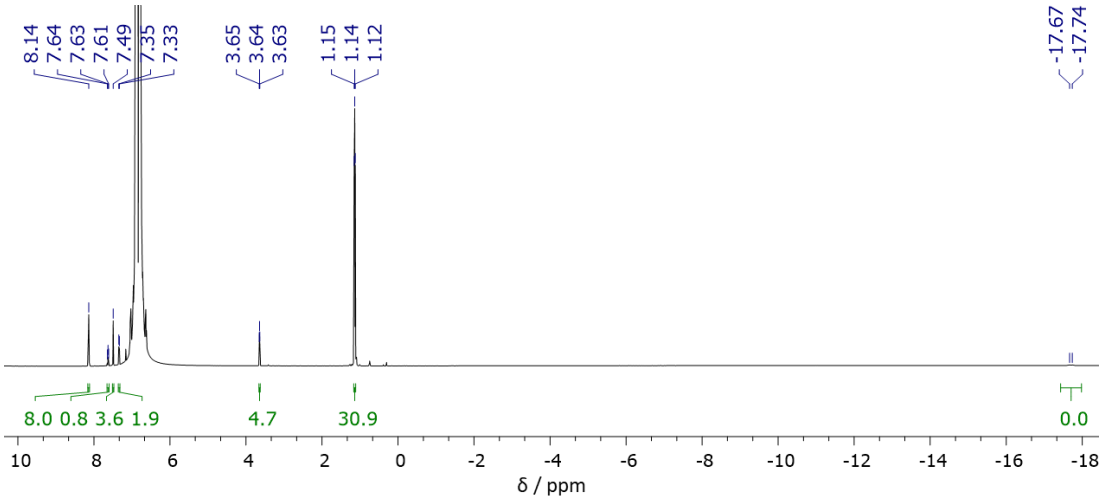

Figure 6.30 – ^{1}H NMR spectrum of **15** (500 MHz, 1,2-$C_6H_4F_2$, 298 K).

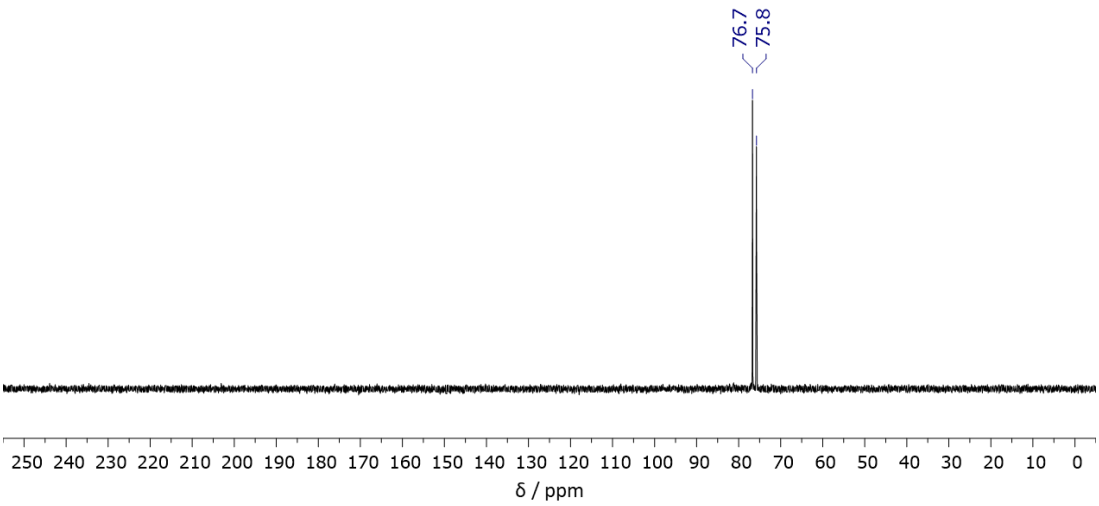

Figure 6.31 – ^{31}P{^{1}H} NMR spectrum of **15** (121 MHz, 1,2-$C_6H_4F_2$, 298 K).

Preparation of VT-NMR samples of 12-15

CD_2Cl_2 solutions of isolated material (20 mmol L^{-1}) for variable temperature NMR analysis were prepared by vacuum transfer of the solvent onto the sample within a J. Young's valve NMR tube pre-fitted with a ceramic spinner. The samples were thawed at 193 K and inserted into a pre-cooled spectrometer (500 MHz) and immediately analysed at 193 K. The samples were thereafter removed from the spectrometer and stored at 193 K before analysis at 298 K. Partial decomposition was observed in some samples analysed at 298 K, since CD_2Cl_2 solutions of **12-15** partially decompose over the course of several hours.

6.3.1 – High-pressure crystallography

High-pressure data of **13** for crystals A and B were collected on the I19 beamline at Diamond Light Source at 293(2) K using Ag-edge synchrotron radiation (λ = 0.48590 Å, 25.5 keV) with a Pilatus 300 K detector. Crystal A (dimensions 0.03 x 0.05 x 0.07 mm) was studied in Daphne-7373 at pressures of 2.5, 4.8, 14.0, 22.4, 25.8, 32.8, 45.1 and 47.4 kbar, with viable datasets obtained up to 25.8 kbar. Crystal B (dimensions 0.03 x 0.04 x 0.08 mm) was studied in paraffin oil at pressures of 8.8, 13.9, 15.4, 20.6, 25.2 and 26.5 kbar, with viable datasets obtained up to 15.4 kbar.

The sample chambers of the Merrill-Bassett diamond anvil cells (DAC) were formed by the 500 μm or 600 μm culet faces of the Boehler-Almax diamonds (for crystals A and B, respectively) and a laser-cut tungsten sheet (Goodfellow Metals, thickness 200 μm) indented to a thickness of *ca*. 120 μm with a gasket hole of diameter 240 μm, drilled using a BETSA electric discharge machine. In each case, the sample crystal was fixed to one culet face by means of high vacuum hydrocarbon grease alongside two ruby chips which allowed for pressure measurement using the ruby fluorescence method.[19] After each pressure ramp, the pressure inside the DAC was allowed to equilibrate for a minimum of 1 hour before data collection was initiated. Pressure measurements were taken immediately before and after each collection and the pressure reported as the average. The average uncertainty in pressure across the study was 0.9 kbar, with specific error bars drawn on Figures as 0.5 times the magnitude of the individual drift plus 0.5 kbar attributed to the inherent uncertainty in the pressure determination given by the ruby fluorescence method.[20] Error bars associated with

bond lengths and angles for specific refinements are drawn on Figures as the esd, as calculated by *SHELXL*.[13]

Cell refinement and data reduction was carried out using the software *CrysAlis*^{PRO}.[11] Special settings (smart background, profile agreement rejection parameters, angle-dependent profile changes) were implemented in the data reduction step to remove contaminating diamond reflections and powder rings from the data. Individual specifications of the exact settings used are contained within the CIFs. Multi-scan absorption corrections were applied with an empirical absorption correction using spherical harmonics, implemented in the *SCALE3 ABSPACK* scaling algorithm[21] through *CrysAlis*^{PRO}.[11] The dataset for **13-β** at 14.0 kbar for crystal A was solved using *SHELXT*.[12] All other structures were solved by isomorphous replacement using an appropriate starting model. Structure solution and refinement were carried out with *SHELXL*[13] using the *Olex2* interface.[14]

Atomic displacements for all non-hydrogen atoms were refined isotopically except for the rhodium atom in certain refinements, which was refined anisotropically where appropriate. All aromatic rings were restrained to an idealised 6-membered ring geometry, and all non-hydrogen atoms comprising the HBcat ligand were geometrically restrained to a planar geometry. Appropriate distance restraints were applied to all B–Ar^{F}, C–O, O–P, B–O bond distances across all refinements, as were all 1,2- and 1,3- distances associated with the CF_3 groups of the counterion and the ^{t}Bu groups of the cation. Where appropriate, the CF_3 group disorder was modelled over two positions. ADP restraints were placed on the counterion to suppress chemically unsensible ADPs in select CF_3 groups, where the combination of geometric restraints and disorder models proved insufficient. The hydrogen atom of HBcat was located with the electron density difference map in all refinements, but in select cases, distance restraints (or constraints) between the rhodium, hydrogen and boron atoms were required to preserve a sensible bonding position. All other hydrogen atoms were automatically generated and refined using a riding model.

6.4 – Data related to Chapter 4

Preparation of $[Rh(COD)_2][BAr^{F20}{}_4]$

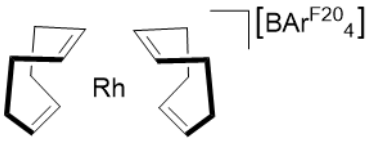

$[Rh(COD)_2][BAr^{F20}{}_4]$ was prepared using a modified procedure for the preparation of $[Rh(COD)_2][BAr^{F}{}_4]$.[8] To a J. Young's flask charged with $[Rh(COD)Cl]_2$ (150.1 mg, 0.30 mmol) and $K[BAr^{F20}{}_4]$ (437.2 mg, 0.60 mmol), CH_2Cl_2 (5 mL) was added. An excess of 1,5-COD (0.1 mL, 0.82 mmol) was added to the yellow reaction mixture, resulting in the formation of a dark red solution which was stirred at room temperature for 30 minutes. The CH_2Cl_2 solution was filtered, and the residue washed twice with CH_2Cl_2 (2 x 2 mL). Analytically pure material was obtained as red crystals by liquid-liquid diffusion of hexane into the filtered CH_2Cl_2 solution at room temperature. Yield: 478.5 mg (0.48 mmol, 80 %).

^{1}H NMR (500 MHz, CD_2Cl_2): δ 5.24 (s, 4H, CH), 2.53 (s, 8H, CH_2).

^{13}C{^{1}H} NMR (126 MHz, CD_2Cl_2): δ 148.6 (br d, $^1J_{CF}$ = 238, *o*-C_6F_5), 138.7 (app dt, $^1J_{CF}$ = 244, $^2J_{CF}$ = 13, *p*-C_6F_5), 136.7 (br t, $^1J_{CF}$ = 244, *m*-C_6F_5), 124.2 (br, *i*-C_6F_5), 108.1 (d,$^1J_{RhC}$ = 8, CH), 30.1 (s, CH_2).

^{19}F{^{1}H} NMR (376 MHz, CD_2Cl_2): δ -133.1 (br, *p*-C_6F_5), -163.7 (t, $^3J_{FF}$ = 20, *o*-C_6F_5), 133.1 (br t, $^3J_{FF}$ = 20, *m*-C_6F_5).

HR ESI-MS (positive ion, 4 kV): 210.9987, $[M - COD]^+$ (calcd 210.9989) m/z.

Anal. Calcd for $C_{40}H_{24}B_2F_{20}Rh$ (998.32 $gmol^{-1}$): C, 48.13; H, 2.42; N, 0.00. Found: C, 48.22; H, 2.34; N, 0.00.

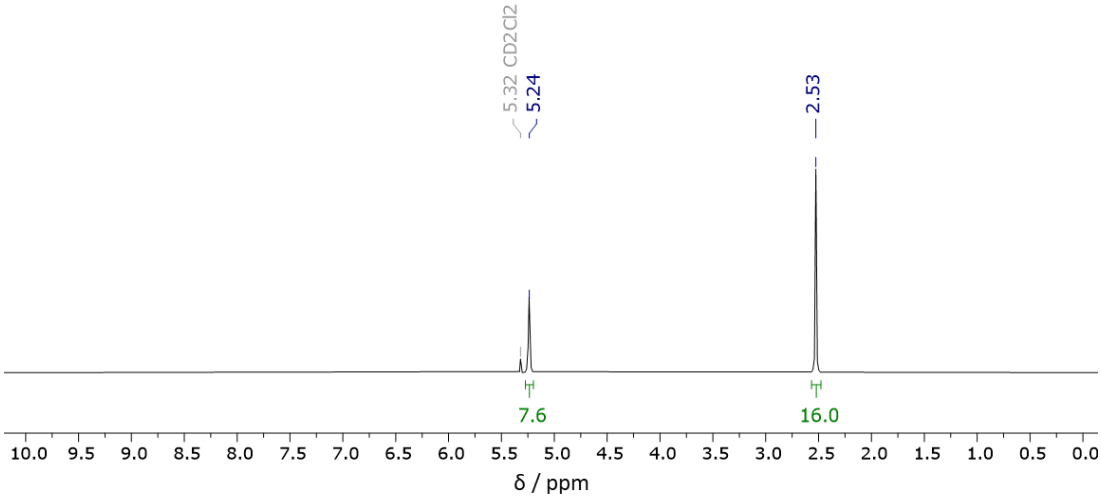

Figure 6.32 – ^{1}H NMR spectrum of [Rh(COD)$_2$][BAr$^{F20}_4$] (500 MHz, CD_2Cl_2, 298 K).

General procedure – NMR scale reactions

A stoichiometric mixture of $[Rh(COD)_2]^+$ salt and pincer ligand (PONOP or PNP) were dissolved in 1,2-$C_6H_4F_2$ ([Rh] = 50 mmol L^{-1}) and allowed to equilibrate for 5 minutes at room temperature before an excess of borane (*ca.* 3 eq.) in 1,2-$C_6H_4F_2$ (HBpin, 0.67 M; HBcat, 0.40 M) was added to the orange solution at room temperature by syringe. The reaction mixture was allowed to stand at room temperature for several hours, during which time the solution turned yellow. In all cases, complete conversion to the rhodium(I) σ-borane complex within 6 hours was confirmed upon *in situ* analysis by ^{1}H, ^{31}P and ^{11}B NMR spectroscopy. Layering the 1,2-$C_6H_4F_2$ solution with hexane afford the product as yellow crystals suitable for analysis by single crystal X-ray diffraction upon diffusion at room temperature.

General stability in solution

In the presence of excess borane, 1,2-$C_6H_4F_2$ solutions of the rhodium σ-borane complexes were persistent at room temperature for up to 48 h. Dissolution of isolated material led to partial decomposition (*ca.* 10–15%) into $[Rh(pincer)(H_2)]^+$ (pincer = PONOP, δ_{31P} 224.4 (J_{RhP} = 126 Hz); PNP, δ_{31P} 81.7 (J_{RhP} = 121 Hz)) within 24 hours at room temperature. The spectroscopic data for these complexes match the literature.[22,23]

Preparation of [Rh(PONOP)(η²-HBpin)][SbF₆], 16

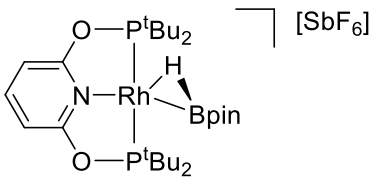

The general procedure detailed above was followed, using PONOP (10.7 mg, 26.8 µmol), [Rh(COD)$_2$][SbF$_6$] (15.0 mg, 27.0 µmol) and a 0.67 M solution of HBpin in 1,2-$C_6H_4F_2$ (120 µL, 80.4 µmol). The product was purified by crystallisation; yellow crystals suitable for X-ray diffraction were produced by liquid-liquid diffusion of hexane into the *in situ* 1,2-$C_6H_4F_2$ solution at room temperature. Yield: 4.6mg (5.1 µmol, 19 %).

^{1}H NMR (500 MHz, 1,2-$C_6H_4F_2$, selected peaks): δ 7.69 (t, $^3J_{HH}$ = 8.1, 1H, 4-py), 1.26 (vt, J_{PH} = 15.6, 36H, ^{t}Bu), 1.15 (s, 12H, HBpin), -14.96 (br s, 1H, HBpin).

^{13}C{^{1}H} NMR (126 MHz, 1,2-$C_6H_4F_2$, selected peaks): δ 164.2 (vt, J_{PC} = 5, 2-py), 147.4 (s, 4-py), 102.7 (vt, J_{PC} = 5, 3-py), 86.1 (s, HBpin{C}), 40.4 (vtd, $^1J_{PC}$ = 8, $^2J_{RhC}$ = 2, ^{t}Bu{C}), 26.9 (vt, J_{PC} = 6, ^{t}Bu{CH_3}), 24.1 (s, HBpin{CH_3}).

^{31}P{^{1}H} NMR (121 MHz, 1,2-$C_6H_4F_2$): δ 217.1 (d, J_{RhP} = 129).

^{11}B NMR (96 MHz, 1,2-$C_6H_4F_2$): 34.92 (br s, HBpin).

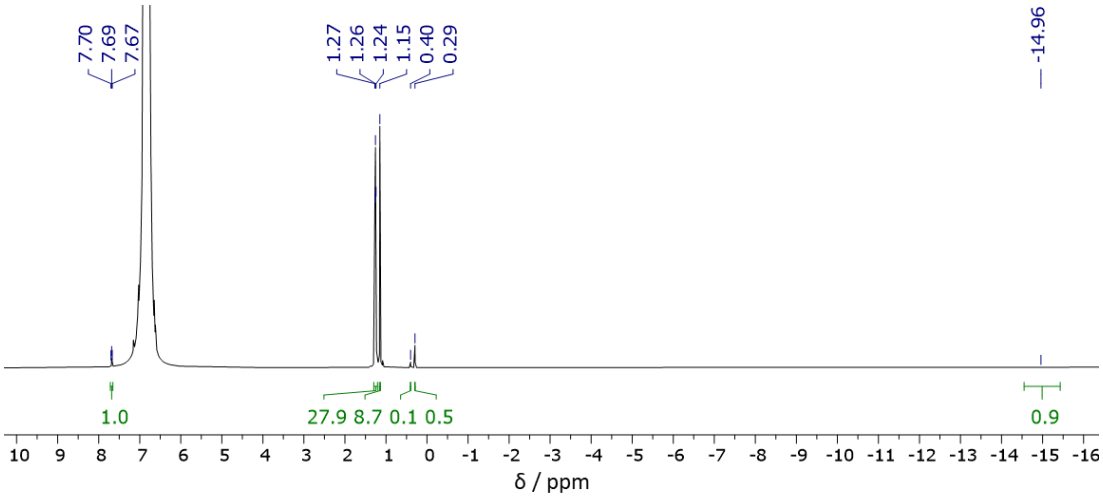

Figure 6.33 – ^{1}H NMR spectrum of **16** (500 MHz, 1,2-$C_6H_4F_2$, 298 K).

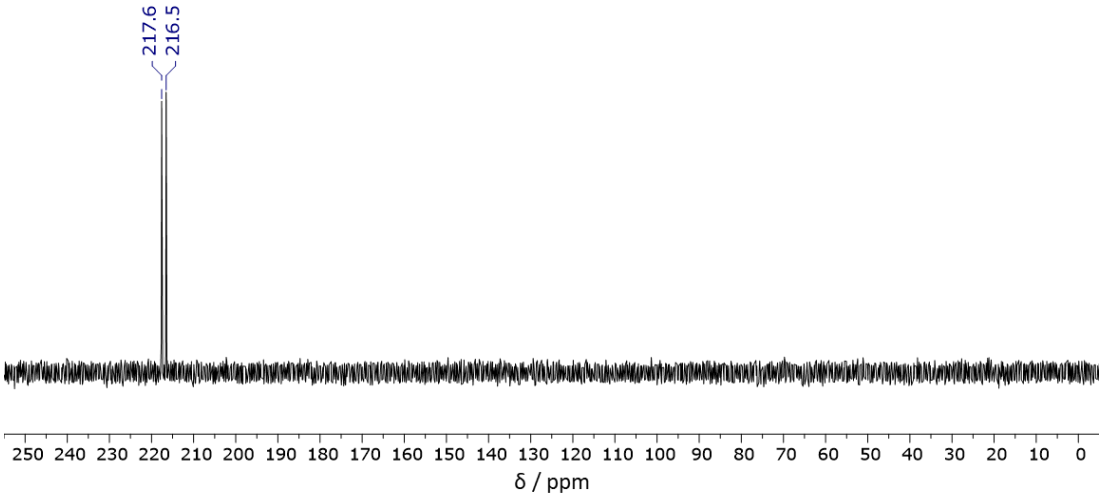

Figure 6.34 – $^{31}P\{^{1}H\}$ NMR spectrum of **16** (121 MHz, 1,2-$C_6H_4F_2$, 298 K).

Preparation of [Rh(PONOP)(η²-HBcat)][SbF₆], 17

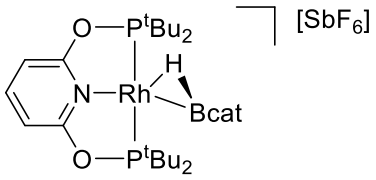

The general procedure detailed above was followed, using PONOP (7.2 mg, 18.0 µmol), $[Rh(COD)_2][SbF_6]$ (10.0 mg, 18.0 µmol) and a 0.40 M solution of HBcat in 1,2-$C_6H_4F_2$ (150 µL, 60.0 µmol). The product could not be purified by crystallisation since it precipitated out of solution as a partially decomposed oil. The NMR data presented herein are for the *in situ* reaction mixtures, which contain excess COD and borane.

^{1}H NMR (300 MHz, 1,2-$C_6H_4F_2$, selected peaks): δ 7.80 (t, $^{3}J_{HH}$ = 8.2, 1H, 4-py), 1.29 (vt, J_{PH} = 15.8, 36H, ^{t}Bu), -13.93 (br s, 1H, HBcat).

^{31}P{^{1}H} NMR (121 MHz, 1,2-$C_6H_4F_2$): δ 217.4 (d, $^{1}J_{RhP}$ = 123).

^{11}B NMR (96 MHz, 1,2-$C_6H_4F_2$, selected peaks): 36.03 (br s, HBcat).

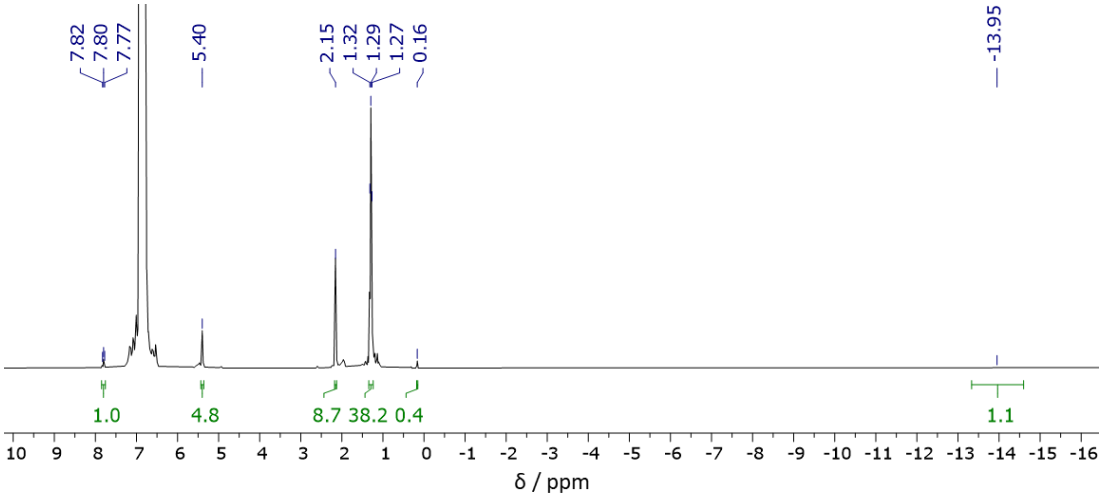

Figure 6.35 – ^{1}H NMR spectrum of **17** (300 MHz, 1,2-$C_6H_4F_2$, 298 K).

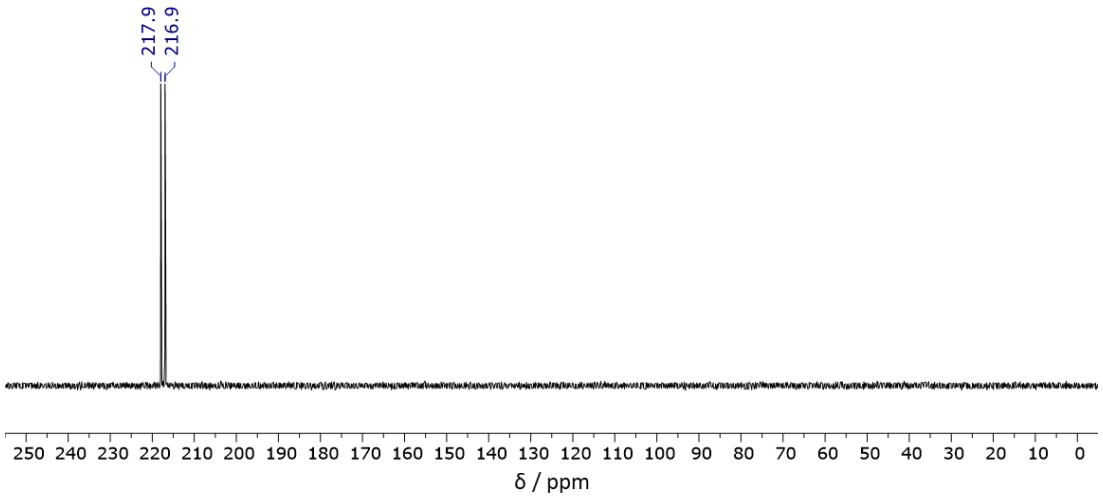

Figure 6.36 – ^{31}P{^{1}H} NMR spectrum of **17** (121 MHz, 1,2-$C_6H_4F_2$, 298 K).

Preparation of [Rh(PNP)(η^2-HBpin)][SbF$_6$], 18

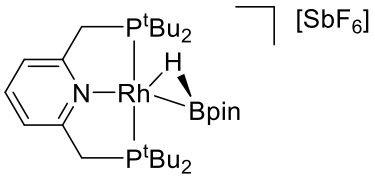

The general procedure detailed above was followed, using PNP (10.7 mg, 26.8 µmol), [Rh(COD)$_2$][SbF$_6$] (15.0 mg, 27.0 µmol) and a 0.67 M solution of HBpin in 1,2-$C_6H_4F_2$ (120 µL, 80.4 µmol). The product was purified by crystallisation; yellow crystals suitable for X-ray diffraction were produced by liquid-liquid diffusion of

hexane into the *in situ* 1,2-$C_6H_4F_2$ solution at room temperature. Yield: 9.2 mg (10.3 µmol, 39 %).

^{1}H NMR (300 MHz, 1,2-$C_6H_4F_2$, selected peaks): δ 7.59 (t, $^{3}J_{HH}$ = 7.8, 1H, 4-py), 7.31 (d, $^{3}J_{HH}$ = 7.8, 2H, 3-py), 3.47-3.49 (m, 4H, PCH_2), 1.17 (vt, J_{PH} = 14.2, 36H, ^{t}Bu), 1.12 (s, 12H, HBpin), -17.58 (br s, 1H, HBpin).

^{13}C{^{1}H} NMR (126 MHz, 1,2-$C_6H_4F_2$, selected peaks): δ 164.4 (vt, J_{PC} = 6, 2-py), 141.0 (s, 4-py), 121.0 (vt, J_{PC} = 5, 3-py), 84.5 (s, HBpin{C}), 36.4 (vt, J_{PC} = 8, PCH_2), 35.3 (vtd, $^{1}J_{PC}$ = 8, $^{2}J_{RhC}$ = 2, ^{t}Bu{C}), 29.0 (vt, J_{PC} = 6, ^{t}Bu{CH_3}), 24.3 (s, HBpin{CH_3}).

^{31}P{^{1}H} NMR (121 MHz, 1,2-$C_6H_4F_2$): δ 73.9 (d, $^{1}J_{RhP}$ = 123).

^{11}B NMR (96 MHz, 1,2-$C_6H_4F_2$): 35.10 (br s, HBpin).

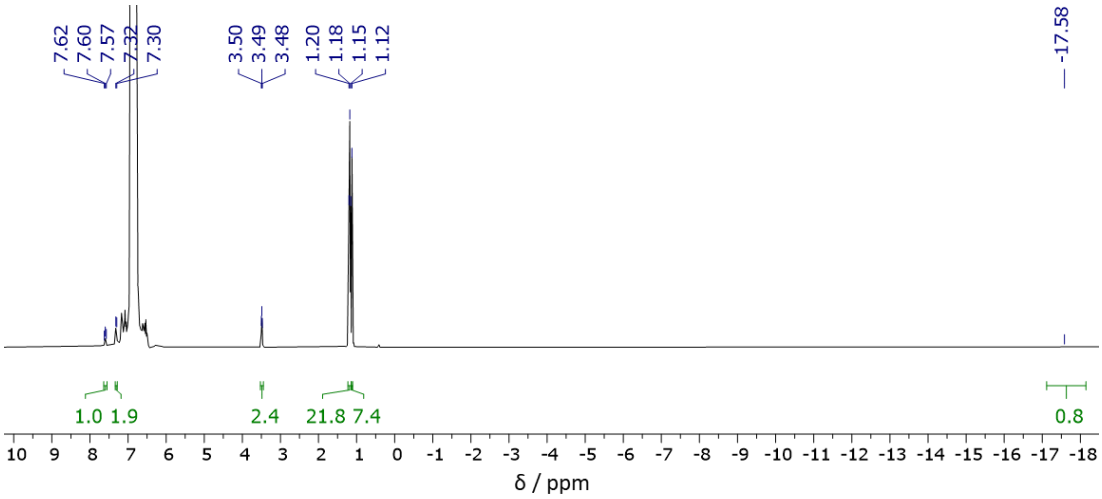

Figure 6.37 – ^{1}H NMR spectrum of **18** (300 MHz, 1,2-$C_6H_4F_2$, 298 K).

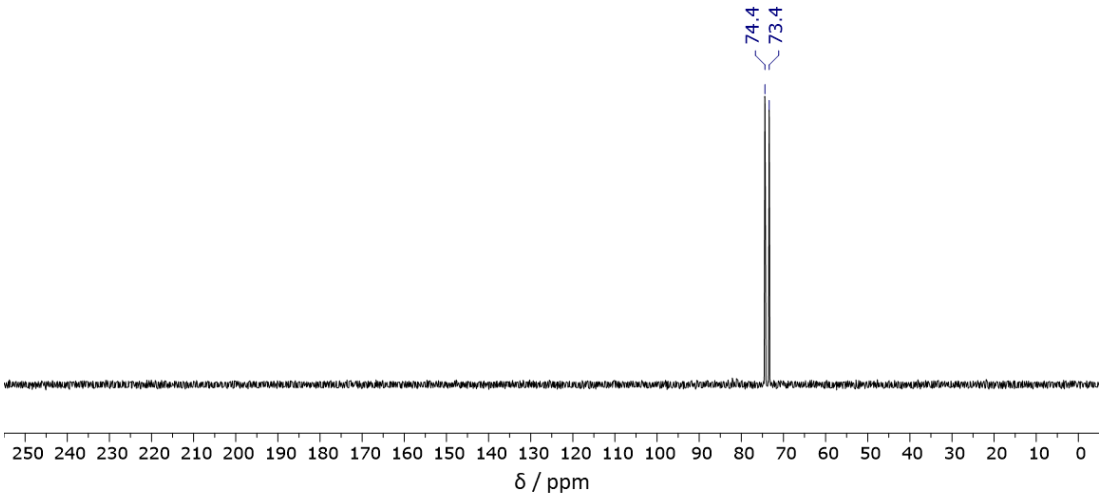

Figure 6.38 - ^{31}P{^{1}H} NMR spectrum of **18** (121 MHz, 1,2-$C_6H_4F_2$, 298 K).

Preparation of [Rh(PNP)(η²-HBcat)][SbF₆] / [Rh(PNP)(H)(Bcat)][SbF₆], co-crystal 19

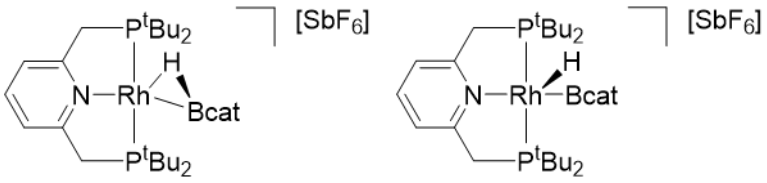

The general procedure detailed above was followed, using PNP (10.2 mg, 25.8 µmol), $[Rh(COD)_2][SbF_6]$ (15.0 mg, 27.0 µmol) and a 0.40 M solution of HBcat in 1,2-$C_6H_4F_2$ (225 µL, 90.0 µmol). The product was purified by crystallisation; yellow crystals suitable for X-ray diffraction studies were produced by liquid-liquid diffusion of hexane into the *in situ* 1,2-$C_6H_4F_2$ solution at room temperature. Yield: 7.7 mg (9.0 µmol, 35 %).

^{1}H NMR (500 MHz, 1,2-$C_6H_4F_2$, selected peaks): δ 7.64 (t, $^3J_{HH}$ = 7.8, 1H, 4-py), 7.41 (d, $^3J_{HH}$ = 7.8, 2H, 3-py), 3.67-3.69 (m, 4H, PCH_2), 1.13 (vt, J_{PH} = 14.6, 36H, ^{t}Bu), -17.84 (br d, J_{RhH} = 40.8, 1H, HBcat).

^{13}C{^{1}H} NMR (126 MHz, 1,2-$C_6H_4F_2$, selected peaks): δ 163.7 (vt, J_{PC} = 6, 2-py), 149.2 (s, HBcat{C}), 141.2 (s, 4-py), 123.4 (s, HBcat{CH}), 121.5 (vt, J_{PC} = 5, 3-py), 111.4 (s, HBcat{CH}), 36.7 (vt, J_{PC} = 8, PCH_2), 35.6 (vtd, J_{PC} = 8, $^2J_{RhC}$ = 2, ^{t}Bu{C}), 28.6 (vt, J_{PC} = 6, ^{t}Bu{CH_3}).

^{31}P{^{1}H} NMR (121 MHz, 1,2-$C_6H_4F_2$): δ 76.3 (d, $^1J_{RhP}$ = 113).

^{11}B NMR (96 MHz, 1,2-$C_6H_4F_2$): 38.91 (br s, HBcat).

IR (KBr, cm^{-1}): 1610 (obscured by HBcat stretch; ν_{BH})

Anal. Calcd for $C_{29}H_{48}BF_6NO_2P_2RhSb$ (854.12 $gmol^{-1}$): C, 40.78; H, 5.66; N, 1.64. Found: C, 38.81; H, 5.42; N, 1.89.

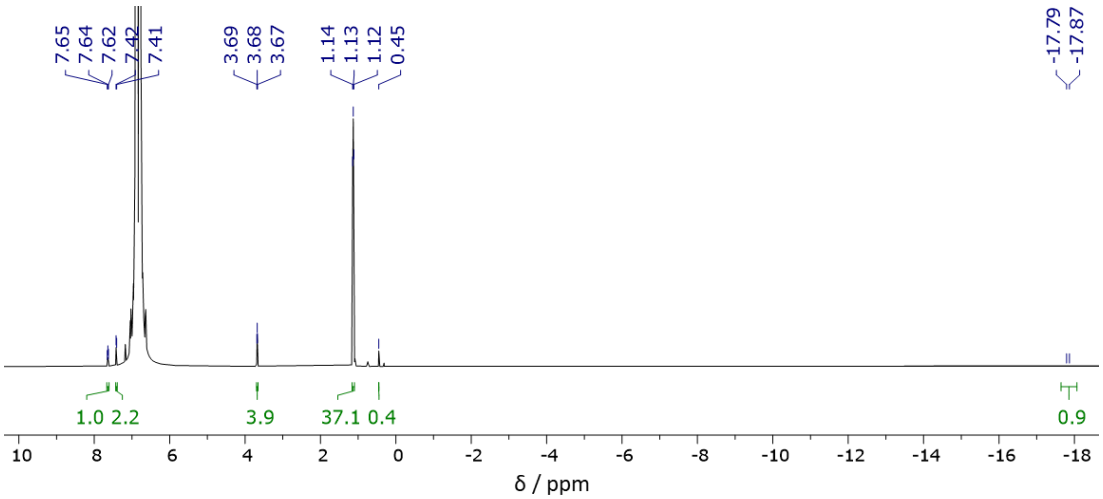

Figure 6.39 – ^{1}H NMR spectrum of **19** (500 MHz, 1,2-$C_6H_4F_2$, 298 K).

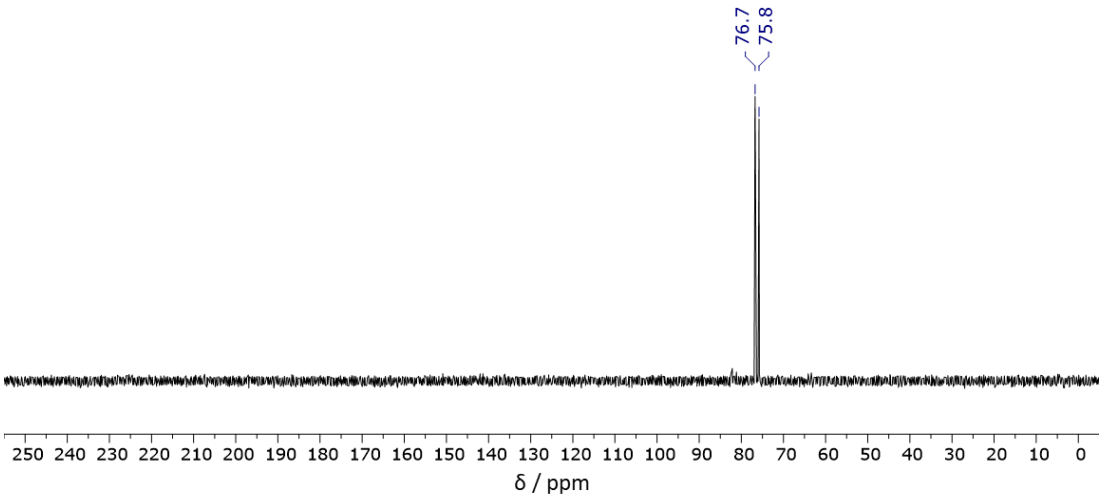

Figure 6.40 – ^{31}P{^{1}H} NMR spectrum of **19** (121 MHz, 1,2-$C_6H_4F_2$, 298 K).

Preparation of [Rh(PONOP)(η^2-HBpin)][BAr$^{F20}{}_4$], 20

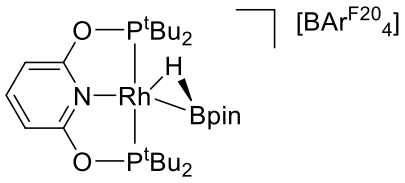

The general procedure detailed above was followed, using PONOP (9.9 mg, 25.0 µmol), [Rh(COD)$_2$][BAr$^{F20}{}_4$] (25.0 mg, 25.0 µmol) and a 0.67 M solution of HBpin in 1,2-$C_6H_4F_2$ (120 µL, 80.4 µmol). The product was purified by crystallisation; yellow crystals suitable for X-ray diffraction studies were produced by

liquid-liquid diffusion of hexane into the *in situ* 1,2-$C_6H_4F_2$ solution at room temperature. Yield: 25.9 mg (19.8 µmol, 79 %).

^{1}H NMR (500 MHz, 1,2-$C_6H_4F_2$, selected peaks): δ 7.64 (t, $^{3}J_{HH}$ = 8.2, 1H, 4-py), 1.26 (vt, J_{PH} = 15.6, 36H, ^{t}Bu), 1.15 (s, 12H, HBpin), -14.94 (br s, 1H, HBpin).

^{13}C{^{1}H} NMR (126 MHz, 1,2-$C_6H_4F_2$, selected peaks): δ 164.4 (vt, J_{PC} = 6, 2-py), 141.0 (s, 4-py), 121.0 (vt, J_{PC} = 5, 3-py), 84.5 (s, HBpin{C}), 36.4 (vt, J_{PC} = 8, PCH_2), 35.3 (vtd, $^{1}J_{PC}$ = 8, $^{2}J_{RhC}$ = 2, ^{t}Bu{C}), 29.0 (vt, J_{PC} = 6, ^{t}Bu{CH_3}), 24.3 (s, HBpin{CH_3}).

The complicated couplings observed in the ^{13}C{^{1}H} NMR spectrum recorded in 1,2-$C_6H_4F_2$ precluded the assignment of the counterion $[BAr^{F20}{}_4]^-$.

^{31}P{^{1}H} NMR (121 MHz, 1,2-$C_6H_4F_2$): δ 217.2 (d, J_{RhP} = 129).

^{11}B NMR (96 MHz, 1,2-$C_6H_4F_2$): 34.50 (br s, HBpin), -16.25 (s, $BAr^{F20}{}_4$).

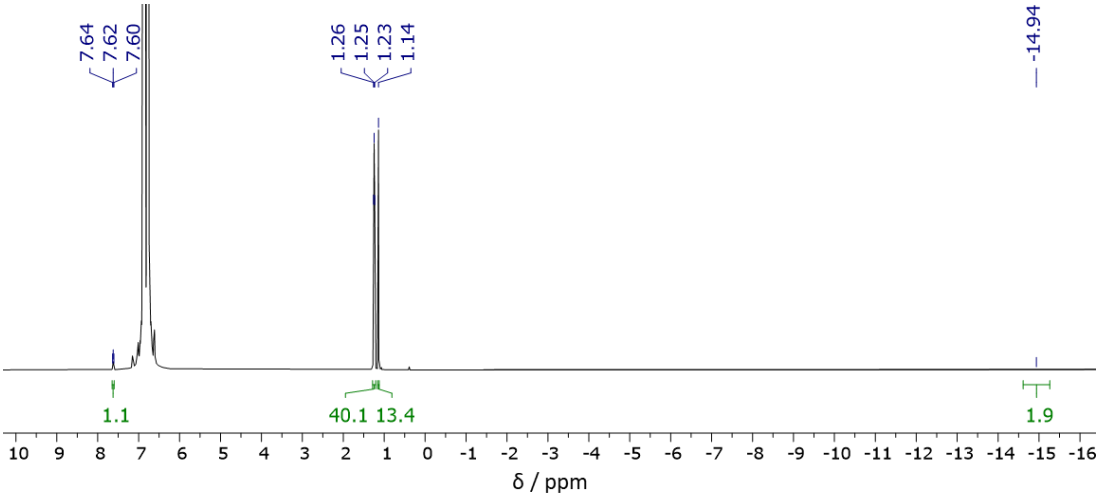

Figure 6.41 – ^{1}H NMR spectrum of **20** (500 MHz, 1,2-$C_6H_4F_2$, 298 K).

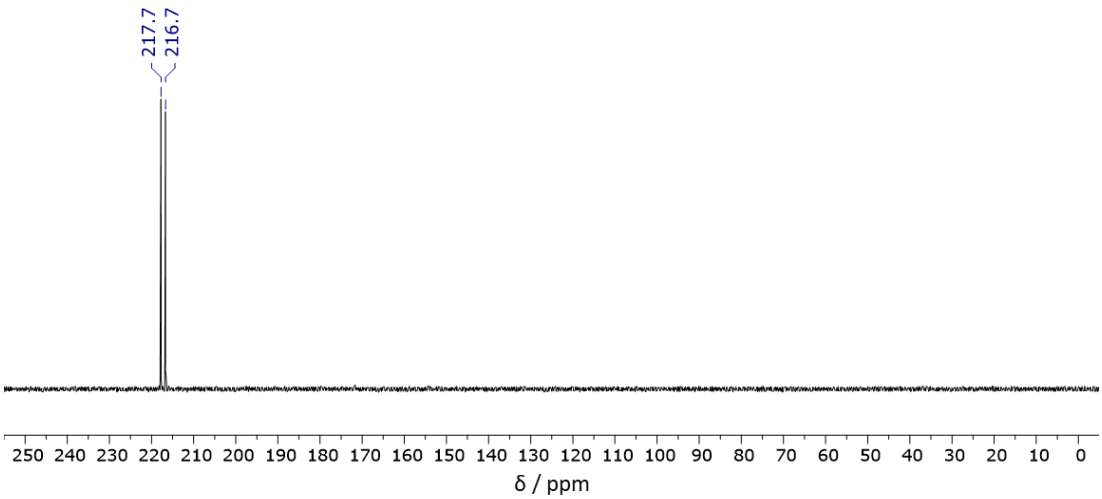

Figure 6.42 – $^{31}P\{^{1}H\}$ NMR spectrum of **20** (121 MHz, 1,2-$C_6H_4F_2$, 298 K).

Preparation of [Rh(PONOP)(η²-HBcat)][BAr$^{F20}_4$], 21

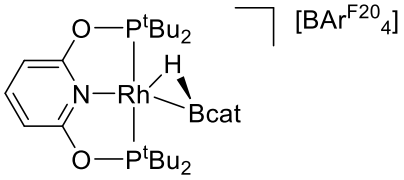

The general procedure detailed above was followed, using PONOP (4.0 mg, 10.1 µmol), [Rh(COD)$_2$][BAr$^{F20}_4$] (10.0 mg, 10.0 µmol) and a 0.40 M solution of HBcat in 1,2-$C_6H_4F_2$ (75 µL, 30.0 µmol). The product could not be purified by crystallisation since it precipitated out of solution as a partially decomposed oil. The NMR data presented herein are for the *in situ* reaction mixtures, which contain two equivalents of COD and excess borane.

^{1}H NMR (300 MHz, 1,2-$C_6H_4F_2$, selected peaks): δ 7.73 (t, $^{3}J_{HH}$ = 8.3, 1H, 4-py), 1.31 (vt, J_{PH} = 15.7, 36H, ^{t}Bu), -13.89 (br s, 1H, HBcat).

^{31}P{^{1}H} NMR (121 MHz, 1,2-$C_6H_4F_2$): δ 217.8 (d, J_{RhP} = 123).

^{11}B NMR (96 MHz, 1,2-$C_6H_4F_2$, selected peaks): 36.28 (br s, HBcat), -16.24 (s, BAr$^{F20}_4$).

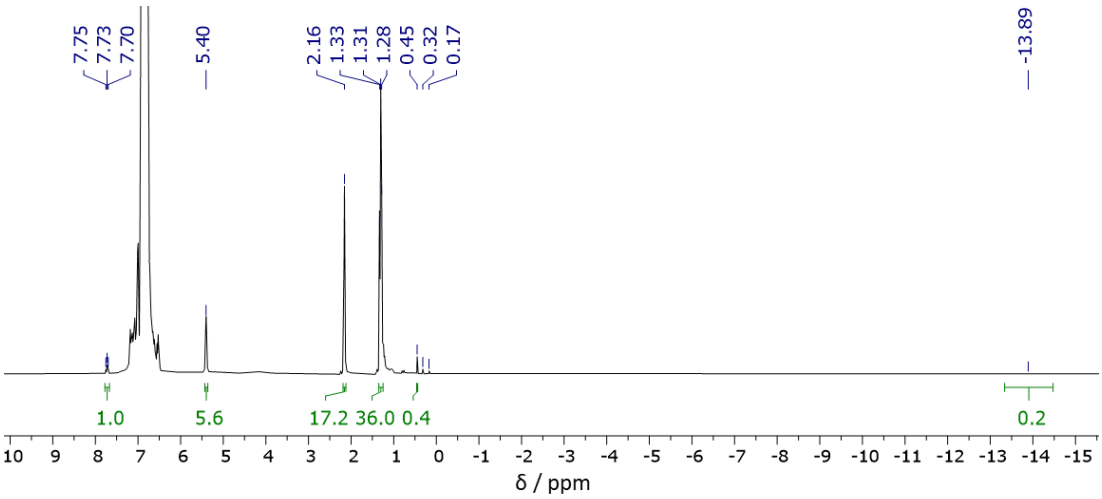

Figure 6.43 – ^{1}H NMR spectrum of **21** (300 MHz, 1,2-$C_6H_4F_2$, 298 K).

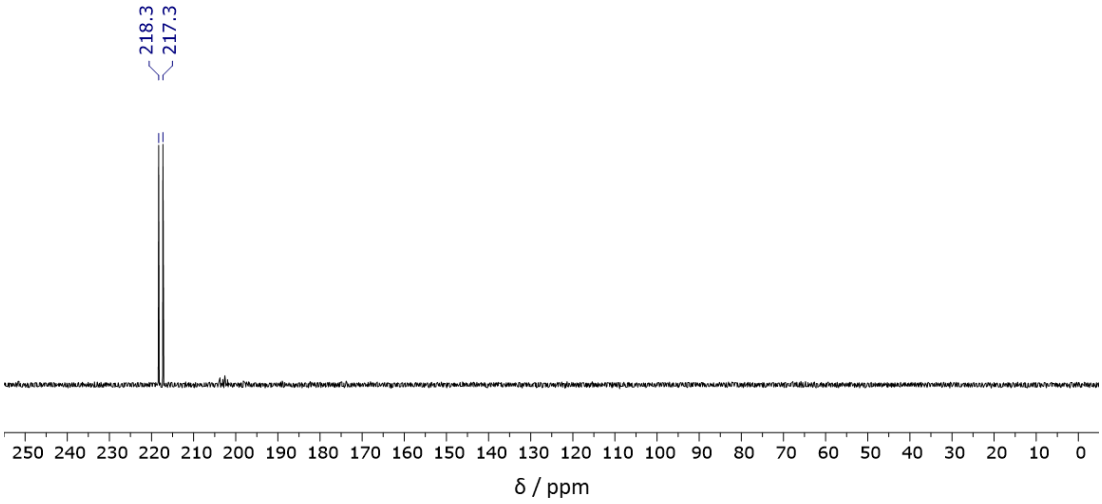

Figure 6.44 – $^{31}P\{^{1}H\}$ NMR spectrum of **21** (121 MHz, 1,2-$C_6H_4F_2$, 298 K).

Preparation of [Rh(PNP)(η²-HBpin)][BAr$^{F20}_4$], 22

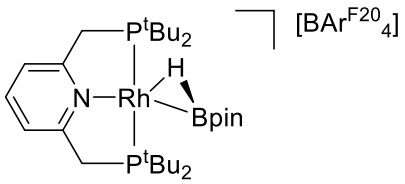

The general procedure detailed above was followed, using PNP (9.9 mg, 25.0 µmol), [Rh(COD)$_2$][BAr$^{F20}_4$] (25.0 mg, 25.0 µmol) and a 0.67 M solution of HBpin in 1,2-$C_6H_4F_2$ (120 µL, 80.4 µmol). The product was purified by crystallisation; yellow crystals suitable for X-ray diffraction studies were produced by liquid-liquid diffusion

of hexane into the *in situ* 1,2-$C_6H_4F_2$ solution at room temperature. Yield: 25.7 mg (19.7 µmol, 79 %).

^{1}H NMR (500 MHz, 1,2-$C_6H_4F_2$, selected peaks): δ 7.57 (t, $^{3}J_{HH}$ = 7.8, 1H, 4-py), 7.24 (d, $^{3}J_{HH}$ = 7.8, 2H, 3-py), 3.44-3.47 (m, 4H, PCH_2), 1.18 (vt, J_{PH} = 14.1, 36H, ^{t}Bu), 1.13 (s, 12H, HBpin), -17.59 (br s, 1H, HBpin).

^{13}C{^{1}H} NMR (126 MHz, 1,2-$C_6H_4F_2$, selected peaks): δ 164.4 (vt, J_{PC} = 7, 2-py), 140.9 (s, 4-py), 120.8 (vt, J_{PC} = 8, 3-py), 84.6 (s, HBpin{C}), 36.4 (vt, J_{PC} = 8, PCH_2), 35.3 (vtd, $^{1}J_{PC}$ = 8, $^{2}J_{RhC}$ = 2, ^{t}Bu{C}), 28.9 (vt, J_{PC} = 6, ^{t}Bu{CH_3}), 24.3 (s, HBpin{CH_3}).

The complicated couplings observed in the ^{13}C{^{1}H} NMR spectrum recorded in 1,2-$C_6H_4F_2$ precluded the assignment of the counterion $[BAr^{F20}{}_4]^-$.

^{31}P{^{1}H} NMR (121 MHz, 1,2-$C_6H_4F_2$): δ 73.9 (d, J_{RhP} = 123).

^{11}B NMR (96 MHz, 1,2-$C_6H_4F_2$): 35.51 (br s, HBpin), -16.26 (s, $BAr^{F20}{}_4$).

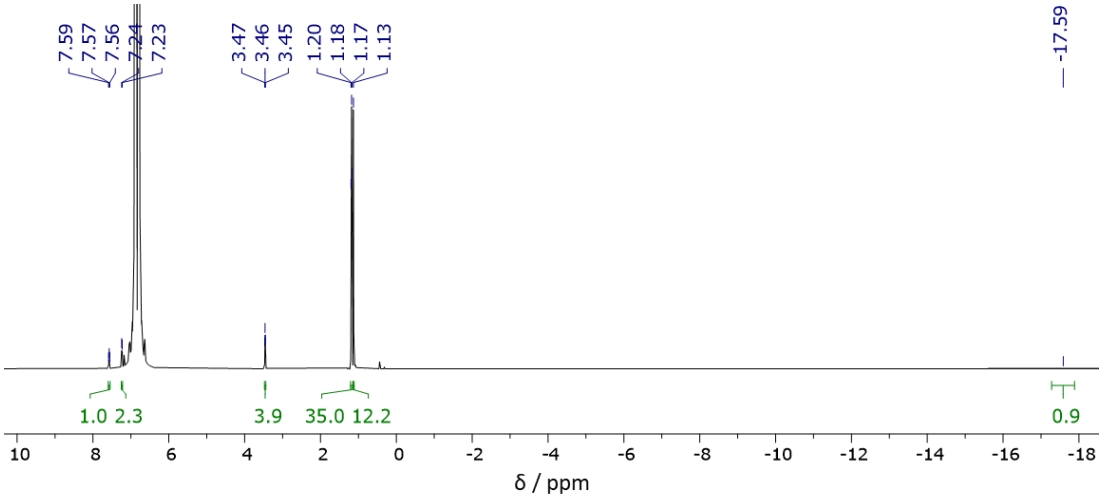

Figure 6.45 – ^{1}H NMR spectrum of **22** (500 MHz, 1,2-$C_6H_4F_2$, 298 K).

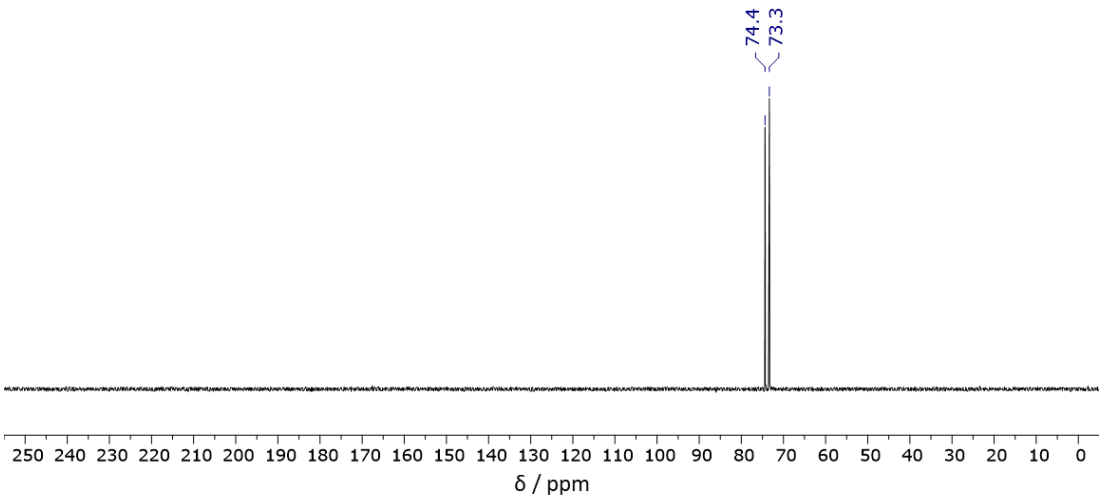

Figure 6.46 – $^{31}P\{^{1}H\}$ NMR spectrum of **22** (121 MHz, 1,2-$C_6H_4F_2$, 298 K).

Preparation of [Rh(PNP)(H)(Bcat)][BAr$^{F20}_4$], 23

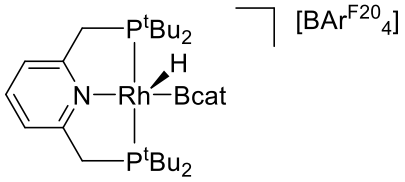

The general procedure detailed above was followed, using PNP (9.9 mg, 25.0 µmol), [Rh(COD)$_2$][BAr$^{F20}_4$] (25.0 mg, 25.0 µmol) and a 0.40 M solution of HBcat in 1,2-$C_6H_4F_2$ (225 µL, 90.0 µmol). The product was purified by crystallisation; yellow crystals suitable for X-ray diffraction studies were produced by liquid-liquid diffusion of hexane into the *in situ* 1,2-$C_6H_4F_2$ solution at room temperature. Yield: 24.3 mg (18.7 µmol, 75 %).

^{1}H NMR (500 MHz, 1,2-$C_6H_4F_2$, 298 K, selected peaks): δ 7.64 (t, $^{3}J_{HH}$ = 7.9, 1H, 4-py), 7.34 (d, $^{3}J_{HH}$ = 7.8, 2H, 3-py), 3.62-3.66 (m, 4H, PCH_2), 1.14 (vt, J_{PH} = 14.4, 36H, ^{t}Bu), -17.72 (br d, J_{RhH} = 40.0, 1H, RhH).

^{13}C{^{1}H} NMR (126 MHz, 1,2-$C_6H_4F_2$, 298 K, selected peaks): δ 163.7 (vt, J_{PC} = 7, 2-py), 149.2 (s, HBcat{C}), 141.1 (s, 4-py), 122.4 (s, HBcat{CH}), 121.3 (vt, J_{PC} = 8, 3-py), 111.4 (s, HBcat{CH}), 36.7 (vt, J_{PC} = 8, PCH_2), 35.7 (vtd, $^{1}J_{PC}$ = 9, $^{2}J_{RhC}$ = 2, ^{t}Bu{C}), 28.5 (vt, J_{PC} = 5, ^{t}Bu{CH_3}).

The complicated couplings observed in the $^{13}C\{^{1}H\}$ NMR spectrum precluded the assignment of the counterion $[BAr^{F20}{}_4]^-$.

$^{31}P\{^{1}H\}$ NMR (121 MHz, 1,2-$C_6H_4F_2$, 298 K): δ 76.2 (d, J_{RhP} = 113).

^{11}B NMR (96 MHz, 1,2-$C_6H_4F_2$, 298 K): 37.39 (br s, HBcat), -16.26 (s, $BAr^{F20}{}_4$).

$^{1}H\{^{11}B\}$ NMR (500 MHz, CD_2Cl_2, 298 K): δ 7.93 (t, $^{3}J_{HH}$ = 7.8, 1H, 4-py), 7.57 (d, $^{3}J_{HH}$ = 7.8, 2H, 3-py), 7.18 (d, $^{3}J_{HH}$ = 5.8, $^{4}J_{HH}$ = 3.3, 2H, HBcat 3-py), 7.06 (d, $^{3}J_{HH}$ = 5.8, $^{4}J_{HH}$ = 3.3, 2H, HBcat 2-py), 3.81-3.84 (m, 4H, PCH_2), 1.30 (vt, J_{PH} = 14.6, 36H, ^{t}Bu), -17.83 (br d, J_{RhH} = 42.3, 1H, HBcat).

$^{31}P\{^{1}H\}$ NMR (202 MHz, CD_2Cl_2, 298 K): δ 76.2 (d, J_{RhP} = 113).

^{11}B NMR (160 MHz, CD_2Cl_2, 298 K): 39.49 (br s, HBcat), -16.65 (s, $BAr^{F20}{}_4$).

$^{1}H\{^{11}B\}$ NMR (500 MHz, CD_2Cl_2, 193 K): δ 7.88 (t, $^{3}J_{HH}$ = 7.8, 1H, 4-py), 7.53 (d, $^{3}J_{HH}$ = 7.8, 2H, 3-py), 7.15 (d, $^{3}J_{HH}$ = 5.8, $^{4}J_{HH}$ = 3.3, 2H, HBcat 3-py), 7.01 (d, $^{3}J_{HH}$ = 5.8, $^{4}J_{HH}$ = 3.3, 2H, HBcat 2-py), 3.72-3.77 (m, 4H, PCH_2), 1.19 (vt, J_{PH} = 13.7, 36H, ^{t}Bu), -18.28 (br d, J_{RhH} = 42.2, 1H, HBcat).

$^{31}P\{^{1}H\}$ NMR (202 MHz, CD_2Cl_2, 193 K): δ 75.3 (d, J_{RhP} = 113).

^{11}B NMR (160 MHz, CD_2Cl_2, 193 K): -17.08 (s, $BAr^{F20}{}_4$).

IR (KBr, cm^{-1}): 1600 (ν_{RhH}), 1569 (ν_{RhB}).

Anal. Calcd for $C_{53}H_{48}B_2F_{20}NO_2P_2Rh$ (1297.41 $gmol^{-1}$): C, 49.07; H, 3.73; N, 1.08. Found: C, 49.32; H, 3.74; N, 1.10.

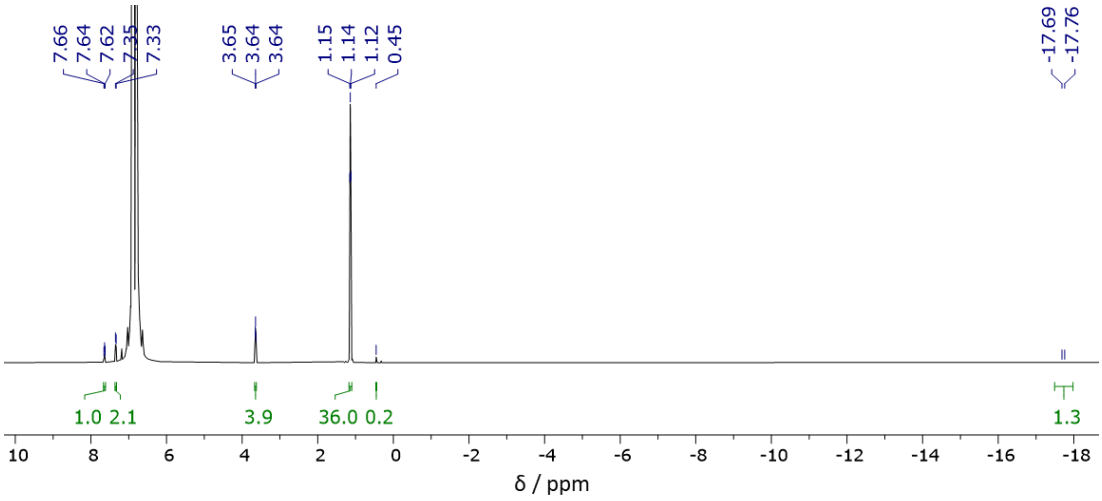

Figure 6.47 – ^{1}H NMR spectrum of **23** (500 MHz, 1,2-$C_6H_4F_2$, 298 K).

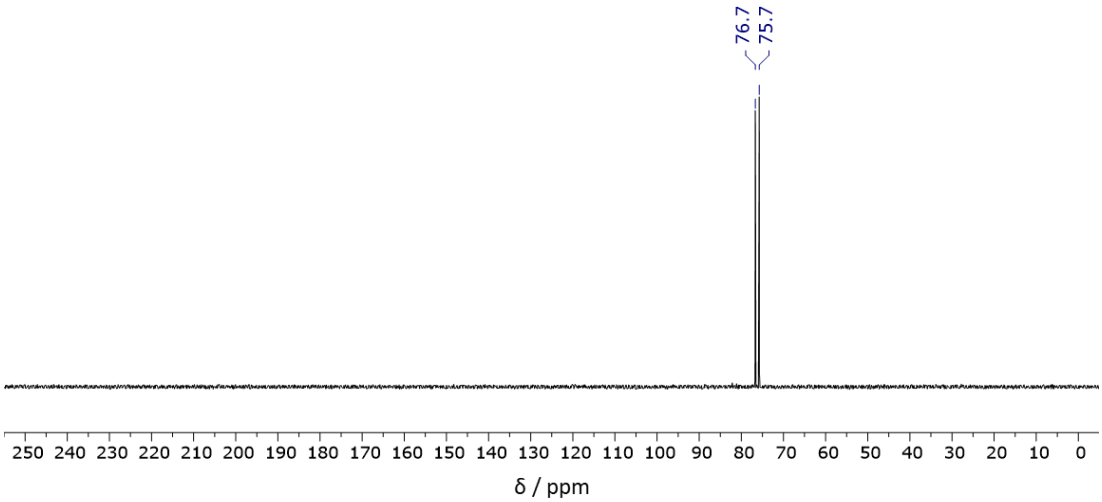

Figure 6.48 – $^{31}P\{^{1}H\}$ NMR spectrum of **23** (121 MHz, 1,2-$C_6H_4F_2$, 298 K).

Preparation of VT-NMR samples of 23

A CD_2Cl_2 solution of isolated material (20 mmol L^{-1}) for variable temperature NMR analysis was prepared by vacuum transfer of the solvent onto the sample within a J. Young's valve NMR tube pre-fitted with a ceramic spinner. The sample was thawed at 193 K and inserted into a pre-cooled spectrometer (500 MHz) and immediately analysed at 193 K. The sample was thereafter removed from the spectrometer and stored at 193 K before analysis at 298 K. Partial decomposition was observed at 298 K, since CD_2Cl_2 solutions of **23** partially decompose over the course of several hours.

Reaction of 23 with carbon monoxide

Dull yellow crystallites of **23** (13.0 mg, 10.0 μmol) in a J. Young's valve NMR tube were placed under an atmosphere of carbon monoxide (1 atm) at room temperature. The sample became bright yellow within 10 minutes but was left to stand at room temperature for 24 hours before the carbon monoxide was removed under a stream of argon. Analysis of the sample by IR spectroscopy indicated quantitative formation of [Rh(PNP)(CO)][BAr^{F20}_4]·HBcat, **24**·HBcat (ν_{CO} = 1981 cm^{-1},[24] ν_{BH} = 2655 cm^{-1}).[25] Treatment of single crystals of **23** with carbon monoxide (1 atm, 24 h) followed by **24**·HBcat, confirming the solid-state reaction to be a single crystal to single crystal transformation. Powdered samples of **23** exposed to carbon monoxide (1 atm, 24 h) were dissolved in CD_2Cl_2 and immediately analysed by NMR spectroscopy,

confirming the quantitative formation of **24** (δ_{31P} 78.3, J_{RhP} = 121 Hz)[24] alongside free HBcat (δ_{11B}: 28.9 (d, $^{1}J_{BH}$ = 194)).[26-28] Over the course of two weeks at room temperature, HBcat partially decomposed (*ca*. 30 %) into a mixture of B_2cat_2 (δ_{11B}: 22.6 (br))[29] and molecular hydrogen (δ_{1H}: 4.60 (s))[30] within the solution, as observed by NMR spectroscopy. The decomposition was thought to be assisted by undetectable amounts of the precursor $[Rh(COD)_2][BAr^{F20}{}_4]$ present in isolated crystalline samples of **23**.[31,32] Exposure of CD_2Cl_2 solutions of **23** (20 mol [Rh] L^{-1}) to carbon monoxide afforded the same products.

Selected data for **24**:

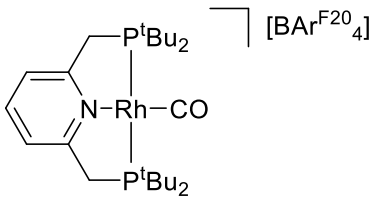

^{1}H NMR (300 MHz, CD_2Cl_2, selected peaks): δ 7.81 (t, $^{3}J_{HH}$ = 7.8, 1H, 4-py), 7.46 (d, $^{3}J_{HH}$ = 7.9, 1H, 3-py), 3.71-3.74 (m, 4H, PCH_2), 1.38 (vt, J_{PH} = 15.1, 36H, ^{t}Bu).

^{13}C{^{1}H} NMR (126 MHz, CD_2Cl_2, 298 K, selected peaks): δ 195.0 (dt, $^{1}J_{RhC}$ = 70, $^{2}J_{PC}$ = 14, RhCO), 165.5 (vtd, $^{2}J_{PC}$ = 12, $^{2}J_{RhC}$ = 2, 2-py), 148.7 (br d, $^{1}J_{CF}$ = 235, *o*-C_6F_5), 141.2 (s, 4-py), 137.8 (br tt, $^{1}J_{CF}$ = 246, $^{2}J_{CF}$ = 15, *m*-C_6F_5), 122.2 (vt, J_{PC} = 11, 3-py), 36.5 (vt, J_{PC} = 16, PCH_2), 36.3-36.5 (obscured vtd, $^{1}J_{PC}$ = 18, $^{2}J_{RhC}$ = 2, ^{t}Bu{C}), 29.5 (vt, J_{PC} = 6, ^{t}Bu{CH_3}).

The complicated couplings observed in the $^{13}C\{^{1}H\}$ NMR spectrum precluded the full assignment of the counterion $[BAr^{F20}{}_4]^-$.

^{31}P{^{1}H} NMR (162 MHz, CD_2Cl_2): δ 78.3 (d, J_{RhP} = 121).

IR (KBr, cm^{-1}): 1981 (ν_{RhCO}).

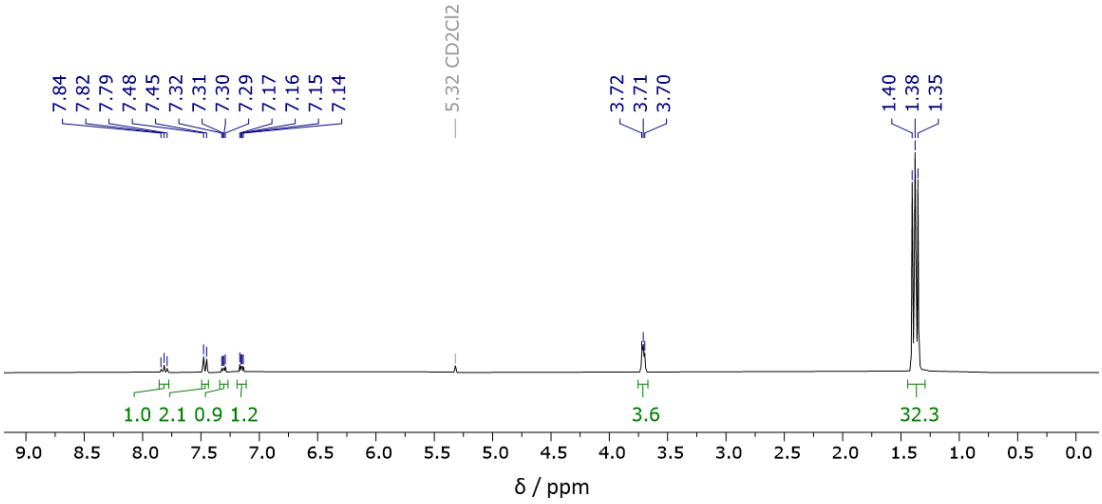

Figure 6.49 – ^{1}H NMR spectrum of **24**, prepared by exposing crystallites of **23** to carbon monoxide for 24 hours before being dissolved in CD_2Cl_2 (300 MHz, CD_2Cl_2, 298 K).

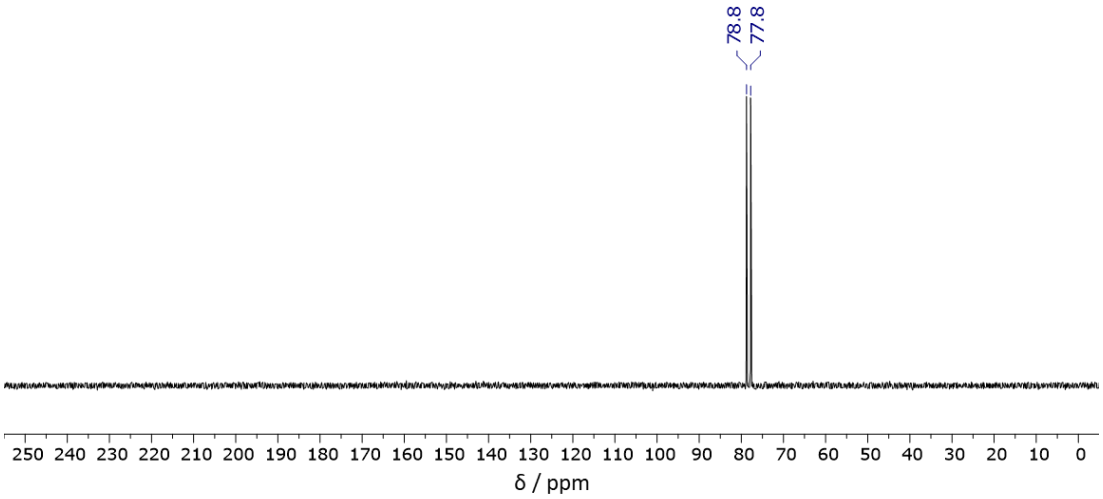

Figure 6.50 – ^{31}P{^{1}H} NMR spectrum of **24**, prepared by exposing crystallites of **23** to carbon monoxide for 24 hours before being dissolved in CD_2Cl_2 (121 MHz, CD_2Cl_2, 298 K).

Reaction of 15 with carbon monoxide

Yellow crystallites of **15** (14.3 mg, 9.7 μmol) in a J. Young's valve NMR tube were placed under an atmosphere of carbon monoxide (1 atm) at room temperature. The sample became bright yellow within 10 minutes but was left to stand at room temperature for 24 hours before the carbon monoxide was removed under a stream of argon. Analysis by IR spectroscopy indicated quantitative formation of [Rh(PNP)(CO)][BAr$^{F}_4$]·HBcat, **F**·HBcat (ν_{CO} = 1981 cm^{-1},[24] ν_{BH} = 2655 cm^{-1}).[25]

Powdered samples of **23** exposed to carbon monoxide were dissolved in CD_2Cl_2 and immediately analysed by NMR spectroscopy, confirming the quantitative formation of the previously reported complex **F** (δ_{31P} 78.3, J_{RhP} = 121 Hz)[9,24] alongside free HBcat (δ_{11B}: 28.9 (d, $^1J_{BH}$ = 194)).[26-28] Over the course of 72 hours at room temperature, HBcat fully decomposed into a mixture of B_2cat_2 (δ_{11B}: 22.6 (br))[29] and molecular hydrogen (δ_{1H}: 4.60 (s))[30] within the solution, as observed by NMR spectroscopy. The decomposition was thought to be assisted by undetectable amounts of the precursor $[Rh(COD)_2][BAr^F{}_4]$ present in isolated crystalline samples of **15**.[31,32] Exposure of CD_2Cl_2 solutions of **15** (20 mol [Rh] L^{-1}) to carbon monoxide afforded the same products.

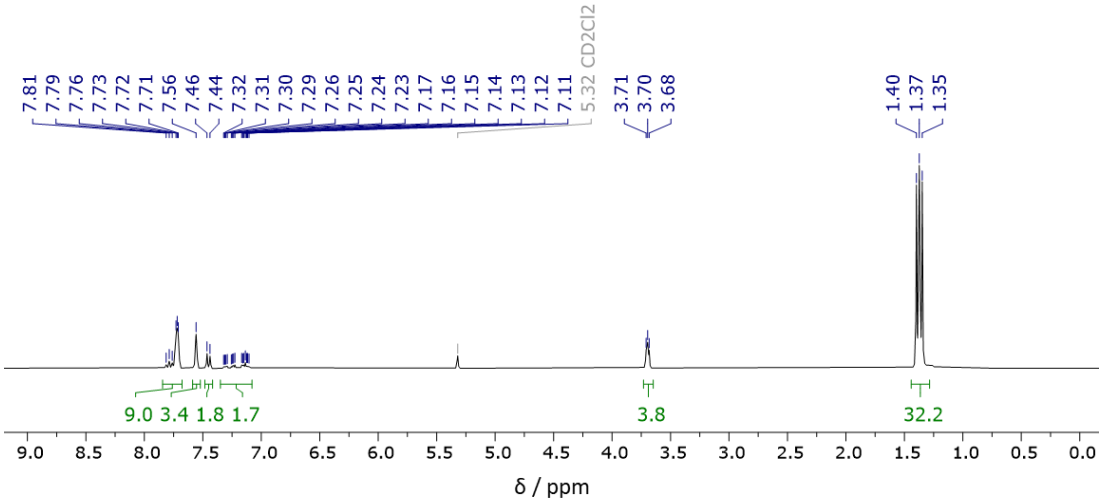

Figure 6.51 – ^{1}H NMR spectrum of **F**, prepared by exposing crystallites of **15** to carbon monoxide for 24 hours before being dissolved in CD_2Cl_2 (300 MHz, CD_2Cl_2, 298 K).

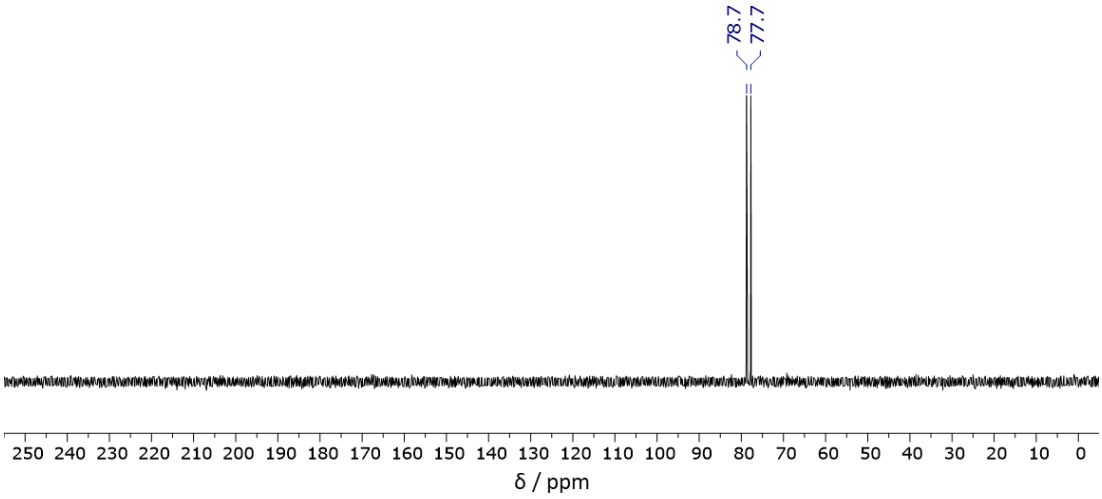

Figure 6.52 – $^{31}P\{^{1}H\}$ NMR spectrum of **F**, prepared by exposing crystallites of **15** to carbon monoxide for 24 hours before being dissolved in CD_2Cl_2 (121 MHz, CD_2Cl_2, 298 K).

6.4.1 – Powder X-ray diffraction

PXRD data for **15**, **19** and **23** were collected on the I11 beamline at Diamond Light Source, England, using synchrotron radiation (λ = 0.82662 Å) at 300 K. Samples were packed into 0.5 mm diameter borosilicate glass capillaries within an Argon atmosphere and sealed with superglue to prevent sample decomposition. Rietveld refinements were carried out using TOPAS *Academic*[18] and fitted to powder simulations derived from the single crystal CIFs.

6.4.2 – High-pressure crystallography

High-pressure data of **19** and **22** were collected on a Rigaku XtaLAB Synergy-S diffractometer using mirror monochromated Mo Kα radiation (λ = 0.71073 Å) generated using a microfocus sealed X-ray tube source and detected at a HyPix Hybrid Pixel Array Detector. Data for **19** and **22** were collected at 300 K and 293 K, respectively. For samples of **19**, crystal A (dimensions 0.09 x 0.11 x 0.20 mm) was studied in Daphne-7575 at 0.9 kbar. Crystal B for **19** (dimensions 0.04 x 0.06 x 0.12 mm) was studied in Daphne-7575 at pressures of 3.5 and 9.5 kbar. Crystal C for

19 (dimensions 0.08 x 0.10 x 0.14 mm) was studied in Daphne-7575 at pressures of 15.5, 20.7, 29.4 and 34.6 kbar.

For samples of **22**, crystal A (dimensions 0.08 x 0.15 x 0.21 mm) was studied in Daphne-7575 at pressures of 4.7, 14.7, 20.3, 25.1 and 32.9 kbar, with viable datasets obtained up to 25.1 kbar. Crystal B of **22** (dimensions 0.06 x 0.09 x 0.16 mm) was studied in Daphne-7575 at pressures of 6.9, 11.2, 18.1, 30.8 and 39.4 kbar, with viable datasets obtained up to 30.8 kbar.

For both studies, the sample chambers of the Merrill-Bassett diamond anvil cells (DAC) were formed by the 500 μm culet faces of the Boehler-Almax diamonds and a laser-cut tungsten sheet (Goodfellow Metals, thickness 200 μm) indented to a thickness of *ca*. 120 μm with a gasket hole of diameter 300 μm, drilled using a BETSA electric discharge machine. In each case, the sample crystal was fixed to one culet face by means of high vacuum hydrocarbon grease alongside two ruby spheres which allowed for pressure measurement using the ruby fluorescence method.[19] After each pressure ramp, the pressure inside the DAC was allowed to equilibrate for a minimum of 24 hours before data collection was initiated. Pressure measurements were taken immediately before and after each collection and the pressure reported as the average. The average uncertainty in pressure across the studies were 0.7 kbar (**19**) and 0.8 kbar (**22**), with specific error bars drawn on Figures as 0.5 times the magnitude of the individual drift plus 0.5 kbar attributed to the inherent uncertainty in the pressure determination given by the ruby fluorescence method.[20] Error bars associated with bond lengths and angles for specific refinements are drawn on Figures as the esd, as calculated by *SHELXL*.[13]

For both studies, cell refinement and data reduction was carried out using the software *CrysAlis*^{PRO}.[11] Special settings (smart background, profile agreement rejection parameters, angle-dependent profile changes) were implemented in the data reduction step, which helped remove contaminating diamond reflections and powder rings from the data. Individual specifications of the exact settings used are contained within the CIFs. Multi-scan absorption corrections were applied with an empirical absorption correction using spherical harmonics, implemented in the *SCALE3 ABSPACK* scaling algorithm[21] through *CrysAlis*^{PRO}.[11] All structures were solved by isomorphous replacement using an appropriate ambient pressure starting model, previously

collected at 150 K. Structure solution and refinement were carried out using *SHELXL*[13] with the *Olex2* interface.[14]

For both studies, atomic displacements for all non-hydrogen atoms were refined isotopically except for the rhodium atoms, which were refined anisotropically. For select refinements of **19**, where appropriate, the antimony atoms were also refined anisotropically.

For refinements of **22**, all aromatic rings were restrained to an idealised 6-membered ring geometry and each Ar^{F20} substituent was restrained to planarity. Where appropriate, 1,2- and 1,3- distance restraints were applied to the Me group and five-membered ring of the HBpin ligand. Appropriate distance restraints were applied to all B–Ar^{F20}, C–F, C–O, and B–O distances across all refinements, as were all 1,2- C–C distances associated with the ^{t}Bu groups of the cation. The hydrogen atom of HBpin was located with the electron density difference map and refined freely in all refinements, but in select cases, B–H distance restraints and ADP restraints were required to preserve sensible values. All other hydrogen atoms were automatically generated and refined using a riding model.

For refinements of **19**, distance restraints were applied to all 1,2- Sb–F, P–C, C–O, and B–O distances across all refinements, as were all 1,2- and 1,3- C–C distances associated with the ^{t}Bu groups of the cation. The hydrogen atom of HBcat and the metal hydride were refined freely, but the B1/B2 and H1/H atoms for the crystallographically unique complexes **19a** and **19b**, respectively, required distance restraints and ADP restraints to preserve sensible values. All other hydrogen atoms were automatically generated and refined using a riding model.

References

1. N. A. Yakelis and R. G. Bergman, *Organometallics*, 2005, **24**, 3579-3581.
2. S. Kundu, W. W. Brennessel and W. D. Jones, *Inorg. Chem.*, 2011, **50**, 9443-9453.
3. E. M. Pelczar, T. J. Emge, K. Krogh-Jespersen and A. S. Goldman, *Organometallics*, 2008, **27**, 5759–5767.
4. I. Chávez, A. Alvarez-Carena, E. Molins, A. Roig, W. Maniukiewicz, A. Arancibia, V. Arancibia, H. Brand and J. M. Manríquez, *J. Organomet. Chem.*, 2000, **601**, 126–132.
5. G. Giordano, R. H. Crabtree, R. M. Heintz, D. Forster and D. E. Morris, *Inorg. Synth.*, 1990, **28**, 88-90.
6. W. H. Bernskoetter, C. K. Schauer, K. I. Goldberg and M. Brookhart, *Science*, 2009, **326**, 553-556.
7. R. A. Widenhoefer and R. E. Kinder, in *Encyclopedia of Reagents for Organic Synthesis*, 2008, DOI: 10.1002/047084289X.rn00893, pp. 1-4.
8. E. Neumann and A. Pfaltz, *Organometallics*, 2008, **24**, 2008-2011.
9. M. R. Gyton, T. M. Hood and A. B. Chaplin, *Dalton Trans.*, 2019, **48**, 2877-2880.
10. P. S. Pregosin, *NMR in Organometallic Chemistry*, Wiley, 2012.
11. CrysAlisPRO, Oxford Diffraction /Agilent Technologies UK Ltd., Yarnton, England.
12. G. M. Sheldrick, *Acta Cryst.*, 2015, **A71**, 3-8.
13. G. M. Sheldrick, *Acta Cryst.*, 2008, **A64**, 112-122.
14. O. V. Dolomanov, L. J. Bourhis, R. J. Gildea, J. A. K. Howard and H. Puschmann, *J. Appl. Cryst.*, 2009, **42**, 339-341.
15. S. Schlecht and J. F. Hartwig, *J. Am. Chem. Soc.*, 2000, **122**, 9435-9443.
16. G. M. Adams, F. M. Chadwick, S. D. Pike and A. S. Weller, *Dalton Trans.*, 2015, **44**, 6340-6342.
17. K. M. van Vliet, N. S. van Leeuwen, A. M. Brouwer and B. de Bruin, *J. Org. Chem.*, 2020, **16**, 398-408.
18. A. A. Coelho, *J. Appl. Cryst.*, 2018, **51**, 210-218.
19. J. D. Barnett, S. Block and G. J. Piermarini, *Rev. Sci. Instrum.*, 1973, **44**, 1-9.
20. W. B. Holzapfel, *J. Appl. Phys.*, 2003, **93**, 1813-1818.
21. R. C. Clark and J. S. Reid, *Acta Cryst.*, 1995, **A51**, 887-897.
22. M. Findlater, K. M. Schultz, W. H. Bernskoetter, A. Cartwright-Sykes, D. M. Heinekey and M. Brookhart, *Inorg. Chem.*, 2012, **51**, 4672-4678.
23. A. B. Chaplin and A. S. Weller, *Organometallics*, 2011, **30**, 4466-4469.
24. M. Feller, E. Ben-Ari, T. Gupta, L. J. W. Shimon, G. Leitus, Y. Diskin-Posner, L. Weiner and D. Milstein, *Inorg. Chem.*, 2007, **46**, 10479−10490.
25. Y. B. Hleba, Doctor of Philosophy, Queen's University, 2007.
26. G. Alcaraz and S. Sabo-Etienne, *Coord. Chem. Rev.*, 2008, **252**, 2395-2409.
27. H. Nöth and M. Warchhold, *Eur. J. Inorg. Chem.*, 2004, **2004**, 1115-1124.
28. H. R. Morales, H. Tlahuext, F. Santiesteban and R. Contrera, *Spectrochim. Acta*, 1984, **40A**, 855-862.
29. W. Clegg, A. J. Scott, C. Dai, G. Lesley, T. B. Marder, N. C. Norman and L. J. Farrugia, *Acta Cryst.*, 1996, **C52**, 2545-2547.
30. G. R. Fulmer, A. J. M. Miller, N. H. Sherden, H. E. Gottlieb, A. Nudelman, B. M. Stoltz, J. E. Bercaw and K. I. Goldberg, *Organometallics*, 2010, **29**, 2176-2179.
31. C. J. Pell and O. V. Ozerov, *J. Org. Chem.*, 2020, **912**, 121143.
32. M. Morimoto, T. Miura and M. Murakami, *Angew. Chem. Int. Ed.*, 2015, **54**, 12659-12663.

Appendix

A1 - Crystallographic tables for complexes **1** and **6**.

Complex	**1**	**6**
Empirical formula	$C_{59}H_{56}BClF_{24}NO_2P_2Rh$	$C_{59}H_{56}BClF_{24}NO_2P_2Rh$
Formula weight	1478.15	1478.15
Temperature/K	150.00(10)	150.00(10)
Crystal system	monoclinic	monoclinic
Space group	$P2_1/n$	$P2_1$
a/Å	12.80372(7)	12.4128(1)
b/Å	14.22720(7)	12.8288(2)
c/Å	35.81668(17)	20.0597(2)
α/°	90	90
β/°	92.7582(4)	96.603(1)
γ/°	90	90
Volume/Å^3	6516.84(6)	3173.14(6)
Z	4	2
ρ_{calc}g/cm^3	1.507	1.547
μ/mm^{-1}	3.954	4.060
F(000)	2984.0	1492.0
Crystal size/mm^3	0.32 × 0.16 × 0.09	0.25 × 0.13 × 0.06
Radiation	Cu Kα (λ = 1.54184)	Cu Kα (λ = 1.54184)
2Θ range for data collection/°	4.94 to 147.28	7.17 to 147.294
Index ranges	-15 ≤ h ≤ 15, -17 ≤ k ≤ 14, -44 ≤ l ≤ 43	-15 ≤ h ≤ 15, -13 ≤ k ≤ 15, -24 ≤ l ≤ 24
Reflections collected	65720	45515
Independent reflections	13057 [R_{int} = 0.0284, R_{sigma} = 0.0196]	11705 [R_{int} = 0.0308, R_{sigma} = 0.0250]
Data/restraints/parameters	13057/4577/1060	11705/4291/1056
Goodness-of-fit on F^2	1.026	1.065
Final R indexes [I>=2σ (I)]	R_1 = 0.0508, wR_2 = 0.1247	R_1 = 0.0379, wR_2 = 0.0980
Final R indexes [all data]	R_1 = 0.0545, wR_2 = 0.1271	R_1 = 0.0391, wR_2 = 0.0995
Largest diff. peak/hole / e Å^{-3}	1.56/-1.31	0.60/-0.87
Flack parameter	-	-0.008(5)

A2 - Crystallographic tables for complexes **A** and **7**.

Complex	**A**	**7**
Empirical formula	$C_{54}H_{53}BCl_2F_{24}NO_2P_2Rh$	$C_{54}H_{53}BCl_2F_{24}NO_2P_2Rh$
Formula weight	1450.53	1450.53
Temperature/K	150.00(10)	150.00(10)
Crystal system	monoclinic	triclinic
Space group	*C*2/*c*	$P\bar{1}$
a/Å	17.00017(12)	12.0374(3)
b/Å	18.20216(14)	12.6040(3)
c/Å	39.8415(3)	20.2577(6)
α/°	90	99.418(2)
β/°	96.5420(6)	92.146(2)
γ/°	90	94.914(2)
Volume/Å^3	12248.28(16)	3016.77(14)
Z	8	2
ρ_{calc}g/cm^3	1.573	1.597
μ/mm^{-1}	4.585	4.654
F(000)	5840.0	1460.0
Crystal size/mm^3	0.43 × 0.21 × 0.08	0.14 × 0.10 × 0.03
Radiation	Cu Kα (λ = 1.54184)	Cu Kα (λ = 1.54184)
2Θ range for data collection/°	7.14 to 147.37	7.14 to 148.592
Index ranges	-16 ≤ h ≤ 20, -22 ≤ k ≤ 22, -49 ≤ l ≤ 48	-15 ≤ h ≤ 14, -13 ≤ k ≤ 15, -24 ≤ l ≤ 24
Reflections collected	73355	47638
Independent reflections	12310 [R_{int} = 0.0955, R_{sigma} = 0.0541]	12093 [R_{int} = 0.0757, R_{sigma} = 0.0579]
Data/restraints/parameters	12310/3813/992	12093/3370/964
Goodness-of-fit on F^2	1.034	1.061
Final R indexes [I>=2σ (I)]	R_1 = 0.0586, wR_2 = 0.1500	R_1 = 0.0560, wR_2 = 0.1474
Final R indexes [all data]	R_1 = 0.0666, wR_2 = 0.1574	R_1 = 0.0642, wR_2 = 0.1563
Largest diff. peak/hole / e Å^{-3}	1.30/-1.27	1.14/-1.97

A3 - Crystallographic tables for complexes **2**, **4** and **5**.

Complex	**2**	**4**	**5**
Empirical formula	$C_{59}H_{62}BClF_{24}NO_2P_2Rh$	$C_{55}H_{55}BCl_2F_{24}NO_2P_2Rh$	$C_{56}H_{58}BClF_{24}NO_2P_2Rh$
Formula weight	1484.20	1464.56	1444.14
Temperature/K	150.00(10)	150.00(10)	150.00(10)
Crystal system	triclinic	triclinic	triclinic
Space group	$P\bar{1}$	$P\bar{1}$	$P\bar{1}$
a/Å	13.2596(3)	13.0302(1)	13.1296(2)
b/Å	22.8240(7)	20.0151(2)	22.1634(3)
c/Å	23.7975(5)	25.4864(3)	23.5199(3)
α/°	65.991(3)	78.940(1)	67.025(1)
β/°	84.847(2)	86.912(1)	86.954(1)
γ/°	87.360(2)	76.369(1)	88.081(1)
Volume/Å^3	6551.9(3)	6339.42(11)	6291.79(16)
Z	4	4	4
ρ_{calc}g/cm^3	1.505	1.534	1.525
μ/mm^{-1}	3.933	4.435	4.078
F(000)	3008.0	2952.0	2920.0
Crystal size/mm^3	0.21 × 0.14 × 0.10	0.41 × 0.21 × 0.07	0.14 × 0.12 × 0.05
Radiation	Cu Kα (λ = 1.54184)	Cu Kα (λ = 1.54184)	Cu Kα (λ = 1.54184)
2Θ range for data collection/°	6.694 to 136.498	5.274 to 147.454	6.742 to 148.174
Index ranges	-15 ≤ h ≤ 15, -27 ≤ k ≤ 27, -28 ≤ l ≤ 28	-15 ≤ h ≤ 16, -24 ≤ k ≤ 24, -30 ≤ l ≤ 31	-15 ≤ h ≤ 16, -27 ≤ k ≤ 27, -29 ≤ l ≤ 29
Reflections collected	120727	124426	122947
Independent reflections	23955 [R_{int} = 0.1217, R_{sigma} = 0.0707]	25388 [R_{int} = 0.0395, R_{sigma} = 0.0284]	25225 [R_{int} = 0.0856, R_{sigma} = 0.0536]
Data/restraints/parameters	23955/9708/2014	25388/9348/1908	25225/9220/1932
Goodness-of-fit on F^2	1.019	1.015	1.036
Final R indexes [I>=2σ (I)]	R_1 = 0.0842, wR_2 = 0.2128	R_1 = 0.0404, wR_2 = 0.1031	R_1 = 0.0553, wR_2 = 0.1447
Final R indexes [all data]	R_1 = 0.1115, wR_2 = 0.2491	R_1 = 0.0433, wR_2 = 0.1059	R_1 = 0.0664, wR_2 = 0.1601
Largest diff. peak/hole / e Å^{-3}	1.88/-1.46	1.01/-0.73	1.71/-1.12

A4 - Crystallographic table for complexes **8** and **9**.

Complex	**8**	**9**
Empirical formula	$C_{54}H_{53}BCl_3F_{24}NO_2P_2Rh$	$C_{53}H_{52}BClF_{24}NO_2P_2Rh$
Formula weight	1485.98	1402.06
Temperature/K	150.00(10)	150.00(10)
Crystal system	monoclinic	triclinic
Space group	$P2_1/c$	$P\bar{1}$
a/Å	13.79152(9)	12.6768(3)
b/Å	23.49706(13)	14.4374(3)
c/Å	19.77529(13)	16.8544(3)
α/°	90	101.5994(16)
β/°	98.1237(6)	95.2483(16)
γ/°	90	96.7276(16)
Volume/Å^3	6344.08(7)	2979.85(10)
Z	4	2
ρ_{calc}g/cm^3	1.556	1.563
μ/mm^{-1}	4.820	0.501
F(000)	2988.0	1412.0
Crystal size/mm^3	0.17 × 0.15 × 0.13	0.20 × 0.14 × 0.10
Radiation	Cu Kα (λ = 1.54184)	Mo Kα (λ = 0.71073)
2Θ range for data collection/°	12.808 to 140.138	5.192 to 52.17
Index ranges	-16 ≤ h ≤ 15, -24 ≤ k ≤ 28, -21 ≤ l ≤ 24	-15 ≤ h ≤ 15, -17 ≤ k ≤ 17, -20 ≤ l ≤ 20
Reflections collected	35993	56867
Independent reflections	11964 [R_{int} = 0.0210, R_{sigma} = 0.0201]	11701 [R_{int} = 0.0413, R_{sigma} = 0.0333]
Data/restraints/parameters	11964/4909/1086	11701/4686/1088
Goodness-of-fit on F^2	1.019	1.063
Final R indexes [I>=2σ (I)]	R_1 = 0.0307, wR_2 = 0.0764	R_1 = 0.0402, wR_2 = 0.0840
Final R indexes [all data]	R_1 = 0.0337, wR_2 = 0.0787	R_1 = 0.0512, wR_2 = 0.0896
Largest diff. peak/hole / e Å^{-3}	0.60/-0.57	0.61/-0.72

A5 - Crystallographic tables for complexes **12-15**.

Complex	**12**	**13**	**14**	**15**
Empirical formula	$C_{59}H_{64}B_2F_{24}NO_4P_2Rh$	$C_{59}H_{56}B_2F_{24}NO_4P_2Rh$	$C_{61}H_{68}B_2F_{24}NO_2P_2Rh$	$C_{61}H_{60}B_2F_{24}NO_2P_2Rh$
Formula weight	1493.58	1485.51	1489.63	1481.57
Temperature/K	150.00(10)	150.00(10)	150.00(10)	150.00(10)
Crystal system	monoclinic	monoclinic	monoclinic	monoclinic
Space group	$P2_1/n$	$P2_1/c$	$P2_1/n$	$P2_1/c$
a/Å	13.28940(9)	18.1285(2)	13.0589(1)	19.2532(4)
b/Å	14.23474(10)	17.9092(2)	14.2536(1)	17.6224(3)
c/Å	35.08634(17)	20.1931(2)	35.8756(4)	19.3155(3)
α/°	90	90	90	90
β/°	92.9395(5)	92.314(1)	93.247(1)	98.960(2)
γ/°	90	90	90	90
Volume/Å^3	6628.59(7)	6550.69(12)	6667.03(10)	6473.5(2)
Z	4	4	4	4
ρ_{calc}g/cm^3	1.497	1.506	1.484	1.520
μ/mm^{-1}	3.550	3.592	3.504	3.608
F(000)	3032.0	3000.0	3032.0	3000.0
Crystal size/mm^3	0.27 × 0.21 × 0.12	0.18 × 0.08 × 0.06	0.18 × 0.16 × 0.10	0.15 × 0.09 × 0.05
Radiation	Cu Kα (λ = 1.54184)	Cu Kα (λ = 1.54184)	Cu Kα (λ = 1.54184)	Cu Kα (λ = 1.54184)
2Θ range for data collection/°	6.702 to 147.28	6.6 to 147.634	4.934 to 147.314	6.828 to 147.034
Index ranges	-16 ≤ h ≤ 16, -17 ≤ k ≤ 17, -42 ≤ l ≤ 33	-22 ≤ h ≤ 22, -15 ≤ k ≤ 22, -18 ≤ l ≤ 24	-16 ≤ h ≤ 16, -16 ≤ k ≤ 17, -43 ≤ l ≤ 38	-23 ≤ h ≤ 18, -21 ≤ k ≤ 21, -23 ≤ l ≤ 23
Reflections collected	67593	52573	38482	37641
Independent reflections	13270 [R_{int} = 0.0274, R_{sigma} = 0.0183]	13059 [R_{int} = 0.0431, R_{sigma} = 0.0280]	13093 [R_{int} = 0.0287, R_{sigma} = 0.0298]	12719 [R_{int} = 0.0458, R_{sigma} = 0.0505]
Data/restraints/parameters	13270/4183/1082	13059/3405/1022	13093/4440/1159	12719/4702/1275
Goodness-of-fit on F^2	1.127	1.027	1.017	1.039
Final R indexes [I>=2σ (I)]	R_1 = 0.0343, wR_2 = 0.0822	R_1 = 0.0329, wR_2 = 0.0812	R_1 = 0.0406, wR_2 = 0.1009	R_1 = 0.0693, wR_2 = 0.1852
Final R indexes [all data]	R_1 = 0.0356, wR_2 = 0.0831	R_1 = 0.0398, wR_2 = 0.0874	R_1 = 0.0476, wR_2 = 0.1059	R_1 = 0.0933, wR_2 = 0.2097
Largest diff. peak/hole / e Å^{-3}	0.42/-0.39	0.40/-0.78	1.47/-0.58	1.32/-1.02

A6 - Crystallographic tables for complexes **16**, **18** and **19**.

Identification code	**16**	**18**	**19**
Empirical formula	$C_{28.5}H_{53}BF_{6.5}NO_4P_2RhSb$	$C_{29}H_{56}BF_6NO_2P_2RhSb$	$C_{58}H_{96}B_2F_{12}N_2O_4P_4Rh_2Sb_2$
Formula weight	894.63	862.15	1708.18
Temperature/K	150.00(10)	150.00(10)	150.00(10)
Crystal system	triclinic	monoclinic	orthorhombic
Space group	$P\bar{1}$	$P2_1/c$	$P2_12_12_1$
a/Å	14.5639(2)	12.7624(2)	12.9296(1)
b/Å	15.7044(2)	16.8191(3)	17.8215(2)
c/Å	16.7452(3)	17.3698(2)	31.0623(3)
α/°	95.625(1)	90	90
β/°	94.853(1)	91.416(1)	90
γ/°	95.136(1)	90	90
Volume/Å^3	3779.29(10)	3727.32(10)	7157.53(12)
Z	4	4	4
ρ_{calc}g/cm^3	1.572	1.536	1.585
μ/mm^{-1}	10.565	10.626	11.066
F(000)	1810.0	1752.0	3440.0
Crystal size/mm^3	0.25 × 0.04 × 0.04	0.27 × 0.06 × 0.02	0.24 × 0.09 × 0.05
Radiation	Cu Kα (λ = 1.54184)	Cu Kα (λ = 1.54184)	Cu Kα (λ = 1.54184)
2Θ range for data collection/°	5.326 to 144.244	6.928 to 147.204	5.69 to 144.25
Index ranges	-17 ≤ h ≤ 15, -19 ≤ k ≤ 19, -20 ≤ l ≤ 20	-15 ≤ h ≤ 15, -20 ≤ k ≤ 19, -21 ≤ l ≤ 20	-11 ≤ h ≤ 15, -21 ≤ k ≤ 22, -37 ≤ l ≤ 38
Reflections collected	42732	14172	40529
Independent reflections	14703 [R_{int} = 0.0423, R_{sigma} = 0.0419]	7274 [R_{int} = 0.0341, R_{sigma} = 0.0450]	13887 [R_{int} = 0.0411, R_{sigma} = 0.0407]
Data/restraints/parameters	14703/55/875	7274/0/408	13887/0/808
Goodness-of-fit on F^2	1.029	1.033	1.053
Final R indexes [I>=2σ (I)]	R_1 = 0.0285, wR_2 = 0.0677	R_1 = 0.0320, wR_2 = 0.0752	R_1 = 0.0369, wR_2 = 0.0952
Final R indexes [all data]	R_1 = 0.0332, wR_2 = 0.0711	R_1 = 0.0375, wR_2 = 0.0790	R_1 = 0.0385, wR_2 = 0.0965
Largest diff. peak/hole / e Å^{-3}	0.91/-1.31	0.81/-1.36	1.15/-1.25
Flack parameter	-	-	-0.003(3)

A7 - Crystallographic tables for complexes **20**, **22**, **23** and **24**.

Identification code	**20**	**22**	**23**	**24**
Empirical formula	$C_{51}H_{52}B_2F_{20}NO_4P_2Rh$	$C_{53}H_{56}B_2F_{20}NO_2P_2Rh$	$C_{53}H_{48}B_2F_{20}NO_2P_2Rh$	$C_{54}H_{48}B_2F_{20}NO_3P_2Rh$
Formula weight	1309.40	1305.45	1297.39	1325.40
Temperature/K	150.00(10)	150.00(10)	150.00(10)	150.00(10)
Crystal system	orthorhombic	triclinic	triclinic	triclinic
Space group	$Pca2_1$	$P\bar{1}$	$P\bar{1}$	$P\bar{1}$
a/Å	20.5241(1)	11.7094(2)	11.6375(2)	12.1335(13)
b/Å	14.2767(1)	14.2312(2)	14.3262(2)	13.4392(14)
c/Å	37.7165(2)	17.4132(2)	17.0942(2)	17.6394(16)
α/°	90	104.046(1)	78.270(1)	86.300(8)
β/°	90	99.239(1)	81.446(1)	80.679(8)
γ/°	90	91.173(1)	88.973(1)	83.559(9)
Volume/Å^3	11051.55(11)	2773.08(7)	2759.18(7)	2817.3(5)
Z	8	2	2	2
ρ_{calc}g/cm^3	1.574	1.563	1.562	1.562
μ/mm^{-1}	4.062	4.016	4.036	3.981
F(000)	5296.0	1324.0	1308.0	1336.0
Crystal size/mm^3	0.25 × 0.18 × 0.09	0.21 × 0.13 × 0.08	0.18 × 0.14 × 0.07	0.16 × 0.09 × 0.05
Radiation	Cu Kα (λ = 1.54184)	Cu Kα (λ = 1.54184)	Cu Kα (λ = 1.54184)	Cu Kα (λ = 1.54184)
2Θ range for data collection/°	6.19 to 147.182	5.31 to 147.262	5.338 to 147.16	6.626 to 147.45
Index ranges	$-25 \le h \le 25$, $-17 \le k \le 15$, $-46 \le l \le 46$	$-12 \le h \le 14$, $-16 \le k \le 17$, $-20 \le l \le 21$	$-14 \le h \le 14$, $-17 \le k \le 17$, $-16 \le l \le 21$	$-15 \le h \le 11$, $-15 \le k \le 16$, $-21 \le l \le 21$
Reflections collected	97559	32580	32918	47850
Independent reflections	21921 [R_{int} = 0.0549, R_{sigma} = 0.0417]	11031 [R_{int} = 0.0184, R_{sigma} = 0.0188]	11001 [R_{int} = 0.0285, R_{sigma} = 0.0305]	10538 [R_{int} = 0.2834, R_{sigma} = 0.2236]
Data/restraints/parameters	21921/1369/1499	11031/1021/827	11001/0/746	10538/1/764
Goodness-of-fit on F^2	1.038	1.022	1.025	1.020
Final R indexes [I>=2σ (I)]	R_1 = 0.0663, wR_2 = 0.1688	R_1 = 0.0207, wR_2 = 0.0524	R_1 = 0.0295, wR_2 = 0.0732	R_1 = 0.1224, wR_2 = 0.3220
Final R indexes [all data]	R_1 = 0.0747, wR_2 = 0.1758	R_1 = 0.0219, wR_2 = 0.0530	R_1 = 0.0319, wR_2 = 0.0751	R_1 = 0.2215, wR_2 = 0.3962
Largest diff. peak/hole / e Å^{-3}	0.48/-1.11	0.32/-0.36	0.60/-1.18	1.15/-1.33
Flack parameter	-0.002(12)	-	-	-

A8 – A Table of selected bond lengths for **24**.

Atoms	Bond length / Å
Rh1–N1	2.101(10)
Rh1–P1	2.307(4)
Rh1–P2	2.306(4)
Rh1–C1	1.842(12)
C1–O1	1.128(14)

A9 – A Table of selected bond and torsion angles for **24**.

Atoms	Bond or torsion angle / °
P1–Rh1–P2	167.67(12)
N1–Rh1–C1	179.2(6)
Rh1–C1-O1	179.0(14)
P1–C7···C8–P2	29.2(8)

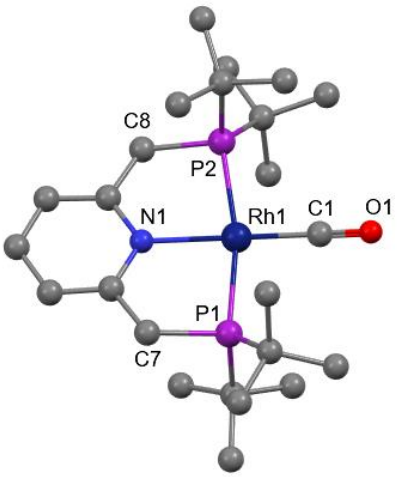

A10 – Partially labelled ball and stick structure of **24**. Anion and hydrogen atoms omitted for clarity.

A11 – Table of fits for the Rietveld refinements of **A** against temperature.

Temperature / K	R_{wp}	*GooF*
300.00	4.5704423	9.6224850
301.66	4.6104800	9.7062600
303.33	4.6061240	9.6966437
305.00	4.6762908	9.8431712
306.66	4.7272474	9.9491742
308.33	4.7721805	10.0488564
310.00	4.7636514	10.0295173
311.66	4.7497636	9.9972003
313.33	4.7503304	9.9993697
315.00	4.7704770	10.0379836
316.66	4.7752078	10.0409491
318.33	4.7680853	10.0247800
320.00	4.7773491	10.0419962
321.66	4.8034742	10.0952963
323.33	4.8207688	10.1316656
325.00	4.8243802	10.1383623
326.66	4.8422563	10.1708939
328.33	4.8394338	10.1614869
330.00	4.8604736	10.2081636
331.66	4.8579558	10.2009145
333.33	4.8866099	10.2571164
335.00	4.8998933	10.3063307
336.66	4.9548437	10.4732945
338.33	5.0386873	10.6512958
340.00	4.9112929	10.3761718
341.66	4.9272747	10.4094341
343.33	4.9308679	10.4151255
345.00	4.9106070	10.3706275
346.66	4.9220192	10.3956641
348.33	4.8866752	10.3203465
350.00	4.8532854	10.2481960
351.66	4.8295915	10.1968006
353.33	4.7582020	10.0450373
355.00	4.7224832	9.9681023
356.66	4.6533362	9.8225237
358.33	4.5759255	9.6581415
360.00	4.4920439	9.4812381
361.66	4.4241842	9.3372025
363.33	4.3601481	9.2029686
365.00	4.3374407	9.1572282
366.66	4.3347964	9.1511106
368.33	4.3187635	9.1155658
370.00	4.2410729	8.9546766
371.66	4.2291542	8.9294702
373.33	4.2270971	8.9245624
375.00	4.2639281	9.0041209
376.66	4.2213582	8.9147784
378.33	4.2224030	8.9139858
380.00	4.2568732	9.0153254
380.00	4.2213580	8.9562840
380.00	4.2224030	8.9848502

A12 - Crystallographic tables for the HP-XRD study of **A-α** (crystal A).

Pressure / kbar	1.9	7.4	9.5
Empirical formula	$C_{54}H_{53}BCl_2F_{24}NO_2P_2Rh$	$C_{54}H_{53}BCl_2F_{24}NO_2P_2Rh$	$C_{54}H_{53}BCl_2F_{24}NO_2P_2Rh$
Formula weight	1450.53	1450.53	1450.53
Temperature/K	293(2)	293(2)	293(2)
Crystal system	monoclinic	monoclinic	monoclinic
Space group	*C*2/*c*	*C*2/*c*	*C*2/*c*
a/Å	17.238(4)	16.6839(18)	16.456(5)
b/Å	18.406(2)	18.059(15)	17.813(4)
c/Å	40.33(6)	39.120(4)	38.46(9)
α/°	90	90	90
β/°	96.56(4)	96.404(9)	96.02(6)
γ/°	90	90	90
Volume/Å^3	12712(19)	11713(10)	11211(27)
Z	8	8	8
ρ_{calc}g/cm^3	1.516	1.645	1.719
μ/mm^{-1}	0.691	0.750	0.784
F(000)	5840.0	5840.0	5840.0
Crystal size/mm^3	0.08 × 0.06 × 0.02	0.08 × 0.06 × 0.02	0.08 × 0.06 × 0.02
Radiation	synchrotron (λ = 0.4859)	synchrotron (λ = 0.4859)	synchrotron (λ = 0.4859)
2Θ range for data collection/°	3.104 to 24.4	3.258 to 26.85	3.126 to 24.578
Index ranges	$-14 \le h \le 14$, $-15 \le k \le 15$, $-16 \le l \le 15$	$-15 \le h \le 15$, $-6 \le k \le 6$, $-37 \le l \le 37$	$-14 \le h \le 14$, $-15 \le k \le 15$, $-15 \le l \le 15$
Reflections collected	16477	19218	12711
Independent reflections	1915 [R_{int} = 0.3882, R_{sigma} = 0.1934]	2226 [R_{int} = 0.2217, R_{sigma} = 0.1327]	1786 [R_{int} = 0.7558, R_{sigma} = 0.3548]
Data/restraints/parameters	1915/3231/392	2226/3136/393	1786/2847/380
Goodness-of-fit on F^2	1.252	1.196	1.421
Final R indexes [I>=2σ (I)]	R_1 = 0.1329, wR_2 = 0.3323	R_1 = 0.1155, wR_2 = 0.3053	R_1 = 0.2081, wR_2 = 0.4694
Final R indexes [all data]	R_1 = 0.2313, wR_2 = 0.3881	R_1 = 0.2144, wR_2 = 0.3674	R_1 = 0.3781, wR_2 = 0.5442
Largest diff. peak/hole / e Å^{-3}	0.67/-0.52	0.55/-0.46	0.45/-0.57

A13 - Crystallographic tables for the HP-XRD study of **A-α** (crystal B).

Pressure / kbar	6.3	8.8	10.6	15.7
Empirical formula	$C_{54}H_{53}BCl_2F_{24}NO_2P_2Rh$	$C_{54}H_{53}BCl_2F_{24}NO_2P_2Rh$	$C_{54}H_{53}BCl_2F_{24}NO_2P_2Rh$	$C_{54}H_{53}BCl_2F_{24}NO_2P_2Rh$
Formula weight	1450.53	1450.53	1450.53	1450.53
Temperature/K	293(2)	293(2)	293(2)	293(2)
Crystal system	monoclinic	monoclinic	monoclinic	monoclinic
Space group	*C*2/*c*	*C*2/*c*	*C*2/*c*	*C*2/*c*
a/Å	16.7475(16)	16.648(2)	16.490(3)	16.289(4)
b/Å	18.064(13)	18.17(2)	17.96(3)	17.61(4)
c/Å	39.279(3)	38.959(6)	38.520(5)	38.192(6)
α/°	90	90	90	90
β/°	96.622(7)	96.026(12)	95.749(14)	95.562(19)
γ/°	90	90	90	90
Volume/Å^3	11804(9)	11717(15)	11348(18)	10904(22)
Z	8	8	8	8
ρ_{calc}g/cm^3	1.632	1.645	1.698	1.767
μ/mm^{-1}	0.744	0.750	0.774	0.806
F(000)	5840.0	5840.0	5840.0	5840.0
Crystal size/mm^3	0.08 × 0.06 × 0.02	0.08 × 0.06 × 0.02	0.08 × 0.06 × 0.02	0.08 × 0.06 × 0.02
Radiation	synchrotron (λ = 0.4859)	synchrotron (λ = 0.4859)	synchrotron (λ = 0.4859)	synchrotron (λ = 0.4859)
2Θ range for data collection/°	3.254 to 26.838	3.254 to 25.624	2.906 to 25.526	3.318 to 24.386
Index ranges	$-15 \le h \le 15$, $-6 \le k \le 6$, $-37 \le l \le 37$	$-15 \le h \le 15$, $-6 \le k \le 6$, $-35 \le l \le 35$	$-14 \le h \le 14$, $-6 \le k \le 6$, $-34 \le l \le 34$	$-14 \le h \le 14$, $-6 \le k \le 6$, $-33 \le l \le 33$
Reflections collected	15536	15022	14110	9394
Independent reflections	2055 [R_{int} = 0.1485, R_{sigma} = 0.1087]	1965 [R_{int} = 0.3929, R_{sigma} = 0.3097]	1973 [R_{int} = 0.3993, R_{sigma} = 0.2113]	1676 [R_{int} = 0.4272, R_{sigma} = 0.3345]
Data/restraints/parameters	2055/1664/341	1965/2680/380	1973/3255/393	1676/3253/393
Goodness-of-fit on F^2	1.388	1.321	1.628	1.641
Final R indexes [I>=2σ (I)]	R_1 = 0.1233, wR_2 = 0.3244	R_1 = 0.1573, wR_2 = 0.3858	R_1 = 0.2125, wR_2 = 0.5112	R_1 = 0.2527, wR_2 = 0.5453
Final R indexes [all data]	R_1 = 0.1946, wR_2 = 0.3778	R_1 = 0.3334, wR_2 = 0.4655	R_1 = 0.3629, wR_2 = 0.5737	R_1 = 0.4304, wR_2 = 0.6230
Largest diff. peak/hole / e Å^{-3}	0.51/-0.53	0.90/-0.49	0.51/-0.67	0.86/-0.65

A14 – A Table of selected bond lengths of **A-α** against pressure. The asterisk denotes the ambient pressure collection conducted at 150 K, for reference.

Pressure / kbar	Rh1–P1 / Å	Rh1–P2 / Å	Rh1–Cl1 / Å	Rh1–N1 / Å	Cl1–C23 / Å
0.0*	2.2841(9)	2.2704(9)	2.3565(9)	2.012(3)	1.777(5)
1.9	2.27(3)	2.06(3)	2.364(18)	2.02(2)	1.610(4)
6.3	2.264(8)	2.268(10)	2.31(3)	2.01(5)	1.84(10)
7.4	2.259(9)	2.249(10)	2.16(4)	1.99(4)	1.65(4)
8.8	2.232(7)	2.192(7)	1.670(18)	2.079(19)	1.671(17)
9.5	2.15(7)	2.13(7)	2.27(3)	1.97(3)	1.59(3)
10.6	2.237(8)	2.193(8)	1.947(17)	1.88(15)	1.481(13)
15.7	2.231(9)	2.227(10)	1.94(2)	1.759(19)	1.327(13)

A15 – A Table of selected bond angles of **A-α** against pressure. The asterisk denotes the ambient pressure collection conducted at 150 K, for reference.

Pressure / kbar	P1–Rh1–P2 / °	N1–Rh1–Cl1 / °	Cl1–C23–Cl2 / °
0.0*	162.10(4)	169.82(8)	113.1(3)
1.9	162.4(5)	169.5(8)	124(6)
6.3	161.8(11)	170.8(7)	113(5)
7.4	164.3(11)	171.3(10)	134(5)
8.8	168.9(4)	164.2(6)	132(19)
9.5	164.2(7)	174(4)	108(4)
10.6	171.4(6)	175.6(6)	133(2)
15.7	174.9(5)	178.3(9)	136(2)

A16 - Crystallographic tables for the HP-XRD study of **A-β** (crystal C).

Pressure / kbar	6.6	7.0	13.5
Empirical formula	$C_{54}H_{51}BCl_2F_{24}NO_2P_2Rh$	$C_{54}H_{53}BCl_2F_{24}NO_2P_2Rh$	$C_{54}H_{53}BCl_2F_{24}NO_2P_2Rh$
Formula weight	1448.52	1450.53	1450.53
Temperature/K	293(2)	293(2)	293(2)
Crystal system	triclinic	triclinic	triclinic
Space group	$P\bar{1}$	$P\bar{1}$	$P\bar{1}$
a/Å	12.9319(17)	12.9257(14)	12.7674(13)
b/Å	22.138(5)	22.132(3)	21.784(4)
c/Å	22.923(5)	22.945(4)	22.461(4)
α/°	67.12(2)	67.171(19)	67.282(19)
β/°	86.58(2)	86.59(2)	87.017(17)
γ/°	87.841(16)	87.893(14)	88.173(13)
Volume/Å^3	6035(2)	6038.4(18)	5753.9(17)
Z	4	4	4
ρ_{calc}g/cm^3	1.594	1.596	1.674
μ/mm^{-1}	0.728	0.727	0.763
F(000)	2912.0	2920.0	2920.0
Crystal size/mm^3	0.07 × 0.05 × 0.03	0.07 × 0.05 × 0.03	0.07 × 0.05 × 0.03
Radiation	synchrotron (λ = 0.4859)	synchrotron (λ = 0.4859)	synchrotron (λ = 0.4859)
2Θ range for data collection/°	3.078 to 26.808	3.258 to 26.864	3.314 to 26.856
Index ranges	$-12 \le h \le 12$, $-21 \le k \le 21$, $-15 \le l \le 15$	$-12 \le h \le 12$, $-21 \le k \le 21$, $-14 \le l \le 15$	$-12 \le h \le 12$, $-20 \le k \le 20$, $-14 \le l \le 14$
Reflections collected	20496	18739	23128
Independent reflections	4395 [R_{int} = 0.1676, R_{sigma} = 0.1615]	4277 [R_{int} = 0.1706, R_{sigma} = 0.1467]	4193 [R_{int} = 0.1511, R_{sigma} = 0.1309]
Data/restraints/parameters	4395/7424/679	4277/8682/705	4193/8470/705
Goodness-of-fit on F^2	2.728	3.180	3.709
Final R indexes [I>=2σ (I)]	R_1 = 0.2850, wR_2 = 0.6215	R_1 = 0.3239, wR_2 = 0.6688	R_1 = 0.3577, wR_2 = 0.7164
Final R indexes [all data]	R_1 = 0.3628, wR_2 = 0.6656	R_1 = 0.3883, wR_2 = 0.7099	R_1 = 0.4422, wR_2 = 0.7600
Largest diff. peak/hole / e Å^{-3}	2.22/-1.30	2.56/-1.38	3.61/-2.12

A17 - Continued crystallographic tables for the HP-XRD study of **A-β** (crystal C).

Pressure / kbar	18.1	26.3	32.0
Empirical formula	$C_{56}H_{57.95}BClF_{24}NO_2P_2Rh$	$C_{56}H_{57.95}BClF_{24}NO_2P_2Rh$	$C_{56}H_{57.95}BClF_{24}NO_2P_2Rh$
Formula weight	1444.10	1444.10	1444.10
Temperature/K	293(2)	293(2)	293(2)
Crystal system	triclinic	triclinic	triclinic
Space group	$P\bar{1}$	$P\bar{1}$	$P\bar{1}$
a/Å	12.6827(12)	12.5069(13)	12.4481(14)
b/Å	21.622(4)	21.283(4)	21.182(4)
c/Å	22.233(4)	21.792(4)	21.581(4)
α/°	67.372(19)	67.61(2)	67.60(2)
β/°	87.200(17)	87.215(19)	87.317(20)
γ/°	88.316(12)	88.495(13)	88.551(14)
Volume/Å^3	5620.4(17)	5356.8(18)	5255.0(18)
Z	4	4	4
ρ_{calc}g/cm^3	1.707	1.791	1.825
μ/mm^{-1}	0.767	0.804	0.820
F(000)	2920.0	2920.0	2920.0
Crystal size/mm^3	0.07 × 0.05 × 0.03	0.07 × 0.05 × 0.03	0.07 × 0.05 × 0.03
Radiation	synchrotron (λ = 0.4859)	synchrotron (λ = 0.4859)	synchrotron (λ = 0.4859)
2Θ range for data collection/°	3.342 to 26.802	3.398 to 26.796	3.416 to 26.836
Index ranges	$-12 \le h \le 12$, $-20 \le k \le 20$, $-13 \le l \le 14$	$-11 \le h \le 11$, $-20 \le k \le 20$, $-14 \le l \le 14$	$-11 \le h \le 11$, $-20 \le k \le 20$, $-13 \le l \le 13$
Reflections collected	22409	16246	15813
Independent reflections	4093 [R_{int} = 0.1600, R_{sigma} = 0.1413]	4074 [R_{int} = 0.2330, R_{sigma} = 0.1920]	3998 [R_{int} = 0.2459, R_{sigma} = 0.1981]
Data/restraints/parameters	4093/8264/705	4074/8266/705	3998/8268/705
Goodness-of-fit on F^2	4.567	3.991	3.608
Final R indexes [I>=2σ (I)]	R_1 = 0.4866, wR_2 = 0.8158	R_1 = 0.5095, wR_2 = 0.8213	R_1 = 0.4810, wR_2 = 0.7937
Final R indexes [all data]	R_1 = 0.5748, wR_2 = 0.8542	R_1 = 0.6105, wR_2 = 0.8596	R_1 = 0.5860, wR_2 = 0.8340
Largest diff. peak/hole / e Å^{-3}	8.07/-3.66	7.57/-3.29	6.33/-2.75

A18 – A Table of selected bond lengths for **A-β** against pressure for the two crystallographically unique complexes A (top) and B (bottom).

Pressure / kbar	Rh1–P1 / Å	Rh1–P2 / Å	Rh1–Cl1 / Å	Rh1–N1 / Å	Cl1–C23 / Å
6.6	2.278(5) 2.178(5)	2.299(5) 2.374(5)	2.263(3) 2.091(11)	2.027(7) 1.978(8)	1.8421(10) 1.848(7)
7.0	2.286(5) 2.157(6)	2.285(6) 2.385(5)	2.277(3) 2.028(1)	2.015(7) 1.988(8)	1.842(1) 1.848(7)
13.5	2.233(6) 1.973(6)	2.260(6) 2.460(6)	2.229(4) 2.134(12)	1.971(7) 1.867(9)	1.8421(10) 1.850(7)
18.1	2.219(7) 2.157(7)	2.214(7) 2.239(7)	2.235(6) 2.313(19)	1.860(11) 1.890(8)	1.648(6) 1.681(7)
26.3	2.184(8) 2.130(8)	2.177(9) 2.203(8)	2.201(7) 2.27(3)	1.844(10) 1.798(14)	1.8026(10) 1.696(6)
32.0	2.167(8) 2.033(8)	2.169(8) 2.269(8)	2.155(6) 2.26(3)	1.826(9) 1.739(13)	1.8359(10) 1.745(6)

A19 – A Table of selected bond angles for **A-β** against pressure for the two crystallographically unique complexes A (top) and B (bottom).

Pressure / kbar	P1–Rh1–P2 / °	N1–Rh1–Cl1 / °	Cl1–C23–Cl2 / °
6.6	158.18(19) 161.3(2)	165.81(18) 168(3)	97.8(2) 97.4(5)
7.0	158.6(2) 160.8(2)	165.61(19) 167.4(3)	98.0(2) 97.5(5)
13.5	159.4(2) 166.1(3)	168(2) 159.2(3)	96.5(2) 95.6(5)
18.1	161.5(3) 163.6(4)	170.4(3) 168.8(4)	99.5(2) 104.2(5)
26.3	161.5(4) 163.7(6)	170.4(4) 168.8(5)	99.1(3) 104.1(6)
32.0	161.2(4) 166.3(5)	169.9(4) 164.9(5)	95.1(2) 99.5(6)

A20 - Crystallographic tables for the HP-XRD study of **13** (crystal A).

Pressure / kbar	2.5	4.8	14.0	22.4	25.8
Empirical formula	$C_{59}H_{56}B_2F_{24}NO_4P_2Rh$	$C_{59}H_{56}B_2F_{24}NO_4P_2Rh$	$C_{59}H_{56}B_2F_{24}NO_4P_2Rh$	$C_{59}H_{56}B_2F_{24}NO_4P_2Rh$	$C_{59}H_{56}B_2F_{24}NO_4P_2Rh$
Formula weight	1485.51	1485.51	1485.51	1485.51	1485.51
Temperature/K	293(2)	293(2)	293(2)	293(2)	293(2)
Crystal system	monoclinic	monoclinic	monoclinic	monoclinic	monoclinic
Space group	$P2_1/c$	$P2_1/c$	$P2_1/c$	$P2_1/c$	$P2_1/c$
a/Å	18.186(2)	18.020(3)	18.2732(19)	18.011(2)	17.923(2)
b/Å	17.958(2)	17.501(3)	16.3352(18)	16.0971(19)	16.012(2)
c/Å	20.14(2)	19.94(3)	19.06(2)	18.79(2)	18.75(2)
α/°	90	90	90	90	90
β/°	92.58(2)	91.84(3)	93.43(3)	93.33(3)	92.91(3)
γ/°	90	90	90	90	90
Volume/Å^3	6572(7)	6285(9)	5678(6)	5440(6)	5373(7)
Z	4	4	4	4	4
ρ_{calc}g/cm^3	1.501	1.570	1.738	1.814	1.836
μ/mm^{-1}	0.645	0.675	0.747	0.779	0.789
F(000)	3000.0	3000.0	3000.0	3000.0	3000.0
Crystal size/mm^3	0.07 × 0.05 × 0.03	0.07 × 0.05 × 0.03	0.07 × 0.05 × 0.03	0.07 × 0.05 × 0.03	0.07 × 0.05 × 0.03
Radiation	synchrotron (λ = 0.4859)	synchrotron (λ = 0.4859)	synchrotron (λ = 0.4859)	synchrotron (λ = 0.4859)	synchrotron (λ = 0.4859)
2Θ range for data collection/°	3.102 to 26.82	3.092 to 26.862	3.052 to 26.782	3.098 to 26.776	3.112 to 26.77
Index ranges	-17 ≤ h ≤ 17, -17 ≤ k ≤ 17, -8 ≤ l ≤ 8	-17 ≤ h ≤ 17, -16 ≤ k ≤ 16, -8 ≤ l ≤ 8	-17 ≤ h ≤ 17, -15 ≤ k ≤ 15, -9 ≤ l ≤ 9	-17 ≤ h ≤ 17, -15 ≤ k ≤ 15, -9 ≤ l ≤ 9	-17 ≤ h ≤ 17, -15 ≤ k ≤ 15, -9 ≤ l ≤ 9
Reflections collected	25151	18820	17440	16795	16494
Independent reflections	2672 [R_{int} = 0.1811, R_{sigma} = 0.0916]	2587 [R_{int} = 0.1698, R_{sigma} = 0.0945]	2278 [R_{int} = 0.1209, R_{sigma} = 0.0707]	2165 [R_{int} = 0.1284, R_{sigma} = 0.0668]	2127 [R_{int} = 0.1456, R_{sigma} = 0.0778]
Data/restraints/parameters	2672/2788/486	2587/2776/460	2278/2790/460	2165/2784/460	2127/3183/473
Goodness-of-fit on F^2	1.052	1.068	1.046	1.051	1.056
Final R indexes [I>=2σ (I)]	R_1 = 0.0837, wR_2 = 0.2051	R_1 = 0.0936, wR_2 = 0.2452	R_1 = 0.0704, wR_2 = 0.1657	R_1 = 0.0774, wR_2 = 0.1883	R_1 = 0.0781, wR_2 = 0.1857
Final R indexes [all data]	R_1 = 0.1352, wR_2 = 0.2425	R_1 = 0.1382, wR_2 = 0.2817	R_1 = 0.0927, wR_2 = 0.1812	R_1 = 0.0996, wR_2 = 0.2070	R_1 = 0.1077, wR_2 = 0.2056
Largest diff. peak/hole / e Å^{-3}	0.32/-0.31	0.45/-0.41	0.42/-0.36	0.51/-0.44	0.60/-0.39

A21 - Crystallographic tables for the HP-XRD study of **13** (crystal B).

Pressure / kbar	8.8	13.9	15.4
Empirical formula	$C_{59}H_{56}B_2F_{24}NO_4P_2Rh$	$C_{59}H_{56}B_2F_{24}NO_4P_2Rh$	$C_{59}H_{56}B_2F_{24}NO_4P_2Rh$
Formula weight	1485.51	1485.51	1485.51
Temperature/K	293(2)	293(2)	293(2)
Crystal system	monoclinic	monoclinic	monoclinic
Space group	$P2_1/c$	$P2_1/c$	$P2_1/c$
a/Å	18.577(4)	18.251(4)	18.216(5)
b/Å	16.577(2)	16.349(2)	16.327(2)
c/Å	19.44(2)	19.06(2)	18.95(3)
α/°	90	90	90
β/°	93.27(5)	92.93(6)	92.93(7)
γ/°	90	90	90
Volume/Å^3	5978(6)	5680(6)	5629(8)
Z	4	4	4
ρ_{calc}g/cm^3	1.651	1.737	1.753
μ/mm^{-1}	0.709	0.746	0.753
F(000)	3000.0	3000.0	3000.0
Crystal size/mm^3	0.08 × 0.04 × 0.03	0.08 × 0.04 × 0.03	0.08 × 0.04 × 0.03
Radiation	synchrotron (λ = 0.4859)	synchrotron (λ = 0.4859)	synchrotron (λ = 0.4859)
2Θ range for data collection/°	3.36 to 26.8	3.056 to 26.82	3.062 to 26.842
Index ranges	$-17 \leq h \leq 17$, $-15 \leq k \leq 15$, $-13 \leq l \leq 13$	$-17 \leq h \leq 17$, $-15 \leq k \leq 15$, $-12 \leq l \leq 12$	$-17 \leq h \leq 17$, $-15 \leq k \leq 15$, $-12 \leq l \leq 13$
Reflections collected	21522	17557	14690
Independent reflections	2477 [R_{int} = 0.4748, R_{sigma} = 0.2962]	2392 [R_{int} = 0.3619, R_{sigma} = 0.1876]	2369 [R_{int} = 0.3706, R_{sigma} = 0.2329]
Data/restraints/parameters	2477/2692/400	2392/2686/400	2369/2695/400
Goodness-of-fit on F^2	1.041	1.154	1.154
Final R indexes [I>=2σ (I)]	R_1 = 0.1247, wR_2 = 0.2772	R_1 = 0.1229, wR_2 = 0.2925	R_1 = 0.1334, wR_2 = 0.3124
Final R indexes [all data]	R_1 = 0.2691, wR_2 = 0.3672	R_1 = 0.2115, wR_2 = 0.3556	R_1 = 0.2427, wR_2 = 0.3869
Largest diff. peak/hole / e Å^{-3}	0.45/-0.49	0.65/-0.67	0.65/-0.55

A22 - Crystallographic tables for the HP-XRD study of **19** (Column 1, crystal A; columns 2-3, crystal B).

Pressure / kbar	0.9	3.5	9.5
Empirical formula	$C_{58}H_{96}B_2F_{12}N_2O_4P_4Rh_2Sb_2$	$C_{58}H_{96}B_2F_{12}N_2O_4P_4Rh_2Sb_2$	$C_{58}H_{96}B_2F_{12}N_2O_4P_4Rh_2Sb_2$
Formula weight	1708.18	1708.18	1708.18
Temperature/K	300.00(10)	300.00(10)	300.00(10)
Crystal system	orthorhombic	orthorhombic	orthorhombic
Space group	$P2_12_12_1$	$P2_12_12_1$	$P2_12_12_1$
a/Å	12.9338(4)	12.8683(3)	12.7419(3)
b/Å	17.86815(18)	17.7842(15)	17.5948(14)
c/Å	30.7579(6)	30.4739(14)	29.5095(12)
α/°	90	90	90
β/°	90	90	90
γ/°	90	90	90
Volume/Å^3	7108.2(3)	6974.0(7)	6615.8(6)
Z	4	4	4
ρ_{calc}g/cm^3	1.596	1.627	1.715
μ/mm^{-1}	1.372	1.399	1.474
F(000)	3440.0	3440.0	3440.0
Crystal size/mm^3	0.20 × 0.11 × 0.09	0.12 × 0.06 × 0.04	0.12 × 0.06 × 0.04
Radiation	Mo Kα (λ = 0.71073)	Mo Kα (λ = 0.71073)	Mo Kα (λ = 0.71073)
2Θ range for data collection/°	3.416 to 49.464	3.436 to 37.712	3.482 to 36.038
Index ranges	$-11 \le h \le 11$, $-21 \le k \le 21$, $-32 \le l \le 32$	$-11 \le h \le 11$, $-11 \le k \le 11$, $-27 \le l \le 27$	$-11 \le h \le 11$, $-11 \le k \le 11$, $-25 \le l \le 25$
Reflections collected	70187	30856	41980
Independent reflections	6865 [R_{int} = 0.0690, R_{sigma} = 0.0345]	3709 [R_{int} = 0.0705, R_{sigma} = 0.0479]	3100 [R_{int} = 0.0786, R_{sigma} = 0.0390]
Data/restraints/parameters	6865/1497/395	3709/1050/370	3100/1050/370
Goodness-of-fit on F^2	1.076	1.087	1.080
Final R indexes [I>=2σ (I)]	R_1 = 0.1296, wR_2 = 0.3143	R_1 = 0.1054, wR_2 = 0.2730	R_1 = 0.1125, wR_2 = 0.2716
Final R indexes [all data]	R_1 = 0.1374, wR_2 = 0.3206	R_1 = 0.1304, wR_2 = 0.3156	R_1 = 0.1262, wR_2 = 0.2935
Largest diff. peak/hole / e Å^{-3}	0.86/-0.95	0.66/-0.86	0.91/-0.83
Flack parameter	0.185(18)	0.13(2)	0.15(2)

A23 - Crystallographic tables for the HP-XRD study of **19** (Crystal C).

Pressure / kbar	15.5	20.7	29.4	34.6
Empirical formula	$C_{58}H_{96}B_2F_{12}N_2O_4P_4Rh_2Sb_2$	$C_{58}H_{96}B_2F_{12}N_2O_4P_4Rh_2Sb_2$	$C_{58}H_{96}B_2F_{12}N_2O_4P_4Rh_2Sb_2$	$C_{58}H_{96}B_2F_{12}N_2O_4P_4Rh_2Sb_2$
Formula weight	1708.18	1708.18	1708.18	1708.18
Temperature/K	300.00(10)	300.00(10)	300.00(10)	300.00(10)
Crystal system	orthorhombic	orthorhombic	orthorhombic	orthorhombic
Space group	$P2_12_12_1$	$P2_12_12_1$	$P2_12_12_1$	$P2_12_12_1$
a/Å	12.63380(19)	12.57770(19)	12.5073(2)	12.4616(3)
b/Å	17.5246(2)	17.4485(2)	17.3543(3)	17.4875(4)
c/Å	28.649(5)	28.304(5)	27.969(5)	26.620(7)
α/°	90	90	90	90
β/°	90	90	90	90
γ/°	90	90	90	90
Volume/Å^3	6343.1(11)	6211.7(10)	6070.9(11)	5801.1(16)
Z	4	4	4	4
ρ_{calc}g/cm^3	1.789	1.827	1.869	1.956
μ/mm^{-1}	1.538	1.570	1.607	1.682
F(000)	3440.0	3440.0	3440.0	3440.0
Crystal size/mm^3	0.14 × 0.10 × 0.08	0.14 × 0.10 × 0.08	0.14 × 0.10 × 0.08	0.14 × 0.10 × 0.08
Radiation	Mo Kα (λ = 0.71073)	Mo Kα (λ = 0.71073)	Mo Kα (λ = 0.71073)	Mo Kα (λ = 0.71073)
2Θ range for data collection/°	3.524 to 39.548	3.544 to 37.676	3.568 to 35.972	3.608 to 34.49
Index ranges	$-12 \le h \le 12$, $-16 \le k \le 16$, $-9 \le l \le 9$	$-11 \le h \le 11$, $-15 \le k \le 15$, $-9 \le l \le 9$	$-10 \le h \le 10$, $-15 \le k \le 15$, $-8 \le l \le 8$	$-10 \le h \le 10$, $-14 \le k \le 14$, $-7 \le l \le 7$
Reflections collected	35692	34759	32452	29152
Independent reflections	2353 [R_{int} = 0.0404, R_{sigma} = 0.0178]	2054 [R_{int} = 0.0397, R_{sigma} = 0.0167]	1797 [R_{int} = 0.0426, R_{sigma} = 0.0159]	1482 [R_{int} = 0.0535, R_{sigma} = 0.0196]
Data/restraints/parameters	2353/1074/365	2054/1070/365	1797/1076/370	1482/1073/360
Goodness-of-fit on F^2	1.219	1.164	1.225	1.757
Final R indexes [I>=2σ (I)]	R_1 = 0.1194, wR_2 = 0.2673	R_1 = 0.1111, wR_2 = 0.2431	R_1 = 0.0968, wR_2 = 0.2100	R_1 = 0.1124, wR_2 = 0.3152
Final R indexes [all data]	R_1 = 0.1206, wR_2 = 0.2680	R_1 = 0.1206, wR_2 = 0.2680	R_1 = 0.0975, wR_2 = 0.2103	R_1 = 0.1149, wR_2 = 0.3187
Largest diff. peak/hole / e Å^{-3}	1.10/-0.91	1.10/-0.91	0.67/-0.68	2.27/-0.80
Flack parameter	0.212(16)	0.185(17)	0.172(17)	0.10(2)

A24 - Table of selected bond lengths for **19a** (top) and **19b** (bottom) as a function of pressure. The asterisk denotes the ambient pressure collection conducted at 150 K, for reference.

Pressure / kbar	**Rh1–P1 / Å**	**Rh1–P2 / Å**	**Rh1–B1 / Å**	**Rh1–N1 / Å**	**B1–H1 / Å**
0.0*	2.3270(16)	2.3338(16)	2.053(9)	2.112(6)	1.33(6)
0.9	2.314(13)	2.347(14)	2.04(4)	2.140(19)	1.43(13)
3.5	2.301(16)	2.309(16)	2.08(7)	2.06(4)	1.54(13)
9.5	2.303(16)	2.307(15)	2.11(9)	2.05(5)	1.59(13)
15.5	2.320(19)	2.322(18)	1.85(9)	2.12(4)	1.45(15)
20.7	2.321(19)	2.325(18)	1.93(6)	2.09(5)	1.45(16)
29.5	2.306(15)	2.309(16)	2.01(3)	2.08(4)	1.41(8)
34.6	2.269(15)	2.279(15)	1.93(4)	2.07(4)	1.42(9)
Pressure / kbar	**Rh2–P3 / Å**	**Rh2–P4 / Å**	**Rh2–B2 / Å**	**Rh2–N2 / Å**	**Rh2–H / Å**
0.0*	2.3072(16)	2.3085(15)	2.012(8)	2.167(5)	1.42(7)
0.9	2.268(15)	2.328(13)	1.99(4)	2.099(17)	1.42(14)
3.5	2.285(14)	2.305(12)	1.88(7)	2.15(3)	1.44(14)
9.5	2.308(16)	2.292(13)	1.94(8)	2.13(4)	1.47(15)
15.5	2.328(19)	2.351(18)	1.78(11)	2.11(7)	1.41(15)
20.7	2.31(2)	2.333(18)	1.87(9)	2.08(7)	1.39(15)
29.5	2.304(15)	2.316(15)	2.11(4)	2.11(7)	1.48(8)
34.6	2.293(16)	2.290(16)	1.93(4)	2.12(12)	1.49(9)

A25 - Table of selected bond angles for **19a** (top) and **19b** (bottom) as a function of pressure. The asterisk denotes the ambient pressure collection conducted at 150 K, for reference.

Pressure / kbar	**P1–Rh1–P2 / °**	**N1–Rh1–B1 / °**
0.0*	165.54(6)	156.8(3)
0.9	165.1(4)	157.7(13)
3.5	165.5(10)	165(2)
9.5	166.3(9)	160(2)
15.5	164.8(9)	161(4)
20.7	165.2(8)	161(4)
29.5	165.2(7)	159(3)
34.6	164.9(7)	161(4)
Pressure / kbar	**P3–Rh2–P4 / °**	**N2–Rh2–B2 / °**
0.0*	162.76(7)	177.6(3)
0.9	163.2(4)	172.2(10)
3.5	162.4(8)	172.7(18)
9.5	162.8(9)	172.2(19)
15.5	165.5(9)	173(3)
20.7	165.3(11)	174(4)
29.5	165.0(10)	175(3)
34.6	165.6(11)	163(3)

A26 - Crystallographic tables for the HP-XRD study of **22** (Crystal A).

Pressure / kbar	4.7	14.7	20.3	25.1
Empirical formula	$C_{53}H_{56}B_2F_{20}NO_2P_2Rh$	$C_{53}H_{56}B_2F_{20}NO_2P_2Rh$	$C_{53}H_{56}B_2F_{20}NO_2P_2Rh$	$C_{53}H_{56}B_2F_{20}NO_2P_2Rh$
Formula weight	1305.45	1305.45	1305.45	1305.45
Temperature/K	293.00(10)	293.00(10)	293.00(10)	293.00(10)
Crystal system	triclinic	triclinic	triclinic	triclinic
Space group	$P\bar{1}$	$P\bar{1}$	$P\bar{1}$	$P\bar{1}$
a/Å	11.6616(4)	11.5115(3)	11.4585(3)	11.4279(3)
b/Å	14.0971(6)	13.8210(5)	13.7141(4)	13.6530(3)
c/Å	17.1094(10)	16.4891(8)	16.2902(8)	16.1691(9)
α/°	104.172(5)	104.806(4)	104.938(4)	105.035(3)
β/°	99.146(4)	98.854(4)	98.781(4)	98.703(3)
γ/°	90.958(3)	90.180(3)	89.969(2)	89.8231(18)
Volume/Å^3	2687.9(2)	2503.60(17)	2442.37(16)	2406.66(16)
Z	2	2	2	2
ρ_{calc}g/cm^3	1.613	1.732	1.775	1.801
μ/mm^{-1}	0.490	0.526	0.539	0.547
F(000)	1324.0	1324.0	1324.0	1324.0
Crystal size/mm^3	0.21 × 0.15 × 0.08	0.21 × 0.15 × 0.08	0.21 × 0.15 × 0.08	0.21 × 0.15 × 0.08
Radiation	Mo Kα (λ = 0.71073)	Mo Kα (λ = 0.71073)	Mo Kα (λ = 0.71073)	Mo Kα (λ = 0.71073)
2Θ range for data collection/°	3.374 to 50.742	3.05 to 50.798	3.076 to 49.456	3.09 to 49.456
Index ranges	$-14 \le h \le 14$, $-16 \le k \le 16$, $-12 \le l \le 12$	$-13 \le h \le 13$, $-16 \le k \le 16$, $-11 \le l \le 11$	$-13 \le h \le 13$, $-16 \le k \le 15$, $-10 \le l \le 10$	$-13 \le h \le 13$, $-16 \le k \le 16$, $-9 \le l \le 9$
Reflections collected	20906	23683	22711	14003
Independent reflections	2970 [R_{int} = 0.0514, R_{sigma} = 0.0316]	2788 [R_{int} = 0.0456, R_{sigma} = 0.0240]	2623 [R_{int} = 0.0271, R_{sigma} = 0.0167]	2605 [R_{int} = 0.0260, R_{sigma} = 0.0195]
Data/restraints/parameters	2970/462/387	2788/462/387	2623/462/387	2605/460/387
Goodness-of-fit on F^2	1.084	1.080	1.093	1.085
Final R indexes [I>=2σ (I)]	R_1 = 0.0650, wR_2 = 0.1591	R_1 = 0.0583, wR_2 = 0.1329	R_1 = 0.0609, wR_2 = 0.1372	R_1 = 0.0601, wR_2 = 0.1400
Final R indexes [all data]	R_1 = 0.0749, wR_2 = 0.1648	R_1 = 0.0646, wR_2 = 0.1365	R_1 = 0.0650, wR_2 = 0.1393	R_1 = 0.0651, wR_2 = 0.1428
Largest diff. peak/hole / e Å^{-3}	0.47/-0.42	0.53/-0.46	0.44/-0.47	0.42/-0.49

A27 - Crystallographic tables for the HP-XRD study of **22** (Crystal B).

Pressure / kbar	6.9	11.2	18.1	30.8
Empirical formula	$C_{53}H_{56}B_2F_{20}NO_2P_2Rh$	$C_{53}H_{56}B_2F_{20}NO_2P_2Rh$	$C_{53}H_{56}B_2F_{20}NO_2P_2Rh$	$C_{53}H_{56}B_2F_{20}NO_2P_2Rh$
Formula weight	1305.45	1305.45	1305.45	1305.45
Temperature/K	293.00(10)	293.00(10)	292.8(3)	293.00(10)
Crystal system	triclinic	triclinic	triclinic	triclinic
Space group	$P\bar{1}$	$P\bar{1}$	$P\bar{1}$	$P\bar{1}$
a/Å	11.6412(5)	11.5545(3)	11.4630(4)	11.3799(2)
b/Å	14.0705(5)	13.9378(4)	13.7354(4)	13.5844(4)
c/Å	17.0322(11)	16.7316(12)	16.3314(11)	15.8652(11)
α/°	104.268(4)	104.640(5)	105.029(4)	104.956(5)
β/°	99.146(4)	98.973(5)	98.804(4)	98.645(4)
γ/°	90.883(3)	90.460(2)	89.942(3)	89.5465(19)
Volume/Å^3	2665.1(2)	2572.0(2)	2452.1(2)	2341.4(2)
Z	2	2	2	2
ρ_{calc}g/cm^3	1.627	1.686	1.768	1.852
μ/mm^{-1}	0.494	0.512	0.537	0.562
F(000)	1324.0	1324.0	1324.0	1324.0
Crystal size/mm^3	0.16 × 0.09 × 0.06	0.16 × 0.09 × 0.06	0.16 × 0.09 × 0.06	0.16 × 0.09 × 0.06
Radiation	Mo Kα (λ = 0.71073)	Mo Kα (λ = 0.71073)	Mo Kα (λ = 0.71073)	Mo Kα (λ = 0.71073)
2Θ range for data collection/°	2.992 to 49.482	3.024 to 49.426	3.072 to 49.456	3.104 to 49.478
Index ranges	-13 ≤ h ≤ 13, -16 ≤ k ≤ 16, -11 ≤ l ≤ 11	-13 ≤ h ≤ 13, -16 ≤ k ≤ 16, -10 ≤ l ≤ 10	-13 ≤ h ≤ 13, -16 ≤ k ≤ 16, -9 ≤ l ≤ 9	-13 ≤ h ≤ 13, -15 ≤ k ≤ 15, -7 ≤ l ≤ 7
Reflections collected	19728	24953	15993	25176
Independent reflections	2887 [R_{int} = 0.0459, R_{sigma} = 0.0338]	2809 [R_{int} = 0.0470, R_{sigma} = 0.0311]	2653 [R_{int} = 0.0376, R_{sigma} = 0.0332]	2553 [R_{int} = 0.0545, R_{sigma} = 0.0352]
Data/restraints/parameters	2887/408/350	2809/408/350	2653/406/350	2553/396/350
Goodness-of-fit on F^2	1.115	1.085	1.111	1.068
Final R indexes [I>=2σ (I)]	R_1 = 0.0893, wR_2 = 0.2395	R_1 = 0.0889, wR_2 = 0.2220	R_1 = 0.0771, wR_2 = 0.1797	R_1 = 0.0871, wR_2 = 0.2047
Final R indexes [all data]	R_1 = 0.1111, wR_2 = 0.2707	R_1 = 0.1074, wR_2 = 0.2461	R_1 = 0.0930, wR_2 = 0.1972	R_1 = 0.1074, wR_2 = 0.2243
Largest diff. peak/hole / e Å^{-3}	1.31/-0.85	1.48/-0.83	1.31/-0.85	0.79/-0.51

A28 – Table of B-Ar^{F20} angles in **22** against pressure. The asterisk denotes the 150 K ambient pressure collection, for reference.

	B–Ar^{F20} (mean molecular plane) angle / °			
Pressure / kbar	**B2–C200–C203 (Ar^{F20}-1)**	**B2–C206–C209 (Ar^{F20}-2)**	**B2–C212–C215 (Ar^{F20}-3)**	**B2–C218–C221 (Ar^{F20}-4)**
0.0*	173.70(9)	172.82(9)	173.83(10)	173.88(9)
4.7	177.4(8)	172.8(5)	174.4(5)	175.7(7)
6.9	177.5(8)	172.1(7)	174.6(7)	176.0(9)
11.2	176.3(10)	170.9(7)	174.7(7)	176.0(9)
14.7	178.4(7)	169.8(5)	173.9(5)	176.5(6)
18.1	179.6(7)	168.8(7)	174.6(7)	177.3(8)
20.3	178.5(8)	168.9(6)	174.4(5)	176.6(6)
25.1	179.7(7)	168(6)	174.5(5)	175.9(5)
30.8	178.0(7)	165.4(9)	174.4(8)	173.6(8)

A29 – Stacked ^{1}H NMR spectra for **15**, **19** and **23** (500 MHz, 1,2-$C_6H_4F_2$, 298 K).

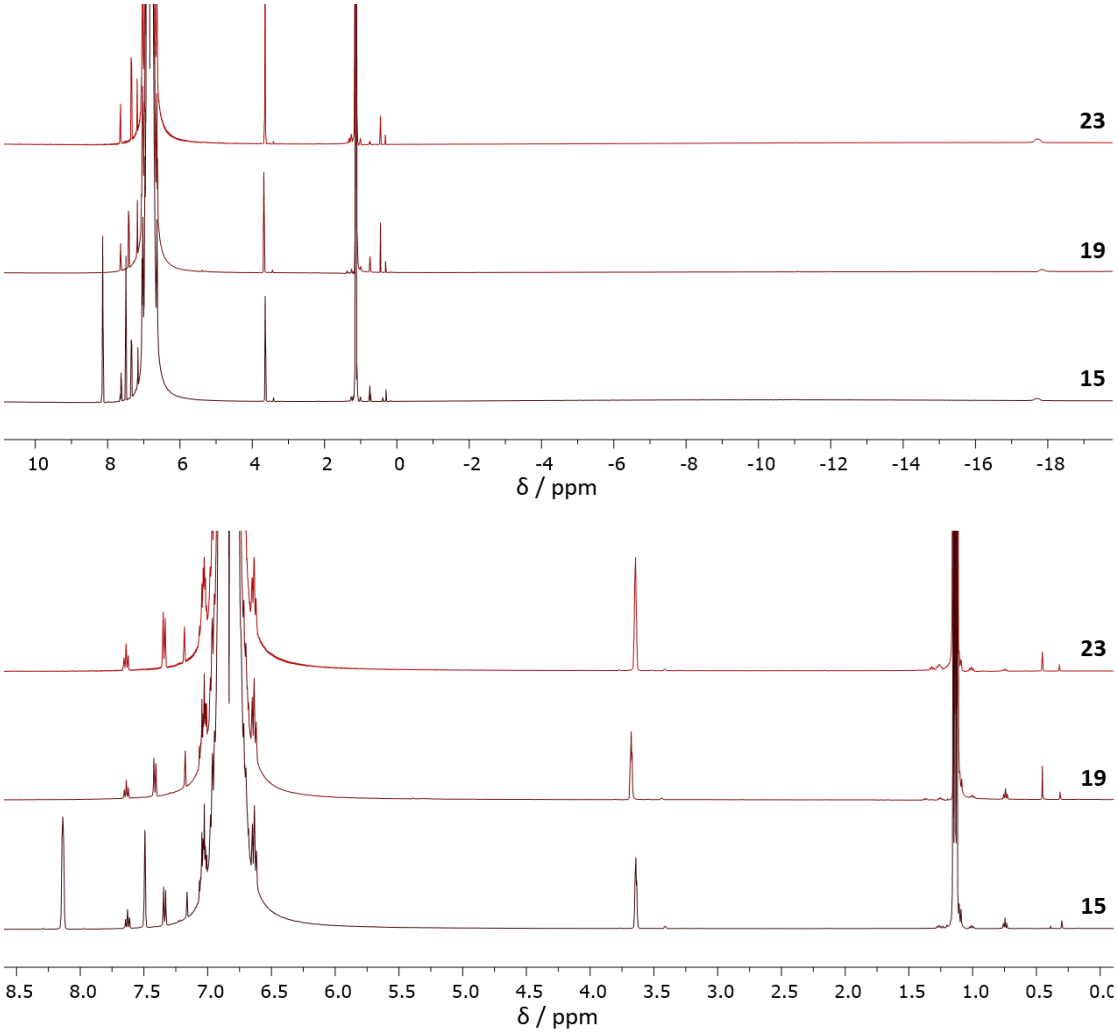

Electronic supporting information:

The folders are divided by technique, followed by the identity of the compound, then (where applicable) by the pressure the dataset was collected at. CheckCIFs are provided, where appropriate.

Ambient pressure XRD data:

- Chapter 2
  - CIF and tables for [Rh(PONOP)(κ_{Cl}-ClPh)][BAr^F_4]
  - CIF and tables for [Rh(PONOP)(Ph)Cl][BAr^F_4]
  - CIF and tables for [Rh(PONOP)(κ_{Cl}-$ClCH_2Cl$)][BAr^F_4]
  - CIF and tables for [Rh(PONOP)(CH_2Cl)Cl)][BAr^F_4]
  - CIF and tables for [Rh(PONOP)Cl][BAr^F_4]
  - CIF and tables for [Rh(PONOP)(κ_{Cl}-$ClCH_2CH_2Cl$)][BAr^F_4]
  - CIF and tables for [Rh(PONOP)(κ_{Cl}-Cl^{i}Pr)][BAr^F_4]

- CIF and tables for [Rh(PONOP)(κ_{Cl}-ClCy)][BAr^F_4]
- CIF and tables for [Rh(PONOP)(H)Cl][BAr^F_4]

- Chapter 3
  - CIF and tables for [Rh(PONOP)(η^2-HBpin)][BAr^F_4]
  - CIF and tables for [Rh(PONOP)(η^2-HBcat)][BAr^F_4]
  - CIF and tables for [Rh(PNP)(η^2-HBpin)][BAr^F_4]
  - CIF and tables for [Rh(PNP)(η^2-HBcat)][BAr^F_4]
- Chapter 4
  - CIF and tables for [Rh(PONOP)(η^2-HBpin)][SbF_6]
  - CIF and tables for [Rh(PNP)(η^2-HBpin)][SbF_6]
  - CIF and tables for [Rh(PNP)(η^2-HBcat)][SbF_6] / [Rh(PNP)(H)(Bcat)][SbF_6] co-crystal
  - CIF and tables for [Rh(PONOP)(η^2-HBpin)][BAr^{F20}_4]
  - CIF and tables for [Rh(PNP)(η^2-HBpin)][BAr^{F20}_4]
  - CIF and tables for [Rh(PNP)(H)(Bcat)][BAr^{F20}_4]
  - CIF and tables for [Rh(PNP)(CO)][BAr^{F20}_4]·HBcat

HP-XRD data:

- Chapter 2
  - CIFs and tables for the *C*2/*c* polymorph (**A-α**) of [Rh(PONOP)(κ_{Cl}-$ClCH_2Cl$)][BAr^F_4] at various pressures
  - CIFs and tables for the $P\bar{1}$ polymorph (**A-β**) of [Rh(PONOP)(κ_{Cl}-$ClCH_2Cl$)][BAr^F_4] at various pressures
- Chapter 3
  - CIFs and tables for [Rh(PONOP)(η^2-HBcat)][BAr^F_4] at various pressures
- Chapter 4
  - CIFs and tables for the [Rh(PNP)(η^2-HBcat)][SbF_6] / [Rh(PNP)(H)(Bcat)][SbF_6] co-crystal at various pressures
  - CIFs and tables for [Rh(PNP)(η^2-HBpin)][BAr^{F20}_4] at various pressures